

Zhongliang Jing
Dmitry Strelets *Editors*

Proceedings of the International Conference on Aerospace System Science and Engineering 2021

Lecture Notes in Electrical Engineering

Volume 849

Series Editors

Leopoldo Angrisani, Department of Electrical and Information Technologies Engineering, University of Napoli Federico II, Naples, Italy

Marco Arteaga, Departament de Control y Robótica, Universidad Nacional Autónoma de México, Coyoacán, Mexico

Bijaya Ketan Panigrahi, Electrical Engineering, Indian Institute of Technology Delhi, New Delhi, Delhi, India
Samarjit Chakraborty, Fakultät für Elektrotechnik und Informationstechnik, TU München, Munich, Germany

Jiming Chen, Zhejiang University, Hangzhou, Zhejiang, China

Shanben Chen, Materials Science and Engineering, Shanghai Jiao Tong University, Shanghai, China

Tan Kay Chen, Department of Electrical and Computer Engineering, National University of Singapore, Singapore, Singapore

Rüdiger Dillmann, Humanoids and Intelligent Systems Laboratory, Karlsruhe Institute for Technology, Karlsruhe, Germany

Haibin Duan, Beijing University of Aeronautics and Astronautics, Beijing, China

Gianluigi Ferrari, Università di Parma, Parma, Italy

Manuel Ferre, Centre for Automation and Robotics CAR (UPM-CSIC), Universidad Politécnica de Madrid, Madrid, Spain

Sandra Hirche, Department of Electrical Engineering and Information Science, Technische Universität München, Munich, Germany

Faryar Jabbari, Department of Mechanical and Aerospace Engineering, University of California, Irvine, CA, USA

Limin Jia, State Key Laboratory of Rail Traffic Control and Safety, Beijing Jiaotong University, Beijing, China

Janusz Kacprzyk, Systems Research Institute, Polish Academy of Sciences, Warsaw, Poland

Alaa Khamis, German University in Egypt El Tagamoa El Khames, New Cairo City, Egypt

Torsten Kroeger, Stanford University, Stanford, CA, USA

Yong Li, Hunan University, Changsha, Hunan, China

Qilian Liang, Department of Electrical Engineering, University of Texas at Arlington, Arlington, TX, USA

Ferran Martín, Departament d'Enginyeria Electrònica, Universitat Autònoma de Barcelona, Bellaterra, Barcelona, Spain

Tan Cher Ming, College of Engineering, Nanyang Technological University, Singapore, Singapore

Wolfgang Minker, Institute of Information Technology, University of Ulm, Ulm, Germany

Pradeep Misra, Department of Electrical Engineering, Wright State University, Dayton, OH, USA

Sebastian Möller, Quality and Usability Laboratory, TU Berlin, Berlin, Germany

Subhas Mukhopadhyay, School of Engineering & Advanced Technology, Massey University, Palmerston North, Manawatu-Wanganui, New Zealand

Cun-Zheng Ning, Electrical Engineering, Arizona State University, Tempe, AZ, USA

Toyoaki Nishida, Graduate School of Informatics, Kyoto University, Kyoto, Japan

Federica Pascucci, Dipartimento di Ingegneria, Università degli Studi "Roma Tre", Rome, Italy

Yong Qin, State Key Laboratory of Rail Traffic Control and Safety, Beijing Jiaotong University, Beijing, China

Gan Woon Seng, School of Electrical & Electronic Engineering, Nanyang Technological University, Singapore, Singapore

Joachim Speidel, Institut of Telecommunications, Universität Stuttgart, Stuttgart, Germany

Germano Veiga, Campus da FEUP, INESC Porto, Porto, Portugal

Haitao Wu, Academy of Opto-electronics, Chinese Academy of Sciences, Beijing, China

Walter Zamboni, DIEM - Università degli studi di Salerno, Fisciano, Salerno, Italy

Junjie James Zhang, Charlotte, NC, USA

The book series *Lecture Notes in Electrical Engineering* (LNEE) publishes the latest developments in Electrical Engineering - quickly, informally and in high quality. While original research reported in proceedings and monographs has traditionally formed the core of LNEE, we also encourage authors to submit books devoted to supporting student education and professional training in the various fields and applications areas of electrical engineering. The series cover classical and emerging topics concerning:

- Communication Engineering, Information Theory and Networks
- Electronics Engineering and Microelectronics
- Signal, Image and Speech Processing
- Wireless and Mobile Communication
- Circuits and Systems
- Energy Systems, Power Electronics and Electrical Machines
- Electro-optical Engineering
- Instrumentation Engineering
- Avionics Engineering
- Control Systems
- Internet-of-Things and Cybersecurity
- Biomedical Devices, MEMS and NEMS

For general information about this book series, comments or suggestions, please contact leontina.dicecco@springer.com.

To submit a proposal or request further information, please contact the Publishing Editor in your country:

China

Jasmine Dou, Editor (jasmine.dou@springer.com)

India, Japan, Rest of Asia

Swati Meherishi, Editorial Director (Swati.Meherishi@springer.com)

Southeast Asia, Australia, New Zealand

Ramesh Nath Premnath, Editor (ramesh.premnath@springernature.com)

USA, Canada:

Michael Luby, Senior Editor (michael.luby@springer.com)

All other Countries:

Leontina Di Cecco, Senior Editor (leontina.dicecco@springer.com)

**** This series is indexed by EI Compendex and Scopus databases. ****


More information about this series at <https://link.springer.com/bookseries/7818>

Zhongliang Jing · Dmitry Strelets
Editors

Proceedings
of the International
Conference on Aerospace
System Science
and Engineering 2021

 Springer

Editors

Zhongliang Jing 
School of Aeronautics and Astronautics
Shanghai Jiao Tong University
Shanghai, China

Dmitry Strelets 
Moscow Aviation Institute
Moscow, Russia

ISSN 1876-1100

ISSN 1876-1119 (electronic)

Lecture Notes in Electrical Engineering

ISBN 978-981-16-8153-0

ISBN 978-981-16-8154-7 (eBook)

<https://doi.org/10.1007/978-981-16-8154-7>

© The Editor(s) (if applicable) and The Author(s), under exclusive license to Springer Nature Singapore Pte Ltd. 2023

This work is subject to copyright. All rights are solely and exclusively licensed by the Publisher, whether the whole or part of the material is concerned, specifically the rights of translation, reprinting, reuse of illustrations, recitation, broadcasting, reproduction on microfilms or in any other physical way, and transmission or information storage and retrieval, electronic adaptation, computer software, or by similar or dissimilar methodology now known or hereafter developed.

The use of general descriptive names, registered names, trademarks, service marks, etc. in this publication does not imply, even in the absence of a specific statement, that such names are exempt from the relevant protective laws and regulations and therefore free for general use.

The publisher, the authors, and the editors are safe to assume that the advice and information in this book are believed to be true and accurate at the date of publication. Neither the publisher nor the authors or the editors give a warranty, expressed or implied, with respect to the material contained herein or for any errors or omissions that may have been made. The publisher remains neutral with regard to jurisdictional claims in published maps and institutional affiliations.

This Springer imprint is published by the registered company Springer Nature Singapore Pte Ltd.

The registered company address is: 152 Beach Road, #21-01/04 Gateway East, Singapore 189721, Singapore

Contents

Simulation Study on Civil Aviation Human Reliability Learning from Incidents Using System Dynamics	1
Yuhe Mao, Yi Lu, Dan Huang, and Shan Fu	
Research on Pressure-Sensing Characteristic of Trailing-Cone	17
Yang Hui, Qu Feizhou, Fang Yang, Li Qiuji, and Yang Xinyu	
Spatial Interpolation Methods for Virtual Rotating Array Beamforming with Arbitrary Microphone Configurations	25
Jiacheng Yang, Ce Zhang, and Wei Ma	
TH-DS-CDMA-Based Robust Frequency-Domain Signal Processing for GNSS Pseudolite Correlators	41
Yingchao Xiao, Wei Wang, Xin Zhang, and Xingqun Zhan	
An Investigation on Rotating Stall in an Aeroengine Transonic Compressor with Inlet Distortion	57
Zhongyu Zhu and Xiaohua Liu	
An Integrated Architecture Design Method for Multi-platform Avionics System	73
Xiang Ni, Miao Wang, Gang Xiao, and Guoqing Wang	
A Group Delay Measurement Method for GNSS Receiver Based on BOC Signal	85
Longlong Li, Xiaoliang Wang, Shufan Wu, and Lang Bian	
Analysis on the Second Ignition Phenomenon Induced by Shock Wave Focusing in a 90° Conical Reflector	95
Yuanchang Li and Bo Zhang	
Research on Attitude Control of Zero-Momentum Spinning Satellite	107
Ning Du, Shufan Wu, Chao Zhong, Wenhui Chen, and Xiaoliang Wang	

Control Parameter Optimization for a Longitudinal Automatic Landing System via a Multi-objective Genetic Algorithm	119
Cheng Chen, Jie Ke, Haonan Xu, Bei Lu, and Qifu Li	
Named Entity Approach for Structured Management of Aeronautical Product Requirements	135
JianKai Lu and ChunKai Hu	
Fault-Tolerant Attitude Control of Spacecraft via Explicit Model Prediction Method	147
Xin Cao, Deren Gong, Qiang Shen, and Shufan Wu	
Simulation Analysis of a Certain Civil Aircraft's Negative Acceleration Flight	163
YaJun Wen	
Design of Aircraft Engine Inlet Radial Distortion Generator	175
Boyang Fang and Xiaoqing Qiang	
Hydraulic Servo System Fault Detection Based on Machine Learning	187
Shengjie Zhou, Yue Wang, Rong Yang, Xingqun Zhan, Xiao Chen, and Xiaoan Gao	
Moving Vehicle Detection in Satellite Video via Background Subtraction and Global-Local Features Fusion Faster R-CNN	197
Dong Wei, Zhongliang Jing, and Han Pan	
A Unified Framework for Joint Moving Object Detection and Tracking in the Sky and Underwater	211
Xia Wu, Han Pan, Meng Xu, Zhongliang Jing, and Min Bao	
Hyperspectral and Multispectral Image Fusion via Regularization on Non-local Structure Tensor Total Variation	225
Meng Xu, Han Pan, Xia Wu, and Zhongliang Jing	
Using an Interpolation Model of the Gravitational Potential for High-Precision Ballistic Calculations	239
A. A. Kuznetsov, I. I. Fukin, S. M. Bazov, and N. A. Zavalova	
Distributed Cooperative Guidance Law with Both Impact Time and Angle Control	249
Ye Chen, Shufan Wu, Hongxu Zhu, Xiaoliang Wang, Quan Li, and Jun Jia	
Effects of Non-uniform Inlet Flow on the Flow Stability of a Transonic Compressor Rotor	261
Zetian Qiu, Yidan Li, and Xiaohua Liu	
Numerical Simulation of 3D Surfaces Icing Near the Moving Wall	269
Andrey Fevralskikh and Vladislav Kupchik	

Modelling Causal Relationship Among Performance Shaping Factors Through Bayesian Network on Aviation Safety 283
 Yifan He, Yi Lu, Dan Huang, and Shan Fu

Adaptive Attitude Control of Uncertain Spacecraft with Attitude and Angular Velocity Constraints 293
 Zeyu Kang, Shufan Wu, Xiaoliang Wang, Chao Zhong, and Qiang Shen

SSS-2A: A 3U CubeSat Project for an In-Orbit Formation Flying Mission 311
 Yixin Huang, Zhongcheng Mu, Sunhao Chu, and Shufan Wu

Scenario-Based Function Modeling Approach for Civil Aircraft Systems 329
 Huang Xu, Chen Yong, and Zhao Meng

Interfacial Properties of Stitched Three-Dimensional Woven Composite/Titanium Alloy Hybrid Board 349
 Chongjing Li

Economic Analysis of Continuous Climb Operation 383
 Donglei Xu, Gang Xiao, and Dongjin Ding

Formation of Aircraft Control Based on a Combination of the Direct Method and the Inverse Problems Method of Dynamics ... 397
 O. N. Korsun, A. V. Stulovsky, V. P. Kharkov, S. V. Nikolaev, and Mounq Htang Om

Identification of the Engine Thrust Force Using Flight Test Data 403
 O. N. Korsun, B. K. Poplavsky, and Mounq Htang Om

Investigation of Plastic Kink-Band in Fiber-Reinforced Composites with Fiber Misalignment Defect 409
 Y. T. Zhang, Y. L. Hu, Y. Yu, Y. Y. Xu, and H. Y. Zhao

Methodology for Formation of an Optimized Verification, Validation and Integration Program for an Aircraft Based on Models of Its Architecture 425
 I. A. Konstantinov, V. A. Kaigorodova, and D. S. Shavelkin

An Investigation on the Flow Mechanism of Complex Fractal Spoiler on Wing 433
 Yanmin Guan and Frank Nicolleau

Compression Performance of Composite Honeycomb Sandwich Structures with Prefabricated Defects 449
 Zhouyu Zheng, Xiuhua Chen, and Huayong Zheng

The Assessment of the Prospects of Composite Materials Manufactured by Vacuum Infusion (VaRTM) 465
 A. E. Protsenko, B. B. Safoklov, V. V. Petrov, and O. S. Dolgov

Routing Optimization Study for LEO Satellite Networks Using the Hybrid GA-SA Algorithm	473
Yuxiao Duan, Shufan Wu, Yixin Huang, and Zhongcheng Mu	
Siamese U-net with Attention Mechanism for Building Change Detection in High-Resolution Remote Sensing Images	487
Yiren Song, Zhongliang Jing, and Minzhe Li	
Analysis of Influencing Factors in Finite Element Simulation of High-Speed Impact of Micro-particles in Space Protection	505
Wei Wang, Shufan Wu, Zhongcheng Mu, and Jiyuan Yi	
SatMVS: A Novel 3D Reconstruction Pipeline for Remote Sensing Satellite Imagery	521
Jiacheng Lu, Yuanxiang Li, and Zongcheng Zuo	
A Kinematics Analysis of Actuation System Based on DCM Method	539
Yige Liu and Xiaohua Liu	
Al-Mg-Sc (1570) Alloy Structure Formation Process	547
V. M. Greshnov, F. F. Safin, R. I. Shaikhutdinov, and I. R. Yanova	
Verifying Aluminum-Air Fuel Cell for Unmanned Aerial Vehicle During Operation in the Field	555
Elizaveta S. Ryzhova, Konstantin V. Pushkin, and Ejen Gurev	
Design Methodology Based on the RFLA Approach	563
Ezhen Gurev, Alexander Dolotovskiy, Maria Voitishina, and Dmitry Slezkin	
Research on Technological Potential for Using Aluminum Alloy Wire in Airborne Smart Cables	573
I. G. Roberov, V. S. Grama, M. A. Kiselev, V. V. Kosyanchuk, and E. Yu Zybin	
Study of the Features of the Flight and Technical Characteristics of a Hybrid Airship	585
S. F. Borodkin, M. A. Kiselev, and M. V. Shkurin	
Model-Based Automated Testing Method for Airborne System	597
Shaofan Zhu, Peipei Xing, and Hao Wang	
Design and Modeling of Remotely Piloted Operations (RPO) Mode for Commercial Aircraft	615
Kelin Zhong, Yong Chen, Yue Luo, and Miao Wang	
The Influence of Wing Deformation on Energy Extraction During Dynamic Soaring	627
Jiangwei Gao, Weigang An, Fuzhen Shi, Wei Wang, and Jianmin Su	

Acoustics Analysis and Experimental Study on Silencer for Commercial Airplane Air Conditioning System 645
Xudong Yan, Xuede Sun, and Dawei Wang

Approaches and Numerical Simulation of Cryogenic Environment in Large Space Environment Simulator 653
Weiwei Shan, Yang Liu, and Ang Li

Development of Portable Friction Stir Welding Equipment for In-Space Manufacturing 663
Peng Li, Wei Zhong, Lijie Guo, Jialiang Zhang, Xiaosong Feng, Fei Li, and Weigang Zhao

Simulation Study on Civil Aviation Human Reliability Learning from Incidents Using System Dynamics



Yuhe Mao, Yi Lu, Dan Huang, and Shan Fu

Abstract Flight safety is the foundation and guarantee of the sustainable development of the civil aviation industry. With the continuous development of the aircraft industry, fewer and fewer accidents are caused solely by mechanical failures. Human factors (HFs) have become the most important cause of aviation accidents, and the research on human reliability is more and more extensive and in depth worldwide. However, many severe aviation disasters still have occurred because of failing to recognize the importance of the implicit warnings or learning from the precursor incidents. Based on the qualitative framework of Human Factor Analysis and Classification System (HFACS), this paper first identifies the HFs which influence the change of human reliability (HR) in the incident learning process. Then, by introducing the theory and method of System Dynamics (SD), an HFACS-SD model is proposed to dynamically and semi-quantitatively analyze the influence of HFs at different levels combined with scenario simulation. This model can effectively deal with the dynamic feedback of issues involving broad factors pervading in learning from incidents, and it provides some suggestions for further improving the human reliability of civil aviation.

Keywords Human Factor Analysis and Classification System (HFACS) · Human Reliability Analysis (HRA) · Aviation incident · System Dynamics (SD)

Y. Mao · D. Huang

School of Aeronautics and Astronautics, Shanghai Jiao Tong University, Shanghai 200240, China
e-mail: myh_healer@sjtu.edu.cn

D. Huang

e-mail: huangdan@sjtu.edu.cn

Y. Lu (✉) · S. Fu

School of Electronic Information and Electrical Engineering, Shanghai Jiao Tong University, Shanghai 200240, China

e-mail: luyi1@sjtu.edu.cn

S. Fu

e-mail: sfu@sjtu.edu.cn

1 Introduction

Flight safety is always the primary goal of the International Civil Aviation Organization (ICAO). In recent years, the civil aviation industry has achieved unprecedented development. However, with the rapid development of civil aviation, safety problems are increasingly prominent. For organizations operating in high-tech and meanwhile high-risk areas such as aviation and space technology, accidents that can be solely blamed on a single mechanical failure or factors beyond the control of the organization are rare [25]. In other words, the safety of civil aircraft is highly dependent on human performance. Human factor (HF) is one of the main concepts used when considering flight performance issues. This concept is extremely broad and serves to characterize various phenomena in aviation practice related to many human activities [19]. Human reliability (HR) is defined as the likelihood that a task will be successfully performed [9], and human reliability analysis (HRA) is developed to identify, model, quantify and reduce the impact of HFs on system failures [18].

The human and organizational factors play significant roles in the occurrence of civil aviation accidents and incidents [27]. According to the statistics offered by ICAO, HF is undoubtedly a crucial cause of severe flight accidents with a large number of casualties and huge property losses. Many of these disasters were caused because of the inability of the personnel and the organization involved to timely and effectively obtain the latent information from distinct incidents so that appropriate action could be taken to reduce the risk of disaster. The unlocking disaster of United Airlines, Flight 811 from Honolulu to New Zealand on February 24, 1989, was definitely caused by the long neglect of the great design flaw in the cargo door, because even a Pan Am B747 already had a cargo door problem as early as 1987. On December 28, 1978, the crash of United Airlines, Flight 173, near Portland International Airport caused ten people's death and severe damage to the aircraft just because of ignoring the fuel shortage while concentrating on fixing a landing gear problem of the captain. Without an effective incident learning system, the precursor incidents are only visible with the benefit of the hindsight that comes from an accident [8]. The analysis of contributing factors of aviation incidents is critical to maintaining and improving safety standards [3]. Identifying the contributing HFs in aviation incidents and the relationship among them is particularly important for improving the level of human reliability and reducing severe accidents caused by HFs.

Traditional HRA methods usually regard people as a part of the system for static quantification of HR. However, compared with technical factors, human behavior is affected by the nonlinear interaction of physiological, psychological, social, cultural and other factors, and its changes are multidimensional and complex. In addition, human behavior in the system is not only governed by the system task but also by the internal factors of the system, as well as the influence of time, space and environment. Thus, the analysis of HR is a cross-field complex problem. Even though many researchers have put forward various quantitative and qualitative methods to integrate them into reliability calculation, still none of them have succeeded.

The Human Factors Analysis and Classification System (HFACS) is one such HRA method that was originally developed for use in aviation but has since been applied in many safety-critical domains [1]. However, it provides only a general framework for qualitative analysis of human factors and cannot be used to quantitatively determine the cause of the accident and give a prediction. Besides, it just communicates analysis results in a textual way, and cannot describe the master-subordinate relationship and time series characteristics between factors [26]. Over the years, many researchers have tried to combine HFACS with other quantitative tools to make up for its shortcomings. For example, Ugurlu et al. [22] combined HFACS with Bayesian Networks and used a new HFACS structure to quantitatively reveal accident formation patterns in the Black Sea. Zhang et al. [24] combined HFACS with System Dynamics (SD) to study the coupling effect of human-organizational factors on pilotage accidents. Among them, SD has been proved to be an effective tool to overcome the qualitative, static and factor-independent defects of HFACS.

System Dynamics (SD), developed by Jay Forrester in the late 1950s, is a top-down modeling approach and focuses on dynamic complexity which arises from the system's structure, feedback and time lags [12]. The SD method has been applied to a wide variety of domains: economics [21], engineering [2], health care [16], aviation [7], etc. It is suitable for dealing with long-term and cyclical problems, taking into account the interrelationships between various factors, and presenting the prediction results of key variables in a dynamic and quantitative form. Obviously, it is a complex process with dynamic feedback and time delays to learn from the precursor events.

In this paper, the HFACS is combined with SD and an HFACS-SD model is proposed to simulate the change of human reliability of civil aircraft crew learning from incidents. The HFACS-SD model dynamically and quantitatively analyzes the relationship between the contributing factors of human reliability in the learning process, through which we can better understand the relationship and correlation strength between different levels.

2 Standard Framework of HFACS

In 1990, James Reason, a psychologist from the University of Manchester in the UK, systematically discussed different viewpoints in the study of human error, typical errors and methods for predicting and preventing errors in his book *Human Error* [11]. In 2000, drawing upon Reason's concept of latent and active failures, Shappell and Wiegmann [20] proposed a Human Factor Analysis and Classification System (HFACS) framework, which adopts the four levels of failure proposed in the REASON model including unsafe acts, preconditions for unsafe acts, unsafe supervision and organizational influences, and details each of them, as shown in Fig. 1.

The lowest level, unsafe acts of crew members, belongs to the dominant factors, which directly leads to the occurrence of accidents. It is a direct manifestation of a system problem, including errors and violations. Errors refer to humans' mental

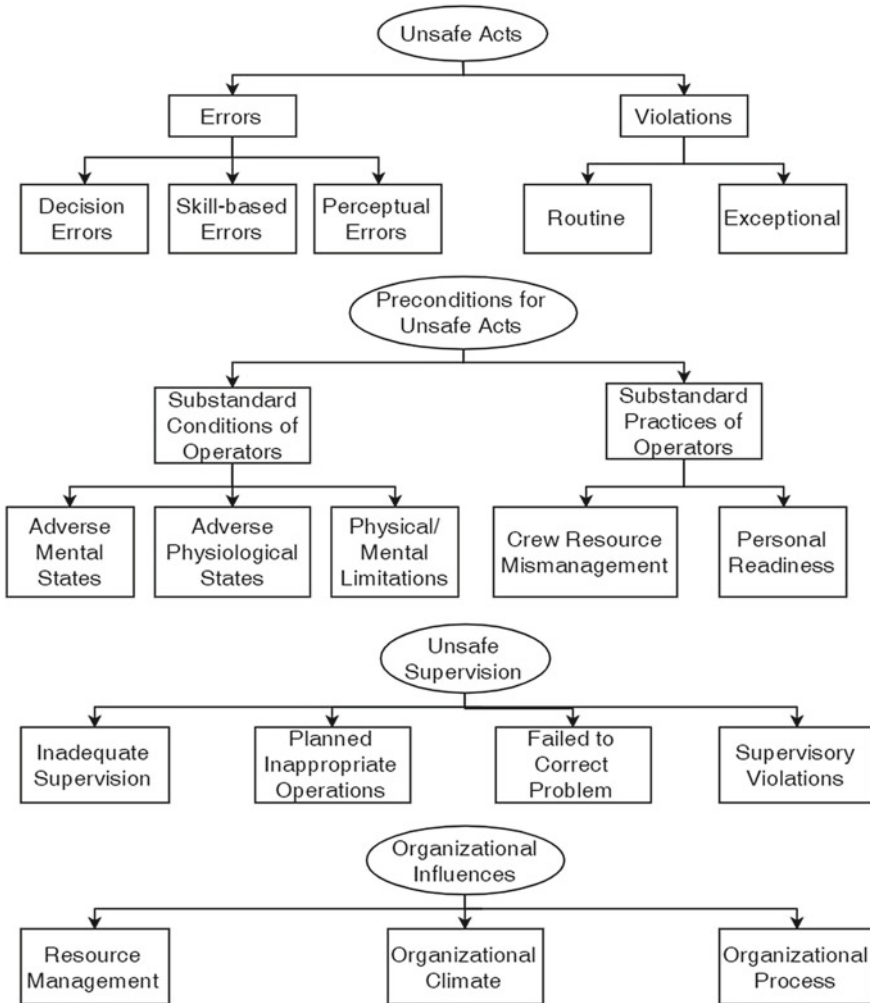


Fig. 1 Standard Framework of HFACS

failure to reach the required state in the situation, or behavior that fails to meet the requirements of the specific task. It include decision errors, referring to acts according to existing while inadequate or inappropriate plans, skill-based errors, referring to basic flight skills that occur without significant conscious thought, and perceptual errors, referring to the errors caused by an improper perception of information in the current situation.

The second level, preconditions for unsafe acts, refers to the direct cause of unsafe acts, including substandard conditions of operators and substandard practices of operators. It is divided into an adverse mental status which affects work performance, adverse physiological status which interferes with safety operation

and physical/mental limitations, referring to the inherent limitation of physical or mental abilities.

The third level, unsafe supervision, is the cause from the organizational level, which is divided into four major types. Inadequate supervision refers to the failure of supervisors and organizers to offer professional guidance, training or supervision. Planned inappropriate operations refer to plans at the organizational level that may lead to an accident. Failed to correct problems refers to neglect and permission of existing problems. As for supervisory violations, it refers to regulators' intentional violation of regulations.

The top level, organizational influences, is always indirect and recessive. Although they are not directly responsible for accidents on the surface, fallible decisions of upper-level management directly affect supervisory practices, as well as the conditions and actions of operators [20]. Organizational influence includes three aspects. Resource management mainly refers to the issues of resource allocation and maintenance decisions. Organizational climate refers to the organizational factors that have an impact on the working efficiency of the members. Organizational process refers to the policies and regulations regularizing the daily work of an organization.

HFACS is one of the most widely used scientific and practical tools for accidents/incidents investigation and analysis, including aviation [13], mining industry [15], construction [17], maritime [14], railways [6], etc. Using the HFACS model can analyze human factors from surface behavior to deep organizational causes, which is of great significance both in determining the cause of accidents/incidents and in putting forward preventive suggestions.

It is noteworthy that the HFACS-SD model could not be exactly correlated to the standard framework of HFACS. In the first place, causal factors referring to Organizational Influences are rarely mentioned in the incident investigations [10]. From a practical point of view, the standard framework might be too specific to correspond accurately from incident reports; it is neither meaningful nor necessary.

3 HFACS-SD Model

HFACS is one of the most commonly used and effective methods to analyze aviation human accidents. However, due to the involvement of the dynamic system of various factors, it is impossible to give an expression of the learning process with a simple qualitative model. SD can use dynamics and feedback to assist decision makers in understanding the structure and characteristics of a complex system [5]. Therefore, in order to effectively analyze the incidents relating to human factors in civil aviation and determine an effective risk-response strategy, it is required to study the interaction between the factors affecting the reliability of flight crew by establishing an SD model based on HFACS, so as to effectively analyze the dynamic process of the influence of different factors on the crew factor reliability.

3.1 HFACS-SD Conceptual Model

A causal loop diagram (CLD) is a visual representation of dynamic interrelationships, which is often used to qualitatively display the cause and effect between different variables. Here from different levels of human factors, the system is analyzed in different sections.

Human Reliability Improving. In general, human reliability improving and incident reducing is a balancing feedback process, as shown in Fig. 2.

The occurrence of the incidents involves the first level of HFACS, unsafe behavior, including errors and violations. It is directly associated with human reliability, which is always defined as the reliability of decision-making and operation of the crew. As for preconditions for unsafe acts, the second level of HFACS, it is expressed as the individual status of the pilot that affects decision-making, and rational allocation of operating resources and effectiveness of the communication that affects operation.

Incident Reporting. In the balancing loop of incident reporting, there are several fundamental components including a number of incidents, number of reported incidents, incident investigation, proposal of safety suggestions, corrective actions and unsafe environment of the system, as shown in Fig. 3.

Unsafe environment of the system is a premise of incidents, which is always caused by inadequate supervision and inadequate cross-check from the third level of HFACS. The effectiveness of the feedback loop and whether it can lead to corrective actions depend on the willingness to report and investigate incidents, the quality of the system and procedures, as well as the ability to prevent loss.

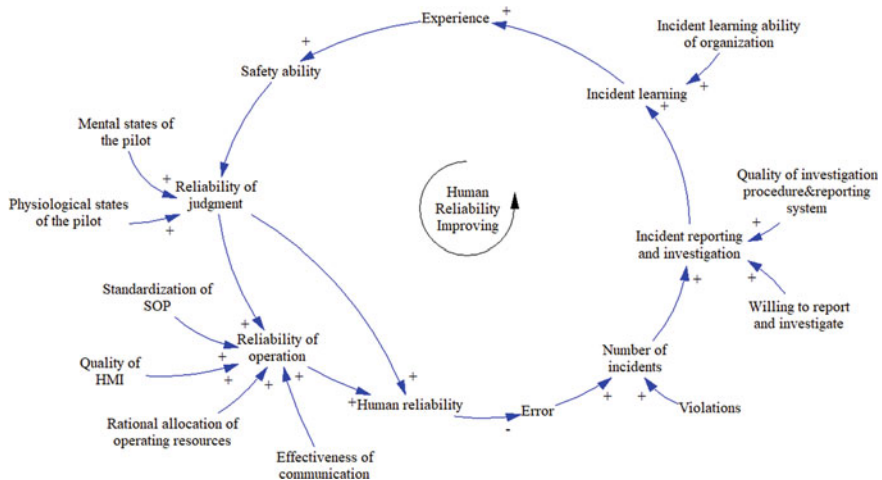


Fig. 2 CLD for human reliability improving

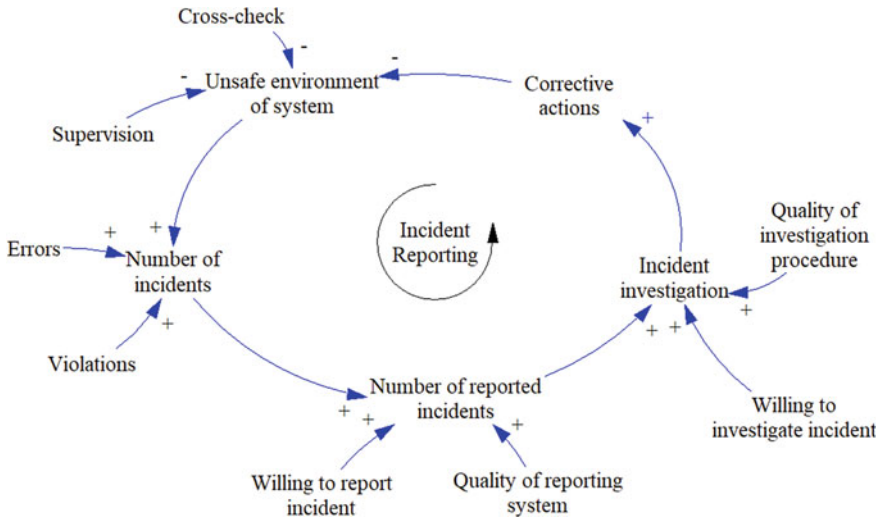


Fig. 3 CLD for incident reporting

Incident Learning. Learning is characterized as a generic feedback cycle including four ordered learning processes, observing, reflecting, creating and acting [4]. In the system of incident learning, there are several fundamental components, experience, safety ability, safety commitment of organization and safety commitment of the individual, as shown in Fig. 4.

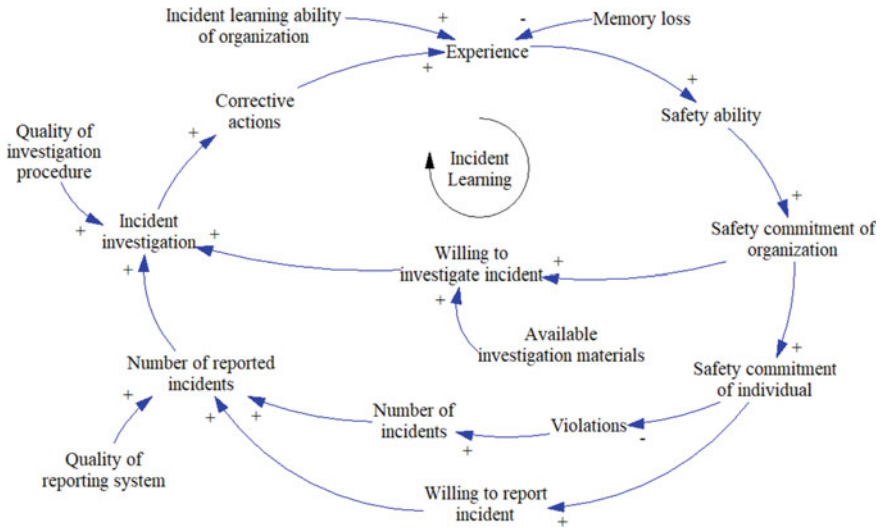


Fig. 4 CLD for incident learning

The goal of incident learning is to reinforce incident reporting by keeping the memory of past incidents alive [8]. Experience is gained through the process of incident reporting, incident investigation, proposal of suggestions and corrective actions taking. Then safety ability, safety commitment of organization and safety commitment of individual are improved in turns, so as to reinforce the loop of incident reporting.

In the system of incident learning, there are mainly two reinforcing feedbacks and one balancing feedback. The improvement of safety commitment of organization and individual can both increase the willingness to report and investigate incidents, thus in turn enhancing the level of experience. On the other hand, personal emphasis on safety will reduce the occurrence of violations, thus reducing the occurrence of incidents.

3.2 HFACS-SD Quantitative Model

Stock-Flow Diagram (SFD) is a quantitative expression of the system structure, which allows examination of the long-term behavior of complex systems by introducing the time dimension.

Identification of Variables. According to the actual characteristics of the variables, they are always divided into five categories: stock (level), flow (rate), data, auxiliary and constant. Stock shows the quantity of study factors, while flows demonstrate factors which come in and out to change the stock level [23]. Table 1 shows the definition of major variables of the HFACS-SD model.

Analysis of HFACS-SD Quantitative Model. As is shown in Fig. 5, different causal feedback loops in the SFD model correspond to different levels of the conceptual model. Different polarities of effect between variables affect the overall characteristics of the feedback loop. Based on the important stocks, here we take one reinforcing feedback loop and two balancing loops as examples.

B_1 (Incident Reporting: $S_2-A_3-A_4-A_5-A_6-F_2-S_2$): This loop reflects the balancing process of controlling the occurrence of incidents by incident reporting and investigation, which is primarily embodied in the elimination of the unsafe environment of the system.

B_2 (Human Reliability Improving: $S_1-A_1-F_2-S_2-A_3-A_4-A_5-F_3-S_3-A_7-A_8-A_9-F_1-S_1$): This loop shows that, under ideal conditions, the organization can gain experience through incident learning, improve the reliability of individual decision-making, then improve the overall level of human reliability, and in turn reduce the occurrence of incidents.

R_1 (Incident Learning: $S_3-A_7-F_5-S_4-A_{11}-F_6-S_5-A_{12}-A_{14}-A_3-A_4-A_5-F_3-S_3$): This loop reflects an increase in organizational and individual commitment to safety through incident learning, and an increase in individuals' willingness to report incidents, which in turn provides more opportunities for incident learning. It is worth noting that memory decay will surely erode the experience accumulated in the process.

Table 1 Definition of variables of HFACS-SD model

Type	Name	Unit	Definition
Stock(S ₁)	Human reliability	Ratio 0–1	INTEG(F ₁ , 0.5)
Stock(S ₂)	Number of incidents	Incident	INTEG(F ₂ , 0)
Stock(S ₃)	Experience	Dml	INTEG(F ₃ -F ₄ , 0)
Stock(S ₄)	Safety commitment of organization	Ratio 0–1	INTEG(F ₅ , 0.5)
Stock(S ₅)	Safety commitment of individual	Ratio 0–1	INTEG(F ₆ , 0.5)
Flow(F ₁)	Change of human reliability	1/Month	(C ₁ -S ₁)*A ₈ *A ₉ /C ₂
Flow(F ₂)	Incident rate	Incident/ Month	C ₃ *((A ₁ + A ₂)/2 + A ₆)/C ₄ /2
Flow(F ₃)	Incident learning	1/Month	C ₈ *A ₅ /C ₉
Flow(F ₄)	Memory loss	1/Month	S ₃ /C ₁₀
Flow(F ₅)	Change of safety commitment of organization	1/Month	(C ₁₇ -S ₄)*A ₇ /C ₁₈
Flow(F ₆)	Change of safety commitment of individual	1/Month	(C ₁₉ -S ₅)*(A ₁₁ -0.75)/C ₂₀
Auxiliary(A ₁)	Errors	Dml	2*(1-S ₁)
Auxiliary(A ₂)	Violations	Dml	4*(1-A ₁₂)
Auxiliary(A ₃)	Number of reported incidents	Incident	S ₂ *A ₁₄ *C ₅
Auxiliary(A ₄)	Incident investigation	Dml	(1-EXP(-0.5*A ₃))*C ₇ *A ₁₃
Auxiliary(A ₅)	Corrective actions	Dml	0.9*A ₄
Auxiliary(A ₆)	Unsafe environment of system	Dml	1-0.6*A ₅ -0.2*A ₇ -0.2*A ₈
Auxiliary(A ₇)	Relative safety ability	Ratio 0–1	(1-EXP(-S ₃))/C ₁₁
Auxiliary(A ₈)	Reliability of decision making	Ratio 0–1	(0.6*C ₁₂ + 0.4*C ₁₃ + A ₇)/4
Auxiliary(A ₉)	Reliability of operation	Ratio 0–1	C ₁₆ *A ₁₆ *C ₁₄ *C ₁₅ *A ₈ *0.6*(1-A ₁₀)
Auxiliary(A ₁₀)	Impact of emergency	Dml	RANDOM NORMAL(0.1, 0.9, 0.5, 1, 2)

(continued)

Table 1 (continued)

Type	Name	Unit	Definition
Auxiliary(A ₁₁)	Relative safety commitment of organization	Ratio 0–1	S ₄ /C ₁₇
Auxiliary(A ₁₂)	Relative safety commitment of individual	Ratio 0–1	S ₅ /C ₁₉
Constant(C ₁)	Expected value of human reliability	Ratio 0–1	0.9

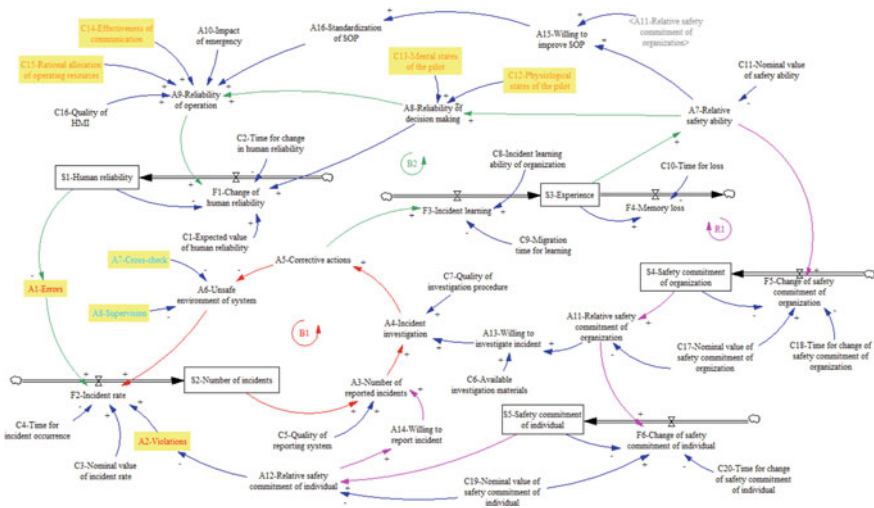


Fig. 5 SFD of HFACS-SD model

4 Simulation Results and Comparative Analysis

4.1 Simulation Results

This paper mainly studies the change of aviation human reliability with time in the process of incident learning. After the transformation from CLD to SFD and the determination of variable equations, it is necessary to judge the rationality of the internal structure of the model and the accuracy of the simulation results.

Comparison of Different Numerical Integration Methods. The comparison between different numerical integration methods is usually used to test the accuracy of the simulation results. In this paper, “Human reliability” is selected to compare the selection of numerical integration methods (Euler, RK4 Fixed). Table 2 shows the comparison result, which indicate that the simulation results of this model are accurate.

Table 2 Comparison results of human reliability (step size = 0.25 month)

Numerical integration method	Time (month)					
	0	30	60	90	120	150
(A) Euler	0.5	0.593163	0.727031	0.832286	0.876811	0.892808
(B) RK4 Fixed	0.5	0.593527	0.727393	0.832202	0.876655	0.892710
(A-B)/B (%)	0	-0.061	-0.050	0.010	0.018	0.011

Extreme Policy Test. Extreme policy test (EPT) refers to the test of various situations that the constant parameters in the SFD model are in the limit state, which can test the structure rationality of the feedback loop in the model.

In the whole system, the level of human reliability shows an S-shaped growth trend. When the pilot's mental state is extremely bad (e.g., anxiety, fatigue), the improvement of human reliability in the incident learning process will slow down and the probability of incidents will increase to some extent. In addition, if the organization has a poor ability of incident learning, the learning process is almost ineffective. Human reliability will increase at a much lower constant speed and incidents will occur at the initial high speed.

The results of EPT show that the structure of the HFACS-SD model is reasonable and the simulation results can quantitatively reflect the change of key variables in the time domain.

4.2 Comparative Analysis

Scenario analysis is usually used to identify key factors and analyze their impact. The model can be simulated and validated in multiple what-if scenarios by setting different constant parameters and comparing and analyzing the running results. Several typical scenarios are analyzed below.

Scenario 1: Adverse Conditions of Incident Reporting and Investigation. In fact, the conditions for the incident reporting and investigation process are unlikely to be perfect. For example, the incident reporting system can never be complete and perfect. Thus, Sino Confidential Aviation Safety Reporting System (SCASS) is established to be a supplement of Aviation Safety Information System of CAAC for collecting information that is not available to the mandatory incident reporting system, following the recommendations of Annex 13 of the ICAO Convention. So, it is necessary to analyze the influence of the inadequate reporting system and the improper investigation procedure on the occurrence of incidents and the increase of HR. The variable "Quality of reporting system" and "Quality of investigation procedure" are reduced from 1 to 0.5 separately, and the comparison result is shown in Fig. 6.

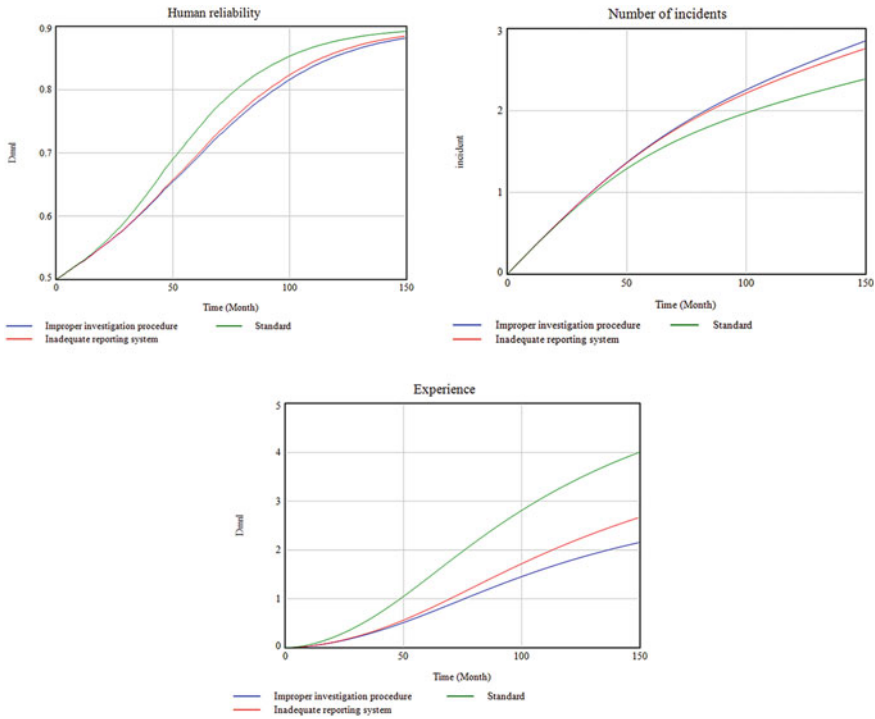


Fig. 6 Comparison results of scenario 1

The simulation results show that poor quality of the reporting system and investigation procedure will both slow down the increase of human reliability to different degrees. Meanwhile, the occurrence rate of incidents will increase considerably.

The adverse conditions of incident reporting and investigation reduce the probability of corrective actions. As a result, the organization cannot learn enough from the incidents. The relative safety ability cannot be improved properly, so various errors and violations are more likely to occur. In short, the adverse conditions for the incident reporting and investigation process have a great negative effect on the improvement of human reliability in the incident learning process.

Scenario 2: Poor Communication. Aviation history marked one of the most tragic mid-air collisions of 349 deaths on November 12, 1996, around 100 km west of Delhi, India. Since then, the importance from the safety angle of proficiency of flight crew in conducting radiotelephony communications in the English language was widely noticed. In 2013, ICAO incorporate “Proficiency in the English language used for radiotelephony communications” into its Language Proficiency Requirements (LPR).

Yearly accident statistics from ICAO indicate an increase of communication problems in accident causes, so it is of significance to analyze the influence of poor

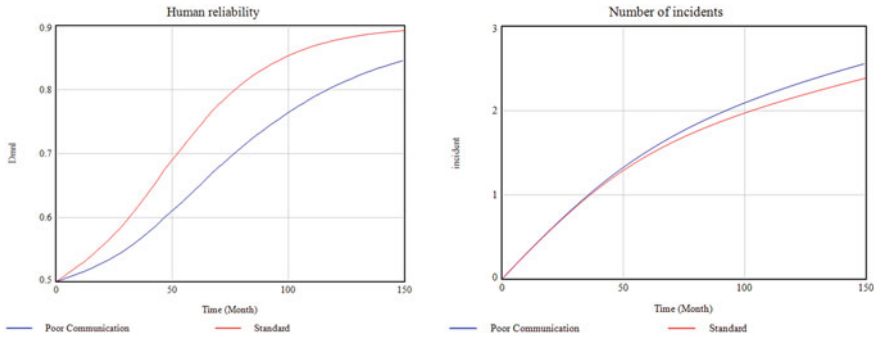


Fig. 7 Comparison results of scenario 2

communication on the occurrence of incidents and the increase of HR. The variable “Effectiveness of communication” is reduced from 1 to 0.5, and the comparison result is shown in Fig. 7.

According to the simulation results, it is obvious that due to the poor communication between pilots, the reliability of operation of the pilot will be greatly reduced, thus significantly smoothing and delaying the increase of human reliability. The number of incidents does not seem to have decreased too much, because poor communication simply increases the probability of making errors and it doesn’t increase the occurrence of violations directly.

Compared with scenario 1, poor communication has a greater negative effect on human reliability, while the influence of it on incident occurrence is less obvious than that in scenario 1.

5 Conclusion

Aiming at dynamically and systematically analyzing the influencing factors of change of aviation human reliability by learning from incidents, this paper proposed an HFACS-SD model based on the theory of Human Factor Analysis and Classification System. The feasibility and correctness of the proposed model are verified by simulations of various typical scenarios.

The main conclusions can be summarized as follows:

- (1) In general, the incident learning process is a reinforcing loop that promotes the improvement of human reliability, and the occurrence of severe aviation accidents and disasters can be slowed down to some extent by effective learning from the precursor incidents.
- (2) Among the four levels of the HFACS model, unsafe acts have the highest correlation with the occurrence of aviation accidents and incidents, while the impact of organizational influence is much less apparent and effective.

- (3) In the incident learning process, adverse conditions of decision-making and operation have a greater negative effect on HR but less influence on incident occurrence, while adverse conditions of incident reporting and investigation have greater influence on incident occurrence but a less negative effect on HR.
- (4) This model can effectively deal with the dynamic feedback of issues involving broad factors pervading in learning from incidents, and it provides some suggestions for further improving the human reliability of civil aviation pilots.

Acknowledgements This research was sponsored by Youth Fund Project of National Natural Science Foundation of China (61803263) and the Startup Fund for Youngman Research at SJTU of China (SFYR at SJTU).

References

1. Hulme A et al (2019) Accident analysis in practice: a review of Human Factors Analysis and Classification System (HFACS) applications in the peer reviewed academic literature. *Proc Hum Fact Ergon Soc Ann Meet* 63(1):1849–1853
2. Bagheri A, Hjorth P (2005) Monitoring for sustainable development: a systemic framework. *Int J Sustain Dev* 8(4):280–301
3. Lyall-Wilson B, Kim N, Hohman E (2019) Modeling human factors topics in aviation reports. *Proc Hum Fact Ergon Soc Ann Meet* 63(1):126–130
4. Carroll JS (1998) Organizational learning activities in high hazard industries: the logics underlying self-analysis. *J Manag Stud* 35:699–717
5. Yang C-C, Yeh C-H (2014) Application of system dynamics in environmental risk management of project management for external stakeholders. *Syst Pract Action Res* 27(3):211–225
6. Li C et al (2019) A hybrid human and organisational analysis method for railway accidents based on STAMP-HFACS and human information processing. *Appl Ergon* 79:122–142
7. Coyle RG (2010) A system dynamics model of aircraft carrier survivability. *Syst Dyn Rev* 8(3)
8. Cooke DL, Rohleder TR (2006) Learning from incidents: from normal accidents to high reliability. *Syst Dyn Rev* 22(3):213–239
9. Evans RA (1976) Reliability optimization. In: Henley EJ, Lynn JW (eds) *Generic techniques in systems reliability assessment*, 1976. Noordhoff International Publishing, Leyden, Netherlands, pp 117–131
10. Tomás M et al (2021) Machine learning and natural language processing for prediction of human factors in aviation incident reports. *Aerospace* 8(2):47–47
11. Reason J (1990) *Human error*. Cambridge University Press, New York, pp 72–95
12. Lewe J-H, Hivin LF, Mavris DN (2014) A multi-paradigm approach to system dynamics modeling of intercity transportation. *Transp Res Part E* 71:188–202
13. Kl B, Soran S (2019) How can an ab-initio pilot avert a future disaster: a pedagogical approach to reduce the likelihood of future failure. *J Aviat* 3(1):1–14
14. Celik M, Cebi S (2008) Analytical HFACS for investigating human errors in shipping accidents. *Accid Anal Prev* 41(1):66–75
15. Lenné MG et al (2012) A systems approach to accident causation in mining: an application of the HFACS method. *Accid Anal Prev* 48:111–117
16. Ghaffarzadegan N, Rahmandad H (2020) Simulation-based estimation of the early spread of COVID-19 in Iran: actual versus confirmed cases. *Syst Dyn Rev* 36(1):101–129
17. Xia N et al (2018) A hybrid BN-HFACS model for predicting safety performance in construction projects. *Saf Sci* 101:332–343

18. Liu P, Qiu Y, Hu J et al (2020) Expert judgments for performance shaping Factors' multiplier design in human reliability analysis. *Reliab Eng Syst Saf* 194
19. Trifonov-Bogdanov P, Vinogradov L, Shestakov V (2013) Civil aviation accidents and incidents classified according to groups of aviation specialists. *Aviation* 17(2):76–79
20. Shappell SA, Wiegmann DA (2001) The human factors analysis and classification system—HFACS. *Hum Fact Aerosp Saf* 1(1):59–86
21. Tauheed L, Wray LR (2006) System dynamics of interest rate effects on aggregate demand. In: Wray LR, Forstater M (eds) *Money, financial instability, and stabilization policy*. Edward Elgar, Cheltenham
22. Özkan U et al (2020) Analyzing collision, grounding, and sinking accidents occurring in the black sea utilizing HFACS and Bayesian networks. *Risk Anal* 40(12):2610–2638
23. Tharmmaphornphilas W, Lohasiriwat H, Vannasetta P (2012) Gold price modeling using system dynamics. *Eng J* 16(5)
24. Zhang X et al (2020) Dynamics simulation of the risk coupling effect between maritime pilotage human factors under the HFACS framework. *J Mar Sci Eng* 8(2)
25. Lu Y et al (2016) System dynamics modeling of the safety evolution of blended-wing-body subscale demonstrator flight testing. *Saf Sci* 89:219–230
26. Lu Y et al (2019) Multiple hierarchy risk assessment with hybrid model for safety enhancing of unmanned subscale BWB demonstrator flight test. *Chin J Aeronaut* 32(12):2612–2626
27. Xue Y, Fu G (2018) A modified accident analysis and investigation model for the general aviation industry: emphasizing on human and organizational factors. *J Saf Res* 67:1–15

Research on Pressure-Sensing Characteristic of Trailing-Cone



Yang Hui, Qu Feizhou, Fang Yang, Li Qiujie, and Yang Xinyu

Abstract This paper provides an analytical method for estimating the pressure-sensing characteristic of a trailing-cone system. The proposed method is based on the mechanics of the cone subjected to the weight and drag of the trailing-cone. The obtained results are compared with wind-tunnel test results. The analysis of such data shows that the proposed methodology is acceptably accurate for estimating the angles of attack of the trailing-cone. And more data need to evaluate the pressure-sensing characteristic estimation agreement, and it could be a promising analysis tool which can be used in flight tests.

Keywords Trailing-cone · Analytical method · Pressure · Angles of attack

1 Introduction

The airspeed of the aircraft is calculated from the total pressure and static pressure from Eq. (1). The measurement of total pressure is generally adequate for the aircraft throughout the normal flight envelope. But the static pressure is affected by the disturbance of the aircraft and usually needs to be corrected to the static pressure of the free stream. Flight test is used to obtain this correction. And various methods are available for obtaining in-flight calibrations (see Refs. [1, 2]). Trailing-cone method is one of these methods, and is widely used because of the good aerodynamic characteristic and can be used in wide flight conditions. The trailing-cone device is illustrated in Fig. 1.

$$P_T - P_S = P_0 \left(\left(1 + 0.2 \left(\frac{V}{a_0} \right)^2 \right)^{3.5} - 1 \right) \quad (1)$$

Y. Hui (✉) · F. Yang · L. Qiujie · Y. Xinyu
Shanghai Aircraft Design and Research Institute, Shanghai 201210, China
e-mail: ya_ben_cool@126.com

Q. Feizhou
Chinese Flight Test Establishment, Xi'an 710089, China

© The Author(s), under exclusive license to Springer Nature Singapore Pte Ltd. 2023
Z. Jing and D. Strelets (eds.), *Proceedings of the International Conference on Aerospace System Science and Engineering 2021*, Lecture Notes in Electrical Engineering 849,
https://doi.org/10.1007/978-981-16-8154-7_2

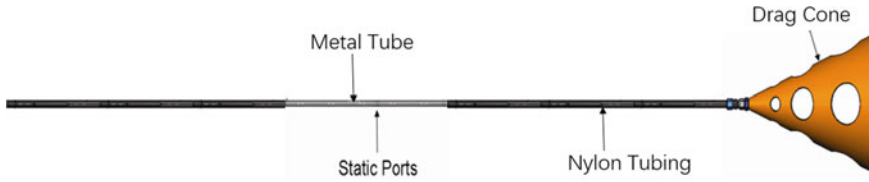


Fig. 1 Trailing-cone system

where P_T is the total pressure and P_S is the static pressure. P_0 and a_0 are the static pressure and speed of the sound at the sea level, respectively. $P_0 = 101,325$ Pa; $a_0 = 340.2940$ m/s. V is the calculated calibrated airspeed for the aircraft.

A lot of investigation of the trailing-cone system and trailing-cone flight technique have been done (see Refs. [3–6]). The static-pressure measurement of the trailing-cone system in stable flight mainly depends on the flight condition, the disturbance of the aircraft, the hose shape and the location of the static ports, and the accuracy of the static sensor. In this paper, the hose shape, i.e. static port inclinations on the pressure-sensing characteristic of the trailing-cone and some wind-tunnel test results are investigated.

2 Pressure-Sensing Characteristic of Various Inclinations

2.1 Wind Tunnel and Test Conditions

The pressure-sensing characteristic of various flow angles is investigated in the wind tunnel. The wind-tunnel test assembly is illustrated in Fig. 2, the tube is fixed by a steel cable. The test conditions are listed in Table 1; the tests were performed with

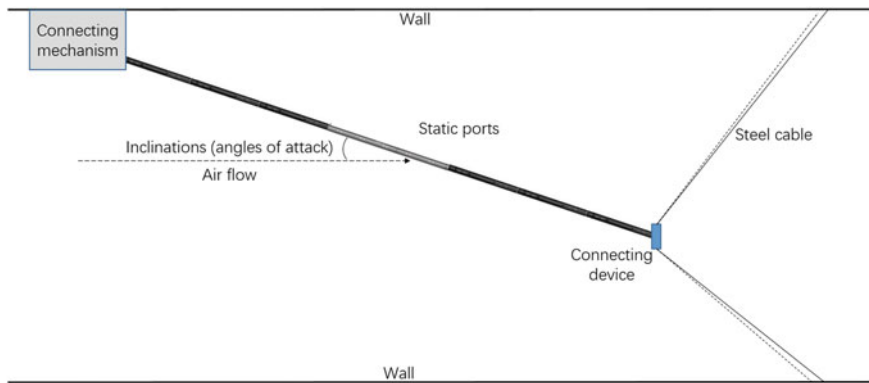


Fig. 2 The sketch of the wind-tunnel test assembly (fixed AOA)

Table 1 The wind-tunnel test conditions (fixed AOA)

Number	Ma	α (deg)				
1	0.4	0	3.256	5.24	6.92	9.082
2	0.785	-0.440	2.764	4.668	8.341	
3	0.82	-0.460	2.608			

$M = 0.4$, $M = 0.785$ and $M = 0.82$. Visual observations of the trailing-cone systems were made during tests, and photographs were obtained by VMD high-speed camera to record momentary inclinations (angles of attack, AOA) and vertical locations of the static-pressure tube.

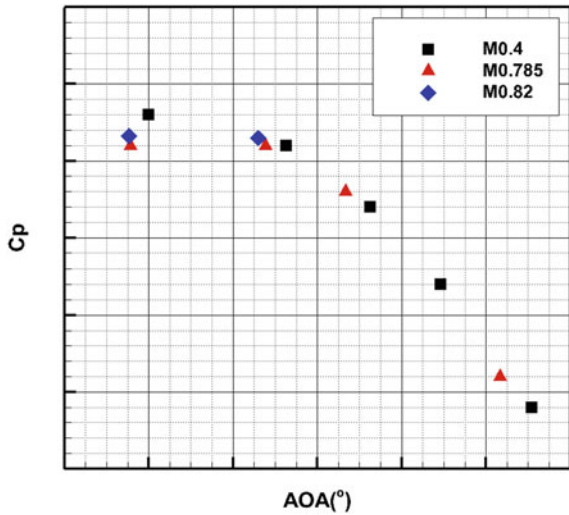
2.2 Wind-Tunnel Results and Discussion

Differences between pressures indicated by the tested device and free-stream static pressure are presented in Fig. 3. The variation of pressure differences is in the coefficient forms C_p defined as in Eq. 2. Figure 3 shows the variation of C_p with various AOA.

$$C_p = \frac{P - P_\infty}{q_\infty} \tag{2}$$

where P is the static pressure measured by the tested device, and P_∞ and q_∞ are free-stream static pressure and dynamic pressure, respectively.

Fig. 3 Variation of pressure difference with AOA



The data in Fig. 3 shows that the pressure-sensing is lower with higher AOA. These data also indicate that the C_p is closely related to AOA, but not to Mach number. This is very important and interesting, but needs more data to confirm it hereafter. If Mach number has little effect on C_p , and C_p just depends on AOA, then AOA of the trailing-cone device in the flight can be obtained and corrected by using this C_p -AOA relationship.

3 Estimation of Trailing-Cone AOA in Flight

3.1 Methodology

The trailing-cone inclinations in the flight can be obtained by additional particular equipment, and it's more accurate than the estimation. But sometimes the additional particular equipment is not available. The estimation of the trailing-cone AOA in flight can be applied.

Figure 4 shows the sketch of forces applied to the cone when the aircraft is a steady flight. D_c is the drag force, T_c is the pulling force and W_c is the weight of the cone. Therefore, the following expressions hold:

$$T_c = \sqrt{(D_c \sin \theta + W_c)^2 + (D_c \cos \theta)^2} \quad (3)$$

$$AOA_c = a \tan \left(\frac{D_c \sin \theta + W_c}{D_c \cos \theta} \right) - \theta \quad (4)$$

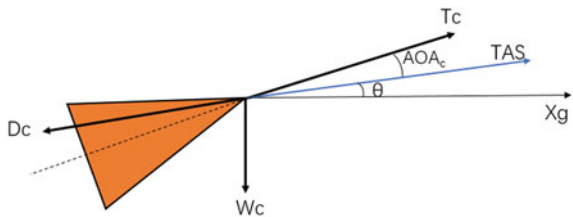
where θ is the flight path angle, and AOA_c is the trailing-cone AOA.

When the flight is level, then $\theta = 0$; the expressions can be simplified to

$$T_c = \sqrt{W_c^2 + D_c^2} \quad (5)$$

$$AOA_c = a \tan \left(\frac{W_c}{D_c} \right) \quad (6)$$

Fig. 4 Sketch of forces applied to the cone



Equation 6 indicates AOA_c increases when W_c increases, whereas AOA_c increases with the decrease of D_c .

The drag of the cone can be calculated through

$$D_c = qC_{Dc}A_c \tag{7}$$

where A_c is the base area of the cone and C_{Dc} is the drag coefficient of the cone.

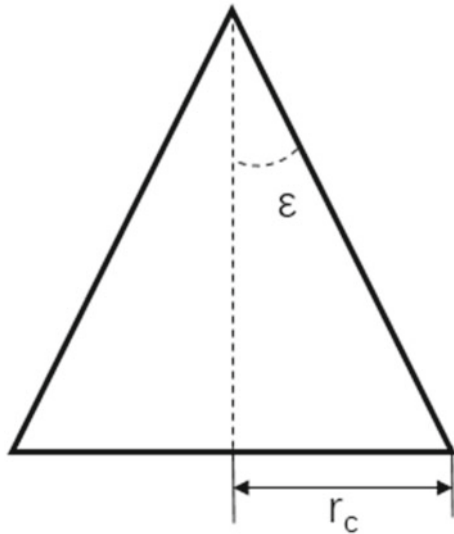
3.2 Drag Coefficient of the Cone

Based on graphical information presented by Hoerner [7] for a three-dimensional cone, the following expression may be used for ϵ up to 30° .

$$C_{Dc} = 0.01\epsilon_{deg} + 0.19003 \tag{8}$$

where ϵ is the half-vertex angle, and must be taken in degree. The ϵ is as illustrated in Fig. 5, and r_c is the base radius of the cone.

Fig. 5 Characteristic dimensions of a cone



3.3 Comparison Between Estimation Results and Wind-Tunnel Results

The wind-tunnel test assembly is as shown in Fig. 6, in which the cone is without any restriction. The cone geometric dimension is $r_c = 6.35$ cm, $\epsilon = 21^\circ$. The total mass of the cone and the connector is 199.65 g, so the $W_c = 1.95657$ N. The estimated drag coefficient calculated from Eq. 8 is 0.40003.

The wind-tunnel test conditions and the results are as listed in Table 2. The drag coefficient calculated from Eq. 8 is 0.40003, and then the estimated AOA is compared to the test results, as listed in Fig. 7. In Fig. 7, the black square symbols are the simulation AOA of the cone, and the red triangle symbols are wind-tunnel test results. Figure 7 shows that the simulation AOA of the cone agrees well with the wind-tunnel test results.

The C_p of the static tube measured in the fixed AOA wind-tunnel test is compared to C_p measured in the free cone wind-tunnel test, as illustrated in Fig. 8. Unluckily, the data is not enough to evaluate the difference.

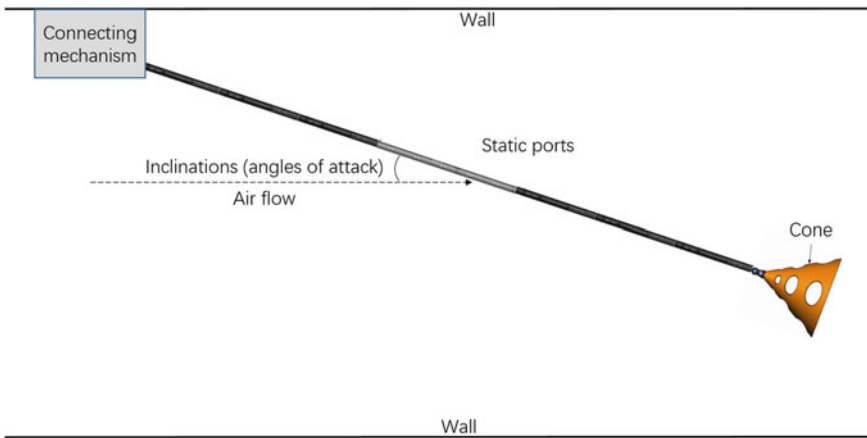


Fig. 6 The sketch of the wind-tunnel test assembly (free cone)

Table 2 The wind-tunnel test conditions and results (free cone)

Number	Ma	q (Pa)	C_p	AOA (deg)
1	0.3	6542.06	-0.0107	3.637
2	0.4	11,052.63	-0.0057	1.948
3	0.6	21,595.74	-0.0047	1.108
4	0.7	29,925.00	-0.004	0.733
5	0.785	34,666.67	-0.0018	0.588
6	0.82	39,166.67	-0.0006	No data

Fig. 7 The estimation AOA of cone compared with wind-tunnel test results

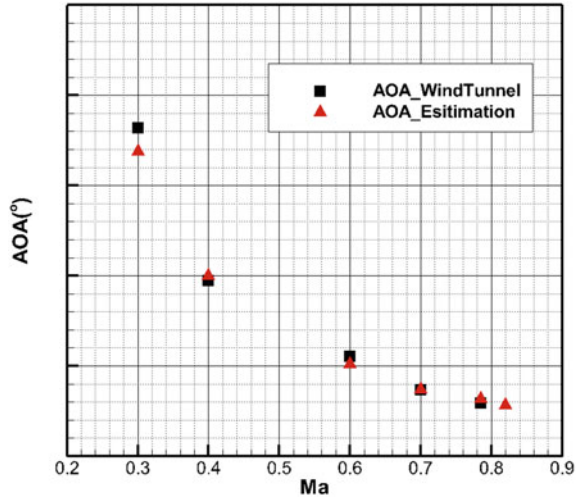
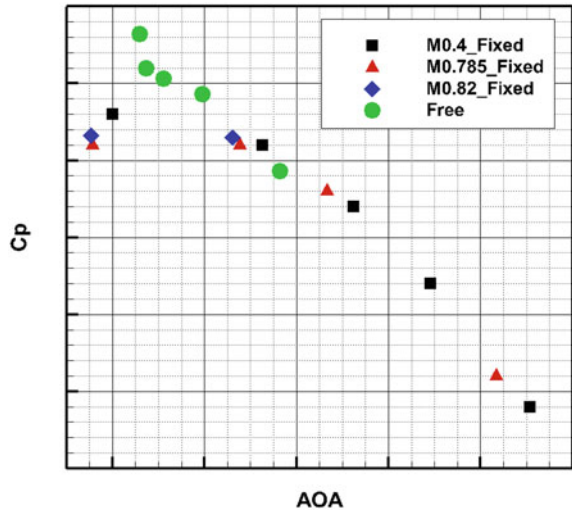


Fig. 8 A comparison of the Cp between the fixed AOA and free cone wind-tunnel test results



4 Outlook

The drag coefficient of the cone can be calculated also using CFD if the half-vertex angle is greater than 30°.

As mentioned in Sect. 2.2, the fixed AOA of cone test data is expected to be more. And the conclusion of the relationship between the pressure-sensing characteristic of the cone and Mach number and the comparison of the estimated pressure-sensing results and wind-tunnel test result is more clear.

The flight test results to estimate the method for determining the AOA and pressure-sensing characteristic of the cone are expected in the future.

5 Conclusion

The engineering method for determining the AOA and pressure-sensing characteristic of the cone is presented. The method is estimated in the wind-tunnel test. The results obtained with such method are compared with data gathered from the wind-tunnel test. The analysis of such data shows that the proposed methodology is acceptably accurate for estimating the AOA of the trailing-cone. With the relationship between the AOA of the trailing-cone and the pressure-sensing characteristic which can be obtained in the wind-tunnel test, the pressure-sensing characteristic in flight at various speeds can be calculated. In this way, it is reasonable to conclude that it constitutes a promising analysis tool which can be used in flight tests.

References

1. Haering Jr EA (1995) Airdata measurement and calibration. NASA Technical Memorandum 104316. NASA
2. Gracey W (1980) Measurement of aircraft speed and altitude. NASA Reference Publication 1046
3. Brown EN (1998) Position error calibration of a pressure survey aircraft using a trailing cone. NCAR Technical Note 313+STR, July 1988
4. Welsler M (2007) F-16B pacer aircraft trailing cone length extension tube investigative study (have cletis). AFFTC-TIM-07- 02, AFFTC, Edwards Air Force Base, California, June 2007
5. Silveira Fo CR (2008) Approximate method for determining the optimum hose length for a trailing cone system. In: 39th annual international symposium, Ft. Worth TX, pp 109–123
6. Jordan Jr. FL, Ritchie VS (1973) Subsonic wind-tunnel tests of a trailing-cone device for calibrating aircraft static-pressure systems. NASA Technical Note 7217. NASA
7. Hoerner SF (1958) Fluid-dynamic drag practical information on aerodynamic drag and hydrodynamic resistance. Midland Park, NJ, USA

Spatial Interpolation Methods for Virtual Rotating Array Beamforming with Arbitrary Microphone Configurations



Jiacheng Yang, Ce Zhang, and Wei Ma

Abstract Virtual rotating array (VRA) beamforming is a robust technique in the identification of rotating sound sources in frequency-domain. Under normal circumstances, the configuration of microphone array is established in ring geometry centered around the rotating axis. Two interpolation methods for arbitrary microphone configurations are proposed by Jekosch and Sarradj (Acoustics 2020). One is to construct a mesh between all stationary microphones using Delaunay-triangulation, another one is a meshless technique based on radial basis function. However, whether other spatial interpolation methods are available in VRA beamforming with arbitrary microphone configurations is still unclear. This paper adds several new spatial interpolation methods in VRA beamforming and detailedly compares the performances of these interpolation methods in simulations. The simulating results demonstrated that all these interpolation methods are successfully applied in VRA beamforming with arbitrary microphone configurations. Inverse distance weighting interpolation method owns the best performance in rotating sound source localization. Additionally, all these interpolation methods have poor spectrum construction capability and sound source strength precision.

1 Introduction

In the past decades, phased microphone array has been increasingly used as a standard technique for sound source localization [16]. The conventional delay-and-sum (DAS) beamforming computes a dirty beamforming map from pressure signals of microphones [15], and is of great simpleness. The spatial resolution and dynamic range of DAS beamforming can be improved by iterative deconvolution algorithms [1, 11–13, 22]. Besides stationary sound source, phased microphone array can also localize moving sound source such as aeroengine fan noise. Beamforming for rotat-

J. Yang · C. Zhang · W. Ma (✉)

School of Aeronautics and Astronautics, Shanghai Jiao Tong University, 800 Dongchuan Road, Shanghai, People's Republic of China
e-mail: mawei@sjtu.edu.cn

© The Author(s), under exclusive license to Springer Nature Singapore Pte Ltd. 2023
Z. Jing and D. Strelets (eds.), *Proceedings of the International Conference on Aerospace System Science and Engineering 2021*, Lecture Notes in Electrical Engineering 849,
https://doi.org/10.1007/978-981-16-8154-7_3

ing source localization (rotating beamforming) has been investigated in the literature, both in time-domain and frequency-domain.

For time-domain rotating beamforming, Sijtsma et al. [23] proposed the rotating source identifier (ROSI). ROSI compensates most of the Doppler effect caused by rotation and may still contain some ghost contributions induced by the Doppler effect, additionally high order rotational symmetry arrays with respect to the rotation axis are able to compensate the ghost contributions [14]. The main defect of ROSI is its extremely low computational efficiency, due to the requirement in over-sampling of the pressure time signals. Therefore, frequency-domain rotating beamforming has been extensively studied in recent years.

For frequency-domain rotating beamforming, Lewis and Joseph [7, 8] proposed the virtual rotating array (VRA) beamforming. The basic idea of VRA beamforming is constructing an array virtually rotating with the same angular speed as the rotating sources. Two algorithms are proposed to calculate pressures at the VRA microphones. The first transforms the modes that are frequency-shifted to compensate for the motion effect [17]. The second resamples the pressures at stationary microphones [5]. The relationship between these two algorithms has been theoretically investigated in Ref. [10]. The main difference between these two algorithms is the interpolation method used to calculate the sound pressures at VRA microphones from pressures at stationary microphones. The first uses Fourier interpolation, while the second uses linear interpolation.

For array configuration, one major constraint of VRA beamforming is that microphones must constitute a ring or several concentric rings around the rotation axis of sound source. This type of array has a poorer performance with regard to side lobe level compared with arbitrary configuration array [20].

In order to apply arbitrary configuration array in VRA beamforming, Jekosch and Sarraj [6] successfully applied two interpolation methods to reconstruct the pressure signals of VRA microphones within a certain accuracy. The first one is to construct a mesh between the stationary microphone positions using Delaunay-triangulation. The second one is a meshless technique based on radial basis function.

A lot of interpolation methods exist in the literature. Until now issues are still unclear and need to be further investigated: (a) Whether other interpolation methods can also be applied in VRA beamforming with arbitrary configuration array? (b) Which one owns the best performance in sound source localization?

The main purpose of this paper is trying to answer the above two questions. Several interpolation methods are applied in VRA beamforming, and their performances are compared in detail. The paper is organized as follows. Theory of VRA beamforming is reviewed in Sect. 2. Interpolation methods are introduced in Sect. 3. Simulations are carried out in Sect. 4. Discussions are presented in Sect. 5. Finally, conclusions are given in Sect. 6.

2 Theory of VRA Beamforming

Figure 1 shows the schematic diagram of VRA beamforming with arbitrary microphone array for rotating source localization. The origin of the coordinate system is placed in the microphone array center. The microphone array center is axially aligned with the axis of rotation of the sound sources. The sound source rotates at an angular speed of Ω . The microphone array contains M microphones, while the scanning plane contains S grids. The position vector of the stationary microphones is $\mathbf{X} = [\mathbf{x}_1, \dots, \mathbf{x}_m, \dots, \mathbf{x}_M]^T$, with $(\cdot)^T$ denoting the non-conjugate transpose. The position vector of the scanning plane grids is $\mathbf{Y} = [\mathbf{y}_1, \dots, \mathbf{y}_s, \dots, \mathbf{y}_S]^T$.

The VRA beamforming is

$$b(\mathbf{y}_{\Omega s}, \omega) = \mathbf{h}^H(\mathbf{y}_{\Omega s}, \omega) \mathbf{C}_v(\omega) \mathbf{h}(\mathbf{y}_{\Omega s}, \omega), \quad s = 1, \dots, S \quad (1)$$

where $(\cdot)^H$ denotes the conjugate transpose, $(\cdot)_{\Omega}$ denotes parameter in rotating reference frame, $(\cdot)_v$ denotes parameter of VRA microphones in rotating reference frame, $\mathbf{y}_{\Omega s}$ is position of the s th rotating grid in rotating reference frame, ω is the angular velocity and $\omega = 2\pi f$ where f is frequency. The beamforming in decibels (dB) is calculated through $10 \log_{10}[b(\mathbf{y}_{\Omega s}, \omega)/p_{\text{ref}}^2]$, where p_{ref} is the reference pressure of 2×10^{-5} Pa.

The parameter

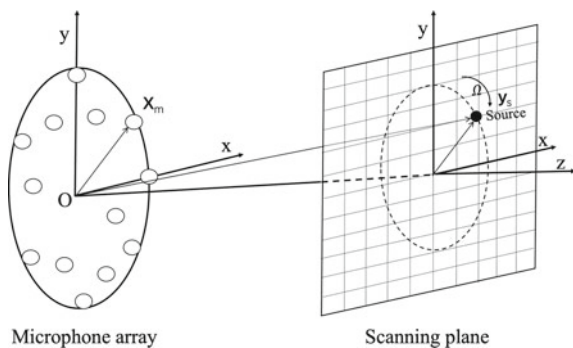
$$\mathbf{h}(\mathbf{y}_{\Omega s}, \omega) = [h(\mathbf{x}_{v1}, \mathbf{y}_{\Omega s}, \omega), \dots, h(\mathbf{x}_{vm}, \mathbf{y}_{\Omega s}, \omega), \dots, h(\mathbf{x}_{vM}, \mathbf{y}_{\Omega s}, \omega)]^T \quad (2)$$

where $h(\mathbf{x}_{vm}, \mathbf{y}_{\Omega s}, \omega)$ is the normalized steering vector from m th virtual microphone to the s th grid at ω , with \mathbf{x}_{vm} the position of the m th virtual microphone in rotating reference frame. In this paper, the steering vector SV-C2 proposed in Ref. [10] is used, while Formulation III in Ref. [19] is used to normalize SV-C2.

The parameter

$$\mathbf{C}_v(\omega) = \epsilon[\mathbf{p}_v(\omega) \mathbf{p}_v^H(\omega)] \quad (3)$$

Fig. 1 Sketch of VRA beamforming with arbitrary microphone array for rotating source localization



is the cross-spectral matrix (CSM), where $\epsilon(\cdot)$ denotes the expectation operation, and

$$\mathbf{p}_v(\omega) = [p(\mathbf{x}_{v1}, \omega), \dots, p(\mathbf{x}_{vm}, \omega), \dots, p(\mathbf{x}_{vM}, \omega)]^T \quad (4)$$

where $p(\mathbf{x}_{vm}, \omega)$ is the complex pressure spectrum at the m th virtual rotating microphone which can be obtained by fast Fourier transformation of pressure time signals $p(\mathbf{x}_{vm}, t)$ at the m th virtual rotating microphone. Due to virtual microphone rotating with the same angular speed as the rotating sources, \mathbf{x}_{vm} does not change with time.

3 Interpolation Methods

Seven interpolation methods, which will be used to calculate the pressure time signals $p(\mathbf{x}_{vm}, t)$, are introduced in this section. Two of them are already applied in VRA beamforming with arbitrary microphone array by Jekosch and Sarradj [6]. These seven interpolation methods are classified into four categories, Delaunay-triangulation, radial basis function, inverse distance weighting, ordinary kriging.

3.1 Category I: Delaunay-Triangulation [18]

In this category, pressure time signals $p(\mathbf{x}_{vm}, t)$ are interpolated through three stationary microphones at neighboring vertices of a mesh obtained by the Delaunay-triangulation. The Delaunay-triangulation is a widely used algorithm to construct a mesh between two-dimensional or three-dimensional discrete points. Delaunay-triangulation maximizes the minimum angle of all the angles of the triangles in the triangulation and avoids sliver triangles. Concerning interpolation methods used in this category, barycentric interpolation was applied by Jekosch and Sarradj [6]. Besides barycentric interpolation, piecewise cubic interpolation is another option.

In category I, interpolation methods with barycentric interpolation and piecewise cubic interpolation will be applied in this paper. These two interpolation methods are denoted by M1 and M2, respectively, in this paper.

3.2 Category II: Radial Basis Functions [2]

The radial basis function interpolation estimates the data of interpolation point by a linear combination of radial basis functions, which depend only on the Euclidean distances between the location of interpolation point and the location of known data points. This approximation process can also be interpreted as a simple kind of neural network.

In this category,

$$p(\mathbf{x}_{vm}, t) = \sum_{i=1}^M \alpha_i(t) \Phi(\|\mathbf{x}_{vm} - \mathbf{x}_{\Omega_i}(t)\|_2) \quad (5)$$

where $\mathbf{x}_{\Omega_i}(t)$ is the position vector of the i th stationary microphone in rotating reference frame, $\Phi(\cdot)$ is the radial basis function, and $\alpha_i(t)$ is weight coefficient of the i th stationary microphone and determined by solving linear system

$$\begin{bmatrix} \Phi(\|\mathbf{x}_1 - \mathbf{x}_1\|_2) & \cdots & \Phi(\|\mathbf{x}_i - \mathbf{x}_1\|_2) & \cdots & \Phi(\|\mathbf{x}_M - \mathbf{x}_1\|_2) \\ \vdots & \ddots & \vdots & \ddots & \vdots \\ \Phi(\|\mathbf{x}_1 - \mathbf{x}_i\|_2) & \cdots & \Phi(\|\mathbf{x}_i - \mathbf{x}_i\|_2) & \cdots & \Phi(\|\mathbf{x}_M - \mathbf{x}_i\|_2) \\ \vdots & \ddots & \vdots & \ddots & \vdots \\ \Phi(\|\mathbf{x}_1 - \mathbf{x}_M\|_2) & \cdots & \Phi(\|\mathbf{x}_i - \mathbf{x}_M\|_2) & \cdots & \Phi(\|\mathbf{x}_M - \mathbf{x}_M\|_2) \end{bmatrix} \begin{bmatrix} \alpha_1(t) \\ \vdots \\ \alpha_i(t) \\ \vdots \\ \alpha_M(t) \end{bmatrix} = \begin{bmatrix} p(\mathbf{x}_1, t) \\ \vdots \\ p(\mathbf{x}_i, t) \\ \vdots \\ p(\mathbf{x}_M, t) \end{bmatrix} \quad (6)$$

where $p(\mathbf{x}_i, t)$ is the pressure time signals of the i th stationary microphone. Please note that the position vector of the i th stationary microphone in rotating reference frame is a variable of time, and thus is expressed as $\mathbf{x}_{\Omega_i}(t)$.

Concerning radial basis function, cubic form interpolation was applied by Jekosch and Sarradj [6]. Besides cubic form interpolation, multiquadric form interpolation is another option.

In category II, interpolation methods with cubic form interpolation and multiquadric form interpolation will be applied in this paper. These two interpolation methods are denoted by M3 and M4, respectively, in this paper.

3.3 Category III: Inverse Distance Weighting [21]

The inverse distance weighting interpolation estimates the data of interpolation point by calculating with a weighted average of the values available at the known points. The weighting values resort to the inverse of the Euclidean distances to each known point when assigning weights.

In this category,

$$p(\mathbf{x}_{vm}, t) = \sum_{i=1}^M \frac{\kappa_i(\mathbf{x}_{vm}, t) p(\mathbf{x}_i, t)}{\sum_{j=1}^M \kappa_j(\mathbf{x}_{vm}, t)} \quad (7)$$

where $\kappa_i(\mathbf{x}_{vm}, t)$ is the inverse distance weighting of the i th stationary microphone to the m th virtual microphone, and

$$\kappa_i(\mathbf{x}_{vm}, t) = \frac{1}{\|\mathbf{x}_{vm} - \mathbf{x}_{\Omega_i}(t)\|_2^\beta} \quad (8)$$

where β is the weighting power exponent.

For determining β , there are two methods. In the first method, β is a constant value. In the second method, β is an adaptive value denoted by $\beta_{\text{ad}}(\mu_x, t)$. $\beta_{\text{ad}}(\mu_x, t)$ is obtained by the following three steps [9]. The first step is to determine the nearest neighbor statistic $R(\mathbf{x}_{vm}, t)$ with the position of virtual microphone \mathbf{x}_{vm} through $R(\mathbf{x}_{vm}, t) = r_{\text{obs}}(t)/r_{\text{exp}}(t)$, with the observed average nearest neighbor distance $r_{\text{obs}}(t) = 1/M_k \sum_{i=1}^{M_k} d_i(t)$, and the expected nearest neighbor distances $r_{\text{exp}}(t) = 1/(2\sqrt{M/A})$, where M_k is the number of nearest neighbor microphones, $d_i(t)$ is the Euclidean distance between the nearest neighbor microphones and the virtual microphone at sampling time t , A is the area of interpolation indexing whose diameter is defined as the furthest distance from the virtual microphone to the stationary microphone. The second step is to normalize the $R(\mathbf{x}_{vm}, t)$ to the parameter μ_x ,

$$\mu_x(t) = \begin{cases} 0 & R(\mathbf{x}_{vm}, t) \leq R_{\min} \\ 0.5 - 0.5 \cos \left[\frac{\pi}{R_{\max}} (R(\mathbf{x}_{vm}, t) - R_{\min}) \right] & R_{\min} < R(\mathbf{x}_{vm}, t) \leq R_{\max} \\ 1 & R(\mathbf{x}_{vm}, t) > R_{\max} \end{cases} \quad (9)$$

where R_{\min} and R_{\max} are nearest neighbor statistical parameter in this algorithm, and are chosen as 0 and 1.5 in this paper. The third step is to determine $\beta_{\text{ad}}(\mu_x, t)$ by applying triangular membership function for different degrees of the adaptive power exponent β_i ($i = 1, 2, \dots, n$) where n is the number of degrees.

In category III, interpolation methods with these two methods for determining β will be applied in this paper. These two interpolation methods are denoted by M5 and M6, respectively, in this paper. In M5, $\beta = 2.0$. In M6, $M_k = 3$, $R_{\min} = 0$, $R_{\max} = 1.5$, and $\beta_{\text{ad}}(\mu_x, t)$ is determined by applying triangular membership function for five degrees of the adaptive power exponent β_i ($i = 1, 2, \dots, 5$),

$$\beta_{\text{ad}}(\mu_x, t) = \begin{cases} \beta_1 & 0.0 \leq \mu_x(t) < 0.1 \\ \beta_1[1 - 5(\mu_x(t) - 0.1)] + 5\beta_2(\mu_x(t) - 0.1) & 0.1 \leq \mu_x(t) < 0.3 \\ \beta_2[1 - 5(\mu_x(t) - 0.1)] + 5\beta_3(\mu_x(t) - 0.1) & 0.3 \leq \mu_x(t) < 0.5 \\ \beta_3[1 - 5(\mu_x(t) - 0.1)] + 5\beta_4(\mu_x(t) - 0.1) & 0.5 \leq \mu_x(t) < 0.7 \\ \beta_4[1 - 5(\mu_x(t) - 0.1)] + 5\beta_5(\mu_x(t) - 0.1) & 0.7 \leq \mu_x(t) < 0.9 \\ \beta_5 & 0.9 \leq \mu_x(t) \leq 1.0 \end{cases} \quad (10)$$

with $\beta_1 = 1.0$, $\beta_2 = 2.0$, $\beta_3 = 3.0$, $\beta_4 = 4.0$, $\beta_5 = 5.0$.

3.4 Category IV: Ordinary Kriging [3]

The ordinary kriging is based on Gaussian process governed by prior covariances. Under suitable assumptions on the priors, the method gives the best linear unbiased prediction at unsampled locations.

In this method,

$$p(\mathbf{x}_{vm}, t) = \sum_{i=1}^M \lambda_i(\mathbf{x}_{vm}, t) p(\mathbf{x}_i, t) \quad (11)$$

where $\lambda_i(\mathbf{x}_{vm}, t)$ is the weighting value of the i th stationary microphone for the m th virtual microphone. The parameter $\lambda_i(\mathbf{x}_{vm}, t)$ is obtained by the following four steps. The maximum distance between arbitrary two stationary microphones in the array is denoted by h_{\max} . The first step is to search microphones from other stationary microphones that satisfy

$$|\mathbf{x}_m - \mathbf{x}_j(m)| \in [h - 0.5 \times (h_{\max}/M), h + 0.5 \times (h_{\max}/M)] \quad (12)$$

for the m th stationary microphone with a giving $h \in (0, h_{\max})$. The second step is to calculate discrete variogram function

$$\gamma(h, t) = \frac{1}{2 \sum_{m=1}^M N(m)} \sum_{m=1}^M \sum_{j=1}^{N(m)} [p(\mathbf{x}_m, t) - p(\mathbf{x}_j(m), t)]^2 \quad (13)$$

where $N(m)$ is the number of stationary microphones that satisfy Eq. 12 obtained in the previous step. The third step is to fit the discrete variogram obtained in the previous step by nonlinear least square estimation. The fourth step is to obtain the weighting value of stationary microphone for the m th virtual microphone by solving linear system

$$\begin{bmatrix} \gamma(h_{11}, t) & \gamma(h_{12}, t) & \cdots & \gamma(h_{1M}, t) & 1 \\ \gamma(h_{21}, t) & \gamma(h_{22}, t) & \cdots & \gamma(h_{2M}, t) & 1 \\ \vdots & \vdots & \ddots & \vdots & \vdots \\ \gamma(h_{M1}, t) & \gamma(h_{M2}, t) & \cdots & \gamma(h_{MM}, t) & 1 \\ 1 & 1 & 1 & 1 & 0 \end{bmatrix} \begin{bmatrix} \lambda_1(\mathbf{x}_{vm}, t) \\ \lambda_2(\mathbf{x}_{vm}, t) \\ \vdots \\ \lambda_M(\mathbf{x}_{vm}, t) \\ -\mu \end{bmatrix} = \begin{bmatrix} \gamma(h_{10}, t) \\ \gamma(h_{20}, t) \\ \vdots \\ \gamma(h_{M0}, t) \\ 1 \end{bmatrix} \quad (14)$$

where h_{ij} ($i, j = 1, 2, \dots, M$) is the Euclidean distance between the i th stationary microphone and j th stationary microphone, h_{k0} ($k = 1, 2, \dots, M$) is the Euclidean distance between the k th stationary microphone and the m th virtual microphone, μ is the expectancy value.

In category IV, interpolation method with a spherical mode used in the third step will be applied in this paper. This interpolation method is denoted by M7 in this paper. In M7, the spherical model used in the third step is

$$\gamma(h, t) = \begin{cases} 0 & h = 0 \\ C_0(t) + C(t) \left[1.5 \frac{h}{a(t)} - 0.5 \left(\frac{h}{a(t)} \right)^3 \right] & h < a(t) \\ C_0(t) + C(t) & h \geq a(t) \end{cases} \quad (15)$$

where $a(t)$, $C_0(t)$ and $C(t)$ are range, nugget value and arch height, respectively.

3.5 Summary

As a summary, there are seven interpolation methods that will be applied in this paper and have listed in Table 1. For all these interpolation methods, the reconstructed pressures time signals of virtual rotating microphone are interpolated through stationary microphones.

In this paper, the calculations will be carried out on an Intel i7-7700HQ CPU with Python. M1 will be implemented by class “LinearNDInterpolator” in Python package Scipy. M2 will be implemented by class “CloughTocher2DInterpolator” in Python package Scipy. M3, M4 will be implemented by class “Rbf” in Python package Scipy. M5 and M6 will be implemented by codes in house. M7 will be implemented by class “OrdinaryKriging” in Python package Pykrige.

4 Simulations

In this section, seven interpolation methods introduced in Sect. 3 are applied in simulations, and their performances are compared.

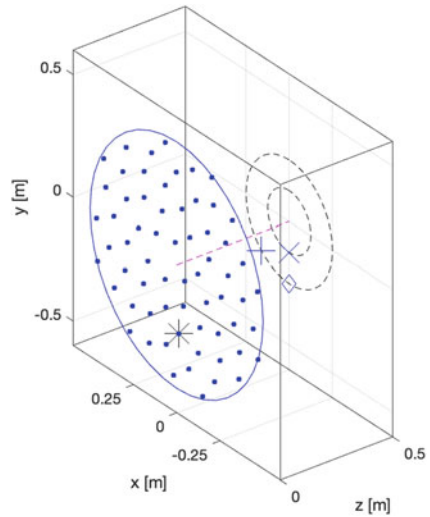
4.1 Simulation Setup

The benchmark case in Herold et al. [4] has been extended for VRA beamforming with arbitrary microphone configuration. Figure 2 shows the sketch of simulations. The microphone array has an aperture of 1.00 m, and contains 64 microphones. The array configuration is designed by the method introduced by Sarraj [20]. The flower parameters of the array used here are $H = 0$ and $V = 5$. The distance between the microphone array and the scanning plane is 0.50 m. Three sources are set at two rings with diameters of 0.125 m and 0.250, and are rotating in the clockwise direction at a constant angular speed of 1500 rpm. The rotation axis is the z axis. The rotation center

Table 1 Summary of interpolation methods

Category type	Methods
Category I:	M1
Delaunay-triangulation	M2
Category II:	M3
Radial basis functions	M4
Category III:	M5
Inverse distance weighting	M6
Category IV: ordinary kriging	M7

Fig. 2 Sketch of simulations. Source 1, blue square point (\diamond); Source 2, blue star point ($+$); Source 3, blue cross point (\times). Magenta rotation axis, magenta dotted line. Blue points, microphones. Reference microphone, black star sign point ($*$)

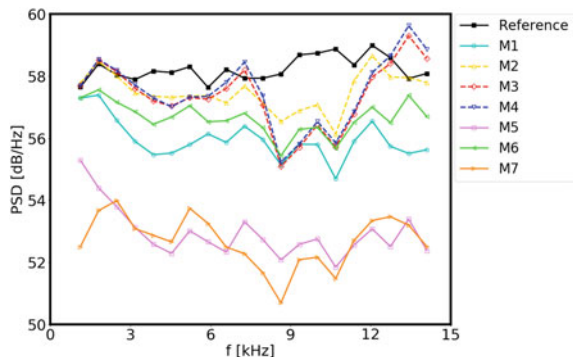


coordinates are (0 m, 0 m, 0.50 m). The original coordinates of these two sources are (0 m, -0.25 m, 0.50 m), (0.161 m, -0.192 m, 0.50 m), and (0 m, -0.125 m, 0.50 m), respectively. Three sources emit white noise. The effective sound pressure levels of these three sources at 1.00 m from these sources are 94 dB, 91 dB, and 88 dB, respectively. The computational grid is with 61×61 grid points. The grid resolution is 0.01 m. The evaluated time is 1.0 s. The sampling rate is 48 kHz. FFT block size is 1024 samples, and FFT window is Von Hann and 50% overlap.

4.2 Spectrum Reconstruction Capability

Spectrum reconstruction capability of interpolation method can be seen from the reconstructed power spectra density (PSD). Figure 3 shows reconstructed spectra of the virtual microphone, whose original position is at the reference microphone

Fig. 3 Reconstructed spectra



marked as a black star sign point (*) in Fig. 2. In order to get accurate PSD of this virtual microphone as reference, a ring array containing 128 stationary microphones is constructed around the rotation axis of sound source. This virtual microphone travels in the ring array during rotation. Then the pressure time signals of this virtual microphone are interpolated by one-dimensional Fourier interpolation method, and the reference PSD is calculated according to the pressure time signals.

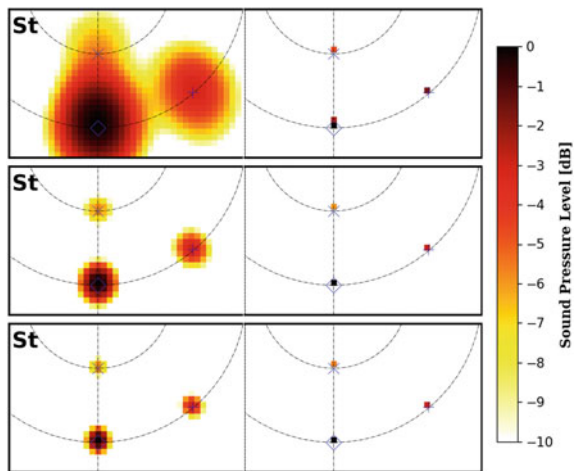
In general, none of these interpolation methods reconstructs precisely the spectrum, whether in terms of trend or strength. M2 is much precise among these interpolation methods. M3 and M4 perform poorly in terms of trends, while M5 and M7 perform poorly in terms of strengths.

4.3 Sound Source Location Precision

Figure 4 shows source maps of conventional beamforming and one deconvolution algorithms, CLEAN-SC for one-third octave band around $f = 2.0, 5.0$ and 8.0 kHz. Figures 5, 6 and 7 show reconstructed source maps of VRA beamforming and deconvolution algorithm CLEAN-SC for one-third octave band around $f = 2.0, 5.0,$ and 8.0 kHz, respectively. Diagonal removal is applied to the CSM.

For VRA beamformings with all interpolation methods, their maps are similar at a frequency. In Fig. 5, VRA beamformings with all interpolation methods have poor spatial resolution, and the locations of the third sound source are difficult to be distinguished. In Figs. 6 and 7, the locations of all the third sound source are distinguished easily, and thus the spatial resolutions of VRA beamformings with all interpolation methods improve obviously. Compared with the beamforming with stationary sound source at the same frequency, VRA beamforming map with each interpolation

Fig. 4 Conventional beamforming and CLEAN-SC maps, $f = 2.0, 5.0$ and 8.0 kHz from top to bottom. Left, conventional beamforming map; right, CLEAN-SC map



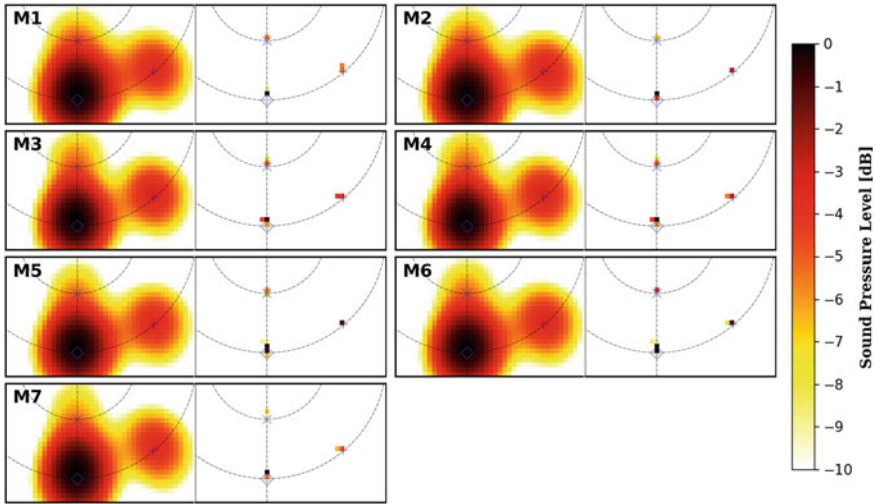


Fig. 5 VRA beamforming and CLEAN-SC maps, $f = 2.0$ kHz. Left, VRA beamforming map; right, CLEAN-SC map

method is not obviously different. This means that each interpolation method has acceptable sound source location precision. Comparing the spatial resolution, VRA beamforming with M5 is the best, even its superiority is subtle.

For CLEAN-SC with each interpolation method, it has better spatial resolutions than the corresponding VRA beamforming, and has estimated precisely all the sound source locations in Fig. 5. However in Figs. 6 and 7, the sound source location precisions of CLEAN-SC decrease obviously, especially for $f = 5.0$ kHz. One exception is the CLEAN-SC with M5.

Considering comprehensively the relative advantages in spatial resolution of VRA beamforming and CLEAN-SC, M5 is the best interpolation method.

4.4 Sound Source Strength Precision

Figures 8, 9 and 10 shows sound source strengths for one-third octave bands of CLEAN-SC from the first sound source to the third sound source. The sound source strength of CLEAN-SC is the summation of sound pressure level in a circle with a diameter of 0.10 m centered on the position of the set sound source. The reference sound source strength is the sound pressure level at the array center due to the sound source. All interpolation methods have poor performances of sound source strength precisions, whether in teams of trend or strength. Moreover, sound source strength

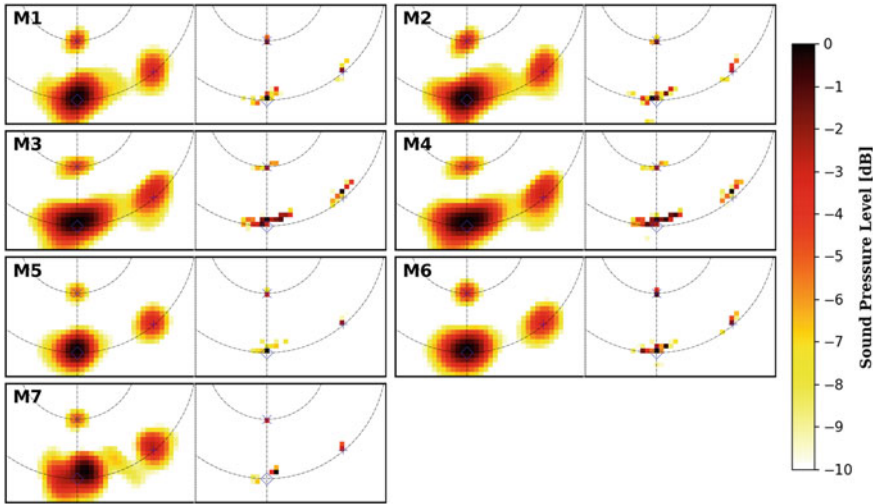


Fig. 6 VRA Beamforming and CLEAN-SC maps, $f = 5.0$ kHz. Left, VRA beamforming map; right, CLEAN-SC map

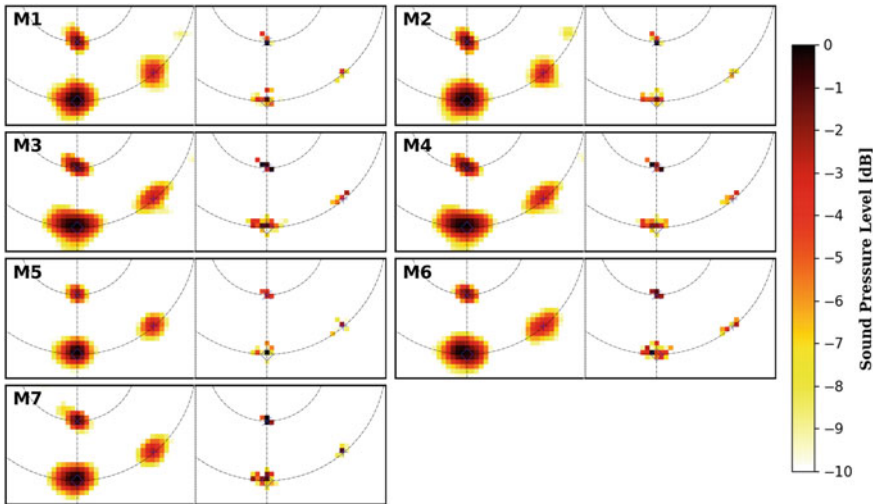


Fig. 7 VRA Beamforming and CLEAN-SC maps, $f = 8.0$ kHz. Left, VRA beamforming map; right, CLEAN-SC map

Fig. 8 Sound source strengths for one-third octave bands of CLEAN-SC for the first sound source

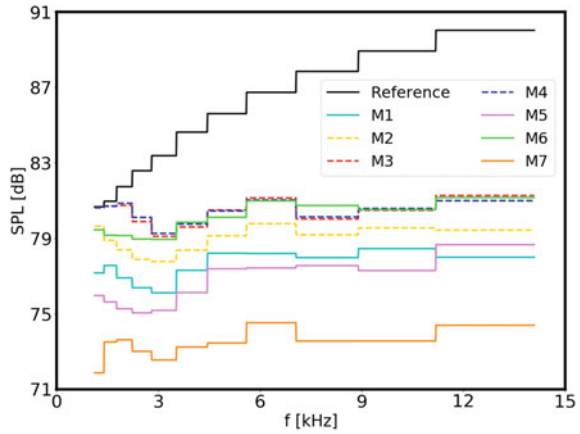
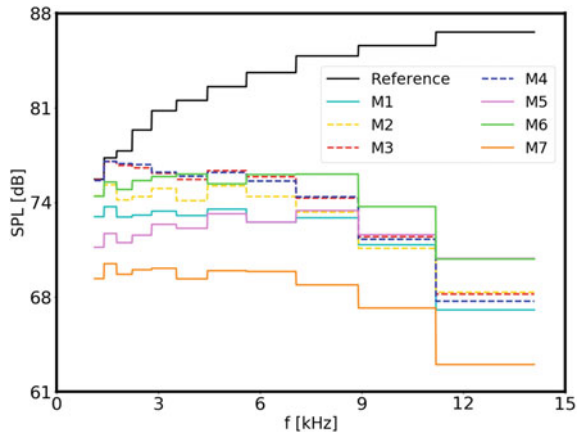


Fig. 9 Sound source strengths for one-third octave bands of CLEAN-SC for the second sound source



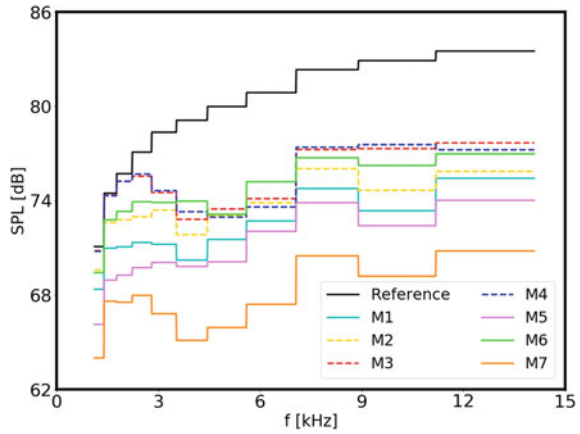
precisions decrease obviously for all interpolation methods at sources 1 and 2 when the frequency increases. M2, M3, M4, and M6 have relatively good performances. M7 behaves the worst.

5 Discussions

In this section, the interrogative sentences at the beginning of each paragraph will guide the discussion in that paragraph.

Why the sound source strength precisions decrease obviously when the frequency increases? Interpolation may smooth distribution fluctuation of pressure time signals. This phenomenon is more obvious when the frequency increases. Thus the error of interpolation is more obvious, and the sound source strength precisions decrease.

Fig. 10 Sound source strengths for one-third octave bands of CLEAN-SC for the third sound source



Why M5 (inverse distance weighting interpolation method) has the best sound source location precision among these methods? The sound source location precision depends on the precision of phase difference between each virtual microphone’s spectrum. Although M5 has poor performance on reconstructing the amplitude of spectrum, it may have good prediction on the phase difference between each virtual microphone’s spectrum.

What are the subsequent investigations in the future? Meshing interpolation method M1 just utilizes only three stationary microphones for reconstructing pressure time signals of virtual microphone. Therefore, whether meshless interpolation methods can only utilize finite neighboring stationary microphones for interpolation deserves to be further explored. Furthermore, the microphone geometry used in this paper is relatively of an uniform arrangement. Thus other geometries of arbitrary microphone configuration can also be a significant research object in VRA beamforming in the future.

6 Conclusions

In this paper, several new spatial interpolation methods are added in VRA beamforming. Performances of seven interpolation methods are detailedly compared for rotating source localization with arbitrary microphone configuration in simulations. All these interpolation methods are successfully applied in VRA beamforming with arbitrary microphone configurations. Inverse distance weighting interpolation method is highly recommended in VRA beamforming with arbitrary microphone configurations owing to its best performance in rotating sound source localization. Additionally, all these interpolation methods have poor spectrum construction capability and sound source strength precision.

Acknowledgements This work is supported by the National Science and Technology Major Project of China (2017-II-003-0015).

References

1. Brooks TF, Humphreys WM (2006) A deconvolution approach for the mapping of acoustic sources (damas) determined from phased microphone arrays. *J Sound Vib* 294:856–879. <https://doi.org/10.1016/j.jsv.2005.12.046>
2. Buhmann MD (2003) Radial basis functions: theory and implementations. Cambridge monographs on applied and computational mathematics. Cambridge University Press. <https://doi.org/10.1017/CBO9780511543241>
3. Cressie N (1990) The origins of kriging. *Math Geol* 22(3):239–252. <https://doi.org/10.1007/bf00889887>
4. Herold G, Ocker C, Sarradj E, Pannert W (2018) A comparison of microphone array methods for the characterization of rotating sound sources. In: Proceedings of the 7th Berlin beamforming conference, 5-6 March, 2018, Berlin, BeBeC-2018-D22 (2018), pp 1–12. <https://doi.org/10.3397/1/376348>
5. Herold G, Sarradj E (2015) Microphone array method for the characterization of rotating sound sources in axial fans. *Noise Control Eng J* 63(6):546–551. <https://doi.org/10.3397/1/376348>
6. Jekosch S, Sarradj E (2020) An extension of the virtual rotating array method using arbitrary microphone configurations for the localization of rotating sound sources. *Acoustics* 330–342 (2020). <https://doi.org/10.3390/acoustics2020019>
7. Lowis CR, Joseph P (2005) Inversion technique for determining the strength of rotating broadband sources in ducts. In: 11th AIAA/CEAS aeroacoustics conference (26th AIAA aeroacoustics conference), 23–25 May 2005, Monterey, AIAA 2005-3018. <https://doi.org/10.2514/6.2005-3018>
8. Lowis CR, Joseph P (2006) Determining the strength of rotating broadband sources in ducts by inverse methods. *J Sound Vib* 295:614–632. <https://doi.org/10.1016/j.jsv.2006.01.031>
9. Lu GY, Wong DW (2008) An adaptive inverse-distance weighting spatial interpolation technique. *Comput Geosci* 34(9):1044–1055. <https://doi.org/10.1016/j.cageo.2007.07.010>
10. Ma W, Bao H, Zhang C, Liu X (2020) Beamforming of phased microphone array for rotating sound source localization. *J Sound Vib* 467 (2020). <https://doi.org/10.1016/j.jsv.2019.115064>
11. Ma W, Liu X (2017) Damas with compression computational grid for acoustic source mapping. *J Sound Vib* 410:473–484. <https://doi.org/10.1016/j.jsv.2017.03.027>
12. Ma W, Liu X (2017) Improving the efficiency of damas for sound source localization via wavelet compression computational grid. *J Sound Vib* 395:341–353. <https://doi.org/10.1016/j.jsv.2017.02.005>
13. Ma W, Liu X (2018) Compression computational grid based on functional beamforming for acoustic source localization. *Appl Acoust* 134:75–87. <https://doi.org/10.1016/j.apacoust.2018.01.006>
14. Ma W, Zhang C (2020) Doppler effect in the time-domain beamforming for rotating sound source identification. *J Acoust Soc Am* 148(1):430. <https://doi.org/10.1121/10.0001570>
15. Merino-Martínez R, Sijtsma P, Snellen M, Ahlefeldt T, Antoni J, Bahr CJ, Blacodon D, Ernst D, Finez A, Funke S, Geyer TF, Haxter S, Herold G, Huang X, Humphreys WM, Leclère Q, Malgoezar A, Michel U, Padois T, Pereira A, Picard C, Sarradj E, Siller H, Simons DG, Spehr C (2019) A review of acoustic imaging methods using phased microphone arrays. *CEAS Aeronaut J* 10(1):197–230. <https://doi.org/10.1007/s13272-019-00383-4>
16. Michel U (2006) History of acoustic beamforming. In: Proceedings of the 1st Berlin beamforming conference, 21-22 November 2006, Berlin, BeBeC-2006-01, pp 1–17
17. Pannert W, Maier C (2014) Rotating beamforming - motion-compensation in the frequency domain and application of high-resolution beamforming algorithms. *J Sound Vib* 333(7):1899–1912. <https://doi.org/10.1016/j.jsv.2013.11.031>

18. Renka RJ, Renka R, Cline A (1984) A triangle-based c^1 interpolation method. *Rocky Mountain J Math* 223–237 (1984). <https://doi.org/10.1216/rmj-1984-14-1-223>
19. Sarradj E (2012) Three-dimensional acoustic source mapping with different beamforming steering vector formulations. *Adv Acoust Vib* 2012:1–12. <https://doi.org/10.1155/2012/292695>
20. Sarradj E (2016) A generic approach to synthesize optimal array microphone arrangements. In: *Proceedings of the 6th Berlin beamforming conference*, 29 February–1 March 2016, Berlin, BeBeC-2016-S4, p 4
21. Shepard D (1968) A two-dimensional interpolation function for irregularly-spaced data. In: *Proceedings of the 23rd ACM national conference*, 27–29 August 1968, pp 517–524. <https://doi.org/10.1145/800186.810616>
22. Sijtsma P (2007) Clean based on spatial source coherence. *Int J Aeroacoust* 6(4):357–374. <https://doi.org/10.1260/147547207783359459>
23. Sijtsma P, Oerlemans S., Holthusen H (2001) Location of rotating sources by phased array measurements. In: *7th AIAA/CEAS aeroacoustics conference and exhibit*, 28 - 30 May 2001, Maastricht, AIAA 2001-2167, pp 1–11. <https://doi.org/10.2514/6.2001-2167>

TH-DS-CDMA-Based Robust Frequency-Domain Signal Processing for GNSS Pseudolite Correlators



Yingchao Xiao, Wei Wang, Xin Zhang, and Xingqun Zhan

Abstract In order to build a seamless national PNT infrastructure based on Beidou system, the absence of Beidou in indoor environments has to be dealt with. Although there are other sensors and approaches to indoor positioning, they cannot be merged into Beidou system smoothly. As a ground transmitter that broadcasts GNSS-like signals, pseudolite has a promising future. Despite these superiorities, pseudolite signals more often than not suffer from joint effects of radio frequency interference and near-far problems. Previous work suggests frequency-domain interference mitigation can suppress jamming effectively while Time-Hopped Direct Sequence Code Division Multiple Access (TH-DS-CDMA) signaling is effective in near-far problem. However, there is little research considering both interference and near-far problem in pseudolite. For the purpose of solving these two problems simultaneously, a frequency-domain interference mitigation method based on TH-DS-CDMA within receiver correlators is proposed in this paper. An adaptive interference detection and mitigation method enabled by thresholding is used to separate the interference and signal in terms of signal power effectively. And the synchronization of TH sequence method called Time-Hopping Starting Index (THSI) is achieved according to the time interval of CDMA signals in different subframe. Simulation shows that the proposed interference mitigation method in frequency domain based on TH-DS-CDMA can effectively provide a stop gap for the combined influence of interference and near-far problem, and the receiver can complete signal acquisition and sequence synchronization successfully, which verifies the validity of the proposed algorithm.

Keywords Time-hopped · Pseudolite · Interference mitigation · Signal acquisition

Y. Xiao · X. Zhang (✉) · X. Zhan
School of Aeronautics and Astronautics Shanghai, Jiao Tong University, Shanghai, China
e-mail: xin.zhang@sjtu.edu.cn

W. Wang
China Satellite Navigation Office, Beijing, China

© The Author(s), under exclusive license to Springer Nature Singapore Pte Ltd. 2023
Z. Jing and D. Strelets (eds.), *Proceedings of the International Conference on Aerospace System Science and Engineering 2021*, Lecture Notes in Electrical Engineering 849,
https://doi.org/10.1007/978-981-16-8154-7_4

1 Introduction

Global Navigation Satellite System (GNSS) can provide global users with ubiquitous positioning and timing services. It has become the first choice of positioning and timing technology to cater for both civilian and military needs [16]. Beidou Navigation Satellite System is the cornerstone of China's synthetical PNT (Positioning, Navigation, and Timing) infrastructure. Compared to other navigation aids, it is the only technology and service system that can both accommodate (a) global positioning and navigation and (b) synchronization with Universal Time Coordinated (UTC). Beidou can't work indoors, since its proper operations depend on line of sight (LOS) between Beidou satellite (transmitter) and users (receiver). Although with the help of weak signal processing technology, indoor positioning with Beidou can be achieved near the window or other openings of the enclosed environment, the positioning accuracy, which typically is about several meters, is not up to the standard; it even loses positioning results in the deep indoor environment. Therefore, while the Beidou system is powerful, it cannot be used indoors. At present, indoor positioning technology is mainly based on a variety of devices such as Wi-Fi, Ultra-Wide Band (UWB), Inertial Measurement Unit (IMU), or physical phenomenon (sound, light, electricity, magnetism), and the positioning accuracy varies from centimeter to meter. It requires additional receiver costs (e.g., GNSS hardware in mobile phone cannot be used to process other wireless signals for indoor positioning purposed without alterations) to combine these indoor positioning technologies with Beidou system. Therefore, traditional indoor positioning technology may not be the best industrialization choice for non-perceptual switching with Beidou system. With this in mind, as a homologous (also known as isomorphic or homogeneous) scheme with the Beidou system, pseudolites have prominent advantages.

Conception of pseudolite existed even before the GPS is fully operational [9]. A pseudolite is a ground transmitter that broadcasts GNSS-like navigational signals to provide Positioning, Navigation and Timing (PNT) services across an area where satellite transmitted GNSS signals have limited coverage or are entirely unavailable. Pseudolites were initially applied to test the GPS receiver. After the successful construction of GNSS, pseudolites were used to solve the problem of satellite navigation in harsh environments [12]. However, whether it is a ground-based or space-based system, pseudolites suffer from serious near-far problem [24, 27]. Distance between GNSS satellites and receivers is more than 20,000 km, and the differential distance between pairs of visible satellite and receiver is not very large, so the received navigation signal power is roughly the same. Under this circumstance, the auto-correlation value of the PRN code is about 24 dB higher than the cross-correlation value, hence the receiver can distinguish different satellite signals and complete the signal acquisition and tracking. In contrast, the differential distance between pairs of pseudolites and receivers is much more remarkable, resulting in the totally different received signal power. Strong signal will seriously affect the acquisition and tracking of weak signal, leading to near-far problem. Therefore, the essence of near-far problem is that the auto-correlation peak of weak signals is less

than the cross-correlation peak of strong signals, which generates cross-correlation interference [22].

In addition to the near-far problem, there are all kinds of wireless communication devices which exist in every corner of modern life, and the mutual interference from different wireless channels also brings challenges to the applications of pseudolites [4].

With the improvement of the performance of GNSS, the research focus has gradually changed from improving the accuracy of positioning and timing to the interference mitigation technology. Up to now, the interference mitigation technology is still a hot research issue in the field of GNSS [13]. Although the DS-CDMA signal adopted by GNSS can provide protection against interference to a certain extent, when the interference is too strong, the receiver may not be able to complete the signal acquisition correctly, thus reducing the system performance [25, 30].

In terms of the interference mitigation, the common solution is to preprocess the received signal based on different characteristics and metrics between interference and signal before signal acquisition. Among all kinds of interference, the high-power narrowband interference has become one of the most common one. At present, there are many interference mitigation methods which can be divided into time domain and transformation domain to deal with narrowband interference. Estimation and elimination filtering is the most popular method in time domain. The principle is to predict the narrowband interference by the non-Gaussian property. The signal can be obtained by subtracting the predicted interference from received signal. Up to now, adaptive notch filtering is the most common time-domain interference mitigation method. Ma et al. proposed an all-pass notch filter to address CWI [23], Chien et al. proposed an adaptive notch filter to deal with interference [8], and Borio et al. used multi-pole notch filter to detect and remove interference [2].

The transformation domain interference mitigation methods focus on the frequency domain. FFT (fast Fourier transform) is used to analyze the spectrum of the received signal, and the interference mitigation is based on the different characteristics of interference and signals in frequency domain. When there is no interference in the received signals, the amplitude of the spectrum is flat. However, when there is narrowband interference in signals, the energy of the narrowband interference is concentrated around a small frequency band. So, it is easier to distinguish and remove the interference in frequency domain. Milstein first applied FFT to narrowband interference mitigation in spread spectrum communication [26], Borio et al. modeled the received signal as Laplace and Cauchy processing in transformation domain, and the zero-memory non-linearity (ZMNL) method was used to deal with the interference in transformation domain [1, 3].

To solve the near-far problem, the existing solutions include: (1) establishing a new CDMA modulation principle, that is, choosing PRN codes with smaller cross-correlation value and longer period [17] using frequency division multiple access (FDMA) technology, that is, different pseudolites broadcast navigation signals at different frequencies; and using time division multiple access (TDMA) or time-hopped technology, that is, different pseudolites broadcast navigation signals at different time periods [20].

Among the above solutions, TDMA is the most commonly used method against near-far problem because of low resource consumption and small changes in receiver architecture [19]. The Australian Locata system which is the most famous pseudolite system does use TDMA technology to reduce the effect of near-far problem [7]. In the signal acquisition of pseudolite based on TDMA, the synchronization of time-hopped sequence is a very essential problem. Only when the received signal is correctly aligned to subframes of the time-hopped sequence, the signal tracking and navigation message demodulation can be achieved and the function of positioning be completed. Because the time-hopped sequence is also a pseudorandom sequence, the synchronization of time-hopped sequence can be accomplished using correlation results. This method has been widely used in ultra-wide band (UWB) system and time-hopped radio system [11, 29].

However, for the pseudolite system, the symbol rate of time-hopped sequence is low, so the correlation method needs a lot of computing resources, resulting in a long synchronization time, which can't meet the requirements of real-time positioning. To solve this problem, Cheong proposed a Time-Hopping Starting Index (THSI) search algorithm [6]. By detecting the active timeslot in multiple subframes, the algorithm determines the starting index in time-hopping sequence, and finally completes the synchronization of the time-hopping sequence. Without considering the detection errors consisting of false alarms and missed detections, the algorithm can achieve a high synchronization accuracy as well as less computation.

Although there have been a lot of researches on interference mitigation in GNSS and TDMA signal in pseudolite, taking both of them into account, that is, the interference mitigation for pseudolite based on TDMA signal system is rare, thus the contributions of this paper are as follows:

- (1) Taking narrowband interference as typical interference, a transform domain interference mitigation scheme in correlators of receiver based on TDMA modulation is presented.
- (2) A time-hopping sequence synchronization scheme for TDMA signals is presented.
- (3) A complete software simulator is designed to verify the scheme with the existing open-source software receiver.

The remainder of this paper is organized as follows. Section 2 first describes the signal model and the strategies adopted for signal acquisition. Then the frequency-domain interference mitigation and time-hopping sequence synchronization scheme are given. The effectiveness of the scheme is verified through simulation in Sect. 3. Summary and conclusion are finally drawn in Sect. 4.

2 Robust Frequency-Domain Signal Processing for Pseudolite Based on TH-DS-CDMA

2.1 GNSS Signal and Acquisition

Without loss of generality, taking the GPS L1 signal as an example. After the received signal from antenna is filtered, down-converted, and digitized by the receiver front end, the output digital signal is [3]

$$y[n] = \sqrt{C}d(nT_s - \tau_0)c(nT_s - \tau_0) \cos(2\pi(f_{IF} + f_0)nT_s + \varphi_0) + \eta_{BB}[n], \quad (1)$$

where the notation $[n]$ is used to denote a discrete-time sequence which is sampled at the frequency $f_s = 1/T_s$, C is the useful received signal power, $d(\cdot)$ is the navigation message, $c(\cdot)$ is pseudorandom noise (PRN) code, τ_0 is the communication delay, f_0 is the Doppler frequency, φ_0 is the initial phase, f_{IF} is the intermediate frequency (IF), $\eta_{BB}[n]$ is modeled as an additive white Gaussian noise (AWGN) with variance $\sigma^2 = N_0 B_{R_x}$, where B_{R_x} is the front-end one-sided bandwidth and N_0 is the power spectral density (PSD) of the input noise.

Because of the good performance of auto-correlation and cross-correlation in PRN code, the PRN number and estimation of received signals' Doppler frequency and code delay can be obtained by comparing the correlation peak value with preset thresholds. Different forms of receivers can be referred to the detailed introduction by Kai [15].

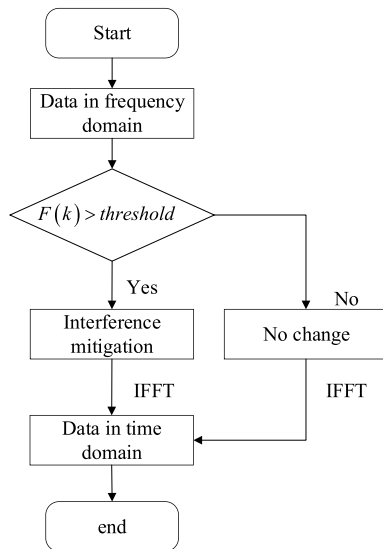
2.2 Frequency-Domain Interference Mitigation Algorithm

Although CDMA signaling is embedded with anti-interference capabilities, the receiver still cannot successfully complete the signal acquisition when the interference is strong enough. So, it is necessary to study the interference mitigation technology. In this paper, the frequency-domain narrowband interference mitigation algorithm is considered.

It is known from the characteristics of narrowband interference that the energy of narrowband interference is mainly distributed in some frequency points of the spectrum. At these frequency points, the interference is powerful, which will greatly influence the performance of the receiver. Therefore, it is necessary to detect and remove the interference before signal acquisition. The processing of frequency-domain interference mitigation is shown in Fig. 1.

The key point of frequency-domain interference mitigation technology is setting of interference detection threshold and interference mitigation scheme. At present,

Fig. 1 Processing of frequency-domain interference mitigation



the common thresholding includes N-Sigma algorithm [5], Consecutive Mean Excision (CME) [14], simplified interference mitigation algorithm [18], and so on. N-Sigma algorithm needs to observe the received signals for a period of time to get the characteristics of the distribution of the received signal, and then generates a reasonable threshold, which makes it complicated. The simplified interference mitigation algorithm is a simplified form of the CME. The algorithm only considers the statistical characteristics of the signal at the frequency points which are not influenced by narrowband interference. The previous calculation results of threshold are directly used in the next threshold calculation, and the weighted factor of the signal mean is set as a fixed value, so the iterative operation of each data block is cancelled, which reduces the computational complexity of the algorithm. The simplified interference mitigation algorithm is easy to implement and design, and therefore it is used to generate the detection threshold in this paper.

The distribution of received signal is Gaussian, whose mean and variance are zero and σ_n^2 , respectively. Since the Discrete Fourier Transform (DFT) is a linear transformation and each spectral line is a weighted sum of independent data, it follows Gaussian distribution with the mean value of zero and variance of $n\sigma_n^2$. The amplitude of the frequency spectrum line follows the Rayleigh distribution and the relationship between the distribution function and the mean value can be obtained as follows [18]:

$$F(x) = \int_0^x f(x)dx = 1 - e^{-\frac{\pi x^2}{4\mu^2}}, \quad (2)$$

where μ is the mean value. According to Eq. (2), if there is no interference, the amplitude of spectrum line which is less than 2μ and 3μ is about 95.68% and 99.91%, respectively. A fixed multiplying coefficient can be selected to generate the interference mitigation threshold according to the coverage ratio of the spectrum line. The selection criteria should take both interference mitigation and signal loss into consideration. Due to the existence of interference, the mean value of the whole spectrum line is affected. In order to get the mean value of the spectrum line as accurately as possible, the iteration is implemented. The mean value of the amplitude of spectral line at t is calculated as follows [18]:

$$\mu(t) = 7/8\mu(t-1) + 1/8 \sum_{k=1}^N A(k) / \sum_{k=1}^N S(k), \quad (3)$$

where $A(k)$ and $S(k)$ are the amplitude and the number of spectrum line which is not affected by interference this time, respectively.

After iterating and obtaining the desired interference detection threshold, the next step is interference mitigation. The simplest mitigation scheme is to set all spectral lines whose amplitude exceeds the threshold to zero. However, when the interference is removed, the amplitude and phase information of the signal at these frequency points will be eliminated as well, resulting in signal loss. Another common interference mitigation method is “threshold-clipping” technology [10, 18]. This method does not set the amplitude of spectral line that exceeds the threshold to zero directly, but decreases it according to the proportion between amplitude and threshold. The processed spectral line retains some amplitude and phase information at the frequency points that are polluted by interference, which reduces signal loss. The formula is as follows [18]:

$$\tilde{R}(k) = \begin{cases} R(k), & 0 \leq |R(k)| \leq H(t) \\ R(k)/8, & H(t) \leq |R(k)| \leq 8H(t) \\ R(k)/64, & 8H(t) \leq |R(k)| \leq 64H(t) \\ R(k)/512, & 64H(t) \leq |R(k)| \leq 512H(t) \\ R(k)/4096, & \text{others} \end{cases}, \quad (4)$$

where $R(k)$ is the spectrum sequence before interference mitigation and $\tilde{R}(k)$ is the spectrum sequence after narrowband interference mitigation.

Compared with M-Estimator [3], “threshold-clipping” technology does not model the received signal as a stochastic process such as Laplace or Cauchy processes and processes all the sampling values, but adopts an adaptive interference detection and mitigation method according to different threshold values. While the interference is removed, the useful signal is retained to the maximum extent, and the error which comes from modeling is reduced as much as possible.

2.3 TH-DS-CDMA Signal for Pseudolite

2.3.1 General TH-DS-CDMA Signal Model

The TH-DS-CDMA signals transmitted by pseudolites are generated by modulating the DS-CDMA signal, $s_{gnss}(t)$ by a pseudorandom TH gating signal $h(t)$.

The pseudorandom TH gating signal $h(t)$ is the dominant part in TH-DS-CDMA signal. It is a binary signal with values in the set $\{0, 1\}$, and it takes a value of one when the pseudolites broadcast signals, or it takes a value of zero. The pseudorandom TH gating signal $h(t)$ is obtained by periodically repeating a basic TH pattern $h_b(t)$ with a duration of T_b . Within a single TH pattern, the signal is divided into several subframes, and each subframe is also divided into several time slots with equal length. In each subframe, a pseudolite broadcasts the navigation signal only in one active time slot. The architecture of the TH-DS-CDMA signal is illustrated in Fig. 2 [20].

From Fig. 2, the TH pattern $h_b(t)$ is divided into N_b subframes, and the duration of each subframe is T_f . Each subframe is divided into N_f time slots, and the duration of each time slot is $T_s = T_f/N_f$. A pseudolite only broadcasts navigation signal in active time slot of a subframe, which effectively reduces the influence of near-far problem.

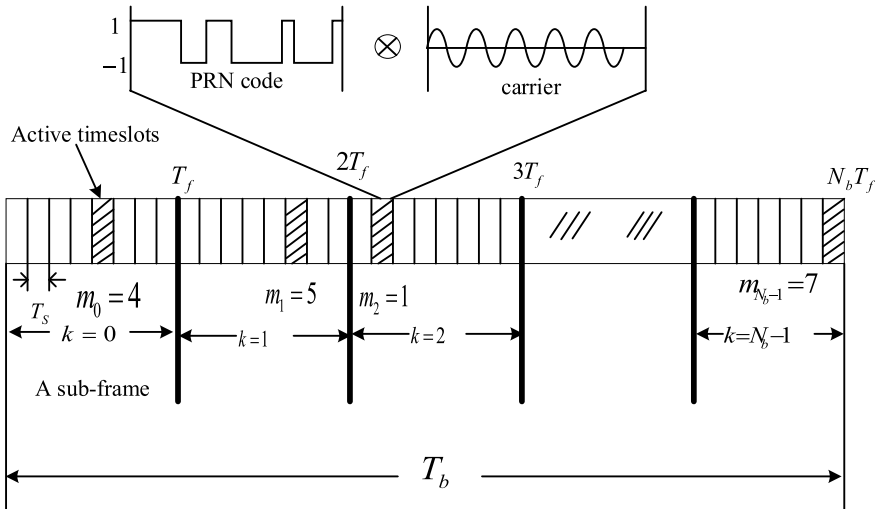


Fig. 2 The architecture of the TH-DS-CDMA signal

2.3.2 Synchronization of TH-DS-CDMA Signal

For TH-DS-CDMA signal, in addition to the signal acquisition and tracking, the synchronization of TH sequence is also essential. Since the TH sequence is a pseudorandom sequence, the synchronization of TH sequence can be achieved through correlation operation which is similar to the signal acquisition in GNSS receiver. However, the correlation operation needs a lot of computing resources to achieve synchronization because it has to deal with the whole sequence of one cycle. Besides that, in the whole sequence of one cycle, navigation signals only exist at the active time slot which results in a lot of computation waste. Therefore, the correlation method is generally not adopted in pseudolite to solve the synchronization problem of TH sequence. The THSI method, described before, can synchronize the whole TH sequence only through a few burst CDMA signal acquisition, which is the common method adopted in synchronizing TH sequence.

The process of THSI algorithm can be achieved as the following pseudocode in Fig. 3:

```

Function Find THSI
1:   For each timeslot TH-DS-CDMA signal acquisition
2:     If this is the first time of TH-DS-CDMA signal acquisition
3:       Let solution set  $F[k]$  equal to all the sub frame number
4:     Else
5:       Calculate the time slot interval  $hop[k]$  from the previous
           and compare it with the sequence to get new solution  $F_m[k+1]$ 
6:     Set the final solution  $F[k+1] = (F[k]+1) \cap F_m[k+1]$ 
7:     If the element number of solution  $c[k]$  equal to 1
           The number of current sub frame equal to  $F[k]$ 
8:     Break
9:     End
10:  End
11:  End

```

Fig. 3 The process of THSI algorithm

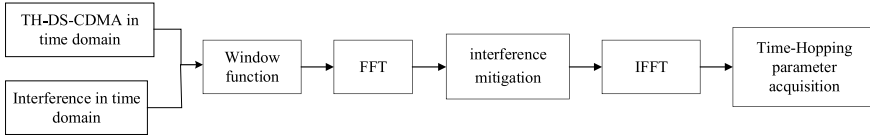


Fig. 4 Frequency-domain interference mitigation method based on TH-DS-CDMA signal

2.4 Robust Frequency-Domain Signal Processing for Pseudolite Based on TH-DS-CDMA

From the analysis of the previous sections, the process of frequency-domain interference mitigation method for pseudolite based on TH-DS-CDMA signal can be obtained which is shown in Fig. 4.

According to the algorithm flow chart, the steps of the method are as follows:

- (1) The time-domain TH-DS-CDMA signal which is polluted by interference needs to go through a window function. The purpose of window function is to cut off the time-domain signal for FFT. Different window functions will cause different spectrum leakage. The discussion on window functions is referred to [21]. And Hanning window function is directly used in this paper.
- (2) Obtain the signal in frequency domain through FFT.
- (3) Do interference detection and mitigation in frequency domain, and IFFT is carried out to obtain the time-domain signal after interference mitigation.
- (4) Conventional signal acquisition algorithm is used for acquisition of the signal which has been processed, and THSI method is used for sequence synchronization.

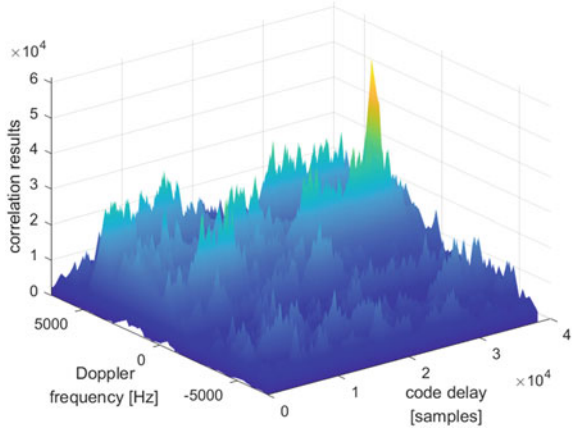
3 Simulation and Verification

The simulation adopts the single-tone interference model [28], and the simulation parameters are given in Table 1 [31].

Table 1 Simulation parameters

Parameters	Value
IF	9.548 MHz
Sampling rate	38.192 MHz
Code rate	1.023 MHz
Code length	1023
Doppler frequency	1000 Hz
Interference frequency	8.548 MHz
Ratio of interference power to signal	50 dB

Fig. 5 The acquisition results without interference mitigation under lower interference



When the receiver does not adopt interference mitigation technology, the acquisition results are shown in Fig. 5.

It can be seen from the results that the signal acquisition fails due to the influence of interference. When the interference mitigation algorithm is adopted, the acquisition results are shown in Fig. 6.

It can be seen from the results that the receiver successfully completes the signal acquisition. Increase the power of interference and make the ratio of interference power to signal at the value of 60 dB. The results are shown in Figs. 7 and 8.

It can be seen from the above simulation results that when the signal is polluted by narrowband interference, the interference will greatly influence the receiver, and the signal acquisition fails. When the interference is removed, the influence is greatly reduced, and the receiver can successfully complete the signal acquisition. The simulation results of different interference power indicate that when the interference power is small (the ratio between interference power and signal is 50 dB), there exists a peak

Fig. 6 The acquisition results with interference mitigation under lower interference

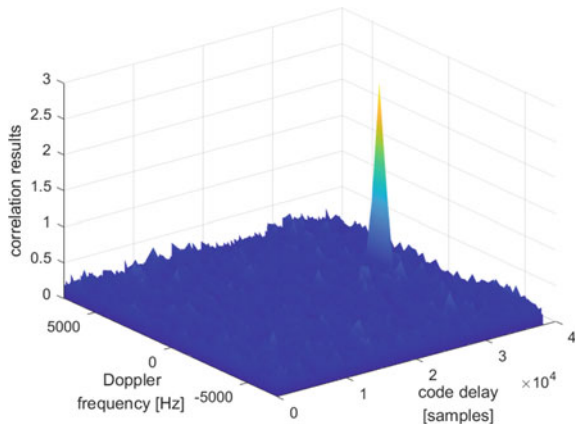


Fig. 7 The acquisition results without interference mitigation under higher interference

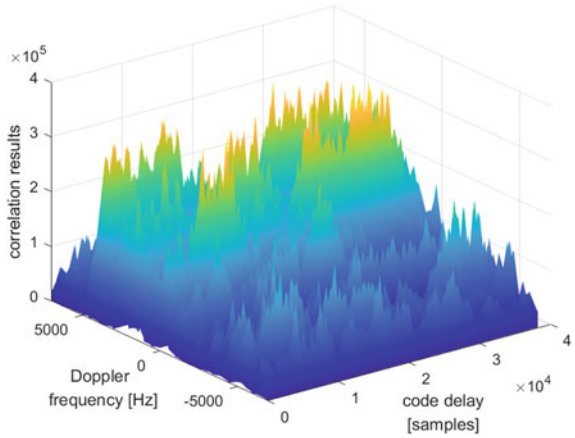
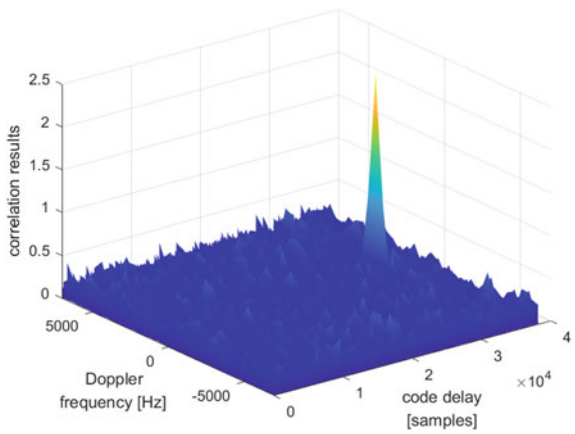


Fig. 8 The acquisition results with interference mitigation under higher interference



in correlation results, but did not exceed the threshold. When the interference power is larger, the signal is completely polluted by interference, resulting in no correlation peak. This also illustrates that although DS-CDMA signal can suppress interference to some extent, when the interference is large, an interference mitigation method is necessary to make sure to complete the signal acquisition correctly.

In order to verify the synchronization performance of the time-hopped sequence, the sequence is set to start at different subframes, and the simulation parameters are shown in Table 2, 3 and 4.

Comparing the simulation results with the original pseudorandom sequence, it can be seen that in the case of 20 subframes, the synchronization of TH sequence can be achieved by completing the burst CDMA signal acquisition up to three times. Since each subframe is divided into 10 time slots with the duration of 1 ms, it takes 30 signal acquisition to achieve sequence synchronization at most. However, the sequence synchronization algorithm based on correlation operation needs 200

Table 2 “Time-Hopped” gate function parameters

Parameters	Value
Signal cycle	200 ms
Total number of subframe	20
Timeslot length	1 ms

Table 3 Pseudorandom “Time-Hopped” gate function

Subframe	Timeslot	Subframe	Timeslot
1	1	11	1
2	3	12	4
3	5	13	9
4	10	14	8
5	10	15	10
6	2	16	7
7	10	17	1
8	10	18	8
9	5	19	9
10	8	20	7

Table 4 Simulation results of sequence synchronization

Start subframe no.	Signal acquisition no.	Current subframe no.
1	3	3
2	3	4
3	3	5
7	3	9
10	2	11
12	3	14
15	2	16
18	2	19

signal acquisition to synchronize the sequence, which cannot meet the real-time requirements. When the number of subframes is much larger, THSI method can significantly reduce the calculation while ensuring the synchronization accuracy, which verifies the correctness and effectiveness of the THSI method.

4 Conclusion

In this paper, the frequency-domain interference mitigation method based on TH-DS-CDMA signal for pseudolites is presented to solve near-far and interference problem. Firstly, the application background of pseudolites is introduced and shows that pseudolites can effectively address the shortage of large error under harsh environment in GNSS. Considering the interference and near-far problem in pseudolite, it is pointed out that the frequency-domain interference mitigation based on TH-DS-CDMA signal modulation can effectively reduce the influence them. Then the frequency-domain interference mitigation and synchronization of time-hopped sequence methods are given. Finally, simulation results based on MATLAB show that the frequency-domain interference mitigation method based on TH-DS-CDMA signal modulation can reduce the influence of narrowband interference and near-far problem in pseudolite well, which verifies the effectiveness of the proposed method.

References

1. Borio D (2017) Myriad non-linearity for GNSS robust signal processing. *IET Radar Sonar Navig* 11:1467–1476
2. Borio D, Camoriano L, Presti LL (2008) Two-pole and multi-pole notch filters: a computationally effective solution for GNSS interference detection and mitigation. In: *International conference on telecommunications*, pp 38–47
3. Borio D, Closas P (2019) Robust transform domain signal processing for GNSS. *Navigation* 66:305–323
4. Borio D, Dovis F, Kuusniemi H, Presti LL (2016) Impact and detection of GNSS jammers on consumer grade satellite navigation receivers. *Proc IEEE* 104:1233–1245
5. Capozza PT, Holland BJ, Hopkinson TM, Landrau RL (2000) A single-chip narrow-band frequency-domain excisor for a Global Positioning System (GPS) receiver. *IEEE J Solid-State Circuits* 35:401–411
6. Cheong JW, Dempster AG, Wayn J (2009) Detection of time-hopped DS-CDMA signal for Pseudolite-based positioning system. In: *Proceedings of international technical meeting of the satellite division of the institute of navigation*, pp 881–891
7. Cheong JW, Wei X, Politi N, Dempster AG, Rizos C (2009) Characterising the signal structure of Locata's Pseudolite-based positioning system. In: *Symposium on GPS/GNSS (IGNSS2009)*
8. Chien YR (2017) Design of GPS anti-jamming systems using adaptive notch filters. *IEEE Syst J* 9:451–460
9. Cobb HS (1997) *GPS pseudolites: theory, design, and applications*. Stanford University
10. Dipietro RC (1989) An FFT based technique for suppressing narrow-band interference in PN spread spectrum communications systems. In: *International conference on acoustics, speech, and signal processing*, pp 1360–1363
11. Fishler E, Poor HV (2004) Low-complexity multiuser detectors for time-hopping impulse-radio systems. *IEEE Trans Signal Process* 52:2561–2571
12. Gan X, Yu B, Wang X, Yang Y, Wang B (2019) A new array pseudolites technology for high precision indoor positioning. *IEEE Access* 7:153269–153277
13. Gao GX, Sgammini M, Lu M, Kubo N (2016) Protecting GNSS receivers from jamming and interference. *Proc IEEE* 104:1327–1338
14. Henttu P, Aromaa S (2002) Consecutive mean excision algorithm. In: *IEEE seventh international symposium on spread spectrum techniques and applications*, vol 2, pp 450–454

15. Kai B, Akos D (2007) A software-defined GPS and galileo receiver: single-frequency approach. Springer Science & Business Media
16. Leick A, Rapoport L, Tatarnikov D (2015) GNSS positioning approaches. John Wiley & Sons Inc.
17. Li TH, Liu JS, Huang ZG, Qin HL (2010) A solution of the near-far effect based on the orthogonality of pseudolite signal. *J Electron Inf Technol* 32:1366–1369
18. Liang JY, Liu HJ, Liang XW, Yang GQ (2004) A simplified method for narrowband interference suppression in satellite spectrum-spread communication. *J Circuits Syst* 9:86–89
19. Liu X (2017) Research on signal design method of pseudolite “Near-Far Effect” based on TDMA technique. In: China satellite navigation conference. Springer, pp 417–429
20. Liu X, Yao Z, Lu M (2021) Robust time-hopping pseudolite signal acquisition method based on dynamic Bayesian network. *GPS Solut* 25:1–14
21. Liu Y (2016) Research and implementation of narrowband interference suppression in satellite navigation system. University of Electronic Science and Technology of China
22. Liu Y, Qin H, Jin T (2011) Threshold setting method for GPS signal acquisition under cross-correlation effect. *J Beijing Univ Aeronaut Astronaut* 37:268–273
23. Ma WJ, Mao WL, Chang FR (2005) Design of adaptive all-pass based notch filter for narrowband anti-jamming GPS system. In: International symposium on intelligent signal processing and communication systems, 2005, pp 305–308
24. Madhani PH, Axelrad P, Krumvieda K, Thomas J (2003) Application of successive interference cancellation to the GPS pseudolite near-far problem. *IEEE Trans Aerosp Electron Syst* 39:481–488
25. Meng X, Liu M, Wang X (2019) Research on narrow band interference resistance of DSSS system assisted by interference suppression technology. *Space Electronic Technology*.
26. Milstein L, Das P (1980). An analysis of a real-time transform domain filtering digital communication system—part II: wide-band interference rejection. *IEEE Trans Commun* 31:21–27
27. Picois AV, Samama N (2014) Near-far interference mitigation for pseudolites using double transmission. *IEEE Trans Aerosp Electron Syst* 50:2929–2941
28. Rusch LA, Poor HV (1994) Narrowband interference suppression in CDMA spread spectrum communications. *IEEE Trans Commun* 42:1969–1979
29. Shao H, Beaulieu NC (2011) Direct sequence and time-hopping sequence designs for narrowband interference mitigation in impulse radio UWB systems. *IEEE Trans Commun* 59:1957–1965
30. Tan X, Su S, Sun X (2020) Research on narrowband interference suppression technology of UAV network based on spread spectrum communication. In: 2020 IEEE international conference on artificial intelligence and information systems (ICAIS). IEEE, pp 335–338
31. Yang F (2019) Research of narrowband interference suppression technology for beidou satellite navigation receiver. Beijing Jiaotong University

An Investigation on Rotating Stall in an Aeroengine Transonic Compressor with Inlet Distortion



Zhongyu Zhu and Xiaohua Liu

Abstract The internal flow stability of the compressor in the aeroengine has always been the top priority for the development of the aviation industry. Rotating stall is one of the most common instability problems in compressors, and stall margin is also an important parameter to measure the aerodynamic performance of compressors. In an actual compressor, it is difficult to achieve an ideal uniform inlet air condition, and inlet distortion will affect the operating conditions of the compressor. In this paper, a three-dimensional simulation of rotor 37 is conducted to study the development process of circumferential distortion and the aerodynamic performance of the compressor. The research results show that as the backpressure increases in the channel corresponding to the circumferentially distorted area, the blockage will occur first, and it will develop in the whole channel, leading to a complete stall. From the perspective of aerodynamic performance, circumferential distortion has an impact on stall margin and adiabatic efficiency, and different types of circumferential distortion have different effects on aerodynamic performance.

Keywords Rotating stall · Circumferential distortion · Numerical simulation

1 Introduction

As one of the core components of aeroengine, compressor is the main component that provides thrust. The problems of flow stability inside compressor seriously limit the development of aeroengine. In fact, every major breakthrough in aeroengine technology is closely related to the breakthrough in compression technology. Therefore,

Z. Zhu · X. Liu (✉)
Shanghai Jiao Tong University, Shanghai, China
e-mail: Xiaohua-Liu@sjtu.edu.cn

Z. Zhu
e-mail: zzy123@sjtu.edu.cn

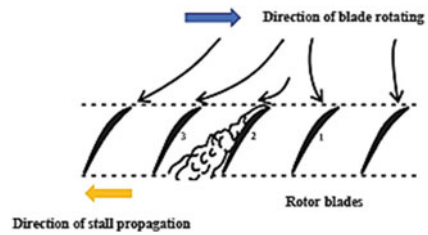
Key Laboratory (Fluid Machinery and Engineering Research Base) of Sichuan Province, Chengdu, China

in the pursuit of high-pressure ratio and high efficiency, it is very necessary to ensure the stable operation of the compressor under various conditions. The corresponding quantity reflecting the stable working range of the compressor is the stall margin. Stall margin is one of the important indicators to measure the design of a compressor. It not only reflects the performance of the compressor, but also determines whether it can be actually used.

The unsteady flow stability problem in compressor mainly includes surge and rotating stall. These unstable conditions will cause the rotor to break away from the original speed, reduce the pressure ratio and efficiency, and even cause the damage of the blade and compressor. In terms of rotating stall, researchers mainly focused on theoretical research and engineering applications. On the one hand, from the perspective of theoretical research, since the 1950s, a large number of scholars at home and abroad began to study this problem [1]. They mainly focused on the development process of stall mass, trying to explain the stall phenomenon from a theoretical point of view. The size of the stall group, the propagation speed, and the hysteresis of exiting the stall after the stall are the hotspots of research. On the other hand, in the actual process, people are more concerned about how to determine the stable working range of a compressor, that is, accurately predict the starting position of the stall. CFD steady calculations converge to obtain a specific flow pattern, and it is stable only under certain small disturbances. In order to be able to adapt to various disturbances, researchers began to seek new stability models [2]. The new stall stability model is based on the theory of small disturbances. It is believed that the compressor's response to small disturbances in the flow field develops linearly before stalling. On this basis, two-dimensional and three-dimensional models for different environments are developed [3]. In the numerical simulation of inlet distortion, considering the complexity of the flow field in the actual compressor, the numerical simulation of inlet distortion is actually difficult to completely restore. Therefore, people often only choose total pressure, total temperature, or swirl flow as a specific type of distortion, and then set the distortion area and distortion intensity, and then study the aerodynamic performance of the compressor under the distortion.

Till now, with the advancement of science and technology, people's research on rotating stalls and the observation of phenomena have deepened the discussion of its internal mechanism and prediction methods. The capture of spike-type stalls has become more and more along with the development of sampling technology. In terms of numerical simulation, with the development of CFD software and computer performance, researchers have become more and more reducible to the real working conditions of the compressor, and the calculation speed and accuracy have been significantly improved. This article aims to explain the phenomenon and principle of rotating stall and inlet distortion. Based on ANSYS-CFX, the ROTOR37 is numerically simulated. We observed the development process of stall under the condition of circumferential distortion, and the aerodynamic performance of the compressor half-stage is also studied.

Fig. 1 Schematic diagram of rotating stall principle



2 The Phenomenon of Rotating Stall and Inlet Distortion

2.1 Rotating Stall

When the speed is constant and the airflow is reduced, the angle of attack of the rotor blades will increase. When the airflow is reduced to a certain level, an unstable flow will be observed, and the compressor will make a special cry and the vibration will increase [4]. The flow field measured behind the moving blade shows that there are one or more low-speed airflow zones rotating along the rotating direction of the moving blade at a certain speed. This unstable condition is called a rotating stall. In other words, Rotational stall is a localized disruption of airflow within the compressor, which continues to deliver compressed air, but at a lower efficiency. Rotational stall is an example of compressor instability that can have catastrophic consequences for an aircraft engine. Jammed airfoils create pockets of relatively stagnant air (called stall cells) that rotate around the circumference of the compressor instead of moving in the direction of flow. The stall cells rotate with the rotor blades, but at a speed of 50–70% of their speed, acting on subsequent aerodynamic surfaces around the rotor when each of them collides with the stall cell. The propagation of instability around the annular space of the flow path is caused by blockage of the stall cell, causing a blowout to an adjacent blade. The adjacent vane is stopped by the shock of the fall, causing the stall cell to “spin” around the rotor [5], as is shown in Fig. 1.

2.2 Inlet Distortion

In a broad sense, for a single component or engine, all inlet conditions that deviate from the uniform and steady state can be regarded as inlet distortion [6]. Inlet distortion will cause the relevant components and the engine to deviate from the expected operating point.

From the perspective of the non-uniform distribution of aerodynamic parameters, the inlet distortion can be roughly divided into four types: total pressure distortion, total temperature distortion, swirl distortion, and rotation distortion. In the actual process, the measurement of the aerodynamic non-uniformity at the inlet section is much more convenient than the measurement of the aerodynamic parameters at the

inlet of the blade row or between the stages. The total temperature and total pressure usually do not change much during the airflow transmission along the inlet, so in engineering, total temperature and total pressure are usually selected as the basis for judging distortion.

Total pressure distortion is the most common and most studied distortion method. Total temperature distortion generally occurs in military aircraft and is usually caused by the inhalation of high-temperature exhaust gas. Swirl distortion is usually caused by the secondary flow caused by the turning of the inlet [7]. When flowing in a curved pipe, it is subject to centrifugal force. The centrifugal force points to the outside of the curved pipe. Therefore, when the fluid flows along the axis of the pipe, it will also flow to the outside of the curved pipe under the action of centrifugal force. The centrifugal force is also large, so it flows outward at a higher secondary flow velocity; rotation distortion usually occurs in multi-stage or multi-axis compressors. When the upstream blade row stalls, the stall group spreads circumferentially. The blade row is a kind of circumferential total pressure distortion. For the convenience of research, the distortion is usually artificially divided into radial distortion and circumferential distortion. Radial distortion means that the aerodynamic parameters only change in the radial direction and are uniform in the circumferential direction. The circumferential distortion is just the opposite, as shown in Fig. 2. Strictly speaking, the actual situation is usually a compound distortion of these two kinds [8].

For different types of inlet distortion, researchers have invested a lot of energy in experimental exploration. In the actual experimental operation, the researchers designed various forms of distortion generators, as shown in the following Fig. 3

Fig. 2 Schematic diagram of F radial distortion and circumferential distortion **a** Radial distortion, **b** Circumferential distortion

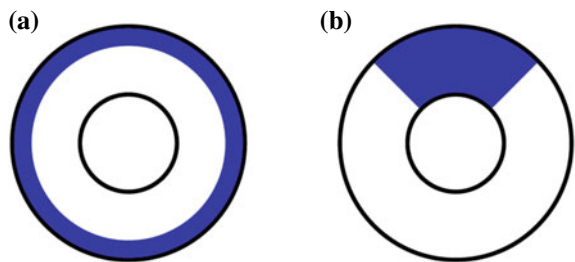
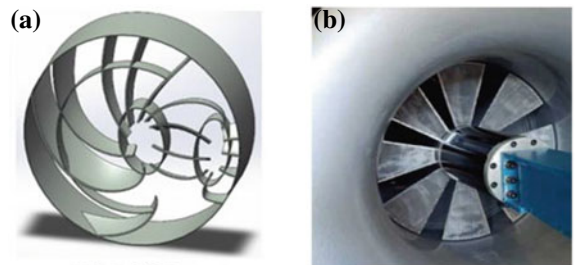


Fig. 3 Common distortion generator [9] **a** swirl distortion generator, **b** rotating distortion generator



[9], and installed them in different positions of the engine to simulate the different distortion conditions encountered during the operation of the compressor.

3 Governing Equations and Turbulence Models

3.1 Governing Equations

This paper adopts the Navier–Stokes equation of Reynolds average, which can be expressed as

$$\frac{\partial}{\partial t} \int_{\Omega} U d\Omega + \int_S \vec{F}_I \cdot d\vec{S} + \int_S \vec{F}_V \cdot d\vec{S} = \int_{\Omega} S_T d\Omega, \quad (1)$$

where Ω represent volume, S represent square, U represent the conserved parameter, \vec{F}_I and \vec{F}_V , respectively, represent inviscid vector flux and viscous vector flux. S_T is the source term, and its expression is

$$U = \begin{bmatrix} \rho \\ \rho v_1 \\ \rho v_2 \\ \rho v_3 \\ \rho E \end{bmatrix}, \quad F_{li} = \begin{bmatrix} \rho v_i \\ \rho v_1 v_i + p \delta_{1i} \\ \rho v_2 v_i + p \delta_{2i} \\ \rho v_3 v_i + p \delta_{3i} \\ (\rho E + p) v_i \end{bmatrix}, \quad F_{vi} = - \begin{bmatrix} 0 \\ \tau_{i1} \\ \tau_{i2} \\ \tau_{i3} \\ q_i + v_j \tau_{ij} \end{bmatrix}, \quad S_T = \begin{bmatrix} 0 \\ \rho f_{e1} \\ \rho f_{e2} \\ \rho f_{e3} \\ W_f \end{bmatrix}, \quad (2)$$

where the total energy and heat flux can, respectively, be expressed as

$$E = e + \frac{1}{2} v_i v_i \quad (3)$$

$$q_i = \kappa \frac{\partial}{\partial x_i} T. \quad (4)$$

In the above formula, κ is the laminar heat transfer coefficient, ρf_{e1} , ρf_{e2} , ρf_{e3} are the components of the external force \vec{f}_e , and W_f is the work done by the external force.

$$W_f = \rho \vec{f}_e \cdot \vec{v}. \quad (5)$$

In order to close the Navier–Stokes equation, the definition of the shear stress tensor must be given according to other flow variables. Only Newtonian fluid is

considered here, and its shear stress tensor is given by

$$\tau_{ij} = \mu \left[\left(\frac{\partial v_j}{\partial x_i} + \frac{\partial v_i}{\partial x_j} \right) - \frac{2}{3} (\nabla \cdot \vec{v}) \delta_{ij} \right]. \quad (6)$$

Among them, μ is the viscosity coefficient, and δ_{ij} is the Kronecker symbol.

$$\delta_{ij} = \begin{cases} 0, & \text{if } i \neq j \\ 1, & \text{if } i = j \end{cases}. \quad (7)$$

3.2 Turbulence Models

The turbulence model is based on the time-averaged Navier–Stokes equation. In the numerical calculation process, different turbulence models will get different results. Therefore, it is necessary to select a suitable turbulence model according to actual needs. Commonly used turbulence models include Baldwin–Lomax zero equation model, Spalart–Allmaras one equation model, SARC one equation model, k-epsilon two-equation model, SST two-equation model, k-omega two-equation model, v2-f four equation model, and EARSM algebraic Reynolds stress model. In this paper, the Spalart–Allmaras (S-A) one equation model is selected for numerical calculation.

The S-A turbulence model is based on the solution of the vortex viscous migration equation, can handle more complex flows, has good robustness, and has low CPU and memory requirements. In 1992, Spalart and Allmaras [10] proposed the solution process of the S-A turbulence model. In 1996, Ashford and Powell [11] supplemented the theory.

The turbulent viscosity coefficient of the S-A model is

$$\nu_t = \tilde{\nu} f_{v1} \quad (8)$$

Among them, $\tilde{\nu}$ is the turbulence working variable, f_{v1} is defined as follows:

$$f_{v1} = \frac{\chi^3}{\chi^3 + c_{v1}}. \quad (9)$$

Among them, χ is the ratio of the turbulent working variable $\tilde{\nu}$ to the molecular viscosity ν

$$\chi = \frac{\tilde{\nu}}{\nu}. \quad (10)$$

The turbulent working variable $\tilde{\nu}$ obeys the migration equation shown below.

$$\frac{\partial \mathbf{v}}{\partial t} + \tilde{\mathbf{V}} \cdot \nabla \tilde{\mathbf{v}} = \frac{1}{\sigma} \left\{ \nabla \cdot [(\mathbf{v} + (1 + c_{b2})\tilde{\mathbf{v}})\nabla \tilde{\mathbf{v}}] - c_{b2}\tilde{\mathbf{v}}\Delta \tilde{\mathbf{v}} \right\} + S_T. \quad (11)$$

Among them, σ , c_{b2} are constants, \mathbf{V} is the velocity vector, S_T is the source term, and the source term includes the generation term S_T and the dissipation term f_w .

$$S_T = \tilde{\mathbf{V}} P(\tilde{\mathbf{v}}) - \tilde{\mathbf{V}} D(\tilde{\mathbf{v}}). \quad (12)$$

Inside the equation:

$$\tilde{\mathbf{v}} P(\tilde{\mathbf{v}}) = c_{b1} S \tilde{\mathbf{v}} \quad (13)$$

$$\tilde{\mathbf{v}} D(\tilde{\mathbf{v}}) = c_{w1} f_w \left(\frac{\tilde{\mathbf{v}}}{d} \right)^2. \quad (14)$$

The generating term P is related to the following formula.

$$\tilde{S} = S f_{v3} + \frac{\tilde{\mathbf{V}}}{k^2 d^2} f_{v2} \quad (15)$$

$$f_{v2} = \frac{1}{(1 + \chi/c_{v2})^3} \quad (16)$$

$$f_{v3} = \frac{(1 + \chi f_{v1})(1 - f_{v2})}{\chi}. \quad (17)$$

Among them, d is the minimum distance from the wall, and S is the vortex intensity. The dissipation term f_w is

$$f_w = g((1 + c_w 3^6)/(g^6 + c_w 3^6))^{(1/6)}. \quad (18)$$

Inside the equation:

$$g = r + c_{w2}(r^6 - r) \quad (19)$$

$$r = \frac{\tilde{\mathbf{v}}}{\tilde{S} k^2 d^2}. \quad (20)$$

The constant term in the model is

$$c_{w1} = \frac{c_{b1}}{k^2} + \frac{(1 + c_{b2})}{\sigma}, c_{w2} = 0.3, c_{w3} = 2, c_{v1} = 7.1, c_{v2} = 5, \\ c_{b1} = 0.1355, c_{b2} = 0.622, k = 0.41, \sigma = 2/3. \quad (21)$$

4 Numerical Simulation of Circumferential Distortion

4.1 Compressor Description

Rotor37 is a transonic compressor rotor designed by NASA-Lewis Research and Design Center. Uder et al. [12] conducted a detailed experimental test on this rotor. The test measurement position is shown in Fig. 4. The flow results (Table 1) used in this paper are taken from the position 1 and 4.

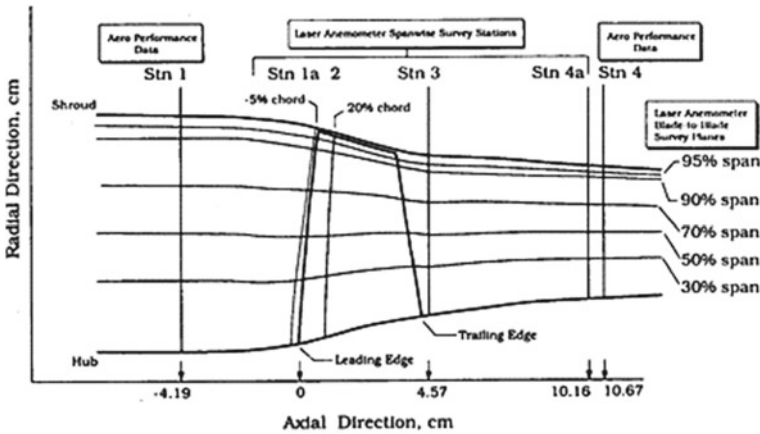


Fig. 4 Positions of measurement station of Rotor37 [14]

Table 1 Main design parameters of Rotor37 [13]

Parameter	Value
Blade number	36
Hub-tip ratio	0.7
Aspect ratio	1.19
Tip consistency	1.29
Rotor tip clearance (mm)	0.356
Rotational speed (r/min)	17,188
Tip tangential velocity (m/s)	454.14
Total pressure ratio	2.106
Total temperature ratio	0.877
Design point mass flow (kg/s)	20.19
Choking point mass flow (kg/s)	20.93

4.2 Computational Mesh and Boundary Conditions

The simulation of this paper was conducted by the commercial computational fluid dynamics software ANSYS-CFX. In order to meet the characteristics of uneven circumferential distortion in the circumferential direction, we have selected the full passage as the calculation domain for numerical calculation, as is shown in Fig. 5. The applied grid consists of 14,400,000 nodes. There are 44 nodes in blade spanwise direction including 7 nodes in blade tip clearance. The grid topology is of HOH-type, with the O-type mesh generated around the rotor and the H-type mesh in inlet and outlet. In order to meet the requirement of S-A turbulence model, the y^+ adjacent to the solid wall was set as 5. To verify the feasibility of the calculation grid, we compared the steady flow calculation results under this grid setting method with the experimental data. It can be found that the calculated results under this grid condition are very close to the actual experimental results, as is shown in Fig. 6. Due to the limitation of calculation conditions, we can think that this kind of 14,400,000-node grid can more accurately reflect the situation of the flow field.

As for the design of circumferential distortion, two different circumferential distortions are designed for comparison. The first case is to simulate the situation

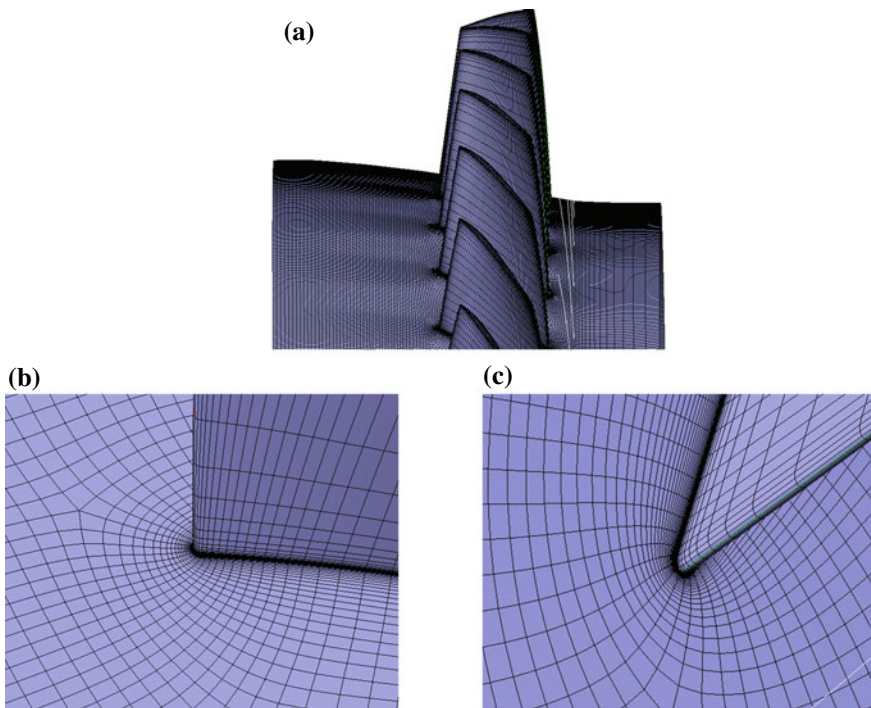


Fig. 5 Different perspectives of the computing grid

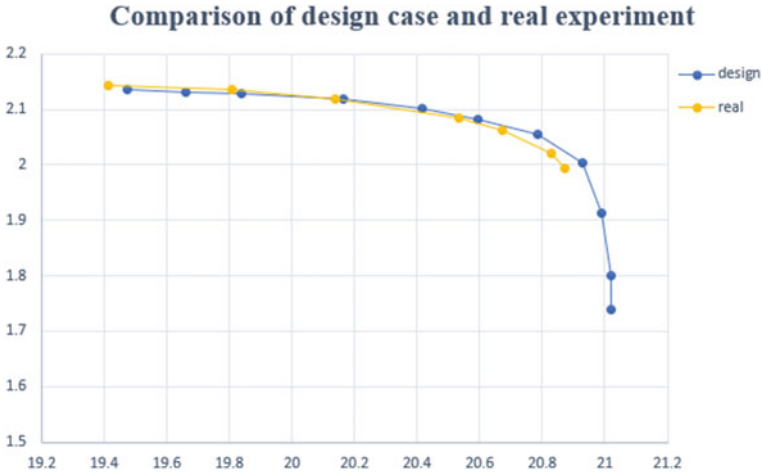


Fig. 6 Comparison of design case and real experiment

of inserting the baffle in the actual experiment. The comparison between the experimental equipment and the numerical simulation effect is shown in Fig. 7. The other case is related to distortion angle. In order to control the area of the two cases to be equal, through calculation, we set the distortion angle as 67.7° , as is shown in Fig. 8. In both cases, the distortion intensity of the distortion area is 2500 Pa. Moreover, we will call these two cases flashboard distortion and angle distortion in the rest part of this paper.

4.3 Influence on Compressor Performance

Figure 9 shows the characteristic line and isentropic efficiency of ROTOR37 with a distorted inlet. From the comparison chart, we can clearly find that the influence of the circumferential distortion on the aerodynamic performance of the two cases is similar. Circumferential distortion has attenuated the flow rate and total pressure ratio of the blocking point, and the flow position of the peak efficiency point of the adiabatic efficiency has also moved downward. It can be found that the adiabatic efficiency also has a small drop, but it may not be very obvious due to the distortion area and even if the length is not large enough. At the same time, comparing the circumferential distortion data in the two cases, it can be found that the plug-in circumferential distortion has a greater impact on the efficiency, and the efficiency at the peak is about 0.03% less than the angle distortion. The stall margin of angle circumferential distortion is 10.686%, and the stall margin of insert plate distortion is 11.144%, which is about 0.5% higher than the former. Therefore, it can be inferred

Fig. 7 Comparison of the experiment and the numerical simulation

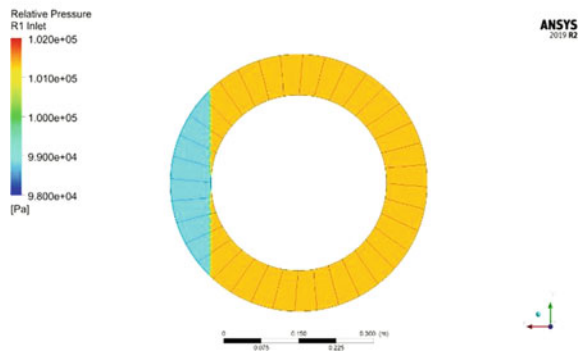
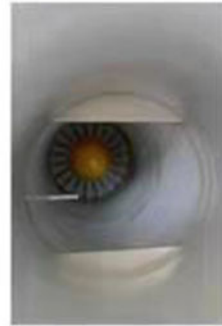
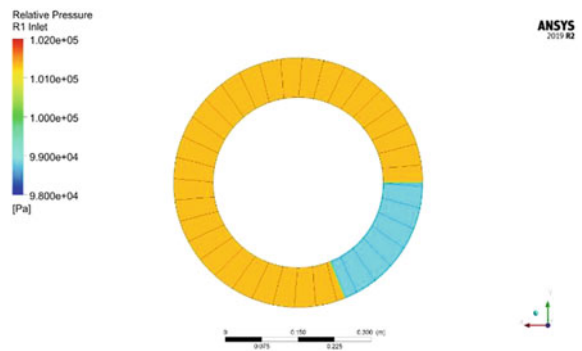
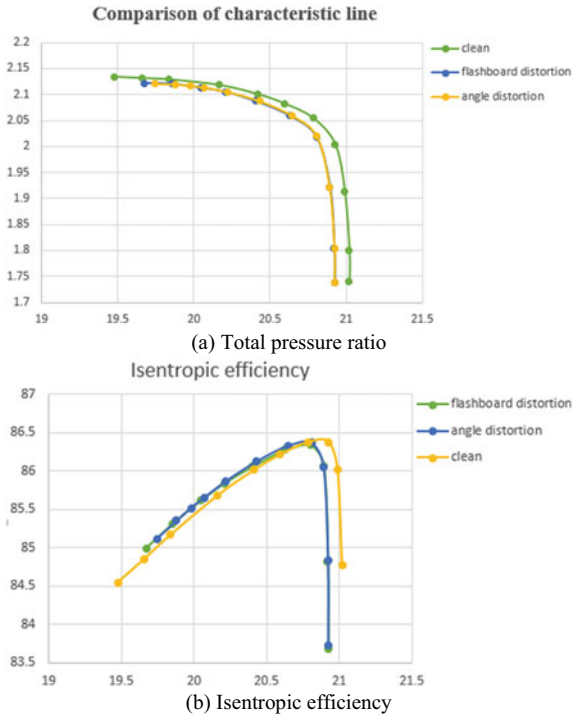


Fig. 8 Numerical simulation of angle distortion



that the circumferential distortion of the insert plate is closer to the rim distortion zone, which has a greater impact on the thermal insulation efficiency, while the angle distortion is closer to the hub and has a greater degree of distortion, which has a greater impact on the flow capacity.

Fig. 9 The characteristic curves of compressors



4.4 Development of Rotating Stall

We can see from the last section that under the influence of circumferential distortion, the characteristic line of ROTOR37 has moved downward overall, and the flow rate of the blocking point, stall margin, and adiabatic efficiency have all been attenuated to a certain extent. In order to explore the mechanism of the impact of circumferential distortion on aerodynamic performance, we tried to restore the flow in the channel from the blocking point to the near-stall point. We derive and integrate the blade-to-blade static entropy distribution map at 90% leaf height corresponding to each backpressure situation. As is shown in Figs. 10 and 11, we, respectively, show the development process of the rotation stall in the full channel under the conditions of the flashboard distortion and the angle distortion. The positive direction along the x-axis in the figure is the process from the blocking point to the near-stall point. In each case, the 36 channels are shown as a plan view cut from the middle at 90% span.

We can clearly find that the static entropy of the gas in the channel corresponding to the circumferential distortion zone is significantly higher than that of the channel corresponding to the normal region. With the attenuation of the mass flow in the

Fig. 10 The development of stall in flashboard distortion

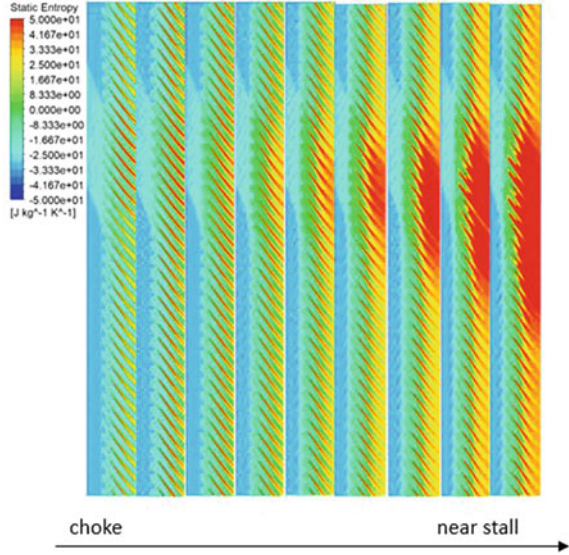
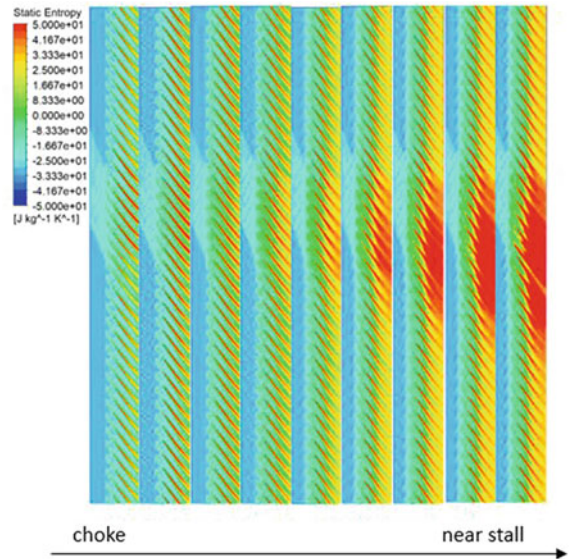


Fig. 11 The development of stall in angle distortion



passage and the increase of the pressure ratio, the gas disorder in the channel corresponding to the distortion zone increases significantly, and diffuses into the surrounding channels, resulting in a significant increase in the degree of congestion in the blade channel, and finally leading to a complete stall and comparing the two cases, it can be found that although the area of the distortion area is the same, the flashboard distortion depends on the larger area of the receiver, so the number of

channels affected by the distortion is more, and the corresponding area with high entropy in the figure is also larger. However, angle distortion, due to the serious congestion in the channel of the distortion zone, and the larger area of the area close to the hub, has a greater impact on the flow capacity of the compressor.

5 Conclusion

As the main complex operating conditions encountered by actual compressors, inlet distortion is of great significance to its research and prevention. With the improvement of calculation conditions, people will pay more attention to the use of simulation methods and conduct research in related fields. In this way, you can use the input conditions to set your own design ideas as you like, and it can also save experimental costs to a large extent.

This paper studies the difference in the impact of the two circumferential distortions on the engine performance and the development process of the rotating stall in the full channel. It can be found that the inlet distortion has a certain negative impact on the overall performance of the compressor. The flow capacity has a greater impact, and more distortion near the rim has a greater impact on efficiency. In addition, observing the rotating stall process under the condition of circumferential distortion, it can be found that the gas in the several channels corresponding to the distortion zone is initially blocked to a certain extent. As the backpressure increases, the degree of blockage in these channels gradually becomes serious and spreads to the surrounding channels, finally leading to the complete development of the stall.

In the future, the study of circumferential distortion will be able to go deep into many aspects, and the significance of its exploration is also significant. On the one hand, there are many forms of circumferential distortion. The total pressure distortion in this article is only a rough restoration of the real situation. The future research on software-recognizable representation methods of complex imported situations will be very valuable. On the other hand, the research on more accurate turbulence models and three-dimensional calculation methods will also be of great significance.

Acknowledgements The first author greatly appreciates the support from China Scholarship Council. This work is partially supported by National Natural Science Foundation of China (No.51976116), Natural Science Fund of Shanghai (No.19ZR1425900), and the Open Research Subject of Key Laboratory (Fluid Machinery and Engineering Research Base) of Sichuan Province (No. rszjj2019022).

References

1. Sears WR (1955) Rotating stall in axial compressors. 6(6):429–455
2. Gong Y, Tan CS, Gordon KA et al (1999) A computational model for short-wavelength stall inception and development in multistage compressors. 121(4):726–734

3. He L (2012) Computational study of rotating-stall inception in axial compressors 13(1)
4. Day IJ (1993) Stall Precursors in Axial Flow Compressors. *J Turbomach* 115(1):1–9
5. Emmons HW, Pearson CE, Grant HP (1955) Compressor surge and stall propagation. *Trans ASME* 77(3):455–469
6. Inoue M, Kuroumaru M, Tanino T et al (2000) Propagation of multiple short-length-scale stall cells in an axial compressor rotor. 122(1):45–54
7. Xu D, He C, Sun D et al (2021) Stall inception prediction of axial compressors with radial inlet distortions. *Aerosp Sci Technol* 109
8. Li F, Li J, Dong X, Sun D, Sun X (2017) Influence of SPS casing treatment on axial flow compressor subjected to radial pressure distortion. *Chin J Aeronaut* 30(02):685–697
9. Dong X et al (2018) Stall margin enhancement of a novel casing treatment subjected to circumferential pressure distortion. *Aerosp Sci Technol* 73:239–255
10. Spalart PR, Allmaras SR (1992) A one equation turbulence model for aerodynamic flows. AIAA-92-0439
11. Ashford GA, Powell KG (1996) An unstructured grid generation and adaptive solution technique for high-reynolds number compressible flow. Von Karman Institute Lecture Series. 1996-06.
12. Suder KL, Chima RV, Strazisar AJ, Roberts WB (1995) The effect of adding roughness and thickness to a transonic axial compressor rotor. *J Turbomach* 117(4):491–505
13. Reid L, Moore RD (1978) Design and overall performance of four highly-loaded, high speed inlet stages for an advanced, high pressure ratio core compressor. NASA-TP-1337
14. Benini E, Biollo R (2006) On the aerodynamics of swept and leaned transonic compressor rotors. In: *Turbo expo: power for land, sea, and air*. Barcelona, Spain

An Integrated Architecture Design Method for Multi-platform Avionics System



Xiang Ni , Miao Wang , Gang Xiao, and Guoqing Wang

Abstract The mission environment presents the trend of systematization, informatization, and strong confrontation in the future, and the mission style also develops from ‘single’ to ‘cluster’. With the development of unmanned system, the unmanned unit will play an increasingly important role in the process of mission execution. The mission execution mode with the collaboration of different kinds of platforms can form an organic system through mutual support and complementary ability. Therefore, it is necessary to launch the research on the architecture design of multi-platform avionics systems for multi-platform collaboration so as to define the interface pattern among different platforms. Firstly, this paper proposes a multi-platform avionics integration method and architecture drawing lessons from the idea of system integration inside the single platform to support task integration for different missions, system function integration for different capabilities, and system resource integration for different aircraft platforms; Then, this paper proposes a collaborative simulation and verification method based on the scenario design tool and the system modeling tool. By constructing the consistency environment of scenario space–time domain and architecture logic domain, the rationality and accuracy of the simulation model are improved. Finally, the comparative analysis between the multi-platform architecture proposed in this paper and the traditional architecture is realized by analyzing the spatial and temporal data of the collaborative simulation model. The superiority of the proposed multi-platform avionics architecture is verified.

Keywords Multi-platform avionics system · Integration method · Model simulation and verification · MBSE

X. Ni · M. Wang (✉) · G. Xiao · G. Wang
Department of Aeronautics and Astronautics, Shanghai Jiao Tong University, Shanghai, China
e-mail: miaowang@sjtu.edu.com

X. Ni
e-mail: ideal-diamond@sjtu.edu.com

1 Introduction

In recent years, the main component of the world's great powers in the missions is still large multi-platform formations. They take advantage of the coordination of multiple platform services to complete the mission. Although large aircraft and other similar platforms can carry more and better equipment with a larger operational range, they have the characteristics of long production cycle, high cost, complex maintenance, and poor operational flexibility. Based on this, some new theories and concepts of how to complete the mission for multi-platform formation are come out. For example, USA will adopt a new theory and concept of operation [1] which transforms the needs of developing complex "chimney" equipment [2] into small manned or unmanned equipment with relatively single function, low complexity and low cost. It can flexibly combine these manned/unmanned units which are like mosaic [3] to complete missions, as well as meet the diverse requirements of mission scenarios and accelerate the product development cycle. However, the multi-platform avionics system is difficult to compatible with the development of multi-platform formation. The multi-platform formation's avionics system encounters the similar problems in the development of the avionics system in the single aircraft. First of all, each platform such as an aircraft needs to be equipped with its own independent resources and interfaces to establish its own independent operation and input/output processing, which makes the system operation increasingly complex with a large number of unnecessary repetitive devices in the aircraft [4]. The overall efficiency of the system will be greatly limited. The operation cost increases in a straight line, which brings out great pressure on the organization of the whole system. Secondly, each platform can only utilize its own resources to support the function which will directly affect the reliability of the system. Once a certain resource and function module of the aircraft fails, it is impossible for the aircraft to use the resource of other platforms to replace the faulty equipment which greatly reduces the reliability of the system. Therefore, the design of an efficient multi-platform avionics system (MPAS) for multi-platform collaboration will become a focus of current and future research.

Some countries have carried out some research on the architecture design of multi-platform avionics system. Cai studied the manned/unmanned cooperative operation and established the structure of cooperative operation without carrying out the task system design [5]; Chen Jun proposed a cooperative decision-making mechanism based on fuzzy cognitive map which improved the autonomous decision-making ability of multi-platform formation [6]. The US military has proposed "open architecture" [7] as a common technical architecture for all kinds of platforms' mission systems to promote the development of open architecture computing environment. The open architecture improves the connectivity and interoperability between different platforms [8] and has been applied in the new generation DDG-1000 of the US Navy, effectively improving the overall efficiency of the formation. The US Department of defense has approved and established the "SoSITE" project [9], which aims to split the loads from a single large air platform to a large number of manned and

unmanned platforms. “SoSITE” project uses the open system architecture method to form a distributed multi-platform avionics system. It proposes the development plan of multi-platform avionics system but it doesn’t design the avionics system further.

This paper introduces a new multi-platform avionics system (MPAS) architecture for multi-platform collaboration by using the idea of avionics system integration for reference. Section 2 presents the integration method of MPAS and a MPAS architecture. Section 3 demonstrates the collaborative simulation verification method based on operation scenario design tool and modeling tool in the specific scenarios. The comparison between the presented architecture and the traditional architecture is shown in Sect. 4 to explain the superiority of the proposed multi-platform mission architecture.

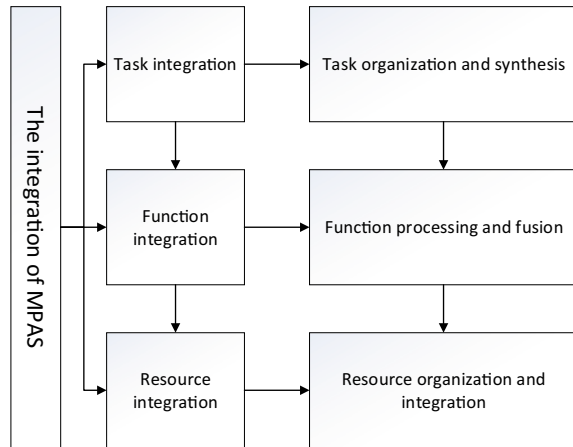
2 Integrated Method and Architecture of MPAS

2.1 Integrated Method of MPAS

The multi-platform avionics system for multi-platform formation is a system to manage task execution, function organization, and resource allocation when multi-platform cooperative formation is performing the mission [10, 11]. In the traditional multi-platform avionics system, each platform uses the communication link to realize the information interaction of each platform, so as to jointly complete the mission [12]. However, each unit can only complete the task depending on its own equipment and function. This kind of system achieves the ability of basic interconnection between different platforms and cannot support the interoperability between platforms. The traditional MPAS is urgent to be improved by the integration of resource, design of integrated function logic, and the integrated allocation of tasks so as to solve the problems such as inconsistent situation awareness, cognitive mismatch, uncertainty of collaborative decision-making, information interaction during action. The limitation of traditional MPAS is similar with the problems encountered by the traditional joint avionics system of aircraft. As a result, this paper creatively takes the integration as the design idea, and proposes a distributed MPAS integrated architecture which is based on the main nodes composed of manned platforms and sub-nodes composed of unmanned platforms. The integrated method constructs the MPAS to improve the efficiency and performance of the formation from three levels which are task, function, and resource (Fig. 1).

- Task integration. MPAS is a complex system to realize the task organization and management of different platforms. Task integration refers to the optimization process of the task sequence and the platform organization takes operation objectives capability and environment into consideration comprehensively. Task integration realizes the better task synthesis and organization which can help the commander make better decisions and determine the role and subtask of manned and unmanned platforms in different tasks.

Fig. 1 Integration method of multi-platform avionics system



- **Function integration.** In the process of task execution, the formation needs to provide different functions such as detection function, calculation function, and hitting function to support the task execution. Function integration refers to the integration of function profession, logic, and capability of main-sub-nodes so that the system has better function distribution and processing efficiency. Function integration is mainly to realize processing and fusion of the functions belonging to different manned and unmanned platforms. The function processing and fusion of MPAS mainly consists of the be-low three parts. Function profession integration, that is, the integration of functions with the same or similar profession of each platform, to clarify the functions of master node and slave node. Function logic integration is to clarify the function processing responsibilities of different nodes, the function processing logic link, and realize the function processing flow. Through function logic integration, the system can determine what the different platforms' functions will deal with and the direction of the information flow. Functional capability integration is to achieve the fusion of different functions to greatly improve the functional capability according to the requirements of functional organization when performing tasks. With the function integration, the function and information interaction between manned and unmanned platforms is defined during the different tasks.
- **Resource integration.** In the process of task execution, different resources such as software and hardware resources are demanded to ensure that the ability of functions can support the completion of tasks. Just like the resource integration of avionics system, resource integration is to realize a better resource organization considering the characteristics of distributed main-sub-nodes. Slave nodes unmanned platforms are equipped with special processing resources, and master node platforms realize general processing resource integration. Based on this, the resource integration of MPAS is mainly to realize the resource organization and integration which is composed of the resource organization of slave nodes and the resource integration of master nodes. The resource organization of slave node, that

is, the slave node unit with single function and simple structure is equipped with special resources. Special resource is the terminal resource devices that realize functions, such as sensors and weapons. The resource integration of master node is to integrate general resources which are used in different tasks to support the functions such as computing resources in the master node platform aimed to improve the processing capacity of the master node. In the traditional MPAS, the platforms are relatively closed because it cannot support the interoperability between platforms. Each unit needs to be equipped with a variety of independent equipment which results in complex structure, limited professional development, rising costs, and other problems. Resource integration can help each platform effectively develop professional ability. Master node with resource integration can process information quickly and improve the processing ability.

2.2 Integrated Architecture of MPAS

Combined with the characteristics of multi-platform and the integration design idea of aircraft avionics system, the integrated architecture of MPAS is proposed as shown in Fig. 2.

For a certain mission, the command center determines the tasks and specific organization mode according to the idea of task integration and sends these information to each manned master node. According to the idea of task integration, the manned master nodes can obtain the specific tasks of the manned master node and the unmanned sub-node and determine the functions in support of the tasks. According to the idea of function integration, the function processing logic and the interaction mode of master–slave node are determined, and the information of the sub-node is transferred to the master node for processing and fusion so as to obtain higher

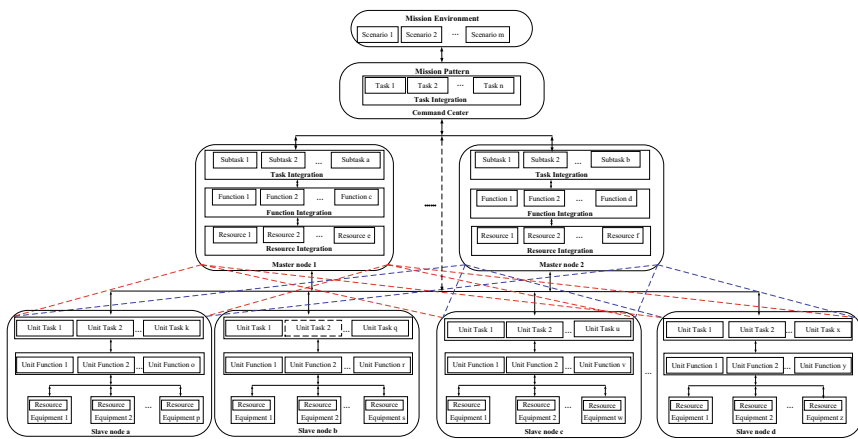


Fig. 2 The integrated architecture of MPAS

function efficiency. In this process, based on the idea of resource integration, the master nodes realize the integration of general resources, and the special resources are distributed in the sub-nodes to realize the optimization of resource allocation and provide more powerful processing capacity for functions.

3 System Modeling and Simulation

3.1 System Modeling

With the increasing complexity of system design, the traditional document-based design method has been unable to meet the design requirements [13]. The model-based system engineering (MBSE) method can analyze the system in different scenarios, establish the activity, interaction and state model of the system, and generate the corresponding functional requirements, operation scenarios, functional interfaces, and logical architecture [14]. Architecture design is a complex work which needs a set of standard modeling criteria to guide the design process. Department of Defense Architecture Framework (DoDAF) is a system architecture description standard [15] adopted by the US military in MBSE. It provides a architecture description method from multiple perspective, which describes the system from eight aspects including capability view, operational view, service view, and system view. DoDAF makes it possible to describe complex systems or systems as a whole and meets the requirements of system engineering. It has become the mainstream and mature architecture description standard in the world.

For complex scenarios, DoDAF description rules are used in system modeling tools such as EA and Rhapsody to build the system description model, which can clearly reflect the internal interaction logic of the formation in the process of task execution from a micro perspective. However, it is difficult to visually and vividly show the process of mission from a macro perspective. The scenario design tool such as STK can provide intuitive two-dimensional and three-dimensional animation demonstration so as to simulate the real scene. At the same time, the data in the process of scenario simulation can be calculated with the help of the analysis engine of scenario design tool, which is convenient for further system efficiency calculation.

3.2 Collaborative Simulation

The model-driven modeling and simulation verification method can be used to analyze the system function under different scenarios from scenario space-time domain and architecture logic domain. At the same time, a large amount of data generated by the model can be used to further analyze the architecture performance and compare it with other architectures under the same standard.

When the complex system is simulated and verified, the scenario model and the system description model are established based on the mission scenario. Through the collaborative simulation verification based on scenario design tool and system modeling tool, scenario design tool can generate mission space–time scene intuitively, provide spatiotemporal data in scene simulation and send trigger event to modeling tool. The system modeling tool receives trigger events and dynamically verifies the system behavior by running state diagram correspondingly. The collaborative simulation verification based on scenario design tool and system modeling tool makes the joint simulation verification of scene space–time domain and architecture logic domain more reasonable and accurate. The model-based collaborative simulation verification process is shown in Fig. 3.

The scenario design tool sends the trigger events to the system modeling tool model and the state of the corresponding unit in the system description model will change to realize the synchronous simulation verification from the macro and micro perspectives. The operational perspective of DoDAF describes the overall operational process of the system. When the scenario model established in the scenario design tool runs, it will send the event trigger information to the system description model built in the system modeling tool. By receiving the trigger information of events, the correctness and accuracy of the model can be verified. Moreover, combined with the macro three-dimensional model of the scenario design tool and the micro description

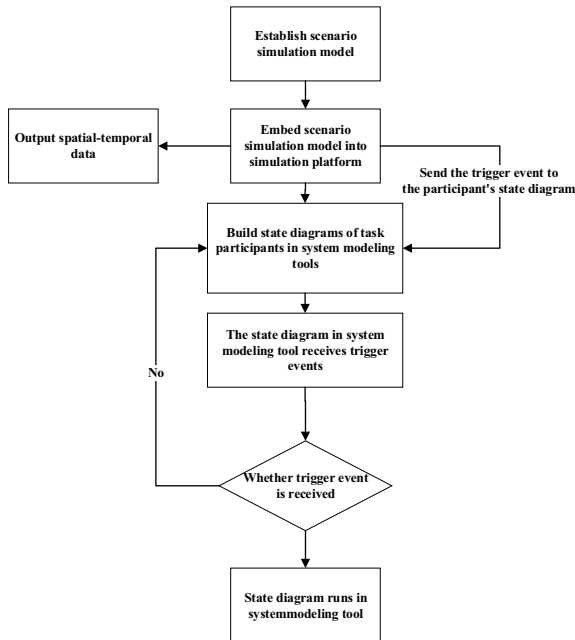


Fig. 3 Collaborative simulation verification process based on operation scenario design tool and system modeling tool

of the system modeling tool, the space–time relationship and information flow of the scenario can be displayed in a vivid and intuitive way. Finally, the scenario model simulation is used to improve the operation efficiency and the system description model simulation is used to improve the accuracy. The time–space state synchronization, action sequence synchronization and dynamic verification of MPAS model are realized. By embedding the scenario model and system description model into the collaborative simulation platform, the collaborative simulation verification based on the scenario design tool and system modeling tool can be realized. The collaborative simulation gets through the scene space–time domain and architecture logic domain which provides strong support for the future architecture comparison.

4 Efficiency Analysis

There are many evaluation methods for multi-platform formation system, which can be chosen depending on the actual situation. Among them, establishing efficiency index evaluation through mathematical analysis is an effective quantitative comparison method [16]. In Ref. [17], a formation system efficiency evaluation method for the mission is proposed. This paper will refer to efficiency evaluation model in reference [17] to calculate and compare the efficiency of two kinds of MPAS architecture in the same scenario such as anti-missile operation.

The efficiency evaluation method is shown in Fig. 4, which consists of two parts: the single efficiency evaluation model based on AHP-Index method and the system operational efficiency evaluation based on stages. The specific calculation method is as follows:

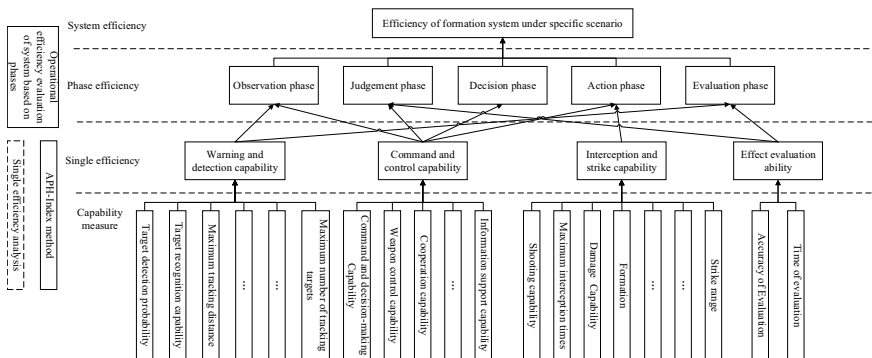


Fig. 4 Combat effectiveness evaluation method for manned/unmanned collaboration formation

(1) Establish the efficiency calculation structure

Make clear the mission profile of operational scenario, that is, the task of each stage and the functional requirements of each phase. At the same time, a single efficiency evaluation index system is established to investigate the single macro capability such as detection capability from multiple detailed capability measures. Finally, the efficiency calculation level as shown in Fig. 4 is established to calculate the final system efficiency from bottom to top.

(2) Calculate the efficiency of the single capability

The efficiency value of single capability is calculated by using the single efficiency evaluation model based on AHP-Index method. The analytic hierarchy process (AHP) is used to compare the capability measures that affect a single capability and quantify the importance to construct the judgment matrix C_{NN} .

$$C_{NN} = \begin{bmatrix} r_{11} & \cdots & r_{1N} \\ \vdots & & \vdots \\ r_{N1} & \cdots & r_{NN} \end{bmatrix}. \tag{1}$$

Then, the consistency of the matrix needs to be checked by comparing the consistency index CI with the random consistency index RI . If $CR < 0.1$, then the matrix consistency is acceptable. Otherwise, the comparison value will be readjusted until the matrix consistency is acceptable.

The corresponding eigenvector $(w_1, w_2, \dots, w_{N-1}, w_N)$ of the maximum eigenvalue of the judgment matrix C_{NN} is the weight of each ability measure that affects the efficiency of single capability. The lowest level capability measures index is calculated by combining the historical data of equipment tested and the expert experience. By comparing the capabilities of foreign similar equipment and considering the capabilities of different architectures, the operational equipment capability is standardized and converted into a dimensionless relative value. Finally, the index of each single capability is evaluated with standardized capability measure index and weight coefficient.

$$I = \prod_{i=1}^N X_i^{w_i}. \tag{2}$$

X_i is the standardized index value of the i -th capability measure of a single efficiency; is the number of capability measures of a single efficiency; refers to the weight coefficient of the i -th capability measure's normalized index value which represents the contribution of different capability measures.

(3) Calculate the efficiency of the each phase

For each mission phase, the index method adopts the "coupling connection" criteria to associate the single efficiency into a whole. The i -th phase efficiency is

$$S_{si} = \sum_{j=1}^{J_p} I_{ij} \cdot \prod_{j=1}^{J_s} I_{ij}, \tag{3}$$

where J_p and J_s are the number of parallel functions used at the same time and the number of serial functions used in sequence, respectively. S_{si} is the j -th single efficiency required in phase i .

(4) Calculate the whole efficiency

By weighting the efficiency of different mission phases, the total efficiency of the architecture in the scenario is obtained.

$$S_e = \sum_{i=1}^n S_{si} \cdot W_i, \tag{4}$$

where W_i is the weight of each phase and n is the number of phase.

Here, the weight of different phases is chosen as (0.225, 0.225, 0.225, 0.225, 0.1). Referring to the capabilities of the US formation, the parameter in the reference and the characteristics of different architectures, the efficiency value of the traditional MPAS, and the presented MPAS architecture is finally obtained (Table 1).

At the same time, the scenario spatial-temporal data can be obtained from the scenario design tool. The scene design tool has rich built-in data interfaces, which can obtain a series of data such as object directory, object spatial-temporal data, sensor attribute value, sensor detection situation, and so on. The data can be further calculated and analyzed to obtain the efficiency evaluation parameters from the aspects such as reconnaissance and detection, command and decision-making, interception, and strike are obtained in Table 2.

Table 1 The efficiency value of two kinds of architecture

Architecture	Value
Traditional architecture	0.655
Integrated architecture	0.816

Table 2 The efficiency evaluation parameters comparison of two architectures

Efficiency type	Efficiency name	Traditional	Integrated
Detection	Time required to find target(s)	15	10
Command and control	Information transmission time (s)	15	10
Strike and interception	Missile hit rate (%)	40%	60%
	Number of aircraft shot down	8	8
Time	Time required to finish mission(s)	6.3	3.3

From the final efficiency value and the data directly obtained from the simulation in Table 2, it can be clearly seen that the integrated architecture's information processing, information fusion, decision analysis, and other capabilities are significantly better than the traditional MPAS architecture. Owing to the integration of task, function, and resource, the performance of integrated architecture is better than the traditional one.

5 Conclusion

In this paper, the MPAS integrated architecture is established referring to the idea of integration in the avionics system.

- The integration method of MPAS is defined, and the integration of MPAS is realized from three levels which are task integration, function integration, and resource integration.
- Through the collaborative simulation and verification based on the scenario design tool and the system modeling tool, the architecture is simulated from the macro and micro point of view to verify its rationality in the specific task scenario. Finally, it is concluded that the MPAS integrated architecture is significantly better than the traditional MPAS architecture through the analysis of efficiency.

References

1. Clark B, Walton TA. (2019) Taking back the seas: transforming the US surface fleet for decision-centric War-fare. Center for Strategic and Budgetary Assessments
2. Zhang X-X (2018) Multi-capability areas weapon system portfolio selection and decision making methods. National University of Defense Technology
3. Clark B, Patt D, Schramm H (2020) Mosaic warfare: exploiting artificial intelligence and autonomous systems to implement decision-centric operations. Center for Strategic and Budgetary Assessments.
4. Wang G, Zhao W (2020) The principles of integrated technology in mission systems. Academic Press
5. Jun-wei C, Hai-ying L, Xin Z (2013) Key Technologies for cooperative combat system of manned/unmanned aerial vehicles. *Command Inf Syst Technol* 4(02):10–14 (in Chinese)
6. Chen J, Zhang X-W, Xu J, Gao X (2015) Human/unmanned-aerial-vehicle team collaborative decision-making with limited intervention. *Acta Aeronauticaet Astronautica Sinica*, 36(11):3652–3665. (in Chinese)
7. Min BK, Kuk S, Seo Y et al (2012) Standard-based integrated management system implemented for heterogeneous distributed systems in naval ship combat management system. In: 2012 IEEE/ACIS 11th international conference on computer and information science
8. Da WANG, Yan-jun ZUO, Jun GUO (2018) New generation surface warship combat system of the US navy system architecture. *Command Control Simul* 40(01):132–140
9. Jones J (2019) System of systems integration technology and experimentation (SoSITE). Defence Advanced Research Projects Agency (DARPA). <https://www.darpa.mil/program/system-of-systems-integration-technology-and-experimentation>

10. Guo-qing WANG, Qing-fan GU, Miao WANG et al (2014) Research on the architecture technology for new generation integrated Mission system. *Acta Aeronautica et Astronautica Sinica* 35(06):1473–1486 (in Chinese)
11. Guo-qing WANG, Qing-fan GU, Miao WANG et al (2015) Concept and architecture for new generation aircraft mission system. *Acta Aeronautica et Astronautica Sinica* 36(8):2735–2752 (in Chinese)
12. Cares J (2006) Distributed networked operations: the foundations of network centric warfare. IUniverse
13. Hart LE (2015) Introduction to model-based system engineering (MBSE) and SysML. In: Delaware valley INCOSE chapter meeting. Ramble-wood Country Club, Mount Laurel, New Jersey, p 30
14. Wang Y, Zhang A, Li D et al (2018) Research on civil aircraft design based on MBSE. In: Asia-Pacific international symposium on aerospace technology. Springer, Singapore, pp 1273–1283
15. DoD U (2009) Department of defense architecture frame-work
16. Yang J, Wang N, Xiao F, Han B (2019) Operation test and evaluation of aircraft carrier formation system. *Command Control Simul* 2019(4). (in Chinese)
17. Wang H (2020) Study on the operational effectiveness evaluation of the ship formation air defense system based on OODA. *Modern Defence Technology* ,48(06):19–25+38. (in Chinese)

A Group Delay Measurement Method for GNSS Receiver Based on BOC Signal



Longlong Li, Xiaoliang Wang , Shufan Wu, and Lang Bian

Abstract Traditional group delay measurement methods include single carrier phase method and spectrum analysis method based on signal autocorrelation function, but these two methods have their own limitations in GNSS receiver group delay measurement. The single carrier phase method cannot measure the group delay of multi filters and downconverters stage connect channel directly, and the measurement accuracy of group delay of spectrum analysis method based on signal autocorrelation function will deteriorate greatly near the zero point of signal power spectrum. In order to solve the above problems, this paper proposes a BOC (bi-nary offset carrier) signal group delay measurement method, which can realize the simple and accurate measurement of GNSS receiver group delay. In this paper, a group delay measurement method is analyzed and simulated by software, and verifies the feasibility and accuracy of the method are verified by simulation.

Keywords BOC navigation signal · Group delay · GNSS receiver

1 Introduction

The non-ideal channel characteristics of GNSS receiver will lead to the distortion of correlation peak, and then affect the ranging error of the receiver, which cannot be modeled and analyzed in the processing, which has become the main error source restricting high-precision positioning. The GNSS receiver channel characteristics can be divided into amplitude frequency characteristics and group delay characteristics. Compared with the amplitude frequency characteristics, the group delay has a greater impact on the correlation peak distortion, so it is necessary to accurately measure the group delay of GNSS receiver.

L. Li · L. Bian
Xi'an Branch of China Academy of Space Technology, Xi'an, China

X. Wang (✉) · S. Wu
The School of Aeronautics and Astronautics, Shanghai Jiao Tong University, Shanghai, China
e-mail: xlwang12321@sjtu.edu.cn

Traditional group delay measurement methods include single carrier phase method and spectrum analysis method based on signal autocorrelation function. Because the GNSS receiver generally contains multi-stage filters and downconverters, the single carrier phase method has high requirements for the measurement of GNSS receiving group delay, which generally requires peripheral equipment such as external mixer, and the measurement process is complex and not universal. The spectrum analysis method based on signal autocorrelation function is to use the frequency spectrum of output correlation function after passing through the channel to calculate the transfer function of the channel, and then to work out the group delay of the channel. Although this method is simple and convenient, it can realize the measurement of group delay of GNSS receiver at one time, but it will deteriorate near the zero point of signal power spectrum, resulting in poor measurement accuracy at the deviation from the center frequency. So, the spectrum analysis method based on signal autocorrelation function unable to meet the requirements of high precision measurement.

In Ref. [1], a mixer group delay measurement method based on spread spectrum signal is given, and contains two methods include based on spread spectrum receiver technology and signal correlation technology. The feasibility of the two methods is proved by simulation experiment, and the measurement method based on spread spectrum receiver technology has higher accuracy, and can be applied to the measurement of group delay in GNSS receiver group delay measurement. In Ref. [2], the group delay measurement technology based on narrow-band spread spectrum signal is proposed. Through simulation analysis, the measurement accuracy of group delay is given, and its engineering application scheme is presented, which can realize high-precision measurement of group de-lay of GNSS receiver.

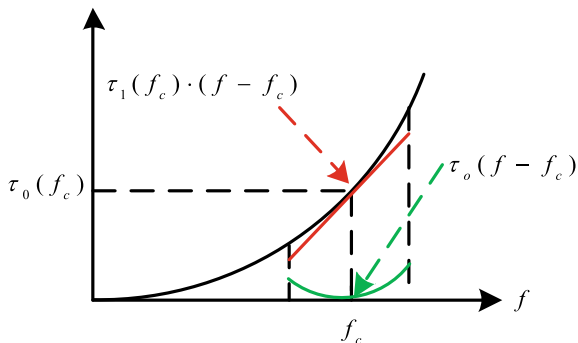
Although the existing group delay measurement technology based on spread spectrum signal can realize the group delay measurement of GNSS receiver, it needs to traverse several times to realize the group delay measurement in the whole receive bandwidth. The measurement and calibration process are relatively complex, and the requirements for measurement equipment are relatively high. The group delay measurement method based on BOC is proposed in this paper. The group delay of the whole receive channel can be obtained by a single measurement. The measurement signal generation can be compatible with the current navigation signal system. In this paper, the realization principle and method are given, and the feasibility and measurement accuracy of the method are analyzed by simulation.

2 Measurement Principles

Suppose we have the transfer function of GNSS receiver $H(f)$, and the corresponding group delay $\tau(f)$, the group delay $\tau(f)$ is expanded by Taylor expansion at any frequency f_c as:

$$\tau(f) = \tau_0(f_c) + \tau_1(f_c) \cdot (f - f_c) + \tau_o(f - f_c) \quad (1)$$

Fig. 1 Group delay decomposition diagram



where, $\tau_0(f_c)$ is the zero order group delay, $\tau_1(f_c)$ is the first-order group delay, $\tau_o(f - f_c)$ is the high-order group delay, Fig. 1 shows the group delay decomposition diagram.

In the design of general GNSS receiver, the fluctuation of group delay in pass-band is relatively gentle, and the group delay between can be approximately linear, namely:

$$\tau_o(f - f_c) \approx 0, \quad -\Delta f < f - f_c < \Delta f \tag{2}$$

Within the $f_c \pm \Delta f$ frequency range, the amplitude frequency response of the channel is generally very flat, and the amplitude fluctuation in the band can be considered unchanged.

In the case that the channel group delay response is linear, if the spread spectrum signals with code rate Δf is used to measure the channel group delay, the linear group delay has no effect on the phase discrimination curve deviation, and the measured group delay result is the zero order group delay $\tau_0(f_c)$ at the center frequency point [3].

For baseband signal BOC(m, n), due to the periodicity of its subcarrier, it can be regarded as the product of BPSK signal and square wave subcarrier. By using Fourier series expansion, the harmonic form expression of BOC signal can be obtained as [4]:

$$r_{\text{BOC}}(t) = c(t) \cdot s(t) = \sum_{k=-\infty}^{\infty} \frac{2}{(2k + 1)\pi} c(t) \cdot \sin(2\pi(2k + 1) \cdot f_{sc} \cdot t) \tag{3}$$

where, $c(t)$ represents spread spectrum code, $s(t)$ represents subcarrier signal and f_{sc} represents subcarrier frequency.

For sinusoidal signal BOC(m, n), the power spectral density can be expressed as follows [5]:

$$S(f) = \begin{cases} f_c \cdot \frac{\sin^2(\pi f/f_c)}{(\pi f)^2} \cdot \tan^2(\frac{\pi f}{2f_{sc}}), & 2m/n = \text{even} \\ f_c \cdot \frac{\cos^2(\pi f/f_c)}{(\pi f)^2} \cdot \tan^2(\frac{\pi f}{2f_{sc}}), & 2m/n = \text{odd} \end{cases} \quad (4)$$

where, f_c is the spread spectrum code rate and f_{sc} represents the subcarrier frequency.

Therefore, after filtering each sideband of the signal separately, each sideband can be used as a narrow-band spread spectrum signal to measure the group delay.

From the above analysis, it can be concluded that the measured aperture of group delay is related to the spectrum code rate, and the relationship is as follows:

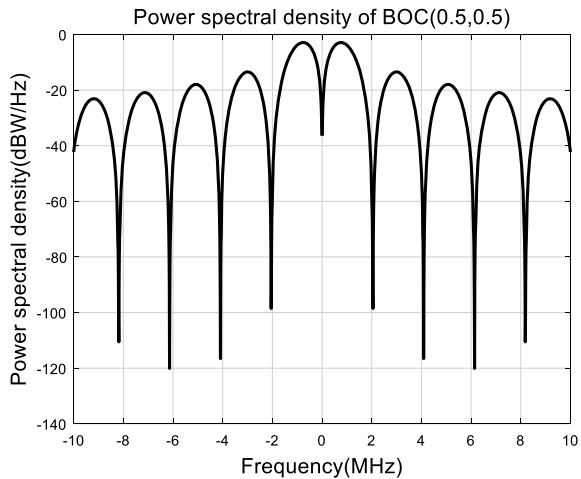
$$\Delta f = 2 \times f_c \quad (5)$$

At the same time, in order to ensure the continuous and uniform measurement of the group delay in the band, the signal with the same spread spectrum code rate and sub carrier rate is used to measure. To the signal BOC(m, n), let $m = n$.

In order to ensure that the group delay measurement within the measured bandwidth has enough resolution, that is, the measurement aperture is required to be small enough. At the same time, in order to ensure the accuracy of group delay measurement, the code rate should not be too small. For GNSS receiver group delay measurement, the spread spectrum code rate $f_c = 511.5$ KHz is selected, that is, the signal BOC(0.5, 0.5) is used for group delay measurement, and the measurement aperture is 1.023 MHz, which can meet the requirements of accuracy and resolution for most group delay measurements. At this condition, the power spectral density of BOC signal is shown in Fig. 2. Filtering processing is performed for each side band, which is equivalent to selecting the narrow-band spread spectrum signal with center frequency f_0 of and bandwidth 1.023 MHz for measure group delay.

$$f_0 = \pm(2k + 1) \cdot f_c, \quad k = 0, 1, 2, \dots, 9 \quad (6)$$

Fig. 2 Power spectral density of BOC (0.5, 0.5)



3 Group Delay Measurement Method of Narrowband Spread Spectrum Signal

The normalized CCF (cross correlation function) curve of narrowband spread spectrum signal passing through GNSS receiver channel is calculated.

$$\text{CCF}(s_{\text{out}}, s_{\text{in}}, \tau) = \frac{\int_0^T s_{\text{out}}(t) \cdot s_{\text{in}}(t + \tau) dt}{\sqrt{\int_0^T |s_{\text{out}}(t)|^2 dt} \cdot \sqrt{\int_0^T |s_{\text{in}}(t)|^2 dt}} \quad (7)$$

where, s_{in} is the input spread spectrum code signal, s_{out} is the spread spectrum code signal output through the receiver channel, τ is the signal delay deviation.

Generally speaking, the signal tracking loop of GNSS receiver adopts uncorrelated DLL loop. For a given distance between early and late correlators, the normalized phase discrimination curve SC (S-curve) is defined as follows:

$$\text{SC}(s_{\text{out}}, s_{\text{in}}, \tau) = |\text{CCF}(s_{\text{out}}, s_{\text{in}}, \tau + \delta/2)|^2 - |\text{CCF}(s_{\text{out}}, s_{\text{in}}, \tau - \delta/2)|^2 \quad (8)$$

Therefore, the group delay measurement using narrow-band spread spectrum signal can be obtained by calculating the zero-crossing deviation of SC.

4 Measurement and Calibration Process of Group Delay Based on BOC Navigation Signal

According to the satellite navigation signal characteristics, the bilateral band-width of each frequency point of most GNSS receiver is no more than 20 MHz, and the bandwidth range of group delay measurement is set to 20 MHz. The process of group delay measurement using BOC (0.5, 0.5) signal is as follows [6]:

Step 1. Input BOC (0.5, 0.5) signal, after passing through GNSS receiver, each sideband of the output signal is filtered independently. For each sideband, the group delay measurement method of narrow-band spread spectrum signal is used to measure the group time $\bar{\tau}(f)$ in the band.

Step 2. Using the tested group delay, the estimated channel transfer function $\hat{H}(f)$ with ideal amplitude frequency characteristics and group delay characteristics consistent with the measured group delay characteristics is generated.

Step 3. Similar to the first step, the simulated transfer function $\hat{H}(f)$ is used to calculate the in-band group delay $\hat{\tau}(f)$.

Step 4. The system deviation $\Delta\tau(f)$ obtained is as follows:

$$\Delta\tau(f) = \hat{\tau}(f) - \bar{\tau}(f) \tag{9}$$

Step 5. The system deviation is used to modify the measured group delay. The modified group delay $\tau(f)$ is obtained as follows:

$$\tau(f) = \bar{\tau}(f) - \Delta\tau(f) \tag{10}$$

The corresponding flow chart is as follows (see Fig. 3):

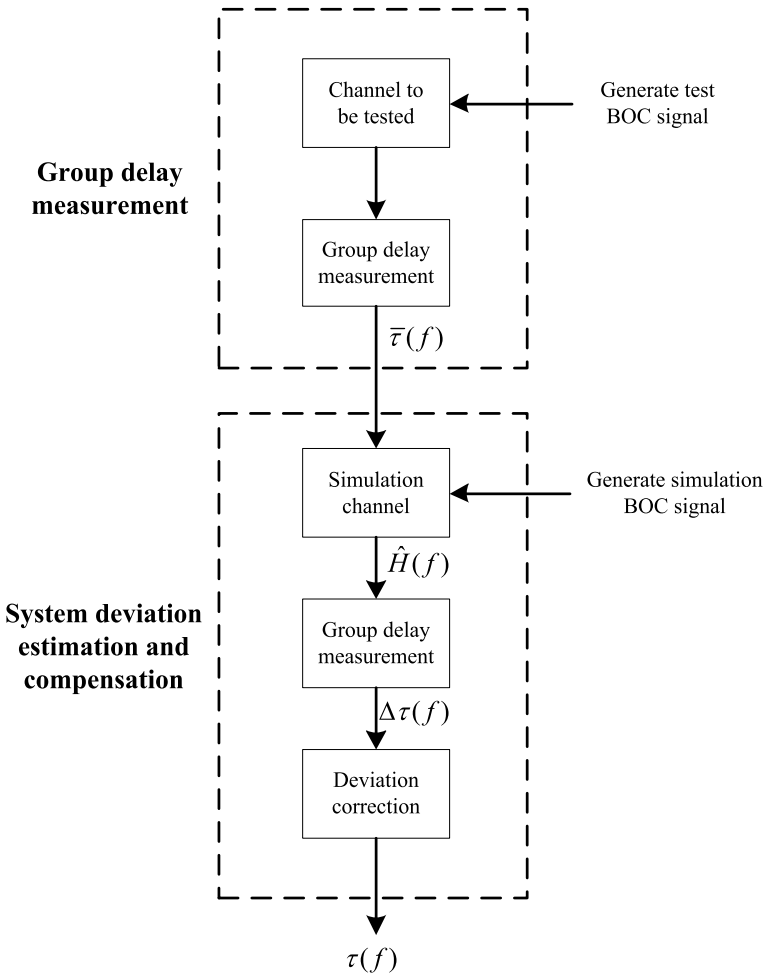


Fig. 3 Flow chart of group delay measurement using BOC (0.5, 0.5) signals

5 Simulation Analysis

In the measurement of group delay of GNSS receiver, the group delay of GNSS receiver is regarded as a whole. In the simulation process, the representative filter group delay which has the greatest influence on GNSS receiver is selected for simulation analysis [7]. Chebyshev filter, Butterworth filter and elliptic filter are usually used in GNSS receiver filter design. This paper selects elliptic filter for simulation analysis. This kind of filter is usually used in receiver design because of its better stopband attenuation characteristics.

Set the single sideband bandwidth of the elliptic filter to 11 MHz, the stopband bandwidth to 20 MHz, the in-band fluctuation to 1 dB, and the out of band attenuation to 30 dB. The group delay of the filter is shown in Fig. 4.

BOC (0.5, 0.5) signals are used to measure group delay, and the results are shown in Fig. 5.

According to the measured group delay, a simulated channel transfer function with ideal amplitude frequency characteristics and group delay that consistent with the measured group delay is generated. The specific method is to interpolate the measured values of group delay by polynomial interpolation, and obtain the phase frequency characteristic curve after integration. The simulated channel amplitude frequency characteristic curve is fixed as constant 1, and the transfer function of the channel is obtained. BOC (0.5, 0.5) signals are generated by simulation, and the time delay value is measured through the method mentioned above. According to the obtained delay value, the deviation of the measured group delay is corrected, and the measured group delay value is finally output. Figure 6 shows the simulation value, measured and corrected group delay value. Figure 7 shows the residual of measured group delay and the corrected group delay.

Fig. 4 Group delay simulation of elliptic filter

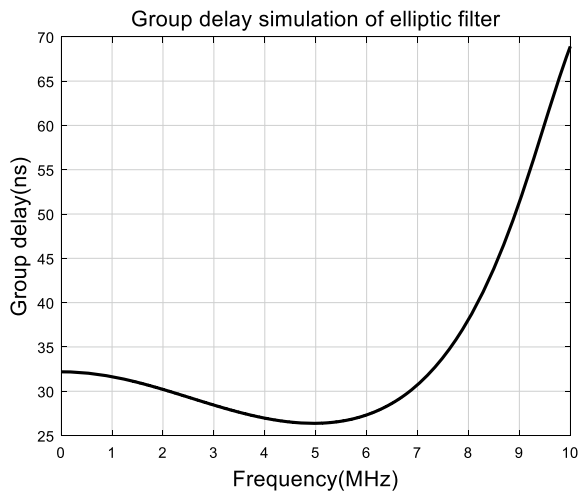


Fig. 5 Group delay measurement of elliptic filter

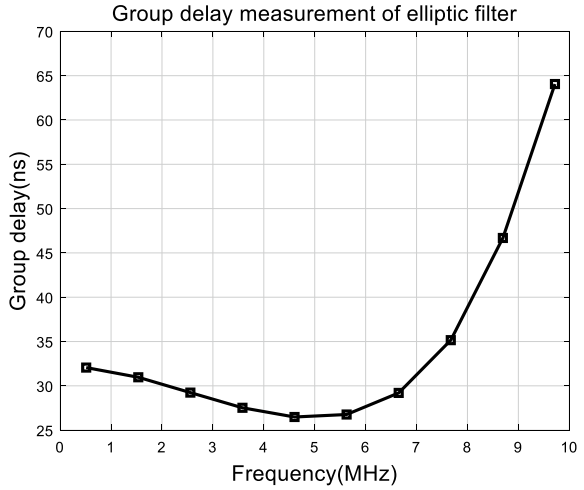
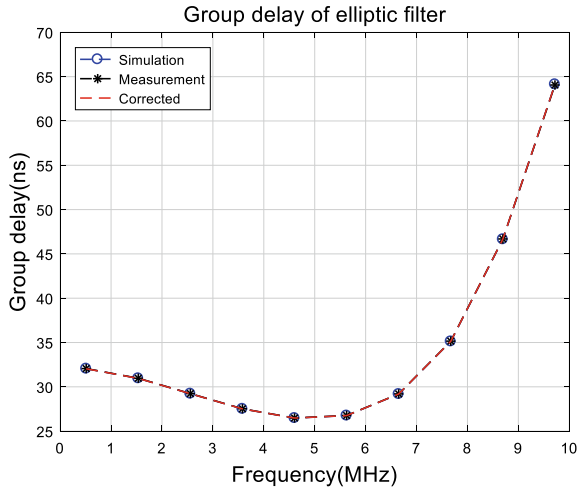


Fig. 6 Group delay test results of elliptic filter

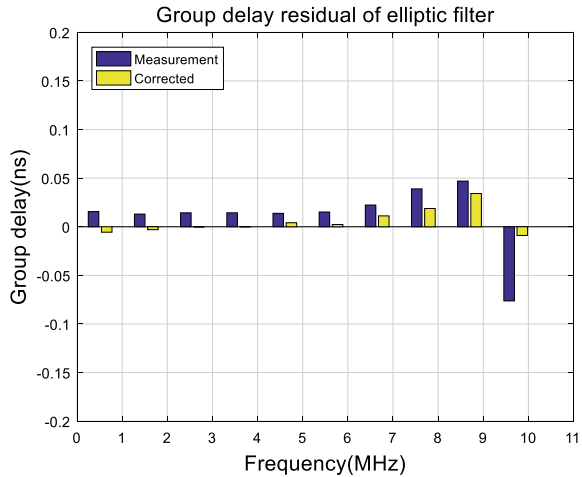


6 Conclusions

Compared with the traditional group delay measurement method, BOC signal can be simpler and more accurate to measure the group delay in the GNSS receiver band, and it can achieve a group delay measurement accuracy of better than 0.1 ns within 20 MHz bandwidth of GNSS receiver.

Because of the phase consistency of BOC Signal side lobe, it can ensure that the in-band group delay characteristics of the equipment under measurement can be completely obtained in a single measurement, which avoids the multiple traversal

Fig. 7 Residual of measured group delay and the corrected group delay



and calibration when using the traditional narrowband spread spectrum signal group delay measurement method, and the process is simpler and more convenient.

Moreover, because the method can ensure that the group delay of different frequency points in the band can be measured at the same time, it can avoid the measurement error caused by inconsistent measurement time, and this leads to higher measurement accuracy. The method proposed in this paper provides a new idea for the convenience and high precision measurement of GNSS receiver group delay, and has high engineering application value.

Acknowledgements This research was funded by Shanghai Nature Science Fund under contract No. 19ZR1426800, Shanghai Jiao Tong University Global Strategic Partnership Fund (2019 SJTU-UoT), WF610561702, and Shanghai Jiao Tong University Young Teachers Initiation Program, AF4130045.

References

1. Sha H, Zhu X, Zhang G, Sun G (2010) Group delay measurement method based on spread spectrum signal. *Modern Electron Technol* 01:8–11. <https://doi.org/10.16652/j.issn.1004-373x.2010.01.028>
2. Xiao Z (2014) Group delay modeling, measurement and calibration technology of high precision navigation receiver. Doctoral dissertation, University of Defense Science and Technology
3. Soellner M, Kohl R, Luetke W, Erhard P (2002, September) The impact of linear and non-linear signal distortions on Galileo code tracking accuracy. In: *Proceedings of the 15th international technical meeting of the satellite division of the institute of navigation (ION GPS 2002)*, pp 1270–1285
4. Yan Z (2015) Analysis of the influence of imperfect channel on BOC Signal Number tracking algorithm performance. Doctoral dissertation, University of Defense Science and Technology
5. Betz JW (2001) Binary offset carrier modulations for radionavigation. *Navigation* 48(4):227–246

6. Yu C, Chen Y (2009, August) A new measurement method for group delay of frequency-translating devices based on software defined radio technology. In: 2009 9th international conference on electronic measurement & instruments. IEEE, pp 1–694
7. Yu Y, Wang M, Guo W, Ma L, Wei Z (2014) Study on the influence of IF bandpass filter group delay on pseudo range measurement in GNSS receiver. *Electron Meas Technol* (03):24–28. <https://doi.org/10.19651/j.cnki.emt.2014.03.006>

Analysis on the Second Ignition Phenomenon Induced by Shock Wave Focusing in a 90° Conical Reflector



Yuanchang Li  and Bo Zhang 

Abstract The shock wave focusing is a promising detonation initiation method that can greatly shorten the deflagration to detonation transition distance. In this work, we conducted experiments under the constant operating pressure in a conical reflector to explore the shock focusing induced ignition in CH₄/O₂/Ar mixture. The second ignition is formed in the conical reflector under certain conditions. The introduction of the second ignition brings a higher pressure peak after ignition. By adjusting the incident shock intensity, three modes of ignition are found in the conical reflex. The pressure peak of combustion and the time to induce the second ignition are systematically investigated.

Keywords Second ignition · Shock wave focusing · Shock tube · Methane

1 Introduction

Detonation is a phenomenon that the mixture of fuel-oxidizer is combusted and the chemical energy is released in an extremely rapid and efficient method. Rather than the deflagration propagating in several hundred meters per second, detonation merges the shock wave and the combustion wave into a high-speed self-sustaining wave which can spread at a speed over two kilometers per second. Previous researchers have done many basic works on the detonation characteristics and detonation initiation [1–4]. Zhang et al. performed a series of experiments that investigated how the different factors, such as blockage ratio [5], wall toughness [6], and the type of fuel [7], influenced the position of detonation initiation and detonation limits. Maxwell et al. provided the burning mechanism of unstable detonations and the images of reaction zone structure in the experiment and numerical simulation [8]. Experiments

Y. Li · B. Zhang (✉)

School of Aeronautics and Astronautics, Shanghai Jiao Tong University, Shanghai, China

e-mail: bozhang@sjtu.edu.com

Y. Li

e-mail: liyuanchang@sjtu.edu.com

carried out by Kellenberger and Ciccarelli [9] showed how a high-speed combustion wave propagated in a channel with obstacles mounted on top and bottom and they found out detonation initiation occurred at the junction of the channel wall and obstacles. Recently, Wang et al. [10–12] studied the detonation behavior of methane-oxygen mixture in tubes with various obstacle configurations.

For the advantages of detonation mentioned above, detonation is naturally considered as a novel and potential method for engines. The detonation-based engine has drawn attention from the public for its simple structure, lightweight, and high thrust-to-weight ratio. It is proven by Hutchins and Metghalchi [13] that the pulse detonation engine has better performance in effectiveness and efficiency under the same pressure ratio compared with the turbine engine. Researchers have come up with many possible structures of detonation engines, e.g., pulse detonation engine (PDE) [14, 15], oblique detonation engines (ODE) [16, 17] and rotating detonation engine (RDE) [18, 19]. Pandey and Debnath [20] made a detailed review of the pulse detonation engine technology and suggested the future scope of PDE design. Peng et al. [21] firstly achieved a methane-air continuous rotating detonation, which contributed a lot to the design of a continuous rotating detonation engine. From the research work mentioned above, it is recognized that the reliable detonation initiation method is the most important part of the design of a detonation-based engine.

To obtain the detonation, deflagration to detonation transition (DDT) is the most common method widely used in the lab. Considering the size limit of a detonation-based engine, it is critical to reduce the induction distance of DDT as much as possible. There are two main approaches to induce DDT, one is using obstacles in the tubes, the other one is using a cross fluidic jet. However, Coopers et al. [22] claimed that using internal obstacles brought an average of 25% thrust loss in single-cycle PDE. Using a fluidic jet brought a new problem that the control of the fluidic jet system brings additional weight and system complexity.

In recent 50 years, shock focusing has been generally recognized by researchers. For shock focusing's high-energy region and self-ignition, it is considered as a promising detonation initiation method for the detonation-based engine. Meshkov [23], Skews and Kleine [24], Bond et al. [25], respectively, gave the images of an incident shock wave propagating to the cavity in nonreactive gas and discussed the flow structure evolution in shock focusing. For the reactive mixture, Gelfand et al. [26, 27] conducted a series of experiments of shock wave focusing in the different reflectors and it is found that the incident shock Mach number is the key to detonation initiation rather than the shape of reflex. Smirnov et al. [28, 29] analyzed the shock focusing in a wedge by numerical simulation and claimed that the probable reason for detonation initiation is the structure of unburnt gas surrounded by high-temperature burnt mixture. Despite adequate experiments and simulations of shock wave focusing have been performed, most of them were conducted in the hydrogen-oxygen mixture and the experiment results of the operating condition of different temperatures under constant pressure were still lacking.

In this study, the shock focusing phenomenon in a 90° conical reflex of different temperatures under the same pressure in a methane-based mixture is investigated. The pressure of operating condition is constantly set as 5 bar and the temperature of the

planar reflector is provided as reference. The results indicate that the second ignition occurs in the conical reflex when the temperature of the operating condition is high enough. With the greater incident shock wave velocity, the time to induce the second ignition declines. The main reason for the second ignition may be the instantaneous high-temperature region produced by that reflected shock wave passed through the junction of the tube wall and reflector edge.

2 Experimental Procedure

A shock tube that can change the shape of reflectors was designed to investigate the shock wave focusing phenomenon and self-ignition characteristics of methane. The shock tube has a total length of 6.1 m, in which both the driver section and the driven section are 3 m in length, the middle double-diaphragm section is 0.1 m, and the inner diameter of the whole tube is 73 mm. The double-membrane structure was adopted. The schematic diagram of the experimental device is shown in Fig. 1. It should be mentioned that for the planar reflex shock tube experiment, the initial pressure of the driven section is abbreviated as P_1 , and the initial pressure of the driver section is abbreviated as P_4 . The pressure behind the incident shock is denoted P_2 , and the pressure and temperature behind the reflected shock are referred as to P_5 and T_5 .

There are two reflectors used in this study: a planar one and a 90° conical one. The depth of the conical reflector is 33 mm and the apex angle is 90° . A hole of 7 mm is located at the tip of the cone for the transducer. The driven gas was mixed at the desired ratio of 6.33: 12.66: 81.01 for methane, oxygen, and argon by volume in the chamber. The pressure of the tube was vacuumed below 100 Pa before the experiment was conducted. The driven section was filled with mixed gas according to the calculated parameters. To obtain the required P_5 , the pressure or sound velocity of the driver gas in the high-pressure section was changed. This experiment used a

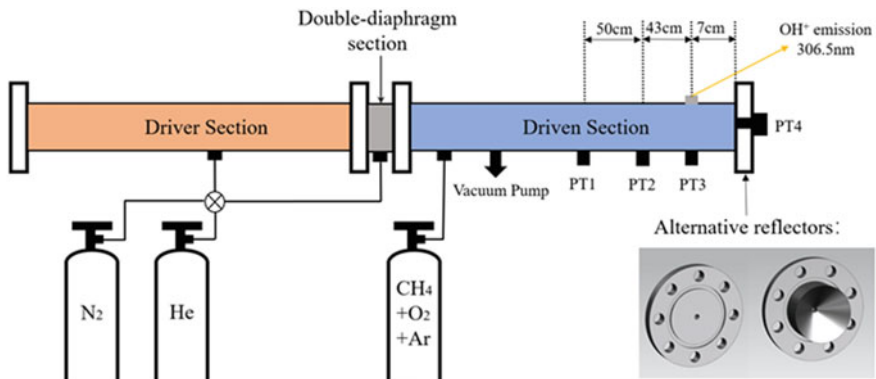
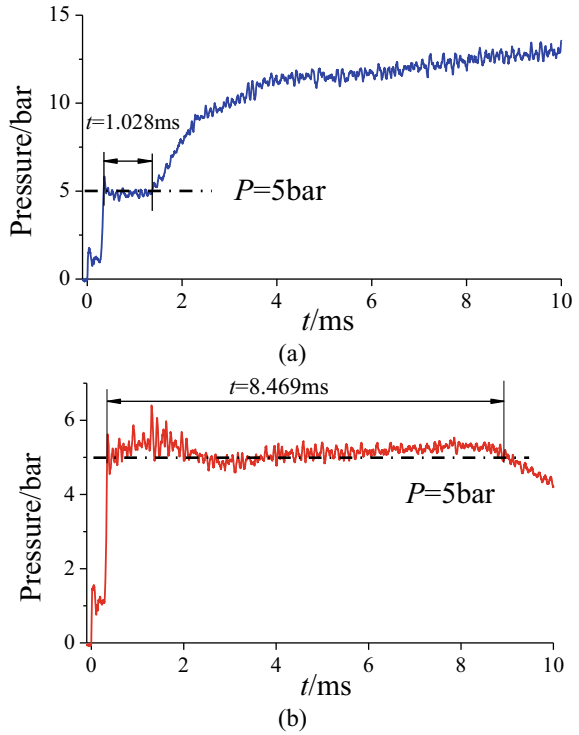


Fig. 1 Schematic diagram of the shock tube with the alternative reflectors

Fig. 2 Pressure traces of PT3 of designed P5 = 5 bar **a** without using tailored condition **b** using tailored condition



mixture of He and N₂ in a certain proportion to change the sound velocity of the driver gas. The experiment was carried out using the method of tailored contact surface condition. A comparison of using regular method and tailored condition is shown in Fig. 2, it is found that the experimental time under tailored condition is greatly extended to more than 8 ms.

The shock wave velocity was measured by four piezoelectric sensors on the side-wall and end wall of the driven section. The detailed distance between them is shown in Fig. 1. The four sensors are marked from PT1 to PT4 with the direction of the shock wave. PT1 and PT3 were PCB piezoelectric sensors, and PT2 and PT4 were Kistler piezoelectric sensors. A quartz optical window with an inner diameter of 8 mm is at the same section of PT4. During the experiment, the photomultiplier tube (PMT) measured the intensity of the emission spectrum of OH radicals at 306.5 nm through this window, which serves as a basis for judging the occurrence of methane ignition. The data of pressure sensors and PMT were recorded by PicoScope 4824 oscilloscope with a sampling frequency of 40Ms/s.

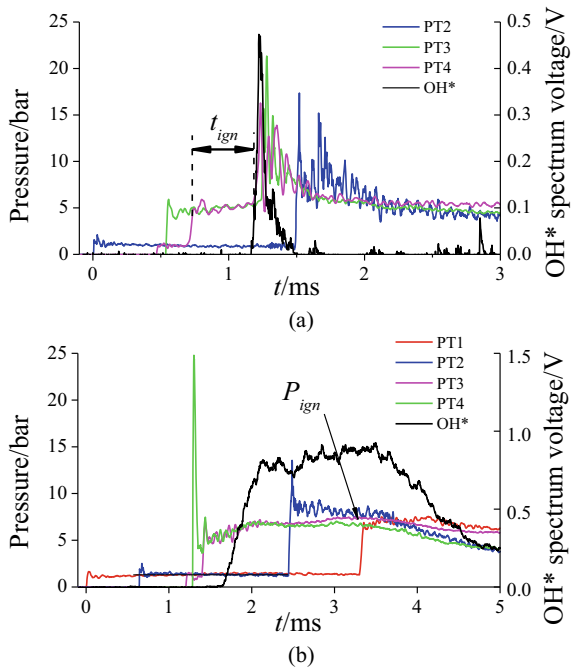
3 Results and Discussions

3.1 Ignition of the Two Reflectors

Figure 3 shows the typical pressure records of two reflectors. For the planar reflector, there is no PT1 signal because PT1 was not installed and it does not affect the experimental results. The time is set to zero when the incident shock wave passes through the section of PT2 in planar reflex and PT1 for conical reflex.

As the planar reflector results are shown in Fig. 2a, the incident shock passes the transducers and then reflects from the end of the tube. The initial condition of this test is $P_1 = 0.1346$ bar and $P_4 = 7.83$ bar with the tailored condition. The incident shock Mach number is 2.652 and the pressure behind the incident shock (P_2) is 1.05 bar which almost equals the result of 1.15 bar calculated by Gaseq [30]. At $t = 0.539$ ms, the shock arrives at the end wall and begins to reflect. From the signals captured by PT3 and PT4, the pressure behind the reflected shock (P_5) is 4.847 bar and the velocity of the reflected shock wave is 395.033 m/s. Giving the initial condition of the experiment, Gaseq’s result is almost equal to the experimental results. Gaseq gets the results that the $P_5 = 4.825$ bar, $T_5 = 1404.2$ K, and velocity of reflected shock is 405.95 m/s. The operating conditions of experiments are proven. At $t = 1.185$ ms, it is found that the pressure rapidly raises and oscillates in the following few microseconds. At the same moment, the PMT voltage sharply rushes

Fig. 3 Pressure records of two reflectors **a** planar reflector of $T_5 = 1400$ K **b** 90° conical reflector of $T_5 = 1175$ K



to a tip which means the ignition occurs. The interval between the beginning of the P_5 platform and the rise of OH* spectrum voltage is defined as “the ignition delay time” (t_{ign}). The ignition delay time is the key parameter of the fuel performance, and in this case, the ignition delay time is 0.977 ms.

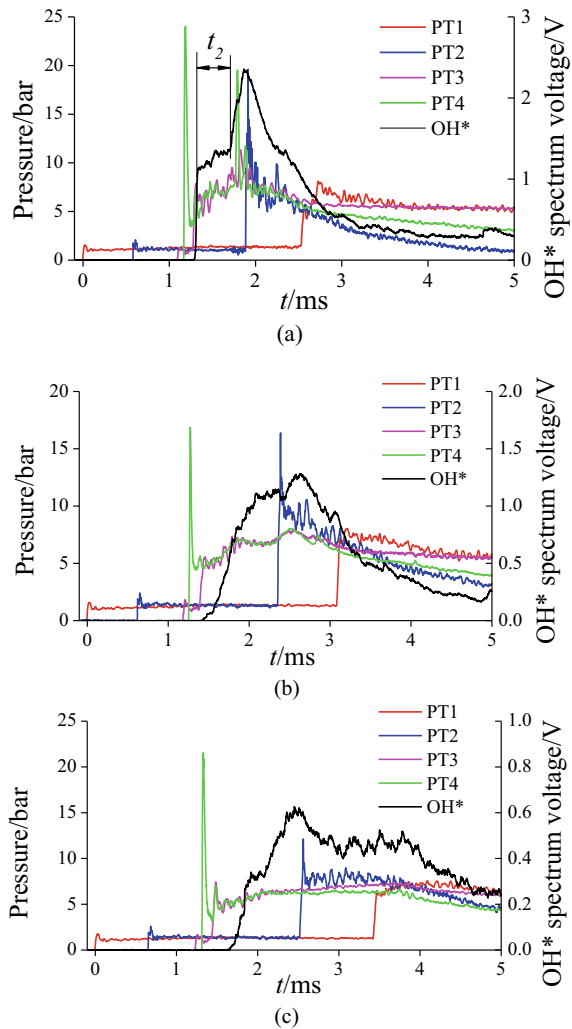
The typical results of the 90° conical reflector are shown in Fig. 3b. It should be mentioned that the design of $T_5 = 1175$ K is for planar reflector and the initial condition of a planar reflector of $T_5 = 1175$ K is used in conical reflex in this experiment. Designed T_5 in conical reflector is just a reference to the initial condition. In this case, $P_1 = 0.1854$ bar and $P_4 = 7.80$ bar (i.e., $N_2 = 1.58$ bar, He = 6.22 bar). In experiment results, $P_2 = 1.31$ bar (1.23 bar for Gaseq) and the incident shock Ma is 2.349. After reflection, the reflected shock velocity is 602.409 m/s. The instantaneous high pressure is recorded by PT4 and the pressure can reach 24.82 bar when the shock arrived at the tip of the cone. Ignition occurs after 0.265 ms after the PT3 meets the reflected shock. The maximum pressure of PT3 after the ignition is defined as P_{ign} and this parameter is used to characterize the pressure rise caused by combustion in the conical reflector. In this case, P_{ign} is 7.539 bar.

3.2 Modes of Ignition in the Conical Reflector

Figure 4 shows three ignition modes of shock wave focusing of different intensities in a 90° conical reflector. Under the relatively strong incident shock condition (i.e., $T_5 = 1350$ K), the second ignition phenomenon is found. The second ignition is manifested as a significant pressure rise after the ignition occurs and a steep rise in the photomultiplier tube signal again. This is a strong second ignition mode. As shown in Fig. 4a, the ignition occurs at the same time the reflected shock arrives at the section of PT3. Although the mixture is ignited after the reflection at $t = 1.319$ ms, the pressure does not have an immediate step rise. In the following 0.389 ms, the pressure slowly increases from 6.51 bar to 9.15 bar and at $t = 1.708$ ms, the second ignition takes place. After the second ignition, the pressure of PT3 climbs to 11.31 bar in a short time. The second ignition is more evident in PT4 and PMT signals. In PT4, the pressure suddenly rushes to a tip of 19.53 bar and then drops back to 7.81 bar. A PMT voltage rise brought by the second ignition is also visible in the figure and the interval of the onset of the second ignition and the first ignition is defined as t_2 . In this case, t_2 is 0.396 ms. It is found that the second ignition contributes to more complete combustion and a higher peak of pressure after ignition.

The probable reason for the second ignition is the shock focusing of the reflected shock at the edge of the cone. After the curved reflected shock wave passes through the junction of the tube wall and the edge of the conical reflector, the reflected shock reflects off the channel wall. This shock wave focusing gives a local high-temperature region at the junction, and it contributes to the second ignition. For the condition of Fig. 4a, the hot spot produces enough heat to ignite the compressed unburnt mixture between the reflected shock and the flame front, and the second ignition is observed in pressure transducers and PMT signals.

Fig. 4 Different modes of ignition in a 90° conical reflector. **a** Strong second ignition mode **b** Weak second ignition mode **c** No second ignition mode



For the relatively weak incident shock wave intensity in Fig. 4b, the second ignition is weakened. The voltage rise of PMT after ignition can be recognized, so the second ignition still occurs. However, compared with the results of Fig. 4a, the pressure rise brought from the second ignition is much smaller. This is referred to as weak second ignition mode. The second ignition occurs at $t = 2.399$ ms, and pressure at the PT3 section slightly rises from 7.345 to 7.840 bar. The pressure rise of the second ignition at the apex of the cone is also feeble. As is shown in Fig. 4c, the pressure remains stable after ignition, and no step rise is found in the PMT signals. This is the no second ignition mode. It means that if the intensity of the incident shock continually

goes down, there is no second ignition obtained in the 90° conical reflector. The hot spot in this case fails to concentrate enough energy to ignite the unburnt mixture.

3.3 Analysis of the Second Ignition

To clarify the second ignition rules in a 90° conical reflector, a series of experiments were conducted and the detailed information of experiment setup and results is shown in Table 1.

In the case of designed $T_5 = 1200$ K and $T_5 = 1175$ K, t_2 is blank because the second ignition did not take place. From the experimental data, it is noted that designed $T_5 = 1200$ K is an important dividing line. For the incident shock intensity larger than that of the $T_5 = 1200$ K case, the combustion is obtained by PMT almost at the same time as the arrival of reflected shock in PT3. t_{ign} is close to zero for Case 1–6. For the weaker shock wave ($T_5 \leq 1200$ K), t_{ign} increases with the decline of incident shock intensity.

Figure 5 shows P_{ign} values under various incident shock velocities. The results do not show too much regularity. For the cases of designed $T_5 \geq 1225$ K, P_{ign} fluctuates between 12 and 15 bar. If the incident shock intensity is weaker than that of designed $T_5 = 1200$ K, P_{ign} floats around 7.2 bar.

Figure 6 shows t_2 as a function of the incident shock wave velocity for the cases of designed $T_5 \geq 1225$ K. A fit of t_2 is provided in Fig. 6 for reference. The experimental data of t_2 are fitted linearly with the incident shock velocity. With the increase in incident shock velocity, t_2 drops linearly. The curve fit between t_2 and incident shock velocity is given as follows:

$$t_2[ms] = -0.001049V[m \cdot s^{-1}] + 9.04507 \quad (1)$$

The determination coefficient of the fit R^2 equals 0.8789, indicating that the fit has reasonable reliability.

Table 1 Experimental data for 90° conical reflector

No.	Designed T_5 /K	P_1 /bar	$P_4(N_2 + He)$ /bar	$V/m \cdot s^{-1}$	P_{ign} /bar	t_{ign} /ms	t_2 /ms
1	1350	0.1436	1.15 + 6.67	831.078	11.312	0	0.396
2	1325	0.1486	1.2 + 6.62	815.475	15.513	0	0.437
3	1300	0.1538	1.26 + 6.56	809.336	13.482	0	0.478
4	1275	0.1593	1.32 + 6.49	803.623	11.584	0.00262	0.581
5	1250	0.1652	1.38 + 6.43	798.811	14.976	0.00455	0.714
6	1225	0.1715	1.44 + 6.36	779.268	12.798	0.00652	0.897
7	1200	0.1782	1.51 + 6.29	769.093	7.251	0.1618	–
8	1175	0.1854	1.58 + 6.22	761.062	7.539	0.2648	–

Fig. 5 P_{ign} of different shock wave intensities for a 90° conical reflector

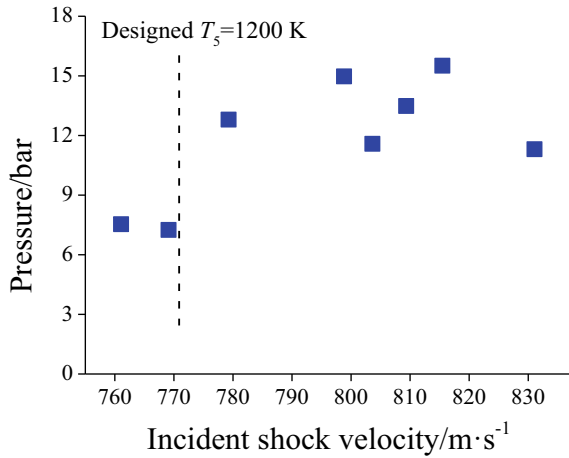
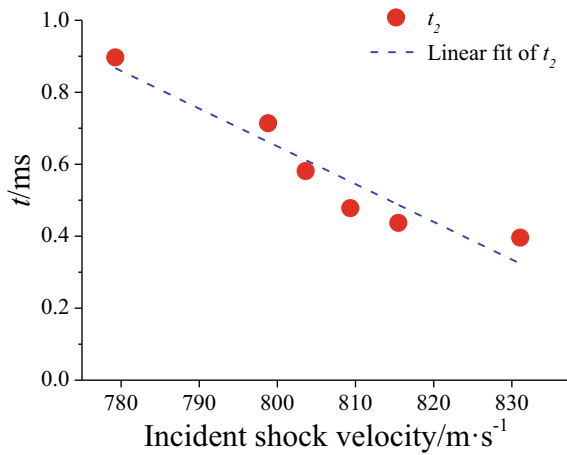


Fig. 6 t_2 of different shock wave intensities (designed $T_5 \geq 1200$ K) for a 90° conical reflector



4 Conclusion

In this study, the second ignition behavior of methane-based mixture in the 90° conical reflector is investigated. The main conclusions are drawn as follows:

- (1) In a 90° conical reflection, the second ignition occurs under relatively high-temperature conditions. The second ignition phenomenon brings more intense combustion and higher ignition pressure. For the initial condition of designed $P_5 = 5$ bar, $T_5 \leq 1200$ K, there will be no second ignition.
- (2) The reason for the second ignition may be that the curved reflected shock wave passes through the junction of the cone edge and the channel wall, and a local hot spot produced by shock wave focusing appears.

- (3) In the second ignition, by increasing the shock wave velocity, it is suggested that the intensity of shock has a great influence on t_2 and P_{ign} . The t_2 drops linearly with the incident shock velocity.

References

1. Lee J (2008) The detonation phenomenon. Cambridge University Press
2. Dorofeev S, Sidorov V, Kuznetsov M, Matsukov I, Alekseev V (2000) Effect of scale on the onset of detonations. *Shock Waves* 10:137–149
3. Lee JHS, Jesuthasan A, Ng HD (2013) Near limit behavior of the detonation velocity. *Proc Combust Inst* 34(2):1957–1963
4. Ciccarelli G, Dorofeev S (2008) Flame acceleration and transition to detonation in ducts. *Prog Energy Combust Sci* 34(4):499–550
5. Zhang B, Liu H (2017) The effects of large scale perturbation-generating obstacles on the propagation of detonation filled with methane–oxygen mixture. *Combust Flame* 182:279–287
6. Zhang B (2016) The influence of wall roughness on detonation limits in hydrogen–oxygen mixture. *Combust Flame* 169:333–339
7. Zhang B, Ng HD, Lee JHS (2012) Measurement and scaling analysis of critical energy for direct initiation of gaseous detonations. *Shock Waves* 22(3):275–9
8. Maxwell B, Bhattacharjee R, Lau-Chapdelaine SSM, Falle S, Sharpe G, Radulescu M (2016) Influence of turbulent fluctuations on detonation propagation. *J Fluid Mech* 818
9. Kellenberger M, Ciccarelli G (2015) Propagation mechanisms of supersonic combustion waves. *Proc Combust Inst* 35(2):2109–2116
10. Wang L, Ma H, Shen Z, Pan J (2019) Effects of bluff bodies on the propagation behaviors of gaseous detonation. *Combust Flame* 201:118–128
11. Wang L, Ma H, Shen Z, Xue B, Cheng Y, Fan Z (2017) Experimental investigation of methane-oxygen detonation propagation in tubes. *Appl Therm Eng* 123:1300–1307
12. Wang L, Ma H, Yongxing D, Shen Z (2019) On the detonation behavior of methane-oxygen in a round tube filled with orifice plates. *Process Saf Environ Prot* 121:263–270
13. Hutchins TE, Metghalchi M (2003) Energy and exergy analyses of the pulse detonation engine. *J Eng Gas Turbines Power* 125(4):1075–1080
14. Kailasanath K (2003) Recent developments in the research on pulse detonation engines. *AIAA J* 41(2):145–159
15. Bellini R, Lu FK (2010) Exergy analysis of a pulse detonation power device. *J Propuls Power* 26(4):875–8
16. Ostrander M, Hyde J, Young M, Kissinger R, Pratt D (1987) Standing oblique detonation wave engine performance. In: Joint propulsion conference
17. Ng HD (2018) Effects of activation energy on the instability of oblique detonation surfaces with a one-step chemistry model. *Phys Fluids* 30:106110
18. Walters IV, Journell CL, Lemcherfi A, Gejji R, Heister SD, Slabaugh CD (2019) Parametric survey of a natural gas-air rotating detonation engine at elevated pressure. In: AIAA scitech 2019 forum
19. Liu Z, Braun J, Paniagua G (2019) Characterization of a supersonic turbine downstream of a rotating detonation combustor. *J Eng Gas Turb Power* 141(3):031501
20. Pandey KM, Debnath P (2016) Review on recent advances in pulse detonation engines. *J Combust* 016:1–16
21. Peng HY, Liu WD, Liu SJ, Zhang HL, Zhou WY (2019) Realization of methane-air continuous rotating detonation wave. *Acta Astronaut* 164:1–8
22. Cooper MA, Jackson S, Austin J, Wintenberger E, Shepherd J (2002) Direct experimental impulse measurements for detonations and deflagrations. *J Propul Power* 18:1033–1041

23. Meshkov EE (1970) Reflection of a plane shock wave from a rigid concave wall. *Fluid Dyn* 5(4):554–558
24. Skews BW, Kleine H (2007) Flow features resulting from shock wave impact on a cylindrical cavity. *J Fluid Mech* 580:481–493
25. Bond C, Hill DJ, Meiron DI, Dimotakis PE (2009) Shock focusing in a planar convergent geometry: experiment and simulation. *J Fluid Mech* 641:297–333
26. Gelfand BE, Khomik SV, Bartenev AM, Medvedev SP, Gronig H, Olivier H (2000) Detonation and deflagration initiation at the focusing of shock waves in combustible gaseous mixture. *Shock Waves* 10(3):197–204
27. Gelfand BE, Khomik SV, Medvedev SP, Gronig H, Olivier H (2001) Visualization of self-ignition regimes in hydrogen-air mixtures under shock waves focusing. *P Soc Photo Opt Ins* 4183:688–695
28. Smirnov NN, Penyazkov OG, Sevrouk KL, Nikitin VF, Stamov LI, Tyurenkova VV (2018) Onset of detonation in hydrogen-air mixtures due to shock wave reflection inside a combustion chamber. *Acta Astronaut* 149:77–92
29. Smirnov NN, Penyazkov OG, Sevrouk KL, Nikitin VF, Stamov LI, Tyurenkova VV (2017) Detonation onset following shock wave focusing. *Acta Astronaut* 135:114–130
30. Gaseq Chemical Equilibrium Program. Version 0.79. New York (Columbia University): Computerized educational systems. <http://www.gaseq.co.uk/gseqdnld.htm>. Accessed 2005/01

Research on Attitude Control of Zero-Momentum Spinning Satellite



Ning Du, Shufan Wu, Chao Zhong, Wenhui Chen, and Xiaoliang Wang

Abstract A thruster-based attitude control method for zero momentum spinning satellite is proposed in this paper. For the spinning satellite rotating synchronously with the long baseline rotating payload, if the satellite spin axis is required to point to the earth's center in real time, the gyroscopic moment generated by the angular momentum and precession angular velocity of the spinning satellite is difficult to overcome. Therefore, a zero-momentum spinning satellite scheme is proposed to make the large flywheel angular momentum offset the satellite spin angular momentum, making the whole satellite a zero-momentum system. The influence of the whole satellite dynamic unbalance disturbance torque on the attitude stability is analyzed. The attitude control of the spinning satellite is transformed into a three-axis stability control problem by defining the semi fixed reference coordinate system. The effectiveness of the proposed method is verified by mathematical simulation.

Keywords Zero-momentum · Spinning satellite · Attitude control · Thruster · Rotating long baseline interferometer

1 Introduction

Rotating long baseline interferometer (RLBI) system usually only needs a single long baseline to achieve direction finding. Compared with traditional multi-channel interferometer and array direction finding, the system complexity and channel consistency requirements are greatly reduced, and the engineering application is becoming more and more extensive [1–3]. The existing method of rotating baseline payload in orbit is that the payload spins around the line of sight (LOS) axis, and the angular

N. Du · S. Wu (✉) · X. Wang
The School of Aeronautics and Astronautics, Shanghai Jiao Tong University, Shanghai, China
e-mail: shufan.wu@sjtu.edu.cn

N. Du · C. Zhong · W. Chen
Institute of Shanghai Aerospace Control Technology, Shanghai, China

momentum of the payload is compensated by the flywheel, so as to avoid the gyro moment generated by the spin angular momentum of the payload interfering with the satellite attitude. Then, the satellite platform only needs three-axis orientation control. For small satellites, the attitude control in the above way requires strict constraints on the payload weight and baseline size. In addition, constrained by the life times of the conductive slip ring of the payload rotating mechanism [4, 5], it is difficult to further improve the life and reliability of the whole satellite. Therefore, with the development of the rotating baseline payload technology, the size and weight of the payload baseline are further increased, and the existing satellite attitude control technology has encountered bottlenecks, so it is necessary to carry out new satellite platform technology research. With the development of high dynamic star sensor technology, the three-axis attitude measurement is gradually feasible when the whole satellite rotates with the payload at high speed [6]. Therefore, based on the integrated design idea of satellite platform and payload [7, 8], this paper proposes the satellite platform spin scheme to meet the working requirements of the payload and avoid the influence of the conductive slip ring on the payload life.

The conventional spin satellite's spin axis is along with the normal direction of the orbital plane, which can avoid the gyro moment generated by the combination of spin angular momentum and orbital angular velocity, and it is easy to realize the payload scanning ground target. The object of this paper is different from the conventional spinning satellite. During the working period of the rotating baseline payload, it is necessary to ensure that the LOS (spin axis) points to the ground target. The combination of spin angular momentum and orbital angular velocity will produce gyro interference torque. At this time, if the reaction flywheel is used for attitude control, the angular momentum of the flywheel will be quickly saturated. If the thruster is used for attitude control, the fuel consumption is too large, so it cannot be realized in engineering. Therefore, this paper proposes a scheme of angular momentum compensation for spin satellite. A large angular momentum compensation mechanism is installed on the spin axis of the satellite to make its angular momentum offset the spin angular momentum of the star. The whole satellite becomes a zero-momentum system to avoid the interference of gyro moment during the precession of the spin axis. The new problem brought by this scheme is that the conventional precession control algorithm and the conventional three-axis attitude control algorithm cannot be used because the dynamic characteristics of the zero-momentum spin satellite are different from those of the conventional spin satellite, so the attitude control method suitable for the zero-momentum spin satellite needs to be redesigned (see Figs. 1 and 2).

In Refs. [9–11], the attitude determination of spinning satellite is based on sun sensor and earth sensor, and the attitude nutation and precession control algorithms are designed. In Ref. [12], the attitude nutation and precession control algorithm of the spinning small satellite is designed on the premise that the three-axis attitude of the satellite can be determined. In Refs. [13, 14], the stability control method of spinning satellite based on geomagnetic field and gravity field is proposed. The above references do not deal with the attitude control of spin satellite after angular momentum compensation. In Ref. [15], a single axis stability control method based on magnetic torque converter and rotor for spinning micro nano satellite is proposed,

Fig. 1 Spin axis pointing requirement

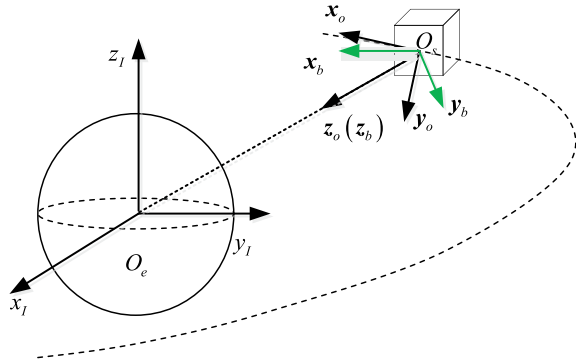
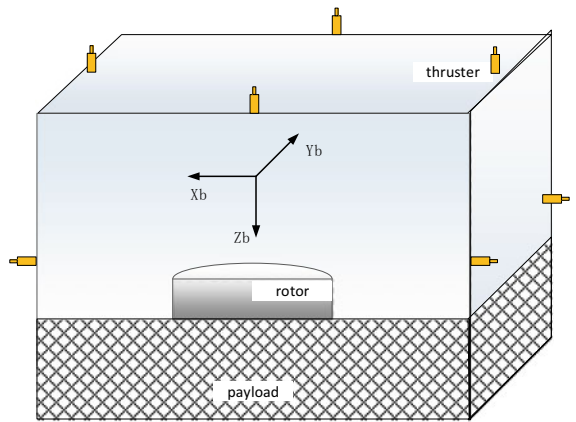


Fig. 2 Satellite structure diagram



but the attitude control method of zero momentum spinning satellite thruster is not involved. Reference [16] is suitable for high angular velocity fast maneuver of three-axis stabilized satellites, but not for spinning satellites. In this paper, according to the characteristics of zero momentum spinning satellite, the dynamic unbalance interference torque caused by inertia product and spin angular velocity is analyzed, and the thruster attitude control algorithm is redesigned through the reference coordinate system design.

2 Disturbance Torque Analysis of Dynamic Unbalance

Due to the high-speed rotation of the satellite, the whole satellite inertia product combined with the spin angular velocity produces obvious dynamic imbalance interference torque, and the whole satellite angular momentum is compensated to 0nms,

no longer has the anti-interference characteristics of the spin satellite, so the interference torque will have a significant impact on the stability of the satellite, so it is necessary to carry out quantitative analysis.

After derivation, the specific form of dynamic unbalance interference torque is as follows:

$$\begin{aligned} \mathbf{T}_d &= \mathbf{A}_{bo} \boldsymbol{\omega}_{ob} \times \mathbf{I} \boldsymbol{\omega}_{ob} = \begin{bmatrix} \cos \Psi & \sin \Psi & 0 \\ -\sin \Psi & \cos \Psi & 0 \\ 0 & 0 & 1 \end{bmatrix} \begin{bmatrix} 0 & -\omega_z & 0 \\ \omega_z & 0 & 0 \\ 0 & 0 & 0 \end{bmatrix} \begin{bmatrix} I_x & -I_{xy} & -I_{xz} \\ -I_{xy} & I_y & -I_{yz} \\ -I_{xz} & -I_{yz} & I_z \end{bmatrix} \begin{bmatrix} 0 \\ 0 \\ \omega_z \end{bmatrix} \\ &= \begin{bmatrix} I_{yz} \omega_z^2 \cos \Psi + I_{xz} \omega_z^2 \sin \Psi \\ -I_{yz} \omega_z^2 \sin \Psi + I_{xz} \omega_z^2 \cos \Psi \\ 0 \end{bmatrix} = \begin{bmatrix} \sqrt{I_{xz}^2 + I_{yz}^2} \omega_z^2 \sin(\Psi + \theta) \\ \sqrt{I_{xz}^2 + I_{yz}^2} \omega_z^2 \cos(\Psi + \theta) \\ 0 \end{bmatrix} \end{aligned} \quad (1)$$

where Ψ is the yaw attitude angle of the satellite relative to the expected coordinate system, θ is the fixed phase angle, ω_z is the satellite spin angular velocity, I_{xz} and I_{yz} are the inertia product of the whole satellite.

Furthermore, it can be seen that the interference angular momentum corresponding to dynamic unbalance has the following form:

$$\mathbf{H}_d = \begin{bmatrix} -\sqrt{I_{xz}^2 + I_{yz}^2} \omega_z \cos(\Psi + \theta) \\ \sqrt{I_{xz}^2 + I_{yz}^2} \omega_z \sin(\Psi + \theta) \\ 0 \end{bmatrix} \quad (2)$$

The interference angular momentum causes periodic fluctuation of the satellite non-spin axis angular velocity, and the fluctuation period is the satellite spin period. The amplitude of angular velocity fluctuation can be estimated as follows:

$$\Delta \boldsymbol{\omega} = \mathbf{I}^{-1} \mathbf{H}_d \approx \begin{bmatrix} -\sqrt{I_{xz}^2 + I_{yz}^2} / I_{xx} \omega_z \cos(\Psi + \theta) \\ \sqrt{I_{xz}^2 + I_{yz}^2} / I_{yy} \omega_z \sin(\Psi + \theta) \\ 0 \end{bmatrix} \quad (3)$$

where I_{xx} and I_{yy} are the main axis inertia of the satellite.

With the help of the estimation formula, the inertia product index of the whole satellite can be put forward reversely under the constraint of the satellite stability index. The main inertia of the satellite's non-spin axis is 430 kgm^2 and the spin angular velocity is $90^\circ/\text{s}$. The stability index was $0.02^\circ/\text{s}$ as example, the inertia product of satellite body coordinate system is required to be less than 0.0955 kgm^2 .

3 Spin Axis Pointing Control Algorithm

Taking the satellite running in the inclined circular orbit and fixed installation of solar wings as an example, it needs to carry out long-term three-axis orientation control to the sun. Under the ground or program-controlled command, it turns into the payload to ground orientation attitude control mode. Therefore, the attitude control task of zero momentum spin satellite is mainly spin axis pointing control. In the long-term operation, the spin axis points to the sun in the opposite direction, and the spin axis continuously points to the earth center during the mission. In addition, it is necessary to control the satellite spin axis angular velocity to ensure that the whole satellite spin angular velocity meets the payload requirements.

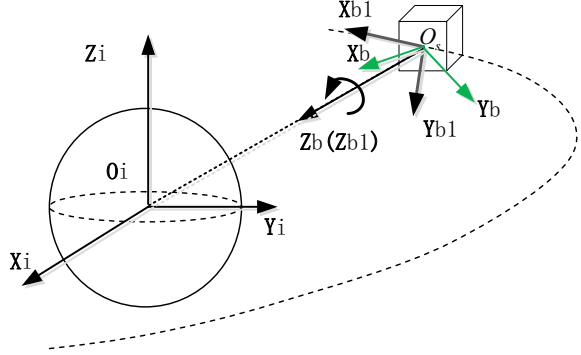
Because the satellite spins at a high speed and the angular momentum of the whole satellite is close to zero after compensation, it is impossible to control the satellite's attitude precession with the help of the spin angular momentum. Due to the high-speed rotation of the satellite, it is impossible to use the conventional three-axis stabilized satellite thruster attitude control algorithm. According to the characteristics of zero momentum spinning satellite, the attitude control algorithm of thruster should be designed, and the influence of thruster delay on thruster frequency and thruster volume should be considered.

Conventional non-spin satellites usually use PD pulse width modulation algorithm as thruster attitude control law, and jet pulse width can be calculated directly from the desired control torque. For the zero-momentum spinning satellite, the satellite body rotates at a high-speed relative to the orbital coordinate system, so the conventional control law cannot be used for attitude control. In order to solve this problem, this project defines a new reference coordinate system $O_{b1}X_{b1}Y_{b1}Z_{b1}$: the reference coordinate system Z_{b1} axis is consistent with the satellite body Z_b axis, the X_{b1} axis is obtained by the cross multiplication of Z_{b1} axis and the orbital plane normal Y_o , and the Y_{b1} axis is determined by the right-hand rule, so the reference coordinate system does not rotate rapidly relative to the orbital coordinate system, and it can reflect the payload LOS direction information. The attitude control of the satellite can be realized when the thrusters output the desired torque in the reference coordinate system (see Fig. 3).

According to the measurement information of star sensor, the component of satellite Z_b axis in orbit coordinate system can be obtained, and then the attitude of reference coordinate system relative to orbit coordinate system can be determined as follows:

$$\begin{aligned} X_{b1} &= \frac{Y_o \times Z_{b1}}{\|Y_o \times Z_{b1}\|} \\ Y_{b1} &= \frac{Z_{b1} \times X_{b1}}{\|Z_{b1} \times X_{b1}\|} \\ Z_{b1} &= Z_b \end{aligned} \quad (4)$$

Fig. 3. Diagram of reference coordinate system



Transformation matrix from orbit coordinate system to reference coordinate system.

$$\mathbf{A}_{b1o} = [\mathbf{X}_{b1} \ \mathbf{Y}_{b1} \ \mathbf{Z}_{b1}]^T \quad (5)$$

The attitude quaternion and angular velocity of the reference coordinate system relative to the orbital coordinate system can be obtained by the following method:

$$\mathbf{q}_{ob1} = dcm2quat(\mathbf{A}_{b1o}) \quad (6)$$

$$\boldsymbol{\Omega}_{ob1_k} = \mathbf{q}_{ob1_k}^{-1} \otimes (2(\mathbf{q}_{ob1_k}^{-1} - \mathbf{q}_{ob1_{k-1}}^{-1})/T) \quad (7)$$

where T is the attitude control period.

After obtaining the attitude and angular velocity information of the reference coordinate system relative to the orbit coordinate system, the command control torque can be calculated according to the conventional PD control law \mathbf{T}_c .

$$\mathbf{T}_c^{b1} = -\mathbf{K}_p \Delta \boldsymbol{\theta} - \mathbf{K}_d \Delta \boldsymbol{\omega} \quad (8)$$

It should be noted that since the thruster is installed in the satellite body coordinate system rather than the reference coordinate system, it is necessary to first transfer the command control torque to the satellite body coordinate system, and then calculate the command pulse width of each thruster

$$\mathbf{T}_c^b = \mathbf{A}_{bb1} \mathbf{T}_c^{b1} \quad (9)$$

$$\mathbf{t}_{on_i} = \frac{T_{c_j} \Delta t}{T_i} (i = x, y, z) \quad (10)$$

where T_c is the desired control torque, $\Delta\theta$ is the attitude control error, $\Delta\omega$ is the angular velocity control error, Δt is the control period, T_i is the nominal torque of each thruster and the jet width of each thruster.

It should be noted that in the process of thruster working delay and thruster start-up, the azimuth of each thruster relative to the reference coordinate system changes rapidly with the satellite rotation, that is, there is a deviation between the actual output torque and the expected torque, which will affect the attitude control accuracy, thruster working times, and total thruster volume. Therefore, it is necessary to analyze and simulate the delay characteristics of the thruster and evaluate the final attitude control accuracy and fuel consumption through mathematical simulation.

4 Mathematical Simulation

The satellite is set to run in a circular orbit with an orbital altitude of 500 km and an orbital inclination of 35° . The rotational inertia of satellite spindle $I_{xx} = 430 \text{ kgm}^2$, $I_{yy} = 430 \text{ kgm}^2$, $I_{zz} = 530 \text{ kgm}^2$, the inertia product $I_{xy} = 0.1 \text{ kgm}^2$, $I_{yz} = 0.1 \text{ kgm}^2$, $I_{xz} = 0.1 \text{ kgm}^2$, the nominal torque of each thruster is 1Nm, and the thrust equivalent delay is 50 ms.

Initial attitude of satellite relative orbit coordinate system $[26.5651 \ 41.8103 \ 26.5651]^\circ$ (123 sequence), initial angular velocity of relative inertial coordinate system $[0.5 \ 0.5 \ 90]^\circ/\text{s}$. It is assumed that the pointing accuracy of payload LOS axis is better than 0.5° . The attitude control bandwidth of PD is 0.375 rad/s (see Figs. 4, 5, 6, 7, 8 and 9).

From the simulation results, it can be seen that the number of thruster injection is related to the attitude control accuracy requirements. Under the current controller parameters, when the attitude maneuver control is in place, the attitude error between reference coordinate system and orbit coordinate system is less than 0.3° . The angular velocity error is less than $0.02^\circ/\text{s}$. The angular velocity error is mainly related to the dynamic unbalance disturbance caused by the inertia product of the satellite. Based on the initial orientation to the sun of the satellite attitude, through attitude maneuver and stability control, the payload LOS can be adjusted in a large range and continuously pointed to the earth center to meet the working conditions of the payload.

5 Conclusions

According to the requirements of rotation and pointing during the operation of rotating baseline payload, a spinning satellite scheme is proposed in this paper. In order to ensure that the line of sight of the payload points to the earth center continuously, it is necessary to overcome the orbit gyro moment interference, so the angular momentum compensation scheme of the spinning satellite is further

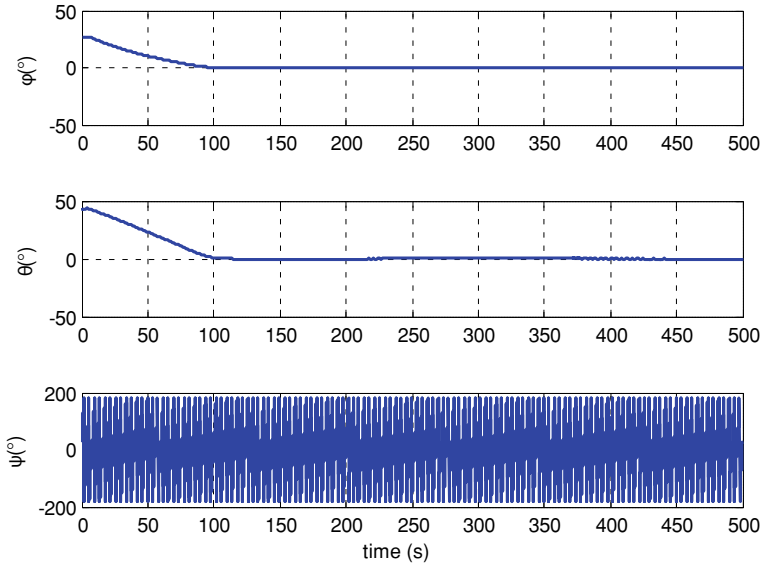


Fig. 4 Attitude angle of satellite body relative to orbit system

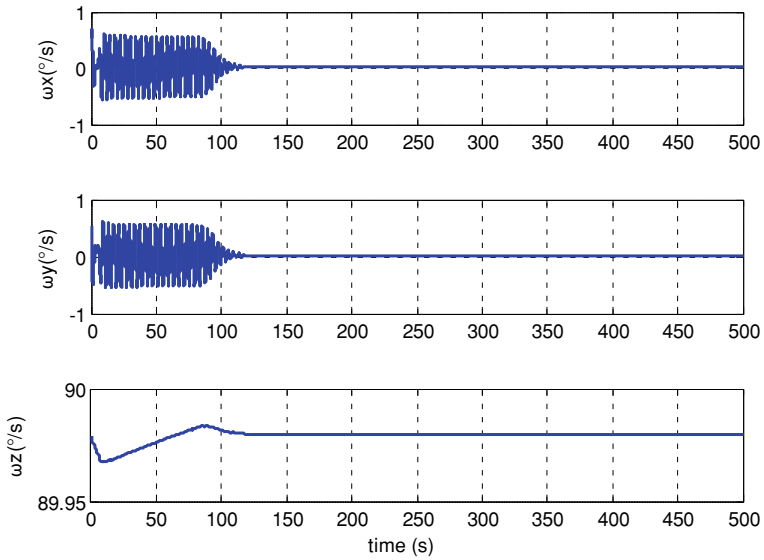


Fig. 5 Angular velocity in satellite relative orbit system

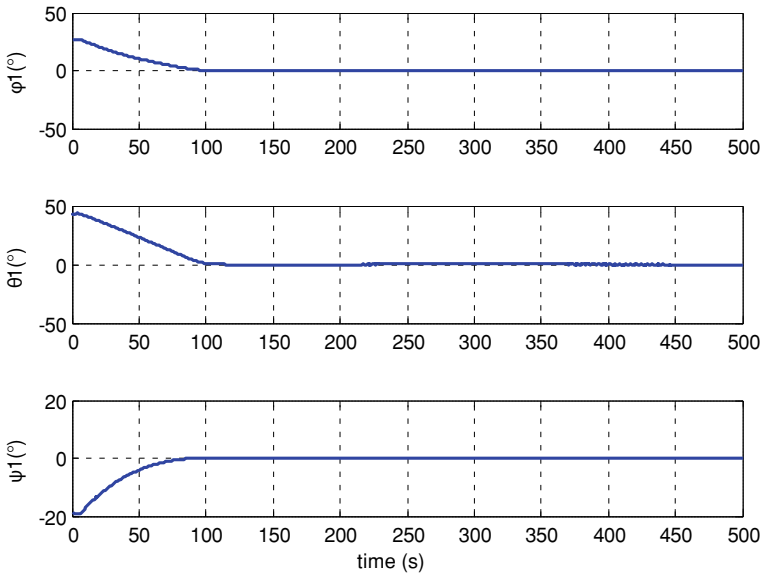


Fig. 6 Attitude angle in reference coordinate system relative to orbit system

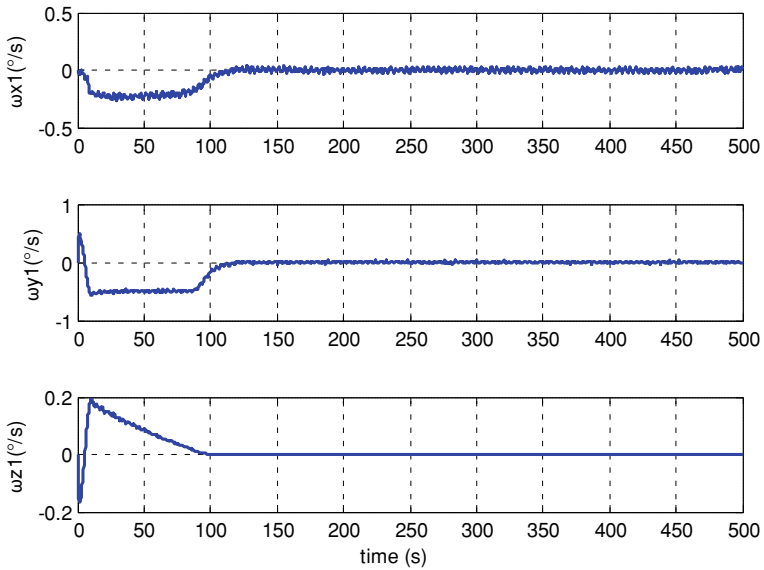


Fig. 7 Angular velocity in reference coordinate system relative to orbit system

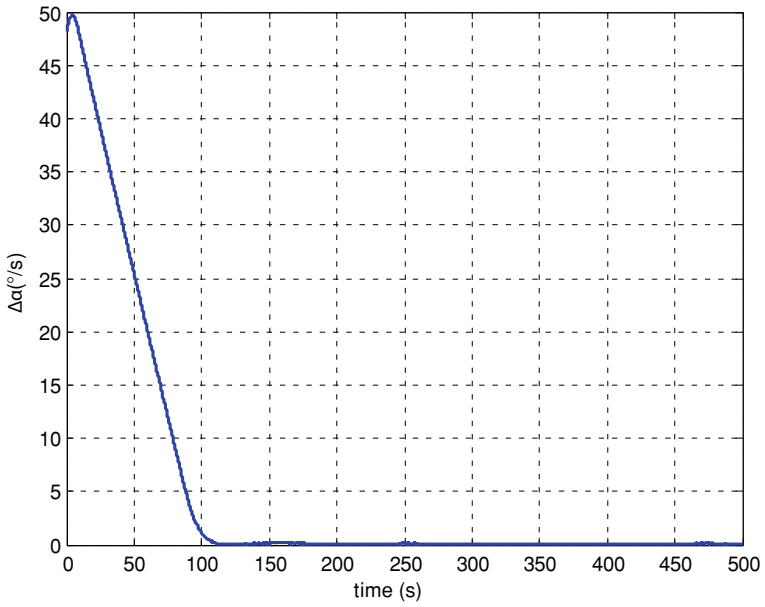


Fig. 8 Angle between the payload LOS and the direction of nadir

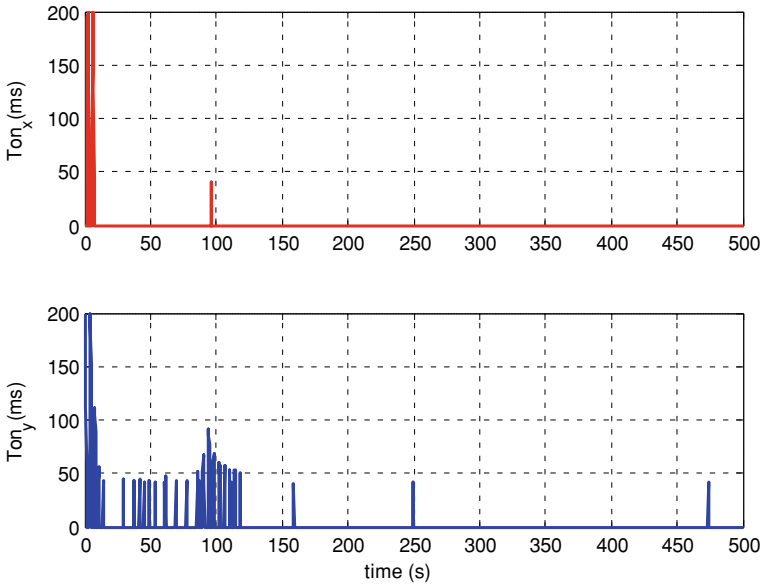


Fig. 9 Rolling and pitching direction pulse width

proposed. Different from conventional spin satellite and dual spin satellite, the precession control of Spin Satellite and the three-axis attitude stabilization control scheme of zero momentum satellite cannot be used. Therefore, this paper deduces the formula of dynamic unbalance interference torque caused by inertia product and spin angular velocity, and analyzes the influence of the interference torque on satellite attitude stability. By designing the reference coordinate system, the attitude control algorithm of the thruster is redesigned. The effectiveness of the proposed algorithm is verified by mathematical simulation.

Acknowledgements This research was funded by SAST-SJTU advanced space technology joint research fund, No. USCAST2019-22. Natural Science Fund of China, No. U20B2054, Shanghai Nature Science Fund No. 19ZR1426800, Shanghai Jiao Tong University Global Strategic Partnership Fund (2019 SJTU-UoT), WF610561702, and Shanghai Jiao Tong University Young Teachers Initiation Program, AF4130045.

References

1. Zhang M, Guo F, Li T et al (2013) A direction-finding method and analysis based on the rotated long baseline interferometer. *Acta Electron Sinica* 41(12):2422–2429. (in Chinese)
2. Xin J et al (2018) Multiple source parameter estimation for rotating interferometer using circular array processing. *J Electron Inf Technol* 40(2):486–492
3. Kawase S (2007) Radio interferometer for geosynchronous satellite direction finding. *IEEE Trans Aerosp Electron Syst* 43(2):443–449
4. Li CJ (2019) Study on the factors affecting wear life of the slip ring of LEO satellite. *Aerosp Shanghai* (36):79:83
5. Liang B, Zhang G (2016) Electrical sliding tribological behavior of Cu/Ag/graphite composite coating. *Rare Metal Mater Eng* 45(8):1961–1966
6. http://www.ty-space.com/pd.jsp?id=33#_pp=2_2835
7. Zu J (2018) An overview of integrated design of platform and payload for remote sensing satellite. *Spacecr Recover Remote Sens* 39(4):87:94
8. Qinghe XU, Lijia FAN, Hongtao GAO et al (2014) Integrated configuration design of platform and payload for remote sensing satellite. *Spacecr Recover Remote Sens* 35(4):9–16 (in Chinese)
9. Guangqian XING (1981) Analysis of jet control dynamics of Spin satellite. *Acta Autom Sinica* 7(1):42–54
10. Yuheng LI, Kechu YI, Peng GUAN (2005) The determination of attitude and control strategies for double spin geostationary satellites. *J Spacecr TT&C Technol* 24(5):19–26
11. Wang H et al (2012) Attitude control method for spin-stabilized satellites based on equiangular precession. *J Spacecr TT&C Technol* 31(4):20–24
12. Lin TIAN, Shijie XU (2009) Research on attitude dynamics modeling and control for Spin-stabilized micro-satellite. *Aerosp Control Alloc* 35(1):47–50
13. Shigehara M (1972) Geomagnetic attitude control of an axisymmetric spinning satellite. *J Spacecr Rocket* 9(6):391–398
14. Thomson WT (1962) Spin stabilization of attitude against gravity torque. *J Astronaut Sci* 9(1). Paper. AAS 9-1-31-3
15. Ovchinnikov MY et al (2020) Single axis stabilization of a fast-rotating satellite in the orbital frame using magnetorquers and a rotor. *Acta Astronaut* 173:195–201
16. Wie B, Weiss H, Arapostathis A (1989) Quaternion feedback regulator for spacecraft eigenaxis rotations. *J Guid Control Dyn* 12(3):375–380

Control Parameter Optimization for a Longitudinal Automatic Landing System via a Multi-objective Genetic Algorithm



Cheng Chen, Jie Ke, Haonan Xu, Bei Lu, and Qifu Li

Abstract It is challenging for control design and parameter optimization of a civil aircraft automatic landing system due to the complex application environment and high tracking precision requirement. In this paper, a parameter optimization method based on the non-dominated sorting genetic algorithm II (NSGA-II) is proposed to reduce the workload of control gain tuning and improve the performance of the autoland system. To facilitate the eventual engineering application, the flying quality indices are explicitly considered when defining the objective function for optimization. The proposed method is applied to design a longitudinal automatic landing system. It greatly simplifies the design process, and simulation results also demonstrate the effectiveness of the method.

Keywords Automatic landing system · Parameter optimization · Non-dominated sorting genetic algorithm II · Flying quality

1 Introduction

Landing is the most important phase of a flight due to the complex flight environment, poor visibility, and high requirement for flight path control [1]. According to the latest statistical summary, most flight accidents occur during the landing phase [2]. Therefore, a stable and reliable automatic landing control system (ALCS) is needed to ensure the landing safety of the aircraft. However, an ALCS involves control for multiple axes (e.g., longitudinal and lateral-directional), multiple loops (e.g., inner loop and outer loop), and different landing phases (e.g., final approach, flare, and decrab), leading to multiple control parameters to be adjusted. An appropriate solution can be obtained via an iterative design process, either manually or auto-

C. Chen · B. Lu · Q. Li (✉)
Shanghai Jiao Tong University, Shanghai, China
e-mail: qifuli@sjtu.edu.cn

J. Ke · H. Xu
Shanghai Aircraft Design and Research Institute, Shanghai, China

© The Author(s), under exclusive license to Springer Nature Singapore Pte Ltd. 2023
Z. Jing and D. Strelets (eds.), *Proceedings of the International Conference on Aerospace System Science and Engineering 2021*, Lecture Notes in Electrical Engineering 849,
https://doi.org/10.1007/978-981-16-8154-7_10

matically repeated. For the manual adjustment method, the control design engineer must have rich experience, and yet the design process is time consuming and the performance cannot be guaranteed to be optimal. With the development of computer technology and optimization algorithms, it is possible to automatically search the optimal control parameters by using the computer-aided design method.

Designing an ALCS is a complex optimization problem with multiple objective functions, which can be transformed into a single-objective optimization problem by using weighting coefficients or the min-max strategy. The problem can be solved by using some local optimization algorithms based on the gradient of the objective function. German Aerospace Center (Deutsches Zentrum für Luft- und Raumfahrt, DLR) used the sequential quadratic programming method and min-max strategy to tune the parameters of flight control systems and developed a set of engineering optimization software called Multi-Objective Parameter Synthesis (MOPS) [3]. Ames Research Center of the US military and University of Maryland used the CONSOL-OPTCAD optimization engine combined with MATLAB/Simulink simulation environment to launch the Control Designer's Unified Interface (CONDUIT) which was applied in the design and development of military aircraft [4]. However, due to the difficulty in determining the weighting coefficients and limitation of the initial design point, the solution of the optimization problem might not be globally optimal. Thus, many multi-objective meta-heuristic optimization algorithms have been adopted in flight control design for parameter tuning [5]. Deng and Duan proposed a pigeon-inspired optimization algorithm and applied it to design the control parameters for an automatic carrier landing system [6]. Hung et al. developed an intelligent multi-objective simulated annealing algorithm, which can be used to tune the parameters of robust proportional-integral-derivative (PID) controllers [7]. Bian, et al. applied a multi-solution particle swarm optimization algorithm for control parameter tuning to keep the safety of aircraft landing in crosswind [8]. In this paper, to deal with the possible conflict between different performance indices, the non-dominated sorting genetic algorithm II (NSGA-II) is applied to obtain the so-called Pareto optimal solution set, which includes appropriate control parameters for different situations.

The flying quality assessment is one of the important steps for testing the performance of a flight control system. Flying qualities are evaluated separately after the flight control system is designed. It is attractive in practical engineering to use flying quality requirements as the cost function for optimization, and complete the control design and performance evaluation at the same stage. In this paper, flying qualities defined in either time or frequency domain are explicitly considered when defining the objective function for ALCS optimization.

The structure of this paper is organized as follows. The framework of the ALCS is first described in Sect. 2. Then, the definition of the multi-objective optimization problem is introduced in Sect. 3. The idea of the formulation of the objective function based on flying qualities is explained as well. In Sect. 4, the process of the multi-objective optimization algorithm is given, which is applied in Sect. 5 to optimize a longitudinal automatic landing system. Finally, the conclusions are drawn in Sect. 6.

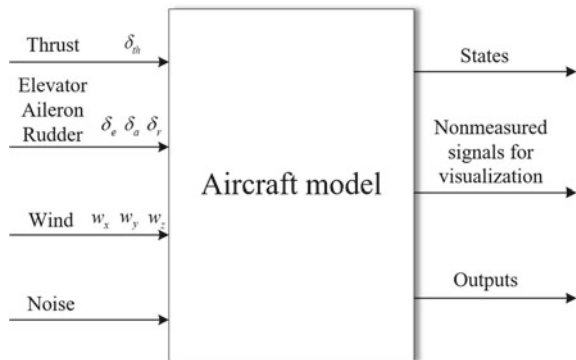
2 Model Description of the Aircraft

In this paper, the civilian aircraft landing challenge, a benchmark aircraft model provided by ONERA and AIRBUS [9], is used as a test platform for control design optimization. Figure 1 shows the structure of the simulation model, which is a 6-DOF rigid-body transport aircraft with 9 inputs including 4 control inputs, 3 wind inputs, and 2 noise inputs and 40 outputs including 16 states, 5 nonmeasured signals for visualization and 19 measurements for feedback control design.

Many advanced control methods have been developed in academia to design control laws for automatic landing systems, such as H_∞ control [10], sliding mode control [11], adaptive control [12], neural network-based control [13], etc. However, there are still gaps between the theory and application, and these advanced control methods are seldom applied to the actual civil aviation aircraft. In industry, the classical PID control method is often used to achieve a satisfactory control performance by adjusting the three terms. In this paper, the PID control structure is adopted for the longitudinal automatic landing system design. The control parameters are optimized to accurately track the glide-slope command generated by the instrument landing system (ILS) [14] and keep the calibrated speed constant even in the presence of disturbances.

The longitudinal control system is composed of two parts: the inner loop and the outer loop. The structure diagram of the inner loop is shown in Fig. 2, in which V_z and V_c are the signal of inertial vertical airspeed and calibrated airspeed. V_{zcmd} and V_{cmd} are the corresponding command signals, respectively. n_z and q are the load factor and pitch rate. The controller structure is chosen as proportional-integral (PI) or proportional (P) control, and $k_i (i = 1, 2, \dots, 10)$ are the control gains which will be designed using the optimization algorithm introduced in the next section. The elevator control command δ_e is generated by the rate tracking system and the engine control command δ_{th} is generated by the autothrottle system. The structure of the outer loop is shown in Fig. 3, in which ΔV is the deviation between the current

Fig. 1 Structure of nonlinear aircraft simulation model



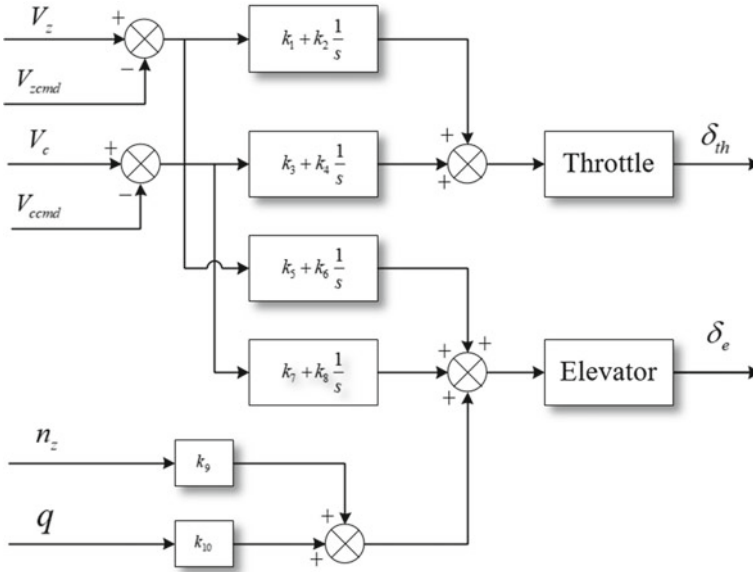
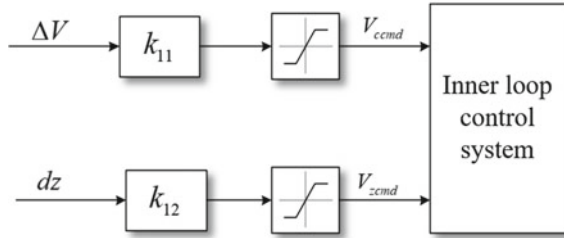


Fig. 2 Structure diagram of longitudinal inner loop flight control system

Fig. 3 Structure diagram of longitudinal outer loop flight control system



velocity and the steady-state value, d_z is the glide deviation calculated by the ILS. Two P controllers are used to control the aircraft attitude and trace a landing path, as well as to keep the flight speed constant.

3 Problem Formulation for ALCS Parameter Optimization

An automatic landing system involves multiple modes, multiple inputs, and multiple outputs with different performance requirements [15], which could be contradictory with each other. Some performance requirements are sometimes compromised to obtain a solution. In order to make a comprehensive analysis of the optimization target, in this section, the automatic landing control problem is formulated as a multi-objective optimization problem by combining multiple performance indices.

3.1 Definition of the Multi-objective Optimization Problem

A generic multi-objective control optimization problem associated with a given dynamic system can be formulated as

$$\begin{aligned} & \min_K J(K) \\ \text{s.t. } & g_i(K) \leq 0 \quad (i = 1, 2, \dots, n_g) \\ & h_i(K) = 0 \quad (i = 1, 2, \dots, n_h), \end{aligned} \quad (1)$$

where $J(K)$ is the vector of different optimization objectives, and $J(K) = [J_1(K), J_2(K), \dots, J_m(K)]$. $K \in D \subseteq R^n$ is defined as a set of control parameters in the searching space D (formed by parameter bounds) which must be optimized to make the cost function J be minimized. $g_i(K)$ and $h_i(K)$ are inequality and equality constraints, respectively.

Unlike the single-objective optimization problem, for the multi-objective optimization problem (1), the superiority of a solution over other solutions cannot easily be determined by comparing their objective function values. The goodness of a solution is determined by the dominance. This implies that the final solution of problem (1) is not a single one for the reason that there is no solution dominating in all objectives. Here, the concept of Pareto optimal solution is used to describe the degree to which the solution satisfies different cost functions J_i . The related definitions are given below.

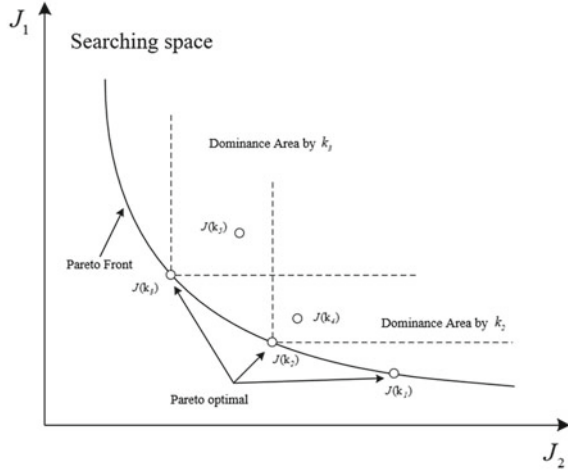
Definition 1 (*Pareto optimal* [16]) In the searching space, if no objective function value $J(K^*)$ can be improved without worsening the rest, the solution K^* is a Pareto optimal, i.e., $\nexists K \in D : J \leq J^*$.

Definition 2 (*Pareto solution set* [16]) The Pareto solution set Θ contains all Pareto optimal solutions, i.e., $\Theta = \{K \in D \mid \nexists K \in D : J \leq J^*\}$.

Definition 3 (*Pareto front* [16]) The Pareto front is the set J^* including the objectives of all the Pareto optimal solutions, i.e., $J^* = \{J \mid K \in \Theta\}$.

To help better understand the above definitions, a visualization of Pareto optimal and Pareto front for two objectives is presented. As shown in Fig. 4, five solutions (k_1, \dots, k_5) in the searching space are calculated to estimate the Pareto solution set. The solutions k_1, k_2, k_3 are Pareto optimal because there are no better solutions for both objectives J_1 and J_2 . However, the solutions k_4, k_5 are not Pareto optimal because some solutions dominate them. In fact, it is impossible to calculate the exact Pareto front that contains infinite solutions. Hence, the corresponding objectives, $J(k_1), J(k_2), J(k_3), \dots$, each of which is confirmed to be Pareto optimal, can be used together to approximate the Pareto front.

Fig. 4 Definition of Pareto optimal and Pareto front for two objectives



3.2 Definition of the Objective Functions

For the optimization design of flight control systems, the objective function is defined based on the flying qualities, which are affected by many factors and are given using different performance indices, either in time domain or frequency domain. The type of time-domain indices such as integrated square error (ISE) [17] or integrated time and absolute error (ITAE) [18] is often used in previous studies. However, the resulting optimization target has no obvious physical meaning, and also it is hard to reflect the influence of control system parameters on the flight over time. In this paper, the flying qualities defined in not only time but also frequency domains are considered to design the objective function, which involves two steps, flying quality specification and index standardization.

A. Flying quality specification

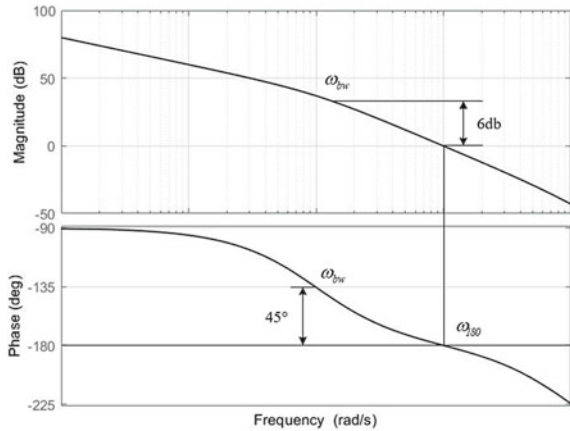
The performance specifications usually considered in flight control design are rise time and overshoot, which both are defined in the time domain to assess the transient response. For the performance of the steady-state response, ISE can be used to quantify the steady-state tracking error. Except these three commonly used time-domain performance specifications, other flying quality indicators given in MIL-STD-1797A include control anticipation parameter (CAP) [19], bandwidth criterion [20] and closed-loop (Neal-Smith) criterion [21], etc.. Table 1 lists the objectives chosen for optimization design of the longitudinal automatic landing system studied in this paper.

Note that the bandwidth criterion is a two-dimensional performance index defined in the frequency domain. It is used to determine the flying quality level based on the values of the prescribed open-loop system bandwidth ω_{bw} and the time delay τ_p . Consider the open-loop pitch attitude response to the pilot control force or displacement input, as shown in Fig. 5. ω_{bw} is the smaller value of the corresponding frequencies

Table 1 Performance indices chosen for optimization design

Objectives	Description	Dimension	Type
R_t	Rise time	1	Time domain
O_s	Overshoot	1	Time domain
ISE	Integral of the squared error value	1	Time domain
Bw_c	Bandwidth criterion	2	Frequency domain

Fig. 5 Definition of bandwidth



when the phase margin is not less than 45° or the gain margin is not less than 6 dB. The time delay is defined as follows:

$$\tau_p = -\frac{(\phi_{2\omega_{180}} + 180^\circ)}{57.3 \times 2\omega_{180}} \tag{2}$$

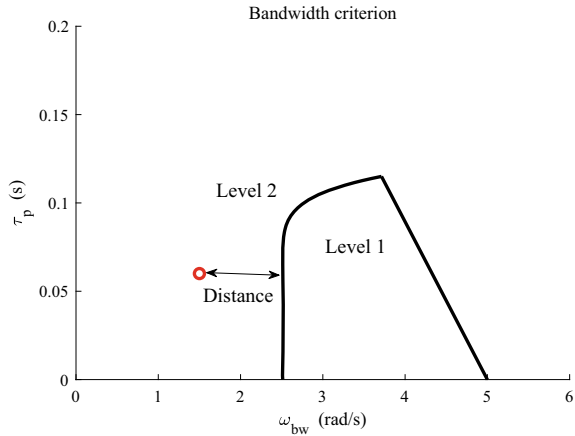
where ω_{180} is the frequency when the phase is equal to -180° and $\phi_{2\omega_{180}}$ is twice the phase angle at the frequency ω_{180} . According to the obtained ω_{bw} and τ_p , the flying quality level of the system can be determined, as shown in Fig. 6.

B. Index standardization

Note that the performance specifications listed in Table 1 are one or two dimensional. In order to consider them together in an optimization process, in this paper, the two-dimensional specifications are transformed to one-dimensional. For each two-dimensional specification, there are two levels of demarcation to define the performance. Take the bandwidth criterion as an example. As shown in Fig. 6, in the area of Level 1, the flying quality is satisfactory and no improvement in control design is needed. The rest area is Level 2, which is unacceptable. Thus, the optimization target is to make the flight control system achieve the Level 1 flying quality.

In the optimization process, a distance algorithm can be used to translate the location of performance points on each of the two-dimensional indicators into a

Fig. 6 Two-dimensional performance demarcation and rate translation



numerical rating. If the design points fall into the Level 1 area, the performance rating is zero. When it falls into the Level 2 area (see the red point shown in Fig. 6), this rating will be calculated by the distance from the border splines between Level 1 and Level 2 and the higher the number, the worse the flight performance.

4 Control Design Using Non-dominated Sorting Genetic Algorithm

After determining the structure of the flight control system and defining the objective function and constraint conditions, the next step is to solve the control parameters using an optimization algorithm. The block diagram of the general control parameter optimization process is shown in Fig. 7. In this research, a fast and genetic algorithm (NSGA-II) [22] is adopted to find the parameters that make the flight control system achieve an optimal performance.

Fig. 7 Block diagram of the general multi-objective control parameter optimization process

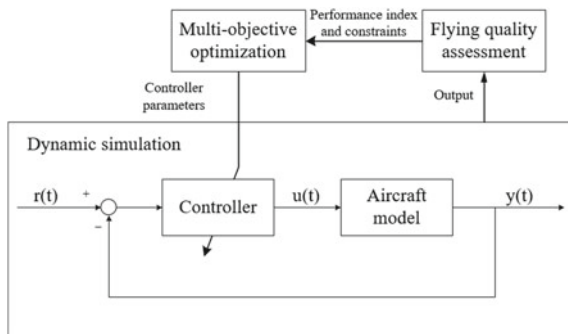
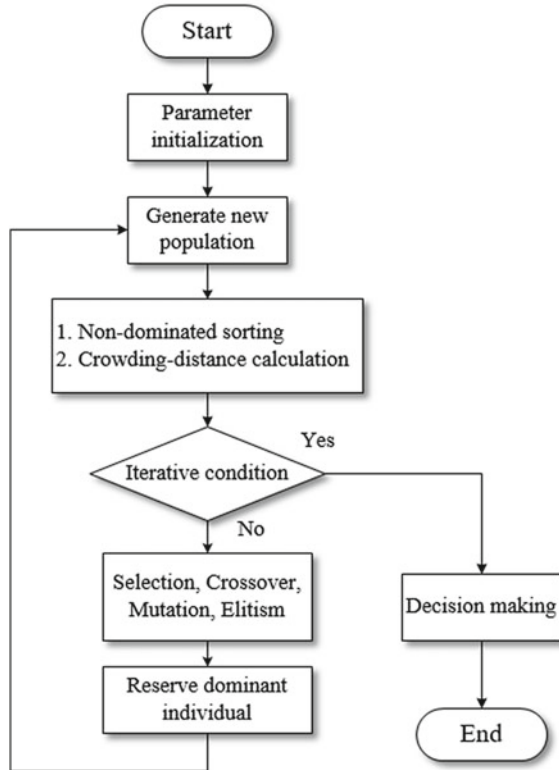


Fig. 8 Flowchart of NSGA-II algorithm



The flowchart of the NSGA-II algorithm is shown in Fig. 8 and it works as follows. At the beginning, the parent population P_t and the new generation population Q_t of size N are randomly generated and mixed to make a fast non-dominant ranking. Meanwhile, the crowding degree of all individuals in each Pareto level is calculated. According to the non-dominant relationship between individuals and the crowding degree, the appropriate individuals are selected to form a new parent population P_{t+1} . Next, the new offspring population Q_{t+1} will be generated by the traditional genetic algorithm process, such as crossover, mutation, etc.. Repeat the above operations until the end condition of the optimization problem is met.

Compared with the traditional single-objective genetic algorithm, NSGA-II is different in the following three aspects:

A. Fast non-dominated sorting

By calculating the dominant number N_p for any individual in the population and the set θ_p for the solutions dominated by it, this stratification of the existing population is realized to guide the solution direction of Pareto optimal. The front with a non-inferior level of 1 is the current Pareto front.

B. Elitist strategy choice

To improve the convergence of the genetic algorithm, the Level 1 Pareto solutions in the parent generation population without crossover and mutation are used to replace the lowest Pareto class individuals in the current population.

C. Crowding-distance computation

The crowding distance is used as the estimation index of individual distribution, and the individuals in this class are ranked according to the objective function. f_m^{\min} and f_m^{\max} are the m th objective function value of the first and the last individual, respectively. $obj(p_{i+1})$ and $obj(p_{i-1})$ are the value of objective functions from two adjacent individuals. The crowding distance of the two boundaries after sorting is set to ∞ . Individual crowding distance is calculated according to the following formula:

$$I(d_1) = I(d_n) = \infty, I_0(d_i) = 0$$

$$I(d_i) = I_0(d_i) + \frac{obj(p_{i+1}) - obj(p_{i-1})}{f_m^{\max} - f_m^{\min}} \quad (3)$$

5 Simulation Results and Analysis

In this section, the NSGA-II algorithm is applied to optimize the longitudinal automatic landing system described in Sect. 2. Firstly, the constraints are defined as shown in Table 2, including the limits of longitudinal control inputs and states for landing. Secondly, the optimization objectives are divided into two categories: hard objective and soft objective. The flying quality index defined using the bandwidth criterion is taken as a hard objective, which must abide by all optimal solutions in the Level 1 region as shown in Fig. 6. The remaining three objectives listed in Table 1, i.e., the rise time, the overshoot, and the ISE, are soft objectives, which adopt a minimization strategy.

The NSGA-II algorithm is used to tune the control parameters and solve the Pareto optimization problem. The results of the tuning process are shown in Fig. 9. For the

Table 2 Constraints of control inputs and states for longitudinal flight control

Variable	Description	Unit	Bound	Rate-limit
EPR	Exhaust pressure ratio	–	(0.95, 1.6)	0.1
δ_e	Elevator deflection	deg	(–25, 25)	20
p	Pitch rate	deg/s	(–30, 30)	30
n_z	Vertical load factor	g	(0.8, 1.2)	0.1

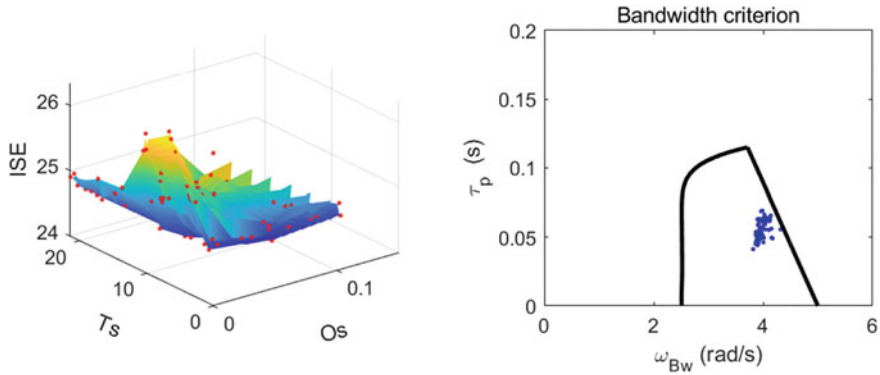
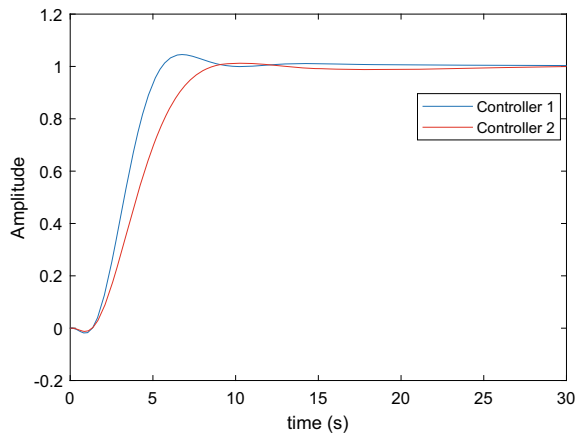


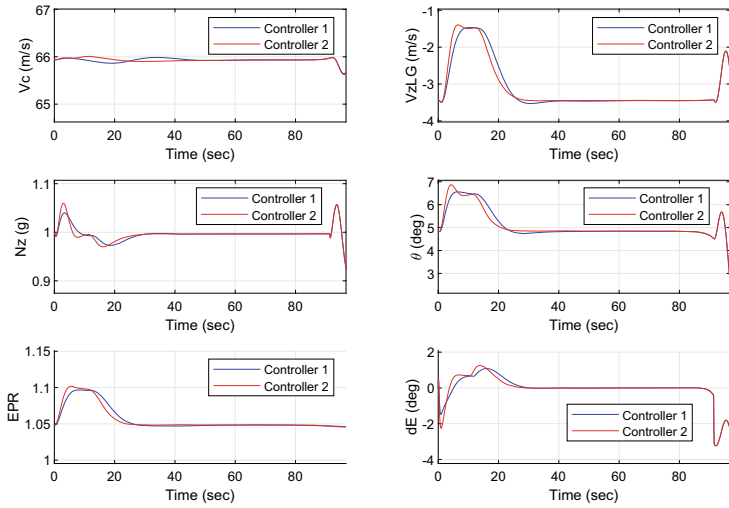
Fig. 9 Pareto front of controller parameters (left) and flying quality evaluated using bandwidth criterion (right)

Fig. 10 Linear simulation response for the V_z command input

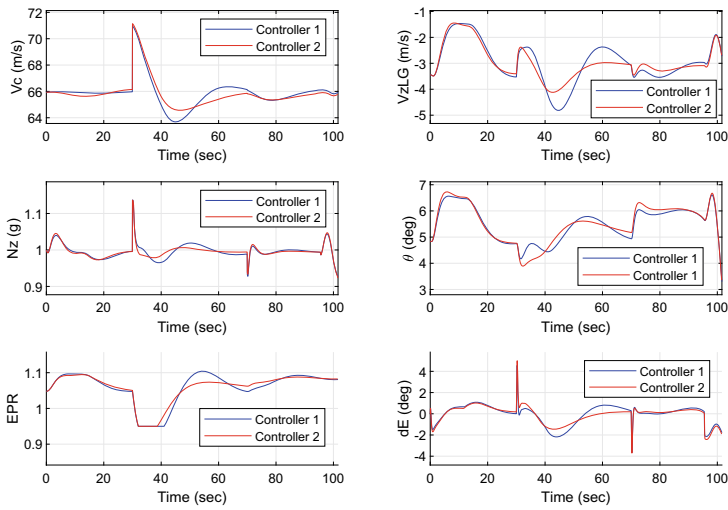


plot on the left side, three axes represent the three soft objectives, respectively. The red points are the Pareto optimal solutions and each point is corresponding to a set of controller parameters that are Pareto dominated. According to the position of each point in the three-dimensional space, the approximate Pareto front is obtained by surface fitting method. Corresponding to the Pareto optimal solutions, the plot on the right side represents their performance assessed using the bandwidth criterion.

Finally, the controller parameters can be determined by selecting a Pareto optimal solution from the Pareto front based on the practical application considerations. In this example, two Pareto optimal solutions are selected, and the corresponding simulation responses are shown in Figs. 10, 11 and 12. Figure 10 shows the linear step responses of the V_z command using these two controllers, for both of which good dynamic performance with zero steady-state tracking error can be obtained. Also, it can be observed that the response obtained using the first controller has a quicker speed but a bigger overshoot. Figures 11 and 12 show nonlinear simulation responses

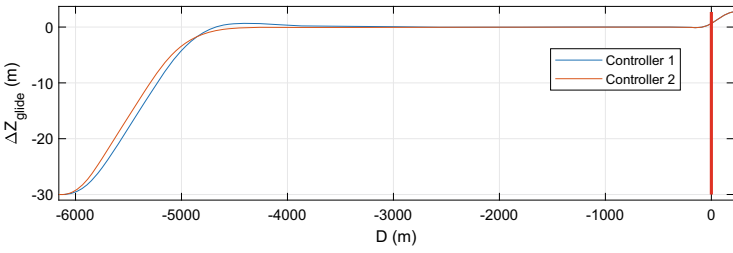
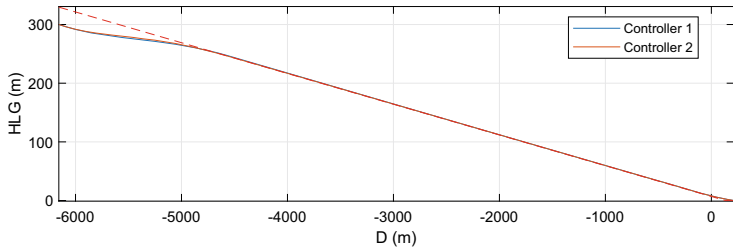


(a) Without wind disturbances

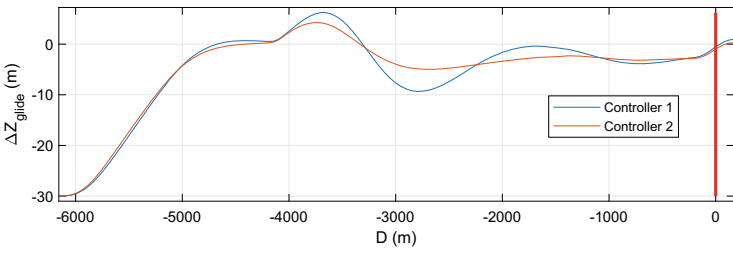
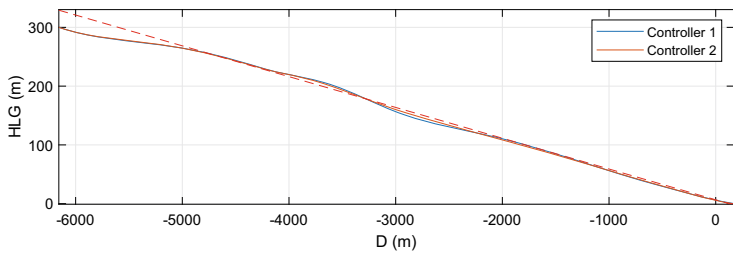


(b) With a deterministic wind disturbance (5 m/s gust w_x)

Fig. 11 Nonlinear simulation responses of longitudinal variables



(a) Without wind disturbances



(b) With a deterministic wind disturbance (5 m/s gust w_x)

Fig. 12 The aircraft trajectory

and aircraft trajectories for with and without wind disturbances, respectively. Overall, acceptable performance is obtained using either of the controllers, which can maintain a constant speed and achieve an accurate trajectory tracking during the landing phase.

6 Conclusion

In this paper, an automatic controller parameter tuning method is proposed for the ALCS design. The tuning process is formulated as a multi-objective optimization problem, for which the performance indices (including rise time, overshoot, and ISE) and the flying quality defined using the bandwidth criterion are considered as the optimization objectives. The NSGA-II algorithm is applied to solve the optimization problem and the solutions are given as Pareto optimal and Pareto front. In the part of analysis, two sets of controllers are selected from the Pareto front, and simulation results show an overall good landing performance for both controllers. This paper presents an alternative flight control system design method, which can improve the design efficiency and guarantee the optimal flying quality. For the next step, this method will be generalized to a complete automatic landing system design, including longitudinal as well as lateral-directional axes.

References

1. Zhao Y, Yue C, Hu H (2016) Gust load alleviation on a large transport airplane. *J Aircr* 53(6):1932–1946
2. Airbus, Commercial Aviation Accidents 1958–2019, A Statistical Analysis (2020)
3. Joos H-D (1999) A methodology for multi-objective design assessment and flight control synthesis tuning. *Aerosp Sci Technol* 3(3):161–176
4. Tischler M, Colbourne J, Morel M, Biezad D, Levine W, Moldoveanu V (1997) Conduit-a new multidisciplinary integration environment for flight control development. In: Guidance, navigation, and control conference, p 3773
5. Marler RT, Arora JS (2004) Survey of multi-objective optimization methods for engineering. *Struct Multidiscip Optim* 26(6):369–395
6. Deng Y, Duan H (2016) Control parameter design for automatic carrier landing system via pigeon-inspired optimization. *Nonlinear Dyn* 85(1):97–106
7. Hung M-H, Shu L-S, Ho S-J, Hwang S-F, Ho S-Y (2008) A novel intelligent multiobjective simulated annealing algorithm for designing robust PID controllers. *IEEE Trans Syst, Man, Cybern-Part A: Syst Humans* 38(2):319–330
8. Bian Q, Nener B, Wang X (2018) Control parameter tuning for aircraft crosswind landing via multi-solution particle swarm optimization. *Eng Optim* 50(11):1914–1925
9. Biannic JM, Boada-Bauxell J (2016) A civilian aircraft landing challenge. Online available from the aerospace benchmark section of the SMAC toolbox. <http://w3.onera.fr/smac>
10. Alpert J (2001) A new approach to fixed-order H-infinity synthesis-application to autoland design. In: AIAA guidance, navigation, and control conference and exhibit (2001), p 4282
11. Bouadi H, Wu H, Mora-Camino F (2011) Flight path tracking based-on direct adaptive sliding mode control. In: 2011 IEEE intelligent vehicles symposium (IV). IEEE, pp 25-30

12. Wang Y, Li Q, Lu B (2018) Automatic landing system design via multivariable model reference adaptive control. *Aerosp Syst* 1(1):63–71
13. Juang J-G, Chien L-H, Lin F (2011) Automatic landing control system design using adaptive neural network and its hardware realization. *IEEE Syst J* 5(2):266–277
14. Gray RA, Maybeck PS (1995) An integrated GPS/INS/baro and radar altimeter system for aircraft precision approach landings. In: *Proceedings of the IEEE 1995 national aerospace and electronics conference. NAECON 1995, vol 1, IEEE*, pp 161–168
15. Parker R, Temoleman J (1967) Automatic landing system 727 airplane. In: *Control and flight dynamics conference*, p 573
16. Miettinen K (2012) *Nonlinear multiobjective optimization*, vol 12. Springer Science & Business Media, Berlin
17. Zhuang M, Atherton D (1991) Tuning PID controllers with integral performance criteria. In: *International conference on control 1991. Control'91, IET*, pp 481–486
18. Davey K, Bounds S (1996) Source-weighted domain integral approximation for linear transient heat conduction. *Int J Numer Meth Eng* 39(10):1775–1790
19. Gautrey J, Cook M (1998) A generic control anticipation parameter for aircraft handling qualities evaluation. *Aeronaut J* 102(1013):151–160
20. Hodgkinson J, Wood J, Hoh R (1983) An alternate method of specifying bandwidth for flying qualities. In: *Guidance and Control Conference*, p 1609
21. Bailey R, Bidlack T (1994) A quantitative criterion for pilot-induced oscillations-Time domain Neal-Smith criterion. In: *21st atmospheric flight mechanics conference*, p 3434
22. Deb K, Pratap A, Agarwal S, Meyarivan T (2002) A fast and elitist multiobjective genetic algorithm: NSGA-II. *IEEE Trans Evol Comput* 6(2):182–197

Named Entity Approach for Structured Management of Aeronautical Product Requirements



JianKai Lu and ChunKai Hu

Abstract Civil aircraft is a typical complex product system. It has the characteristics of high technology intensiveness, strong interdisciplinary, high system integration, long development cycle, large project investment, and complex project management. The development process of civil aircraft usually involves many stakeholders, and each stakeholder will put forward its own requirements for the aircraft development process. Therefore, the number of requirements documents and requirements items summarized in the hands of product suppliers will be very large. One way to solve the above problems is to adopt a structured expression of requirements, so that the subject, object, realization function, attribute parameter, and category involved in each requirement can be clearly expressed in the database. Aiming at the extraction of attributes such as subject and object in the demand, this topic uses the related algorithm of named entity recognition in natural language processing to identify the corresponding entity. I built a word segmentation and NER model based on the Hidden Markov Model, which has achieved good results on the test data set.

Keywords Systems engineering · NER · NLP · HMM

1 Introduction

1.1 The Basic Problem of NER

Information extraction is the core step of the structured management of aviation product requirement. Structured management refers to the process of structural analysis of demand documents entered in free text, extracting unstructured information from electronic medical records, and converting it into structured information.

J. Lu (✉) · C. Hu

School of Aeronautics and Astronautics, Shanghai Jiao Tong University, Shanghai, China

e-mail: lj_k_1stprc@sjtu.edu.cn

C. Hu

e-mail: 13236558677@163.com

The structured analysis process often uses relevant knowledge of aviation product terminology dictionaries, uses advanced technology in the field of natural language processing, and needs to strictly follow aviation product access standards, such as MIL-STD-1750A and so on.

1.2 Difficulties in Applying Named Entity Recognition to Aviation Product Requirements

There are few domestic researches on corpus in the aviation field, and this article lacks relevant reference materials. Moreover, aviation-related data at home and abroad has a certain degree of confidentiality. It is difficult to obtain sufficient data training models in this article, which makes it difficult to implement some deep learning models with relatively high data requirements.

2 Literature Review of Named Entity Recognition

2.1 Introduction to Named Entity Recognition

The term “Named Entity” (NE) was first used at the sixth Message Understanding Conference (MUC-6). Named entity recognition is one of the subtasks of information extraction. The purpose is to locate named entities in unstructured text. Different from English and other languages composed of words, if you want to complete the task of named entity recognition in Chinese, you must first complete the leading subtask: word segmentation. After having a correct word segmentation result, it is possible to discuss the identification of entities and the determination of entity relationships. The form and the construction of language vocabulary make it relatively difficult to recognize named entities in Chinese.

There are already some mature word segmentation tools, such as Jieba, SnowNLP, PkuSeg, THULAC, HanLP, and so on. But for the aviation industry, these universal word segmentation tools may not be sufficiently robust.

The named entity recognition of the requirements document in the aviation field also requires the construction of an ontology in the field. Previous literature used ontology to describe design-related functions, to assist function-oriented engineering design, and to describe and model the abstract concepts of conceptual design.

2.2 *Commonly Used Models and Methods for Named Entity Recognition*

Rule-based Approaches. Rule-based named entity recognition requires manual input of rules. Erik F. Tjong Kim Sang and Fien De Meulder [2] used a named entity identification method that matches certain rules and set up a standard to test the effectiveness of the method. In the test of English and German test corpus, good results have been achieved. The corresponding English corpus has a 14% error rate, and the corresponding German has a 6% error rate.

Wu [5] built a semantic parsing module with a complete system of named entity recognition based on a rule matching network. In the matching network design process, by introducing a rule configuration system, the rules are classified and hierarchically processed to reduce the computational complexity in the rule matching process. Improved matching speed.

However, rule-based named entity recognition can only play a well role under the premise that the corpus does not change much and the manual rules can exhaust the rules of the input corpus. This not only makes the model's portability poor but also makes it difficult to respond to the complex needs of multiple stakeholders.

Unsupervised Learning Approaches. Michael Collins and Yoram Singer [3] converted words into tokens and then use clustering methods to find similar entities. Zhao [4] studied the application of metric learning technology in unsupervised problems. Compared with other classification problems, the salient feature of metric learning technology is that it does not directly learn the target task classifier, but indirectly through the similarity measurement between learning samples. Achieve classification tasks.

Deep learning techniques for NER. Deep learning is a very commonly used machine learning method in recent years. Deep learning has a multi-layer neural network, which has very strong learning ability and excellent data migration ability. Therefore, deep learning can be applied to the work of named entity recognition. The supervised deep learning relationship extraction method can solve the main problems of manual feature selection and feature extraction error propagation in classic methods and combine low-level features to form more abstract high-level features to find distributed feature representations of data [6].

However, the model of named entity recognition based on deep learning is often too complicated, requires a lot of data, is poor in interpretability, and lacks the ability of model transfer [7].

2.3 Research on Named Entity Recognition in a Specific Field

By studying various named entity recognition methods, Zou Tao proposed an efficient recognition strategy for named entities in the field of electronic products, which is the preliminary work in the project "World Information Technology and Product Level Library Construction"-through computer intelligence methods to identify Named entities such as product technical parameters in the field of electronic products provide solutions, and provide underlying support for quantitative intelligence analysis and vertical search that may be carried out in the next step [8]. This strategy organically combines rule-based and statistical identification methods through a cascading model, inherits the advantages of rule-based and statistical identification methods, and fully considers the trade-off between text characteristics and human and material resources in the field of electronic products. Finally, the named entity recognition system in this field is realized, and 19 types of named entities such as the technical parameters of electronic products are selected, and comparative experiments are carried out to prove the recognition effect of the system, and satisfactory results are obtained.

Zhang Yunzhong combined the characteristics of the three entities and the dependencies between the entities, proposed a complex medical named entity recognition method based on multi-neural network collaboration, and realized sentence-level model migration, solved the number and quality of training data sets, and finally obtained. The second place in the evaluation task. In addition, the improved method of this method won the first place in CCKS2019 evaluation task 1, which confirmed its effectiveness and generalization ability [9].

Aiming at the problems of traditional agricultural named entity recognition methods relying on artificial feature templates, insufficient feature information extraction, and inconsistent labeling caused by multiple entity names in the construction of agricultural intelligent question and answering system, Zhao [10] proposed an attention mechanism-based agricultural text named entity recognition method.. Use continuous bag-of-words model (CBOW) to pre-train the input word vector to enrich the feature information of the word vector and alleviate the impact of word segmentation accuracy on performance; introduce a document-level attention mechanism to obtain similar information between entities to ensure that entities are in different contexts Under the label consistency; based on the bidirectional long-term short-term memory network (BiLSTM) and conditional random field (CRF) model to build a model framework suitable for entity recognition in the agricultural field. Compared with the other three recognition methods, the accuracy of the model in corpora of different scales has been improved to a certain extent, which has obvious performance advantages.

3 Language Model

3.1 Early Language Model

The earliest language model is the n-gram model. Suppose we want to predict the probability $P(w|h)$ of a word w appearing behind a sentence, this model can estimate this probability. Suppose the history is “Pooh likes to eat” and we want to know the probability that the next word is “honey”:

$$P(\text{honey}|\text{Pooh likes to eat}) \tag{1}$$

We only need to count the number of occurrences of each word after the sentence "Pooh likes to eat" in a large enough relevant corpus, and count each situation as a probability. So we get “When history h is known, what is the probability that w will appear later”, as follows:

$$P(\text{honey}|\text{Pooh likes to eat}) = \frac{C(\text{Pooh likes to eat honey})}{C(\text{Pooh likes to eat})} \tag{2}$$

This model will lead to a very serious consequence that is data sparsity: if we continue to increase the dimensionality of the data, then the storage space requirements will increase exponentially, and most of the storage locations are 0. In this way, we need a more flexible method to predict the probability of a word appearing based on historical data. In order to express the probability of each specific word, we can use a chain model:

$$P(X_1 \dots X_n) = P(X_1)P(X_2|X_1)P(X_3|X_{1:2}) \dots P(X_n|X_{1:n-1}) = \prod_{k=1}^n P(X_k|X_{1:k-1}) \tag{3}$$

Applying the chain rule to words, we get

$$P(w_{1:n}) = P(w_1)P(w_2|w_1)P(w_3|w_{1:2}) \dots P(w_n|w_{1:n-1}) = \prod_{k=1}^n P(w_k|w_{1:k-1}) \tag{4}$$

Such a formula can be used to describe the conditional probability in a sentence.

3.2 Bidirectional Encoder Representations from Transformers Model (BERT)

Pre-training a language model with a certain model seems to be a more reliable method. From the previous ELMo of AI2, to the fine-tune transformer of OpenAI, to this BERT of Google, all are applications of pre-trained language models. The BERT model is different from the other two:

1. It replaces a small number of words with Mask or another random word with a reduced probability when training a two-way language model. I personally feel that the purpose of this is to force the model to increase the memory of the context. As for this probability, I guess Jacob set it casually.
2. Added a loss to predict the next sentence. This looks rather new.

The reason for the high-performance of BERT is actually due to two points. In addition to the improvement of the model, more importantly, it uses a large data set (BooksCorpus 800 M + English Wikipedia 2.5G words) and large computing power (corresponding to a large model). Pre-training on related tasks has achieved a monotonous increase in performance on the target task.

The two-way model of this model is different from Elmo. Most people have misunderstood the size of his two-way contribution on novelty. I think this detail may be the reason for his significant improvement over Elmo. Elmo spells a left-to-right and a right-to-left. He opened a window directly during training and used a sequential cbow.

3.3 Bidirectional and Auto-Regressive Transformers Model (BART)

We can think of BART as a combination of BERT with a two-way encoder and GPT2 with a left-to-right decoder. At the same time, the BERT model adds a causal decoder to the bidirectional encoder architecture of BERT and replaces the cloze task of BERT with more complex pre-training tasks.

The most important pre-training task of BERT is to predict the masked token and use the entire input to obtain more complete information for more accurate prediction. This is effective for tasks that allow the use of information after position i to predict position i , but it is not useful for tasks such as text generation, where predictions of position i can only depend on previously generated words. The GPT pre-training task uses the idea of autoregressive, using the information that has been decoded to predict the next position. This mode is more effective for generating tasks but worse for downstream tasks that can use global input to get output. The BART model can achieve the best of both worlds.

Both Bart and T5 replace the text span with a mask during pre-training and then let the model learn to reconstruct the original document. In the summary generation task,

the input sequence is the document we want to summarize, and the output sequence is a fact summary. The Seq2Seq architecture can be directly used for summary tasks without any new operations, and pre-training tasks are also very suitable for downstream tasks. The numbers in the following table confirm this: in the CNN/Daily Mail abstract summary task, all new Seq2Seq models do much better than those old less-fancy models, and BART performs particularly well.

4 NER Based on Hidden Markov Model

4.1 HMM Model

Machine learning methods are increasingly being used in named entity recognition. Compared with rule-based methods, machine learning methods are most beneficial for higher maintainability, adaptability, training, and economy. At the base of a sequence of token $T_1^n = t_1 t_2 \dots t_n$, NER tries to find an optimal tag sequence to optimize: $\log P(T_1^n | G_1^n) = \log P(T_1^n) + \log \frac{P(T_1^n, G_1^n)}{P(T_1^n) \cdot P(G_1^n)}$ is the mutual information of T_1^n and G_1^n . For simplifying the calculation of mutual information between the two. It is necessary to assume that mutual information is independent: $MI(T_1^n, G_1^n) = \sum_{i=1}^n MI(t_i, G_i^n)$.

Bring into the front, we get:

$$\log P(T_1^n | G_1^n) = \log P(T_1^n) - \sum_{i=1}^n \log P(t_i) + \sum_{i=1}^n \log P(t_i | G_i^n) \quad (5)$$

In HMM, there are 5 basic elements: $\{N, M, A, B, \pi\}$, the following is an introduction to these 5 basic elements in combination with the sequence marking task:

N: A limited set of states. Here, it refers to the label behind each word.

M: A finite set of observations. Here, it refers to each word itself.

A: State transition probability matrix. Here, it refers to the probability of transferring from one label to the next one.

B: Observation probability matrix, that is, emission probability matrix. Here, it refers to the probability of generating a certain word under a certain label.

π : Initial probability matrix. Here, it refers to the initialization probability of each label.

The above elements can all be counted from the training corpus. Finally, we can calculate the label sequence behind the word sequence by applying the Viterbi algorithm based on these statistical values.

4.2 Sequence Labeling Method

The entity tagging method in this article is mainly based on the BIO tagging strategy in sequence tagging, where the beginning of the entity is represented by B, the part after the beginning of the entity is represented by I, and the non-entity is represented by O. The BIO labeling method labels the separated target entities into the following format: “B-X”, “I-X” or “O”. Where X indicates that the current segment belongs to the X type, it can be seen that “B-X” indicates that the current segment belongs to the head and has the attribute X, and “I-X” indicates that the current segment belongs to the non-head and has the attribute X.

4.3 Test Results and Analysis

The test results use general standards in the field of entity labeling such as precision rate, recall rate and F1 value as a reference. Among them are the total number of words in the corpus, the number of entities recognized by the system, the number of entities correctly recognized by the system, and other parameter feedback. The test results are shown in Table 1.

4.4 Recurrent and Convolutional Neural Network Fusion Model

BLDC-NER model structure. In recent years, NER methods based on neural networks and language models have been proposed one after another. Compared with CNN, RNN is more suitable for processing sequential text, but RNN has the problem of vanishing gradient. LSTM is usually used to solve the problem of vanishing gradient of ordinary RNN, but LSTM only alleviates this problem, while CNN can capture global information. For the task of named entity recognition, in order to cover

Table 1 Result of HMM

Type	Data
Total number of words in the corpus	1145
System identification entity	1188
Identify entities correctly	883
Accuracy	0.8967
Precision	0.7433
Recall rate	0.7712
F1 value	0.757

more original information, ordinary CNN will deepen the number of layers of the network, and finally make the model huge and difficult to train.

The overall structure of the BLDC-NER model is shown in Fig. 1. The model consists of three parts, namely the BERT layer, the BiLSTM-DCNN layer, and the decoding layer (Fig. 2).

The model first uses the BERT layer to encode each character in the input text and obtain the dynamic semantic vector of each character. Then use the BiLSTM-DCNN layer to further semantically encode the word vector sequence. BiLSTM can capture the contextual timing information of the current character, and the DCNN module can obtain the global information of the input text, and merge the two encoded vectors so that the model can obtain the text The contextual time sequence information can also capture the global semantic features of the input text, and the output semantic code contains richer feature information. Finally, the fused semantic vector is input

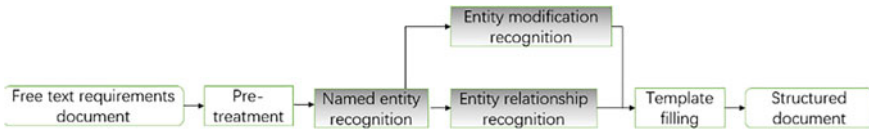
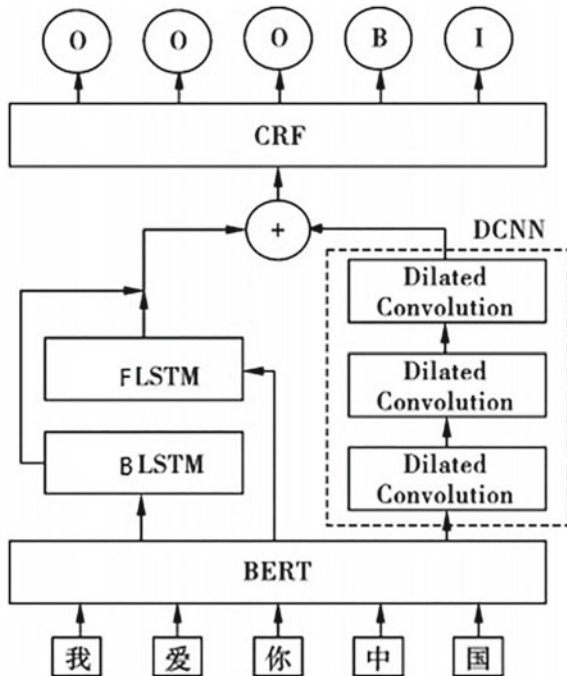


Fig. 1 Structured regular process after free text requirements document

Fig. 2 The overall structure of the BLDC-NER model



to the CRF layer for decoding, and the CRF layer can learn the constraint information between tags to improve the final prediction result.

BERT layer. BERT uses Transformer’s encoder as a feature extractor to construct a language model by masking language modeling and predicting the relationship between sentences. The task of masking language modeling is to randomly cover 15% of the words in each sentence, and let the model predict these words. This method is no longer simply splicing the positive and reverse sentence codes together, but to achieve two-way semantics modeling. Some tasks in natural language processing need to understand sentences. The training task of predicting the relationship between sentences is to learn the correlation between sentences.

BiLSTM-DCNN. The BiLSTM-DCNN layer is a combination of the BiLSTM layer and multiple DCNN modules, and the output feature vectors of the two are fused so that the feature vector contains richer feature information.

BiLSTM is a combination of forward LSTM and reverse LSTM. One-way LSTM can only capture text above or below information, while BiLSTM can capture two-way information.

LSTM structure expression formula is

$$f_t = \sigma(W_f x_t + V_f h_{t-1} + b_f) \quad (6)$$

$$i_t = \sigma(W_i x_t + V_i h_{t-1} + b_i) \quad (7)$$

$$o_t = \sigma(W_o x_t + V_o h_{t-1} + b_o) \quad (8)$$

$$\tilde{c}_t = \tanh(W_c x_t + V_c h_{t-1} + b_c) \quad (9)$$

$$c_t = f_t * c_{t-1} + i_t * \tilde{c}_t \quad (10)$$

$$h_t = o_t * \tanh(c_t) \quad (11)$$

Decoding layer. For the observation sequence $X = (x_1, x_2, \dots, x_n)$ and the corresponding label sequence $Y = (y_1, y_2, \dots, y_n)$, when the conditional random field is trained, the training set is used to obtain the conditional probability model $P(Y|X)$ through the maximum likelihood estimation method; when forecasting, the conditional probability P is obtained through the observation sequence $P(Y|X)$ the largest output sequence.

Analysis of test results. In order to verify that the BERT-based embedding is better than the traditional word vector and to verify that the recognition of the BLDC-NER model is more accurate, this paper conducts experiments and comparisons on various data sets. The experimental results are shown in Table 2.

Table 2 The experimental results of the BLDC-NER model

Dataset	Model	P\R\F ₁
MSRA	<i>BLDC-NER</i>	90.04\90.14\90.09
RESUME	<i>BLDC-NER</i>	90.37\90.75\90.56

5 Conclusion

For Hidden Markov Model, judging from the three parameters of recall rate, accuracy rate, and F1 value in the test results, the correct rate of entity recognition based on HMM is ideal and it can correctly identify aviation entities, which proves that this scheme based on statistics and rules is practical value. However, there are still some shortcomings in the identification of aviation entities and problem:

- (1) The aircraft was confused with the airport, resulting in no aviation entity being identified.
- (2) The amount of training sample text data is not large enough.

The BLDC-NER model proposed in this paper can better capture the rich feature information in long-sequence texts and use dynamic vector encoding Chinese characters to solve the shortcomings of traditional word vectors. The F1 value on the SRA and RE SUME data sets is 94.78, 95.68%, the recognition results surpassed models such as Lattice and BERT-BiLSTM-CRF. The model in this paper has certain advantages in the task of Chinese named entity recognition.

However, at the time of writing this article, due to the lack of sufficient computing resources and sufficient data for aviation product requirements documents, in the BLDC-NER model training corpus of the aviation industry was not used. The next step is to further expand the scope of the corpus and define more comprehensive entity categories. So as to satisfy the construction of knowledge graph in this field.

References

1. Liu Y, Lin S, Chen Y (2017) The application of Xiaoshu ontology in design information and knowledge management [J]. *Sci Technol Rev* 35(22):65–70
2. Sang EF, De Meulder F (2016) Introduction to the CoNLL-2003 shared task: Language-independent named entity recognition. arXiv preprint cs/0306050 (2003). Author F, Author S Title of a proceedings paper. In: Editor F, Editor S (eds) CONFERENCE 2016, LNCS, vol 9999. Springer, Heidelberg, pp 1–13
3. Nadeau D, Turney PD, Matwin S (2006) Unsupervised named-entity recognition: generating gazetteers and resolving ambiguity. In: Proceedings of the 19th international conference on advances in artificial intelligence: Canadian society for computational studies of intelligence (AI'06). Springer-Verlag, Berlin, Heidelberg. https://doi.org/10.1007/11766247_23, pp 266–277
4. Zhao S (2020) Research on Chinese knowledge graph question answering based on joint training and unsupervised method [D]. Harbin Institute of Technology
5. Wu Y (2018) Research and implementation of semantic processing system based on rule matching [D]. Harbin Institute of Technology

6. Li D, Zhang Y, Li D, Lin D (2020) Summary of research on entity relationship extraction methods [J]. *Comput Res Dev* 57(07):1424–1448
7. LeCun Y, Bengio Y, Hinton G (2015) Deep learning. *Nature* 521(7553):436
8. Tao Z (2010) Research on a named entity recognition method in the field of electronic products [D]. Xidian University
9. Zhang Y, Ji B, Yu J, Liu H (2021) Recognition method of named entity in electronic medical records based on multi-neural network cooperation [J]. *Comput Appl Softw* 38(02):179–184
10. Zhao P, Zhao C, Wu H, Wang W (2021) Agricultural text named entity recognition based on attention mechanism [J]. *Trans Chin Soc Agric Mach* 52(01):185–192
11. Jurafsky D, Martin JH (2008) *Speech and language processing: an introduction to natural language processing, computational linguistics, and speech recognition*
12. Devlin J, Chang M-W, Lee K, Toutanova K (2018) BERT: pre-training of deep bidirectional transformers for language understanding (cite arxiv:1810.04805Comment: 13 pages)
13. Zhou G, Su J (2002) Named entity recognition using an HMM-based chunk tagger. In: *Proceedings of the 40th annual meeting of the association for computational linguistics*
14. Feng J, Li Z, Zhang D, Zou J (2020) Named entity recognition of bridge detection text based on hidden Markov model [J]. *Transp World* (08):32–33
15. Chen Y et al (2013) Toward a scientific ontology based concept of function [J]. *Artif Intell Eng Design Anal Manuf* 27(3):241–248
16. Wu WX, Quning FJ (2021) Chinese named entity recognition and application based on the fusion of loop and convolutional neural network [J]. *J Lanzhou Inst Technol* 28(03):77–82

Fault-Tolerant Attitude Control of Spacecraft via Explicit Model Prediction Method



Xin Cao, Deren Gong, Qiang Shen, and Shufan Wu

Abstract In this paper, the problem of spacecraft attitude control with soft faults of actuators is investigated. A robust fault-tolerant controller is proposed in spacecraft with the explicit model predictive control. Firstly, Fault model of the actuator is established with the method based on explicit model prediction. Then, considering the model uncertainty and the system state disturbance, the control problem based on the spacecraft actuator failure state was transformed into the multi-parametric quadratic programs (MPQP) under the constraints. Finally, a recursive process of combining and replacing solutions is given to extract the required explicit control laws. By designing the terminal cost function and constraint set appropriately, it is proved that the MPC controller is robust to the constraints applied in the closed loop of the uncertain system and the input to the stability of the origin state.

Keywords Passive fault-tolerant control · Model predictive control · Multiparameter programming · Dynamic programming · Fault-tolerant control in spacecraft

1 Introduction

In the spacecraft attitude control, failure of an actuator may cause irreparable damage and inevitably appear disturbance and uncertainty. Therefore, the design of the control system should not only be robust to disturbances and uncertainties, but also be fault-tolerant. Control systems that maintain overall stability and acceptable levels under fault conditions are called fault-tolerant control systems (FTC).

With the continuous development of fault diagnosis technology, the corresponding fault-tolerant control methods are also gradually developed, especially the method

X. Cao · D. Gong (✉) · Q. Shen · S. Wu
Shanghai Jiao Tong University, Shanghai, China
e-mail: drgong@sjtu.edu.cn

X. Cao
e-mail: cxcbbbs@sjtu.edu.cn

based on analytical model. This method is often divided into two categories, namely, passive fault-tolerant control (PFTC) method and active fault-tolerant control method (AFTC). AFTC method is to adjust the parameters of the controller according to the fault (after the fault occurs) to compensate for the fault, and the structure needs to be changed if necessary. Obviously, this method requires a designed control algorithm. However, this method can improve the performance of the controlled system. Generally speaking, most active fault-tolerant controls require fault diagnosis (FD) subsystems or modules to obtain fault-related information [1]. By contrast, PFTC method is based on the idea of robust control [2]. In related reports, passive fault-tolerant control is often divided into reliable stabilization, simultaneous stabilization, and integrity. Passive fault-tolerant control method is essentially a robust control technology, which is effective only for faults in a specific range, and generally speaking, it is more conservative [3].

At present, different FTC methods have been proposed, but Model Predictive Control (MPC) has not been used to solve the control problem of spacecraft actuators under passive FTC. The main problem of MPC is the large amount of calculation online, which limits its wide application. Considering the limited power supply, data storage, and computing resources of spacecraft, an explicit predictive control (EMPC) is proposed to solve this problem [4]. In this method, the optimal solution of the closed-loop system is obtained offline. The original MPC problem is modified by dynamic programming and multi-parameter programming, and it is transformed into a multi-stage optimization problem [5]. However, for the design of spacecraft actuators, there is no robust fault-tolerant controller for disturbance and uncertainty.

In this paper, the factors such as actuator failure, disturbance, and model uncertainty are combined into the predictive control problem of spacecraft linear systems, robust fault-tolerant explicit control laws under state and input constraints are derived. On the basis of the work of Kourama, the algorithm adopts the method of combining dynamic programming with multi-parameter programming [6]. By using the idea of constraint rearrangement, the control problem based on the failure state of spacecraft actuator is transformed into a constrained multi-parameter optimization problem. Finally, the recursive process of combinatorial and substitution solutions is given to obtain the required explicit control law.

2 Problem Formation

Considering the following satellite model assumptions:

- All state variables in the model are based on the satellite body-fixed frame O_b .
- The origin of O_b coincides with the center of gravity of the satellite, the inertial matrix of a satellite is $\mathbf{I} = \text{diag}\{i_{11}, i_{22}, i_{33}\}$.
- The satellite's reaction wheel generates internal control torque around the satellite's main axis, the axial inertia of the momentum wheel is \mathbf{I}_s , The axis of rotation in the ontology coordinate system is $\mathbf{C} = [0, 1, 0]^T$.

- Satellite external control moment $\sum \boldsymbol{\tau}_{\text{control}} \triangleq \boldsymbol{\tau} = [\tau_1, \tau_2, \tau_3]^T$, provided by thrusters, can act directly on the angular velocity of the satellite's main axis, the only interfering moment to be considered is the gravity gradient moment.

2.1 Satellite Attitude Model

A preliminary and relatively complex satellite model can be described as

$$\begin{aligned}
 \dot{\omega}_{ib}^b &= \mathbf{J}^{-1}[-\mathbf{S}(\omega_{ib}^b)(\mathbf{I}\omega_{ib}^b + \mathbf{C}\mathbf{I}_s\omega_s) + \boldsymbol{\tau}_e - \mathbf{J}^{-1}\mathbf{C}\boldsymbol{\tau}_a] \\
 \dot{\omega}_s &= -\mathbf{C}^T\mathbf{J}^{-1}[-\mathbf{S}(\omega_{ib}^b)(\mathbf{I}\omega_{ib}^b + \mathbf{C}\mathbf{I}_s\omega_s) + \boldsymbol{\tau}_e] + [\mathbf{C}^T\mathbf{J}^{-1}\mathbf{C} + \mathbf{I}_s^{-1}]\boldsymbol{\tau}_a \\
 \dot{\eta} &= -\frac{1}{2}\boldsymbol{\epsilon}^T\omega_{ob}^b \\
 \dot{\boldsymbol{\epsilon}} &= \frac{1}{2}[\eta\mathbf{I} + \mathbf{S}(\boldsymbol{\epsilon})]\omega_{ob}^b
 \end{aligned} \tag{1}$$

where \mathbf{J} is the satellite's overall inertia matrix, \mathbf{I} is the inertial matrix of the satellite, \mathbf{I}_s is the axial inertia matrix of reaction wheel, \mathbf{C} is the matrix for the reaction wheel, ω_s is the angular velocity of the reaction wheel, $\boldsymbol{\tau}_a$ is the reaction wheel control torque.

$$\boldsymbol{\tau}_e = \sum \boldsymbol{\tau}_{\text{control}} + \sum \boldsymbol{\tau}_{\text{disturbance}}, \quad \sum \boldsymbol{\tau}_{\text{control}} \triangleq \boldsymbol{\tau} = [\tau_1, \tau_2, \tau_3]^T \tag{2}$$

$$\mathbf{S}(\omega_{ib}^b) \triangleq \boldsymbol{\omega}^\times = \begin{bmatrix} 0 & -\omega_z & \omega_y \\ \omega_z & 0 & -\omega_x \\ -\omega_y & \omega_x & 0 \end{bmatrix}, \quad \boldsymbol{\omega} = \begin{bmatrix} \omega_x \\ \omega_y \\ \omega_z \end{bmatrix}. \tag{3}$$

2.2 Satellite Attitude Model

Model in (1) must be differentiated relative to the total state vector, the total state vector is currently selected as $x = [\omega_1, \omega_2, \omega_3, \omega_s, \eta, \varepsilon_1, \varepsilon_2, \varepsilon_3]^T$. In this way, the nonlinear control law $\mathbf{f}(\mathbf{x}, \mathbf{u}) = [\dot{\omega}_{ob}^b, \dot{\omega}_s, \dot{\eta}, \dot{\boldsymbol{\epsilon}}]^T \triangleq [f_1, \dots, f_8]^T$. The linearized system can be expressed as follows:

$$\begin{cases} \dot{\mathbf{x}} = \mathbf{A}\mathbf{x} + \mathbf{B}\mathbf{u} \\ \mathbf{y} = \mathbf{C}\mathbf{x} + \mathbf{D}\mathbf{u} \end{cases} \tag{4}$$

Considering the observability and controllability of linear systems, select equilibrium point $\mathbf{x}^p = [0, 0, 0, 0, 1, 0, 0, 0]^T$, $\mathbf{u}^p = [0, 0, 0, 0]$, the solution formula

of the state equation is used to ensure that the continuous state equation and the discretized state equation have the same solution at the sampling time. Transform the state-space model of discrete system into the following form:

$$\begin{cases} \mathbf{x}((k+1)T) = G(T)\mathbf{x}(kT) + H(T)\mathbf{u}(kT) \\ \mathbf{y}(kT) = C(T)\mathbf{x}(kT) + D(T)\mathbf{u}(kT) \end{cases} \quad (5)$$

Decoupling this system into a six-degree-of-freedom state system, the matrix in (6) is as follows:

$$\mathbf{A} = \begin{bmatrix} 0 & 0 & (1-k_x)\omega_0 & 0 & -8k_x\omega_0^2 & 0 \\ 0 & 0 & 0 & 0 & 0 & \frac{-6k_y i_{22}\omega_0^2}{\kappa} \\ (k_z-1)\omega_0 & 0 & 0 & 0 & 0 & 0 \\ \frac{1}{2} & 0 & 0 & 0 & 0 & 0 \\ 0 & \frac{1}{2} & 0 & 0 & 0 & 0 \\ 0 & 0 & \frac{1}{2} & 0 & 0 & 0 \end{bmatrix}$$

$$\mathbf{B} = \begin{bmatrix} \frac{1}{i_{11}} & 0 & 0 \\ 0 & \frac{1}{\kappa} & 0 \\ 0 & 0 & \frac{1}{i_{33}} \\ 0 & 0 & 0 \\ 0 & 0 & 0 \\ 0 & 0 & 0 \end{bmatrix}, \quad (6)$$

where

$$k_x = \frac{i_{22} - i_{33}}{i_{11}}, \quad k_y = \frac{i_{11} - i_{33}}{i_{22}}, \quad k_z = \frac{i_{22} - i_{11}}{i_{33}}, \quad \kappa = i_{22} - i_s.$$

3 Fault Model Prediction Description

3.1 Linear Discrete System Under Spacecraft Failure

The state equation of linear discrete spacecraft is as follows:

$$x_{k+1} = f(x_k, u_k) = Ax_k + B\Omega_k u_k + Wd_k, \quad (7)$$

where $x_k \in R^n$, $u_k \in R^m$, $d_k \in R^s$ are state, input, and disturbance vector respectively, subject to constraints $\mathcal{X} = \{x \in R^n | Gx \leq \mu\}$ and $\mathcal{U} = \{u \in R^m | Hu \leq \gamma\}$ are convex polyhedron, $G \in R^{n \times m}$, $\mu \in R^{n \times m}$, $H \in R^{m \times m}$, $\gamma \in R^{m \times m}$; additionally,

unknown disturbances d_k are restricted to $d_i^L \leq d_{k,i} \leq d_i^U$ ($i = 1, \dots, r$), system coefficient matrix A , B are uncertain matrices; unknown boundary matrix $\Delta A \Delta B$ are defined as follows:

$$\Delta A \in A = \{ \Delta A \in \mathbb{R}^{n \times n} | -\varepsilon_a |A_0| \leq \Delta A \leq \varepsilon_a |A_0| \} \quad (8)$$

$$\Delta B \in B = \{ \Delta B \in \mathbb{R}^{n \times n} | -\varepsilon_b |B_0| \leq \Delta B \leq \varepsilon_b |B_0| \}, \quad (9)$$

where A_0 B_0 are nominal matrices, use $|X|$ represent $\{|X_{ij}|\}$, $X = \{X_{ij}\}$, $u_{k,i}$ stands for the i th actuator of time k and $u_{k,i}^F$ denotes its defective form written as

$$\varepsilon_{k,i} \in R = \{ \varepsilon_{k,i} \in \mathbb{R} | 0 \leq \varepsilon_{k,i} \leq \varepsilon_i^U \leq 1 \}, \quad (10)$$

whereas $\varepsilon_{k,i}$ and ε_i^U indicate the corresponding failure percentage at time instant k and its upper bound, respectively. Therefore, $\varepsilon_{k,i} = 0$ indicates the state of health while $\varepsilon_{k,i} = 1$ indicates the correspondence of input is completely invalid. Now let's define

$\Omega_k \triangleq I_m - \varepsilon_k$, $\varepsilon_k \triangleq \text{diag}\{\varepsilon_{k,1}, \dots, \varepsilon_{k,m}\}$, I_m denote the unit matrix of order m , $u_k^F = \Omega_k u_k$, so the MPC problem under constraints is defined as[7]:

$$\min_{U^t} J = \sum_{k=0}^{N-1} [\bar{x}_{k|t}^T Q \bar{x}_{k|t} + u_{k|t}^T R u_{k|t}] + \bar{x}_{N|t}^T P \bar{x}_{N|t}, \quad (11)$$

where

$$\bar{x}_{k+1|t} = A_0 \bar{x}_{k|t} + B_0 u_{k|t}, k = 0, 1, 2, \dots, N-1 \quad (12)$$

$$x_{k+1|t} = A x_{k|t} + B \Omega_k u_{k|t} + W d_{k|t}, k = 0, 1, 2, \dots, N-1 \quad (13)$$

$$u_{k|t} \in \mathcal{U} = \{ u \in R^m, H u \leq \gamma \}, k = 0, 1, 2, \dots, N-1 \quad (14)$$

$$x_{N|t} \in X_f = \{ x \in R^n, G_f x \leq \mu_f \} \quad (15)$$

and $\forall \Delta A_{0|t}, \dots, \Delta A_{k-1|t}$ satisfies (5), $\forall \Delta B_{0|t}, \dots, \Delta B_{k-1|t}$ satisfies (6) $\forall \alpha_{0|t}, \dots, \alpha_{k-1|t}$ satisfies (7).

A control sequence $U^t = \{u_{0|t}, \dots, u_{N-1|t}\}$ is a robust solution for the explicit/multi-parametric MPC problem, $x_{0|t} = x_t$, the matrices Q , P are positive semi-definite, R is positive definite and X_f contains the origin in its interior. N is the prediction length. At each sampling time, the objective of this work is to obtain a control sequence U and in extension the optimal control variables u_t for the

optimization as functions of the state variables x_t (7), it is obvious that deriving the control variables utas explicit functions of the states x_t is not possible with the current nominal mp-MPC methods which meets the constraints of all allowable values of disturbance, uncertainty, and actuator fault. In order to be applied to multi-parameter programming, it is assumed that the objective function only punishes the behavior of nominal systems (such as Kourama 2013). This closed-form solution of the problem is named as a robust fault-tolerant explicit control law.

3.2 Model Prediction Dynamic Programming

In this step, based on the ideas of multi-stage decomposition, problem (11)–(13) with N decision variables is expressed as a multi-stage optimization problem where the time instant t represents each of the stages of the problem with N optimization problems and one decision variable, that is

$$\min_{U_t} J = \sum_{k=0}^{N-1} [\bar{x}_{k|t}^T Q \bar{x}_{k|t} + u_{k|t}^T R u_{k|t}] + \bar{x}_{N|t}^T P \bar{x}_{N|t} \quad (16)$$

where

$$\begin{aligned} \bar{x}_{k+1} &= A_0 \bar{x}_k + B_0 u_k, k = i, \dots, N-1 \\ x_i \in \mathcal{X}, u_i \in \mathcal{U}, x_{i+1} \in X_{i+1} &= \{x \in R^n, G_{i+1} x \leq \mu_{i+1}\}. \end{aligned} \quad (17)$$

The optimization problem (16) is solved stage wise, starting from $i = N-1$ and solving it repetitively backwards until $i = 0$, where effects of all uncertain parameters are captured as $x_{i+1} = A x_i + B \Omega_i u_i$, where the only optimization variable is the control variable u_i at the current stage and only the state and input constraints at the current stage are considered [8].

3.3 Model Prediction Constraint Arrangement

The key step in the proposed method is to rearrange the constraint beat to ensure the robustness and fault tolerance of our controller, all constraints (17)–(20) can be rewritten as

$$\begin{aligned} G_{i+1} A_0 x_i + G_{i+1} \Delta A_i x_i + G_{i+1} B_0 u_i - G_{i+1} B_0 \varepsilon_i u_i + \\ G_{i+1} \Delta B_i u_i - G_{i+1} \Delta B_i \varepsilon_i u_i + G_{i+1} W d_i \leq \mu_{i+1}, \end{aligned} \quad (18)$$

Considering the perturbation, uncertainty and worst case of actuator failure, the model constraint prediction is rearranged as follows:

$$\begin{aligned}
 & G_{i+1}A_0x_i + G_{i+1}B_0u_i \\
 & + \max(G_{i+1}\Delta A_i x_i - G_{i+1}B_0\varepsilon_i u_i + G_{i+1}\Delta B_i u_i \\
 & - G_{i+1}\Delta B_i \varepsilon_i u_i + G_{i+1}Wd_i) \leq \mu_{i+1}
 \end{aligned} \tag{19}$$

$$-y_i \leq x_i \leq y_i \tag{20}$$

$$-v_i \leq u_i \leq v_i. \tag{21}$$

3.4 Multi-parametric Programming

The convexity of (16) can be used to derive a convex multi-parameter programming problem by considering the assumptions as follows [9]:

- Considering $\varphi_i = [u_i^T, y_i^T, v_i^T]^T$ as the optimization variable.
- Considering $\theta_i = [x_i^T, u_{i+1}^T, \dots, u_{N-1}^T]^T$ as the optimization parameters.
- Considering objective function only penalizes the nominal system $\bar{x}_{k+1} = A_0\bar{x}_k + B_0u_k$, therefore $\bar{x}_{k+1} = A_0^{k-i+1}x_i + \sum_{j=i}^k A_0^{k-j}B_0u_j$ ($k = i, \dots, N - 1$).

The design of robust controller control law for spacecraft is transformed into the multi-parameter quadratic optimization problem as follows:

$$\min_{\varphi_i} \left\{ \frac{1}{2} \varphi_i^T H_i \varphi_i + \theta_i^T F_i \varphi_i \right\} \tag{22}$$

$$A_{ci} \varphi_i \leq b_{ci} + B_{ci} \theta_i, \tag{23}$$

where

$$\begin{aligned}
 H &= R + \sum_{i=t}^{N-1} B_0^T (A_0^{i-1-t})^T Q A_0^{i-1-t} B_0 \\
 H &= R + \sum_{i=t}^{N-1} B_0^T (A_0^{i-1-t})^T Q A_0^{i-1-t} B_0 \\
 F &= \left[\left(\sum_{t+1}^{N-1} 2(A_0^{i-t})^T Q A_0^{i-1-t} \right)^T \times \left(\sum_{i=t+2}^{N-1} 2B_0^T (A_0^{i-t-2})^T Q A_0^{i-1-t} B_0 \right) \right. \\
 &\quad \left. \times \left(\sum_{i=t+3}^{N-1} 2B_0^T (A_0^{i-t-3})^T Q A_0^{i-1-t} B_0 \right)^T \cdots (B_0^T P A_0^{N-1-t} B_0) \right]
 \end{aligned}$$

In addition, A_{ci}, b_{ci}, B_{ci} is simply obtained from constraints (18)–(20). By using the transformation $z_i \triangleq \varphi_i + H_i^{-1} F_i^T \theta_i$, the problem is converted to the standard form of the multi-parameter quadratic programming problem, which is

$$\min_{z_i} \frac{1}{2} z_i^T H_i z_i \quad (24)$$

$$A_{ci} z_i \leq b_{ci} + S_i \theta_i, \quad (25)$$

where $S_i = A_{ci} H_i^{-1} F_i^T + B_{ci}$, it should be a positive symmetric definite matrix, a problem solved by Yalmip in the multi-parameter toolbox, the solution in MPT takes the form of [10]:

$$\begin{aligned}
 u_i &= K_i^j \theta_i + k_i^j \\
 \text{if } \theta_i \in \mathcal{CR}_i^j &= \left\{ \theta A_{\theta_i}^j \theta \leq b_{\theta_i}^j \right\}.
 \end{aligned} \quad (26)$$

At the end of the current stage, the t -robust controllability set for the feasibility constraint in (17) can be obtained either by performing set theoretic computations, or by taking the union that allowable constraint region of the next stage is calculated as follows:

$$\mathcal{X}_i = \bigcup_j \mathcal{CR}_i^j. \quad (27)$$

At the end of each phase, the solution of form (26) is obtained through this method, but the expected control law is only a function of x_i . These formulas (28)–(30) show how to extract the required explicit control law by combining the solution of previous and current stages which are obtained from the algorithm:

$$u_i = K_{x_i}^r x_i + K_{u_i}^r u_{pre} + k_i^r \text{ if } A_{x_i}^r x_i + A_{u_i}^r u_{pre} \leq b_{\theta_i}^r \quad (28)$$

$$u_{pre} = K_{pre}^q x_{i+1} + k_{pre}^q \text{ if } A_{pre}^q x_{i+1} \leq b_{pre}^q, \quad (29)$$

where $u_{pre} = [u_{i+1}^T, \dots, u_{N-1}^T]^T$ and $K_{pre}^q, k_{pre}^q, A_{pre}^q, b_{pre}^q$ are obtained at the end of previous stage for the critical region, \mathcal{CR}_{pre}^q , rewrite the system using the nominal model $x_{i+1} = A_0 x_i + B_0 u_i$ in the following form:

$$\begin{bmatrix} I_m & -K_{u_i}^r \\ -K_{pre}^q B_0 & I_{m \times (N-i-1)} \end{bmatrix} \begin{bmatrix} u_i \\ u_{pre} \end{bmatrix} = \begin{bmatrix} k_i^r \\ k_{pre} \end{bmatrix} + \begin{bmatrix} K_{x_i}^r \\ K_{pre}^q A_0 \end{bmatrix} x_i. \quad (30)$$

It is possible to find two critical regions from $A_{x_i}^r x_i + A_{u_i}^r u_{pre} \leq b_{\theta_i}^r$ and $A_{pre}^q A_0 x_i + A_{pre}^q B_0 u_i \leq b_{pre}^q$, which is the critical region for the sequence from u_i to u_{N-1} , An empty intersection indicates that there is no feasible solution in the current $r - q$ combination. This procedure is required to being repeated at the end of each stage. In this way, the control problem based on the failure state of spacecraft actuator is transformed into a multi-parameter optimization problem under constraints.

4 Simulation

4.1 2U Cubic Satellite Parameters Initialized

Table 1 summarizes some of the main physical parameters. These values were used in the previous analysis and will be used in the simulation section of this paper [11], adopting the satellite attitude kinematics and dynamics model in the paper, the operating altitude of the micro-nano satellite is 17125 km, the moment of inertia of the satellite on three axes is $I = \text{diag}\{4.251, 4.330, 3.669\} [kg m^2]$, [12] the satellite's state variable is $x = [\omega_1, \omega_2, \omega_3, \eta, \alpha_1, \alpha_2, \alpha_3]^T$, $\omega_1, \omega_2, \omega_3$ are, respectively, satellite triaxial angular velocities, $\eta, \alpha_1, \alpha_2, \alpha_3$ are the corresponding quaternions, respectively. In order to facilitate tracking and control, the state quantity of the satellite is set as $x = [\omega_1, \omega_2, \omega_3, \alpha_1, \alpha_2, \alpha_3]^T$. The fixed sampling time is 0.1 s, and the state constraint is

Table 1 Observation from the state partition

Observe	Fixed manipulation	Value
ω_1, ε_1	$\omega_2, \varepsilon_2, \omega_3, \varepsilon_3$	$case1 = [0, 0, 0, 0]$
ω_2, ε_2	$\omega_2, \varepsilon_2, \omega_3, \varepsilon_3$	$case2 = [0, 0, 0, 0]$
ω_3, ε_3	$\omega_2, \varepsilon_2, \omega_3, \varepsilon_3$	$case3 = [0, 0, 0, 0]$

$$-[0.5; 0.5; 0.5; 0.5; 0.5; 0.5] \leq X \leq [0.5; 0.5; 0.5; 0.5; 0.5; 0.5];$$

The input constraint is:

$$-[0.484; 0.484; 0.039] \leq U \leq [0.484; 0.484; 0.039];$$

The state matrix is $Q = \text{diag}(200,200,200,1,1,1)$;

The input matrix is $R = \text{diag}(100,200,100)$;

The uncertainty of system model is $\sigma = 0.1$, upper limit of the fault $\alpha^U = 0.5$. The predicted step size is $N = 4$, and the system control partition obtained by offline calculation is shown in Table 1.

4.2 Simulation Results

In order to study the high performance of the designed controller, the behavior of the closed-loop system starting from any initial condition x_0 is simulated. As can be seen from Fig. 1, which illustrates the explicit region of the satellite rolling angular velocity and rolling angle, the explicit region of the satellite pitch velocity and pitch angle is depicted in Fig. 2. Figure 3 also reflects the explicit region of the yaw angular velocity and yaw angle.

Taking pitch angle and yaw angle as an example, their control law partitions are indicated in Fig. 4, corresponding to u_1, u_2, u_3 from top to bottom. In this way, different control law permutation and combination under different states can be obtained.

Figure 5 demonstrates the state partitions of all angular velocities when the roll angle, pitch angle, and yaw angle are special values of zero; Fig. 6 illustrates the

Fig. 1 Feasible critical region of the observation1

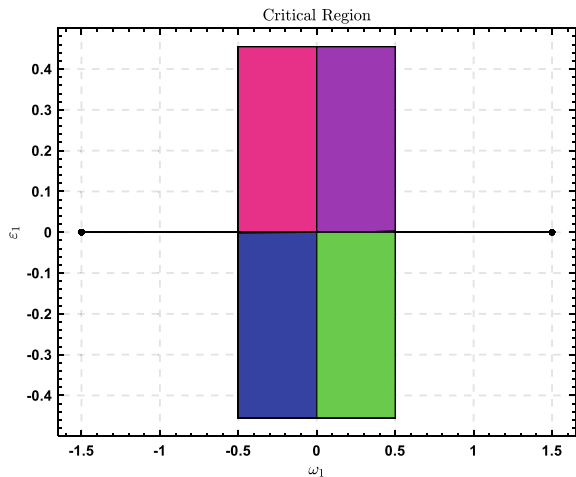


Fig. 2 Feasible critical region of the observation2

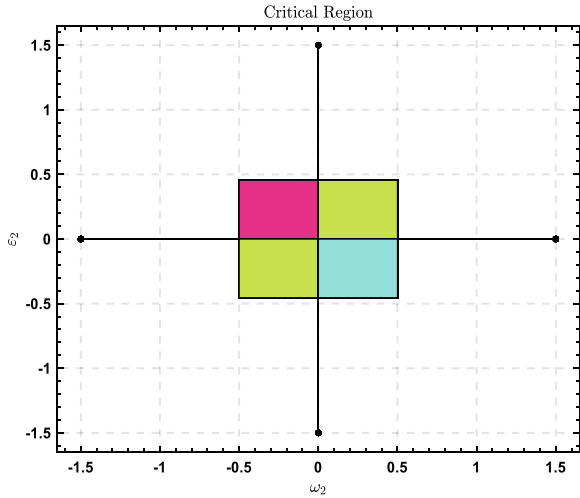
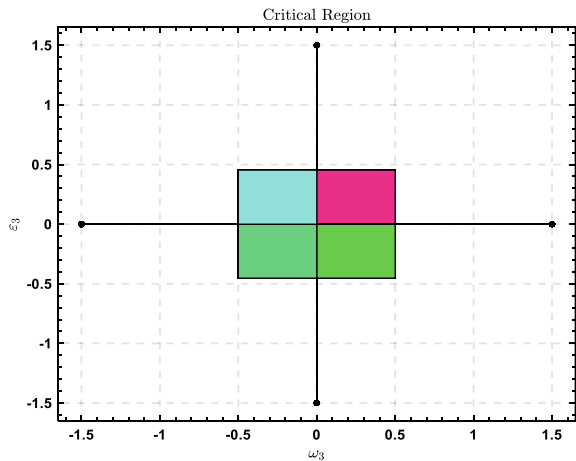


Fig. 3 Feasible critical region of the observation3



state partitions of all Euler parameters when the roll velocity, pitch velocity, and yaw velocity are special values of zero.

In order to study the high performance of the designed controller, the behavior of the closed-loop system starting from any initial condition $x_0 = [0.1; 0.2; 0.5; 0.3; 0.4; 0.1]$ is simulated. The system is affected by random allowable disturbance, uncertainty, and actuator failure. Figure 7 shows the curve of the three control laws changing with time, it can be seen that the control input basically reaches the balance at 4 s.

In Fig. 8 three curves of angular velocity over time are shown and Fig. 9 reflects curves of Euler quaternions over time, indicating that after a fault occurs, the system can quickly and timely search for an emergency plan through explicit predictive

Fig. 4 Feasible region of the control law

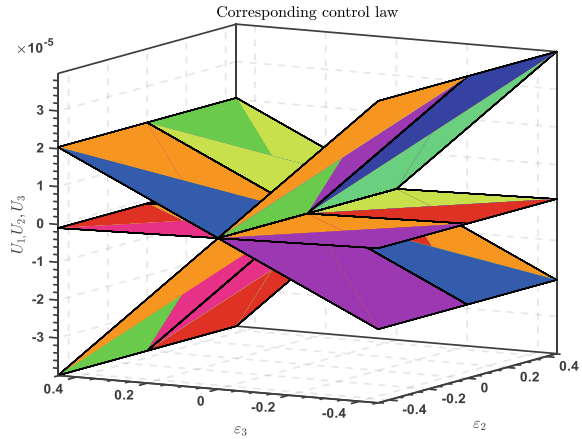
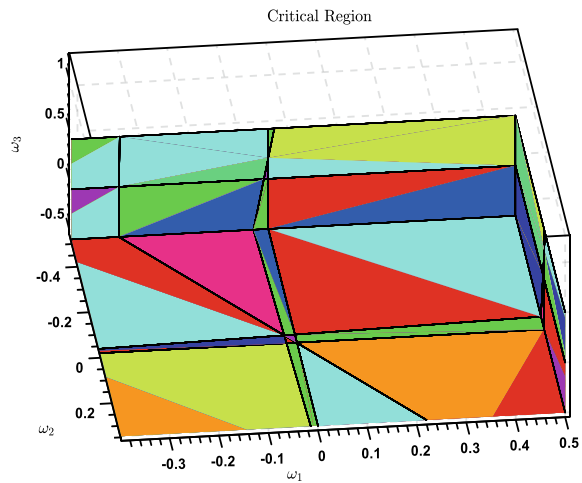


Fig. 5 Feasible region of all angular velocities



control, so as to stabilize the spacecraft attitude quickly. Especially, the transient response is faster and the steady-state accuracy is higher.

5 Conclusion

In this work, a new methodology was applied in micro-satellite to deal with a robust fault-tolerant explicit solution as an EMPC problem with objective quadratic function and linear state and input constraints. The micro-satellite system was exposed to unknown bounded disturbances, actuator failures as well as model uncertainties. A multi-stage optimization program was implemented by using the multi-parametric

Fig. 6 Feasible region of all Euler parameters

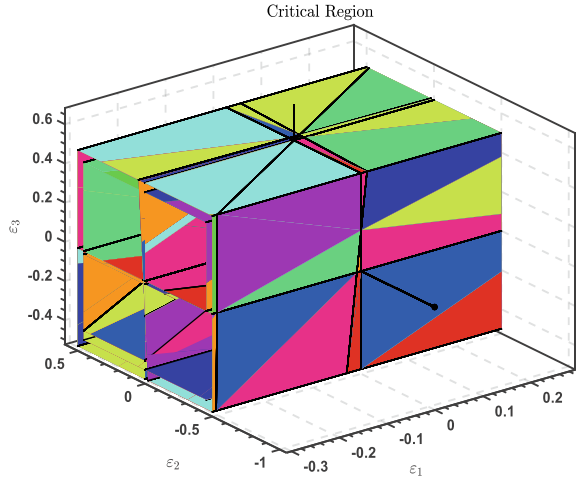
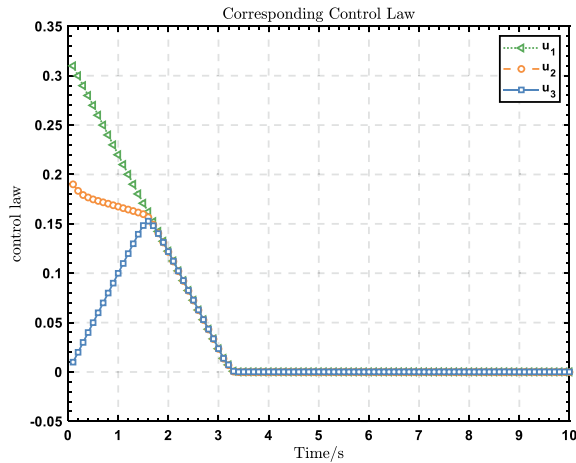


Fig. 7 Feasible region of control law



programming and dynamic programming approaches. Furthermore, an implemented constraint rearrangement formulation was imposed which ensures the immunity of the attitude system to the worst situation such as disturbances, uncertainties, and faults. Additionally, a recursive process was used to combine the stage-by-stage solutions and to extract the expected explicit control law. The numerical simulations show that the proposed controller is obviously successful in achieving high performance in quality as well as in the presence of parametric uncertainty, external disturbance, actuator failure, and control input constraints. At the same time, it provides an idea for cooperative control and distributed control of multi-spacecraft.

Fig. 8 Simulation results of the angular velocity

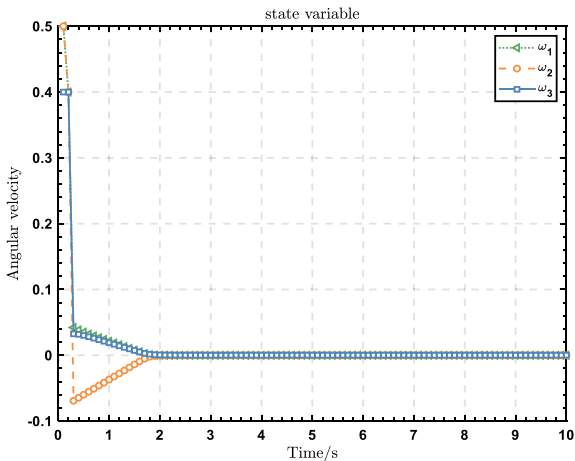
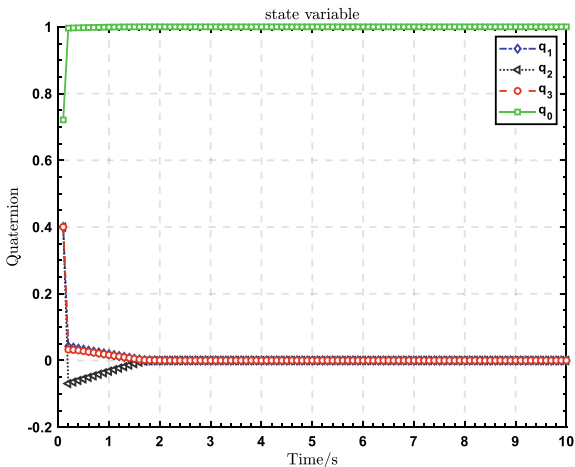


Fig. 9 Results of the Euler parameters with time



Acknowledgements This work is partially supported by National Natural Science Foundation of China, No. U20B2054, National Key R&D Program of China, No. 2020YFC2200800. We wish to thank Qiang Shen for his help with the initial implementation of the algorithm, and Deren Gong for suggesting improvements to the original manuscript.

References

1. Blanke M, Kinnaert M, Lunze J, et al (2006) Diagnosis and fault-tolerant control[M]. Springer, Berlin
2. Benosman M, Lum KY (2010) Application of passivity and cascade structure to robust control against loss of actuator effectiveness[J]. Int J Robust Nonlinear Control IFAC-Affiliated J 20(6):673–693

3. Jiang J, Yu X (2012) Fault-tolerant control systems: a comparative study between active and passive approaches[J]. *Annu Rev Control* 36(1):60–72
4. Borrelli F, Bemporad A, Morari M (2017) Predictive control for linear and hybrid systems[M]. Cambridge University Press
5. Kouramas KI, Faísca NP, Panos C et al (2011) Explicit/multi-parametric model predictive control (MPC) of linear discrete-time systems by dynamic and multi-parametric programming[J]. *Automatica* 47(8):1638–1645
6. Sheikhhahaei R, Alasty A, Vossoughi G (2018) Robust fault tolerant explicit model predictive control[J]. *Automatica* 97:248–253
7. Kouramas KI, Panos C, Faísca NP et al (2013) An algorithm for robust explicit/multi-parametric model predictive control[J]. *Automatica* 49(2):381–389
8. Tøndel P, Johansen TA, Bemporad A (2003) An algorithm for multi-parametric quadratic programming and explicit MPC solutions[J]. *Automatica* 39(3):489–497
9. Krogstad T, Gravdahl J T, Tondel P (2005) Explicit model predictive control of a satellite with magnetic torquers[C]. In: Proceedings of the 2005 IEEE International Symposium on, Mediterrean Conference on Control and Automation Intelligent Control. IEEE, pp 491–496
10. Sakizlis V, Kakalis NMP, Dua V et al (2004) Design of robust model-based controllers via parametric programming[J]. *Automatica* 40(2):189–201
11. Wei C, Chen Q, Liu J et al (2021) An overview of prescribed performance control and its application to spacecraft attitude system[J]. *Proc Inst Mech EngPart I J Syst Control Eng* 235(4):435–447
12. Arefkhani H, Sadati SH, Shahravi M (2020) Satellite attitude control using a novel constrained magnetic linear quadratic regulator[J]. *Control Eng Pract* 101:104466

Simulation Analysis of a Certain Civil Aircraft's Negative Acceleration Flight



YaJun Wen

Abstract In this article, the dynamic simulation model of a civil aircraft is used to analyze the flight action of negative acceleration in detail. The simulation results show that the maneuverability of the aircraft is better when the aircraft is of small weight and rear center of gravity, which is helpful to extend the negative normal overload time of the aircraft. In order to make the aircraft enter the negative normal overload for a longer time, the aircraft can climb steadily for a period of time behind the pull sidestick, and the operation of push sidestick can be carried out at a larger pitch angle and speed. After the pilot pushes the sidestick quickly, the elevator will fluctuate, and the elevator deflection can be stabilized faster by pulling the sidestick in a small amplitude. For the longitudinal position of the sidestick, it is recommended to maintain between -10.8° and -9.8° , the value of the normal overload can be maintained between -0.15 and -0.25 g, and the time for the aircraft to enter the negative normal overload can also be maintained above 7.5 s.

Keywords Negative acceleration flight · The normal overload · Position of the sidestick

1 Introduction

Negative acceleration flight of civil aircraft is a complicated and comprehensive test subject. When the normal overload value of the aircraft is less than 0 due to the emergency situation, the fuel system and lubricating oil system in the aircraft will float due to weightlessness, which may affect the normal operation of the system function, or even cause more serious problems. Therefore, for the negative acceleration test flight of civil aircraft, China, the United States and many other countries have clearly given relevant requirements in the airworthiness regulations. That is, in all model designs and tests, negative acceleration analysis and testing must be carried out.

Y. Wen (✉)
COMAC Flight Test Center, Shanghai, China
e-mail: wj23npu@163.com

And the aircraft must be designed in such a way that the fuel system, lubricating oil system, power supply system, power unit, and relevant accessories will not have any fault when the negative acceleration is made in the flight envelope [1].

However, in China, there is little experience to learn from in negative acceleration flight test, and the understanding of negative acceleration flight test remains in the analysis of flight test data. This paper uses the test flight data of a certain type of civil aircraft to verify the accuracy of the dynamics simulation model and uses the model to conduct a detailed simulation of the test flight of the negative acceleration from the principle of flight.

2 Flight Maneuver Analysis

According to the requirements of Section 25.943 in CCAR25 [2], when the aircraft flies with negative acceleration within the flight envelope, there must be no dangerous failures in the flight action. And the normal overload value at the center of gravity of the aircraft should be maintained between -1 and 0 g, and the duration should be at least 7 s. The engine should be in the maximum continuous state, and the total flight time under the condition of negative acceleration should not be less than 20 s. In order to meet the requirements of the clauses, the negative acceleration flight test generally enters a state where the normal overload value is less than 0 g by manipulating the aircraft to perform a parabolic flight test. The parabolic flight test scheme is shown in Fig. 1, which is generally divided into four stages: accumulation speed stage (shown in 1–2), jump stage (shown in 2–3), entry and maintenance stage (shown in 3–4–5), and recovery level flight stage (shown in 5–6–7).

At present, this method is used for negative acceleration test flight of civil aircraft. During the flat flight phase, the aircraft is lifted up by pull sidestick to accumulate potential energy, which can obtain a longer maintenance time of negative normal overload value. Meanwhile, the maneuverability of the aircraft is greatly improved and the safety of flight test is increased. However, for pilots, it is difficult to grasp the

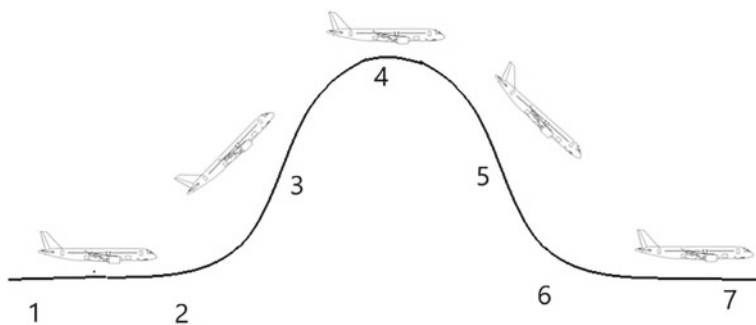


Fig. 1 Schematic diagram of flight test plan

timing of push sidestick at state point 3 and the timing of pull sidestick at state point 5. How to quantify the whole flight test action to specific parameters such as speed, pitch angle and provide intuitive reference for pilots is the key to ensure efficient and safe completion of the flight test task.

3 Principle Analysis

Considering that the pilot performs the test flight through the longitudinal operation of the sidestick, in the aircraft-body coordinate frame, the aircraft motion is simplified as no sideslip and no roll flight. And the engine thrust is along the direction of the flight speed. Then the relationship between normal overload and aircraft motion is as follows [3]:

$$n_z = \frac{V \frac{d\gamma}{dt}}{g} + \cos(\gamma) \quad (1)$$

From formula (1), it can be concluded that the normal overload value is related to flight speed and the flight-path angle rate. This formula can well explain the change law of normal overload when the aircraft makes negative acceleration action. Taking g as the fixed value and considering that the variation range of V and $\cos(\gamma)$ is very small in a short time, n_z is mainly related to $\frac{d\gamma}{dt}$. when $n_z < 0$, the smaller the position of push sidestick, the smaller the $|\frac{d\gamma}{dt}|$, and the smaller the $|n_z|$, it is more likely to maintain a longer negative overload time.

4 Analysis of Negative Acceleration Action

Therefore the weight, center of gravity, the pitch angle and speed of state point 3, and the deflection of push sidestick all have an effect on $\frac{d\gamma}{dt}$, so this article will analyze the n_z from several aspects. And in the flight, in order to facilitate the driver's intuitive judgment, this article takes the pitch angle and velocity as the reference in the negative acceleration flight test. The pitch angle and speed can be directly reflected through the pilot display. The simulation model has passed the model accuracy verification. We select a section of negative acceleration flight test data for comparison, and find that the error of n_z is less than 2%, the average error of θ is 2.3%, and the error of elevator deflection is 1.3%.

4.1 The Effect of Weight and Center of Gravity

This section first analyzes the influence of different weight and different center of gravity on Δt_{n_z} . The flight-path angle rate is related to the aerodynamic force. And in practice, the weight and center of gravity of the aircraft affect the aerodynamic force. Because of the change of weight and center of gravity, the flight attitude of the aircraft will change accordingly. The push sidestick action is shown in Fig. 2. When the pitch angle and velocity of state point 3 reach 20° and 260 km respectively, push the sidestick quickly to -10.8° within 0.5 s, and then keep the sidestick position unchanged at -10.8° .

Table 1 shows the Δt_{n_z} at different weights and different center of gravity. It can be seen from the table that when the weight is small, the center of gravity has little effect on n_z , which is about 7.4 s. With a small weight, the smaller the lift moment required by the wing, the better the maneuverability of the aircraft. When the weight is heavy, the position of the center of gravity has a great influence on n_z . With the increase of the lift moment required by the wing under the front center of gravity,

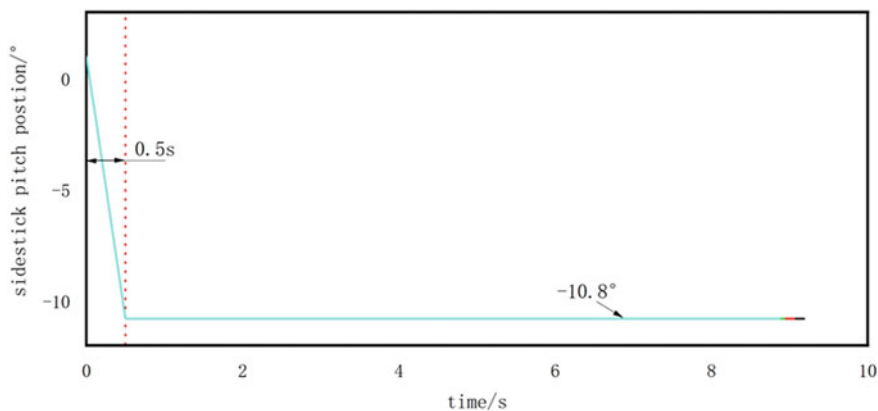


Fig. 2 Schematic diagram of the Sidestick operation

Table 1 Influence of different weight and different center of gravity on Δt_{n_z}

weight/%mac	$\Delta t_{n_z}/s$	weight/%mac	$\Delta t_{n_z}/s$
50/15	7.4375	60/30	7.125
50/22	7.4375	65/15	1.1875
50/30	7.4375	65/22	7
55/15	7.375	65/30	6.9375
55/22	7.3125	70/15	0
55/30	7.25	70/22	6.875
60/15	7.4375	70/30	6.875
60/22	7.125		

the maneuverability of the aircraft becomes more difficult. When the weight is 70 t and the center of gravity is 15, the aircraft cannot enter the load overload. Therefore, for negative acceleration flight, it is recommended to select small weight and rear center of gravity for flight test.

4.2 The Effect of the State Point 3

If the aircraft is flying in a vertical plane, when $n_z = \cos(\gamma)$, the aircraft is in a straight flight state; when $n_z > \cos(\gamma)$, $d\gamma/dt > 0$, the airplane flight trajectory is curved upward; when $n_z < \cos(\gamma)$, $d\gamma/dt < 0$. The aircraft's flight trajectory bends downwards. In the 2–3–4 stage, the aircraft's flight trajectory gradually changes from upward bending to downward bending, and n_z changes from greater than 1 to less than 1. It is particularly important how the normal overload of the aircraft changes from greater than 1 to less than 1 in this stage. If in the 2–3–4 stage, after the aircraft bends upwards, it climbs straight for a period of time so that the normal overload is equal to 1, and then starts to bend downwards, it will definitely affect the time for the aircraft to enter the negative overload. Therefore, the aircraft attitude of state point 3 is very important. This section will study the level flight state, speed and pitch angle of state point 3.

4.2.1 The Effect of Different Level Flight Speeds

In this section, three speeds of 260, 280, and 300 km are selected to establish a stable level flight and pull the sidestick. After reaching a pitch angle of 20° and a speed of 260 km, a fast push is performed to -10.8° and held for 0.5 s. Then keep the putter position at -8.8° and observe the change of Δt_{n_z} . The results are shown in Table 2.

It can be seen from Table 2 that the time of negative normal overload value is longer after flying at higher speed and entering negative acceleration action. The curves of n_z , elevator deflection and speed with time are shown in Fig. 3. The three vertical red dotted lines in the figure are the time points of push sidestick when the speed and pitch angle reach 260 km and 20° respectively. Compared with the level flight speed of 260 km, when the level flight speed is 280 km and 300 km, it needs to climb steadily for a period of time before the speed reaches 260 km, and its normal overload value is equal to 1 in front of the push sidestick. Therefore, after pushing sidestick, the normal overload value can enter the negative value stage earlier and maintain a longer time.

Table 2 The time of negative normal overload at different level flight speeds

velocity/km	260	280	300
$\Delta t_{n_z}/s$	7.5625 s	8 s	8.25 s

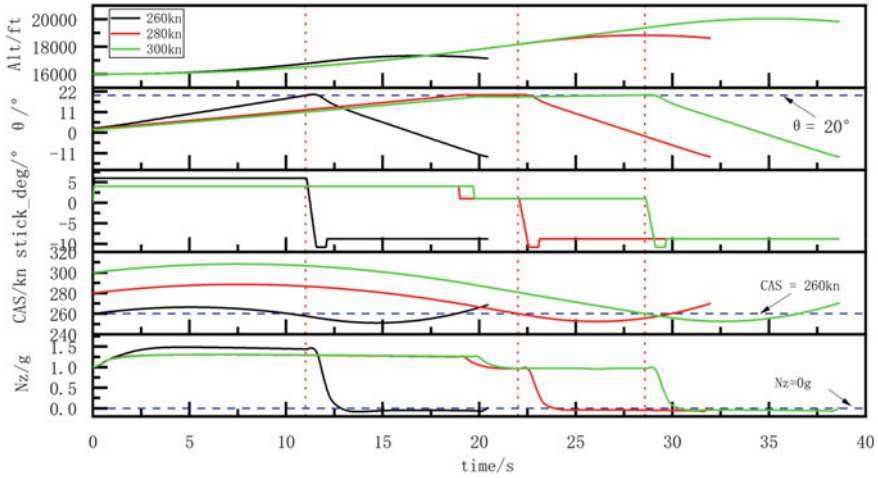


Fig. 3 The variation curves of n_z , $\frac{dy}{dt}$, deLR with time at different level flight speed

Therefore, after reaching the specified pitch angle, a stable climb for a period of time can increase the time of the load overload. However, it can also be seen from Table 2 that the maintenance time of the negative overload value of 300 km level flight is not much longer than that of 280 km level flight. And considering that there are errors in the simulation model when putting the sidestick, it is recommended that the level flight speed be around 280 km.

4.2.2 The Effect of Different Pitch Angles at State Point 3

In this section, the pitch angle is used as a variable. When the aircraft pull sidestick climb to the pitch angle of 20°, 24°, and 28° respectively and the speed is 260 km, the sidestick position is quickly pushed to -10.8°. And hold for 0.5 s, then return to -9.8° to observe the time when the aircraft enters the negative normal overload. The results are shown in Table 3.

The curves for the three cases are shown in Fig. 4. The red color is the time line of the three push rods. From the curve of the pitch angle we can see that the slope is basically the same in all three cases due to the same amount of push rod. But the overload value of n_z at 28° fluctuates greatly and is close to 2 g, which is easy to cause unsafe flight test. The pitch angle can be changed more widely when the push sidestick is started at 24° than at 20° and 24°. Therefore the $\frac{dy}{dt}$ stays at a certain

Table 3 The time of negative normal overload at different pitch angle

$\theta/^\circ$	20	24	28
$\Delta t_{n_z}/s$	7.5625	8.625	8.6875

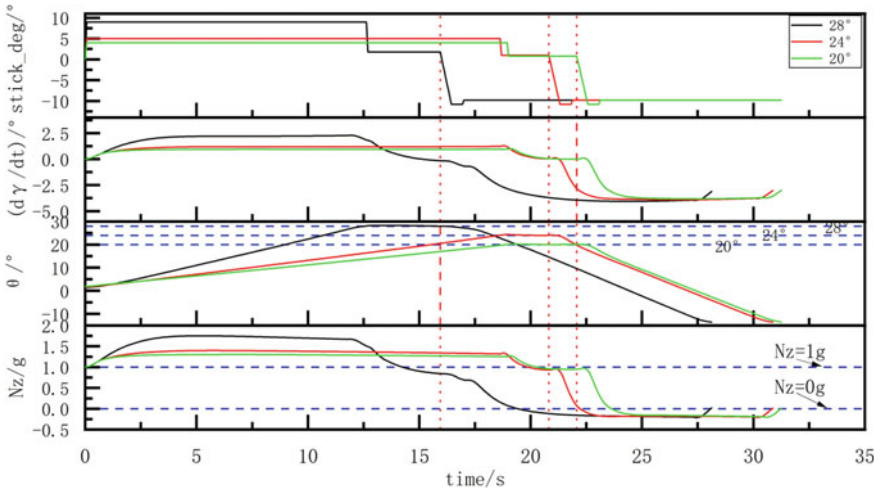


Fig. 4 The variation curves of n_z , $\frac{d\gamma}{dt}$, deLR with time at different pitch angle

value longer, and the Δt_{n_z} is also longer. Therefore, in conjunction with the actual flight test, the pitch angle for the push sidestick is recommended at 24° about.

4.2.3 The Effect of Different Aircraft Speed at State Point 3

This section considers the effect of different aircraft speeds on Δt_{n_z} at state point 3. When the aircraft pull sidestick climb to speeds of 250 km, 260 km, 270 km, and 280 km respectively and the pitch angle is 20°, the sidestick position is quickly pushed to -10.8° . And hold for 0.5 s, then return to -9.8° to observe the time when the aircraft enters the negative normal overload. The results are shown in Table 4.

Figure 5 shows the variation curves of n_z , deLR, $d\gamma/dt$ with time. The higher the speed of the aircraft at the push sidestick, the earlier the aircraft enters the negative overload range and the longer the value of Δt_{n_z} . When $n_z > 0$, the greater the speed, the smaller the elevator deflection, and the smaller the value of $|d\gamma/dt|$, which is consistent with the analysis of the previous formula. When $|d\gamma/dt|$ is smaller, the time that the pitch angle change from 20° to -15° is also longer, and Δt_{n_z} increases. Therefore, at state point 3, you can choose to operate the sidestick with a larger initial speed for increasing the negative normal overload time.

Table 4 The time of negative normal overload at different speed

Velocity/km	250	260	270	280
$\Delta t_{n_z}/s$	7.1875	7.5625	8.0625	8.375

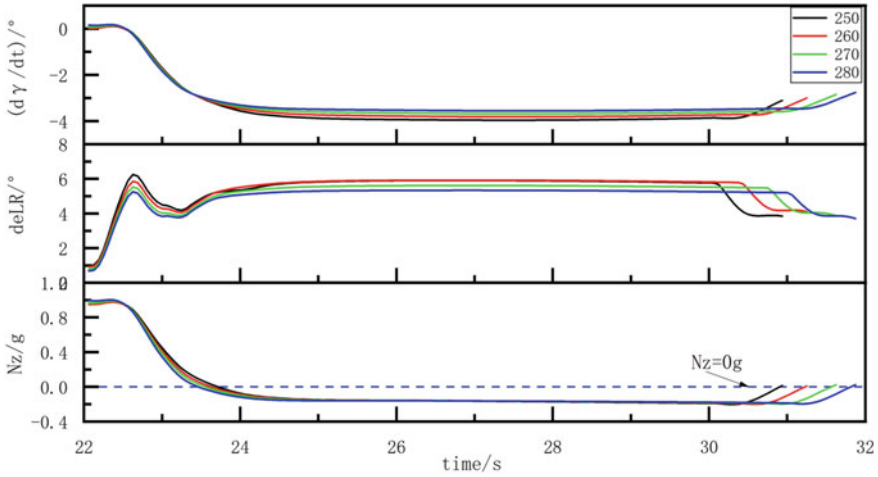


Fig. 5 The variation curves of n_z , $\frac{d\gamma}{dt}$, deLR with time at different aircraft speed

4.3 The Effect of Different Push-Sidestick Actions

This section mainly studies the influence of different push-sidestick actions on n_z at the same state point 3. The state points 3 used in this section are all the same. The aircraft flies steadily and levelly at 280 km, and pull the sidestick. When the aircraft reaches a speed of 260 km and a pitch angle of 20° , the sidestick is pushed quickly.

Observing the elevator deflection in the previous figure, it can be obtained that after a quick push, the elevator surface has a small fluctuation, and then it is gradually deflected to a certain value. First we study a small return of the sidestick after a quick push. The results are shown in Table 5 and Fig. 6. After the sidestick is pushed to a certain value, the elevator fluctuates back. Then with the stabilization of the sidestick position, the elevator deflection gradually stabilizes to a certain value. In combination with the value of Δt_{n_z} in the table, the larger the initial push sidestick, the faster the $\frac{d\gamma}{dt}$ changes, so that the n_z enters the negative value earlier. Then the small return to -9.8° helps the elevator to stabilize faster, so the Δt_{n_z} is greater. Therefore, during the test flight of this action, the pilot can push the sidestick by a large margin and maintain it for about 0.5 s, then return it by a small margin.

The elevator deflection is mainly affected by the sidestick position. The elevator deflection is different under different sidestick position, resulting in different moments. Therefore, after putting the sidestick to 12.8° and maintaining it for 0.5 s,

Table 5 The time of negative normal overload at different sidestick position

stick_deg/ $^\circ$	-8.8	-9.8	-10.8	-11.8
Δt_{n_z} /s	7.5	7.5625	7.5625	7.75

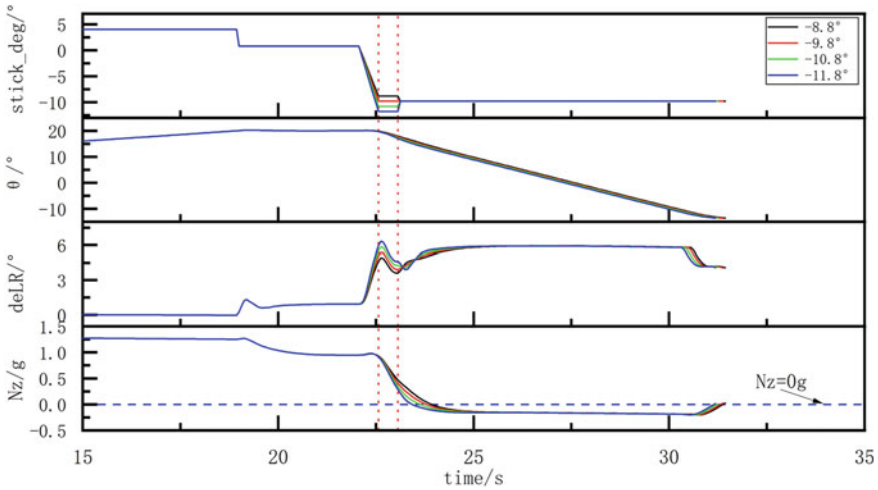


Fig. 6 The variation curves of n_z , $\frac{d\gamma}{dt}$, deLR with time at different sidestick position

Table 6 The time of negative normal overload at different sidestick position

stick_deg/°	-14.8	-13.8	-12.8	-11.8	-10.8	-9.8	-8.8	-8.3
$\Delta t_{n_z}/s$	6.1875	6.1325	6.5625	6.875	7.1875	7.625	8.25	2.1875

we further analyzed the influence of different sidestick position on Δt_{n_z} . The results are shown in Table 6.

It can be seen from the table that the greater the position of the sidestick after 1 s, the longer the Δt_{n_z} . until the sidestick position reaches -8.3° , the Δt_{n_z} decreases sharply, which is consistent with the results shown in the previous formula. No matter how you put the sidestick, the Δt_{n_z} keeps the maximum when the stick is returned to -8.8° , which can reach 8.25 s. We compared the Δt_{n_z} when putting the sidestick directly to -8.8° under the same state point 3, which is 7.75 s. It can be seen that a small return of the sidestick position helps to lengthen Δt_{n_z} , which is the same as the result in Table 5.

Figure 7 show the variation curves of n_z , $d\gamma/dt$, deLR with time. The smaller the sidestick position, the smaller the elevator deflection, the smaller the $|d\gamma/dt|$, the longer the Δt_{n_z} . But it also causes the value of $|n_z|$ to be smaller within Δt_{n_z} . When the sidestick position is -8.8° , the value of n_z is less than 0, but it is close to 0. But when the sidestick position is too large, such as -14.8° , -13.8° , the value of n_z is between -0.7 and -0.6 g. For test flight, there is no need for such a large negative overload value, and Δt_{n_z} is also less than 7 s. Therefore, the selection of the sidestick position is best between -9.8° and -10.8° , and the value of n_z is between -0.15 and -0.25 g, and Δt_{n_z} is greater than 7 s.

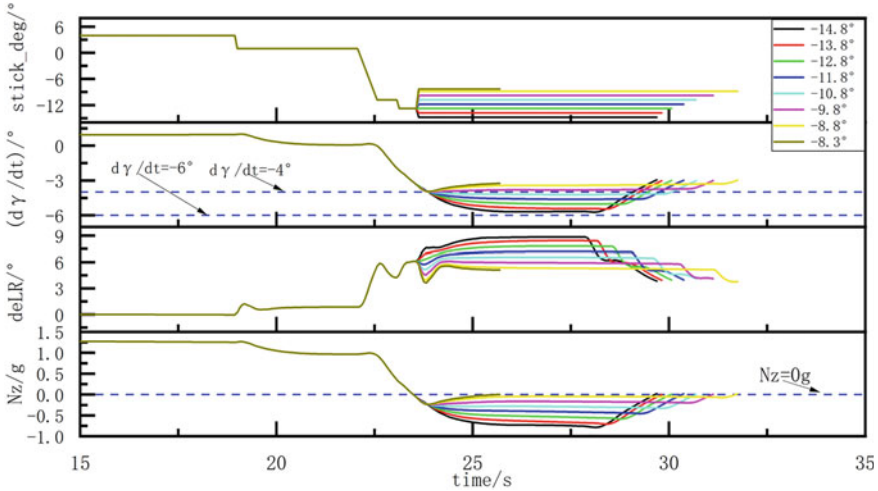


Fig. 7 The variation curves of n_z , $\frac{d\gamma}{dt}$, deLR with time at different sidestick position

5 Conclusion

In this paper, a dynamic simulation model is used to conduct a detailed simulation analysis of negative acceleration flight from the principle of flight. The relevant results are as follows:

- (1) When the weight is small and the center of gravity is back, the aircraft has better maneuverability, which helps to extend the negative normal overload time of the aircraft.
- (2) In order to make the aircraft enter the negative normal overload for a longer time, the aircraft can be allowed to climb stably for a period of time behind the pull sidestick and carry out the push sidestick operation with a larger pitch angle and speed.
- (3) After the driver pushes the sidestick quickly, the elevator surface will fluctuate. The sidestick can be returned in a small range to make the elevator deflection faster and more stable.
- (4) It is recommended to maintain the sidestick position between -10.8° and -9.8° , and its n_z value between -0.15 and -0.25 g. The time for the aircraft to enter the negative normal overload can also be maintained for more than 7.5 s.

Acknowledgements This work is partially supported by Rong Jin. He provided me with a lot of ideas for the paper and guided me how to carry out the simulation work. And my colleagues also provided suggestions for revising my paper. Thank them for their help. The authors also gratefully acknowledge the helpful comments and suggestions of the reviewers, which have improved the presentation.

References

1. Meiqian L, Jinzhou W, Hongliang L (2011) Negative acceleration flight test technique study for civil aircraft fuel system. *Sci Technol Eng* 12:8820–8823 (in Chinese)
2. CCAR-25-R3 (2001) China civil aviation regulations Part 25: Airworthiness standards for transport category airplanes. Civil Aviation Administration of China. (in Chinese)
3. Chen YL, Shen HL (2016) Aircraft flight dynamics. In: *Aircraft mobility and agility*

Design of Aircraft Engine Inlet Radial Distortion Generator



Boyang Fang and Xiaoqing Qiang

Abstract The design of the inlet radial distortion generator is the key technology of the compressor component performance test and aerodynamic stability test. This paper designed several radial distortion generators composed of annular metal wires for high-pressure compressor and core engine inlet to simulate the actual total pressure profile of the incoming flow. The design of the radial distortion generator uses the principle of airflow flowing through different metal wires to produce different magnitudes of flow losses to generate the required radial total pressure distribution. Through numerical simulation of wire distortion generations with different diameters, quantities, and arrangements, and iteratively adjusted the generator's parameters, the total pressure distribution at the target position of the distortion generator finally meets the target design requirements.

Keywords Radial distortion · Distortion generator · Compressor · Numerical simulation · Total pressure loss

1 Introduction

During the development of aero engines, compressor component performance tests and aerodynamic stability tests are essential, and inlet distortion research is an important task [1]. Among the disturbance factors affecting compressor stability, the inlet total pressure distortion is particularly important. If the total pressure distortion is too high, it may cause compressor instability and bring serious consequences [2]. Therefore, the experimental study on the effect of inlet distortion on the aerodynamic stability of high bypass ratio turbofan engines and establishing a reasonable analysis

B. Fang · X. Qiang (✉)
Shanghai Jiao Tong University, Shanghai, China
e-mail: qiangxiaoqing@sjtu.edu.cn

B. Fang
e-mail: fangby@sjtu.edu.cn

and calculation method is of great significance to the development of high bypass ratio turbofan engines [3].

According to the distortion parameters, inlet distortion can be divided into total pressure distortion, total temperature distortion, swirl distortion, static pressure distortion, plane wave, and compound distortion. And according to the different spatial distribution, the total inlet pressure distortion can be divided into radial distortion, circumferential distortion, and combined radial and circumferential distortion. At present, the mechanism of radial inlet total pressure distortion affecting compressor aerodynamic stability is only considered from the aspects of decreasing the local axial velocity and increasing the inlet angle of attack. It is generally believed that the influence of radial inlet total pressure distortion is negative, which means the stability boundary shifts to the right. Besides, due to the strong radial mixing effect in the compressor blade channel, the radial non-uniformity of the flow parameters gradually decreases along the flow direction. So the influence of radial total pressure distortion on the aerodynamic stability of the compressor is generally less than that of circumferential total pressure distortion. However, the influence of inlet radial total pressure distortion cannot be ignored. In addition to theoretical and numerical analysis [4–6], it is also necessary to conduct key research in the stability verification test [7].

It is widely used to install a distortion generator upstream of the engine inlet to simulate the total pressure distortion of the engine inlet under a certain condition, to conduct the engine stability test [8]. Distortion generator includes distortion net, simulation board, spoiler, free jet simulator, and random frequency generator. The three main pressure distortion generators used are grid pressure distortion generator [9], variable lip pressure distortion generator [10], and baffle pressure distortion generator [11]. This paper studies the distortion generator of the annular metal wire structure. Dai et al. [12] studied the radial total pressure distribution generator of the non-uniform annular wire and found that with the increase of the inlet Mach number, the total pressure loss in the downstream of the distortion generator gradually increased, and the total pressure loss in the upstream of the channel increased more obviously than that in the downstream part, making the dimensionless total pressure change more dramatically along the radial direction. Deng et al. [13] point out that, under the inlet radial total distortion condition, the total pressure distortion index of the flow field behind the fan is larger than that in front of the fan, and it has a certain influence on the velocity field. Zhang et al. [14] pointed out that the drag coefficient of the wire distortion net is largely related to the incoming Mach number and the consistency of the metal wire.

To the best of our knowledge, there is no summary of the total pressure distribution after the wire distortion generator in the literature and does not quantitatively analyze the influence of the wire on the total pressure distribution of the downstream flow field. Therefore, for the subsequent research and design of the distortion generator, further analysis of the influence of the metal wire is required. The purpose of this research is to analyze the influence of different distributions of wire distortion generators on the total pressure loss, and the relationship between solidity ratio and total pressure distribution, so that the design of the wire distortion generator has a

more intuitive data basis. In this paper, according to the principle that the airflow through different metal wires causes different magnitudes of flow losses, several radial distortion generators of annular metal wires are designed. Through numerical simulation of the flow field of wire distortion generators with different diameters, quantities, and arrangement modes, iterating the parameters of distortion generators repeatedly, then study the physical mechanism of wire turbulence, summarize the law of its distortion index. Finally, the total pressure distribution of the radial distortion simulator at its target position meets the design requirements.

The paper is organized as follows: First, introduce the basic theory of the distortion generator. Design the numerical model of the distortion generator, then carry out the two-dimensional numerical simulation through the designed model. Finally, summarize the simulation results.

2 Fundamentals of Calculation

The radial distortion generator designed in this paper is a distortion generator composed of several annular metal wires distributed along the radial direction. The principle is to use airflow to flow through metal wires of different diameters to generate flow losses (friction loss and shock loss) of different magnitudes, thereby forming a total pressure distribution along the radial direction. The total pressure loss of airflow through the distortion generator can be expressed as

$$\Delta P^* = P_0^* - P_1^* = K \cdot \frac{1}{2} \rho_0 V_0^2 \quad (1)$$

In the formula, K is the loss coefficient, ρ_0 is the airflow density in front of the distortion generator, V_0 is the airflow velocity in front of the distortion generator, P_0^* is the total pressure in front of the distortion generator, and P_1^* is the total pressure behind the distortion generator.

One of the calculation methods of loss coefficient K [15, 16] is as follows:

$$K = \frac{\varphi S}{(1 - S)^2} \quad (2)$$

The curve of the drag coefficient φ is related to the Mach number, the consistency of the metal wires, Reynolds number, etc. S is the solidity ratio of the distortion generator, which is equal to the ratio of the blocked area of the wire to the total area. The larger the value, the larger the blockage area of the wire, and the greater the total pressure loss caused by the distortion generator. For a uniformly distributed wire distortion generator, the solidity ratio is calculated as follows [14]:

$$S = \frac{d}{m} \quad (3)$$

In the formula, d is the diameter of metal wire and m is the center distance.

To analyze the influence of metal wires under different diameters on total pressure loss, the single variable method was used to adjust the diameter of the wire. Nine cases with the solidity ratio ranging from 0.1 to 0.5 were calculated. After summarizing the rules, a distortion generator with a non-uniform annular arrangement of metal wires with different diameters was further designed.

3 Model Design

3.1 Design Scheme

The component units of the radial distortion generator are the casing and the metal wire. Its main principle is the airflow through the metal wire produces related losses. The simplified model is shown in Fig. 1. The distortion generator has periodic characteristics in the circumferential direction. To simplify the calculation, this paper did not directly perform CFD numerical simulation on the distortion generator but numerically simulates the multi-cylinder turbulence problem in a two-dimensional plane, to obtain the total pressure loss distribution under each solidity ratio.

3.2 Numerical Model

The distortion generator is composed of several metal wires arranged in a radial direction, so the object of the two-dimensional calculation is several cylinders with a fixed diameter. Determine the calculation domain of this two-dimensional plane cylinder turbulence numerical simulation according to the flow channel parameters

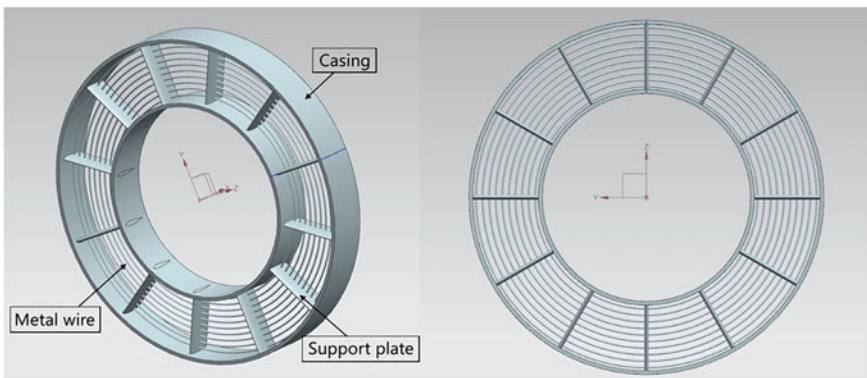


Fig. 1 Simplified distortion generator model

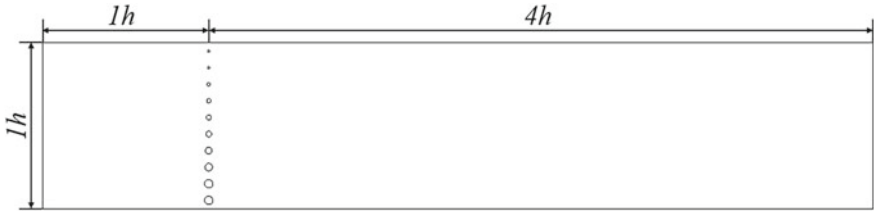


Fig. 2 Calculation domain diagram

of compressor inlet straight section, as shown in Fig. 2. The width of the calculation domain is equal to the height of the compressor inlet. The distance of the inlet section from the center of the distortion generator is one time the height of the flow channel, and the outlet section is four times the height of the flow channel from the center of the distortion generator.

The computational domain uses ICEM for grid division, adopts a structured grid method, uses O-shaped grids at the cylinder, and H-shaped grids for the rest. The cylindrical area and the wake mixing area behind the cylinder were performed with corresponding mesh refinement. The first layer mesh thickness of the cylinder wall is set at $20 \mu\text{m}$. For further research, this paper analyzes the grid independence of all the nine generator models with a solidity ratio from 0.1 to 0.5. This article carries on the numerical simulation to the model with 800,000 and 3.1 million grids, respectively. Figure 3 shows the radial total pressure distribution at the outlet section under the two grid numbers with a diameter of 6 mm. The solid line is the radial

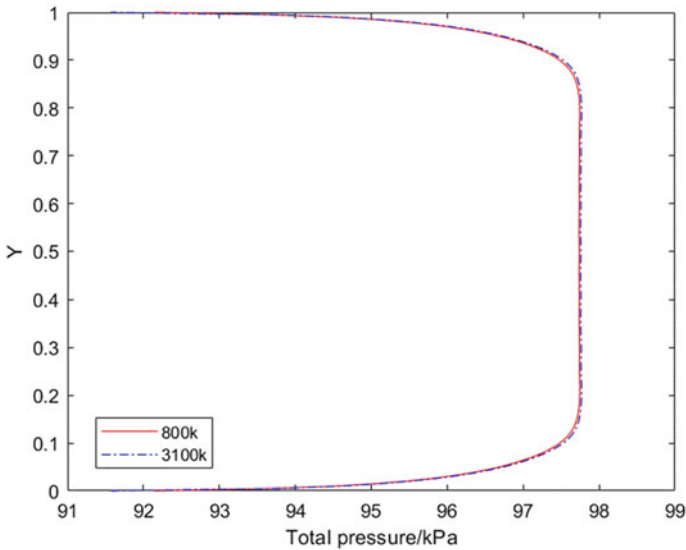


Fig. 3 Radial total pressure distribution of outlet section under two kinds of mesh numbers

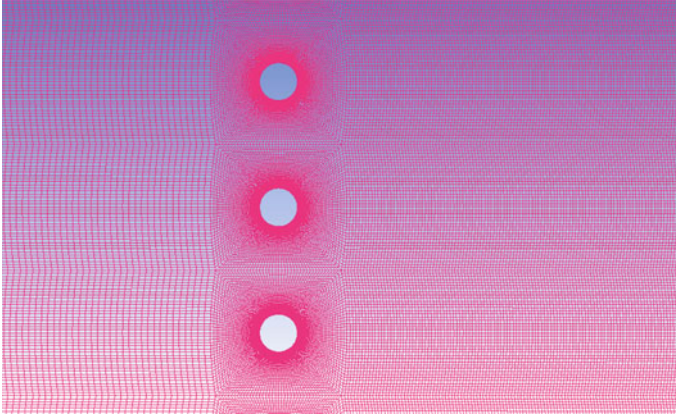


Fig. 4 Two-dimensional calculation grid

total pressure distribution of the outlet section under 800,000 mesh number, and the dotted line is the total pressure distribution under 3.1 million mesh number. It can be seen from the figure that the total pressure distribution of the flow field after the distortion generator under the two grid numbers is the same, and the grid number only plays a minor role in the wake mixing. Its difference has a negligible impact on the overall analysis. To simplify the calculation, a total mesh number of about 800,000 was used for numerical simulation. The mesh details are shown in Fig. 4.

4 Results of Two-Dimensional Numerical Simulation

4.1 *Two-Dimensional Numerical Simulation of Uniform Placement of Distortion Generator*

Fluent is used to solve the numerical simulation of two-dimensional cylinder turbulence of distortion generator. The turbulence model is the SST $k-\omega$ model. The inlet boundary uses pressure inlet boundary, the total pressure is set at 101325 Pa, the outlet boundary uses pressure outlet boundary, and the static pressure is set at 90000 Pa. The inlet Mach number of the distortion generator is distributed within a reasonable range. The remaining boundary conditions are wall boundary conditions. The operating pressure is 0. Use CFX-Post for post-processing, mainly compared the wake mixing situation after the distortion generator, the inlet Mach number, and the total pressure loss at the outlet section under different diameters. The results are shown in Figs. 5, 6, and 7.

This paper mainly studies the total pressure distribution after the distortion generator, so the radial distribution of the total pressure at different axial positions after

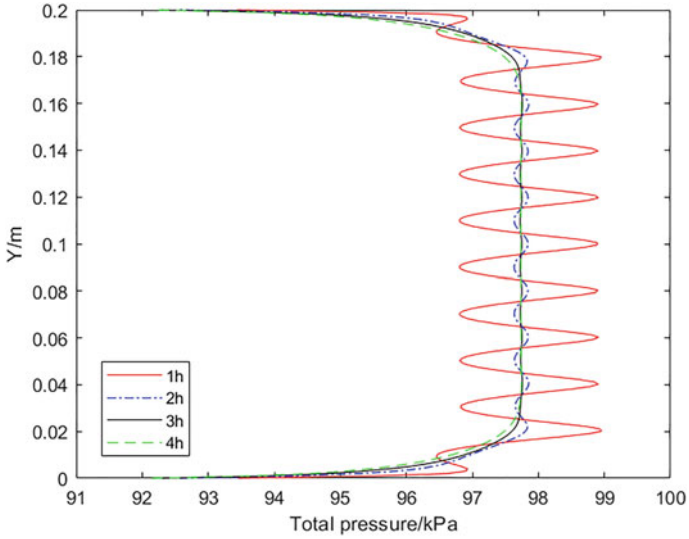


Fig. 5 Radial total pressure distribution at different axial section

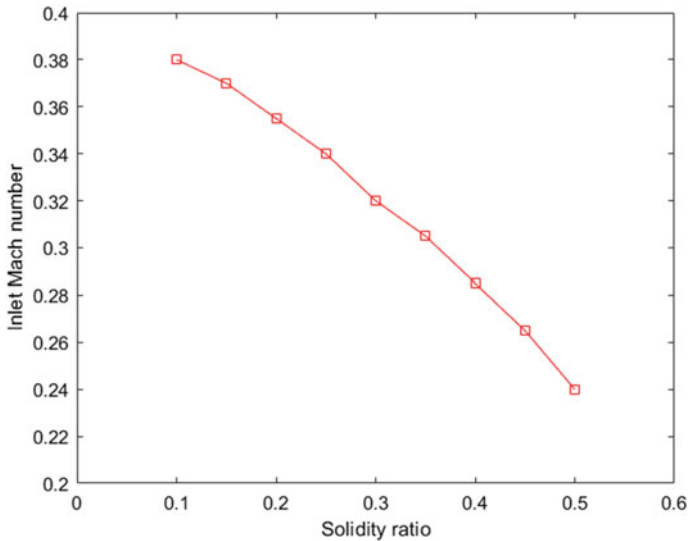


Fig. 6 Relationship between inlet Mach number and solidity ratio

the distortion generator is used to represent the wake mixing situation. Figure 5 shows the radial distribution of the total pressure at different axial sections behind the distortion generator. The abscissa is the total pressure, and the ordinate is the relative channel height.

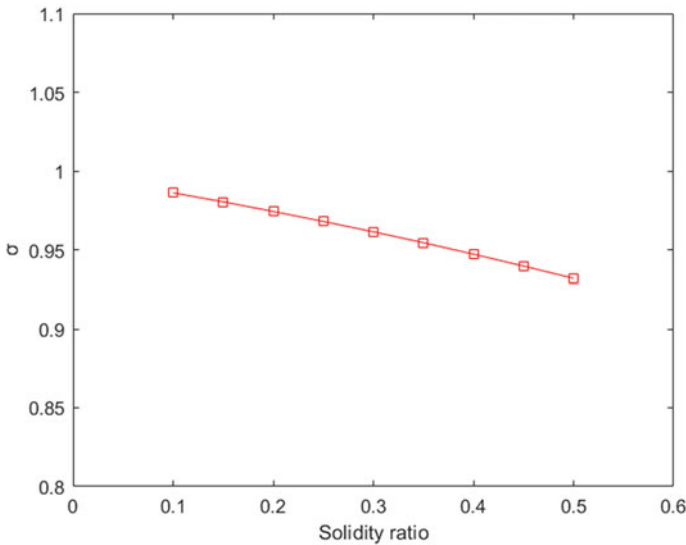


Fig. 7 Relationship between the total pressure recovery coefficient of the outlet section and solidity ratio

It can be seen from Fig. 5, the total pressure distribution at each axial position decreases on both sides close to the wall, which is due to the energy dissipation of the viscous layer on the wall. In the area far away from the wall (10–90% of the channel height), the radial distribution of the total pressure at different axial positions is different. The closer to the distortion generator, the greater the radial fluctuation of the total pressure. The farther away from the distortion generator, the smaller the radial fluctuation of the total pressure. It should be because the wake near the distortion generator has not been completely mixed after the airflow flows through cylinders, and the wake between each cylinder influences each other, resulting in the fluctuation of the total pressure along the radial direction. And it can be seen from the figure that the total pressure fluctuation is closely related to the cylindrical distribution. With the development of the airflow downstream, the wake flow gradually completes mixing, and the radial fluctuation of the total pressure also decreases with mixing. When the airflow is 3–4 times the channel height behind the distortion generator, the mixing is nearly complete, and the radial distribution fluctuation of the total pressure is within a reasonable range.

The relationship between inlet Mach number and solidity ratio is shown in Fig. 6. Under the same boundary conditions, with the increase of solidity ratio, inlet Mach number decreases, and the decreasing trend is close to a linear relationship.

To better analyze the total pressure distribution of the section at the exit, the total pressure distribution is represented by the total pressure recovery coefficient σ in a dimensionless way and its calculation formula in Eq. 4.

$$\sigma = \frac{P_{t.out}}{P_{t.in}} \tag{4}$$

where σ is the total pressure recovery coefficient, $P_{t.out}$ is the average total pressure of the outlet section, and $P_{t.in}$ is the total pressure of the inlet section. The relationship between the total pressure recovery coefficient of the outlet section and the solidity ratio is shown in Fig. 7, which is similar to the relationship between the inlet Mach number. With the increase of the solidity ratio, the total pressure recovery coefficient decreases, the radial total pressure loss increases, and the decreasing trend is close to a linear relationship. According to Eq. 2, with the increase of solidity ratio S , the resistance coefficient K will increase so that the total pressure loss before and after the distorted generator will increase. Finally, the radial total pressure of the outlet section will decrease with the increase of solidity ratio.

4.2 Two-Dimensional Preliminary Design of Non-uniform Distortion Generator

According to the numerical simulation results of the two-dimensional uniform arrangement, the distortion generator with the non-uniform arrangement was preliminarily designed to verify the turbulent influence under the non-uniform arrangement and whether the radial total pressure distribution at the outlet meets the expectation. Figures 8, 9, and 10 show a set of two-dimensional models of the non-uniformly arranged distortion generator and the numerical simulation results of the total radial pressure at the outlet. The distortion generator is composed of ten metal wires, and its two-dimensional plane model is shown in Fig. 8. The solidity ratio of the channel gradually increases from top to bottom so that the expected radial total pressure at the outlet is distributed in a decreasing trend from top to bottom. Figure 9 shows the total pressure contour of the two-dimensional model of the distortion generator. After the

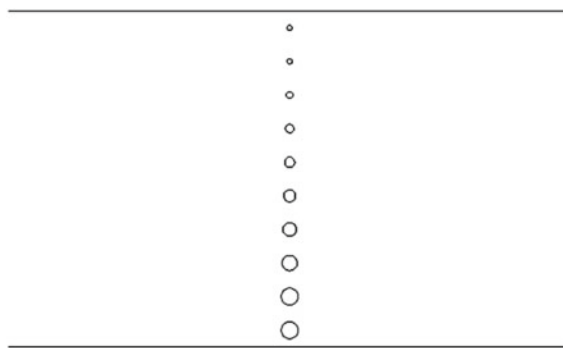


Fig. 8 Two-dimensional model of a non-uniform arranged distortion generator

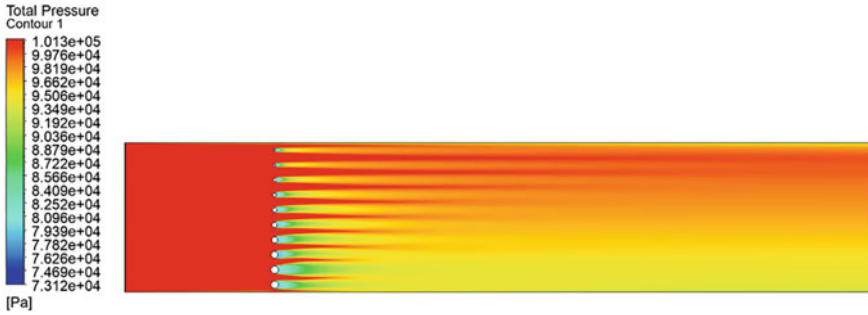


Fig. 9 Total pressure contour of a non-uniform arranged distortion generator

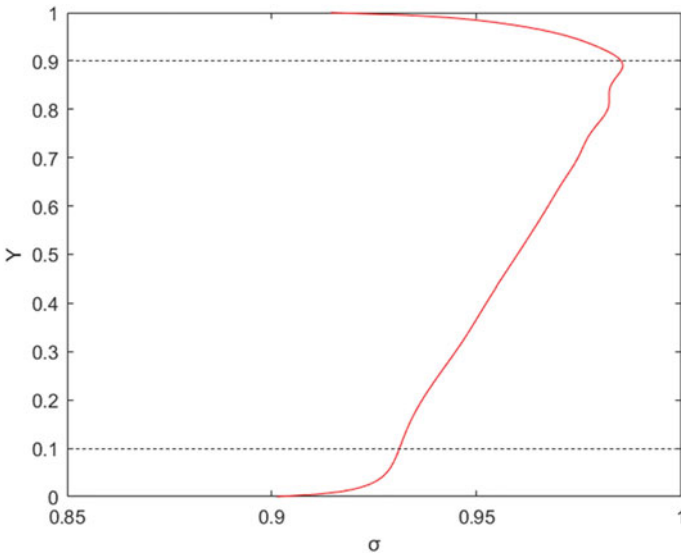


Fig. 10 Radial total pressure distribution at the outlet of a non-uniform arranged distortion generator

airflow flows through the distortion generator, wake flows with different parameters are generated behind each cylinder, which influences each other and gradually mix in the flow process until the exit is nearly completely mixed.

Figure 10 shows the change of the total pressure recovery coefficient at the exit with the height of the channel, where the abscissa is the total pressure recovery coefficient, the ordinate is the relative channel height. It can be seen from the figure, the total pressure recovery coefficient of the area relative to the channel height of 10–90% is roughly in line with the linear relationship, and its value accords with the results of two-dimensional numerical simulation of uniform placement of distortion generator. In the area with a small solidity ratio, the total pressure loss is small and

the total pressure recovery coefficient is large. Due to the energy loss of the viscous layer, the total pressure recovery coefficient on both sides near the wall decreases.

5 Conclusion

In this paper, the numerical simulation of the two-dimensional uniform and non-uniform design of the wire distortion generator is carried out. The following conclusions are obtained:

- (1) Under the same pressure boundary conditions, with the increase of solidity ratio of the distortion generator, the inlet Mach number decreases, and the total pressure recovery coefficient at the outlet section decreases. After the air flows through the distortion generator, it takes 3–4 times the channel height to make the wake close to complete mixing. The closer to the distortion generator, the greater the radial total pressure distribution be fluctuated by the wire wake.
- (2) According to the numerical simulation results of the distortion generator with non-uniform distributed wires, the design of the distortion generator can refer to the numerical simulation results of the distortion generator with uniform distributed wires. By reasonably arranging the wire of different diameters, the total radial pressure can be distributed as expected.
- (3) The CFD numerical simulation of the distortion generator has the effect of a viscous layer near the wall, resulting in a decrease in the total pressure at both ends of the channel, which is different from the fully developed area in the center.

References

1. Zhong Y, Ma H, Guo J, Li J (2021) Review of ground test data processing method of aeroengine inlet total pressure distortion. *Aeroengine* 47(01):72–85
2. Qiao W, Cai Y, Chen Y (2001) Effect of pressure and temperature distortion orientation on turbine engine stability. *J Propuls Technol* 04:307–310
3. Guo J, Hu J, Tu B, Wang X, Wang Z (2020) Numerical simulation of high bypass ratio turbofan engine with total pressure inlet distortion. *J Aerosp Power* 35(05):1029–1041
4. Choi M, Vahdati M, Imregun M (2011) Effects of fan speed on rotating stall inception and recovery. *J Turbomach* 133(4). <https://doi.org/10.1115/1.4003243>
5. Fidalgo VJ, Hall CA, Colin Y (2012) A study of fan-distortion interaction within the NASA Rotor 67 transonic stage. *J Turbomach* 134(5). <https://doi.org/10.1115/1.4003850>
6. Hu J, Zhao Y, Ding N, Lai A (2013) Investigation of influence of inlet distortion on high bypass ratio turbofan engine stability. *Aeroengine* 39(06):6–12
7. Tu B, Hu J (2012) Effect of total pressure distortion on aerodynamic stability of compressor. *J Propuls Technol* 33(02):167–173
8. Zhang T, Zhao Y, Zhao W, Chen B-Y (2017) Design and research of movable total pressure distortion generator. *J Propuls Technol* 38(12):2706–2715

9. Sivapragasam M (2019) Flow field behind a complex total pressure distortion screen. *Proc Inst Mech Eng Part G J Aerosp Eng*
10. Chen X, Mao J (1992) Method of the combination of varying-lip and plate simulation total pressure distortion flow field. *China Acad J* 08:418–422
11. Zhang X, Li J, Song G, Zhou Y, Xie H (2019) Numerical simulation on flat baffle inlet distortion of axial compressor. *J Aerosp Power* 34(05):1153–1165
12. Dai X, Wang Z, Chen L, Zhou K (2019) Design and research of radial total pressure distribution simulator. *J Propuls Technol* 40(03):682–690
13. Deng T, Lei P, Gao X, Wu Y (2017) Research on influence of radial total pressure distortion on forward and backward fan flow. *J Civil Aviat Univ China* 35(02):24–30
14. Zhang S, Ren W, Tu B, Ding Y (2013) CFD numerical simulating investigation on distortion net. *J Shenyang Aerosp Univ* 30(05):27–32
15. Mccarthy JH (2006) Steady flow past non-uniform wire grids. *J Fluid Mech* 19(4):491–512
16. Peacock RE, El-Attar MA, Robinson GD (1981) Asymmetric distortion generation in a variable height annulus. *J Aircr* 18(2):65–66

Hydraulic Servo System Fault Detection Based on Machine Learning



Shengjie Zhou, Yue Wang, Rong Yang, Xingqun Zhan, Xiao Chen,
and Xiaoran Gao

Abstract Servo systems are widely used in aerospace and other fields. To ensure the safety of the system operation, the fault detection of servo systems is very important. Servo system fault detection often uses comparative differential judgment method, which requires the establishment of a reliable model. On the one hand, servo system models are usually built using mathematical and physical methods by combining the transfer functions of the various components the actual servo system have into an algorithm that calculates the input–output relationship. On the other hand, machine learning algorithms can also be used to model the servo system. In this paper, we address this issue by developing a rocket data prediction model based on the LSTM algorithm using publicly available data provided by Shanghai Aerospace Control Technology Institute. After deriving the results, the results are evaluated by using R-squared metrics and some improvement outlooks are provided for the subsequent research.

Keywords Machine learning · Fault detection · LSTM

S. Zhou · Y. Wang · R. Yang · X. Zhan (✉)
Shanghai Jiao Tong University, Shanghai, China
e-mail: xqzhan@sjtu.edu.cn

S. Zhou
e-mail: Z_chark@sjtu.edu.cn

Y. Wang
e-mail: johnld@sjtu.edu.cn

R. Yang
e-mail: rongyang@sjtu.edu.cn

X. Chen · X. Gao
Shanghai Aerospace Control Technology Institute, Shanghai, China
e-mail: alexcdq@163.com

X. Gao
e-mail: gaoxiaoran123@163.com

1 Introduction

Due to the advancement of technology and the increasing demand for functionality in the market, industrial systems tend to be integrated and precise. The hydraulic servo system [1] has the characteristic that the output will change more precisely with the change of input, also has the advantages of fast response, strong control ability and stability, which is widely used in machinery, aerospace and other fields.

Because of the increasing unity and complexity of industrial systems, a small error in the system may cause the collapse of the entire system, resulting in unavoidable safety problems and property damage, so it is necessary to perform fault detection on the system.

There are some characteristics to judge the quality of fault detection [2], which are false alarm rate and leakage rate; sensitivity and robustness; fault locating ability; and accuracy. These metrics give the evaluation criteria in terms of the response speed, accuracy, correctness, and stability of the fault diagnosis methods, respectively.

There are also many model-based methods to perform fault testing of the system [3]. On the one hand, we can have the evaluation of the system done by technicians in the relevant field [2]. The advantage of such an approach is that the mathematical model of the system does not depend on any historical state and the current system error can be calculated by virtue of the current inputs. However, the disadvantage is that building out a complete system model requires a deeper understanding of the whole system, the difficulty of building it increases greatly with the complexity of the system; On the other hand, relying on the development of computer artificial intelligence technology, we can obtain the output corresponding to the input at any moment by processing the processed data with machine learning method after collecting the data [4], which avoids the shortcomings of the first method to some extent.

In this study, a model based on LSTM (Long Short-Term Memory Network) is trained with the pendulum angle control information and telemetry information of the hydraulic servo system collected by sensors. The pendulum angle control information and current telemetry information at any moment are used as input to make the prediction of the telemetry information at the next moment, and the accuracy of the model is evaluated.

This paper will be divided into the following parts: Sect. 2 is the general introduction of hydraulic servo system fault monitoring; Sect. 3 is the data source and processing; Sect. 4 is the model training method and results; and Sect. 5 is the conclusion and the outlook of the subsequent research.

2 The General Introduction of Hydraulic Servo System Monitoring

In this paper, we use the model comparison monitoring principle for fault detection [5], and the principle of this method is shown in the following Fig. 1.

We first need to establish a model of the hydraulic servo system, the model's input is the current state information and control angle information and the output is the next moment of the state information. After successfully establishing the model with reliable accuracy, we put the control information and state information of the previous moment into the model, then compare the output of the model with the real state information of the current state,

$$\begin{cases} \|r\| < Threshold, \text{ fault-free} \\ \|r\| \geq Threshold, \text{ have a fault} \end{cases}$$

where r is the difference between the real value and the analog output, which is called the compared differences. When the compared differences are greater than the previously set threshold, we consider the system to have a fault, while when the compared differences is less than the threshold, we consider the system to be fault-free.

Because of the large number of system state quantities, we need to set thresholds for each state quantity of the system so as to locate the fault occurrence location more precisely.

To improve the trustworthiness of fault detection, the key lies in three aspects, which are:

- the trustworthiness of the system model;
- the trustworthiness of the sensor accuracy; and
- the reasonableness of the threshold value.

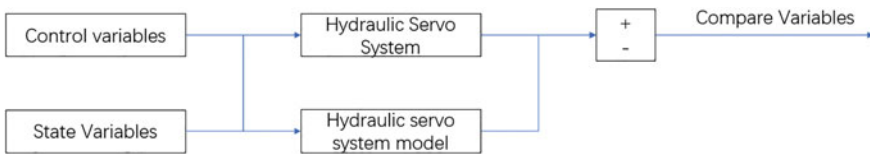


Fig. 1 Fault monitoring schematic

3 The Data Source and Processing

3.1 The Data Source

The data for this study were obtained from publicly available data on the servo system collected by Shanghai Aerospace Control Technology Institute. There are 10 time points from August 2020 to November 2020 for the control and state information of the system collected by three CPUs. The information collected by the three CPUs is compared with each other to prove the accuracy of the collected information.

3.2 The Data Processing

The information contained in the file can be divided into control information and state information, where the control information is the pendulum angle control information of the four servo devices (corresponding to the four mechanisms in the servo actuator), and the state information is the actuator feedback, actuator current, actuator differential pressure, and actuator output D/A. At the same time, in order to increase the accuracy, 12 other features are added. There are four state quantities in each group, corresponding to the four mechanisms, as shown in the following table:

By observing the data, we find that the control information is not present at every moment and the sampling frequency is 0.02 s. The state quantity is recorded from the moment $t = 0$, and is collected every 0.04 s. We correspond the time coordinates of the two one by one and interpolate the state quantity information to calculate so that the number of control information and state quantity information is the same.

The data points where the control information is not equals 0 can be use as the dataset.

4 The Model Training Method and Results

4.1 LSTM Algorithm

We need some machine learning methods which can process time series forecast, such as RBN (Radial Basis Networks) [6], CNN (Convolutional Neural Networks) [7], etc. In this study, we choose LSTM method.

LSTM [8] belongs to RNN (Recurrent Neural Networks) [9] algorithm; each neural network cell contains input layer, output layer, hidden layer, and adds forgetting gate, input gate and output gate. These gates allow forgetting and memory functions to extract the temporal properties of the servo information. According to

the LSTM neural network document of PyTorch [10], the specific formula of LSTM is shown below:

$$i_t = \sigma(W_{ii}x_t + b_{ii} + W_{hi}h_{t-1} + b_{hi}) \quad (1)$$

$$f_t = \sigma(W_{if}x_t + b_{if} + W_{hf}h_{t-1} + b_{hf}) \quad (2)$$

$$g_t = \tanh(W_{ig}x_t + b_{ig} + W_{hg}h_{t-1} + b_{hg}) \quad (3)$$

$$o_t = \sigma(W_{io}x_t + b_{io} + W_{ho}h_{t-1} + b_{ho}) \quad (4)$$

$$c_t = f_t \odot c_{t-1} + i_t \odot g_t \quad (5)$$

$$h_t = o_t \odot \tanh(c_t) \quad (6)$$

where h_t is the state of hidden layer at moment t , c_t is the state of the cell at moment t , i_t, f_t, g_t, o_t , are the input, forget, cell, and output gate at moment t , respectively, and σ refers to the sigmoid function, while \odot refers to the Hadamard product.

In this study, we use the control and state quantities at time $t-1$ as input with an input feature dimension of 32 and the state quantity at time t as output with a feature dimension of 28. The number of hidden layers of the model is 2 and the feature dimension of the hidden layer is 50.

4.2 Analysis of Experimental Results

To evaluate the accuracy of the model, we introduce the following 4 metrics.

MSE. MSE (Mean Squared Error) is calculated as follows:

$$MSE = \frac{1}{m} \sum_{i=1}^m (y_i - \hat{y}_i)^2 \quad (7)$$

where m is the number of data, y_i is the true value of data, and \hat{y}_i is the predicted value of data. The mean square error is similar to the loss function of the model, which can show the distance between the predicted value and the actual true value, and the smaller the MSE, the more accurate the model.

RMSE. RMSE (Root Mean Squared Error) is calculated as follows:

$$RMSE = \sqrt{\frac{1}{m} \sum_{i=1}^m (y_i - \hat{y}_i)^2} \quad (8)$$

where m is the number of data, y_i is the true value of data, and \hat{y}_i is the predicted value of data. The root mean square error is similar in meaning to the root mean square error, but since the root mean square error is the sum of the squares of the errors, it is relatively less intuitive, while the root mean square error can be more intuitively described after opening the square to become the root mean square error.

MAE. MAE is calculated as follows:

$$MAE = \frac{1}{m} \sum_{i=1}^m |(y_i - \hat{y}_i)| \quad (9)$$

where m is the number of data, y_i is the true value of data, and \hat{y}_i is the predicted value of data. MAE is the average of the absolute values of the relative errors, which can describe the accuracy of the model more obviously.

R-square. R-square is calculated as follows:

$$R^2 = \frac{SSR}{SST} = \frac{\sum_{i=1}^n (\hat{y}_i - \bar{y})^2}{\sum_{i=1}^n (y_i - \bar{y})^2} \quad (10)$$

where m is the number of data, y_i is the true value of the data, \hat{y}_i is the predicted value of the data, and \bar{y} is the average of the true values. R-squared ranges from 0 to 1. The closer to 1 means the higher the reasonableness of the model (Table 1).

4.3 Experimental Results

After model learning from the relevant data, we can obtain the model accuracy metrics for each data item, as shown in the Table 2.

We can find that the values corresponding to all the output data are small in terms of MSE, RMSE, and MAE, so we cannot clearly determine whether the model is accurate or not based on this.

From the R-square, we find that the R-square index of each feature is higher than 0.9, which indicates that the model is reasonable.

Table 1 Parameters and parameter designation

Parameters	Parameter designation
Rudder 1A swing angle control signal	1D1A
Rudder 2A swing angle control signal	1D2A
Rudder 1B swing angle control signal	1D1B
Rudder 2B swing angle control signal	1D2B
Actuator 1A feedback	1D1Af
Actuator 2A feedback	1D2Af
Actuator 1B feedback	1D1Bf
Actuator 2B feedback	1D2Bf
Actuator 1A current	1D1AI
Actuator 2A current	1D2AI
Actuator 1B current	1D1BI
Actuator 2B current	1D2BI
Actuator 1A voltage difference	1D1APyc
Actuator 2A voltage difference	1D2APyc
Actuator 1B voltage difference	1D1BPyc
Actuator 2B voltage difference	1D2BPyc
Actuator 1A output D/A	1D1ADA
Actuator 2A output D/A	1D2ADA
Actuator 1B output D/A	1D1BDA
Actuator 2B output D/A	1D2BDA
Actuator 1A oil level	11AUym
Actuator 2A oil level	12AUym
Actuator 1B oil level	11BUym
Actuator 2B oil level	12BUym
Actuator 1A pressurize	11APcy
Actuator 2A pressurize	12APcy
Actuator 1B pressurize	11BPcy
Actuator 2B pressurize	12BPcy
Input pressure of actuator 1A	11APry
Input pressure of actuator 2A	12APry
Input pressure of actuator 1B	11BPry
Input pressure of actuator 2B	12BPry

Table 2 The model accuracy metrics for each data item

Output	MSE	RMSE	MAE	R2
1D1Af	0.003377	0.058113	0.211003	0.97094
1D2Af	0.002994	0.054718	0.244446	0.945687
1D1Bf	0.002605	0.051039	0.171605	0.965231
1D2Bf	0.003473	0.058931	0.273874	0.959636
1D1AI	0.001809	0.042537	0.137833	0.963024
1D2AI	0.002068	0.045475	0.165984	0.971534
1D1BI	0.001702	0.041256	0.112587	0.975018
1D2BI	0.001816	0.042618	0.117671	0.959549
1D1APyc	0.003585	0.059874	0.310761	0.949913
1D2APyc	0.004102	0.064043	0.335393	0.957568
1D1BPyc	0.003913	0.062556	0.325096	0.9438
1D2BPyc	0.003201	0.056582	0.247349	0.961129
1D1ADA	0.001742	0.04174	0.122993	0.9695
1D2ADA	0.002159	0.046461	0.161271	0.967148
1D1BDA	0.001723	0.041514	0.113595	0.974296
1D2BDA	0.002225	0.047172	0.15465	0.954429
11AUym	0.002619	0.051176	0.19379	0.922762
12AUym	0.00292	0.054038	0.208806	0.922587
11BUym	0.002394	0.048924	0.168295	0.928577
12BUym	0.002355	0.048526	0.164028	0.925104
11APcy	0.002174	0.046622	0.153095	0.942865
12APcy	0.002937	0.054194	0.224313	0.951616
11BPcy	0.002789	0.052808	0.221763	0.952881
12BPcy	0.002186	0.04675	0.157486	0.951317
11APry	0.001909	0.043693	0.133331	0.953226
12APry	0.002653	0.051504	0.208047	0.970934
11BPry	0.002311	0.048076	0.180613	0.960046
12BPry	0.002408	0.049067	0.166709	0.971161

5 Conclusion and Future Outlook

5.1 Conclusion

This study provides a feasible solution for servo system fault detection using the LSTM algorithm. The machine learning model is trained using publicly available data from Shanghai Aerospace Control Technology Institute, which does not require a deep understanding of the whole system and is easy to implement.

Finally, the MSE, RMSE, MAE, and R-squared parameters of the output results are calculated and the accuracy while reliability of the model results are analyzed and then the corresponding outlook is proposed.

5.2 Future Outlook

After the selection of the characteristic quantity and the change of the training times of the model, the R-square index of each characteristic value in the model is higher than 0.9, which indicates that the hydraulic servo system model is reasonable. We hope to establish the machine learning model of the electronic servo system by selecting appropriate datasets and features through similar methods, then evaluate the results of the model.

Acknowledgements This work is supported by Shanghai Aerospace Control Technology Institute for the public data collected on the servo system, which provided sufficient material for this study.


The authors also gratefully acknowledge the helpful comments and suggestions of the reviewers, which have improved the presentation.

References

1. Sohl GA, Bobrow JE (2002) Experiments and simulations on the nonlinear control of a hydraulic servosystem. In: Proceedings of the 1997 American control conference (Cat. No.97CH36041). IEEE
2. Jiaqi Z, Xixiang Y, Yuqiang C, Liang L (2021) Overview of application of fault detection and diagnosis based on machine learning. *Comput Meas Control* 29(03):1–9
3. Gertler JJ (2002) Fault detection and diagnosis in engineering systems. *Control Eng Pract* 10(9):1037–1038
4. Mitchell TM (2003) *Machine learning*. McGraw-Hill
5. Ji DONG (2019) Research on fault monitoring method of hydraulic servo actuator based on model comparison. *Metrol Meas Technol* 39(5):20–28
6. Wichert A, Sa-Couto L, Radial basis networks
7. Ketkar N (2017) *Convolutional neural networks*. Springer International Publishing
8. Gers FA, Schmidhuber J et al. (2000) Learning to forget: continual prediction with LSTM. *Neural Comput*
9. Boden M (2001) A guide to recurrent neural networks and backpropagation. <http://www.hh.se/staff/mibo/publications/rn2.pdf>
10. pytorch Official Documents. <https://pytorch.org/docs/stable/generated/torch.nn.LSTM.html?highlight=lstm#torch.nn.LSTM,last>. Accessed 2021/06/25

Moving Vehicle Detection in Satellite Video via Background Subtraction and Global–Local Features Fusion Faster R-CNN



Dong Wei, Zhongliang Jing , and Han Pan

Abstract With the successful operation of the Jilin-1 constellation and other staring satellites in recent years, satellite videos have become new resources for real-time tasks such as surveillance. However, it is difficult to detect small objects in satellite videos due to the high resolution of the satellite video, and the low contrast between the objects and background. This paper develops a novel small moving vehicle detection scheme by exploiting the spatial–temporal information of satellite video. The proposed method consists of four stages: (i) pre-processing, to filter, adjust the contrast, and register the satellite video frame by frame; (ii) extracting the candidate moving vehicle region based on the improved ViBe method; (iii) detecting the vehicle both moving and stationary by the global–local features fusion Faster R-CNN; and (iv) merging the detected results from previous stages to propose the final results, accidental miss detection will be recalled by the inter frame compensation module. Experimental results show that the proposed method demonstrates better performance even when compared to some state-of-the-art methods.

Keywords Moving vehicle detection · Satellite video · Background subtraction

1 Introduction

With the rapid development of earth observation system, the development and application of remote sensing satellite are constantly innovating and deepening. Video satellite is a new type of earth observation satellite which appears in recent 10

D. Wei · Z. Jing (✉) · H. Pan
School of Aeronautics and Astronautics, Shanghai Jiao Tong University, Shanghai, China
e-mail: zljing@sjtu.edu.cn

D. Wei
e-mail: 847628070@sjtu.edu.cn

H. Pan
e-mail: hanpan@sjtu.edu.cn

years [1]. It can gaze at a certain area and obtain more dynamic information by video recording than traditional satellites, which is especially suitable for observing dynamic targets and analyzing their instantaneous characteristics. Getting benefits from the wide monitoring range and second-level time resolution, satellite video has important application potential in the fields of real-time vehicle monitoring in large commercial areas, rapid response to natural disasters, major project monitoring, and military security. At present, several video satellites have been launched worldwide for video capture. For example, SkyBox Imaging launched two video satellites SkySat-1 and SkySat-2 in 2013 and 2014 [2], and Chang Guang Satellite Technology Co. Ltd launched Jilin-1-1 and Jilin-1-2 satellites in 2015 which can shoot color videos with meter resolution. Nowadays, nine video satellites have been launched as a part of the Jilin-1 constellation [3].

Although there have been many researches on satellite video object detection and tracking, there are still many challenges: (i) small uneven movement of the background, which seriously affects the background model; (ii) low contrast between objects and the background (e.g., roads), which is a challenge to the algorithm that depends on the brightness difference between the target and the environment; (iii) tiny objects compared with large scale. For the reason that the ground sampling distance (GSD) of video satellite is generally about 1 m, a vehicle only occupies several pixels in the frame, as well as little color and texture information. Therefore, the current mainstream deep learning object detection methods cannot be directly applied to this scene.

The current researches are mainly divided into two technical routes. One is to improve the moving object detection algorithm suitable for daily scenes, which makes full use of the motion information. The other is to use deep learning method to assist detection. Some researchers proposed schemes to solve the problems above, such as modifying the network structure to adapt to small object detection, designing the algorithm to make the neural network perceive the motion information and appearance information at the same time.

To deal with the problems, this paper proposes a novel framework for small moving vehicle detection by exploiting the spatial-temporal information of satellite video. The proposed method consists of four stages: (i) pre-processing; (ii) motion branch: extracting the candidate moving vehicle region based on background subtraction method; (iii) appearance branch: detecting vehicle either moving or stationary by global-local features fusion Faster-RCNN, which is specifically designed for object detection in satellite video, to deal with noise and false detections such as building roofs; and (iv) merging the detections of the motion branch and appearance branch to form the final results, missed detections are recalled according to the temporal and spatial information in adjacent frames.

The remainder of the paper is organized as follows. Section 2 introduces the related works of satellite video moving detection. Section 3 describes the method of the whole process in detail. In Sect. 4, detailed description about the dataset, metrics, and experiments are presented. Finally, we give our conclusion in Sect. 5.

2 Related Work

At present, the research of satellite video object detection is mainly two routes, one is to achieve moving object detection according to the traditional moving object detection frameworks, the other is to use traditional methods to extract motion information and combine with deep learning to obtain more accurate detection.

The traditional moving object detection methods in still camera video can be divided into three categories, such as frame difference, optical flow, and background subtraction. These three kinds of algorithms have their own advantages and are usually suitable for different situations.

Frame difference is the simplest method of motion detection. The foreground target is obtained by calculating the difference between two or more consecutive frames. However, there are many problems in this method. Once the background is slightly different, it will produce false positives and the complete contour of moving objects is usually not available. Therefore, although the method is simple and fast, it is still not suitable for satellite video detection.

The optical flow method [4] calculates the temporal and spatial variation trend of the brightness value of each pixel, and calculates the velocity vector field, so as to obtain the spatial position of the dynamic object. Optical flow method can be divided into dense optical flow and sparse optical flow. Sparse optical flow can get faster speed by calculating the motion of some feature points.

Recently, the background subtraction method is similar to the frame subtraction method, with the basic idea to obtain the foreground through the difference. However, the background subtraction method maintains a constantly updated background model instead of directly differentiating the current frame from other frames. The core of background modeling method is background modeling algorithm, such as Gaussian mixed model (GMM) [5], improved Gaussian mixed model (GMMv2) [6], Visual Background Extractor (ViBe) [7], K Nearest Neighbor (KNN) [8], etc.

Each of these three methods has its own advantages, and many researches on moving object detection in satellite video based on the above three methods have been widely carried out. [9] proposed a method in the view of the characteristics of moving vehicles usually on the road, to accumulate the trajectory information to form a general road range which can assist the detection of moving objects. [10] introduced a process based on background difference method, which has corresponding judgment methods for moving and ghost targets, but too many parameters were set manually, which affects generalization. From the noise perspective, each frame was regarded as the sum of two parts in [11], namely, the original image and the random 2D noise signal diagram. Using probabilistic distribution to model, the noise is helpful to distinguish potential objects. [12] proposed an improved inter-frame difference method and movement trajectories accumulation method to eliminate pseudo-motion.

The traditional methods mainly considered motion information, but ignored appearance information. The deep learning method makes full use of appearance information. However, the appearance information in satellite video is lost seriously, so the traditional detection method and deep learning method are generally combined in the current methods. A shallow CNN was proposed in [13] to extract heatmap and then to detect objects by thresholding the heatmap. In [14], the merging occurred on the input side, the results of frame difference were superposed with the original frames as the input of the Faster R-CNN. Moreover, different from regarding task as detection problem, in [15], how to deal with the boxes proposed by motion branch was regarded as a classification problem, and the classification was carried out through a shallow network with the resized motion candidates as input. Besides, [16] proposed a new algorithm to fuse the results of object detection and motion detection on pixel level, but it ignored the missing detection of both the two detectors.

Based on these previous works, our work synthesized the meaningful modules of the above methods and constructed the novel framework to detect moving objects with both traditional motion detection methods and deep learning methods.

3 Methodology

The proposed framework consists of four main steps: (i) pre-processing; (ii) motion branch, to extract the potential proposals by background subtraction model; (iii) appearance branch, to regress and classify vehicles by deep learning method; and (iv) merging results of the two branches with an inter-frame compensation module. The framework is shown in Fig. 1, and will be detailed discussed following.

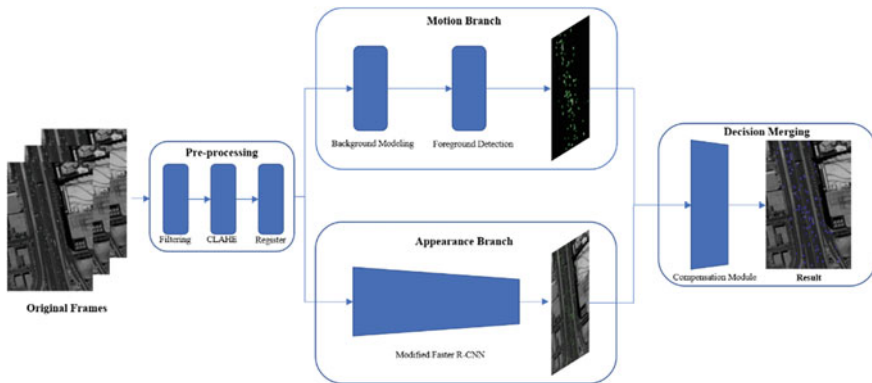


Fig. 1 Flowchart of the proposed framework

3.1 *Pre-processing*

The pre-processing step was an important foundation for the success of subsequent motion branch detection, which was mainly composed of three parts, filtering, contrast processing, and registration.

Filtering before image processing is a routine step. The commonly used filters are mean filter, median filter and Gaussian filter. Mean filter and median filter can only control the smoothing intensity of the filter by controlling the size of the window. But the moving object in satellite video usually has only a few pixels in one dimension, using these two filters will cause excessive blur of the object and loss of little feature details. Gaussian filter can suppress noise by controlling sigma parameters, which can get smoother image and reduce the impact of noise on image quality.

Due to the large coverage area of satellite video, its local contrast is low. This is very disadvantageous for building background model to distinguish foreground from background, so it is necessary to improve local contrast. In this paper, Contrast Limited Adaptive Histogram equalization method (CLAHE) was used for contrast processing [17]. The image was divided into several sub-regions, the histogram of each block was cut, and the contrast limited histograms of each sub-region were equalized. As well, the center point of each sub-region was bilinear interpolated, so as to achieve not only the local histogram equalization to adapt to the different gray distribution of different parts of the image but also the global histogram equalization to coordinate the gray distribution.

The key step in satellite video preprocessing is registration. Because of the inter-frame jitter caused by camera jitter and other factors, the background modeling method directly used for satellite video was relatively poor. Therefore, inter-frame registration is needed to compensate for the background change caused by global motion. In this paper, we use the feature point registration method. Firstly, to detect the Shi-Tomasi points [18] of the current frame, and then to use the forward-backward LK optical flow method [19] to track these feature points, so as to get the position of the points in the next frame. According to the corresponding feature points of the two frames, we can calculate the homographic matrix by applying Random Sample Consensus (RANSAC) [20]-based robust method. Then, the compensated frame calculated by the current frame and the homographic matrix could be conducted.

3.2 *Motion-Based Branch*

The main purpose of the motion branch is to detect the moving foreground target with as little noise as possible. Many classical background modeling methods need a large number of video frames to build the background model, but the duration of satellite video is generally less than 2 minutes, or even only tens of seconds, so the cost is relatively expensive. Therefore, this paper used an improved ViBe algorithm to build the background model. The ViBe method only needs one frame to form the

background model, and it can be updated continuously. On the basis of this, the ghost can be reduced as much as possible by a semaphore mechanism.

The principle of ViBe method is to use random update and neighborhood update mechanism in background modeling, which mainly includes three steps: template initialization, foreground detection, and background model update. For template initialization, to randomly select a pixel from its eight neighborhood N times to fill the background template of every pixel in the frame. Then denoting the background template as $M(x)$.

Then, to denote the Euclidean distance of the pixel in frame and its corresponding points in the background model as D . Also, setting two parameters discrimination threshold R and count threshold C . Count the number of background points whose D bigger than R , whenever the number larger than C , this pixel can be regarded as background point; otherwise, it is considered as the foreground point.

In the template update, this paper used a conservative update strategy. When the pixel $V(x)$ is judged to be the background, a value in the background sample $M(x)$ was randomly selected and replaced with $V(x)$ in the updating process, and the background template sample value in the $V(x)$ neighborhood was updated with equal probability.

However, if there were moving objects in the first frame, these moving objects would be added to the background model, resulting in ghost phenomenon. In order to solve this problem, the semaphore mechanism was applied on the ViBe method. To set a semaphore on each foreground pixel which would increase once, the pixel is judged as foreground consecutively. If the semaphore value exceeded the threshold α , it was judged as ghost, and then converted into background pixels. The reason for the above mechanism is that the moving object in the static background will not stay at a certain position for a long time.

After morphological processing and contour generation, the candidate proposals of motion branches can be obtained.

3.3 *Appearance-Based Branch*

The purpose of motion branch was to detect moving objects, but at the same time, it will also generate false detection, such as building roofs and accidental noise. Therefore, the appearance branch can be used to distinguish whether the detected proposals are vehicle or not. The object in satellite video is different from the common object detection task. In Common Objects in Context (COCO) dataset [21], the object less than 32×32 pixels is defined as a small object, but the object in satellite video is usually only ten to dozens of pixels in size, and the GSD is usually about 1 m, so the texture information and color information of each object are very poor. For such reasons, the mainstream deep learning model cannot be directly applied in the framework.

Based on Faster R-CNN [22] and attention mechanism [23], this paper proposed the global–local features fusion Faster R-CNN method which can utilize context information to assist detection and recognition. Compared with single image, one advantage of video is that there is information association in context. In video object detection, frames are divided into key frame, local frame, and global frame. The key frame is the current frame to be detected, the local frame is the frame within a certain range before and after the key frame, and the global frame is a random frame in the video. On the basis of the key frame features, using the information of local frames and global frames can assist detection of the key frame. The global frames can provide the appearance information and texture information of the category to help the key frame to determine the category, while the local frames can provide the location information to help the key frame locate the object, thus offering help in both regression and classification.

This paper used the basic framework of Faster R-CNN to expand and fuse the global information and local information. For each key frame, its adjacent N frames were regarded as local frames, and M frames were randomly selected from the video sequence as global frames, where the N and M were determined by the calculating power. And all the three kinds of frames were firstly fed into the Region of Interests (ROI) generator of Faster R-CNN to generate ROIs. Aggregation between features was executed through relation module [24], which was inspired by multi-head attention. It aimed to enhance each instance by measuring the relation features as the weighted sum of encoded position information and appearance features from other instances. Meanwhile, the relation distillation tactic [25] was introduced to save computational power and avoid the negative impact of too many invalid ROIs on the training process. The standard of distillation was the ranking of ROI scores for every non-key frame, and the top $K\%$ ROIs were taken for subsequent operation in Fig. 2.

For the reason that the quality of global information was lower than that of local information, the global information was directly aggregated on the ROI proposals

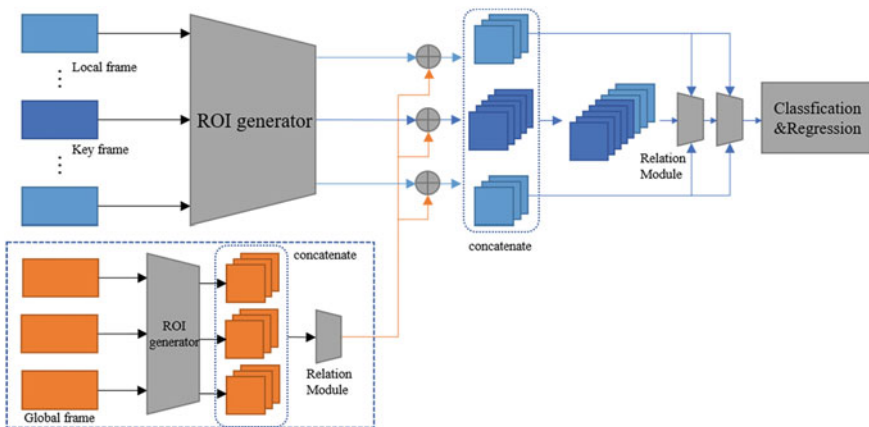


Fig. 2 Structure of the global–local feature fusion Faster R-CNN

of key frame and local frames, and then the local ROIs after global aggregation were distilled and concatenated with the key ROIs. The concatenated tensor and the local feature tensor were aggregated twice to mine the local information as much as possible. Finally, to extract the key ROIs in the concatenated tensor for regression and classification.

3.4 Decision Merging

The main idea of decision merging is to select the final results based on the appearance branch and motion branch. In the motion branch, we got the motion candidate proposals, which contained real objects and false detections. In the appearance branch, we obtained the appearance candidate proposals, namely, stationary vehicle objects and moving vehicle objects, through deep learning model. Then, by selecting from two sets of candidate proposals, we can get the candidate objects more accurately.

For the reasons that the counter of moving object detection is usually larger than that of the object itself, and even several adjacent objects may be connected, the measurement scale was not Intersection over Union (IoU), but Intersection over Appearance (IoA), that was, the ratio of the intersection part to the appearance candidate box. We set the threshold of IoA as 0.3 to determine the real object.

In addition, the appearance detector and motion detector inevitably miss some true values, a strategy of detecting the leakage is used. For the reason that the movement of the vehicle is continuous, that is, it is impossible to disappear suddenly or move to another place, so the existence of the vehicle can be determined according to the spatiotemporal coherence. The specific strategy was to perform IoU operation between the results of the previous frame and the current frame. If IoU is less than the given threshold or even cannot match, denoting the unmatched box in previous frame as surviving box, then the discarded motion proposals and appearance proposals are investigated during the decision merging of the current frame. If there is one proposal in the discarded set which can match the surviving box, it will be added to the result set. Meanwhile, initializing a semaphore to monitor the surviving box, the semaphore was added one for each re-matching until the semaphore reached the threshold. At this time, the object was considered to be lost and to remove it from the result set.

4 Experiments and Results

4.1 Datasets

In this paper, we choose the dataset of *LasVegas* satellite video dataset [26] which was widely used in previous studies. This experimental video was taken by SkySat-1

satellite over Las Vegas on March 25, 2014. The dataset contains 700 frames, with the GSD of 1.1 m and resolution of 1920*1080. The annotation mainly concentrates on two area of interest, and each vehicle occupies about 10 pixels.

Besides the *Las Vegas* dataset, the *VEDAI* dataset [27] is used to train the basic Faster R-CNN part of the appearance branch to perform better generalization. The *VEDAI* dataset has about 1200 frames of satellite imagery with the GSD of 12.5cm × 12.5cm and nine categories. We combine the car, pick-up and van as a new vehicle class. After down-sampling, the dataset is in the same resolution level of satellite video which is convenient for transfer learning.

4.2 Metrics

According to the usual practice, we use box-level metrics to evaluate the performance of the algorithm. By calculating the IoU score between the ground truth and the detected boxes, the detected results can be divided into 4 parts, that are, true positive (TP), false negative (FN), true negative (TN), and false positive (FP). The TP means the detected box is the correct result, the FN represents identifying the ground truth as background. While the FP represents the false alert that mistakenly regard fake objects as true objects.

On the basis of these three indexes, we can calculate the precision, recall and F1-score.

$$P = \frac{TP}{TP + FP} \quad (1)$$

$$R = \frac{TP}{TP + FN} \quad (2)$$

$$F1 = \frac{2 * P * R}{P + R} \quad (3)$$

The precision is the ratio of the right ones in all detected boxes, and the recall is the correctly detected boxes over all ground truth. No doubt that the higher the precision and recall, the better the detection performance, but usually these two indicators are difficult to improve at the same time. So, F1-score, as the harmonic mean of precision and recall, was used as the main metric in this paper.

Table 1 Results of different BGS methods on *LasVegas* datasets

Method	Precision	Recall	F1-score
GMM	0.482838	0.498424	0.490507
GMMv2	0.029226	0.132175	0.047867
KNN	0.050037	0.199556	0.080012
CNT	0.066785	0.359497	0.112643
GMG	0.052204	0.116525	0.072104
Improved ViBe	0.525120	0.557086	0.540631

4.3 Results and Comparisons

Comparison of Different Methods in the Motion Branch

Apart from the ViBe method discussed above, there are several mature methods for moving object detection in a steady background suitable for different situation. To achieve better performance, we selected five different methods to generate motion proposals, including GMM, GMMv2, KNN, CouNT (CNT), and Geometric Multi-grid (GMG). By testing these methods on the *LasVegas* dataset, the results are shown in Table 1 and Fig. 3.

From Table 1, the performance of KNN, GMMv2, CNT, and GMG were greatly affected by the changes of light though the video has been preprocessed. Except for these methods, the improved ViBe method was better than the GMM whether on precision or recall. The experiment shows that the improved ViBe method is a better choice for the motion branch.

Comparison of Different Methods in the Appearance Branch

The experiments of appearance branch were to compare the proposed method with the baseline of Faster R-CNN and YOLOv4 [28] which chosen by other previous studies. Also, the RDN [25], which is one of the state-of-art methods in video object detection, was also added as a competitor.

During training, the parameters of the global–local features fusion network is as following. After training the Faster R-CNN network on the *VEDAI* dataset, the whole appearance branch was trained on a TITAN X with SGD. The initial learning rate was 10^{-3} with the decay of 10^{-4} for the first 8 k iterations, while for the next 8 k iterations, the learning rate was 10^{-4} and 10^{-5} . Besides, the anchor size of the RPN was set as 8, 12, and 16 with the ratios of {1:2, 1:1, 2:1}. The number of proposals depended on the frame category, it was 300 for key frame and 50 for other frames. Moreover, the M and N were set as 10 and 25.

Table 2 shows that the recall and F1-score of our method was better than the others, and the precision was better than Faster R-CNN and YOLO v4 and in the similar level of RDN. So, the proposed appearance detection method is remarkable.

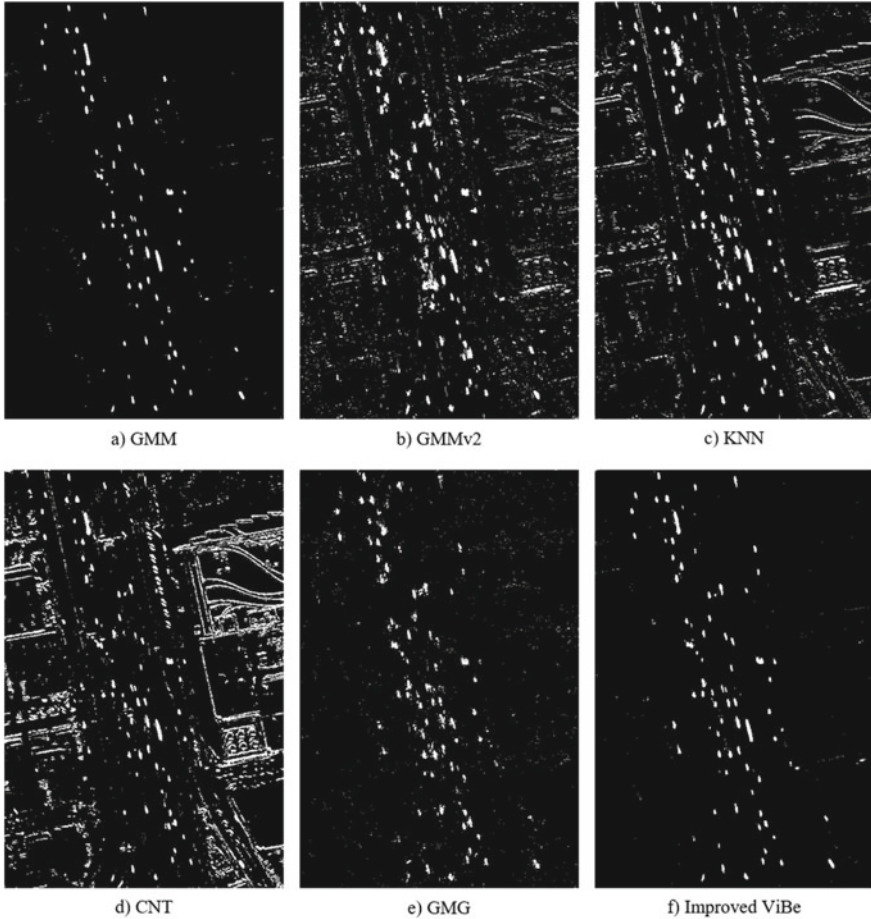


Fig. 3 Results of different BGS methods on *Las Vegas* datasets

Table 2 Results of different object detection models

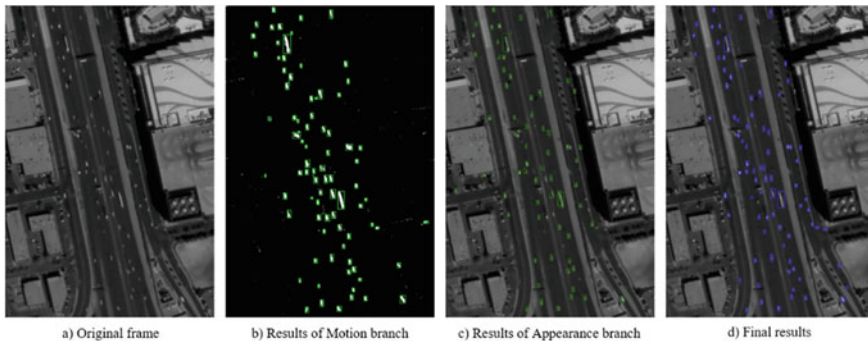
Method	Precision	Recall	F1-score
Faster R-CNN	0.670	0.468	0.551
YOLO v4	0.620	0.588	0.621
RDN	0.863	0.630	0.728
Ours	0.858	0.807	0.832

Results of the Whole Framework

The previous experiments indicated that the improved ViBe method and the global-local features fusion Faster R-CNN were the best model for motion branch and appearance branch. In this set of experiments, we evaluated the performance of the

Table 3 Results of different satellite moving object detection methods

Method	Precision	Recall	F1-score
Ours (no compensation)	0.901	0.783	0.838
Ours (with compensation)	0.894	0.848	0.871
E-LSD	0.796	0.938	0.861
RPCA-PCP	0.902	0.781	0.837

**Fig. 4** Results of different steps in the proposed framework

compensation module and the decision merging module, as well as compared our algorithm with other algorithms.

As shown in Table 3, after integrating the inter frame compensation branch, the recall increased greatly by about 6%, with no loss of the precision. E-LSD [29] obtained the best recall result and the RPCA-PCP [30] got the best precision score, however, our framework achieve the best F1-score in the experiments. This indicates our algorithm balance the precision and recall, resulting in the better comprehensive performance. Figure 4 shows the results of different steps in our method.

5 Conclusion

In this paper, a new framework for satellite video object detection is proposed, which consists of three main modules, that are motion branch, appearance branch, and decision merging module. After pre-processing of the input video, the frames are processed by motion and appearance branch, respectively, to extract motion and appearance candidate regions. The decision merging module merges the two sets of candidate regions with inter frame compensation module. Experimental results show that the proposed method can achieve better results than the state-of-the-art methods.

On the other hand, this framework is not an end-to-end model. Also, in order to make up the missed detection of either motion branch or appearance branch, a semaphore mechanism is introduced to the framework. However, it may be more perfect to be replaced by object tracking method to achieve better results further.

Acknowledgements This work was supported in part by the National Natural Science Foundation of China (Number 61673262, 61603249).

References

1. Kopsiaftis G, Karantzas K (2015) Vehicle detection and traffic density monitoring from very high resolution satellite video data. 2015 IEEE international geoscience and remote sensing symposium (IGARSS): IEEE; p 1881–1884
2. Murthy K, Shearn M, Smiley BD, Chau AH, Levine J, Robinson MD (2014) SkySat-1: very high-resolution imagery from a small satellite. In: Sensors, systems, and next-generation satellites XVIII: international society for optics and photonics; 2014, p 92411E
3. Li D, Wang M, Jiang J (2020) China's high-resolution optical remote sensing satellites and their mapping applications. In: Geo-spatial information science, pp 1–10
4. Brox T, Bruhn A, Papenbergh N, Weickert J (2004) High accuracy optical flow estimation based on a theory for warping. In: European conference on computer vision. Springer.; pp 25–36
5. Friedman N, Russell S (2013) Image segmentation in video sequences: a probabilistic approach. arXiv preprint arXiv:13021539
6. Kaew TraKul Pong P, Bowden R (2002) An improved adaptive background mixture model for real-time tracking with shadow detection. In: Video-based surveillance systems. Springer. pp 135–44
7. Barnich O, Van Droogenbroeck M (2010) ViBe: a universal background subtraction algorithm for video sequences. *IEEE Trans Image Process* 20(6):1709–1724
8. Zivkovic Z, Van Der Heijden F (2006) Efficient adaptive density estimation per image pixel for the task of background subtraction. *Pattern Recogn Lett* 27(7):773–780
9. Yang T, Wang X, Yao B, Li J, Zhang Y, He Z et al (2016) Small moving vehicle detection in a satellite video of an urban area. *Sensors* 16(9):1528
10. Xu A, Wu J, Guo Z, Pan S, Xin S (2017) Motion detection in satellite video. *J Remote Sens GIS*. 6(2):1–9
11. Ao W, Fu Y, Hou X, Xu F (2019) Needles in a haystack: Tracking city-scale moving vehicles from continuously moving satellite. *IEEE Trans Image Process* 29:1944–1957
12. Chen X, Sui H, Fang J, Zhou M, Wu C (2020) A novel AMS-DAT algorithm for moving vehicle detection in a satellite video. *IEEE Geosci Remote Sens Lett*
13. Pflugfelder R, Weissenfeld A, Wagner J (2020) On learning vehicle detection in satellite video. arXiv preprint arXiv:200110900
14. Feng J, Liang Y, Ye Z, Wu X, Zeng D, Zhang X et al (2020) Small object detection in optical remote sensing video with motion guided R-CNN. In: IGARSS 2020–2020 IEEE International Geoscience and Remote Sensing Symposium, IEEE, pp 272–275
15. Chen R, Li X, Li S (2020) A lightweight CNN model for refining moving vehicle detection from satellite videos. *IEEE Access* 8:221897–221917
16. Al-Shakarji N, Bunyak F, Aliakbarpour H, Seetharaman G, Palaniappan K (2019) Multi-cue vehicle detection for semantic video compression in georegistered aerial videos. In: Proceedings of the IEEE/CVF conference on computer vision and pattern recognition workshops 2019, pp 56–65

17. Reza AM (2004) Realization of the contrast limited adaptive histogram equalization (CLAHE) for real-time image enhancement. *J VLSI Signal Process Syst Signal, Image Video Technol* 38(1):35–44
18. Tommasini T, Fusiello A, Trucco E, Roberto V. Making good features track better. In: *Proceedings 1998 IEEE computer society conference on computer vision and pattern recognition (Cat No 98CB36231)*. IEEE, pp 178–183
19. Kalal Z, Mikolajczyk K, Matas J. Forward-backward error: Automatic detection of tracking failures. In: *2010 20th international conference on pattern recognition: IEEE; 2010*. pp 2756–2759
20. Fischler MA, Bolles RC (1981) Random sample consensus: a paradigm for model fitting with applications to image analysis and automated cartography. *Commun ACM* 24(6):381–395
21. Lin T-Y, Maire M, Belongie S, Hays J, Perona P, Ramanan D et al (2014) Microsoft coco: Common objects in context. In: *European conference on computer vision*. Springer, 2014. pp 740–755
22. Ren S, He K, Girshick R, Sun J (2015) Faster r-cnn: towards real-time object detection with region proposal networks. *arXiv:150601497*
23. Vaswani A, Shazeer N, Parmar N, Uszkoreit J, Jones L, Gomez AN et al. (2017) Attention is all you need. *arXiv preprint arXiv:170603762*
24. Hu H, Gu J, Zhang Z, Dai J, Wei Y (2018) Relation networks for object detection. In: *Proceedings of the IEEE conference on computer vision and pattern recognition 2018*, pp 3588–3597
25. Deng J, Pan Y, Yao T, Zhou W, Li H, Mei T (2019) Relation distillation networks for video object detection. *Proceedings of the IEEE/CVF international conference on computer vision 2019*, pp 7023–7032
26. Zhang J, Jia X, Hu J (2019) Local region proposing for frame-based vehicle detection in satellite videos. *Remote Sens* 11(20):2372
27. Razakarivony S, Jurie F (2016) Vehicle detection in aerial imagery: a small target detection benchmark. *J Vis Commun Image Represent* 34:187–203
28. Bochkovskiy A, Wang C-Y, Liao H-YM (2020) Yolov4: Optimal speed and accuracy of object detection. *arXiv preprint arXiv:200410934*
29. Zhang J, Jia X, Hu J (2019) Error bounded foreground and background modeling for moving object detection in satellite videos. *IEEE Trans Geosci Remote Sens* 58(4):2659–2669
30. Wright J, Peng Y, Ma Y, Ganesh A, Rao S. Robust principal component analysis: exact recovery of corrupted low-rank matrices by convex optimization. In: *Proceedings of the 22nd international conference on neural information processing systems 2009*, p 2080–2088

A Unified Framework for Joint Moving Object Detection and Tracking in the Sky and Underwater



Xia Wu, Han Pan, Meng Xu, Zhongliang Jing, and Min Bao

Abstract The ability to detect and locate the moving object in a video is a fundamental procedure in applications of computer vision. However, these tracking methods still face some challenges, and are contradictory among different tasks. In this paper, a unified framework for joint moving object detection and tracking in the sky and underwater is proposed. This framework meets the requirements of two real applications: (i) tracking unmanned aerial vehicle (UAV) in the sky; and (ii) tracking unmanned underwater vehicle (UUV) in water. It consists of three key steps: (i) moving object detection by pixel classification; (ii) data association by blob detection; and (iii) object tracking by efficient convolution operator. Finally, analysis on the accuracy of the proposed framework is provided. Experimental results on real-world datasets and object tracking benchmark (OTB) demonstrate the advantage of the tracking method compared with some state-of-the-art trackers, in terms of accuracy and robustness. In addition, to the best of the authors' knowledge, there is no previously published work for joint moving target detection and tracking in the sky and underwater.

This work was supported in part by the National Natural Science Foundation of China under Grant 61603249, Grant 61673262, and the Wuhan Second Ship Design and Research Institute.

X. Wu · H. Pan (✉) · M. Xu · Z. Jing (✉)
Shanghai Jiao Tong University, 200240 Shanghai, SH, China
e-mail: hanpan@sjtu.edu.cn

Z. Jing
e-mail: zljing@sjtu.edu.cn

X. Wu
e-mail: wuxia2016@sjtu.edu.cn

M. Xu
e-mail: sjtuxm@sjtu.edu.cn

M. Bao
Xidian University, 710071 Shaanxi Xi'an, China
e-mail: mbao@xidian.edu.cn

Keywords Background subtraction · Tracking · Pixel classification · Unmanned aerial vehicles · Unmanned underwater vehicles

1 Introduction

Moving object tracking is widely applied to various domains [1, 2], such as unmanned aerial vehicle (UAV), robotics, and visual surveillance. The goal of moving object tracking is to estimate trajectory of a target in an image sequence or a video. In recent years, discriminative correlation filter (DCF)-based approaches have revealed extraordinary performance on different object tracking benchmarks, both in accuracy and robustness [3–9].

However, these tracking methods require careful analysis involving different situations. Some issues such as deformation, occlusion are critical due to their great impact on the success of the operation. For tracking UAV in the sky, traditional detection methods have a limited model structure for handling diverse datas [10, 11]. For tracking UUV in underwater with an imaging sonar, it is restricted because of the scale change, occlusion, and fast movement of the objects [12, 13].

To address these gaps, we bring up a new framework to study the common characteristics of moving object detection and tracking from a unified perspective. Especially, the versatility of joint moving detection and tracking in the sky and underwater remains unknown. In addition, to the best of the authors' knowledge, it is the first time to introduce a unified framework for the study of tracking UAV in the sky and tracking UUV in underwater.

In this paper, a unified framework for joint moving object detection and tracking is proposed. The proposed framework employs a novel scheme by pixel classification [14] and efficient convolution operation (ECO) [9]. In order to validate the effectiveness of the proposed framework, extensive experiments are performed on object tracking benchmark (OTB) [15] in two real situations: (1) tracking UAV in the sky; (2) tracking UUV in water.

To summarize, the main contributions of this work are three-fold:

1. A unified framework for joint moving object detection and tracking is proposed, which tracks the target automatically and provides a robust appearance model of the target.
2. The effectiveness of the proposed framework is illustrated on real-world datasets, i.e., moving UAV in the sky and moving UUV in underwater. The qualitative and quantitative results show that the proposed method is effective in the two applications.
3. Extensive tracking experiments are carried out on OTB and demonstrate that the proposed framework performs favorably compared with other state-of-the-art trackers in terms of accuracy and robustness.

2 Related Work

2.1 Background Subtraction for Moving Object

Background subtraction is a fundamental technique for isolating the moving parts of a scene by segmenting it into background and foreground [14], as shown in Fig. 1.

The background subtraction techniques can be classified into three major categories, namely, parametric models [16–18], sample-based models [19–21], and neural network-based models [22–25].

A classical parametric background subtraction method is the Gaussian mixture model (GMM) [17], which models each pixel as a Gaussian distribution. However, these parametric methods are prone to fail in the face of illumination variation. To improve the performance of GMM, some methods have been proposed [18, 26], but these variants are still easy to fail when sudden illumination variation, high dynamic scene, and hard shadow occur.

Sample-based methods based on stored sample feature values (e.g., codebook methods [19] and other different variants [21]) can address the highly difficult problem of accurately modeling all types of shadows in an image sequence or a video, by exploiting the recurrence of similar shadow values at pixel level to match with the samples in the model. However, these methods are not suited for foreground segmentation when facing high dynamic scenes.

Some neural network-based models [22, 23, 25] employ convolutional neural networks (CNN) instead of manually extracting features to fuse the fine-scale and coarse-scale feature information efficiently [25], which is more accurate but computationally intensive.

2.2 Tracking UAV in the Sky

UAVs are widely applied in various fields, such as surveillance, rescuing, and agriculture, etc. [1, 27]. However, tracking maneuvering UAV in an uncertain environment is a challenging task because of appearance variation, background clutter, and severe

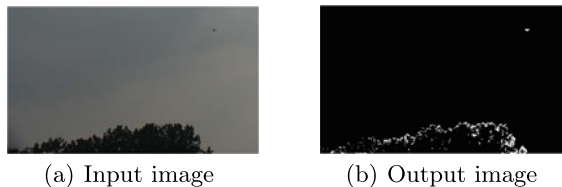


Fig. 1 An example of background subtraction result. The left image is the input image, the right image is the segmentation result. Foreground pixels are marked in white

occlusion [11]. The methods of tracking UAV can be divided into two mainstream directions, one is based on correlation filtering [3, 4, 6, 8], and the other is based on deep learning [28–32].

The minimum output sum of squared error (MOSSE) [3] was the pioneer of applying correlation filtering into moving object tracking. In 2012, circulant matrices and kernel function were firstly introduced in the circulant structure of tracking-by-detection with kernels (CSK) [4] based on MOSSE, to reduce complexity and achieve high tracking speed. Later, a novel adaptive tracker named discriminative scale space tracking (DSST) [6] was proposed, which can be integrated with other tracking algorithms without scale estimation. The first tracker to make use of background information is background-aware correlation filter for moving tracking (BACF) [8], which can efficiently model the variety of both the foreground and background of the object over time.

In recent years, deep learning methods have attracted extensive attention in the field of tracking UAVs. Some siamese networks balanced accuracy and speed in moving object tracking, such as Siamese [33], SiameseFC [28]. Accurate tracking by overlap maximization (ATOM) [31] decomposed the tracking task into two tasks of classification and estimation, which can demonstrate impressive speed.

Furthermore, a new algorithm named continuous convolution operator for tracking (CCOT) [7] was proposed, which utilized an implicit interpolation model to integrate multi-resolution deep feature maps in the continuous spatial domain, can surprisingly lead to sub-pixel accurate localization. And later, efficient convolution operator (ECO) [9] developed CCOT behind the problems of computational complexity and over-fitting, improved both speed and accuracy simultaneously.

2.3 Tracking UUV in Underwater with Imaging Sonar

For tracking maneuvering UUV in underwater with an imaging sonar, the typical algorithms include:

(1) tracking algorithm developed on Kalman filter (KF) [34], including extended Kalman filter (EKF) [35], unscented Kalman filter (UKF) [36], etc.; (2) tracking algorithm based on the probability hypothesis density (PHD) [27, 37, 38]; (3) multi-target tracking algorithm based on data association [39].

Multiple KF-based algorithms [34–36] can be developed for underwater multi-target environments and inaccurate targets, but the convergence speed is slow and high-dimensional accuracy will be reduced.

It is apposite for the PHD-based algorithms [37, 38] to be adopted in underwater environments with low signal-to-noise, but the tracking accuracy is insufficient.

Data association algorithms [39], which models the seabed topography as a Gaussian Process random field on a Chow-Liu tree, can cope with degenerate cases. However, it is limited for different applications.

3 The Proposed Framework of Joint Moving Object Detection and Tracking

The proposed framework of joint moving object detection and tracking, as shown in Fig. 2, is proposed for tracking UAV in the sky and tracking UUV in underwater. The proposed framework consists of three modules: (1) moving object detection; (2) data association; (3) object tracking.

First, a background subtraction algorithm through pixel classification is employed to detect the moving target in a video, and segment all frames into foreground and background. The foreground pixels are marked in white, while the background pixels are marked in black respectively.

Second, the blob detection algorithm in opencv libraries [40] can contribute to connect pixels that share some common property (e.g., grayscale value) in an image, and gives an initial location of the object.

Third, the location is transmitted to the tracking module based on ECO [9], for the purpose of tracking the moving target in an image sequence. Once ECO fails to track the maneuvering target, the pixel classification with following blob detection algorithm will be called again to detect the moving target. In addition, the pixel classification algorithm is aroused every $25 \times n$ frames in order to improve the success rate and robustness.

3.1 Moving Object Detection

This subsection presents the detection module of the proposed framework in real scenes, based on pixel classification. In this module, background is stationary or moving very slowly, while foreground object has fast movement.

As a general background subtraction algorithm, pixel classification based on [14] has no specific requirements for video stream, color space, and scene content. To

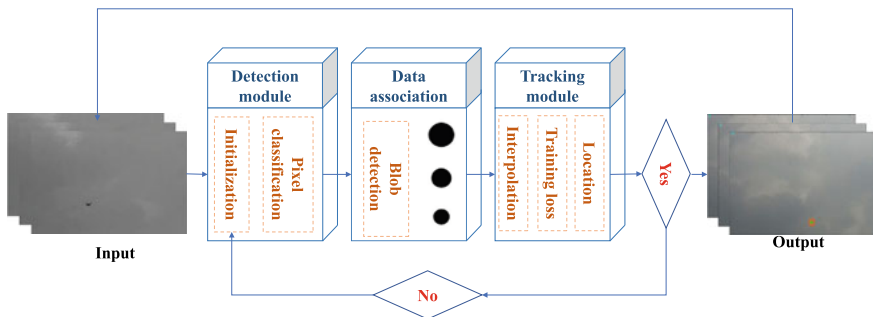


Fig. 2 The proposed framework of joint moving object detection and tracking

introduce it in more details, this method can be divided to three parts: (1) pixel classification; (2) model initialization; (3) update strategy.

Pixel classification means classifying pixels according to some patterns, and determines whether the current pixel belongs to background. This method stores a sample set for each pixel, and the values in this set are its previous pixel value and its neighbor point values. In the following step, each new pixel value is compared with the stored sample set to determine whether it belongs to the background.

Initialization is a vital process of modeling the background. In this method, the model is initialized through only one frame of image, because a frame image may contain pixel distribution information of space and time. For each pixel, its sample values are selected randomly from its neighbor pixels. The initialization method are more sensitive to noise, with smaller computation and faster speed. However, it is limited when the object is moving too fast, because it may introduce ghost area.

The updated strategy of this method for each pixel differs from those based upon the classical belief that the oldest values should be replaced first, the background model is substituted by choosing random values taken in the past at the same location or in the neighborhood.

3.2 *Data Association by Blob Detection*

A blob is a group of pixels that share some common property in an image. In our framework, the input of blob detection is an image with only white and black pixels. The aim of blob detection is to identify and mark the regions where the dark connected. Opencv provides an efficient way to detect blobs and filter them based on different characteristics, which can be called directly with some minor tuning.

3.3 *Efficient Convolution Operator Based on Background Subtraction*

The tracking module of the proposed framework built on ECO [9] can estimate and track the objects' real position, which is initialized by the result of pixel classification. ECO is developed on CCOT [7], which introduced an implicit interpolation model to continuous spatial domain. These two algorithms can accomplish precise integration of multi-resolution deep feature maps. The algorithm is shown below.

The training sample x_j contains D feature channels x_j^1, \dots, x_j^D , which are extracted from the same image patch. For each feature channel d , an interpolation operator J_d is introduced as

$$J_d \{x^d\} (t) = \sum_{n=0}^{N_d-1} x^d[n] b_d(t - \frac{T}{N_d} n), \quad (1)$$

Algorithm 1 The tracking module of the proposed framework based on ECO.

Input: x_j : the training samples; L_0 : the initialization location of the moving target;

Output: the location results in the images patch.

for each image in an image sequence, **do**

the interpolation operator $J_d \{x^d\} (t) = \sum_{n=0}^{N_d-1} x^d[n] b_d(t - \frac{T}{N_d} n)$;

the factorized convolution operator $S_{Pf} \{x\} = \sum_{d=1}^D p_{d,c} f^c * J_d \{x^d\} = f * P^T J \{x\}$;

the expected loss $E(f) = \sum_{l=1}^L \pi_l \|S_{Pf} \{x_j\} - y_0\|_{L^2}^2 + \sum_{d=1}^D \|w f^d\|_{L^2}^2$;

end for

return *result*

where $b_d \in L^2(T)$ is an interpolation function obtained by cubic spline kernel and $x^d[n]$ is acted as weights for each shifted function b_d .

Similar to other discriminative methods, the target is localized by maximizing the confidence scores in an image region. Differently, the confidence scores S_f are defined on a continuous spatial domain, which is parameterized by a set of constitutional filters $f = (f^1, f^2, \dots, f^D) \in L^2(D)^T$, where f^i is the continuous filter for feature channel i .

To reduce the number of parameters in the model, a factorized convolution approach is introduced, which factors the multi-channel filters as the matrix-vector product Pf , where $P = (p_{d,c})$ is a $D \times C$ matrix. The factorized convolution operator can be expressed as

$$S_{Pf} \{x\} = \sum_{d=1}^D p_{d,c} f^c * J_d \{x^d\} = f * P^T J \{x\}. \quad (2)$$

In the following step, the convolution responses from all filters are summed to produce the final confidence function. To reduce the training samples, a Gaussian mixture model (GMM) is employed to evaluate the expectation E , the component m with $\pi_m = \gamma$ and $\mu_m = x_j$ of GMM can be applied to minimize the expected loss

$$E(f) = \sum_{l=1}^L \pi_l \|S_{Pf} \{x_j\} - y_0\|_{L^2}^2 + \sum_{d=1}^D \|w f^d\|_{L^2}^2. \quad (3)$$

The update strategy adopts a sparse updating scheme, which updates the model for every several frames, has a substantial efficient on the overall computational complexity of the learning process.

4 Experiments and Results

To demonstrate the effectiveness of the proposed framework, extensive experiments are carried out: (1) tracking UAV in the sky; (2) tracking UUV in underwater.

The proposed method is compared with some state-of-the-art trackers, such as CCOT in [7], BACF in [8], CSRDCF in [41], AutoTrack in [42], and ARCF & ARCFH in [43]. The proposed framework is validated on OTB to demonstrate the effectiveness and robustness.

The extensive experiments are conducted on a PC with an i7-7700K processor (4.20 GHz), 8GB RAM. Several tracking methods are implemented in Matlab language.

4.1 Real-World Datasets in the Sky and Underwater

Some real datasets for joint moving object detection and tracking are collected.

For tracking UAV in the sky, a PTZ camera [44] with resolution 1920×1280 with 30 fps is utilized to capture some videos of moving UUV in the sky.

For the application of tracking UUV, a multi-beam imaging sonar, i.e., BluePrint M750d [45], is employed to capture the real-world datasets. The sonar works at 750 kHz/1.2 MHz universal dual frequency, which can provide a navigation distance of up to 120 m and high-resolution images for near-field target recognition.

4.2 Evaluation Metrics

One-pass evaluation (OPE) [15] is one of the most conventional metrics to evaluate the tracking average accuracy and success rate of trackers, where the initialization comes from the result of background subtraction.

The robustness of a tracker is as well as an essential index, which can be evaluated by temporal robustness evaluation (TRE) [15] and spatial robustness evaluation (SRE) [15]. The proposed framework evaluated TRE by starting at 20 different frames and SRE by starting with 12 different bounding boxes.

4.3 Experimental Results

Tracking UAV in the Sky This subsection reports the experimental results of the proposed method for tracking UAV in the sky. Some raw images and the corresponding detection results for initiating consecutive tracker are presented in Fig. 3. It can be seen that pixel classification can successfully extract the moving UAV from the real environment.

Then, the blob detection method in opencv libraries is employed to connect pixels in an image so that the appearance of the target can be connected as one or more circles, as shown in Fig. 4. The center of the circle can be served as the initial location

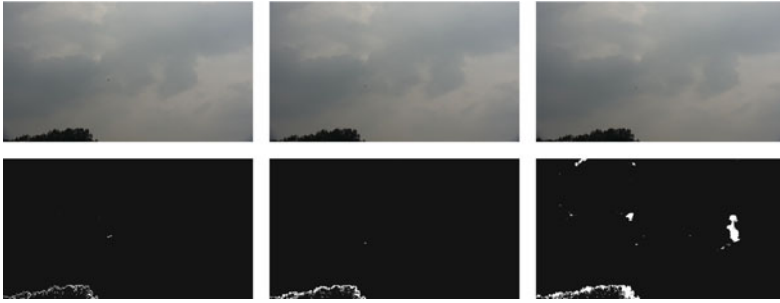


Fig. 3 Some raw images and the corresponding detection results for moving UAV in the sky. The raw images are on the upper row, and the corresponding detection results are on the lower row. The foreground pixels are shown in white



Fig. 4 The blob detection of the background results. The appearance of the target is connected into a circle or circles

of the moving target, and the radius or the sum of the radii can be utilized to calculate the size of the target.

After the blob analysis of the background subtraction results, ECO tracker is applied to estimate the location of the moving UAV from the image sequences, as shown in Fig. 5. These results indicate that the proposed framework can successfully achieve moving UAV detection automatically, and tracking UAV adaptively with a good performance in both accuracy and robustness.

Tracking UUV in Underwater Compared with tracking UAV in the sky, the environment in underwater is more complex. To cope with this problem, prior knowledge can be utilized to restrict the object in a small range, which can filter some noises and clutters.

The first step is to detect the moving UUV by pixel classification in a video. Then, the blob detection is employed to perform a more detailed analysis and restrict the object in a small range. In the last step, ECO tracker is employed to estimate the location of the moving UUV in underwater. The results shown in Fig. 6 demonstrate that the proposed framework can be successfully applied into UUV tracking in underwater with an imaging sonar.

The trajectory of the moving targets are shown as follows. The UAV is shown in Fig. 7, moving back and forth across the sky. The UUV is shown in Fig. 8, moving from side to side. Note that “*” represents the starting point and “o” represents the end point.



Fig. 5 Some tracking results of UAV in the sky, the objects are in the bounding box. The number in the upper left corner represents the frame number of the image

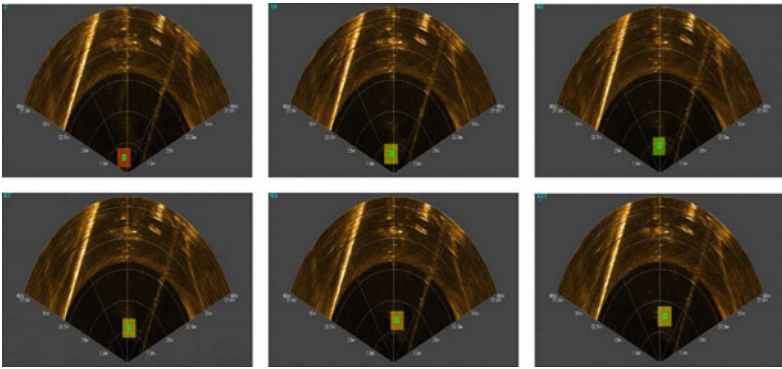


Fig. 6 Some tracking results of UUV in underwater, the objects are in the bounding box. The number in the upper left corner represents the frame number of the image. The orange area indicates the search area of each frame

Fig. 7 Motion curve of UAV

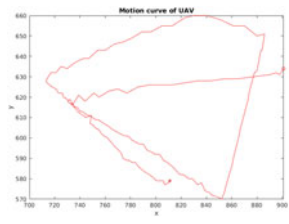
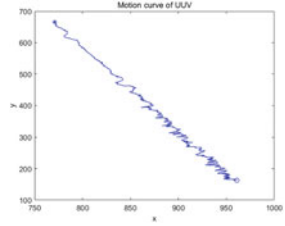


Fig. 8 Motion curve of UUV



Overall Performance on OTB Benchmark Finally, the proposed framework is compared with some competing trackers on OTB benchmark. Figure 9 provides the success rate and precision plots of these trackers on three different metrics: OPE, TRE, and SRE.

In Table 1, we compare our approach with other trackers, in terms of precision, success rate, and speed. It is evident that the ECO tracker is superior to other trackers both in precision and success rate. The ECO-HC tracker achieves the fast speed, which is another hand-crafted feature version of ECO based on histogram of oriented gradient (HOG) and color.

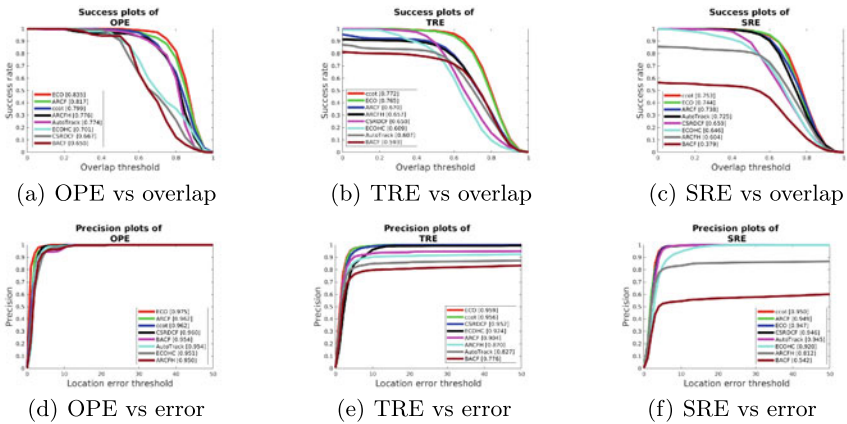


Fig. 9 Plots of OPE, SRE, and TRE. The performance score for each tracker is shown in the legend

Table 1 Comparison results of state-of-the-art trackers in terms of precision, success rate, and speed on the OTB benchmark

Name	CSRDCF	CCOT	ECO	ECO-HC	AutoTrack	BACF	ARCF	ARCFH
Precision	0.960	0.962	0.975	0.951	0.954	0.954	0.962	0.950
Success rate	0.667	0.799	0.835	0.701	0.774	0.650	0.817	0.776
Speed	9.95	0.51	3.56	72.88	54.05	66.87	36.45	63.02

5 Conclusions

In this paper, a unified framework for joint moving object detection and tracking in the sky and underwater is proposed. The effectiveness of the proposed method is validated on two situations: (1) tracking UAV in the sky; (2) tracking UUV in underwater.

Some real-world datasets are applied to verify the proposed method, such as UAV datasets captured by a PTZ camera, and UUV datasets captured by a multi-beam imaging sonar.

The experimental results on OTB indicate that the proposed framework is superior to some competing trackers in both accuracy and robustness. It is evident that the proposed framework can be applied to tracking moving UAV in the sky and tracking UUV in underwater successfully.

References

1. Zhongliang J, Han P, Yuankai L, Peng D (2018) Non-cooperative target tracking: fusion and control. Algorithms and advances. Springer International Publishing, Berlin
2. Pan H, Jing Z, Qiao L, Li M (2018) Visible and infrared image fusion using ℓ_0 -generalized total variation model. *Sci China Inf Sci* 61(4):049103
3. Bolme DS, Beveridge JR, Draper BA, Lui YM (2010) Visual object tracking using adaptive correlation filters. In: *IEEE computer society conference on computer vision and pattern recognition 2010*, pp 2544–2550
4. Henriques J, Caseiro R, Martins P, Batista J (2012) Exploiting the circulant structure of tracking-by-detection with kernels 7575:702–715
5. Danelljan M, Häger G, Khan FS, Felsberg M (2015) Learning spatially regularized correlation filters for visual tracking. In: *2015 IEEE international conference on computer vision (ICCV)*, 2015, pp 4310–4318
6. Danelljan M, Hager G, Khan FS, Felsberg M (2017) Discriminative scale space tracking. *IEEE Trans Pattern Anal Mach Intell* 39(8):1561–1575
7. Danelljan M, Robinson A, Shahbaz Khan F, Felsberg M (2016) Beyond correlation filters: learning continuous convolution operators for visual tracking. *ECCV* 9909:472–488
8. Galoogahi HK, Fagg A, Lucey S (2017) Learning background-aware correlation filters for visual tracking. In: *IEEE international conference on computer vision (ICCV) 2017*, pp 1144–1152
9. Danelljan M, Bhat G, Khan FS, Felsberg M (2017) Eco: Efficient convolution operators for tracking. In: *2017 IEEE conference on computer vision and pattern recognition (CVPR)*, pp 6931–6939
10. Gladh S, Danelljan M, Khan FS, Felsberg M (2016) Deep motion features for visual tracking. In: *2016 23rd international conference on pattern recognition (ICPR)*, 2016, pp 1243–1248
11. Wu H, Li W, Li W, Liu G (2020) A real-time robust approach for tracking uavs in infrared videos. In: *Proceedings of the IEEE/CVF conference on computer vision and pattern recognition (CVPR) workshops*
12. Maki T et al. (2019) Autonomous tracking of sea turtles based on multibeam imaging sonar: toward robotic observation of marine life. In: *12th IFAC conference on control applications in marine systems, robotics, and vehicles CAMS 2019. IFAC-PapersOnLine*, vol 52, no 21, pp 86–90

13. Jiang M, Feng X, Song S, Herrmann JM, Li S (2019) Underwater loop-closure detection for mechanical scanning imaging sonar by filtering the similarity matrix with probability hypothesis density filter. *IEEE Access* 9:1
14. Barnich O, Van Droogenbroeck M (2011) Vibe: a universal background subtraction algorithm for video sequences 20(6)
15. Wu Y, Lim J, Yang M (2013) Online object tracking: a benchmark. In: *IEEE conference on computer vision and pattern recognition 2013*, pp 2411–2418
16. Bouwmans T (2011) Recent advanced statistical background modeling for foreground detection: a systematic survey. *Recent Patents Comput Sci* 4:147–176
17. Stauffer C, Grimson WEL (1999) Adaptive background mixture models for real-time tracking. In: *Proceedings. 1999 IEEE computer society conference on computer vision and pattern recognition (Cat. No PR00149)*, vol 2, pp 246–252
18. Lee D-S (2005) Effective gaussian mixture learning for video background subtraction. *IEEE Trans Pattern Anal Mach Intell* 27(5):827–832
19. Kim K et al. (2005) Real-time foreground-background segmentation using codebook model. *Real-Time Imag* 11(3):172–185. Special issue on video object processing
20. Krungkaew R, Kusakunniran W (2016) Foreground segmentation in a video by using a novel dynamic codebook. In: *2016 13th international conference on electrical engineering/electronics, computer, telecommunications and information technology (ECTI-CON)*, pp 1–6
21. Varghese A, Sreelekha G (2017) Sample-based integrated background subtraction and shadow detection. *Ipsj Trans Comput Vis Appl* 9(1):25
22. Chang O, Constante P, Gordon A, Singaña M (2017) A novel deep neural network that uses space-time features for tracking and recognizing a moving object *J Artif Intell Soft Comput Res* (2), in press
23. Kang K, Li H, Yan J, Zeng X, Yang B, Xiao T, Zhang C, Wang Z, Wang R, Wang X, Ouyang W (2018) T-cnn: tubelets with convolutional neural networks for object detection from videos. *IEEE Trans Circuits Syst Video Technol* 28(10):2896–2907
24. Maddalena L, Petrosino A (2008) A self-organizing approach to background subtraction for visual surveillance applications. *IEEE Trans Image Process* 17(7):1168–1177
25. Vijayan M, Raguraman P, Mohan R (2021) A fully residual convolutional neural network for background subtraction. *Pattern Recognit Lett* 146:63–69
26. Chen M, Wei X, Yang Q, Li Q, Wang G, Yang M (2018) Spatiotemporal gmm for background subtraction with superpixel hierarchy. *IEEE Trans Pattern Anal Mach Intell* 40(6):1518–1525
27. Li XR, Jilkov VP (2010) Survey of maneuvering target tracking. Part ii: motion models of ballistic and space targets. *IEEE Trans Aerosp Electron Syst* 46(1):96–119
28. Bertinetto L, Valmadre J, Henriques JF, Vedaldi A, Torr P (2016) Fully-convolutional siamese networks for object tracking 2016:850–865
29. Mueller M, Smith N, Ghanem B (2016) A benchmark and simulator for uav tracking
30. Mandal M, Kumar LK, Vipparthi SK (2020) Mor-uav: a benchmark dataset and baselines for moving object recognition in uav videos. *Assoc Comput Mach*
31. Danelljan M, Bhat G, Khan FS, Felsberg M (2019) Atom: accurate tracking by overlap maximization. *IEEE/CVF conference on computer vision and pattern recognition (CVPR) 2019*, pp 4655–4664
32. Fu C, Zhang Y, Huang Z, Duan R, Xie Z (2019) Part-based background-aware tracking for uav with convolutional features. *IEEE Access* 7:79 997–80 010
33. Chopra S, Hadsell R, LeCun Y (2005) Learning a similarity metric discriminatively, with application to face verification. In: *2005 IEEE computer society conference on computer vision and pattern recognition (CVPR'05)*, vol 1, pp 539–546
34. Modalavalasa N (2012) An efficient implementation of tracking using kalman filter for underwater robot application. *Int J Comput Sci Eng Inf* 2(2):67–78
35. Rao J, Dinesh U, Koteswara Rao S, Jagan B (2017) Active sonar target tracking using extended kalman filter. *Int J Pure Appl Math* 117(12):301–309

36. Kumar D (2021) Hybrid unscented kalman filter with rare features for underwater target tracking using passive sonar measurements. *Optik - Int J Light Electron Opt* 226(3):165813
37. Jeong TT (2007) Particle phd filter multiple target tracking in sonar image. *IEEE Trans Aerosp Electron Syst* 43(1):409–416
38. Xie S, Chen J, Luo J, Xie P, Tang W (2012) Detection and tracking of underwater object based on forward-scan sonar. In: *Intelligent robotics and applications*. Springer, Berlin, pp 341–347
39. Wang J, Shan T, Englot B (2019) Underwater terrain reconstruction from forward-looking sonar imagery. In: *International conference on robotics and automation (ICRA) 2019*, pp 3471–3477
40. “Opencv,” <https://opencv.org/>. Accessed 20 April 2021
41. Lukežić A, Vojčić T, Zajc LC, Matas J, Kristan M (2017) Discriminative correlation filter with channel and spatial reliability. In: *2017 IEEE conference on computer vision and pattern recognition (CVPR)*, 2017, pp 4847–4856
42. Li Y, Fu C, Ding F, Huang Z, Lu G (2020) Autotrack: towards high-performance visual tracking for uav with automatic spatio-temporal regularization. In: *2020 IEEE/CVF conference on computer vision and pattern recognition (CVPR)*, 2020, pp 11 920–11 929
43. Huang Z, Fu C, Li Y, Lin F, Lu P (2019) Learning aberrance repressed correlation filters for real-time uav tracking. In: *ICCV*
44. Ptz camera. <http://www.sectec.com.cn/products/>. Accessed 13 April 2021
45. The blueprint m750d. <https://www.blueprintsubsea.com>. Accessed 13 April 2021

Hyperspectral and Multispectral Image Fusion via Regularization on Non-local Structure Tensor Total Variation



Meng Xu, Han Pan, Xia Wu, and Zhongliang Jing

Abstract Hyperspectral and multispectral image fusion plays an important role in the fields such as image restoration, space robotics, remote sensing, computer vision, etc. The fused images take advantages of the high spectral resolutions of hyperspectral images and the high spatial resolutions of multispectral images. So there has been a recent outgrowth of interests of research in this field. However, the local structural image regularity and non-local image self-similarity are not yet explored in existing fusion methods. This paper develops a novel method for fusing hyperspectral and multispectral images with non-local structure tensor total variation regularization. Specifically, the weight function to measure self-similarity in non-local domain is introduced on the basis of the definition of structure tensor. Therefore, the proposed method can exploit the regularity and self-similarity of spatial-spectral image's non-local structures simultaneously. In addition to the general formulation of non-local structure tensor variation, this paper presents the discrete non-local structure tensor variation for hyperspectral and multispectral image fusion whose measurements are discrete. This method can provide an alternative way to measure the image variation of multi-band image. The resulting problem is solved by alternating direction method of multipliers (ADMM), a simple but powerful algorithm for convex optimization problems. The optimization problem is handled by a splitting variables strategy, which is implemented by introducing four auxiliary variables regarding to the required fused image. The iteration related to the proposed non-local structure

This work was supported in part by the National Natural Science Foundation of China under Grant 61603249, Grant 61673262, and the Wuhan Second Ship Design and Research Institute.

M. Xu · H. Pan (✉) · X. Wu · Z. Jing (✉)

School of Aeronautics and Astronautics, Shanghai Jiao Tong University, 200240 Shanghai, China
e-mail: hanpan@sjtu.edu.cn

Z. Jing

e-mail: zljing@sjtu.edu.cn

M. Xu

e-mail: sjtuxm@sjtu.edu.cn

X. Wu

e-mail: wuxia2016@sjtu.edu.cn

© The Author(s), under exclusive license to Springer Nature Singapore Pte Ltd. 2023
Z. Jing and D. Strelets (eds.), *Proceedings of the International Conference on Aerospace System Science and Engineering 2021*, Lecture Notes in Electrical Engineering 849,
https://doi.org/10.1007/978-981-16-8154-7_18

tensor regularization term is solved by the proximal mapping method. The solutions of other iterations are given through fast Fourier transforms. Extensive computational experiments are performed on various datasets. The results of index evaluation demonstrate the effectiveness of the proposed method. These results also indicate non-local structure tensor total variation regularization has obvious advantages over the state-of-the-art fusion methods.

Keywords Image fusion · Non-local tensor regularization · Optimization method

1 Introduction

Multiple multiband imaging instruments, i.e., hyperspectral and multispectral sensors, have been promising tools to intelligent environment sensing [1–6]. They have been used in several applications such as restoration, space robotics [7, 8], remote sensing, etc. However, compared to RGB cameras, these sensors have the limitation of low spatial resolution [9]. This study aims to reconstruct a high-resolution image using a number of observations of the same scene. This task is extremely difficult on account of environmental conditions, imaging model [10], and regularization methods [11].

To achieve this task, it is of great interest to exploit nonlinear structures of hyperspectral and multispectral images. Several avenues have been explored in the literature, such as sparse representation [12, 13], total variation [14], matrix factorization [15, 16] (MF). Among the available regularization methods, total variation (TV) is one of the successful priors on image gradient domain [14]. The key idea of TV is to evaluate the image variation with ℓ_1 norm. TV has been applied to different fusion problems, such as hyperspectral sharpening, hyperspectral and multispectral image fusion, multiple multiband image fusion. However, this regularization method has some fundamental limitations, such as staircase effect and loss of texture.

Recently, an efficient regularizer with non-local weighted average of the image gradients is presented in [17]. It can improve the limitations of total variation. This regularizer presents an approach to model complex image structures, such as long-range dependencies or non-localized patterns. Specially, a non-local differential operator is defined on the basis of structure tensor. The latter is utilized to describe the local features of the image variation. This regularization method provides a potential to represent the non-local structures of the underlying multi-sensor images.

In this study, a new method of hyperspectral and multispectral image fusion is examined by considering a new problem formulation and regularization. The image non-local structures are exploited. To the best of the authors' knowledge, there is no previously published work about hyperspectral and multispectral image fusion via regularization on non-local structure tensor total variation. The contributions of this study are summarized as follows

1. A new fusion model for hyperspectral and multispectral image fusion is proposed. It is characterized by taking account of spatial dependence modeling, i.e., non-local structure tensor regularization method. The non-local structure tensor is fabricated by using a weighting function, which represents the non-local image self-similarity to replace the Gaussian convolution kernel in structure tensor.
2. An alternating minimization algorithm based on the framework of ADMM is proposed to solve the new fusion model. Utilizing the solutions provided by this algorithm, the efficiency of the proposed fusion model is investigated on the fusion of hyperspectral and multi-spectral images.

The paper is organized as follows. In Sect. 2, the details of the proposed method and its fusion model with non-local structure tensor total variation regularization are described. In Sect. 3, the resulting optimization framework and algorithms are presented. In Sect. 4, several numerical experiments are conducted. The comparisons with existing methods are demonstrated. Finally, we conclude our work in Sect. 5.

2 Fusion Model

This section has three subsections. The first one is about the representations of the hyperspectral and multispectral imaging models. Then the non-local structure tensor total variation and its discrete version are discussed. In the last subsection, the optimization problem combining the two parts above is given.

2.1 Imaging Models

Just like RGB images, hyperspectral images (HSIs) and multispectral images (MSIs) are generally indicated by 3D arrays. But in this study, we first convert HSIs and MSIs into 2D matrices whose rows have the same amounts with spectral bands. Each row of the matrices puts down the lexicographically ordered pixels of every band. So the observed data of hyperspectral images can be represented by matrix $I_h \in \mathbb{R}^{b_h \times s_h}$, with b_h bands and spatial dimension s_h . And let $I_m \in \mathbb{R}^{b_m \times s_m}$ denote the observed multispectral images. According to the definitions and properties of HSIs and MSIs, it is obviously that $b_h > b_m$ and $s_h < s_m$. What we want to obtain are the images with high spatial and high spectral resolution, which means the estimated data should be the matrices $J \in \mathbb{R}^{b_h \times s_m}$.

Based on the analysis mentioned above, the model of hyperspectral measurements is

$$I_h = JBM + N_h, \quad (1)$$

where the matrix $B \in \mathbb{R}^{s_m \times s_m}$ is a spatial blurring matrix describing the highly blur of hyperspectral images in spatial resolution; the matrix $M \in \mathbb{R}^{s_m \times s_h}$ accounts for

a uniform subsampling of the HSIs so its columns are a subset of the columns of the identity matrix; N_h is an additional noise which is independent identically distributed (i.i.d.). To reduce the complexity of computation, fast Fourier transform (FFT) is used to compute convolutions and matrix inversion, which are usually costly operations. Because these operations are based on the assumption that this model meets circular boundary conditions. Simões et al. [14] has the experimental finding that these conditions do not lead to any significant artifacts in the fused image, while allowing a dramatic reduction in the amount of computation. For simplicity, the assumptions that B is band independent and the noise is identically distributed across bands are also made.

The model of multispectral measurements is shown as follow

$$I_m = VJ + N_m, \quad (2)$$

where $V \in \mathbb{R}^{b_m \times b_h}$ is a matrix represents the spectral response condition of the multispectral instrument and N_m is the i.i.d. noise in multispectral measurements.

Hyperspectral data can be viewed as sparse data. Some results about hyperspectral data in [18] indicate that four eigenvalues are sufficient to account for over 99% of the total energy in the scene. That means J can get in the following form

$$J = EX, \quad (3)$$

where $E \in \mathbb{R}^{b_h \times b_a}$ is a matrix that contains the basis of subspace spanned by the columns of the J only and $X \in \mathbb{R}^{b_a \times s_m}$ is the corresponding coefficient matrix for forming the images we desire. So the operations on J are equivalent to the operations on X . By dimensionality reduction, the computational work can be done more efficiently and the variables estimated reduce significantly, which can improve the accuracy of the solution.

Then (1) can be replaced by

$$I_h = EXBM + N_h, \quad (4)$$

where N_h in this equation also takes account of the error due to dimensionality reduction.

2.2 Non-local Structure Tensor Regularization

To exploit the local structural image regularity and the non-local image self-similarity in natural images, the details of non-local structure tensor TV (NLSTV) are presented. The main idea of NLSTV is to combine these two important image properties to structure a more useful regularization method [17].

All the elements in one line of the matrix X mean all pixels representing spatial resolution in one same spectral band. After extracting each row from matrix X , b_a

smooth grayscale images are obtained. For these scale images, structure tensor of i -th channel at a spatial location \mathbf{m} is defined as

$$S_g X^i(\mathbf{m}) = g_\sigma * (\nabla X^i(\mathbf{m})^T \nabla X^i(\mathbf{m})), \tag{5}$$

where g_σ is a Gaussian convolution kernel with standard deviation σ .

Replacing the Gaussian convolution kernel with a non-negative weighting function $\omega(\mathbf{m}, \mathbf{n})$ that assigns appropriate weights between pairs of points (\mathbf{m}, \mathbf{n}) in image domain $\Omega \subseteq \mathbb{R}^{s_m}$, the non-local structure tensor is given as follow

$$S_\omega X^i(\mathbf{m}) = \int_\Omega \omega(\mathbf{m}, \mathbf{n}) \nabla X^i(\mathbf{n})^T \nabla X^i(\mathbf{n}) d\mathbf{n}. \tag{6}$$

Inspired by the non-local means filter, an effective denoising method comparing regions rather than pixels [19], the weighting function is taken as

$$\omega(\mathbf{m}, \mathbf{n}) = e^{-\frac{d_\sigma(X^i(\mathbf{m}), X^i(\mathbf{n})))}{\beta^2}}, \tag{7}$$

where the ‘‘region distance’’ $d_\sigma(\cdot)$ is defined as

$$d_\sigma(X^i(\mathbf{m}), X^i(\mathbf{n})) = \int_W G_\sigma(\mathbf{t}) |X^i(\mathbf{m} + \mathbf{t})^T - X^i(\mathbf{n} + \mathbf{t})^T|^2 d\mathbf{t} \tag{8}$$

and G_σ is a Gaussian kernel having σ as its standard deviation. W is the search window for \mathbf{t} . β is a filtering parameter.

Since most important information is encoded in the eigenvalues of the non-local structure tensor [17], the non-local structure tensor regularization is based on total variation (TV) is formed by taking advantages of this critical finding. Therefore, the family of NLSTV functions is defined as

$$NLSTV_p(X^i(\mathbf{m})) = \int_\Omega \left(\sum_{i=1}^{s_m} \delta_i^{p/2}(\mathbf{m}) \right)^{1/p} d\mathbf{m}, \tag{9}$$

where $\delta_i, i = 1, \dots, s_m$ are the eigenvalues of the non-local structure tensor. Obviously, NLSTV is established by computing the ℓ_p norms of the square roots of these eigenvalues.

The above is the general formulation of non-local structure tensor variation. However, it cannot be applied to hyperspectral and multispectral image fusion directly. Because the integral involved is continuous yet the existence of uniform subsampling matrix M makes the measurements of hyperspectral instrument discrete. That means a discrete version of NLSTV is needed.

Firstly, a direct non-local gradient operator $D_\omega : \mathbb{R} \mapsto \Gamma \triangleq \mathbb{R}^{s_m \times s_m}$ is introduced from [17]. When this gradient operator is applied on the n -th pixel of X^i , we can get a $s_m \times s_m$ matrix with the following form

$$D_\omega X_n^i = \left[\sqrt{\omega_{n,1}} \nabla (X_1^i)^T, \dots, \sqrt{\omega_{n,s_m}} \nabla (X_{s_m}^i)^T \right], \quad (10)$$

where $\nabla (X_n^i)^T$ is the discrete gradient of n -th pixel in $(X^i)^T$ and $\omega_{n,m}$ is the discrete weight about the pair of pixels (n, m) . This discrete version of weight has the identical layout with (7), except the definition of the region distance $d_\sigma(n, m)$. Here a specified discrete weighting function g_w of size $\tau \times \tau$ is used to replace the Gaussian kernel in (8), then what we will get is

$$d_\sigma(n, m) = \sum_{j=-\tau/2}^{\tau/2} g_w(j) \left| (X_{n+j}^i)^T - (X_{m+j}^i)^T \right|^2. \quad (11)$$

Once these aforementioned works have been completed, the discrete non-local structure tensor can be expressed in terms of the direct non-local gradient operator refer to (6), namely

$$S_\omega X_n^i = D_\omega X_n^i (D_\omega X_n^i)^T. \quad (12)$$

Calculate the eigenvalues $\delta_{n,m}$ of non-local structure tensor is equivalent to calculate the singular values $\sigma_{n,m}$ of non-local gradient, for $n = 1, \dots, s_m$ and $m = 1, \dots, s_m$, since

$$\delta_{n,m} = \sigma_{n,m}^2. \quad (13)$$

Then, the discrete NLSTV can be established by the following expression

$$NLSTV_p(X^i) = \sum_{n=1}^{s_m} \left(\sum_{m=1}^{s_m} \sigma_{n,m}^p \right)^{1/p} = \sum_{n=1}^{s_m} \|D_\omega X_n^i\|_{S_p}, \quad (14)$$

which can be obtained by using the definition of the Schatten norm of order p . And for notation simplicity, we take the $\sum_n \|\cdot\|_{S_p}$ as $\|\cdot\|_{1,p}$.

2.3 Problem Formulations

Let $\|X\|_F \triangleq \sqrt{\text{Tr}(XX^T)}$ denote the Frobenius norm of X . Then the optimization problem regard to hyperspectral and multispectral image fusion is formulated on the basis of our observation models mentioned in Sect. 2.1 and the proposed discrete NLSTV. The detailed description of the optimization problem is shown as follows

$$\underset{X}{\text{minimize}} \quad \frac{1}{2} \|I_h - EXBM\|_F^2 + \frac{\lambda_m}{2} \|I_m - VEX\|_F^2 + \lambda_\tau \tau(X) + \phi(X). \quad (15)$$

The first two terms are data-fitting terms, indicating that the estimated image should have the capacity to explain the observations according to the model. The third term is the regularizer function, which is defined as

$$\tau(X) = \sum_{i=1}^{b_a} \|D_\omega X^i\|_{1,p}. \quad (16)$$

It indicates the sum of discrete NLSTV on spacial pixels of per bands. And

$$\phi(X) = \sum_{i=1}^{b_a} \iota_{\mathcal{C}}(X^i) \quad (17)$$

is the sum of indicator function values about every rows of matrix X . $\iota_{\mathcal{C}}$ is the indicator function of a convex set \mathcal{C} . As for the parameters λ_m and λ_τ , they are be used to control the relative importance of the various terms.

This optimization problem has three main difficulties that need to be deal with. The first difficulty is that the discrete NLSTV is highly nonlinear, non-quadratic and non-smooth due to the nature of total variation. The second one is the large size of X increases the computational complexity. And that the presence of the downsampling operator M preventing a direct use of the Fourier transform in optimizations is the last difficulty. However, the alternating direction method of multipliers (ADMM), a simple but powerful algorithm [20], can deal with these difficulties providing the linear systems' solution of equations on each iteration. The next section will describe the details of the optimization method.

3 Optimization Scheme

We employ ADMM algorithm to deal with the proposed problem. By introducing four auxiliary variables regarding to X , the optimization problem can be given as follows:

$$\begin{aligned} & \underset{X, Y_1, Y_2, Y_3, Y_4}{\text{minimize}} && \frac{1}{2} \|I_h - EY_1M\|_F^2 + \frac{\lambda_m}{2} \|I_m - VEY_2\|_F^2 + \lambda_\tau \tau(Y_3) + \phi(Y_4) \\ & \text{subject to} && Y_1 = XB \\ & && Y_2 = X \\ & && Y_3 = X \\ & && Y_4 = X. \end{aligned} \quad (18)$$

After that, the augmented Lagrangian is established by considering penalty items only:

$$\begin{aligned}
& L_\mu(X, Y_1, Y_2, Y_3, Y_4, Z_1, Z_2, Z_3, Z_4) \\
&= \frac{1}{2} \|I_h - EY_1M\|_F^2 + \frac{\mu}{2} \|XB - Y_1 - Z_1\|_F^2 \\
&\quad + \frac{\lambda_m}{2} \|I_m - VEY_2\|_F^2 + \frac{\mu}{2} \|X - Y_2 - Z_2\|_F^2 \\
&\quad + \lambda_\tau \tau(Y_3) + \frac{\mu}{2} \|X - Y_3 - Z_3\|_F^2 \\
&\quad + \phi(Y_4) + \frac{\mu}{2} \|X - Y_4 - Z_4\|_F^2,
\end{aligned} \tag{19}$$

where $Z_i, i = 1, 2, 3, 4$ are the so-called scaled dual variables, and μ is the penalty parameter whose value is positive. This form of the augmented Lagrangian is permitted because the final result of penalty is that the equality constraints hold, which means the term consist of the Lagrangian multiplier equals zero.

Then the iterations about primal variable X , auxiliary variables $Y_1 - Y_4$ and dual variables $Z_1 - Z_4$ are carried out respectively. The first two iterations are performed by splitting the primal minimization problem into several smaller minimization sub-problems.

The first minimization sub-problem is

$$\begin{aligned}
X^{k+1} \in \underset{X}{\operatorname{argmin}} \quad & \frac{\mu}{2} \|XB - Y_1^k - Z_1^k\|_F^2 + \frac{\mu}{2} \|X - Y_2^k - Z_2^k\|_F^2 \\
& + \frac{\mu}{2} \|X - Y_3^k - Z_3^k\|_F^2 + \frac{\mu}{2} \|X - Y_4^k - Z_4^k\|_F^2
\end{aligned} \tag{20}$$

which the solution is obviously get by

$$X^{k+1} = [BB^T + 3I]^{-1} \times [(Y_1^k + Z_1^k)B^T + (Y_2^k + Z_2^k) + (Y_3^k + Z_3^k) + (Y_4^k + Z_4^k)]. \tag{21}$$

In order to reduce the influence of the increase of the amount of calculation caused by the introduction of auxiliary variables, we perform the computation through FFT, which has complexity $\mathcal{O}(b_s \times s_m \log s_m)$.

The minimization sub-problem involving Y_1 is shown as follows

$$Y_1^{k+1} \in \underset{Y_1}{\operatorname{argmin}} \quad \frac{1}{2} \|I_h - EY_1M\|_F^2 + \frac{\mu}{2} \|X^{k+1}B - Y_1 - Z_1^k\|_F^2. \tag{22}$$

Taking advantage of the definition about the uniform sub-sampling matrix M , the solution is get by combining $Y_1^{k+1}M$ and $Y_1^{k+1}\overline{M}$, where \overline{M} is the matrix that selects the pixels which is not selected by M [14]. So the solutions regarding to $Y_1^{k+1}M$ and $Y_1^{k+1}\overline{M}$ are

$$Y_1^{k+1}M = [E^T E + \mu I]^{-1} \times [E^T I_h + \mu (X^{k+1}B - Z_1^k)]M \tag{23}$$

$$Y_1^{k+1}\overline{M} = (X^{k+1}B - Z_1^k)\overline{M}. \tag{24}$$

In this step, FFT can also be employed to give the computation with the complexity $\mathcal{O}(b_s \times s_m \log s_m)$.

The minimization sub-problem concerning Y_2 is

$$Y_2^{k+1} \in \operatorname{argmin}_{Y_2} \frac{\lambda_m}{2} \|I_m - VEY_2\|_F^2 + \frac{\mu}{2} \|X^{k+1} - Y_2 - Z_2^k\|_F^2 \quad (25)$$

which has the solution

$$Y_2^{k+1} = [\lambda_m E^T V^T V E + \mu I]^{-1} \times [\lambda_m E^T V^T I_m + \mu (X^{k+1} - Z_2^k)] \quad (26)$$

with the complexity $\mathcal{O}(b_s \times s_m)$.

Y_3 is computed by solving the following minimization sub-problem

$$Y_3^{k+1} \in \operatorname{argmin}_{Y_3} \frac{1}{2} \|Y_3 - X^{k+1} + Z_3^k\|_F^2 + \frac{\lambda_\tau}{\mu} \tau(Y_3). \quad (27)$$

After derivation, the result we can get from the definition of Frobenius norm is

$$\|Y_3 - X^{k+1} + Z_3^k\|_F^2 = \sum_{i=1}^{b_a} \|Y_3^i - (X^i)^{k+1} + (Z_3^i)^k\|_F^2. \quad (28)$$

This leads to that this minimization sub-problem in terms of Y_3 can be divided into b_a smaller minimization sub-problems, namely

$$(Y_3^i)^{k+1} \in \operatorname{argmin}_{Y_3^i} \frac{1}{2} \|Y_3^i - (X^i)^{k+1} + (Z_3^i)^k\|_F^2 + \frac{\lambda_\tau}{\mu} \|D_\omega Y_3^i\|_{1,p} \quad (29)$$

which corresponds to the evaluation of the proximal map of the function $\lambda_\tau \|D_\omega Y_3^i\|_{1,p}$ scaled by μ . Based on this, we make use of the definition of the proximal operator [21] to give the solutions of these sub-problems as

$$(Y_3^i)^{k+1} = \operatorname{prox}_{\frac{\lambda_\tau}{\mu} \|D_\omega \cdot\|_{1,p}} \left((X^i)^{k+1} - (Z_3^i)^k \right). \quad (30)$$

And these can continue to be decomposed as

$$\begin{aligned} (Y_3^i)_n^{k+1} &= \operatorname{prox}_{\frac{\lambda_\tau}{\mu} \|D_\omega \cdot\|_{s_p}} \left((X^i)_n^{k+1} - (Z_3^i)_n^k \right) \\ &= \operatorname{argmin}_{(Y_3^i)_n} \frac{1}{2} \left((Y_3^i)_n - (X^i)_n^{k+1} + (Z_3^i)_n^k \right)^2 + \frac{\lambda_\tau}{\mu} \|D_\omega (Y_3^i)_n\|_{s_p}. \end{aligned} \quad (31)$$

This is a kind of problems finding the minimal value of a number, which is much simpler than finding the minimal value of a vector.

In the same way, the minimization sub-problem regard to the last auxiliary variable Y_4

$$Y_4^{k+1} \in \underset{Y_4}{\operatorname{argmin}} \quad \frac{1}{2} \|Y_4 - X^{k+1} + Z_4^k\|_F^2 + \frac{1}{\mu} \phi(Y_4) \quad (32)$$

is decomposed into b_a smaller minimization sub-problems, which has the similar from with (29)

$$(Y_4^i)^{k+1} \in \underset{Y_4^i}{\operatorname{argmin}} \quad \frac{1}{2} \|Y_4^i - (X^i)^{k+1} + (Z_4^i)^k\|_F^2 + \iota_C(Y_4^i) \quad (33)$$

where correspond to the projection of $(X^i)^{k+1} - (Z_4^i)^k$ on the convex set \mathcal{C} . A simple convex set is given as $\mathcal{C} \triangleq \{Y_4^i \in \mathbb{R}^{s_m} : 0 \leq (Y_4^i)_n \leq \gamma, \forall n = 1, \dots, s_m\}$. Therefore, the projection in this case can be computed by $\Pi_{\mathcal{C}}(Y_4^i) = \min(\max(0, Y_4^i), \gamma)$.

After performing the optimizations mentioned above, the following are used to update the dual variables

$$\begin{aligned} Z_1^{k+1} &= Z_1^k - (X^{k+1}B - Y_1^{k+1}) \\ Z_2^{k+1} &= Z_2^k - (X^{k+1} - Y_2^{k+1}) \\ Z_3^{k+1} &= Z_3^k - (X^{k+1} - Y_3^{k+1}) \\ Z_4^{k+1} &= Z_4^k - (X^{k+1} - Y_4^{k+1}). \end{aligned}$$

The complexity of these steps is dominated by the FFT too so that it is $\mathcal{O}(b_s \times s_m \log s_m)$ in per iteration.

A summary of the above optimization process is displayed in Algorithm 1. The code of implementing the whole process is written in Matlab programming language.

Y^k denotes the combination $[Y_1^k, Y_2^k, Y_3^k, Y_4^k]$ and Z^k denotes $[Z_1^k, Z_2^k, Z_3^k, Z_4^k]$.

4 Experimental Results and Discussion

In this section, we assess the performance of the proposed fusion method by testing it on publicly available hyperspectral datasets. To evaluate the fusion performance of the proposed fusion method, the relative dimensionless global error in synthesis [22] (ERGAS), averaged spectral angle mapper (SAM), and universal image quality index [23] (UIQI) are measured.

The proposed method is compared with other state-of-the-art methods, such as coupled non-negative matrix factorization [16] (CNMF), total variation (TV)-based method [14], and low tensor-train rank representation (LTRR)-based method [24]. The competing algorithms are evaluated with default parameters.

Algorithm 1 Hyperspectral and multispectral image fusion algorithm based on NLSTV

```

1: Input: data  $I_h, I_m$ ; regularization parameters  $\lambda_m, \lambda_\tau$ ; initializations
    $Y_1^0, Y_2^0, Y_3^0, Y_4^0, Z_1^0, Z_2^0, Z_3^0, Z_4^0, k := 0$ ; penalty parameter  $\mu$ ; matrices  $E, M, V, B$ 
2: Out:  $X^{k+1}$ 
3: while stopping criterion is not satisfied do
4:    $X^{k+1} \leftarrow \underset{X}{\operatorname{argmin}} L_\mu(X, Y^k, Z^k)$ 
5:    $Y_1^{k+1} \leftarrow \underset{Y_1}{\operatorname{argmin}} L_\mu(X^{k+1}, Y_1, Z_1^k)$ 
6:    $Y_2^{k+1} \leftarrow \underset{Y_2}{\operatorname{argmin}} L_\mu(X^{k+1}, Y_2, Z_2^k)$ 
7:    $Y_3^{k+1} \leftarrow \sum_{i=1}^{b_a} \operatorname{prox}_{\frac{\lambda_\tau}{\mu} \|D_\omega \cdot\|_{1,p}} \left( (X^i)^{k+1} - (Z_3^i)^k \right)$ 
8:    $Y_4^{k+1} \leftarrow \sum_{i=1}^{b_a} \Pi_C(Y_4^i)$ 
9:    $Z_1^{k+1} \leftarrow Z_1^k - (X^{k+1} B - Y_1^{k+1})$ 
10:   $Z_2^{k+1} \leftarrow Z_2^k - (X^{k+1} - Y_2^{k+1})$ 
11:   $Z_3^{k+1} \leftarrow Z_3^k - (X^{k+1} - Y_3^{k+1})$ 
12:   $Z_4^{k+1} \leftarrow Z_4^k - (X^{k+1} - Y_4^{k+1})$ 
13:   $k \leftarrow k + 1$ 
14: end while

```

4.1 Datasets

Three semi-synthetic datasets are used in our experiments, i.e., *Botswana*, *Indian Pines*, and *Washington DC Mall*. The resolutions of these datasets are 400×240 , 400×400 , and 400×300 , respectively. These datasets are generated according to the Wald’s protocol. The real-world hyperspectral datasets are taken for the reference images.

4.2 Experimental Results

Table 1 reports the performance evaluation of all the competing methods. The bold font in Table 1 indicates the best results. It can be seen that the proposed method

Table 1 Numerical results of hyperspectral and multispectral image fusion on three datasets

Datasets	Botswana			Indian pines			Washington DC Mall		
	ERGAS	SAM	UIQI (%)	ERGAS	SAM	UIQI (%)	ERGAS	SAM	UIQI (%)
CNMF	1.5030	2.6568	93.08	1.1561	1.9536	79.50	1.0353	2.1314	96.52
LTRR	1.4379	2.8973	92.89	1.0835	2.2114	80.14	1.0374	2.1333	96.52
TV	1.3670	2.1117	95.85	0.6770	0.9817	93.62	1.2821	1.0406	96.48
Our	0.8734	1.4802	98.11	0.3817	0.5006	96.63	1.2696	0.8314	96.73

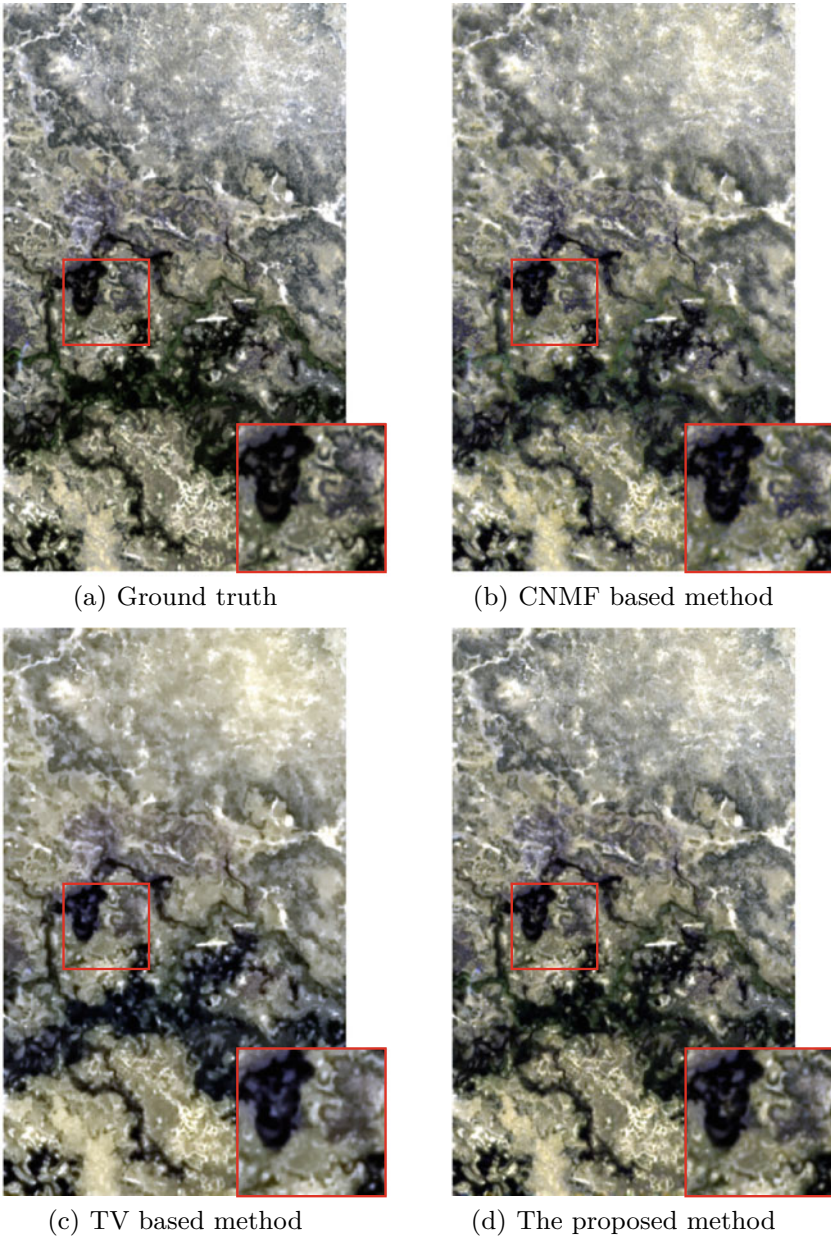


Fig. 1 Visual fusion results of hyperspectral and multispectral image fusion on *Botswana* dataset. Color image composites of the bands (14, 20, and 2). **a** Ground truth; **b** CNMF-based method; **c** TV-based method; **d** The proposed method

achieves the best fusion performance. Especially, the results of the proposed method on *Botswana* and *Indian Pines* datasets are much better than the other three methods.

The visual results of all competing methods are presented in Fig. 1. The outcome of CNMF-based method is presented in Fig. 1b. The comparison result of TV-based method is provided in Fig. 1c. The details of our method are shown in Fig. 1d. As for the absent of LTRR-based method, it is because there is little difference between LTRR-based method and CNMF-based method according to the results of three indicators in Table 1. After comparing the visual results of the three methods with the ground truth in Fig. 1a, it is found that the proposed method has a better reproduction of texture details and the color fits the ground truth better than the others. It can be seen that the proposed method can give good fused results.

5 Conclusion

In this study, a novel hyperspectral and multispectral image fusion method with non-local structure tensor regularization is proposed. The proposed method utilizes the non-local image self-similarity properties and performs on the domain of non-local gradient. An efficient optimization method is proposed to solve the resulting problem with the framework of ADMM. Extensive experiments were performed on a number of hyperspectral image datasets. The experimental results indicate that the proposed method outperforms several state-of-the-arts fusion methods.

References

1. Reed JM, Hutchinson S (1996) Image fusion and subpixel parameter estimation for automated optical inspection of electronic components. *IEEE Trans Indust Electron* 43(3):346–354
2. Luo RC, Lai CC (2014) Multisensor fusion-based concurrent environment mapping and moving object detection for intelligent service robotics. *IEEE Trans Indust Electron* 61(8):4043–4051
3. Huang S, Chen B (2014) Automatic moving object extraction through a real-world variable-bandwidth network for traffic monitoring systems. *IEEE Trans Indust Electron* 61(4):2099–2112
4. Rezaee H, Abdollahi F (2014) A decentralized cooperative control scheme with obstacle avoidance for a team of mobile robots. *IEEE Trans Indust Electron* 61(1):347–354
5. Leung H, Mukhopadhyay SC (2015) *Intelligent environmental sensing*, vol 13. Springer
6. Ko S, Yu S, Kang W, Park C, Lee S, Paik J (2017) Artifact-free low-light video enhancement using temporal similarity and guide map. *IEEE Trans Indust Electron* 64(8):6392–6401
7. Pan H, Jing Z, Liu R, Jin B (2012) Simultaneous spatial-temporal image fusion using kalman filtered compressed sensing. *Opt Eng* 51(5):057005
8. Zhongliang J, Han P, Yuankai L, Peng D (2018) *Non-cooperative target tracking. Fusion and control - algorithms and advances*. Springer International Publishing, Berlin
9. Dong W, Fu F, Shi G, Cao X, Wu J, Li G, Li X (2016) Hyperspectral image super-resolution via non-negative structured sparse representation. *IEEE Trans Image Process* 25(5):2337–2352

10. Kunkel B, Blechinger F, Lutz R, Doerffer R, van der Piepen H, Schroder M (1988) Rosis (reflective optics system imaging spectrometer)-a candidate instrument for polar platform missions. In: *Optoelectronic technologies for remote sensing from space*, vol 868. International Society for Optics and Photonics, pp 134–142
11. Vogel CR (2011) *Computational methods for inverse problems*. Society for Industrial and Applied Mathematics
12. Akhtar N, Shafait F, Mian A (2015) Bayesian sparse representation for hyperspectral image super resolution. In: *2015 IEEE conference on computer vision and pattern recognition (CVPR)*, June 2015, pp 3631–3640
13. Wei Q, Bioucas-Dias J, Dobigeon N, Tournet J (2015) Hyperspectral and multispectral image fusion based on a sparse representation. *IEEE Trans Geosci Remote Sens* 53(7):3658–3668
14. Simões M, Bioucas-Dias J, Almeida LB, Chanussot J (2015) A convex formulation for hyperspectral image superresolution via subspace-based regularization. *IEEE Trans Geosci Remote Sens* 53(6):3373–3388
15. Kawakami R, Wright J, Tai Y-W, Matsushita Y, Ben-Ezra M, Ikeuchi K (2011) High-resolution hyperspectral imaging via matrix factorization. In: *IEEE conference on computer vision and pattern recognition (CVPR)*, Jun 2011, pp 2329–2336
16. Yokoya N, Yairi T, Iwasaki A (2012) Coupled nonnegative matrix factorization unmixing for hyperspectral and multispectral data fusion. *IEEE Trans Geosci Remote Sens* 50(2):528–537
17. Lefkimiatis S, Osher S (2015) Nonlocal structure tensor functionals for image regularization. *IEEE Trans Comput Imag* 1(1):16–29
18. Keshava N, Mustard JF (2002) Spectral unmixing. *IEEE Signal Process Mag* 19(1):44–57
19. Li J, Liu H, He J, Yang P (2018) Application of non-local mean filtering in real head mr image*. In: *Australian New Zealand control conference (ANZCC) 2018*, pp 330–333
20. Boyd S, Parikh N, Chu E, Peleato B, Eckstein J (2011) Distributed optimization and statistical learning via the alternating direction method of multipliers. *Now foundations and trends*
21. Combettes PL, Wajs VR (2005) Signal recovery by proximal forward-backward splitting. *Multiscale Model Simul* 4(4):1168–1200. <https://doi.org/10.1137/050626090>
22. Wald L (2000) Quality of high resolution synthesised images: is there a simple criterion? In: *Third conference fusion of earth data: merging point measurements, raster maps and remotely sensed images*. SEE/URISCA (2000), pp 99–103
23. Wang Z, Bovik AC (2002) A universal image quality index. *IEEE Signal Process Lett* 9(3):81–84
24. Dian R, Li S, Fang L (2019) Learning a low tensor-train rank representation for hyperspectral image super-resolution. *IEEE Trans Neural Netw Learn Syst* 30(9):2672–2683

Using an Interpolation Model of the Gravitational Potential for High-Precision Ballistic Calculations



A. A. Kuznetsov, I. I. Fukin, S. M. Bazov, and N. A. Zavalova

Abstract This article provides a study on the feasibility of applying gravitational potential interpolation for high-precision ballistic calculations.

Keywords Interpolation · Ballistics · High-performance computing

1 Annotation

The paper is devoted to the implementation of a high-precision integrator of the spacecraft ballistic motion, taking into account the impact of gravitational potential, the computation of which is accelerated by means of cubic spline interpolation. The contribution of error of the interpolation model to the numerical computations of the spacecraft motion in low-Earth orbits is also analyzed.

2 Introduction

As is well known, the problem of the motion of the center of mass of a body with mass m is a Cauchy problem for the first-order equation:

$$\frac{d\vec{y}}{dt} = f(t, \vec{y}), \quad y(t_0) = y_0$$

The unknown vector function is a vector of coordinates and velocities, and the right part is a vector of velocities and accelerations:

A. A. Kuznetsov (✉) · I. I. Fukin · S. M. Bazov · N. A. Zavalova
Moscow Institute of Physics and Technology, Dolgoprudny, Russia
e-mail: kuznetsov.aa@mipt.ru

I. I. Fukin
e-mail: fukin.ii@mipt.ru

$$\vec{y} = (\vec{r}, \vec{v})^T, \quad \vec{f} = (\vec{v}, 1/m\vec{F})^T$$

Among the forces acting on a spacecraft, we can distinguish the gravitational force of the Earth, the potential of which in a spherical ECEF system can be written as [1]:

$$V(r, \varphi, \lambda) = \frac{GM}{r} \sum_{n=0}^N \left(\frac{a}{r}\right)^n \sum_{m=0}^n [C_{n,m} \cos(m\lambda) + S_{n,m}(m\lambda)] P_{n,m}(\sin(\varphi))$$

The minus sign is omitted here for convenience. The gravitational force is calculated by the formula:

$$\vec{F} = m\nabla V$$

Here, GM and a are the gravitational parameter and the equatorial radius of the Earth, the numbers $C_{n,m}$ и $S_{n,m}$ are the series coefficients (the model parameters), and $P_{n,m}(t)$ are the associated Legendre polynomials. The number N is the order of the gravitational potential, which determines the accuracy of its calculation and as a result the force acting on the spacecraft. In modern models, the maximum order of gravity potential reaches 360 (EGM96) and 2190 (EGM2008 and EGM2020). The algorithms for calculating the gravitational force proposed in [1] or [2], due to recurrent formulas, reduce asymptotic complexity to $O(N^2)$ (Fig. 1).

Figure 2 shows the daily error of the ballistic calculation, depending on the order of the potential N . Forecast obtained by taking into account 256 terms of the first

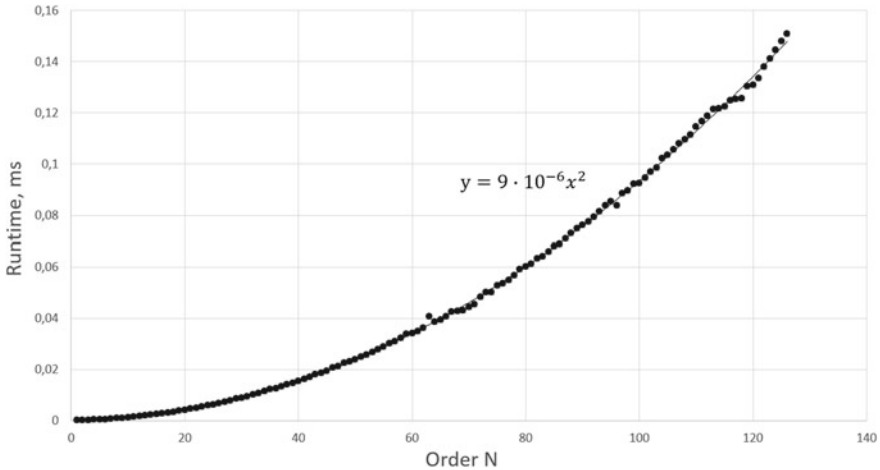


Fig. 1 Dependence of the calculation time of the gravitational force on the gravitational potential of the order N

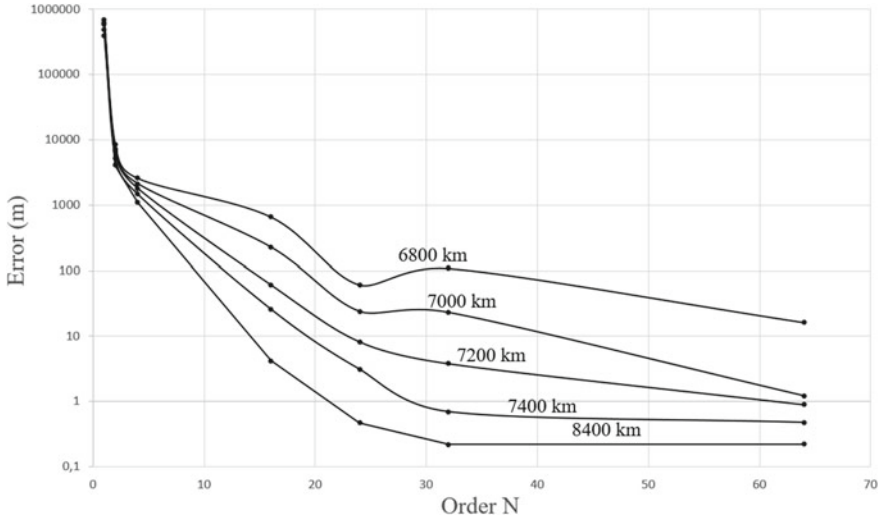


Fig. 2 Daily error in determining the position of the device depending on the order of gravitational potential for different heights

sum of the expansion (1) was taken as a standard. The integration was performed using the Everhart-15 method. The numerical integration error did not exceed 1 m.

It can be seen that for the ballistic prediction of low-orbit spacecraft with a daily accuracy of less than 10–3 m, it is necessary to use the gravitational potential with an order more than 64. This fact greatly increases the computational complexity of ballistic algorithms and leads to the idea of interpolating the potential to speed up calculations.

3 Derivatives of the Gravitational Potential

For further discussion, we will use the uniform representation of the gravitational potential [2]. To do this, we will introduce new variables r, s, t and u as follows:

$$\vec{r} = r(s, t, u)^T$$

$$r = |\vec{r}|$$

If we define functions:

$$r_m(s, t) = \text{Re}(s + it)^m$$

$$i_m(s, t) = \text{Im}(s + it)^m$$

then the gravitational potential can be written as:

$$V(r, s, t, u) = \frac{GM}{r} \sum_{n=0}^N \left(\frac{a}{r}\right)^n \sum_{m=1}^n [C_{n,m} r_m(s, t) + S_{n,m} i_m(s, t)] P_{n,m}(u)$$

Using functions:

$$\begin{aligned} D_{n,m}(s, t) &= C_{n,m} r_m(s, t) + S_{n,m} i_m(s, t) \\ E_{n,m}(s, t) &= C_{n,m} r_{m-1}(s, t) + S_{n,m} i_{m-1}(s, t) \\ F_{n,m}(s, t) &= S_{n,m} r_{m-1}(s, t) - C_{n,m} i_{m-1}(s, t) \\ G_{n,m}(s, t) &= C_{n,m} r_{m-2}(s, t) + S_{n,m} i_{m-2}(s, t) \\ H_{n,m}(s, t) &= S_{n,m} r_{m-2}(s, t) - C_{n,m} i_{m-2}(s, t) \end{aligned}$$

and notation:

$$\rho_0 = \frac{GM}{r}, \quad \rho_1 = \frac{a}{r} \rho_0, \quad \rho_n = \frac{a}{r} \rho_{n-1}$$

It is possible to determine the gravitational potential:

$$V(r, s, t, u) = \sum_{n=0}^N \rho_n \sum_{m=0}^n P_{n,m}(u) D_{n,m}(s, t),$$

its gradient:

$$\vec{F} = m(a_1 + a_4s)\vec{i} + m(a_2 + a_4t)\vec{j} + m(a_3 + a_4u)\vec{k} \tag{1}$$

$$\begin{aligned} a_1 &= \sum_{n=0}^N \frac{\rho_{n+1}}{a} \sum_{m=0}^n P_{n,m}(u) m E_{n,m} \\ a_2 &= \sum_{n=0}^N \frac{\rho_{n+1}}{a} \sum_{m=0}^n P_{n,m}(u) m F_{n,m} \\ a_3 &= \sum_{n=0}^N \frac{\rho_{n+1}}{a} \sum_{m=0}^n P_{n,m+1}(u) m D_{n,m} \\ a_4 &= - \sum_{n=0}^N \frac{\rho_{n+1}}{a} \sum_{m=0}^n P_{n+1,m+1} D_{n,m} \end{aligned}$$

and the Hess matrix using recurrent formulas also described in [2] and [3]. However, the first- and second-order derivatives are not sufficient for accurate interpolation. In this connection, the authors obtained an expression for the third mixed derivative:

$$\frac{\partial^3 V}{\partial x \partial y \partial z} = b_1 + b_2 + b_3 + b_4 + b_5$$

$$b_1 = \sum_{n=0}^N \frac{\rho_{n-3}}{a^3} \sum_{m=0}^n m(m-1)(m-n-1) P_{n,m}(u) H_{n,m}(s, t)$$

$$b_2 = st(1-u^2) \sum_{n=0}^N \frac{\rho_{n-3}}{a^3} \sum_{m=0}^n P_{n+2, m+3}(u)$$

$$b_3 = -stu \sum_{n=0}^N \frac{\rho_{n-3}}{a^3} \sum_{m=0}^n (n+m+5) P_{n+2, m+2}(u) D_{n,m}(s, t)$$

$$b_4 = s \sum_{n=0}^N \frac{\rho_{n-3}}{a^3} \sum_{m=0}^n m(n-m+1) P_{n+2, m+1}(u) F_{n,m}(s, t)$$

$$b_5 = t \sum_{n=0}^N \frac{\rho_{n-3}}{a^3} \sum_{m=0}^n m(n-m+1) P_{n+2, m+1}(u) E_{n,m}(s, t)$$

It is worth noting that the summands in the obtained sums can also be calculated recursively, which does not significantly increase the number of arithmetic operations of the algorithm.

4 Building an Interpolant

The gravitational potential was interpolated using a cubic three-dimensional spline having the third order of accuracy [4]. To construct it, an interpolation area was divided into cubes, in each of which a local spline of the form was constructed:

$$f(x, y, z) = \sum_{i,j,k=0}^3 a_{ijk} x^i y^j z^k$$

The definition of a local spline is to find 64 unknown coefficients a_{ijk} in each cube of the interpolation area. The solution to this problem is reduced to solving a system of linear algebraic equations with a nonsingular matrix of size 64 by 64. The matrix of the system is determined by dimensions of the cube in which the interpolation is performed, and the right part of the system is determined by the values of the functions

$$V, \frac{\partial V}{\partial x}, \frac{\partial V}{\partial y}, \frac{\partial V}{\partial z}, \frac{\partial^2 V}{\partial x \partial y}, \frac{\partial^2 V}{\partial x \partial z}, \frac{\partial^2 V}{\partial y \partial z}, \frac{\partial^3 V}{\partial x \partial y \partial z}$$

in the eight vertices of the cube.

The spline constructed in this way is a continuously differentiable function in the entire interpolated area. The force, in this case, can be determined using the formula:

$$\vec{F} = m \nabla V = m \vec{i} \sum_{n=1, l, r=0}^3 a_{nlr} n x^{n-1} y^l z^r + m \vec{j} \sum_{l=1, n, r=0}^3 a_{nlr} l x^n y^{l-1} z^r + m \vec{k} \sum_{r=1, n, l=0}^3 a_{nlr} r x^n y^l z^{r-1}$$

5 Results

To perform the interpolation, a set of meshes with a similar structure (hollow cubes) with a uniform partition in all three directions was constructed (Fig. 3).

The dependence of information weight of the interpolant on the grid size as expected was linear; namely, 1 million nodes of the interpolant occupied 1 GB of information.

Figure 4 shows the dependence of the interpolation error on the grid size in one direction. Since the cubic spline has a third order of accuracy, the error should decrease with the third order as the number of nodes increases in one direction. The resulting order of accuracy was 2.9, which is in good agreement with the theory.

When using the interpolant, a one-time calculation of the effective force ceases to depend on the order of the gravitational potential N, it only affects the time of

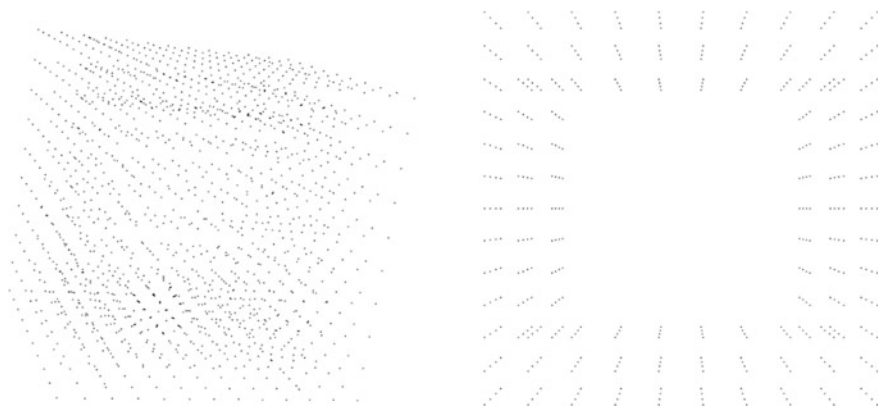


Fig. 3 View of the grid for the gravitational potential interpolation (left) and the view of this grid in the section (right)

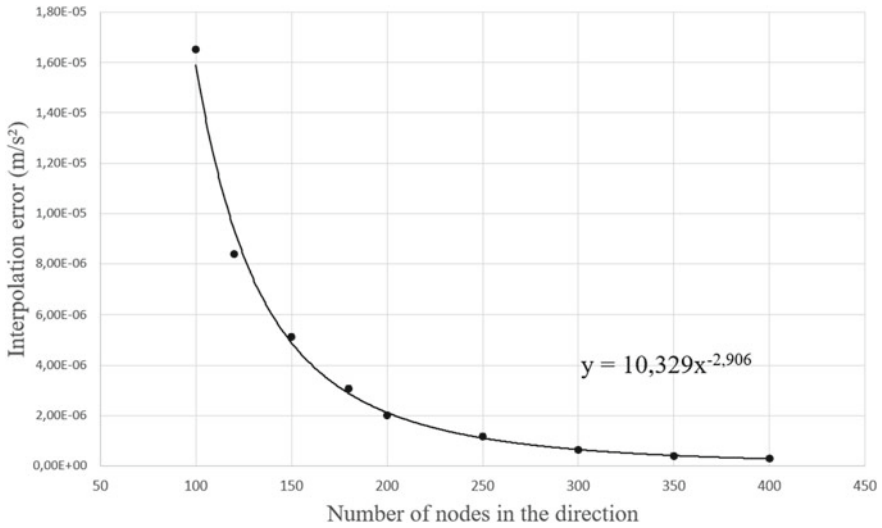


Fig. 4 Accuracy of the interpolation depending on the number of nodes in the direction

calculating the interpolation coefficients. In this regard, there is a significant acceleration of the calculation of the gravitational force. Figure 5 shows the ratio of the time taken to calculate the gravitational force using formula (1) and using the interpolation model. The graph shows that when calculating the force with an order of up to 100, the gain in execution time approaches three orders of magnitude.

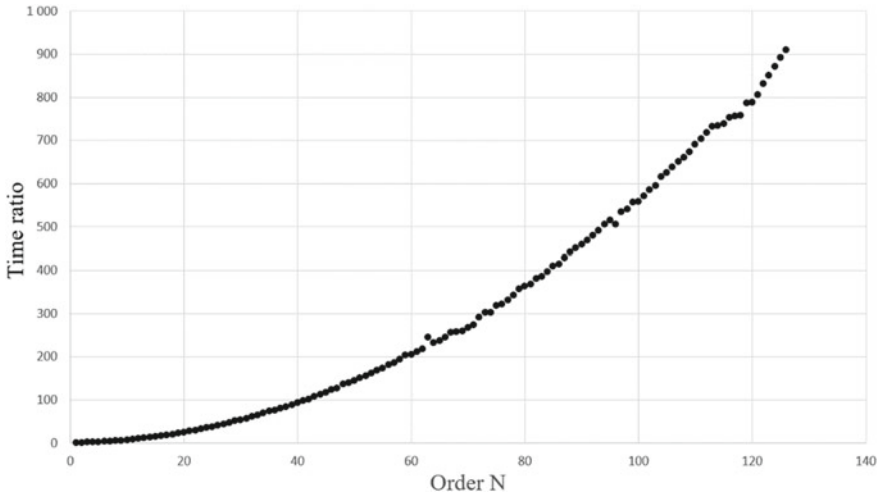


Fig. 5 The ratio of the times of the direct calculation of the gravitational force and the calculation using the interpolation model depending on the order of the potential N

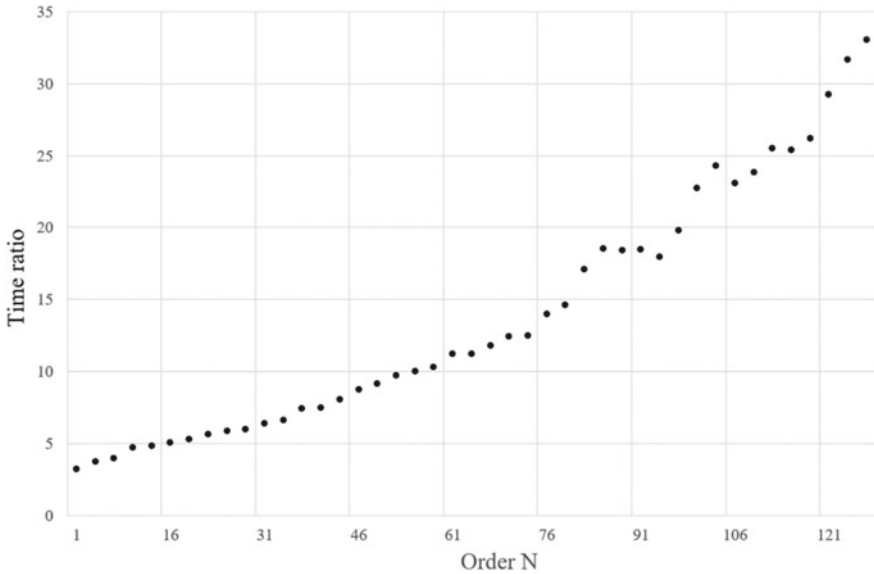


Fig. 6 The ratio of integration times of the equations of motion using the direct force calculation and using the interpolation model as a function of the order of potential N

When integrating the equations of motion, the most computationally expensive operation is to calculate forces acting on a spacecraft. Therefore, using an interpolation model, the time spent on integrating the motion is also significantly reduced. Figure 6 shows the ratio of integration times using a direct and an interpolation model. In this case, the resulting gain is less significant, but it reaches one or two orders of magnitude.

When using an interpolation model, it is important to investigate an issue related to the error that this model introduces in the integration of the equations of motion. For this purpose, calculations were made with an integration time of 1 day. The Everhart-15 method was used for the integration. The error of the method was no more than 10^{-3} m. The initial conditions were set randomly, the altitude of the orbit varied from 6800 to 7200 km, and the eccentricity was assumed to be zero. Other Keplerian parameters were distributed evenly over their domain of definition. Figure 7 shows the error associated with using the time-dependent interpolation model. The trajectory obtained by direct calculation of the force was chosen as the reference. The order N of the gravitational potential used was chosen to be 64. Grid size for the interpolation was $27 \cdot 10^6$, which corresponded to 27 GB of information. The vertical axis shows the maximum error for all calculations (the difference between the solution with the interpolation model and the direct force calculation), and the horizontal axis shows the flight time of the spacecraft.

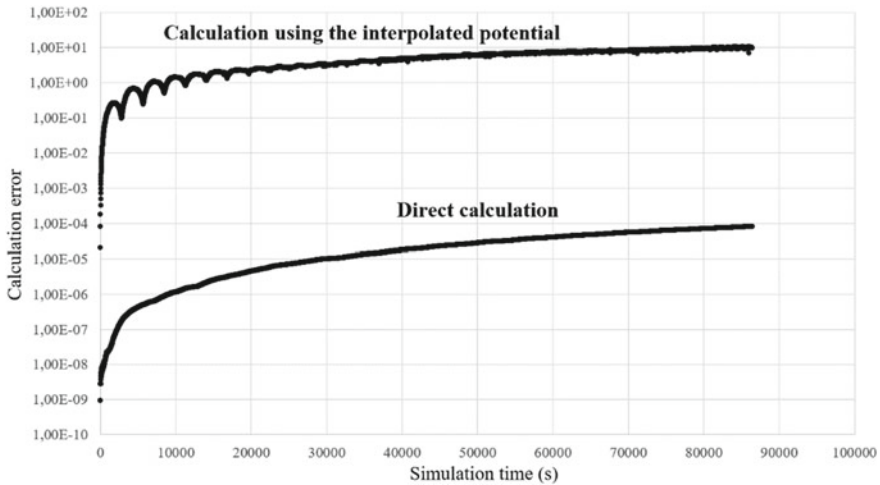


Fig. 7 Daily position error caused by the integration method and by the use of interpolation model

6 Conclusion

In this paper, an interpolation model of the gravitational potential used to accelerate ballistic calculations was constructed. It was shown that acceleration in the calculation of gravitational force at a large value of the order of gravitational potential can reach three orders of magnitude, and the acceleration of the integration of the equations of motion—one or two orders of magnitude. At the same time, the dependence of error for motion in low-Earth orbits associated with the use of the interpolation model was determined by numerical calculations.

Acknowledgements The work was supported by the Foundation for Advanced Studies in the framework of the project “Integral-D”.

References

1. Petit G, Luzum B (2010) IERS conventions (2010). In: Bureau international des Poids et mesures sevres (France) (2010)
2. Pines S (1973) Uniform representation of the gravitational potential and its derivatives. *AIAA J* 11(11):1508–1511
3. Lundberg JB, Schutz BE (1988) Recursion formulas of legendre functions for use with nonsingular geopotential models. *J Guid Control Dyn* 11(1):31–38
4. Lekien F, Marsden J (2005) Tricubic interpolation in three dimensions. *Int J Numer Methods Eng* 63(3):455–471

Distributed Cooperative Guidance Law with Both Impact Time and Angle Control



Ye Chen, Shufan Wu, Hongxu Zhu, Xiaoliang Wang, Quan Li, and Jun Jia

Abstract Aiming at the problem of how to control the impact time and angle of missile simultaneously in multi-missile cooperation to achieve a saturated attack on a target, a distributed cooperative guidance law was proposed based on the leader–follower model. Firstly, the guidance geometry and the relative motion equations were established. Secondly, the cooperative guidance strategy of PNG and distributed cooperative guidance was adopted based on the consensus algorithm. The modified component of PNG and tangential acceleration were derived to control the impact time and angle of the missile cluster. Finally, simulation results demonstrate the effectiveness of the designed method. The guidance law has the merits of no center node, applicable to missiles with unsteady velocity, concise analytical expression, and low communication cost.

Keywords Leader–follower · Cooperative guidance · Angle constraint · Consensus algorithm

1 Introduction

With the enhancement of the modern battlefield defense system and the increasing number of hostile targets, the penetration and strike ability of one single missile have been severely challenged, and it cannot meet some complex needs. Therefore, multi-missile cooperative guidance has gradually become a research hotspot. By cooperating with each other, multiple missiles can format with different terminal impact angles which could achieve saturation attack on a target.

Y. Chen · S. Wu (✉) · H. Zhu · X. Wang
Shanghai Jiao Tong University, Shanghai, China
e-mail: shufan.wu@sjtu.edu.cn

Q. Li · J. Jia
Institute of Shanghai Electro-Mechanical Engineering, Shanghai, China

The communication between missiles is the key to closed-loop cooperative guidance [1]. The communication topology between missiles can usually be divided into centralized and distributed. Centralized communication means that one or more missiles in the missile cluster can communicate with all missiles. The estimated value of time-to-go of each missile is given to the missile with global communication [2], and the maximum value is taken as the time-to-go of the missile cluster so as to achieve time coordination. Distributed communication means that each missile can only communicate with a number of missiles adjacent to it. Sun and Xia [3] proposed a networked distributed cooperative guidance method based on graph theory. On the basis of [3], the adaptive variable coefficient was designed, which has a simpler form [4]. The centralized communication topology has high communication cost and poor robustness, and the distributed one has less communication volume and strong anti-jamming ability, and the latter performs better than the other. In view of the existing literatures, most of them only consider time coordination [5–14], and few studies control the impact time and angle simultaneously. Therefore, it is of great significance to design the distributed impact time and angle cooperative guidance law.

At the same time, cooperative guidance architecture is also an important concept in the design of cooperative guidance law. Zhao et al. [15] first proposed a two-layer cooperative guidance architecture applicable to the two communication topologies. The bottom guidance control adopted the bias proportional guidance law with a time constraint, and the upper coordination control selected the time-to-go as the coordination variable among missiles. On this basis, by designing different bottom guidance laws and coordination variables, multi-missile cooperative guidance can be realized with different requirements. Zhang et al. [16] first applied the formation control of leader–follower to the multi-missile cooperative guidance and proposed the leader–follower cooperative guidance architecture. The idea is to achieve the consistency of some state variables of the follower and the leader by designing the cooperative guidance component. But in the studies based on the above architectures, few consider angle constraint. Therefore, it is also of great significance to design the time and angle cooperative guidance law based on some kind of cooperative guidance architecture.

In this paper, a novel cooperative guidance law is proposed with impact angle constraint. It consists of two parts: the first has the form of proportional navigation guidance law, which guarantees missiles hit the target, and the second is distributed cooperative strategy, which achieves multi-missile simultaneous arrival with desired impact angle. The devised guidance law possesses the following attractive features:

- (1) The proposed guidance law has a concise analytical expression, which is convenient for application.
- (2) The proposed guidance law adopts the consensus algorithm which has a fast convergence rate.
- (3) The proposed guidance law does not need the estimation of time-to-go, which makes the guidance precision higher.

2 Problem Formulation

This section first presents the communication topology of missiles and then establishes a missile-target engagement model.

Consider a scenario in which four missiles intercept a target cooperatively. The communication topology is distributed. Four missiles are denoted as M_0, M_1, M_2, M_3 . The information interaction mode between each missile is shown in Fig. 1.

As it can be seen from the figure, adjacent two-way communication is adopted between missiles. It has the merits of little communication and strong robustness.

The engagement geometry between missiles and targets is shown in Fig. 2. The target is stationary.

The relative motion equations between missile $M_i(i = 0, 1, 2,3)$ and target are as follows:

Fig. 1 Multi-missile distributed communication network

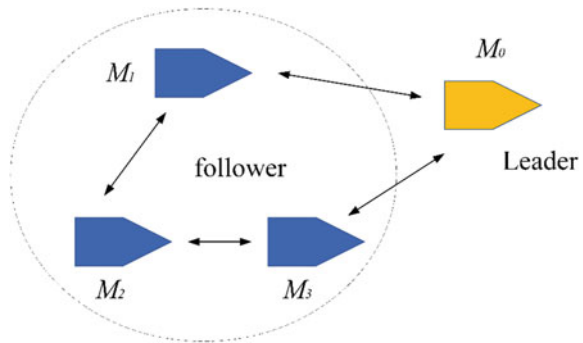
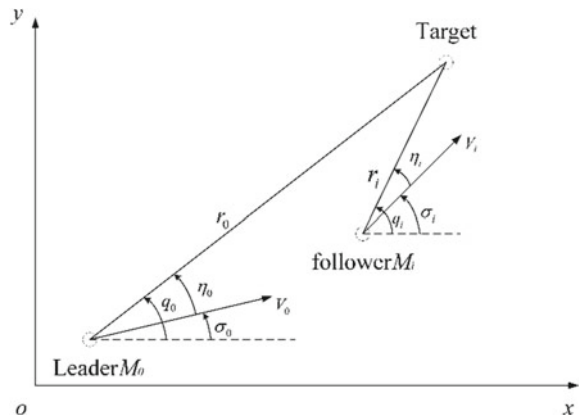


Fig. 2 Relative motion model of missiles and targets



$$\begin{aligned}
\dot{r}_i &= -V_i \cos \eta_i \\
r_i \dot{q}_i &= V_i \sin \eta_i \\
q_i &= \sigma_i + \eta_i \\
\dot{\sigma}_i &= a_i / V_i \\
\dot{V}_i &= a_{ip}
\end{aligned} \tag{1}$$

in which V_i is the speed of M_i ; a_i and a_{ip} are the normal acceleration and tangential acceleration of M_i , respectively. r_i and q_i are the relative distance and line-of-sight angle between M_i and target, σ_i is the heading angle of M_i and η_i is the leading angle.

3 Proposed Cooperative Guidance Law

3.1 General Analysis

M_i adopts the cooperative guidance strategy combining PNG and distributed cooperative guidance, which can be defined as

$$a_i = N_i V_i \dot{q}_i + a_{i2} \tag{2}$$

where the former term is the acceleration expression of PNG, a_{i2} is the distributed cooperative guidance command used to coordinate the state of each missile.

Substituting formula (2) into formula (1), we obtain

$$\begin{cases} \dot{r}_i = -V_i \cos \eta_i \\ \dot{\eta}_i = (1 - N_i) \frac{V_i \sin \eta_i}{r_i} - \frac{a_{i2}}{V_i} \\ \dot{q}_i = \frac{V_i \sin \eta_i}{r_i} \\ \dot{V}_i = a_{ip} \end{cases} \tag{3}$$

The state-space form of the above equation is

$$\begin{bmatrix} \dot{r}_i \\ \dot{\eta}_i \\ \dot{q}_i \\ \dot{V}_i \end{bmatrix} = \begin{bmatrix} -V_i \cos \eta_i \\ (1 - N_i) \frac{V_i \sin \eta_i}{r_i} \\ \frac{V_i \sin \eta_i}{r_i} \\ 0 \end{bmatrix} + \begin{bmatrix} 0 & 0 \\ -\frac{1}{V_i} & 0 \\ 0 & 0 \\ 0 & 0 \end{bmatrix} \begin{bmatrix} a_{i2} \\ a_{ip} \end{bmatrix} \tag{4}$$

Letting $x_i = [r_i \ \eta_i \ q_i \ V_i]^T$, $u_i = [a_{i2} \ a_{ip}]^T$, the relative motion equation of M_i ($i = 0, 1, 2, 3$) and target can be simplified as

$$\dot{x}_i = f(x_i) + g_i u_i \tag{5}$$

where f and g_i are determined by the formula (4).

For the problem of multi-missile cooperative attack, if $r_i = r_j$, $\eta_i = \eta_j$ or $r_i = r_j$, $\eta_i = -\eta_j$ can be guaranteed at the end of guidance, then multiple missiles can hit the target simultaneously [17]. On this basis, this paper further achieves the coordination of impact angles, which requires each missile to hit the target at different angles. That is, $q_i = q_j + \Delta q_{ij}$, where Δq_{ij} is the deviation of the expected impact angle between M_i and M_j . Then the problem is transformed into a distributed consensus algorithm design problem.

3.2 Distributed Cooperative Guidance Law

For convenience, define $\xi_{1i} = r_i$, $\xi_{2i} = \dot{r}_i$, $\xi_{3i} = q_i$, $\xi_{4i} = \dot{q}_i$ and derivate ξ_{2i} and ξ_{4i} , so we obtain

$$\begin{cases} \dot{\xi}_{2i} = \ddot{r}_i = -a_{ip} \cos \eta_i + V_i \sin \eta_i \cdot \dot{\eta}_i = \\ \frac{V_i^2 \sin^2 \eta_i (1 - N_i)}{r_i^2} - a_{ip} \cos \eta_i - a_{i2} \sin \eta_i \\ \dot{\xi}_{4i} = \ddot{q}_i = \frac{r_i}{r_i} \dot{V}_i + \frac{V_i \cos \eta_i}{r_i} \dot{\eta}_i - \frac{V_i \sin \eta_i}{r_i^2} \dot{r}_i = \\ \frac{V_i^2 \sin \eta_i \cos \eta_i (2 - N_i)}{r_i^2} + \frac{\sin \eta_i}{r_i} a_{ip} - \frac{\cos \eta_i}{r_i} a_{i2} \end{cases} \tag{6}$$

The state-space form of formula (6) can be rewritten as

$$\begin{bmatrix} \dot{\xi}_{2i} \\ \dot{\xi}_{4i} \end{bmatrix} = \begin{bmatrix} \frac{V_i^2 \sin \eta_i (1 - N_i)}{r_i} \\ \frac{V_i^2 \sin \eta_i \cos \eta_i (2 - N_i)}{r_i^2} \end{bmatrix} + \begin{bmatrix} -\cos \eta_i & -\sin \eta_i \\ \frac{\sin \eta_i}{r_i} & -\frac{\cos \eta_i}{r_i} \end{bmatrix} \begin{bmatrix} a_{ip} \\ a_{i2} \end{bmatrix} \tag{7}$$

The equation above is a nonlinear system, using the control command below to transform it into a linear system.

$$\begin{bmatrix} a_{ip} \\ a_{i2} \end{bmatrix} = \begin{bmatrix} -\cos \eta_i & -\sin \eta_i \\ \frac{\sin \eta_i}{r_i} & -\frac{\cos \eta_i}{r_i} \end{bmatrix}^{-1} \left\{ \begin{bmatrix} v_{i1} \\ v_{i2} \end{bmatrix} - \begin{bmatrix} \frac{V_i^2 \sin^2 \eta_i (1 - N_i)}{r_i} \\ \frac{V_i^2 \sin \eta_i \cos \eta_i (2 - N_i)}{r_i^2} \end{bmatrix} \right\} \tag{8}$$

where v_{i1} and v_{i2} are equivalent inputs.

For $\xi_{1i} = r_i$, $\xi_{3i} = q_i$, the regular expressions can be obtained as

$$\begin{cases} \dot{\xi}_{1i} = \xi_{2i} \\ \dot{\xi}_{2i} = v_{i1} \\ \dot{\xi}_{3i} = \xi_{4i} \\ \dot{\xi}_{4i} = v_{i2} \end{cases} \tag{9}$$

In summary, by designing the transformation formula (8), the problem of using the original control inputs a_{ip} and a_{i2} to stabilize the nonlinear system (7) has been transformed into the problem of using the new control inputs v_{i1} and v_{i2} to stabilize the linear system (9).

Letting $x_i = [\xi_{1i} \ \xi_{2i} \ \xi_{3i} \ \xi_{4i}]^T$, $u_i = [v_{i1} \ v_{i2}]^T$, the state-space form of formula (9) is

$$\dot{x}_i = Ax_i + Bu_i \tag{10}$$

where $A = \begin{bmatrix} 0 & 1 & 0 & 0 \\ 0 & 0 & 0 & 0 \\ 0 & 0 & 0 & 1 \\ 0 & 0 & 0 & 0 \end{bmatrix}$, $B = \begin{bmatrix} 0 & 0 \\ 1 & 0 \\ 0 & 0 \\ 0 & 1 \end{bmatrix}$.

From formula (10), the distributed cooperative guidance strategy is designed as follows:

$$u_i = -K_2 \sum_{j \in \Omega_i} \alpha_{ij} (x_i - x_j) \tag{11}$$

where α_{ij} is the term of the adjacency matrix, Ω_i is the neighbor set of M_i , and K_2 is the gain matrix.

Under this strategy, the multi-missile system can be rewritten in the following matrix form:

$$\dot{x} = (I_N \otimes A - L \otimes BK_2)x \tag{12}$$

where $x = [x_1^T \ x_2^T \ x_3^T \ \dots \ x_N^T]^T$, L is a Laplace matrix under the directed action topology, and I_N is a unit matrix of $N \times N$.

In the process of multi-missile cooperative guidance, each missile adds distributed cooperative guidance command on the basis of PNG. In this section, in order to coordinate the impact time and angle of the multi-missile system, each missile needs to adjust the axial flight speed and direction at the same time. In other words, the control command includes both tangential acceleration a_{ip} and normal acceleration a_i .

Substitute formula (11) into formula (8), then we obtain

$$\begin{aligned} \begin{bmatrix} a_{ip} \\ a_{i2} \end{bmatrix} &= \begin{bmatrix} -\cos \eta_i & -\sin \eta_i \\ \frac{\sin \eta_i}{r_i} & -\frac{\cos \eta_i}{r_i} \end{bmatrix}^{-1} \cdot \\ &\left\{ -K_2 \sum_{j \in \Omega} \alpha_{ij} \left(\begin{bmatrix} r_i \\ \dot{r}_j \\ q_i \\ \dot{q}_i \end{bmatrix} - \begin{bmatrix} r_j \\ \dot{r}_j \\ q_j \\ \dot{q}_j \end{bmatrix} \right) - \begin{bmatrix} \frac{V_i^2 \sin^2 \eta_i (1-N_i)}{r_i} \\ \frac{V_i^2 \sin \eta_i \cos \eta_i (2-N_i)}{r_i^2} \end{bmatrix} \right\} \end{aligned} \quad (13)$$

The equation above can finally achieve the consistency of the range-to-go and impact angle of M_i and M_j . In order to make a certain impact angle deviation between each missile, the impact angle deviation term Δq_{ij} (the desired impact angle deviation between M_i and M_j) is introduced, then the formula (13) can be rewritten as follows:

$$\begin{aligned} \begin{bmatrix} a_{ip} \\ a_{i2} \end{bmatrix} &= \begin{bmatrix} -\cos \eta_i & -\sin \eta_i \\ \frac{\sin \eta_i}{r_i} & -\frac{\cos \eta_i}{r_i} \end{bmatrix}^{-1} \cdot \\ &\left\{ -K_2 \sum_{j \in \Omega} \alpha_{ij} \left(\begin{bmatrix} r_i \\ \dot{r}_j \\ q_i \\ \dot{q}_i \end{bmatrix} - \begin{bmatrix} r_j \\ \dot{r}_j \\ q_j + \Delta q_{ij} \\ \dot{q}_j \end{bmatrix} \right) - \begin{bmatrix} \frac{V_i^2 \sin^2 \eta_i (1-N_i)}{r_i} \\ \frac{V_i^2 \sin \eta_i \cos \eta_i (2-N_i)}{r_i^2} \end{bmatrix} \right\} \end{aligned} \quad (14)$$

Note that the normal acceleration of the missile a_i can be obtained from formula (2), and the tangential acceleration a_{ip} and distributed cooperative guidance command a_{i2} can make the range-to-go and impact angle meet the requirements. The pure proportional navigation guidance law ensures that the missile can hit the target and the terminal leading angle is 0° . To avoid the missile cluster being far away from the target (the terminal leading angle is 180°), the leader M_0 is guided by PNG, and then the asymptotic consistent convergence of the follower state is realized by the formula (14), which can ensure the coordination of impact time and angle while hitting the target.

4 Simulation

Consider the following guidance scenario: the number of missile cluster is 4. The missile with the longest flight time under PNG is selected as the leader, which is marked as M_0 , and the other three followers are marked as M_i ($i = 0, 1, 2, 3$). According to the information of range-to-go, leading angle, LOS angle, and so on, the leader and the follower interact with each other under the given communication topology during the engagement. The target is stationary and the position is (20000, 500 m). The missile cluster is required to intercept the target simultaneously, and the absolute deviation of the impact angle between the adjacent missiles is expected to

Table 1 Initial conditions of missiles

Missiles	Initial position/m	Initial heading angle/°	Initial velocity/m · s ⁻¹
M0	(9000, 7000)	-20	240
M1	(12,000, -10,000)	80	280
M2	(32,000, -6000)	135	280
M3	(33,000, 6000)	-150	280

be 90°, that is, the terminal velocity direction of each missile is vertical or opposite. The proportional navigation coefficient of $M_i= (i = 0, 1, 2, 3)$ equals 5, and the initial conditions of each missile are shown in Table 1.

The PNG (guidance law 1), time cooperative guidance law [1] (guidance law 2), and the cooperative guidance law designed in this section (guidance law 3) are simulated, respectively, while the initial conditions of each missile remain unchanged, the flight trajectories of the missile cluster under different guidance laws are shown in Figs. 3, 4 and 5.

As can be seen from Figs. 3, 4 and 5, all the three guidance laws can achieve the missile cluster hitting the target accurately. Figure 3 shows that the trajectory of each missile is almost the straight line between the missile and the target under PNG, which is also the merit of PNG, that is, it can make the missile hit the target in the shortest time. Figure 4 shows that the trajectory of each missile is more curved under the time cooperative guidance law, which is due to the addition of time constraint, and the missile with short flight time is bent under the control command to achieve the same impact time as the missile with the long flight time. Figure 5 shows that the trajectory of each missile is the most curved under the guidance law proposed in this paper. On the one hand, the missile needs to bend around to achieve the same impact time; on the other hand, it needs to control the impact angle to meet the requirement.

Fig. 3 Missile trajectories under guidance law 1

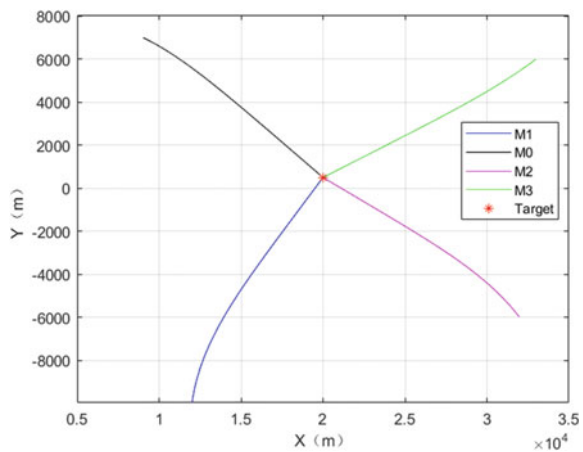


Fig. 4 Missile trajectories under guidance law 2

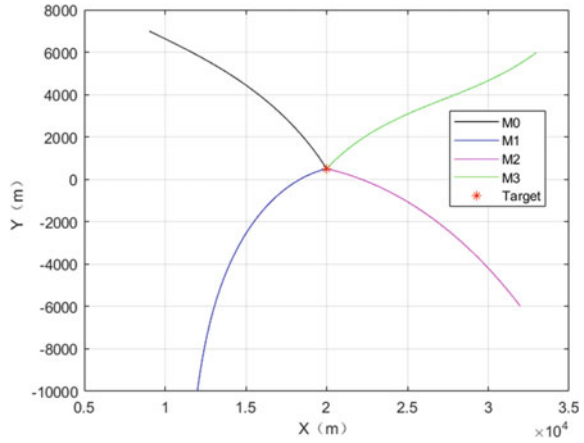
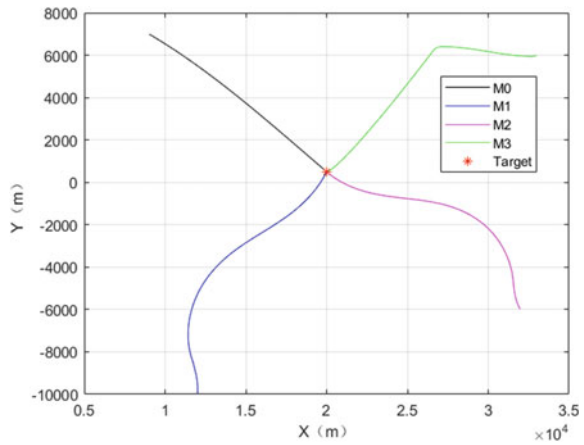


Fig. 5 Missile trajectories under guidance law 3



Analyze the impact time, impact angle, and corresponding errors of missiles in detail, and the results are shown in Tables 2, 3 and 4.

It can be seen from Table 2 that the impact time of each missile in the missile cluster is different under PNG, and the flight time of the leader M_0 is the longest, which is 53.3 s. Under the guidance law 2, the impact time can be effectively controlled and

Table 2 Comparison of impact time

Missiles	GL1/s	GL2/s	GL3/s
M0	53.3	54.8	53.3
M1	47.7	54.8	53.3
M2	48.9	54.8	53.3
M3	50.4	54.8	53.3

Table 3 Comparison of impact angle

Missiles	GL1/°	GL2/°	GL3/°
M0	-33.2	-50.3	-33.2
M1	45.5	10.5	56.9
M2	155.8	170.2	146.6
M3	-158.8	-140.5	-123.3

Table 4 Comparison of impact angle error and impact time error

Errors	Expected errors	GL1	GL2	GL3
$q_0 - q_1$	-90°	-78.7°	-60.8°	-90.1°
$q_0 - q_2$	-180°	-189°	-220.5°	-179.8°
$q_0 - q_3$	90°	125.6°	90.2°	90.1°
$t_0 - t_1$	0 s	5.6 s	0 s	0 s
$t_0 - t_2$	0 s	4.4 s	0 s	0 s
$t_0 - t_3$	0 s	2.9 s	0 s	0 s

is slightly longer than the flight time of M_0 under PNG. Under the guidance law 3, the impact time of each missile is the same and is equal to the flight time of M_0 under PNG, which verifies the effectiveness of the proposed method. Table 3 shows that the impact angle of the missile cluster is uncontrolled under guidance laws 1 and 2, and the terminal heading angles of each missile are irregular. Under the guidance law 3, the terminal heading angles of four missiles are -33.2° , 56.9° , 146.6° , and -123.3° , respectively, which meets the requirement that the terminal velocity direction of each missile is vertical or opposite. Table 4 shows the characteristics of three guidance laws more intuitively, PNG cannot control the impact time and angle, and there is a big deviation between the actual value and the expected value. The time cooperative guidance law can control the impact time, but the impact angle deviation is quite different from the expected value. The distributed cooperative guidance law shows good performance in both impact time and angle achievement.

Figures 6 and 7 give the variation of the heading angle and range-to-go of each missile.

As can be seen from Fig. 6, the heading angles of four missiles eventually converge to their expected values. Figure 7 shows that the range-to-go of all missiles decreases to zero at about 53.3 s. A large number of simulations verify the effectiveness of the distributed cooperative guidance law with impact angle constraint.

Fig. 6 Heading angle variations of missile cluster

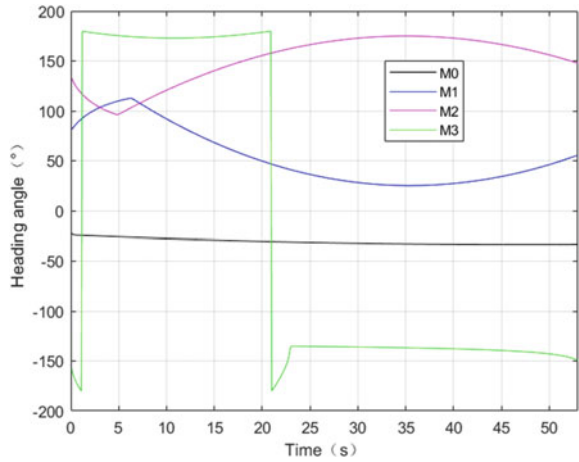
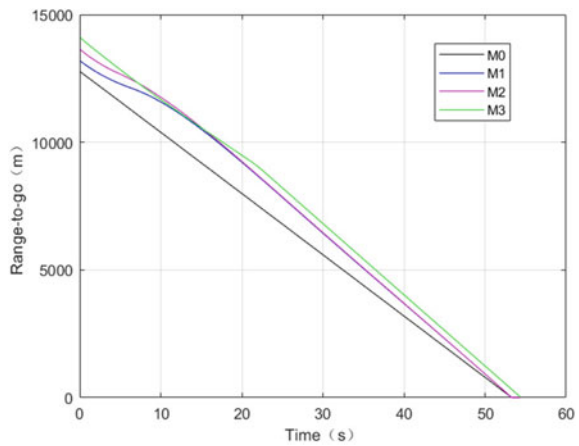


Fig. 7 Range-to-go of missile cluster



5 Conclusion

A distributed cooperative guidance law based on the leader–follower model is proposed in this paper, and the cooperative guidance strategy of PNG and distributed cooperative guidance are adopted. The modified component of pure proportional guidance and tangential acceleration are derived to control the impact time and angle of the missile cluster. Four missiles are simulated and analyzed to attack one target cooperatively. Two guidance laws, PNG and time cooperative guidance law, are compared to demonstrate the effectiveness of the proposed method. How to handle maneuvering targets and some other constraints is an important direction for future research.

Acknowledgments This work is partially supported by the Shanghai Academy of Spaceflight Technology Industry-University Research Cooperation Fund under Grant USCAST2020-8 & USCAST2020-20, and the Natural Science Fund of Shanghai under Grant 19ZR1426800.

References

1. Li K, Wang J, Lee CH et al (2020) Distributed cooperative guidance for multivehicle simultaneous arrival without numerical singularities. *J Guid Control Dyn* 43(7):1365–1373
2. Jeon IS, Lee JI, Tahk MJ (2006) Impact-time-control guidance law for anti-ship missiles. *IEEE Trans Control Syst Technol* 14(2):260–266
3. Sun X, Xia Y (2012) Optimal guidance law for cooperative attack of multiple missiles based on optimal control theory. *Int J Control* 85(8):1063–1070
4. Zou L, Ding QX, Zhou R (2010) Distributed cooperative guidance for multiple heterogeneous networked missiles. *J Univ Aeronaut Astronaut* 36(12):1432–1435 (in Chinese)
5. Zou L, Kong FE, Zhou R et al (2012) Distributed adaptive cooperative guidance for multi-missile salvo attack. *J Beijing Univ Aeronaut Astronaut* 38(1):128–132 (in Chinese)
6. Wang J, Zhang R (2018) Terminal guidance for a hypersonic vehicle with impact time control. *J Guid Control Dyn* 41(8):1790–1798
7. Enjiao Z, Chao T, Wang S et al. (2015) An adaptive parameter cooperative guidance law for multiple flight vehicles. In: *AIAA atmospheric flight mechanics conference*, vol 2709
8. Sun X, Zhou R, Hou D et al (2014) Consensus of leader-followers system of multi-missile with time-delays and switching topologies. *Optik* 125(3):1202–1208
9. Jeon IS, Lee JI, Tahk MJ (2010) Homing guidance law for cooperative attack of multiple missiles. *J Guid Control Dyn* 33(1):275–280
10. Zhao J, Yang S, Xiong F (2019) Cooperative guidance of seeker-less missile with two leaders. *Aerosp Sci Technol* 88:308–315
11. Wang Y, Dong S, Ou L et al (2014) Cooperative control of multi-missile systems. *IET Control Theory Appl* 9(3):441–446
12. Zhao J, Zhou R (2016) Obstacle avoidance for multi-missile network via distributed coordination algorithm. *Chin J Aeronaut* 29(2):441–447
13. Li G, Wu Y, Xu P (2018) Adaptive fault-tolerant cooperative guidance law for simultaneous arrival. *Aerosp Sci Technol* 82:243–251
14. Wang X, Zheng Y, Lin H (2015) Integrated guidance and control law for cooperative attack of multiple missiles. *Aerosp Sci Technol* 42:1–11
15. Zhang Y, Wang X, Wu H (2015) A distributed cooperative guidance law for salvo attack of multiple anti-ship missiles. *Chin J Aeronaut* 28(5):1438–1450
16. Zhao SY, Zhou R (2008) Multi-missile cooperative guidance using coordination variables. *Acta Aeronaut Astronaut Sin* 29(6):1605–1611 (in Chinese)
17. Zhang YA, Macxs GX, Wang XP (2009) Time-cooperative guidance for multi-missiles: A leader-follower strategy. *Acta Aeronaut Astronaut Sin* 30(6):1109–1118 (in Chinese)

Effects of Non-uniform Inlet Flow on the Flow Stability of a Transonic Compressor Rotor



Zetian Qiu, Yidan Li, and Xiaohua Liu

Abstract Progressing advance concerning acquiring higher pressure ratio in an aeroengine compressor has been achieved, which attracts much attention in recent years. Distortion at the flow entrance creates deterioration in the performance of aerodynamics and thermodynamics in transonic compressors, which usually leads to unsteady flow phenomena such as surge and rotating stall. This paper focuses on the investigation of the non-uniform inlet flow field in the tip and hub region of a compressor rotor blade, and radial pressure distortion is paid main attention in this work. The results show that non-uniform flow entrance condition causes deteriorator impacts on the stability of the axial flow compressor. Furthermore, hub radial pressure distortion alleviates the occurrence of unsteady phenomena presented by smaller surge flow rate than clean flow entrance condition.

Keywords Inlet distortion · Aeroengine compressor · Compressor stability

Z. Qiu · X. Liu (✉)
Shanghai Jiao Tong University, Shanghai, China
e-mail: Xiaohua-Liu@sjtu.edu.cn

Z. Qiu
e-mail: qzerty_95@sjtu.edu.cn

Y. Li
AECC Commercial Aircraft Engine Co, Ltd, Shanghai, China
e-mail: yidanli@sjtu.edu.cn

X. Liu
Key Laboratory (Fluid Machinery and Engineering Research Base) of Sichua-N Province, Chengdu, China

1 Introduction

The development of transonic aeroengine compressors has achieved significant advancement, especially with the progress of non-intrusive measurement techniques and computational fluid dynamics. To acquire much superior performance of aerodynamics and thermodynamics, the stability of air-breathing propulsion system is an unavoidable question for the pursuing researchers. Different from design condition, the non-uniform flow entrance condition is frequently occurring in the flight of both commercial and military aircraft, which gradually emerges from unperceived problems in recent decades, because the performance of the compressor weighs high on the inlet condition. The distorted flow could happen in enormous condition, caused by the flow separation at a large angle of attack at the inlet lip when aircraft takes off, inhaled ground vortex, and the dramatic growth of the boundary layer under adverse pressure gradient conditions [1].

Various analytic researches have devoted themselves to the effect of distorted inlet flow condition in a transonic compressor. Hah et al. [2] paid main attention to the effects of circumferential distortions in inlet total pressure on the flow field, describing the principle of interactions between the unsteady passage shock and the boundary layer of the blade. Spakovszky et al. [3] first attempted active feedback control experimentally to control rotating stall in a single-stage transonic axial compressor with inlet distortion. Some researchers have tried the model study method to investigate inlet distortion. Ferrand et al. [4] illustrated a method to evaluate single and multistage compressors' response to steady and unsteady inlet distortions. This work was also able to evaluate the appearance of unstable regimes and their characterization. Yao et al. [5] established a numerical simulation procedure to analyze the total pressure distortion transfer and the total temperature distortion generation. Xu et al. [6] established a stall inception prediction model to predict the stall limit under radial inlet distortions.

This paper focuses on the investigation of the non-uniform inlet flow field in the tip and hub region of a compressor rotor blade, and radial pressure distortion is paid main attention in this work.

2 Computational Simulation Setup

2.1 Target Rotor

The transonic compressor NASA Rotor 37(R37) is composed of 36 blades with a tip clearance of 0.356 mm. It was used as a 'blind' test case for turbomachinery CFD by the Turbomachinery Committee of the IGTI. Table 1 has shown other main design specifications of the following considered axial compressor rotor. Suder et al. [7] have conducted a detailed experimental test about this isolated rotor from which the experimental measurement positions are shown in Fig. 1. The experimental statistics this paper used were undertaken for stations 1 and 4 [8].

Table 1 Main design parameters of R37 [9]

Parameters	Value
Blade number	36
Hub-tip ratio	0.7
Aspect ratio	1.19
Tip solidity	1.29
Tip clearance (mm)	0.356
Design speed (r/min)	17,188
Tip speed (m/s)	454.14
Total pressure ratio	2.106
Adiabatic efficiency	0.877
Mass flow rate of design point (kg/s)	20.19
Mass flow rate of chock point (kg/s)	20.93

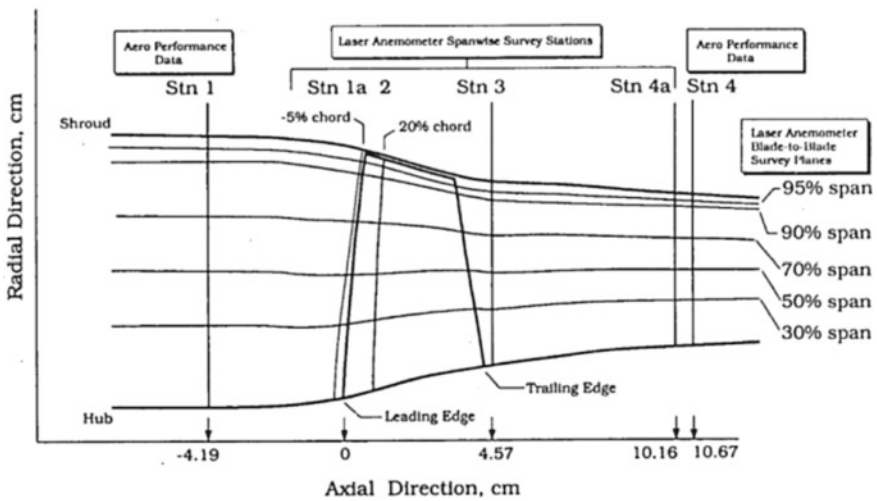


Fig. 1 Positions of measurement station [10]

2.2 Grid Independence Verification

CFX software in this research is chosen to generate high-quality meshes and obtain the CFD solution for the steady-state case for the transonic rotor. The development of the grid has significant importance for the CFD solution as it affects the solution values. Also, CFX software including module TurboGrid, CFX-Pre, and CFX-Solver Manager is recognized for its outstanding accuracy, robustness, and speed when simulating turbomachinery, such as pumps, fans, compressors, and gas and hydraulic turbines.

In order to study solution dependence upon mesh refinement, three different 3D meshes were generated for the steady calculation, having the total number of grids as 1.25 million, 1.5 million, and 1.75 million, respectively. Furthermore, the flow condition is specified for a clean inlet with a total pressure of 1 atm and a total temperature of 288.15 K at design RPM 17,188 and changed outlet static pressure. However, no-slip conditions are used on walls, and periodic conditions are applied to the periodic surfaces. Three-dimensional steady compressible Reynolds-averaged Navier–Stokes equations have been solved by using the Spalart–Allmaras (SA) turbulence model.

Figure 2 has evidently shown that the performance map which was calculated by 1.5 million mesh is similar to 1.25 million. Thus, reaching the requirement of grid independence, the mesh with 1.5 million grids was adopted in this paper to ensure accuracy and calculation efficiency.

2.3 Validation Between Computational and NASA Experimental Results

To authenticate simulation results, the computational results of the mesh mentioned in the last chapter having 150 million grids are compared with the NASA experimental data in the R37 experimental report [10] to verify the rationality of boundary condition and turbulence model used in this paper.

Figure 3 presents a characteristic map among normalized mass flow rate vs. pressure ratio and isentropic efficiency of the compressor under design, respectively.

The characteristic map between both operating conditions is very similar and shows high agreement between the computational and experimental results.

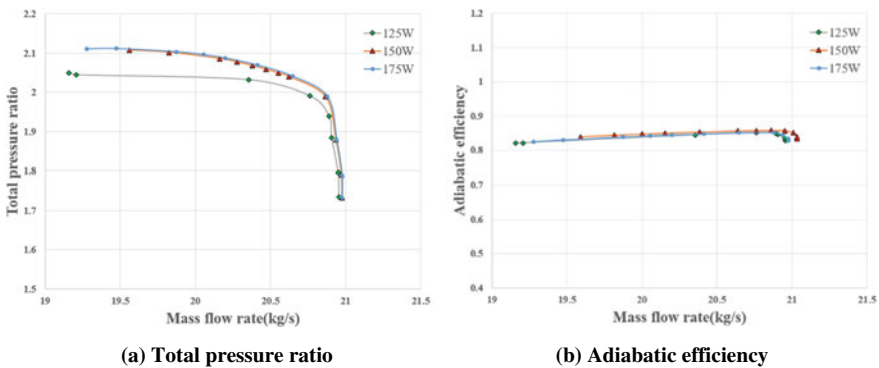


Fig. 2 The performance map of three different precision meshes

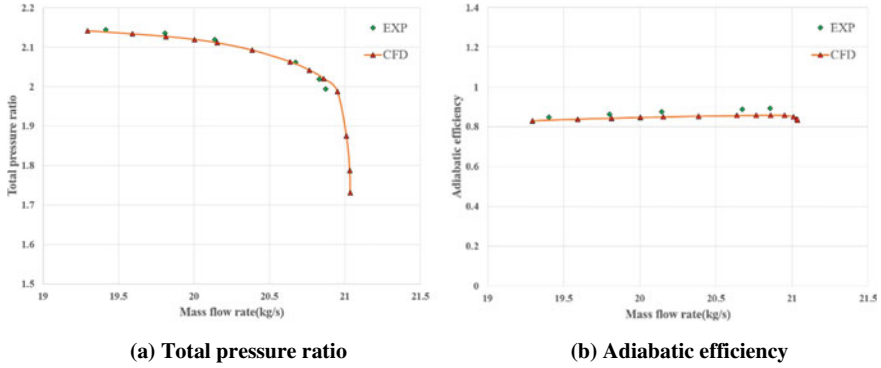


Fig. 3 The performance map for computational and experimental results

Table 2 The distortion boundary condition

Case	Distorted area	Distorted strength (Pa)
I	None	None
II	20% height at hub	2500
III	20% height at tip	2500

2.4 Computational Grid with Inlet Distortion

To illustrate the effects of the distorted inlet condition on the stability of the axial compressor rotor, this research focuses on the radial inlet pressure distortion in the tip and hub areas of the rotor.

For hub and tip radial inlet pressure, the distortion boundary condition is specified by the list shown in Table 2. Compared with the clean flow condition that is uniform 1 atm total pressure at the entrance, in such a way, the total pressure of 20% region of the blade height is distorted by 2500 Pa at tip and hub, respectively.

Figure 4 visualized the computational simulation of distorted inlet flow condition which is shown in Table 2. As apparently shown, the blue region is the distorted area which is 98825 Pa total pressure, while the orange region is uniform at 1 atm. However, the green region is the transition area for simulating a natural decrease of P-total.

3 Results and Analysis

Figure 5 presents the characteristic map of a combined hub, tip, and none inlet radial pressure distortion. The results show that with the non-uniform inlet flow, the choke mass rate decreases from 21.034 kg/s to minimum 20.848 kg/s at tip distortion. Contrary to common sense that non-uniform inlet flow condition certainly pushes

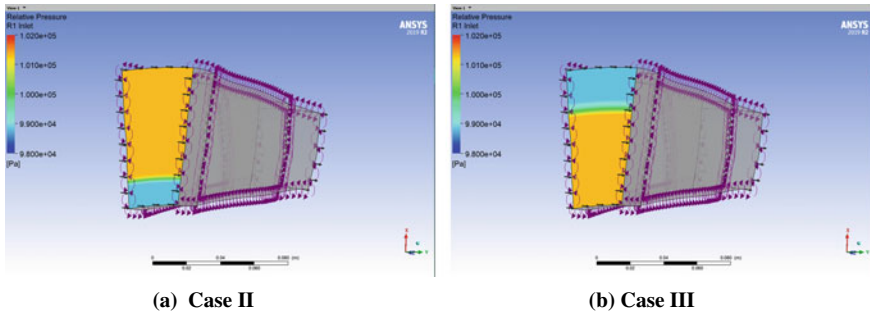


Fig. 4 The distortion area and strength

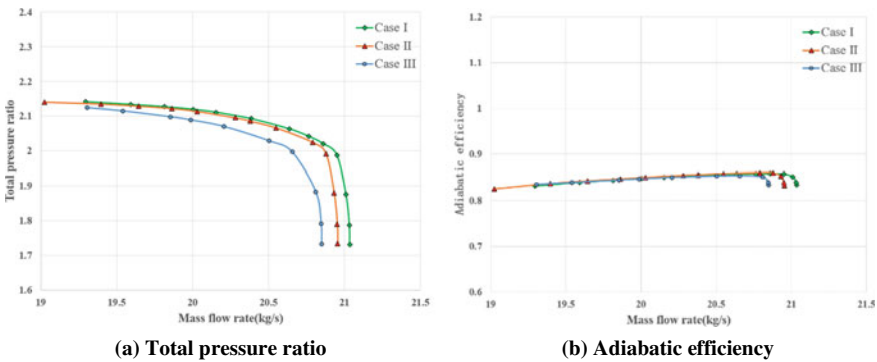


Fig. 5 The performance map of Cases I, II, and III

the occurrence of unsteady phenomena, the hub radial has smaller choking mass flow but has enlarged the stability range.

With the same pressure distortion strength, under the hub radial distorted pressure condition, the rotor reaches the choking point at mass flow 19.025 kg/s, much less than the tip radial distorted condition, even less than uniform condition.

4 Conclusion

This paper chooses the CFD method to investigate the influence of inlet distortion on the stability of compressor rotor, obtaining the conclusion as follows:

- (1) Under the hub radial distorted pressure condition, the rotor can reach a smaller choking mass point, much less than in uniform condition.
- (2) Hub radial pressure distortion is capable of enhancing the flow stability range of the compressor, whereas tip radial inlet flow distortion has shown the deterioration impacts of the compressor performance.

Acknowledgments This work is partially supported by the National Natural Science Foundation of China (No. 51976116), Natural Science Fund of Shanghai (No. 19ZR1425900), and the Open Research Subject of Key Laboratory (Fluid Machinery and Engineering Research Base) of Sichuan Province (No. rszjj2019022).

References

1. Chen H (2020) Investigation of compressor flow instabilities based on global linear stability analysis. Beihang University, Beijing
2. Hah C, Rabe DC, Sullivan TJ, Wadia AR (1998) Effects of inlet distortion on the flow field in a transonic compressor rotor. *ASME J Turbomach* 120(2):233–246
3. Spakovszky ZS, Weigl HJ, Paduano JD, van Schalkwyk CM, Suder KL, Bright MM (1999) Rotating stall control in a high-speed stage with inlet distortion: part i—radial distortion. *ASME J Turbomach* 121(3):510–516
4. Ferrand P, Chauvin J (1982) Theoretical study of flow instabilities and inlet distortions in axial compressors. *ASME J Eng Power* 104(3):715–721
5. Yao J, Gorrell SE, Wadia AR (2010) High-fidelity numerical analysis of per-rev-type inlet distortion transfer in multistage fans—part i: simulations with selected blade rows. *ASME J Turbomach* 132(4):041014
6. Xu D, He C, Sun D, Sun X (2021) Stall inception prediction of axial compressors with radial inlet distortions. *Aerosp Sci Technol* 109:106433. ISSN 1270-9638
7. Suder KL (1995) Experiment and computational investigation of the tip clearance flow in a transonic axial compressor rotor. NASA-TM-106711
8. Benini E, Biollo R (2006) On the aerodynamics of swept and leaned transonic compressor rotors. In: *ASME turbo expo 2006: power for land, sea, and air*, pp 283–291
9. He C, Sun D, Sun X (2018) Stall inception analysis of transonic compressors with chord-wise and axial sweep. *J Turbomach* 140(4):041009
10. Dunham J (1998) CFD validation for propulsion system components (No. AGARD-AR-355). Advisory Group for Aerospace Research and Development Neuilly-Sur-Seine, France

Numerical Simulation of 3D Surfaces Icing Near the Moving Wall



Andrey Fevral'skikh and Vladislav Kupchik

Abstract The capabilities of the method of 3D surfaces icing numerical simulation near the moving ground using Ansys FENSAP ICE software are investigated. The finite-length cylinder and the WIG craft layout are accepted as surfaces of icing accretion. The icing simulation multi-stage method includes the automatic generation of fluid domain mesh taking into account the icing form on the surface before the next stage of simulation. The results of icing numerical simulation above the ground of unswept wing GLC305 and finite-length cylinder have a good agreement with the results of the experiment. The non-dimensional rate of the cylinder and the WIG vehicle icing versus the ground clearance are determinate: the dependences have the nonlinear type, and it is in the agreement with the typical nonlinear influence of the ground effect on the aerodynamics. The forms of cylinder icing for different ground clearance determinate by numerical simulation are presented. The results of numerical simulation show that the method used in Ansys FENSAP ICE software in conjunction with the automatic re-meshing is applicable for the ground effect icing problem.

Keywords CFD · Icing · Ground effect aerodynamics

1 Introduction

The numerical simulation of icing (NSI) approach based on the computational fluid dynamics (CFD) used in the Ansys FENSAP-ICE software is the popular method of determination of icing form on the in-flight aircraft surface [6, 9, 10, 13]. At the same time, the known methods of icing process studies using the NSI approach are not suitable directly for the low-flying aircraft, amphibious craft, aircraft on the take-off mode, which move near the ground. The reasons for this are based on the three facts. Firstly, when the non-dimensional distance between moving aircraft's wing and earth surface $\bar{h} \leq 1$ ($\bar{h} = h/c$, h —distance in meters, c —wing chord),

A. Fevral'skikh (✉) · V. Kupchik
Moscow Aviation Institute (National Research University), Moscow, Russian Federation

the ground effects on the aerodynamic characteristics (ground effect influence [12]), on the characteristics of flight stability, on the structure of velocity field near the aircraft and therefore on the icing form [4]. Secondly, the liquid content in the air near the earth's surface has different characteristics than far from the earth's surface: the droplet diameter, the density of water droplets in the air, the droplet distribution, and other characteristics. Thirdly, the different reasons for ice accretion can be like a splash generated from the water surface, the ice rain, the snowflakes, in addition to the droplets hanging in the air.

The problem of the aerodynamic characteristics changing versus the ground clearance \bar{h} is well researched for different wings and aircraft layouts using both the experiments in the wind tunnel and the CFD modeling [2, 5, 7, 12]. In the present study the ice accretion on the 3D surfaces moving near the ground and the aerodynamic characteristics changing caused by the ice accretion versus the ground clearance are investigated according to the finite length cylinder and the wing-in-ground effect vehicle layout.

2 Numerical Simulation Method

2.1 Computational Domain

The numerical simulation of ground effect aerodynamics is completed using the finite-size space around the 3D surfaces situated near the ground in the computational domain. It is assumed that the 3D surfaces are fixed, the fluid flows into the computational domain through the inlet boundary and flows out through the outlet boundary, and the bottom boundary moves with the velocity value equal to the value of the fluid velocity on the inlet. The cylinder with length 1730 mm and diameter 51 mm, and the WIG vehicle layout with the take-off mass of 1.8 tons are applied as the 3D surfaces. The values of distances between the 3D surface and the domain

Table 1 The domain boundaries characteristics

Domain boundary	Distance between boundary and cylinder, in RL	Distance between boundary and WIG vehicle, in RL	Boundary conditions type
Inlet	59	10	Velocity inlet
Outlet	59	25	Pressure outlet
Top	26	15	Slip wall
Side	1	15	Slip wall
Bottom	0.1...26	0.1...15	Moving wall
Symmetry	0	0	Symmetry

boundaries are shown in Table 1, where the RL is the reference length equal to the diameter of the cylinder and is equal to the wing mean chord for the WIG vehicle.

2.2 Algorithm of Simulation

The numerical simulation of ice accretion with Ansys FENSAP-ICE includes five steps in one stage of simulation: numerical simulation of aerodynamics using Ansys Fluent, numerical simulation of droplet impingement using Ansys FENSAP-ICE's DROP3D module, numerical simulation of crystallization using Ansys FENSAP-ICE's ICE3D module, remeshing using Ansys Fluent Meshing, and transferring results information for next aerodynamic simulation. It is assumed that the droplet motion and ice accretion do not influence the air motion in one stage duration. For long-time process simulation, the 10 stages with different simulation times are used. The process of results transfer is automatic.

2.3 Model of Aerodynamics

The numerical simulation of compressible air motion in the computational domain is based on the application of the finite-volume method to the solving of Reynolds-averaged Navier–Stokes Eqs. (1)–(4).

$$\frac{\partial \rho}{\partial t} + \nabla \cdot (\rho \vec{u}) = 0 \quad (1)$$

$$\frac{\partial(\rho \vec{u})}{\partial t} + \nabla \cdot (\rho \vec{u} \vec{u}) = -\nabla p + \nabla \cdot (\tau_m + \tau_t) \quad (2)$$

$$\frac{\partial(\rho E)}{\partial t} + \nabla \cdot (\rho \vec{u} H) = \nabla \cdot (\vec{u} \cdot \tau + \vec{q}) \quad (3)$$

$$\rho = pm/(RT) \quad (4)$$

where ρ —air density, $\vec{u} = \{u, v, w\}$ —velocity vector, p —pressure, $E = C_V T + 0.5(u^2 + v^2 + w^2)$ —full energy, $H = C_P T + 0.5(u^2 + v^2 + w^2)$ —full enthalpy, τ —viscous tensor, $\vec{q} = -\frac{C_P \mu(T)}{Pr} \nabla T$ —heat flow, $\mu(T)$ —viscosity, C_P and C_V —specific-heat capacity for constant pressure and constant volume, respectively. For the determination of Reynolds stress, the Menter's SST k - ω turbulence model is used [8] with the viscous heating model.

The special boundary conditions on the 3D surface are used to provide the ice accretion. High roughness (Icing) is applied as the roughness model with specified

sand-grain roughness height of 0.0005 m and roughness constant of 0.5 on the first stage of multi-stage simulation. The temperature on the boundary is the temperature of adiabatic stagnation plus 10 K.

2.4 Model of Droplet Motion and Impingement

The model of droplet motion and impingement is presented by Eqs. (5)–(6).

$$\frac{\partial \alpha}{\partial t} + \vec{\nabla} \cdot (\alpha \vec{V}_d) = 0 \quad (5)$$

$$\frac{\partial(\alpha \vec{V}_d)}{\partial t} + \vec{\nabla} [\alpha \vec{V}_d \otimes \vec{V}_d] = \frac{C_D Re_d}{24K} \alpha (\vec{V}_a - \vec{V}_d) + \alpha \left(1 - \frac{\rho_a}{\rho_d}\right) \frac{1}{Fr^2} \quad (6)$$

where α —the concentration of droplets; \vec{V}_a —velocity of air; \vec{V}_d —velocity of droplets; C_D —the drag coefficient; Fr —Froude number; ρ_a and ρ_d —air and water density; the droplets Reynolds number Re_d ; \otimes —is the Kronecker product of two matrices; an inertial parameter K and the local Froude number Fr are obtained by (7), (8), and (9), respectively.

$$Re_d = \frac{\rho_a d \vec{V}_{a\infty} \|\vec{V}_a - \vec{V}_d\|}{\mu_a} \quad (7)$$

$$K = \frac{\rho_d d^2 \vec{V}_{a\infty}}{18L} \quad (8)$$

$$Fr = \frac{\|\vec{V}_{a\infty}\|}{\sqrt{Lg}} \quad (9)$$

where d —the droplet diameter; L —a characteristic length; $\vec{V}_{a\infty}$ —velocity of air at the inlet; μ_a —the dynamic viscosity of air.

The drag coefficient is obtained by (10).

$$C_D = \begin{cases} \left(\frac{24}{Re_d}\right)(1 + 0.15 Re_d^{0.687}), & Re_d \leq 1300 \\ 0.4 & Re_d > 1300 \end{cases} \quad (10)$$

The collection efficiency, β , is the non-dimensional parameter that represents the amount of water that impacts the surface per unit time (11).

$$\beta = -\frac{\alpha(\vec{u}_d \cdot \vec{n})}{\alpha_\infty \|\vec{u}_{d\infty}\|} \tag{11}$$

where \vec{n} —the vector of the surface normal, $\vec{u}_{d\infty}$ —velocity of droplets and α_∞ —concentration of droplets on the inlet boundary.

In the present study for icing simulation, the monodisperse droplet distribution is used.

2.5 Model of Ice Accretion

On each solid surface activated by ice accretion, the icing caused by the impinging droplets is solved for the thin liquid film. The film may run back and may be forced by the shear stresses created by the airflow. The determination of the liquid film form is applied as the grid vertex motion, and the height of the motion is calculated using the surface thermodynamic conditions.

It is assumed that the normal to the wall component of the film velocity \vec{V}_f is the function of the air shear stress $\vec{\tau}_{a,wall}$ (12).

$$\vec{V}_f(\vec{x}) = \frac{h_f}{\mu_f} \vec{\tau}_{a,wall}(\vec{x}) \tag{12}$$

where h_f —the film height; $\vec{x} = (x_1, x_2)$ —coordinates on the wall.

For the determination of the film height h_f , the system of two partial differential Eqs. (13) and (14) for a surface is solved.

$$\rho_f \left(\frac{\partial h_f}{\partial t} + \vec{\nabla} \cdot (V_f h_f) \right) = V_\infty LWC\beta - \dot{m}_{evap} - \dot{m}_{ice} \tag{13}$$

$$\begin{aligned} \rho_f \left(\frac{\partial h_f \tilde{T}_f}{\partial t} + \vec{\nabla} \cdot (V_f h_f c_f \tilde{T}_f) \right) = & \left(c_f (\tilde{T}_\infty - \tilde{T}_f) + \frac{\vec{V}_d^2}{2} \right) V_\infty LWC\beta \\ & - L_{evap} \dot{m}_{evap} - (L_{fusion} - c_s \tilde{T}) \dot{m}_{ice} \\ & + \sigma \varepsilon (T_\infty^4 - T_f^4) - c_h (\tilde{T}_f - \tilde{T}_{ice,rec}) \end{aligned} \tag{14}$$

where V_f —velocity of fluid on the wall, LWC —liquid water content (kg/m^3), \dot{m}_{evap} —mass rate of evaporation, \dot{m}_{ice} —mass rate of icing; $\rho_f, c_f, c_s, \sigma, \varepsilon, L_{fusion}, L_{evap}$ —physical properties of the fluid and the solid. In Eqs. (13) and (14) h_f is the film thickness, \tilde{T}_f is the equilibrium temperature at the air/water film/ice/wall interface, \dot{m}_{ice} is the instantaneous mass accumulation of ice. To close the system of Eqs. (13)–(14) the relations (15) are used.

$$\begin{cases} h_f \geq 0 \\ \dot{m}_{ice} \geq 0 \\ h_f \tilde{T}_f \geq 0 \\ \dot{m}_{ice} \tilde{T}_f \leq 0 \end{cases} \quad (15)$$

The relations (15) mean that the model predicts no liquid water when the equilibrium temperature is below the freezing point (0 °C), and that no ice if there is a film that is above 0 °C.

2.6 Remeshing and Transferring Data

After determination of h_f as the field of values on the surfaces of icing, the faceted geometry model of new wall surfaces is created. For the next stage of icing simulation, it is necessary to create a new mesh model and to transfer the data of roughness. In the present study, the automatic meshing is implemented as script execution in Ansys Fluent Meshing. The launching of Ansys Fluent Meshing, the transfer data, and the start of the next stage of ice simulation are provided using the shell script (*.sh).

3 Validation of Icing Simulation Method

The validation of the icing numerical simulation method is completed using the experimental data of icing of unswept wing and cylinder above the ground. The data of numerical simulation and the experimental data are in good agreement.

3.1 Validation with Unswept Wing

The conditions of icing of unswept wing GLC305 are presented in Table 2 [11]. The ice form determinate by numerical simulation and in an experiment are presented in Fig. 1; a good agreement is observed.

Table 2 The conditions of unswept wing icing

Velocity, m/s	Angle of attack, grad	Droplet diameter, microns	Temperature, K	Time of icing, s	LWC, g/m ³
90	4.5	20	258	264	0.405

Fig. 1 The result of experimental and numerical simulation of unswept wing icing: full line—ice form above the ground; stipple line—ice form near the ground with $\bar{h} = 0.1$

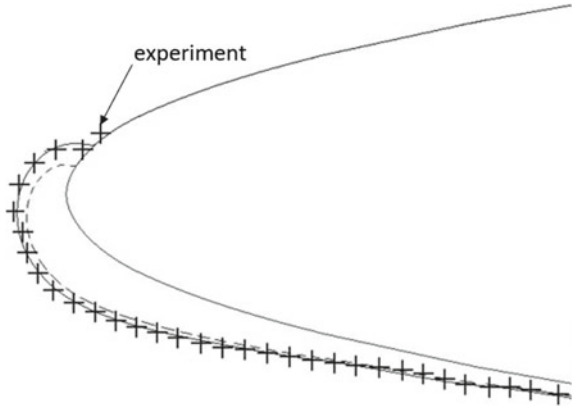


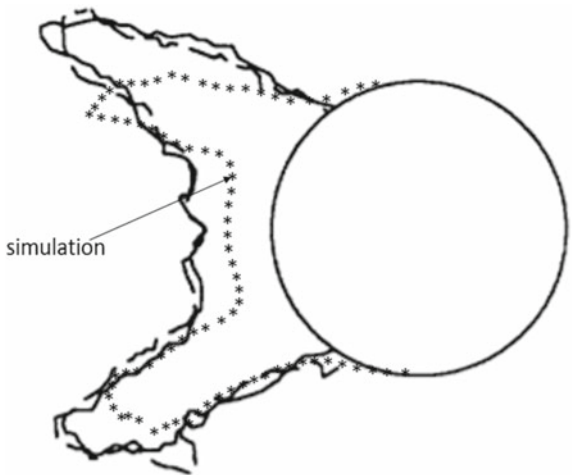
Table 3 The conditions of finite-length cylinder icing

Diameter, m	Velocity, m/s	Droplet diameter, microns	Total temperature, K	Time of icing, s	LWC, g/m ³
0.051	94	30	265.15	468	1.3

3.2 Validation with Finite-Length Cylinder

The conditions of icing of a finite-length cylinder are presented in Table 3 [1]. The ice forms determinates by numerical simulation and in the experiment are presented in Fig. 2 and have a good agreement. The differences between the ice shape obtained

Fig. 2 The result of experimental and numerical simulation of finite-length cylinder icing above the ground



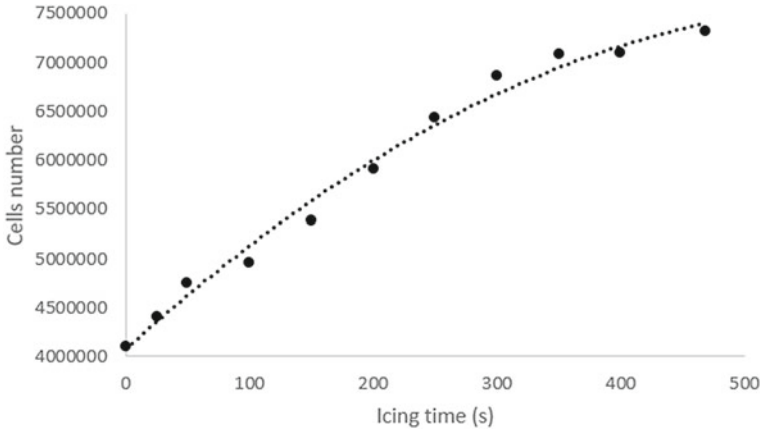


Fig. 3 Cells number for validation case of cylinder icing

as a result of numerical simulation and the ice shape obtained in the experiment may be due to the lack of information about the experimental conditions.

A significant increase in the number of grid cells was noted during the simulation (almost doubled). The growth rate of cells number is shown in Fig. 3.

4 Results of Cylinder Icing Simulation

For the analysis of icing rate for wing with the different ground clearance, the expression for non-dimensional rate determination (16) is suggested by [4].

$$\bar{q}_{ice} = \frac{d\bar{m}_{ice}}{d\bar{t}} = \frac{d(m_{ice}g/F)}{d(Vt/b)} \tag{16}$$

where b —a characteristic length of a body (chord length or cylinder diameter); F —the lift force of wing or the drag force of cylinder. For the cylinder, the lifting force is zero due to its symmetry; therefore, the drag force is applied to the cylinder.

The conditions of cylinder icing used in the numerical simulation are presented in Table 3. Non-dimensional icing rate dependence on the ground clearance for the cylinder is shown in Fig. 4.

Figure 5 shows the drag force dependence on the ground clearance for cylinder before and after icing calculations.

Figure 6 shows the change of ice cover during the calculation for two cases of simulation: when $\bar{h} = 0.3$ and $\bar{h} = 1$ at different time steps.

The geometry of ice build-ups on a cylindrical surface for motion with different values of ground clearance is shown in Fig. 7.

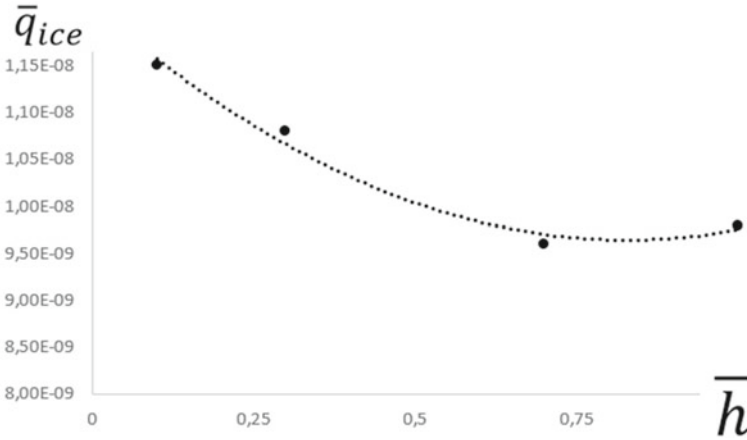


Fig. 4 The non-dimensional icing rate versus the ground clearance for the cylinder

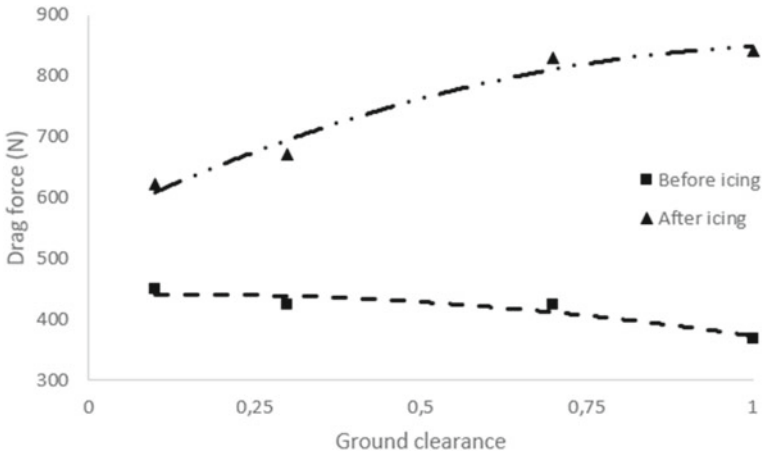


Fig. 5 The drag force versus the ground clearance for cylinder before and after icing

5 Results of WIG Craft Icing Numerical Simulation

The conditions of WIG craft icing used in the numerical simulation are presented in Table 4. The description of the WIG craft is presented in [3]. The dependence of the non-dimensional icing rate on the ground clearance for the WIG craft is shown in Fig. 8. The places of icing for motion with ground clearance $\bar{h} = 0.2$ are presented in Fig. 9.

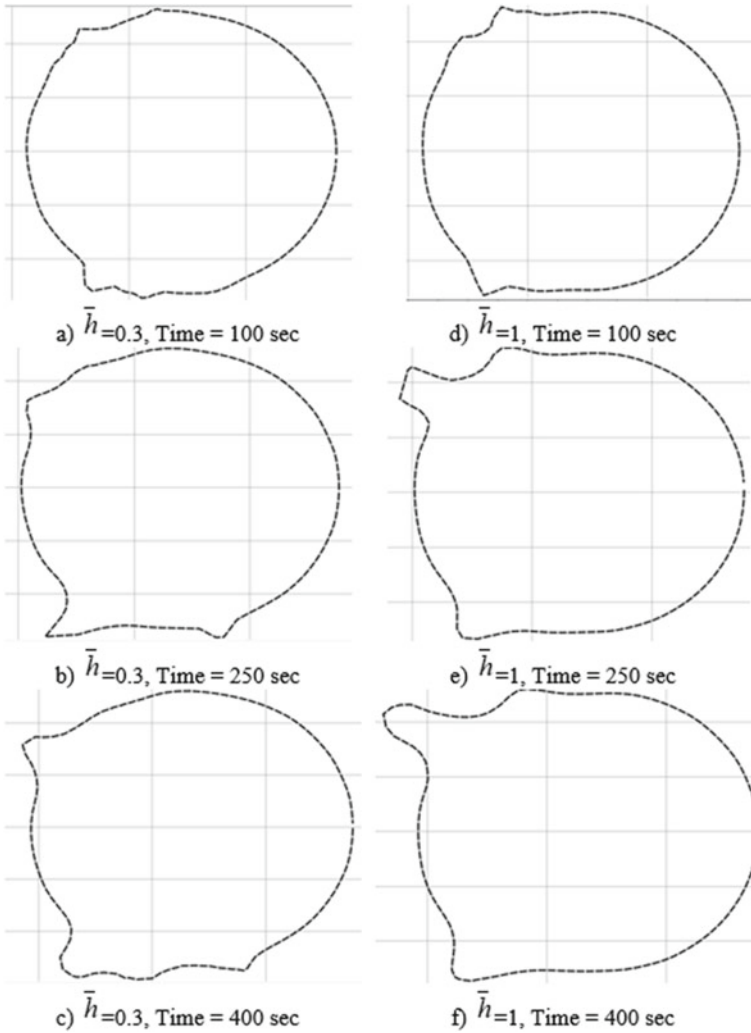


Fig. 6 Ice forms at different moments of time near the ground and above the ground

6 Conclusion

The results of the numerical simulation method of the 3D surfaces icing near the moving ground using Ansys FENSAP-ICE software are investigated here. The finite length cylinder and the WIG craft are applied as the 3D surfaces. The rate of icing and the aerodynamic characteristics versus the ground clearance determinate are given by the results of numerical simulation.

The results of icing simulation on cylinder have a good agreement with the experimental data without moving wall. The dependence of the icing rate on the ground

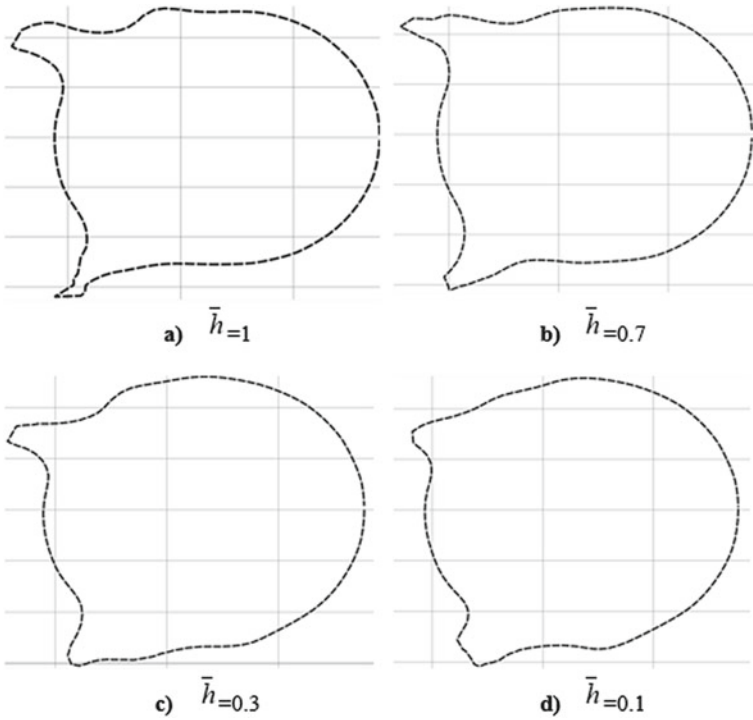


Fig. 7 Ice build-ups on a cylindrical surface at the various ground clearance

Table 4 The conditions of WIG craft simulation

Velocity, m/s	Angle of attack, grad	Droplet diameter, microns	Temperature, K	Time of icing, s	LWC, g/m ³
30	4.5	70	268	264	3

Fig. 8 The non-dimensional icing rate versus the ground clearance

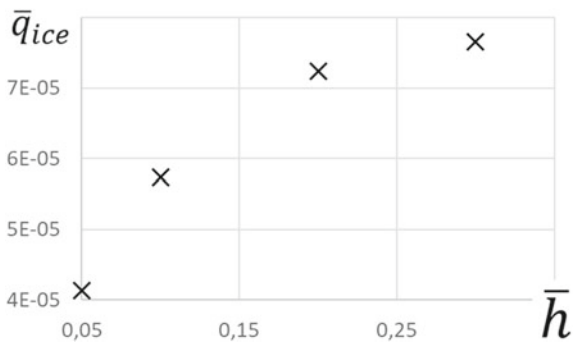
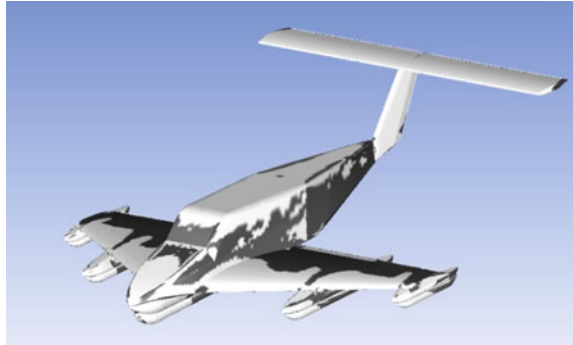


Fig. 9 The places of WIG craft icing determinate by numerical simulation for $\bar{h} = 0.2$



clearance for the cylinder and the WIG craft has a nonlinear type. It is supposed that the change of icing rate with the ground clearance increase is connected with the change in air velocity field near the 3D surfaces, which is illustrated by the dependences of the drag force of the cylinder and the lift force of the WIG vehicle on the ground clearance.

References

1. Anderson DN (1994) Rime-, mixed- and glaze-ice evaluations of three scaling laws. NASA Technical memorandum 106461. AIAA-94-0718
2. Bil C, Fung MC, Cheung SCP, Marzocca P (2015) CFD analysis of a wing-in-ground-effect (WIGE) vehicle. SAE Technical Paper Series <https://doi.org/10.4271/2015-01-2571>
3. Fevralskikh AV (2017) Development of design methodology of air-hydrodynamic layout of an amphibious air-cushion vehicle with aerodynamic unloading based on numerical simulation. Dissertation, Nizhny Novgorod State Technical University n.a. R.E. Alekseev
4. Fevralskikh AV (2019) Wing icing of ground-effect vehicle: numerical simulation. *Transa Krylov State Res Centre* 4(390):2019. <https://doi.org/10.24937/2542-2324-2019-4-390-117-124>
5. Gramuzov EM, Lyubimov VI, Fevralskikh AV, Smirnov KV, Sosnov AV (2019) Automated optimization of wing and horizontal fins layout of a groundplane based on numerical simulation of aerodynamics. *Mar Intell Technol* 3(45):38–47
6. Geiger P (2020) Simulation of in-flight rime icing using a non-body-fitted mesh. <http://hdl.handle.net/10012/15810>
7. Lee J (2018) Computational analysis of static height stability and aerodynamics of vehicles with a fuselage, wing and tail in ground effect. *Ocean Eng* 168:12–22
8. Menter E (1993) Zonal two equation $k-\omega$ turbulence models for aerodynamic flows. 24th fluid dynamics conference, (Orlando), AIAA paper-93-2906
9. Ozcer I, Baruzzi G, Desai M, Yassin M (2019) Numerical simulation of aircraft and variable-pitch propeller icing with explicit coupling. SAE Technical Paper. <https://doi.org/10.4271/2019-01-1954>
10. Ozcer I, Switchenko D, Baruzzi G, Chen J (2019) Multi-shot icing simulations with automatic re-meshing. SAE Technical Paper <https://doi.org/10.4271/2019-01-1956>
11. Pueyo A, Brette C, Vafa S, Akel I (2007) A Comparison exercise of ice accretion simulations with 2D and 3D solvers. SAE Technical Paper. <https://doi.org/10.4271/2007-01-3338>

12. Rozhdestvensky KV (2006) Wing-in-ground effect vehicles. *Prog Aerosp Sci* 42:211–283. <https://doi.org/10.1016/j.paerosci.2006.10.001>
13. Tran P, Baruzzi G, Akel I, Habashi WG, Narramore JC (2004) FENSAP-ICE applications to complete rotorcraft configurations. *J Aerosp SAE Trans*

Modelling Causal Relationship Among Performance Shaping Factors Through Bayesian Network on Aviation Safety



Yifan He, Yi Lu, Dan Huang, and Shan Fu

Abstract Aviation safety is greatly influenced by pilot performance reliability. To assess the reliability, many human reliability analysis (HRA) methods are developed. Currently, in most HRA methods performance shaping factors (PSFs) are used to represent internal and external factors which contribute to human error. Up to now, the effects of PSFs are usually considered to be independent. However, more and more evidences show that causal relationships do exist among PSFs and neglecting that interrelationship will make the assessed human error rate to be too optimistic or too conservative. This paper builds a Bayesian network (BN) to represent interrelated relationships based on investigation of 50 human factor related aviation mishap reports of US Airforce from 2011 to 2019. The causal dependency of PSFs is derived from Human Factor Analysis and Classification System (HFACS) framework. And an Expectation–Maximization algorithm is used to quantify the dependency, which reduces the heavy reliance on expert judgement. Through sensitivity analysis we find that 2 key factors influencing cognitive error are negative state of operator and deteriorating technical condition, implying these factors have greater influence on the cognitive process of operator such as interpreting task demand and information perception. The proposed BN model can be used to identify the primary PSFs influencing pilot performance, providing targeted risk mitigating suggestions.

Keywords Aviation safety · Accident investigation · Bayesian model · Human reliability analysis

Y. He · D. Huang

School of Aeronautics and Astronautics, Shanghai Jiao Tong University, Shanghai 200240, China
e-mail: hyfsjtu@sjtu.edu.cn

D. Huang

e-mail: huangdan@sjtu.edu.cn

Y. Lu (✉) · S. Fu

School of Electric Information and Electrical Engineering, Shanghai Jiao Tong University, Shanghai 200240, China

e-mail: luyi1@sjtu.edu.cn

S. Fu

e-mail: sfu@sjtu.edu.cn

1 Introduction

Currently, more and more aviation accidents were caused by human failure. According to statistics, 60% of aviation accidents are at least partial attributable to human error during 1984–2017 [1]. Therefore, it is extremely important to study the reliability of human-being, find out the factors which cause operator to make errors, and take corrective measures such as improving cockpit ergonomic design and personnel training to improve the safety of aviation.

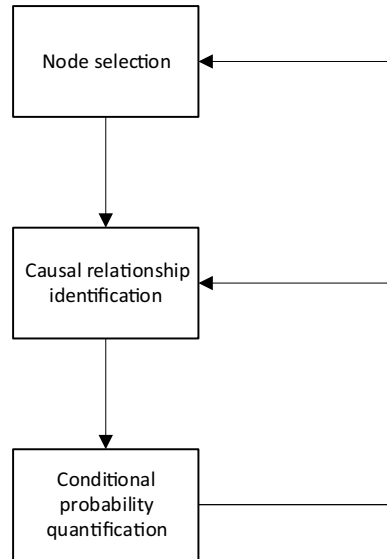
According to definition given by Swain and Guttman, human reliability is the probability that an operator correctly system-required task in a required time [2]. Over the past decades, many HRA (Human Reliability Analysis) methods had been proposed to quantify human error probability [3]. Most HRA methods introduce PSFs (Performance Shaping Factors) such as stress, man–machine interface and training trying to find the causes of the accidents. Human error rate is considered as a function of the states of PSFs. Most HRA methods assume independency between PSFs, however, more and more evidences show that causal relationships do exist among PSFs and neglecting that interrelationship will make the assessed human error rate to be too optimistic or too conservative [4]. Only few methods such as CREAM, SPAR-H mention interrelationship between PSFs but fail to quantify it [4, 5]. Some efforts had been made to deal with the dependency between PSFs over the years. Some researchers use fuzzy inference rules to assess the dependency [6], while others use Analytic Network Process which presents a quantitative way to address the interrelationship [7]. For example, Adedigba introduces Bayesian network in chemical process industry to account for dependencies among causal factors [8]. Groth uses correlation and factor analysis to get the data-driven dependency network, which reduces the heavy reliance on expert judgement [9].

The rest of this paper is organized as follows. Section 2 gives a brief introduction of BN model and HFACS framework. In Sect. 3, a BN model depicting causal relationships among PSFs and human error is built based on the analysis of 50 military aircraft mishap reports. Conditional probability tables (CPTs) are learnt by EM algorithm using commercial Bayesian network building software GeNIe. Finally, the last section summarizes the main work and the conclusions.

2 Method

2.1 Bayesian Network

BN is proposed by Pearl in 1988, which represents Bayes Theorem in an intuitive graph. BN is consisted of 2 part, directed acyclic diagram (DAG) and conditional probability table (CPT). The nodes in BN represent variables, while the directed edges connecting nodes depict causal relations. Just as the name implies, the CPT contains conditional probability of a node given the states of its parent nodes. The model

Fig. 1 BN modeling process

building can be divided into 2 parts, qualitative analysis and quantitative analysis. Qualitative part includes node selection and structure refinement. Quantitative part includes conditional probability elicitation. After the model is built, sensitivity analysis will be conducted to verify the model. The model building process is iterative, as Fig. 1 indicates.

Bayesian network has intuitive graphical representation and ability to merge data from different sources [10]. The scarcity of mishap data of aviation industry makes Bayesian network an ideal tool to construct the interrelationship between PSFs combining objective data and expert subjective judgement.

2.2 HFACS

Human factor analysis and classification framework (*HFACS*) is based on Cheese model presented by Reason [11]. Reason views the process of accident as 4 layers, namely organizational influence, unsafe supervision, preconditions for unsafe action, and unsafe action [12]. The 4 layers act like barriers to prevent the accident from happening, and the weakness in each layer is like the whole in cheese. As Fig. 2 shows, HFACS explores each layer further and defines specific expressions for each layer, and it is oriented to use in aviation safety analysis field (Fig. 2).

The data analyzed by the authors are collected according to HFACS framework. Up to now, most research limit to statistical analysis, counting accident proportion by each possible cause [14]. Few studies the interrelationship between each possible problem. Identifying the interrelationship would contribute to produce more accurate

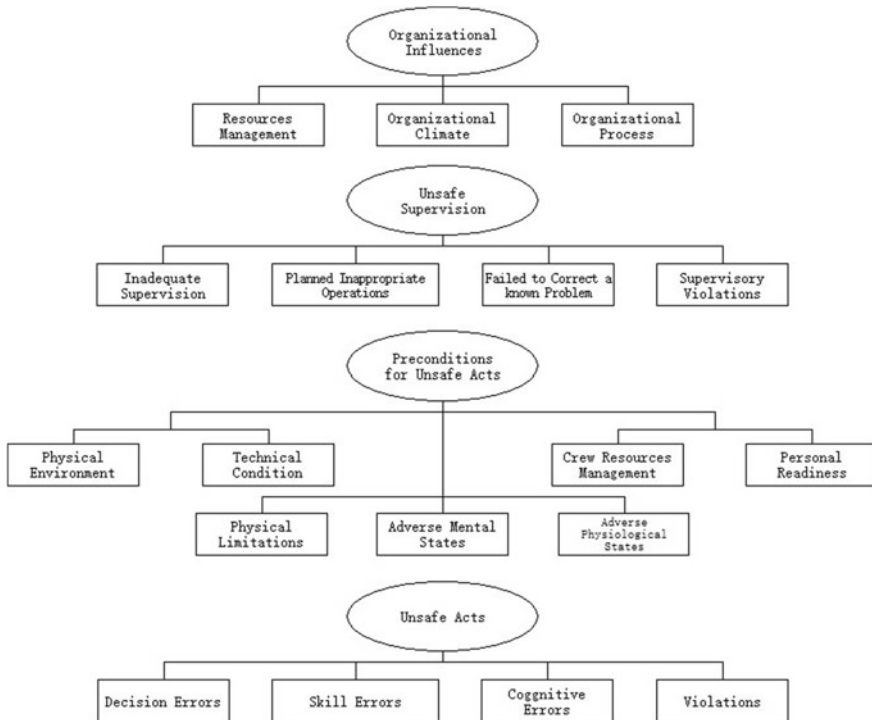


Fig. 2 HFACS framework [13]

human error probability prediction, which is useful for probabilistic safety analysis. Besides, it will provide a better understanding of causal relationship among each factor, making it possible to take effective measures to reduce risk from the root.

3 Bayesian Network for Aviation Accidents

3.1 Construct the BN Structure from HFACS

The node selection is based on aircraft mishap reports investigation. 50 accidents reports are analyzed from 2011 to 2019 of US Airforce. It is an open source database. The accident investigation board reports are available at <https://www.airforcemag.com/docs/type/accident/>. Then human error analysis data is mapped into HFACS framework. The nodes which occurred frequently are chosen and some nodes are merged due to data limitation. For example, poor man-machine interface, display, and checklist design are merged into one node, named ‘deteriorating technical condition’.

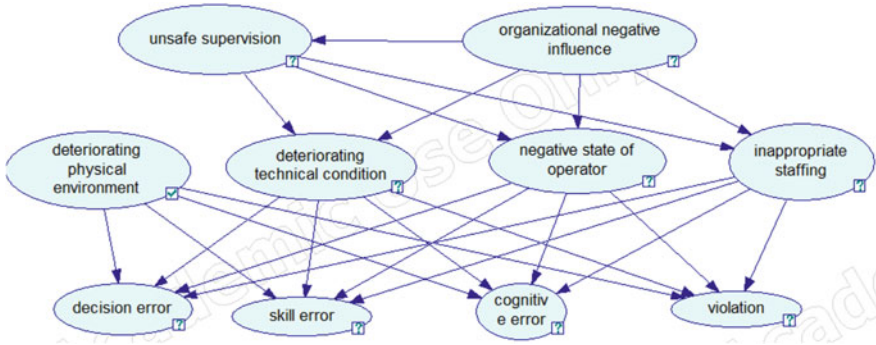


Fig. 3 BN structure identification

Table 1 Data sample

Event	2014–1	2014–2
Decision error	Absent	Present
Skill error	Absent	Absent
Cognitive error	Absent	Absent
Violation	Absent	Absent
Physical environment	Present	Absent
Technical condition	Absent	Absent
Operator state	Present	Absent
Inappropriate staffing	Absent	Absent
Unsafe supervision	Absent	Present
Organizational influence	Absent	Present

Causal relationships among nodes are elicited with literature review [15]. Figure 3 shows the result of structure identification.

Table 1 shows example of data mapped into BN nodes. Since the mishap reports are organized according to HFACS, little data mapping work is needed which minimizes the loss of valuable information. For quantitative analysis, we arrange the PSFs for each event in a table. For each event, the states of PSFs are coded as ‘Absent’ or ‘Present’. Table 1 exemplifies the arranged data.

3.2 Calculation of BN Node Marginal and Conditional Probabilities

The Expectation–Maximization algorithm is used to calculate CPT. After CPT parameters are learnt, DAG can be adjusted according to expert judgement then the process goes iteratively until the parameters converge. Traditional way to get

CPT is to elicit expert judgement, which is time-consuming and lacks theoretical support. What’s worse, the input of CPT for a node grows exponentially when its parent nodes increase. For example, in a BN where all nodes are binary variables if one node has n parents, the CPT of the node has 2^n inputs. Many algorithms have been developed to reduce the computation load. Typical algorithm is Noisy-Or [16, 17]. It can reduce parameter number from 2^n to n .

However, this algorithm has a strong assumption that each parent node is independent, which contradicts with the goal of using Bayesian networks to study inter-relationships among PSFs. Noisy-Leaky algorithm takes the factor which cannot be explicitly expressed into consideration by introducing leaky probability [18].

Recursive Noisy-Or relaxes the assumption about parent nodes independency in Noisy-Or, which expands the adaptability of it. The above algorithms all require nodes to be binary variables, which cannot reflect the reality comprehensively. For example, the experience of pilot could have more than 2 states such as ‘high’, ‘medium’, and ‘low’. Therefore, Noisy-Max algorithm is proposed to deal with multi-state variables [19].

In statistics, an expectation–maximization (EM) algorithm is an iterative method to find maximum likelihood estimate of parameters in statistical models, where the model depends on unobserved latent variables [20].

4 Results

For nodes which do not have parent nodes, their marginal probability is illustrated in below. The result is quite surprising. As Table 2 shows, in 50 accident reports, only 28% of them are recorded with deteriorating physical environment (DPE). This means 78% of accidents occurred in good weather and visibility. This is not hard to explain though. Pilots may lose vigilance in good physical environment. And Table 3 indicates that only 24% of total reports recorded with organizational negative influence (ONI). This may due to organizational influence is latent factor, which is not apparent to be observed directly (Tables 2 and 3).

Table 2 Marginal probability for DPE

DPE	State
Present	0.28
Absent	0.72

Table 3 Marginal probability for ONI

ONI	State
Present	0.24
Absent	0.76

Table 4
Conditional probability for ONI

ONI		Present	Absent
State of US	Present	0.5	0.24
	Absent	0.5	0.76

The conditional probability for ONI is listed in Table 4. For node ‘unsafe supervision (US)’, when ONI is present, probability of US being present is 50%. When ONI is absent, probability of US being present is 23.68%. This indicates that ONI has a negative influence on US, which confirms our daily experience.

For node ‘unsafe supervision (US)’, when ONI is present, probability of US being present is 50%. When ONI is absent, probability of US being present is 23.68%. This indicates that ONI has a negative influence on US, which confirms our daily experience (Table 4).

Table 5 lists the result of conditional probability for node US. For node ‘negative state of operator (NSO)’, when US and ONI are both present, the probability of NSO being present is 66.67%. Through sensitivity analysis, it is found that US has greater influence on NSO than ONI does. This may be due to ONI influence the mental state of operator in an indirect way compared to US (Table 5).

For node ‘cognitive error (CE)’ has 4 parent nodes, namely ‘deteriorating physical environment (DFE)’, ‘deteriorating technical condition (DTC)’, ‘inappropriate staffing (IS)’, and NSO. Sensitivity analysis for CE is indicated in Table 6. Through sensitivity analysis, it is derived that 2 key influence factors are NSO and DTC. In other words, NSO and DTC have greater influence on the cognitive process of operator such as interpreting task demand and information perception (Table 6).

However, there are some CPTs being counter-intuitive which needs to be corrected by experts. Because the size of the data set is relatively small (only 50 records are collected), the learning results may not be valid. Virtual environment experiments and simulations provide a possible solution for data shortage [21, 22]. However, the

Table 5 Conditional probability for US

US		Present		Absent	
ONI		Present	Absent	Present	Absent
State of NSO	Present	0.67	0.67	0.5	0.41
	Absent	0.33	0.33	0.5	0.59

Table 6 Sensitivity analysis for CE

Node	State	CE = Present	state	CE = Present	Increase percent (%)
DPE	Absent	0.40	Present	0.45	12.5
DTC	Absent	0.40	Present	0.50	25
NSO	Absent	0.28	Present	0.55	96.4
IS	Absent	0.40	Present	0.44	10

validity of simulation data is yet to be proved. This paper is an attempt to derive insights of PSFs relationships from accident reports data. It urges to establish a more comprehensive database which includes successful flight data [23].

5 Conclusion

This paper develops a Bayesian network to present causal relationships among PSFs bases on accident investigation reports of US Airforce. Firstly, PSFs are selected from HFACS framework. Secondly, Expectation–Maximization algorithm is used to calculate the conditional dependency among PSFs, which can be used to validate expert subjective experience. Finally, conditional dependency of PSFs learnt from statistical data is analyzed. Some of the conditional probability table calculated by EM algorithm may be counterintuitive, which may due to inadequate data or limitation of expert cognition.

However, during the development of the model, some deficiencies have emerged. Due to the scarcity of accidents, the size of database is relatively small, which may affect the efficiency of parameter learning. Simulation experiment can be designed to validate the efficiency of the model. The BN model is able to identify the primary PSFs dominantly influencing pilot error, which helps take corrective measures such as devise training methods accordingly to mitigate negative influences of these factors. The model presented in this paper is intended for incorporating statistic data to enhance HRA, and lays a foundation for developing task-based analysis in the near future.

Acknowledgements This research was sponsored by Youth Fund Project of National Natural Science Foundation of China (61803263) and the Startup Fund for Youngman Re-search at SJTU of China (SFYR at SJTU).

References

1. Boyd DD (2017) A review of general aviation safety (1984–2017). *Aerospace Med Hum Perform* 657–664
2. Swain AD, Guttman HE (1983) *Handbook of human-reliability analysis with emphasis on nuclear power plant applications* Final report, pp. 699
3. Patriarca R, Ramos M, Paltrinieri N, Massaiu S, Costantino F, Di Gravio G, Boring RL (2020) Human reliability analysis: Exploring the intellectual structure of a research field. *Reliab Eng Syst Saf* 107102
4. Gertman DI, Blackman HS, Marble JL, Byers JC, Smith CL (2005) The SPAR-H human reliability analysis method (NUREG/CR-6883, INL/EXT-05–00509)
5. Hollnagel E (1998) Cognitive reliability and error analysis method (CREAM), pp 262–275
6. Wang L, Wang Y, Chen Y, Pan X, Zhang W, Zhu Y (2020) Methodology for assessing dependencies between factors influencing airline pilot performance reliability: a case of taxiing tasks. *J Air Trans Manag* 101877

7. De Ambroggi M, Trucco P (2011) Modelling and assessment of dependent performance shaping factors through analytic network process. *Reliabil Eng Syst Saf* 849–860
8. Adedigba SA, Khan F, Yang M (2016) Process accident model considering dependency among contributory factors. *Proc Saf Environ Protect* 633–647
9. Groth KM, Mosleh A (2012) Deriving causal Bayesian networks from human reliability analysis data: a methodology and example model. *Proc Inst Mech Eng Pt O J Risk Reliab* 361–379
10. Pearl J (2000) *Causality: models, reasoning, and inference*. Cambridge University Press
11. Shappell S, Detwiler C, Holcomb K, Hackworth C, Boquet A, Wiegmann DA (2007) Human error and commercial aviation accidents: an analysis using the human factors analysis and classification system. *Fact* 227–242
12. Reason J (2000) *Human error: models and management*. *West J Med* 393–396
13. Li WC, Harris D, Yu CS (2008) Routes to failure: analysis of 41 civil aviation accidents from the Republic of China using the human factors analysis and classification system. *Accid Anal Prevent* 426–34
14. Tvaryanas AP, Thompson WT, Constable SH (2006) Human factors in remotely piloted aircraft operations: HFACS analysis of 221 mishaps over 10 years. *Aviat Space Environ Med* 724
15. Chang YHJ, Mosleh A (2007) Cognitive modeling and dynamic probabilistic simulation of operating crew response to complex system accidents. Part 2: IDAC performance influencing factors model. *Reliabil Eng Syst Saf* 1014–1040
16. Díez F (2001) Parameter adjustment in Bayes networks. the generalized noisy OR-gate. In: *Proceedings of the 9th conference on uncertainty in artificial intelligence. UAI*
17. Ashrafi M, Davoudpour H, Khodakarami V (2017) A Bayesian network to ease knowledge acquisition of causal dependence in CREAM: application of recursive noisy-OR gates. *Qual Reliab Eng Int* 479–491
18. Fallet-Fidry G, Weber P, Simon C, Iung B, Duval C (2012) Evidential network-based extension of leaky noisy-OR structure for supporting risks analyses. In: *IFAC proceedings volumes*. 672–677
19. Díez FJ, Galán SF (2003) Efficient computation for the noisy MAX. *Int J Intell Syst* 165–177
20. Dempster A, Laird N, Rubin D (1977) Maximum likelihood from incomplete data via the EM algorithm. *J R Stat Soc* 1–38
21. Musharraf M, Bradbury-Squires D, Khan F, Veitch B, MacKinnon S, Imtiaz S (2014) A virtual experimental technique for data collection for a Bayesian network approach to human reliability analysis. *Reliabil Eng Syst Saf* 1–8
22. Musharraf M, Smith J, Khan F, Veitch B, MacKinnon S (2016) Assessing offshore emergency evacuation behavior in a virtual environment using a Bayesian Network approach. *Reliabil Eng Syst Saf* 28–37
23. Sundaramurthi R, Smidts C (2013) Human reliability modeling for the next generation system code. *Ann Nucl Energy* 137–156

Adaptive Attitude Control of Uncertain Spacecraft with Attitude and Angular Velocity Constraints



Zeyu Kang, Shufan Wu, Xiaoliang Wang, Chao Zhong, and Qiang Shen

Abstract In this paper, the rest-to-rest reorientation problem of the uncertain spacecraft with multiple attitude constrained zones and angular velocity limitations is studied. In order to deal with attitude and angular velocity constraints concurrently, two types of logarithmic potential functions are proposed, where the ineffective attitude constraints are excluded in the design of attitude potential function by introducing a warning angle. In addition, we also designed a projection operator-based adaptive law to estimate the upper bounds of the inertia uncertain parameters and the environmental disturbances, so that the estimation process conforms to the physical meaning of the parameters. Combining the two potential functions and the parameters adaptation law, an adaptive controller is constructed to asymptotically stabilize the attitude reorientation error while satisfying the attitude and the angular velocity constraints. Simulation example of an uncertain spacecraft with rest-to-rest attitude maneuver

This work is supported by (1) National Natural Science Foundation of China under Grant, U20B2054. (2) Shanghai Sailing Program under Grant, 20YF1421600. (3) Natural Science Foundation of Shanghai under Grant, 20ZR1427000. (4) SAST-SJTU advanced space technology joint research fund, USCAST2019-22.

Z. Kang · S. Wu (✉) · X. Wang · Q. Shen
Shanghai Jiao Tong University, Shanghai 200240, Republic of China
e-mail: shufan.wu@sjtu.edu.cn

Z. Kang
e-mail: kangzeyu@sjtu.edu.cn

X. Wang
e-mail: xlwang12321@sjtu.edu.cn

Q. Shen
e-mail: qiangshen@sjtu.edu.cn

C. Zhong
Institute of Shanghai Aerospace Control Technology, Shanghai 200240, Republic of China
e-mail: zhongchao0327@163.com

© The Author(s), under exclusive license to Springer Nature Singapore Pte Ltd. 2023
Z. Jing and D. Strelets (eds.), *Proceedings of the International Conference on Aerospace System Science and Engineering 2021*, Lecture Notes in Electrical Engineering 849,
https://doi.org/10.1007/978-981-16-8154-7_24

subject to constraints on attitude and angular velocity is carried out, and the obtained results verify the effectiveness of the proposed adaptive attitude controller.

Keywords Inertia uncertainty · Attitude constraint · Angular velocity constraint

1 Introduction

In recent years, the spacecraft attitude control is a research hotspot, which is to reorientate the spacecraft to the desired orientation. Researchers have proposed many methods to improve the performance and autonomy of spacecraft attitude control, such as inverse optimal control [1], adaptive control [2], fuzzy adaptive control [3], backstepping control [4], integral-type sliding mode control [5], nonlinear model predictive control [6] and others. In order to improve the safety and maneuverability of spacecraft, large-angle reorientation under attitude and angular velocity constraints as well as inertia uncertainties have been extensively studied recently.

The scientific spacecraft is usually equipped with light-sensitive spaceborne equipment, such as telescope and interferometer, which are required to change its pointing direction while keeping away from exposing to bright celestials. There are two main methods to solve this attitude-constrained control problem, i.e., the path planning-based method and the potential function-based method. Since the path planning-based methods [7] have complex structure and expensive computation, it is not conducive to spaceborne calculation. In contrast, the potential function-based methods incorporate the negative gradient of artificial potential into the controller design, resulting in an analytic attitude controller that is suitable for real-time onboard computation. In [8], a Gaussian function-based potential function was used for spacecraft attitude controller design. In [9], Lee constructed a convex logarithmic-type potential function, with an attitude controller that guarantees asymptotic error convergence and satisfies the attitude constrained of the attitude forbidden and mandatory regions. In [10], a quadratic potential function was proposed to parametrize attitude-constrained regions. In [11], considering the pointing deviation of the spaceborne equipment while avoiding the attitude-constrained zones, a virtual attitude controller is designed by using robust logarithmic potential function.

Another practical constraint in spacecraft attitude controller design is the predefined bound of angular velocity determined by performance requirement or saturation limit of rate gyros. To satisfy the angular velocity constraint, Wie developed a cascade quaternion feedback controller for large-angle slew problem by using saturation functions [12], whereas the stability analysis was not provided. In [13], a nonlinear attitude controller combined with a control allocation strategy was proposed to achieve attitude reorientation despite actuator saturation limitation and angular velocity constraints. In [14], the fault-tolerant attitude tracking problem was studied when there are actuator failures and angular velocity constraints in controller design. In [15], a bounded adaptive controller was designed to achieve attitude stabilization of spacecraft subject to angular rate constraint, where the neural network approx-

imation and command filter accounting for actuator saturation compensation and the assigned angular velocity respectively are utilized. In [16], Shen presented an adaptive controller to solve the constrained rigid body reorientation problem, where multiple attitude-constrained zones and angular rate limits are taken into account. However, the aforementioned methods do not consider the spacecraft inertia uncertainty, which may deteriorate the control performance.

In this work, we designed an adaptive attitude controller to achieve asymptotic redirection for inertia uncertain spacecraft under attitude-constrained zones and angular velocity constraints. First, two logarithmic potential functions are constructed to describe potential fields of attitude constraints and angular velocity limitations, respectively. Then, an adaptive attitude controller considering inertia uncertainty is designed to stabilize the spacecraft asymptotically. Finally, the effectiveness of the proposed adaptive attitude controller is verified by using a numerical simulation. The main contributions of this work are summarized as follows:

- (1) In contrast to the existing potential function-based attitude controllers [8–10, 16], the proposed adaptive controller can not only satisfy the attitude and angular velocity constraints but also deal with the inertia uncertainty and external disturbances of spacecraft, thus improving the performance of the controller.
- (2) The warning angle is introduced into the attitude potential function design, which can speed up the convergence rate of the error.
- (3) The proposed adaptive controller uses a smooth projection operator to design the adaptation law for inertia uncertainty and external disturbances, making the estimated parameters closer to their physical values.

2 Preliminaries

2.1 Spacecraft Dynamic Model

The attitude of spacecraft is described by unit quaternion

$$\mathbb{Q}_u = \{ \mathbf{Q} = [\mathbf{q}^T, q_0]^T \in \mathbb{R}^3 \times \mathbb{R} \mid \mathbf{q}^T \mathbf{q} + q_0^2 = 1 \}, \quad (1)$$

where $\mathbf{q} \in \mathbb{R}^3$ is the vector part and $q_0 \in \mathbb{R}$ represents the scalar part. Let $\mathbf{Q}_d \in \mathbb{Q}_u$ denotes the desired attitude. The unit-quaternion error $\mathbf{Q}_e = [\mathbf{q}_e^T, q_{e0}]^T = [q_{e1}, q_{e2}, q_{e3}, q_{e0}]^T \in \mathbb{Q}_u$ can be obtained as $\mathbf{Q}_e = \mathbf{Q}_d^* \odot \mathbf{Q} = [\mathbf{q}_e^T, q_{e0}]^T$, where \odot is the quaternion multiplication operator, and the quaternion conjugate or inverse is defined as $\mathbf{Q}^* = [-\mathbf{q}^T, q_0]^T$. Moreover, in the desired reference frame \mathcal{N} , we denote $\boldsymbol{\omega}_d$ as the desired angular velocity. In addition, this paper focuses on the rest-to-rest reorientation control, and hence $\boldsymbol{\omega}_d = 0$.

Then, the dynamics and kinematics model of the spacecraft with inertial uncertainty can be described as [17]:

$$\mathbf{J}\dot{\boldsymbol{\omega}} = -\mathbf{S}(\boldsymbol{\omega})\mathbf{J}\boldsymbol{\omega} + \mathbf{u} + \mathbf{d}, \tag{2}$$

$$\dot{\mathbf{q}}_e = \frac{1}{2} \begin{bmatrix} \mathbf{S}(\mathbf{q}_e) + q_{e0}\mathbf{I}_3 \\ -\mathbf{q}_e^T \end{bmatrix} \boldsymbol{\omega} \tag{3}$$

where the matrix $\mathbf{S}(\mathbf{x}) \in \mathbb{R}^{3 \times 3}$ denotes a skew-symmetric matrix, the vector $\boldsymbol{\omega} \in \mathbb{R}^3$ is the angular velocity of the spacecraft in the body frame \mathcal{B} with respect to an inertial frame \mathcal{I} , $\mathbf{u} \in \mathbb{R}^3$ denotes the resultant control torque acting on the spacecraft, and the environmental disturbance is denoted as $\mathbf{d} \in \mathbb{R}^3$.

Assumption 1 The environmental disturbance \mathbf{d} of the spacecraft is assumed to be upper bounded by $\|\mathbf{d}\| \leq d_{\max}$ with d_{\max} being a positive scalar, and $\|\cdot\|$ is the Euclidean norm.

The uncertain inertia matrix $\mathbf{J} \in \mathbb{R}^{3 \times 3}$ of the spacecraft is decomposed as

$$\mathbf{J} = \mathbf{J}_0 + \mathbf{J}_1, \tag{4}$$

where \mathbf{J}_0 and \mathbf{J}_1 denote the nominal/known part and unknown part of the inertia \mathbf{J} , respectively. Here, we also assume that \mathbf{J}_1 is bounded, i.e., $\|\mathbf{J}_1\| \leq J_{1,\max}$. Then, the dynamics in (2) can be written as

$$\mathbf{J}_0\dot{\boldsymbol{\omega}} = -\mathbf{S}(\boldsymbol{\omega})\mathbf{J}_0\boldsymbol{\omega} + \mathbf{u} + \mathbf{d} - \mathbf{J}_1\dot{\boldsymbol{\omega}} - \mathbf{S}(\boldsymbol{\omega})\mathbf{J}_1\boldsymbol{\omega}. \tag{5}$$

Motivated by [17], the following lemma is developed:

Lemma 1 *The nonlinear term $\mathbf{d} - \mathbf{J}_1\dot{\boldsymbol{\omega}} - \mathbf{S}(\boldsymbol{\omega})\mathbf{J}_1\boldsymbol{\omega}$ in (5) satisfies*

$$\|\mathbf{d} - \mathbf{J}_1\dot{\boldsymbol{\omega}} - \mathbf{S}(\boldsymbol{\omega})\mathbf{J}_1\boldsymbol{\omega}\| \leq Dh(\mathbf{q}_e, \boldsymbol{\omega}), \tag{6}$$

where the scalar $D \triangleq \max(\|\mathbf{d}\| + D_0\|\mathbf{J}_1\|, (D_0 + r_4)\|\mathbf{J}_1\|)$ being an unknown positive scalar satisfies $\|D\| \leq D_{\max}$, and $h(\mathbf{q}_e, \boldsymbol{\omega}) = 1 + \|\mathbf{q}_e\| + \|\boldsymbol{\omega}\| + \|\boldsymbol{\omega}\|^2$.

Proof According to the kinematics (3) and dynamics (2), $\dot{\boldsymbol{\omega}}$ can be expressed as a function of \mathbf{q}_e , $\boldsymbol{\omega}$ and \mathbf{u} , i.e., $\dot{\boldsymbol{\omega}} = f(\mathbf{q}_e, \boldsymbol{\omega}, \mathbf{u})$. Since \mathbf{u} can be expressed as $\mathbf{u} = g(\mathbf{q}_e, \boldsymbol{\omega})$, we have

$$\dot{\boldsymbol{\omega}} = f(\mathbf{q}_e, \boldsymbol{\omega}, g(\mathbf{q}_e, \boldsymbol{\omega})).$$

Assuming that the function f is linear with respect to \mathbf{q}_e , $\boldsymbol{\omega}$, $\boldsymbol{\omega}^T\boldsymbol{\omega}$, then taking Euclidean norm on both sides of the above equation yields

$$\begin{aligned} \|\dot{\boldsymbol{\omega}}\| &\leq r_0\|\boldsymbol{\omega}\| + r_1\|\boldsymbol{\omega}\|^2 + r_2\|\mathbf{q}_e\| + r_3 \\ &\leq D_0(1 + \|\mathbf{q}_e\| + \|\boldsymbol{\omega}\| + \|\boldsymbol{\omega}\|^2), \end{aligned}$$

where r_0, r_1, r_2 and r_3 are unknown positive constant, $D_0 = \max(r_0, r_1, r_2, r_3)$. Consequently, the following inequality holds:

$$\begin{aligned}
\|\mathbf{d} - \mathbf{J}_1 \dot{\boldsymbol{\omega}} - \mathbf{S}(\boldsymbol{\omega}) \mathbf{J}_1 \boldsymbol{\omega}\| &\leq \|\mathbf{d}\| + \|\mathbf{J}_1\| \|\dot{\boldsymbol{\omega}}\| + r_4 \|\mathbf{J}_1\| \|\boldsymbol{\omega}\|^2 \\
&\leq \|\mathbf{d}\| + D_0 \|\mathbf{J}_1\| (1 + \|\mathbf{q}_e\| + \|\boldsymbol{\omega}\| + \|\boldsymbol{\omega}\|^2) + r_4 \|\mathbf{J}_1\| \|\boldsymbol{\omega}\|^2 \\
&\leq \|\mathbf{d}\| + D_0 \|\mathbf{J}_1\| + D_0 \|\mathbf{J}_1\| \|\mathbf{q}_e\| + D_0 \|\mathbf{J}_1\| \|\boldsymbol{\omega}\| + (D_0 + r_4) \|\mathbf{J}_1\| \|\boldsymbol{\omega}\|^2 \\
&\leq Dh(\mathbf{q}_e, \boldsymbol{\omega}),
\end{aligned}$$

where $D \triangleq \max(\|\mathbf{d}\| + D_0 \|\mathbf{J}_1\|, (D_0 + r_4) \|\mathbf{J}_1\|)$.

Since the unknown positive constant r_4 , $\|\mathbf{d}\|$ and $\|\mathbf{J}_1\|$ are bounded, the unknown positive constant D can be assumed to satisfy $\|D\| \leq D_{\max}$ with D_{\max} being an unknown positive constant.

2.2 Attitude Constrained Zones

Supposing that the pointing direction of the sensitive spaceborne equipment is expressed as \mathbf{y}_i in the body frame \mathcal{B} , and the corresponding pointing direction in the inertial frame \mathcal{I} is derived by

$$\mathbf{y}'_i = \mathbf{Q} \odot \mathbf{y}_i \odot \mathbf{Q}^* = \mathbf{y}_i - 2(\mathbf{q}^T \mathbf{q}) \mathbf{y}_i + 2(\mathbf{q}^T \mathbf{y}_i) \mathbf{q} + 2q_0 (\mathbf{y}_i \times \mathbf{q}) \quad (7)$$

where \mathbf{x}_j is the normalized vector pointing toward the certain bright object in the inertial frame \mathcal{I} . As depicted in Fig. 1, in order to avoid the bright object, the angle between the \mathbf{y}'_i and \mathbf{x}_j (i.e., β_i^j) is required to be strictly greater than θ_i^j . That is, the constraint $\beta_i^j > \theta_i^j$ with $0 < \theta_i^j < \pi$ should be maintained, which can be formulated as

$$\mathbf{x}_j \cdot \mathbf{y}'_i < \cos(\theta_i^j). \quad (8)$$

Substituting (7) into (8) leads to

$$2\mathbf{q}^T \mathbf{y}_i \mathbf{q}^T \mathbf{x}_j - \mathbf{q}^T \mathbf{q} \mathbf{x}_j^T \mathbf{y}_i + q_0^2 \mathbf{x}_j^T \mathbf{y}_i + 2q_0 \mathbf{q}^T (\mathbf{x}_j \times \mathbf{y}_i) < \cos(\theta_i^j). \quad (9)$$

Then, the constraint (9) can be further written as [9]

$$\mathbf{Q}^T \mathbf{M}_i^j \mathbf{Q} < 0, \quad (10)$$

where the matrix \mathbf{M}_i^j associated with the j th bright celestial object and the i th sensitive spaceborne equipment ($j = 1, \dots, m$ and $i = 1, \dots, n$) is defined as

$$\begin{aligned}
\mathbf{M}_i^j &= \begin{bmatrix} \mathbf{A}_i^j & \mathbf{b}_i^j \\ \mathbf{b}_i^{jT} & d_i^j \end{bmatrix}, \mathbf{b}_i^j = \mathbf{x}_j \times \mathbf{y}_i, d_i^j = \mathbf{x}_j^T \mathbf{y}_i - \cos(\theta_i^j), \\
\mathbf{A}_i^j &= \mathbf{x}_j \mathbf{y}_i^T + \mathbf{y}_i \mathbf{x}_j^T - (\mathbf{x}_j^T \mathbf{y}_i + \cos(\theta_i^j)) \mathbf{I}_3.
\end{aligned} \quad (11)$$

Fig. 1 Schematic diagram of the attitude-constrained zone

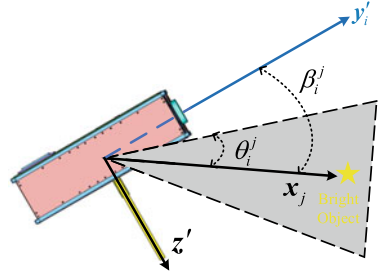
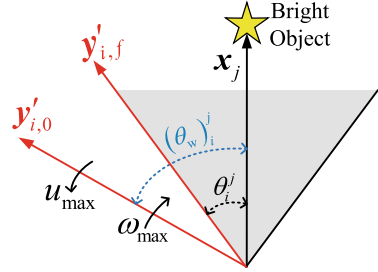


Fig. 2 Demonstration of warning angle



As a consequence, the set of attitudes $\mathcal{Q}_{F_i^j} \subseteq \mathcal{Q}_u$ that are outside of the j th attitude constrained zone for the i th sensitive equipment can be described as

$$\mathcal{Q}_{F_i^j} = \left\{ \mathcal{Q} \in \mathcal{Q}_u \mid \mathcal{Q}^T M_i^j(\theta_i^j) \mathcal{Q} < 0 \right\}. \quad (12)$$

Generally, we need to take into consideration the attitude-constrained zones that are related to all n sensitive spaceborne instrument and their associated m bright celestial objects.

In addition, the concept of warning angle is introduced to specify the necessary attitude-constrained zones that are to be considered in the potential function design.

As shown in Fig. 2, the warning angle inspired by [11] can be obtained as

$$(\theta_w)_i^j = \frac{1}{2} \frac{J_{\max}}{u_{\max}} \omega_{\max}^2 + \theta_i^j, \quad (13)$$

where J_{\max} is the inertia of the major principal axis, u_{\max} is the maximum torque acted to decelerate the spacecraft, ω_{\max} is the maximum angular velocity.

Remark 1 The defined warning angle helps to exclude the ineffective attitude constraints in the potential function design. To be more specific, if the angle between the normalized vector x_j pointing to a bright object and the pointing direction vector y_i' is greater than the warning angle, i.e., $\beta_i^j > (\theta_w)_i^j$, the influence of the j th attitude constrained zone to the i th sensitive spaceborne equipment can be ignored in the construction of the potential field.

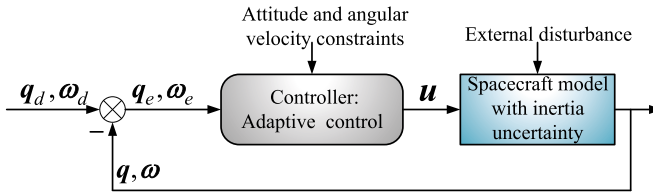


Fig. 3 Structure diagram of the spacecraft attitude control

2.3 Angular Velocity Constraints

In practical spacecraft missions, angular velocity constraints may be required as a result of the limited measurement range of the rate gyroscopes or scientific mission requirements. The set of allowable angular velocity is expressed as

$$W = \{ \omega \in \mathbb{R}^3 \mid |\omega_i| \leq \omega_{i,\max} \}, \tag{14}$$

where $\omega_{i,\max} (i = 1, 2, 3)$ is the limitation of allowable angular velocity for each axis.

3 Problem Statement

The schematic diagram of the attitude control system is shown in Fig. 3, where two problems to be solved in this work are summarized as follows:

Problem 1 (Potential function) Considering the warning angle, design potential functions for the attitude and angular velocity constraints.

Problem 2 (Adaptive Control) Leveraging the proposed potential functions, design an adaptive attitude controller with the projection operator in the adaptive law to achieve asymptotic attitude control despite the presence of the attitude constraints and angular velocity constraints.

4 Potential Function Design

In this section, we solve the Problem 1, where two logarithmic potential functions are proposed for attitude and angular velocity constraints, respectively.

4.1 Potential Function Design for Attitude Constrained Zones

A logarithmic potential function $V_1(\mathbf{Q}) : \mathcal{Q}_p \rightarrow \mathbb{Q}_u$ for the attitude constrained zones is proposed as

$$V_1(\mathbf{Q}) = \|\mathbf{Q}_d - \mathbf{Q}\|^2 \left[\sum_{j=1}^m \sum_{i=1}^n -\alpha k_{ij} \log \left(-\frac{\mathbf{Q}^T \mathbf{M}_i^j(\theta_i^j) \mathbf{Q}}{2} \right) \right] \quad (15)$$

where α is a positive weighting constant, and the parameter k_{ij} relating to the warning angle is defined as

$$k_{ij} = \begin{cases} 0, & \text{if } \beta_i^j > (\theta_w)_i^j \\ 1, & \text{if } \beta_i^j \leq (\theta_w)_i^j. \end{cases} \quad (16)$$

Remark 2 Compared with the existing potential function proposed in [11], the proposed one in (15) considers the effects of the warning angle. When the i th spaceborne sensitive equipment points away from the corresponding j th constrained zone, according to Remark 1, the j th constrained zone can be ignored, i.e., $k_{ij} = 0$. As a result, the unnecessary constrained zones are not taken into account in the potential function design.

4.2 Potential Function Design for Angular Velocity Constraint

In addition, to incorporate the angular velocity constraints defined in (14) in attitude controller design, a logarithmic potential function V_2 is designed as

$$V_2(\boldsymbol{\omega}) = \frac{1}{2} \sum_{i=1}^3 \log \left(\frac{\omega_{i,\max}^2}{\omega_{i,\max}^2 - \omega_i^2} \right). \quad (17)$$

The above potential function satisfies the following lemma:

Lemma 2 *The potential function $V_2(\boldsymbol{\omega})$ has the following three properties:*

- $V_2(\mathbf{0}) = 0$;
- $V_2(\boldsymbol{\omega}) > 0$, for all $\boldsymbol{\omega} \in \mathbf{W} \setminus \{\mathbf{0}\}$;
- $\nabla^2 V_2(\boldsymbol{\omega}) > 0$ is positive for all $\boldsymbol{\omega} \in \mathbf{W}$.

Proof Based on the defined logarithmic potential function $V_2(\boldsymbol{\omega})$, it is trivial to verify that $V_2(0) = 0$. In addition, the following inequality

$$\frac{\omega_{i,\max}^2}{\omega_{i,\max}^2 - \omega_i^2} > 1 \quad (18)$$

holds for all $\omega \in \mathbf{W} \setminus \{0\}$, which subsequently yields

$$\log \left(\frac{\omega_{i,\max}^2}{\omega_{i,\max}^2 - \omega_i^2} \right) > 0, \quad (19)$$

hence, $V_2(\omega) > 0$, for all $\omega \in \mathbf{W} \setminus \{0\}$.

As the third property of Lemma 2, due to the fact that the three terms in the potential function $V_2(\omega)$ are independent, it is sufficient to only have a detailed analysis to one of the three terms. Taking ω_1 as an example, we have

$$V_2(\omega_1) = \log \left(\frac{\omega_{1,\max}^2}{\omega_{1,\max}^2 - \omega_1^2} \right). \quad (20)$$

The gradient of $V_2(\omega_1)$ can be calculated as

$$\nabla V_2(\omega_1) = \frac{\omega_1}{\omega_{1,\max}^2 - \omega_1^2}. \quad (21)$$

Consequently, the Hessian $\nabla^2 V_2(\omega_1)$ can be given as

$$\nabla^2 V_2(\omega_1) = \frac{\omega_{1,\max}^2 + \omega_1^2}{(\omega_{1,\max}^2 - \omega_1^2)^2} > 0. \quad (22)$$

Therefore, it is clear that $\nabla^2 V_2(\omega) > 0$ if $\omega \in \mathbf{W}$.

5 Adaptive Controller Design

In this section, the Problem 2 is solved by leveraging the proposed potential functions, leading to an adaptive attitude controller that realize the spacecraft attitude redirection in the presence of inertia uncertainty. The adaptive controller is designed as

$$\begin{aligned} \mathbf{u} = & \mathbf{S}(\omega) \mathbf{J}_0 \omega - k_1 \mathbf{q}_e^T \mathbf{q}_e \Phi \frac{\tanh(\omega)}{\|\omega\|} - k_2 \Phi \omega - 2k_3 \Phi \mathbf{q}_e \\ & + k_4 \Phi \text{Vec}[(\nabla V_1^* \odot \mathbf{Q})] - \hat{D}_{\max} h(\omega, \mathbf{q}_e) \tanh(\Phi^{-1} \omega) \end{aligned} \quad (23)$$

where $\Phi = \lambda \mathbf{J}_0^{-1}$ with $\lambda = \text{diag}\{(\omega_{1,\max}^2 - \omega_1^2), (\omega_{2,\max}^2 - \omega_2^2), (\omega_{3,\max}^2 - \omega_3^2)\}$, and k_1, k_2, k_3 and k_4 are positive constants, \hat{D}_{\max} is the estimate of the unknown scalar D_{\max} in Lemma 1.

To construct the adaptive law for \hat{D}_{\max} , we assume that the unknown scalar D_{\max} for \mathbf{D} is also bounded. Define two convex sets as

$$\begin{aligned}\Omega_{D_{\max}} &\triangleq \{D_{\max} \in \mathbb{R} \mid D_{\max}^2 < \epsilon\}, \\ \Omega_{\hat{D}_{\max}} &\triangleq \{\hat{D}_{\max} \in \mathbb{R} \mid \hat{D}_{\max}^2 < \epsilon + \delta\},\end{aligned}\quad (24)$$

where $\epsilon > 0$ and $\delta > 0$ are two known constants. The updating scheme for \hat{D}_{\max} is given by

$$\dot{\hat{D}}_{\max} = \text{Proj}(\hat{D}_{\max}, \Psi), \quad \Psi \triangleq h(\boldsymbol{\omega}, \mathbf{q}_e) \|\boldsymbol{\Phi}^{-1}\boldsymbol{\omega}\|, \quad (25)$$

where the projection operator is constructed as

$$\text{Proj}(\hat{D}_{\max}, \Psi) \triangleq \begin{cases} r\Psi, & \text{if } \hat{D}_{\max}^2 < \epsilon \\ r(\Psi - \frac{(\hat{D}_{\max}^2 - \epsilon)\Psi\hat{D}_{\max}}{\delta\hat{D}_{\max}^2}\hat{D}_{\max}), & \text{if } \hat{D}_{\max}^2 \geq \epsilon \end{cases} \quad (26)$$

where r is a positive constant. The above parameter updating law is locally Lipschitz continuous and guarantees that the estimate \hat{D}_{\max} is always within the convex set defined in (24), i.e., $\hat{D}_{\max} \in \Omega_{\hat{D}_{\max}}$ if $\hat{D}_{\max}(0) \in \Omega_{\hat{D}_{\max}}$.

The stability of the attitude control system is summarized as follows:

Theorem 1 *Consider the attitude kinematics and dynamics of an inertia uncertain spacecraft, as modeled in (3) and (5). The potential function-based attitude controller in (23) combined with an adaptive law in (25) solves the Problem 2, so that $\lim_{t \rightarrow \infty} \mathbf{q}_e(t) = 0$ and $\lim_{t \rightarrow \infty} \boldsymbol{\omega}(t) = 0$ and that attitude and angular velocity constraints are satisfied.*

Proof Choose the following Lyapunov candidate:

$$V = 2k_3(\mathbf{q}_e^T \mathbf{q}_e + (1 - q_{e0})^2) + 2k_4 V_1 + V_2 + V_D, \quad (27)$$

where $V_D = \frac{1}{2r} \tilde{D}_{\max}^2$, and $\tilde{D}_{\max} = \hat{D}_{\max} - D_{\max}$ is the estimation error of the D_{\max} . Taking time derivative of V leads to

$$\dot{V} = 2k_3 \mathbf{q}_e^T \boldsymbol{\omega} + 2k_4 \nabla V_1^T [\frac{1}{2} \mathbf{Q} \otimes \mathbf{v}(\boldsymbol{\omega})] + \boldsymbol{\omega}^T \boldsymbol{\Phi}^{-1} \mathbf{J}_0 \dot{\boldsymbol{\omega}} + \frac{1}{r} \tilde{D}_{\max} \dot{\hat{D}}_{\max}. \quad (28)$$

Then, substituting the adaptive controller defined in (23) and adaptive law designed in (25) into the foregoing equation yields

$$\begin{aligned}\dot{V} = & 2k_3 \mathbf{q}_e^T \boldsymbol{\omega} - k_4 \boldsymbol{\omega}^T \text{Vec}[\nabla V_1^* \otimes \mathbf{Q}] + \frac{1}{r} \tilde{D}_{\max} \dot{\hat{D}}_{\max} \\ & + \boldsymbol{\omega}^T \boldsymbol{\Phi}^{-1} \left(-k_1 \mathbf{q}_e^T \mathbf{q}_e \frac{\tanh(\boldsymbol{\omega})}{\|\boldsymbol{\omega}\|} - k_2 \boldsymbol{\Phi} \boldsymbol{\omega} + k_4 \boldsymbol{\Phi} \text{Vec}[(\nabla V_1^* \otimes \mathbf{Q})] \right) \\ & - 2k_3 \boldsymbol{\Phi} \mathbf{q}_e - \hat{D}_{\max} h(\boldsymbol{\omega}) \tanh(\boldsymbol{\Phi}^{-1} \boldsymbol{\omega}) + \mathbf{d} - \mathbf{J}_1 \dot{\boldsymbol{\omega}} - \mathbf{S}(\boldsymbol{\omega}) \mathbf{J}_1 \boldsymbol{\omega},\end{aligned}\quad (29)$$

where $k_3 \nabla V_1^T [\mathbf{Q} \otimes \mathbf{v}(\boldsymbol{\omega})] = -k_3 \boldsymbol{\omega}^T \text{Vec}[\nabla V_1^* \otimes \mathbf{Q}]$ is using. Then, by substituting (6) further research can be obtained

$$\begin{aligned} \dot{V} &\leq -k_1 \|\mathbf{q}_e\|^2 - k_2 \|\boldsymbol{\omega}\|^2 - \tilde{D}_{\max} h(\boldsymbol{\omega}, \mathbf{q}_e) \|\boldsymbol{\Phi}^{-1} \boldsymbol{\omega}\| + \frac{1}{r} \tilde{D}_{\max} \dot{\tilde{D}}_{\max} \\ &\leq -k_1 \|\mathbf{q}_e\|^2 - k_2 \|\boldsymbol{\omega}\|^2 + \frac{1}{r} \tilde{D}_{\max} (\dot{\tilde{D}}_{\max} - r h(\boldsymbol{\omega}, \mathbf{q}_e) \|\boldsymbol{\Phi}^{-1} \boldsymbol{\omega}\|) \\ &\leq -k_1 \|\mathbf{q}_e\|^2 - k_2 \|\boldsymbol{\omega}\|^2 + \frac{1}{r} \tilde{D}_{\max} (\dot{\tilde{D}}_{\max} - r \Psi) \end{aligned} \quad (30)$$

which is negative semi-definite if

$$\frac{1}{r} \tilde{D}_{\max} (\dot{\tilde{D}}_{\max} - r \Psi) \leq 0. \quad (31)$$

According to the adaptive updating law of \hat{D}_{\max} in (25), $\frac{1}{r} \tilde{D}_{\max} (\dot{\tilde{D}}_{\max} - r \Psi) \leq 0$ if $\|\hat{D}_{\max}\|^2 < \epsilon$. Furthermore, if $\|\hat{D}_{\max}\|^2 \geq \epsilon$ and $\Psi \hat{D}_{\max} > 0$, then we have

$$\begin{aligned} \frac{1}{r} \tilde{D}_{\max} (\dot{\tilde{D}}_{\max} - r \Psi) &= \frac{1}{r} \tilde{D}_{\max} (r(\Psi - \frac{(\hat{D}_{\max}^2 - \epsilon) \Psi \hat{D}_{\max}}{\delta \hat{D}_{\max}^2} \hat{D}_{\max}) - r \Psi) \\ &= -(\frac{(\hat{D}_{\max}^2 - \epsilon) \Psi \hat{D}_{\max}}{\delta \hat{D}_{\max}^2} \tilde{D}_{\max} \hat{D}_{\max}) \leq 0 \end{aligned} \quad (32)$$

Since $\tilde{D}_{\max} \hat{D}_{\max} = \hat{D}_{\max}^2 - D_{\max} \hat{D}_{\max} \geq 0$ when $\hat{D}_{\max}^2 \geq \epsilon$. Therefore, we have the result that (31) is satisfied by using the proposed adaptive law. Therefore, we have that \dot{V} satisfies

$$\dot{V} \leq -k_1 \|\mathbf{q}_e\|^2 - k_2 \|\boldsymbol{\omega}\|^2 \leq 0. \quad (33)$$

Consequently, by invoking Barbalat's Lemma [19], it is clear that $\lim_{t \rightarrow \infty} \mathbf{q}_e(t) = 0$ and $\lim_{t \rightarrow \infty} \boldsymbol{\omega}(t) = 0$.

Remark 3 Note that in (23), the term of the positive scalars k_1 and k_3 is related to the attitude convergence rate, when their values are increased, the attitude convergence speed will be accelerated, but excessive angular velocity causes the sensitive equipment to enter the attitude constrained zones. The scalars k_2 and k_4 are analogous to the damping terms. When the angular velocity increases, the degree of damping increases, making the state trajectory smoother. In addition, k_4 represents the influence of the attitude-constrained zones. When k_4 becomes larger, it is easier to avoid the attitude-constrained zones.

Table 1 Parameters of attitude constraints

Constrained zones	Center vector (inertial frame)	Angle, deg
Zone 1 (CZ1)	[0;-1;0]	30
Zone 2 (CZ3)	[0.68;0.67;0.28]	20
Zone 3 (CZ3)	[0.38;0;0.925]	25
Zone 4 (CZ4)	[-0.813;0.548;-0.192]	30

6 Simulation Results

The nominal part inertia of spacecraft is

$$\mathbf{J}_0 = \begin{bmatrix} 20 & 0 & 0 \\ 0 & 15 & 0 \\ 0 & 0 & 20 \end{bmatrix} \text{ kg} \cdot \text{m}^2,$$

and the unknown part is set to $\mathbf{J}_1 = 0.1\mathbf{J}_0$. The environmental disturbance is assumed to be

$$\mathbf{d} = 10^{-2} \begin{bmatrix} -1 + 4 \sin(0.03t) + 3 \sin(0.1t + \pi/2) \\ 1.5 - 3 \sin(0.05t + \pi/2) - 1.5 \sin(0.02t) \\ 1 + 2 \sin(0.1t) - 1.5 \sin(0.04t + \pi/2) \end{bmatrix} \text{ N} \cdot \text{m}.$$

The reaction wheels are installed on the x , y , z axes of the spacecraft body coordinate frame \mathcal{B} and are limited by $|\tau_i| \leq 0.25 \text{ N}\cdot\text{m}$ for $i \in \{1, 2, 3\}$. As a result, the output torque needs to satisfy $\|\mathbf{u}\| \leq 0.433 \text{ N}\cdot\text{m}$. Moreover, the maximal angular velocity about each axis is set to be $6^\circ/\text{s}$, i.e., $\|\boldsymbol{\omega}\| \leq 10.4^\circ/\text{s}$.

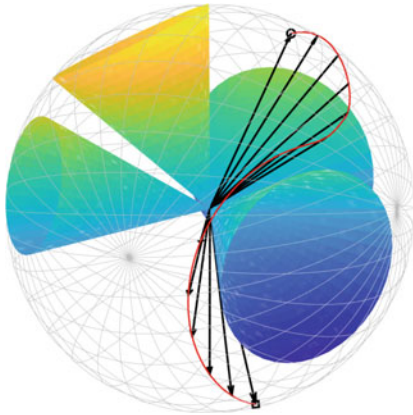
In the simulation, the spacecraft is equipped a sensitive spaceborne equipment, whose boresight vector is along the spacecraft body axis \mathbf{y} . Four attitude constrained zones, which do not overlap with each other, are considered and their details can be found in Table 1. Here, the initial angular velocity is set to be $\boldsymbol{\omega}(0) = [0, 0, 0]^T$ $^\circ/\text{s}$ and the initial attitude is assumed to be $\mathbf{Q}(0) = [-0.352, 0.12, 0, 0.9284]^T$. The desired attitude is $\mathbf{Q}_d = [0.7024, 0.6790, 0, 0.2133]^T$, which is chosen to be outside of four attitude forbidden zones. According to (13), the corresponding warning angles of 4 constrained zones can be obtained as $(\theta_w)_1^1 = 73.6^\circ$, $(\theta_w)_1^2 = 63.6^\circ$, $(\theta_w)_1^3 = 68.6^\circ$ and $(\theta_w)_1^4 = 73.6^\circ$.

6.1 Overall Simulation Result

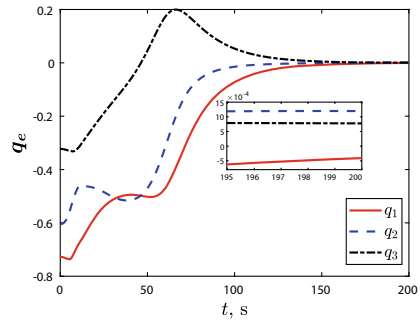
In this subsection, the overall attitude control result under the proposed controller is given. The controller parameters are given in Table 2.

Table 2 Control gains

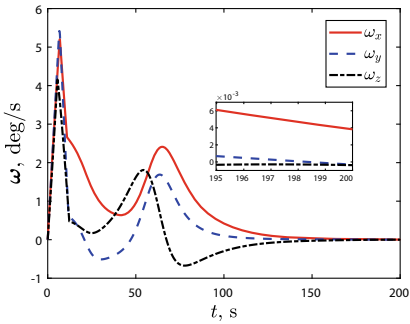
Control schemes	Control gains
The proposed controller (23)	$k_1 = 0.02, k_2 = 120, k_3 = 4, k_4 = 5, \alpha = 0.18, r = 0.2, \varepsilon = 1.5, \delta = 10^{-3}$
Controller (58) in [9]	$\alpha = 160, k_1 = 5.4$
PD controller in [20]	$k_p = 20, k_d = 100$



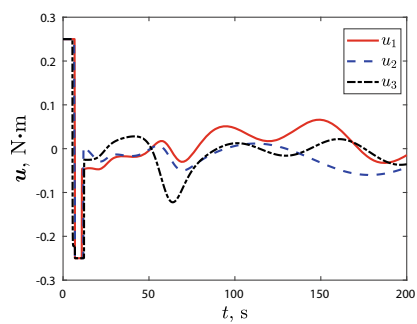
(a) Motion trajectory of sensitive equipment in 3-D



(b) Attitude error vector q_e



(c) Angular velocity vector ω



(d) Actuator output torque u

Fig. 4 Time response of the simulation results under the angular velocity limit of $6^\circ/s$

Fig. 5 The time response of the estimate of the unknown parameter D

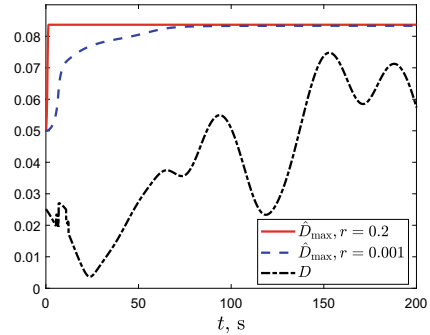


Figure 4 shows the overall simulation results with angular velocity limits $6^\circ/\text{s}$. The 3D trajectories of the sensitive spaceborne equipment pointing direction are depicted in Fig. 4a, it is observed that the proposed adaptive controller (23) based on potential functions (15) and (17) avoids all attitude-constrained zones under the condition of angular velocity limitation. It not only protects the sensitive equipment but also realizes the attitude redirection maneuver.

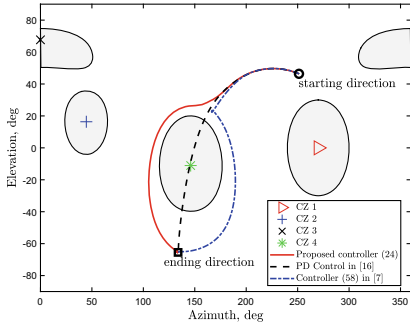
According to Fig. 4b and c, the steady-state attitude error and the angular velocity errors are less than 1.2×10^{-3} and $6 \times 10^{-3}^\circ/\text{s}$, respectively. Both the attitude and angular velocity convergence errors show that the proposed attitude controller (23) can effectively handle the inertia parameter uncertainty and external disturbance despite angular velocity limits. Since the controller output is limited directly in the simulation system, the bang-bang control will appear in the controller output, as shown in Fig. 4d.

As for the estimation of external disturbance and inertial uncertainty, the introduction of projection operator (26) can improve the estimation speed and meet the physical meaning of estimation parameters, as shown in Fig. 5. It is clear that a bigger r only speeds up the estimation without changing the upper bound of the estimated value when other parameters do not change.

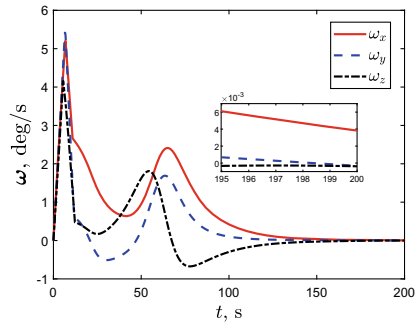
6.2 Comparison Simulation Results

In this subsection, we compare the proposed adaptive controller (23) with existing attitude controllers. For comparison, the controller (58) in [9] and the PD controller in [20] are also implemented. The control gains of three controllers are given in Table 2.

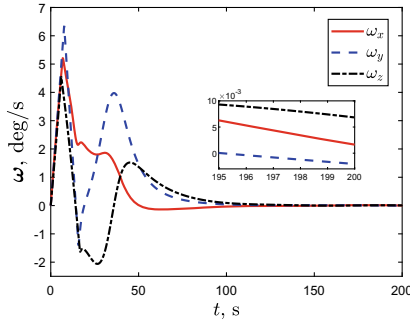
The 2D projection of the pointing direction of sensitive instrument under three controllers is depicted in Fig. 6a. It is observed that trajectories using the PD controller violate attitude constraints, whereas the proposed adaptive controller and the controller (58) in [9] can satisfy attitude constraints.



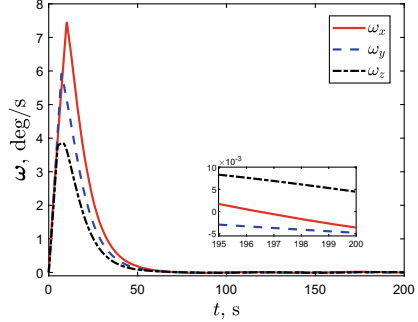
(a) Motion trajectory of sensitive equipment in 2-D under three controllers



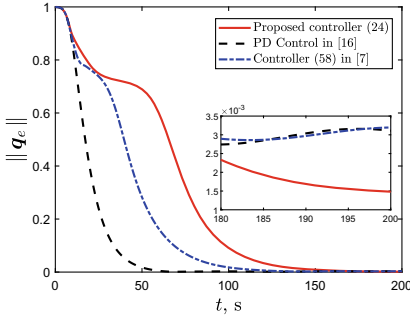
(b) Angular velocity vector ω using the proposed controller



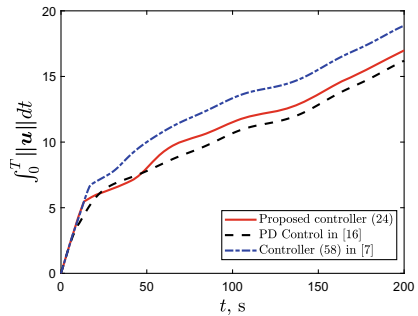
(c) Angular velocity vector ω using the controller (58) in [9]



(d) Angular velocity vector ω using the PD controller in [20]



(e) Attitude error $\|q_e\|$ under three controllers



(f) Energy consumption under three controllers

Fig. 6 Simulation results under three controllers

The angular velocity comparison of the three controllers is presented in Fig. 6b–d, it is clear that the proposed controller satisfies the angular velocity limit of 6 °/s, and both other controllers violate the limit value. The attitude error comparison of the three controllers is presented in Fig. 6e. Since the warning angle is considered in the potential function of the proposed controller, its convergence rate is equivalent to that of PD controller at the beginning of simulation, resulting in improved convergence rate when compared with that of the controller (58) in [9]. Moreover, the proposed controller (23) considers the inertia uncertainty and external disturbance, so the robustness of the controller and control accuracy of attitude error and angular velocity are higher than that of the other two controllers.

In addition, using $\int_0^T \|\mathbf{u}\| dt$ (T is the simulation time) to evaluate the overall energy consumption, it is clear from Fig. 6f that the proposed controller and the controller (58) in [9] spend more energy than the PD controller, which is due to the fact that it has to ensure the spaceborne equipment pointing direction meet the attitude constraints. Then, since the controller (58) in [9] does not consider the angular velocity limit, it takes more energy to accelerate and decelerate with a larger angular velocity than the proposed controller.

7 Conclusions

This work presents a potential function-based adaptive attitude controller to accomplish the attitude redirection for inertia uncertainty spacecraft under attitude constrained zones and angular velocity limitations. By introducing the concept of warning angle, two kinds of logarithmic potential functions are utilized to deal with the attitude constraint and the angular velocity constraint simultaneously. Leveraging the proposed potential functions, we further designed a projection operator-based adaptive law to guarantee that the estimation process conforms to the physical meaning of the estimated parameters. The simulation results demonstrate that the proposed adaptive controller can achieve rest-to-rest attitude redirection despite the presence of inertia uncertainty, angular velocity limitation, multiple attitude-constrained zones, and external disturbances.

References

1. Luo WC, Chu Y-C, Ling K-V (2005) Inverse optimal adaptive control for attitude tracking of spacecraft. *IEEE Trans Autom Control* 50(11):1639–1654. <https://doi.org/10.1109/TAC.2005.858694>
2. Gennaro SD (2003) Output stabilization of flexible spacecraft with active vibration suppression. *IEEE Trans Aerosp Electron Syst* 39(3):747–759. <https://doi.org/10.1109/TAES.2003.1238733>
3. Wang H, Liu PX, Zhao X, Liu X (2020) Adaptive fuzzy finite-time control of nonlinear systems with actuator faults. *IEEE Trans Cybern* 50(5):1786–1797. <https://doi.org/10.1109/TCYB.2019.2902868>

4. Kristiansen R, Nicklasson PJ, Gravdahl JT (2008) Spacecraft coordination control in 6DOF: integrator backstepping vs passivity-based control. *Automatica* 44(11):2896–2901. <https://doi.org/10.1016/j.automatica.2008.04.019>
5. Shen Q, Wang D, Zhu S, Poh EK (2015) Integral-type sliding mode fault-tolerant control for attitude stabilization of spacecraft. *IEEE Trans Control Syst Technol* 23(3):1131–1138. <https://doi.org/10.1109/TCST.2014.2354260>
6. Dong L, Yan J, Yuan X, He H, Sun C (2019) Functional nonlinear model predictive control based on adaptive dynamic programming. *IEEE Trans Control Syst Technol* 49(12):4206–4218. <https://doi.org/10.1109/TCYB.2018.2859801>
7. Angelis ELD, Giuliotti F, Avanzini G (2015) Single-axis pointing of underactuated spacecraft in the presence of path constraints. *J Guid Control Dyn* 38(1):143–147. <https://doi.org/10.2514/1.G000121>
8. McInnes CR (1994) Large angle slew maneuvers with autonomous sun vector avoidance. *J Guid Control Dyn* 17(4):875–877. <https://doi.org/10.2514/3.21283>
9. Lee U, Meshahi M (2014) Feedback control for spacecraft reorientation under attitude constraints via convex potentials. *IEEE Trans Aerosp Electron Syst* 50(4):2578–2592. <https://doi.org/10.1109/TAES.2014.120240>
10. Shen Q, Yue C, Goh CH (2017) Velocity-free attitude reorientation of a flexible spacecraft with attitude constraints. *J Guid Control Dyn* 40(5):1293–1299. <https://doi.org/10.2514/1.G002129>
11. Kang Z, Shen Q, Wu S (2021) Constrained attitude control of over-actuated spacecraft subject to instrument pointing direction deviation. *IEEE Control Syst Lett* 5(6):1958–1963. <https://doi.org/10.1109/LCSYS.2020.3044984>
12. Wie B, Lu J (1995) Feedback control logic for spacecraft eigenaxis rotations under slew rate and control constraints. *J Guid Control Dyn* 18(6):1372–1379. <https://doi.org/10.2514/3.21555>
13. Hu Q, Li B, Zhang Y (2013) Robust attitude control design for spacecraft under assigned velocity and control constraints. *ISA Trans* 52(4):480–493. <https://doi.org/10.1016/j.isatra.2013.03.003>
14. Shen Q, Yue C, Goh CH, Wu B, Wang D (2018) Rigid-body attitude tracking control under actuator faults and angular velocity constraints. *IEEE/ASME Trans Mechatron* 23(3):1338–1349. <https://doi.org/10.1109/TMECH.2018.2812871>
15. Li M, Hou M, Yin C (2016) Adaptive attitude stabilization control design for spacecraft under physical limitations. *J Guid Control Dyn* 39(9):2179–2183. <https://doi.org/10.2514/1.G000348>
16. Shen Q, Yue C, Goh CH, Wu B, Wang D (2018) Rigid-body attitude stabilization with attitude and angular rate constraints. *Automatica* 90:157–163. <https://doi.org/10.1016/j.automatica.2017.12.029>
17. Shen Q, Wang D, Zhu S, Poh K (2015) Finite-time fault-tolerant attitude stabilization for spacecraft with actuator saturation. *IEEE Trans Aerosp Electron Syst* 51(3):2390–2405. <https://doi.org/10.1109/TAES.2015.130725>
18. Khalil HK (1996) Adaptive output feedback control of nonlinear systems represented by input-output models. *IEEE Trans Autom Control* 41(2):177–188. <https://doi.org/10.1109/9.481517>
19. Khalil H (2002) *Nonlinear systems*, 3rd ed. Upper Saddle River, Prentice-Hall. [https://doi.org/10.1016/s0005-1098\(01\)00289-8](https://doi.org/10.1016/s0005-1098(01)00289-8)
20. Wie B (2008) *Space vehicle dynamics and control*. Am Inst Aeronaut Astronaut. <https://doi.org/10.2514/4.860119>

SSS-2A: A 3U CubeSat Project for an In-Orbit Formation Flying Mission



Yixin Huang, Zhongcheng Mu, Sunhao Chu, and Shufan Wu

Abstract The Student Small Satellite (SSS) project is an education and training program for university students to have hands-on experience on the satellite design, development, and implementation practice. It consists of 3 Micro/Nano satellites forming an in-orbit formation flying for technology demonstration and some in-orbit experiments. SSS-1 is a microsatellite of 30 kg mass, being developed by a consortium of 4 countries, with Beihang University as the lead, and being participated by teams from Pakistan, Iran, and Turkey. SSS-2A is a 3U CubeSat, being developed by the Shanghai Jiao Tong University. And the SSS-2B is another 3U CubeSat, being developed by a team from Turkey, together with support from Thailand. This paper mainly introduces the SSS project and further presents the detailed system design and development of the SSS-2A CubeSat, including its main system constitution, main payload selection, and the latest development status and schedule. Technical details of each subsystem will also be discussed and analysed. Some simulation results will be given to show the design performance. It is going to be launched before the end of 2021.

Keywords CubeSat · Formation flying · AIS · Micro-propulsion

This work is supported by (1) China State Key Laboratory of Robotics (Grant No: 19Z1240010018) (2) The office of military and civilian integration development committee of Shanghai (Grant No: 2019-jmrh1-kj3).

Y. Huang · Z. Mu · S. Chu · S. Wu (✉)
Shanghai Jiao Tong University, Shanghai 200240, Republic of China
e-mail: shufan.wu@sjtu.edu.cn

Y. Huang
e-mail: huangyxethan@sjtu.edu.cn

Z. Mu
e-mail: muzhongcheng@sjtu.edu.cn

S. Chu
e-mail: Chu1220@sjtu.edu.cn

© The Author(s), under exclusive license to Springer Nature Singapore Pte Ltd. 2023
Z. Jing and D. Strelets (eds.), *Proceedings of the International Conference on Aerospace System Science and Engineering 2021*, Lecture Notes in Electrical Engineering 849,
https://doi.org/10.1007/978-981-16-8154-7_25

1 Introduction

The CubeSat concept was developed by California Polytechnic State University and Stanford University in 1999, which set up a set of standards to help university or institution worldwide to perform aerospace missions for science and exploration. A CubeSat is a type of miniaturized satellite which has a volume of exactly one liter (10cm cube) and has a mass of less than 1.33 kg. A CubeSat typically uses commercial off-the-shelf components (COTS) for its components. Due to the standard mechanical and electrical interface, the CubeSat has been worldwide accepted and has developed commercial values of Micro/Nano satellite, which further produced a lot of spin-off high-tech companies dedicated to the CubeSat community. The standard 10cm×10cm×10cm basic CubeSat is called '1U' which means one unit. Based on 1 unit, 'nU' CubeSat can be built and developed flexibly and quickly. The CubeSat standard has brought the Nanosat world into a 'CubeSat Era' [1, 2].

In the early 2000s, it was generally precepted that the CubeSats are just designed to fulfil the requirements of training students and amateur demands [3]. Later on, it was demonstrated that CubeSats could also be used for other applications, such as science missions and testing of new technologies [4]. Nowadays, CubeSats are being considered as a competitive solution for space exploration as they keep equilibrium among crucial variables of a space mission, such as cost, development time, lifetime, reliability and maintenance service. Also, CubeSats represent a trend in miniaturization of spacecraft and associated technologies [5–7].

For CubeSats constellation, there are two research directions. One is to increase the number of satellites to enhance re-visit frequency and coverage, where all the satellites operate similar functions with the same payloads. Another direction is to use a formation or constellation with multiple CubeSats with different payloads to execute an integrated mission. Some commercial companies like Planet Labs, SpaceX, and OneWeb have already demonstrated the former methods by launching a large amount of nano-satellites, while the later direction is more oriented towards distributed payloads or multiple functional satellites forming a network to provide integrated services, which is foreseen an important trend for many applications with low-cost CubeSats. This paper presents a three satellite formation flying mission to verify inter-satellite communication based on low-cost and off-the-shelf CubeSat technologies. This project is funded by Asia-Pacific Space Cooperation Organization (APSCO).

APSCO is a non-profit inner-governmental organization, and it is headquartered in Beijing. By resource sharing in space science, technology, and application, APSCO promotes multilateral cooperation for its members: Bangladesh, China, Iran, Mongolia, Pakistan, Peru, Thailand and Turkey, Indonesia, Mexico and Egypt. APSCO is established for cooperation in the peaceful use of outer space, cooperative activities are focused on capacity-building in its member states through education, training and knowledge-sharing platforms. The outcome of cooperative activities is shared equally among all members.

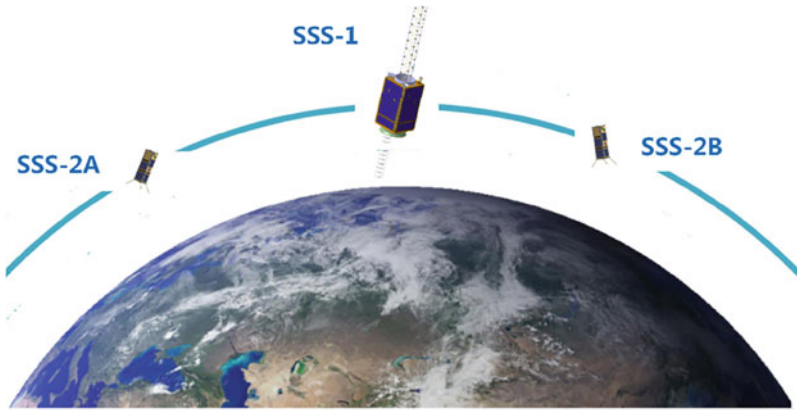


Fig. 1 The APSCO student small satellite mission

The Student Small Satellite (SSS) project is funded by APSCO for training university students to have hands-on experience on the satellite design, development, and implementation practice. The SSS project includes three satellites: one Microsatellite named SSS-1, two CubeSats named SSS-2A and SSS-2B, and the three satellites are targeted to be launched together in 2021. Figure 1 shows the mission concept of the three satellites.

The SSS-1 is a 30 kg Microsatellite with dimension of no more than $350 \times 350 \times 650 \text{ mm}^3$, and it is being developed by a team consisted of 4 countries, include China, Pakistan, Iran and Turkey, Bei Hang University from China takes the lead. Both the SSS-2A/2B are 3U CubeSats, carrying inter-satellite communication payload and micro-propulsion to demonstrate space satellite constellation technologies. SSS-2A is being developed by the Shanghai Jiao Tong University team from China, together with the Pakistan team from the Institute of Space Technology, and the SSS-2B is being developed by a team from Turkey, together with support from Thailand.

This paper further presents the detailed design and development of the SSS-2A CubeSat, including analyses of mission requirements, main system constitution, payloads selection, and the latest development progress. Technical details of each subsystem will be discussed and the design will be justified. Some component specifications and simulation results will be given to show the design performance.

2 Mission Analyses

The performance and capacity of a CubeSat are always constrained by its limited volume, mass, and especially available power onboard. While many space missions need multiple functions linked each other to be provided for different customers to meet

multiple requirements. In the SSS mission, the following fundamental requirements are addressed.

- (1) Demonstrating formation flying capabilities with the 3 satellites in orbit.
- (2) Monitoring the global marine traffic information with an on-board AIS receiver.
- (3) Demonstrating CubeSats adaptive networking technology with an inter-satellite communication system.

2.1 CubeSats Formation Flying

A formation flying (FF) mission involves a set of distributed satellites, capable of autonomous cooperation with another in order to maintain the desired formation. For FF missions, small satellites are suitable, because a large number of satellites can serve as distributed instruments for imaging and other applications agilely with low cost [8]. A typical example is the European QB50 project consisting of 50 CubeSats being launched into a near-circular highly inclined orbit at an expected altitude of about 320 km for formation flying [9].

Micro-propulsion system is essential for orbit correction or maintenance. CubeSat can play more functions and tasks when being placed as a constellation or formation network, where orbital maintenance is a basic requirement. SSS-2A is designed to carry a MEMS cold-gas micro-propulsion module, which is a COTs developed by a commercial company from China, it was demonstrated in a space mission in 2015 successfully.

2.2 Marine Traffic Monitoring from Space

Automatic Identification System (AIS) is a vessel identification system being used for ships over 300 ton and all passenger ships, to broadcast its identification, location, course and speed to other ships and land station to avoid collisions. Satellite AIS is also used for maritime domain awareness, search and rescue, environmental monitoring and maritime intelligence application [10]. Vessels carrying AIS transponders can be tracked by AIS stations located along coast lines. When out of range of networks, Satellite AIS (S-AIS) can track the location of vessels remotely, especially over open oceans and beyond the reach of terrestrial-only AIS systems.

There is apparently a growing interest in satellite-based AIS, which was first proposed in 2003. In 2004, FFI of Norway further investigated the feasibility of AIS messages receiving onboard small satellites and produced prototypes. In 2005 and 2006, Norway launched two 1U CubeSat, NCube-1 and NCube-2, with space-based AIS receiver for test [11]. In 2010, Norway launched AISSAT-1, which is a Nanosatellite and weighs 6 kg, sized by 20×20×20 cm. AISSAT-1 works on polar orbit with a height of 600 km, and successfully collects and transmits downwards

all the ship information about Norway's surrounding sea in a great amount [12]. Besides, the U.S launched TACSAT-2 in 2006, which carried AIS receiver to monitor ships within 2000 sea miles for United States' Coral Guard [13]. After that, countries including Canada, Japan, and multiple European countries followed to study space-based AIS receiver and have built multiple regional AIS system as a result. ORBCOMM became the first commercial service provider of satellite AIS since early 2009. Its next 18 ORBCOMM Generation2 (OG-2) satellites plan to carry AIS receivers.

2.3 Inter-Sat Adaptive Network

With the explosive increase in the number of launched Nano satellites, the highlighted interesting problem is how to build proper communication for CubeSat networks in low earth orbit (LEO), to enhance different services: data collection, internet access, and call inside and outside of the system [14].

Gamalink is a space collaborative project aiming at developing an innovative solution for space communication and attitude determination [15]. The adaptive networking technology is explored by the newly developed Gamalink [16], as an experimental payload. In SSS-2A project, the payload is an advanced component developed by the Tekever Ltd in Portugal which is mainly based on Software-defined Radio (SDR) and Mobile wireless Ad-hoc Networks (MANETs) [16]. The Gamalink component includes the ad-hoc network capability for Inter-satellite link, a GPS receiver and a radio-based attitude determination algorithm. Meanwhile, CubeSat Space Protocol (CSP) will be used to operate inter-satellite communication in this mission. In 2015, the Gamalink was successfully applied in the TW-1 mission and implemented inter-satellite adaptive network experiment [17].

3 Satellite System Design

SSS-2A is a 3U CubeSat with body mounting and deployable solar panels, and passive thermal control except for battery where a heater is applied to ensure certain temperature. Figure 2 shows the external layout of SSS-2A. The satellite chooses solar synchronous orbit of 500km altitude with 10:30 AM as local time of descending node.

The satellite's body coordinate system (O-XYZ) origin is defined in the cubesat center, and the three-axis definition is consistent with the separation mechanism coordinates:

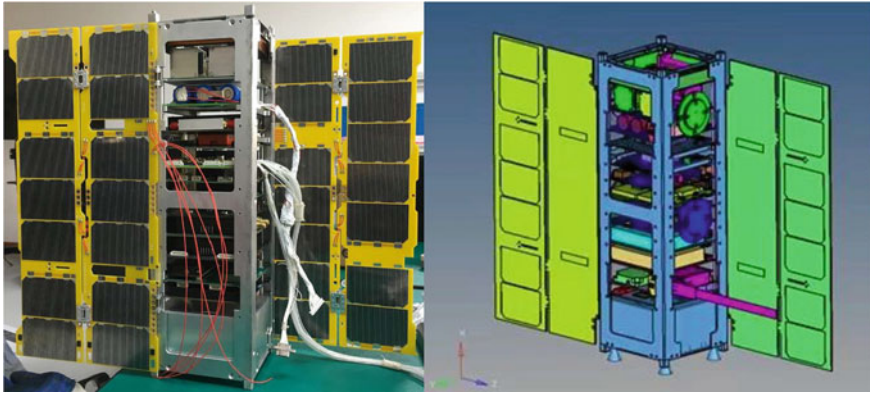


Fig. 2 SSS-2A external equipment layout

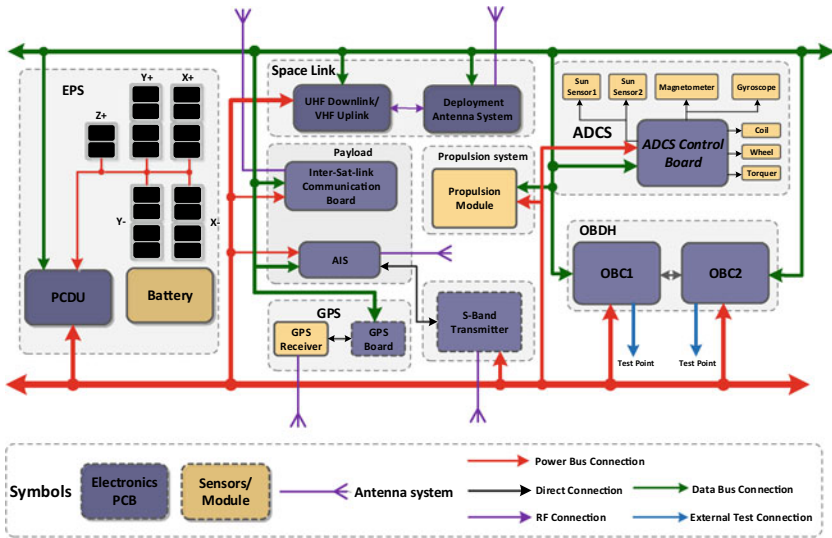


Fig. 3 SSS-2A system block diagram

- (1) The Z axis points to the direction in which the separation mechanism door is opened;
- (2) The X axis points to the installation direction of the internal PC104 of the satellite;
- (3) The Y axis is determined by the rule of the right hand coordinate system.

Figure 3 shows a general system configuration diagram of SSS-2A, indicating data flow, subsystem components and RF connections.

SSS-2A Cubsat is designed and developed according to international Cubesat standard, which mainly includes payload, structure, thermal control, electrical power system (EPS), on-board computer (OBC), attitude and orbit control (AOCS), TT&C,

data transmission and other subsystems. The satellite adopts unified TT&C and satellite affair design. The subsystems are outlined as follows:

(1) Structure

The SSS-2A satellite adopts standard 3U CubeSat structure. The main structure is a frame panel design and single machine stacked installation.

(2) Thermal control

A passive thermal control scheme is used to control the temperature of the whole satellite in the range of $-10\text{ }^{\circ}\text{C} \sim +35\text{ }^{\circ}\text{C}$.

(3) EPS

High efficiency solar array panels and lithium batteries are used for power supply. For different load requirements, the EPS adopts three batteries in series with bus voltage of 11.1 V–12.6 V.

(4) OBC

The satellite subsystem adopts the core processor based on ARM7 architecture and CAN bus communication protocol, intra-satellite communication and management are implemented through the standard PC104 interface of CubeSat.

(5) Attitude control

The three-axis stabilization is realized by magnet control. Sensors are consisted of two sun sensors, one MEMS gyroscope and one three-axis magnetometer. Actuators include four wheels and magnetorquers. The satellite also carries a cold gas micro-propulsion with 4 mN thrust to implement satellite orbit maneuver.

(6) TT&C

UHF/VHF band is used for the telemetry and telecontrol. The uplink rate is 1200 bps, and the downlink rate is 9600 bps.

(7) Data transmission

The satellite uses a S-band data transmitter to transmit payload data, and the maximum data rate could reach 20Mbps.

Based on the mission objectives and tasks assigned to SSS-2A, the satellite system configuration is specified as given in Table 1. A brief introduction for each subsystem comes along in the following table.

Table 1 SSS-2A system specifications

Subsystem	Item	Specification
Structure	Dimension	340.5 × 100 × 100 mm
ADCS	Attitude determination accuracy	≤ 2° (3σ)
	Pointing accuracy	≤ 5° (3σ)
	Pointing stability	≤ 0.1°/s
Thermal	Internal temperature	−10 °C ~ +35 °C
EPS	Bus voltage	10V ~ 12.6 V
	Battery properties	2.6 Ah, 1 year lifetime
TT&C	Frequency	UHF/VHF
	Modulation	BPSK
	Uplink	1200 bps
	Downlink	9600 bps
Data transmitter	Date rate	Maximum 20 Mbps
	Frequency	S band
	Modulation	QPSK
OBC	Process capacity	> 20 MIPS
	Process storage	RAM> 2M, Flash> 256 K

3.1 Integrated Electronic System

The OBC takes the task of managing and processing the whole-satellite data. It schedules satellite task, manages and controls the operation of the satellite equipment and modules efficiently and reliably, manages the time on the satellite, collects and monitors the satellite status, and coordinates with the payload subsystem to complete on-orbit mission. The OBC of SSS-2A consists of 2 cold backup board components, each board has the same design, and Fig. 4 shows the OBC board.

The application software running on the satellite OBC, which is referred as Satellite Flight Software or simply Flight Software (FSW), can be regarded as a system-level entity. It plays a relevant role in implementing space mission to meet complex requirements and is the main interface during the space mission operational phase. The FSW provides all the necessary functions for nominal operations of the satellite. Moreover, it enables the ground users to control and to supervise its various subsystems for the whole mission. Additionally, the FSW manages the mission phases, the satellite modes, the ground interface, the AOCS, the thermal control, the satellite health managements (also referred to as Failure Detection, Isolation, and Recovery (FDIR)), and the on-board mission operation execution. The FSW is in charge of managing the decision-making processes with limited autonomy degree.

For the EPS a space-proven COTS product for CubeSat is chosen. Its photovoltaic solar panel can supply over 30 W power. A maximum power point tracking (MPPT) circuit is adopted for optimal power generation. It has 3 input channels which can

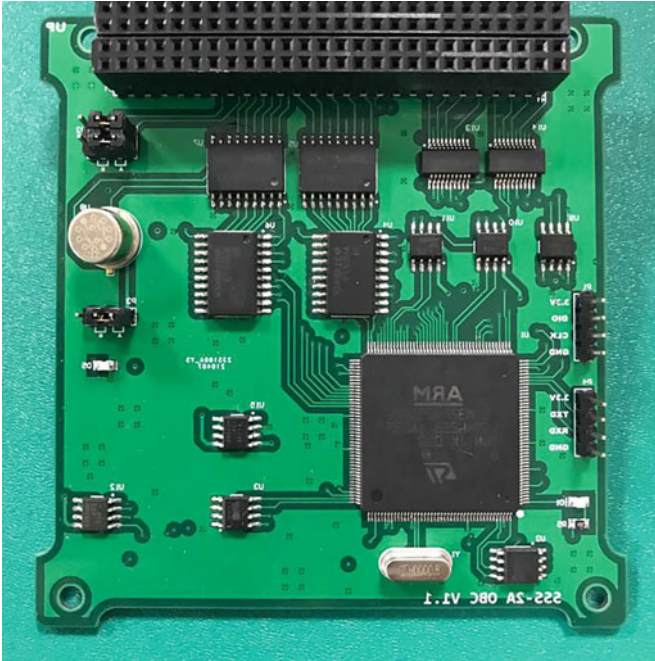


Fig. 4 The on board computer



Fig. 5 The electrical power system

set the power-point with 3 different options independently. The measures for battery under-voltage and over-voltage protection are taken. The number of the regulated power has two 5 V buses and one 12 V bus. The EPS is shown in Fig. 5.

In the simulation, after SSS-2A being released in orbit, each orbit period has a light time of 59.84 min and a shadow time of 34.78 min. Average power output of the solar array each orbit is 14.98 W. When the CubeSat is in shadow zone, the Lithium-battery alone can supply over 20 W power, when in solar zone, the battery and solar panels can together provide over 30 W power together.

3.2 Communication System

For TM/TC, a UHF downlink and VHF uplink full duplex transceiver is chosen and the data rate is chosen as 9.6 kbps to leave more communication budget margin though the selected transmitter has a much higher capacity. For data transmission, an S-band transmitter is used, working at frequency of 2405 MHz. Except as a downlink for payload data, the S-band transmitter is also as a backup of TM/TC. Figure 6 shows the UHF/VHF transceiver and the USB transmitter.

3.3 AOC System

The AOCS is designed for the required spacecraft attitude and orbit control during all mission phases and in particular for high pointing accuracy during science observation. The major tasks are

- (1) Stabilization of the spacecraft after separation from the launcher.
- (2) Autonomous attitude acquisition and determination.
- (3) Stabilization and control of the attitude in 3 axes with pointing and stability requirements.
- (4) Orbit maneuver during formation flying.

Table 2 shows the mainly configuration of the AOCS in SSS-2A, and sensors and actuators being used.

The ADCS has 3 modes in orbit, detumbling mode, sun pointing mode and nadir pointing mode. After separation, the SSS-2A will use a magnetometer, a gyro and a magnetorquer to damp the initial angular rate of the CubeSat. In this mode, Bdot can be obtained by differential measurement of the magnetometer, and then the corresponding magnetic moment can be determined. The magnetic moment of the magnetorquer interacts with the Earth magnetic field to generate a control torque to damp the rate. Detumbling mode simulation results are showed in Fig. 7.

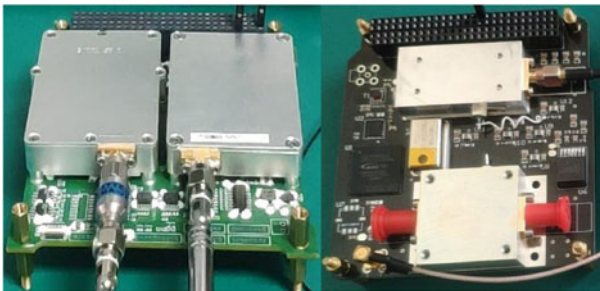


Fig. 6 UHF/VHF transceiver and USB transmitter

Table 2 Configuration of the AOCS system

Unit	Item
Fine sun sensor (×2)	FOV: 120°
	Accuracy: ±0.5°
	Sampling period: 10 ms
Ggyroscope (×1)	Range: −225°/s ~ 225°
	Accuracy: 0.007°/s
Magnetometer (×2)	Range: −400000~400000 nT
	Resolution: 700 nT
	Sampling period: 10 ms
	Output frequency: 10 Hz
Magnetorquer (×1)	Magnetic moment: > 300 mAm2
Reaction wheel (×4)	Nominal rotating speed: ±8000 rpm
	Nominal torque: 0.023 mNm
	Momentum storage: 1.77 mNms

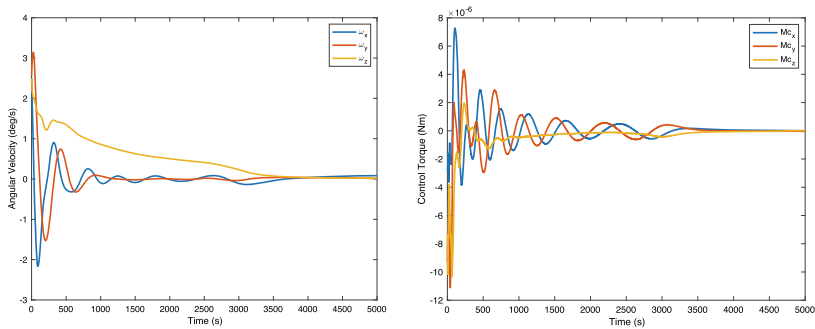


Fig. 7 Angular velocity and control moment simulation in the detumbling mode

After the end of the rate damping, the sun pointing should be achieved in the first orbits for energy charging. The magnetorquer is used to implement the sun pointing control to ensure the energy demand. The attitude determination units involved in the work are sun sensors and magnetometers. A three-axis magnetic control scheme for the sun pointing is adopted. Figure 8 shows results of sun pointing mode simulation.

In the nadir pointing mode, the dual-vector attitude determination is performed with the magnetometer and the sun sensor outputs. When in the shadow area or the sun sensor output is invalid, the double vector EKF attitude setting scheme is adopted; the 3-axis reaction wheel is used for the main attitude control actuators, which is showed in Fig. 9.

The magnetorquer can be used to unload the speed of the momentum wheel. When there is a reaction wheel failure and the Y-direction reaction wheel is normal, the three-axis wheel control scheme is switched to the biased momentum control

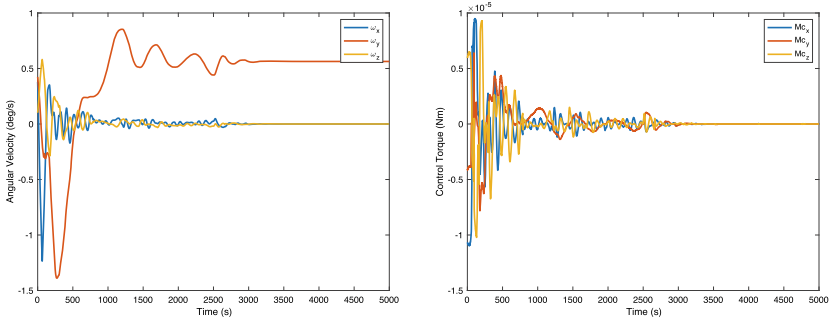


Fig. 8 Angular velocity and control moment simulation in the sun pointing mode

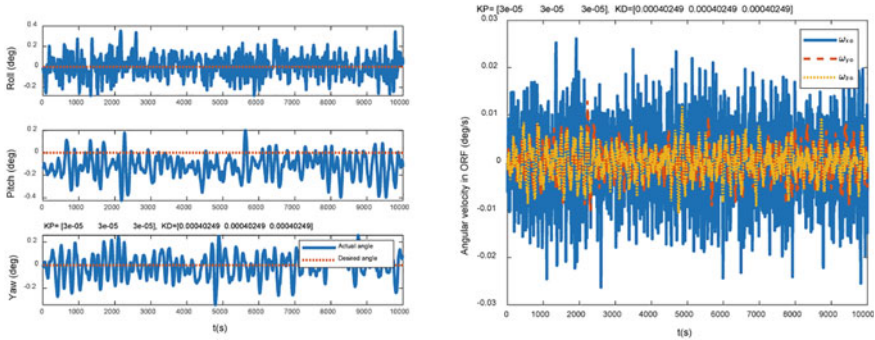


Fig. 9 Nadir pointing mode simulation results (3-axis reaction wheel)

mode. If the Y-direction reaction wheel fails, a three-axis magnetic control scheme is adopted, which is showed in Fig. 10.

Figure 11 shows the MEMS Micro-propulsion system, and it can carry 50g propellant and provide 4mN thrust (1mN each nozzle) for orbit maneuver during formation flying. The volume of the propulsion is 10×10×5cm, which is a standard CubeSat component.

The orbital control strategy design of the orbital mission needs to comprehensively consider the constraints of propulsion, measurement and control, attitude control, etc. and arrange the orbital control reasonably, so that the control quantity can meet the accuracy requirements of the measuring rail within the scope of propulsion capability, and it has the feasibility of measurement control, in line with engineering practice. Parameters of propulsion system are listed in the following:

- (1) Total thrust: 4 mN (including 4 nozzles, 1 mN for each nozzle);
- (2) Minimum thrust: 5 μN;
- (3) Minimum thrust adjustment step size: 5 μN;
- (4) Minimum pulse width time: 1 ms;
- (5) Longest pulse width: 30 min;

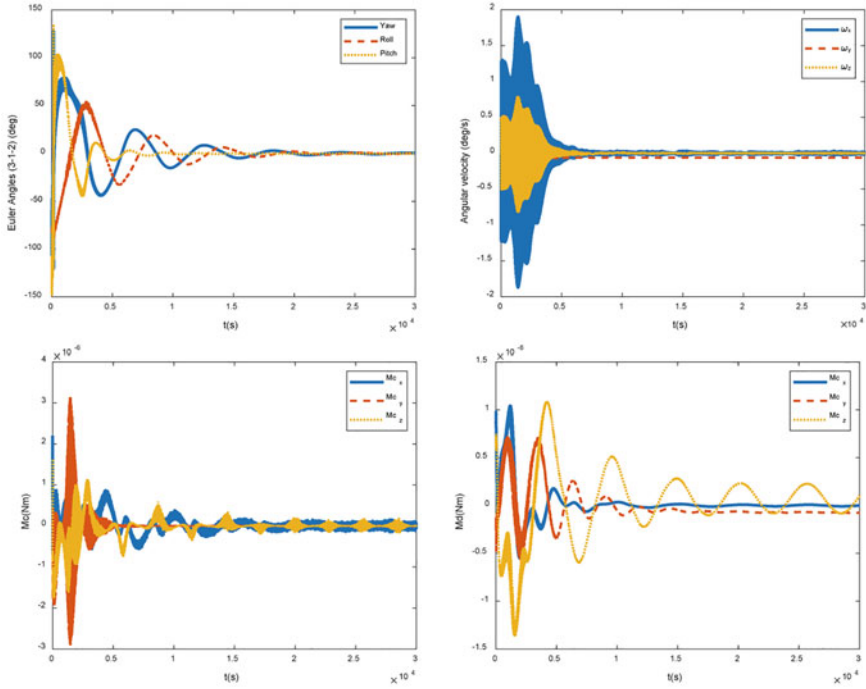
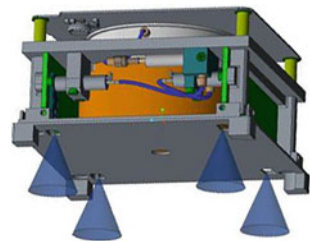


Fig. 10 Nadir pointing mode simulation results (Y-axis wheel + magnetorquer)

Fig. 11 The MEMS Micro-propulsion system



3.4 Payloads System

The Gamalink inter-satellite communication payload is from the Tekever Ltd in Portugal. Figure 12 shows the architecture of the Gamalink. This inter-sat communication payload is mainly based on two novel technologies: Software defined Radio (SDR) and Mobile wireless Ad hoc networks. The device has two segments: the space segment and the ground segment. The device for the space segment includes the ad hoc network capability for Inter-Satellite Link (ISL), a GPS receiver and a radio-based attitude determination algorithm.

Fig. 12 The inter-sat communication payload

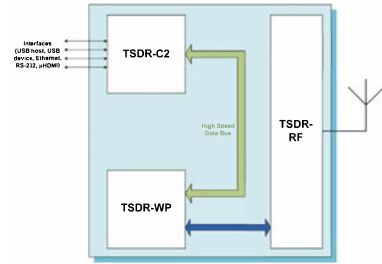


Fig. 13 The AIS payload



The automatic identification system (AIS) is an automatic tracking system that uses transponders on ship and is used by vessel traffic services (VTS). The ship-based and shore-based AIS system is limited by the distance, the ability in global ocean monitoring does not perform well. With the development of CubeSat, Sat-based AIS system can provide large-scale service for e-Navigation, and Ocean Information Services.

In the SSS-2A CubeSat, the AIS receiver is developed in house and the technology is going to be validated. The AIS payload is composed of receiver and antenna, the receiver is attached on a PCB board, and it has a standard PC104 CubeSat interface. A test interface can be connected to the ground system for standalone test. Figure 13 shows the interfaces with the satellite.

4 Project Implementation and Management Plan

Different from conventional aerospace project development process, the SSS-2A omits engineering model manufactures phase on the basis of full consideration in the preliminary phase. The development process greatly saves the project time and cost, which is adapted to the CubeSat manufacture, and the process is described as follows (Fig. 14).

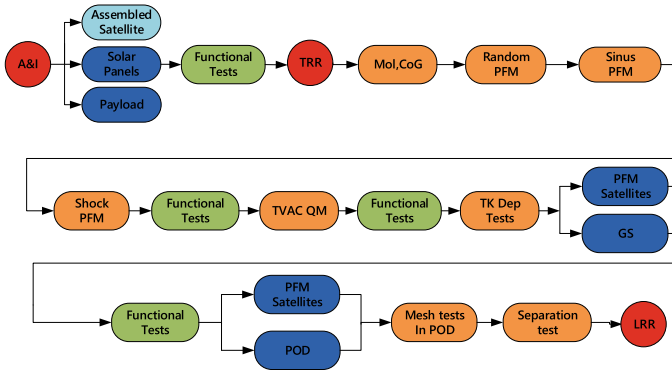


Fig. 14 SSS-2A project development process

According to the technical activities and implementation schedule, the SSS project main milestones are listed in Table 3.

After launching, the APSCO SSS-2A satellite is planned to be operated for 6 months. The mission operation is divided into four phases, the objectives of each phase are shown in the following:

(1) Launch and Early Orbit Phase

After launching, necessary systems are activated into normal mode.

(2) In-orbit Test Phase

All systems are functionally certified and the satellite is in its operational orbit. The ground station is ready for TM/TC mission.

(3) In-orbit Demonstration Phase

This phase overlaps the in-orbit test phase and continues until the experimental elements have been checked functionally, and the data and processing algorithms are calibrated and validated.

(4) Routine Operation Phase

The satellite will work constantly until the half-year design lifetime.

Table 3 Project main milestones

Phases	Milestones	Description
Phase 0	T0	Project SSS kicked off Phase 0 finished
Phase A	T0+4m	Conceptual satellite design finished Subsystem proposal determinations finished Preliminary requirements review Phase A finished
Phase B	T0+10m	Preliminary satellite design finished Preliminary design review Phase B finished
Phase C	T0+14m	Flight model development finished Engineering model subsystem/equipment delivered
	T0+19m	Flight model environment tests finished Flight model functional and software validation test finished
	T0+24m	Satellite AIT readiness review
	T0+30m	SSS joint test finished Satellite-LV test finished SSS Joint AIT readiness review Phase C Finished
Phase D	T0+32m	Launch On-orbit assessment Phase D finished

5 Conclusions

This paper mainly introduces the SSS-2A CubeSat project and further analyzes the mission requirements and presents the detailed design and development of the satellite, including its system integration, main payloads selection, subsystems design specifications and project schedule. The main tasks of the SSS-2A CubeSat are monitoring global marine traffic information with an on-board AIS receiver, demonstrating

the formation flying based on a MEMS micro-propulsion system and demonstrating inter-satellite adaptive networking communication technology.

In addition to the CubeSat system design, this paper introduces the scope and meaning of the SSS project. As an international cooperative project, it is aiming at training university students to have hands-on experience on the satellite design, development, and implementation practice. Besides, SSS project can provide a potential platform for further space cooperation and technology exchange between Asia-Pacific countries in the future.

References

1. De Pasquale D, Charania A (2011) Nano/microsatellite launch demand assessment 2011. SpaceWorks Commercial
2. Su R, Zhang K, Song H (2013) Summarization of very small satellite development. *Spacecraft Eng* 22(6):104–111
3. Villela T, Costa CA, Brandão AM, Bueno FT, Leonardi R (2019) Towards the thousandth CubeSat: a statistical overview. *Int J Aerosp Eng* 2019 (2019). <https://doi.org/10.1155/2019/5063145>
4. Crusan J, Galica C (2019) NASA's Cubesat launch initiative: enabling broad access to space. *Acta Astronaut* 157:51–60. <https://doi.org/10.1016/j.actaastro.2018.08.048>
5. Lemmer K (2017) Propulsion for cubesats. *Acta Astronaut* 134:231–243. <https://doi.org/10.1016/j.actaastro.2017.01.048>
6. Shields J, Pong C, Lo K, Jones L, Mohan S, Marom C, McKinley I, Wilson W, Andrade L (2017) Characterization of CubeSat reaction wheel assemblies. *J Small Satell* 6(1):565–580
7. Imken TK, Stevenson TH, Lightsey EG (2015) Design and testing of a cold gas thruster for an interplanetary CubeSat mission. *J Small Satell* 4(2):371–386
8. Hadaegh FY, Chung SJ, Manohara HM (2014) On development of 100-gram-class spacecraft for swarm applications. *IEEE Syst J* 10(2):673–684. <https://doi.org/10.1109/JSYST.2014.2327972>
9. Gill E, Sundaramoorthy P, Bouwmeester J, Zandbergen B, Reinhard R (2013) Formation flying within a constellation of nano-satellites: The QB50 mission. *Acta Astronaut* 82(1):110–117. <https://doi.org/10.1016/j.actaastro.2012.04.029>
10. Challamel R, Calmettes T, Gigot CN (2012) A European hybrid high performance Satellite-AIS system. In: 2012 6th advanced satellite multimedia systems conference (ASMS) and 12th signal processing for space communications workshop (SPSC), pp 246–252. IEEE (2012). <https://doi.org/10.1109/ASMS-SPSC.2012.6333084>
11. Eide E, Ilstad J (2003) NCUBE-1, the first Norwegian CUBESAT student satellite. In: European rocket and balloon programmes and related research, vol 530 (2003), pp 85–88
12. Narheim B, Hellenen O, Olsen O, Olsen R, Rosshaug H, Beattie A, Kekez D, Zee R (2011) AISSat-1 early results. In: Small satellite conference
13. Schoneman S, Amorosi L, Laidley M, Wilder K, Hunley B (2007) Minotaur-family launch vehicles responsive launch demonstration for the TacSat-2 mission. In: AIAA SPACE 2007 conference and exposition, p 6145
14. Bulanov D, Ocheretyanyy K, Wang Y, Chen QB (2018) Inter-satellite communication for LEO CubeSat network: QoS parameters and feasibility of massive MIMO. *J Commun Technol Electron* 63(10):1174–1182. <https://doi.org/10.1134/S1064226918100054>
15. Soret B, Smith D (2019) Autonomous routing for LEO satellite constellations with minimum use of inter-plane links. In: ICC 2019-2019 IEEE international conference on communications (ICC), pp 1–6. IEEE (2019). <https://doi.org/10.1109/ICC.2019.8761787>

16. Rodrigues P, Oliveira A, Mendes R (2011) SDR-based ad hoc space networks (SASNETs). In: IAC-11-B2. 1.3, 62nd IAC
17. Wu S, Chen W, Chao C (2016) The STU-2 CubeSat mission and in-orbit test results. In: 30th Annual AIAA/USU conference on small satellites

Scenario-Based Function Modeling Approach for Civil Aircraft Systems



Huang Xu, Chen Yong, and Zhao Meng

Abstract As an important approach and tool in model-based system engineering, functional modeling can help engineers to clarify customer requirements, establish functional architecture and generate solution concepts, and it has a wide range of application prospects in the aviation field. However, most existing functional modeling methods do not fully consider how to formalize the generated functional architecture solutions and cannot effectively represent functional logic, especially involved in complex interactions among the system, the user, and the operation environment. Therefore, this paper proposes a scenario-based functional modeling approach for civil aircraft systems. This method combines the concept of scenario in software engineering, builds the aircraft operation scenario model, further establishes the requirement, structure, behavior, and parameter model, and elaborates the functional interaction logic among the aircraft systems. Taking the primary flight control system in the aircraft deceleration on the ground scenario as an example, the functional model of the control spoiler extending and retracting is established and simulated, which demonstrates that the functional modeling approach is applicable to the functional design of civil aircraft system.

Keywords Functional modeling · Scenario · Model-based systems engineering · SysML

H. Xu · C. Yong (✉) · Z. Meng
School of Aeronautics and Astronautics, Shanghai Jiao Tong University, Shanghai, China
e-mail: aerocy@sjtu.edu.cn

H. Xu
e-mail: hx19970422@sjtu.edu.cn

Z. Meng
e-mail: magicmeng@sjtu.edu.cn

1 Introduction

The traditional document-based systems engineering (DBSE) approach used to be the main design approach for aircraft. However, with the development and application of automation, computer, and aircraft flight control technology, the traditional design approach has been difficult to meet the requirements of engineering technology [1]. Therefore, the traditional DBSE has been gradually replaced by the more graphical and visualized model-based systems engineering (MBSE) [2]. As an important approach and tool of MBSE, functional modeling can provide a systematic design approach to help engineers transform product functions into solutions, thereby greatly improving the efficiency of product design and saving costs [3].

Because functional modeling plays such an important role, there has been a lot of exploration in this field in recent years in academia and industry.

Erden et al. [4] use the term "functional modeling" to refer to the activity of developing a system model based on the functions of the system. Eisenbart [5] provides a disciplinary review of functional modeling approaches. Srinivasan et al. [6] reviewed the development of functional definition and functional representation. Carroll [7] first proposed to apply the interaction design method based on actual scenarios to the usability engineering of interactive products. Campbell [8] proposed a design method to realize the functional design of electromechanical systems. In 2007, Pahl and Beitz [9] proposed a system design method, which regarded function design as a process of decomposing the overall function into sub-functions. In addition, Xue et al. [10] designed a method for flight management software package, which effectively reduced the research and development cost and improved its safety. Gui [11] et al. proposed a function design method of scenario integration for intelligent system and proposed a kind of thinking for the application of scenario in intelligent system.

Despite the contributions of existing functional modeling approaches, they still have many shortcomings: 1. Most existing functional modeling approaches focus on generating solution principles for desired functions, but do not fully consider how to formalize the generated functional architecture solutions. 2. Although there are a few functional representation schemas, engineers still lack ways to effectively represent functional logic, especially involved in complex interactions among the system, the user and the operation environment.

Therefore, based on the universal system modeling language SysML, a scenario-based functional modeling approach for civil aircraft system is established in this study. The approach describes the functional interaction logic and control logic of complex systems. At the same time, taking the aircraft deceleration on the ground scenario as an example, this paper establishes the functional interaction model of the primary flight control system (PFCS) in the Cameo System Modeler software environment and performs the simulation and verification of the functional logic.

The rest of this paper is organized as follows. The aircraft-level functional modeling method is presented in Sect. 2. In Sect. 3, the modeling methods of system-level structure, behavior and parameters are described. Taking aircraft deceleration

on the ground scenario as an example, the functional model of the primary flight control system to control spoiler extending and retracting is established, and the simulation results of the above functional model are given in Sect. 4. In Sect. 5, the conclusions are drawn, and future work is presented.

2 Aircraft-Level Functional Modeling

2.1 Scenario Definition

Originating from software engineering, the term scenario is defined to express the interactions between user activities and a software system [12, 13]. In system engineering, scenario can be given a similar meaning, that is, a set of concrete interaction activities of satisfying or failing to satisfy a goal (or set of goals) [14]. By defining the scenario, engineers can clarify the stakeholders’ need of the system and establish a link among the user, the system, and the environment. Therefore, a scenario can refine a customer need into more detailed description.

In a scenario, there are several main contextual elements: Actors, Goal, Time, Location, Precondition, Postcondition. Here, actors mainly refer to the people or external systems interacting with the system; goals are the objects to be achieved by using the system in the scenario; time and location tell when and where this scenario occurs; precondition and postcondition respectively describe the state of the system before and after executing the scenario.

Hereby, the set of contextual elements of a certain scenario can be obtained, as shown in Fig. 1.

Scenario name: To control the aircraft to take off
Contextual elements: { <i>Actors:</i> [polit, tower controller, crew], <i>Goals:</i> “control the aircraft to accelerate and take off”, <i>Time:</i> “N/A” <i>Location:</i> “take-off runway” <i>Preconditions:</i> “the aircraft stops at the beginning of the takeoff runway” <i>Postconditions:</i> “the aircraft leaves the ground” }

Fig. 1 The set of contextual elements of a scenario

2.2 Scenario Modeling

The corresponding scenario model can be established after clarifying the contextual elements. In this study, the internal module diagram (IBD) in SysML is used to define the operating environment of the aircraft, which mainly included the following steps:

1. Create a block representing “Operating Environment”, establish its IBD, and create an “Aircraft System” object.
2. Establish all stakeholders in the “Operation Environment” Block, such as pilot, tower controller, crew, and etc., making these stakeholders part of the operation environment.
3. Associate the aircraft and stakeholders in the IBD, such as connecting the aircraft and the pilot through the Connector relationship, indicating the interaction between them.

Based on the above method, the external operating environment of the aircraft in a scenario can be defined, as shown in Fig. 2.

After the establishment of the aircraft operating environment, the aircraft system structure involved in this scenario can be defined according to the general aircraft architecture division. Using the block definition diagram (BDD), the elements of each system and their attributes can be defined in this model. In SysML, the BDD can display different types of model elements and relationships to illustrate the information of the system structure.

When the operating environment and basic structure of the aircraft are defined, a series of activities that need to be performed by users, systems, and environments can be established according to the goal and conditions in this scenario. Thus, an activity

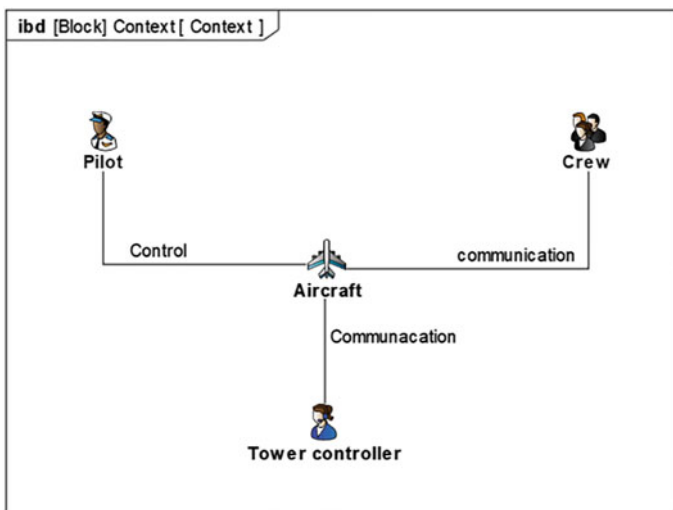


Fig. 2 The IBD of the operating environment

diagram is needed to illustrate the behavior of each element. In SysML, activity diagrams can represent continuous and concurrent behaviors, as well as events that occur over time [15]. An activity diagram of aircraft operation in a certain scenario is shown in Fig. 3.

2.3 Requirement Modeling

In order to establish the requirement model in a typical operation scenario of the civil aircraft, firstly, the customer need in this scenario should be transformed into identifiable (functional) requirements. The requirement decomposition method established in this paper uses requirement diagram to decompose customer needs at all levels. The main steps are as follows:

First, establish the aircraft-level parent requirement element "Aircraft level requirement". The ID attribute of this element is the requirement number, that is, ID = 1, and the text attribute is a natural language-based requirement description, that is, "The aircraft shall meet the aircraft level requirement"; Then, create a system-level requirement under this element with different attributes of ID and text. Finally, a "containment" relationship is established between the parent requirement

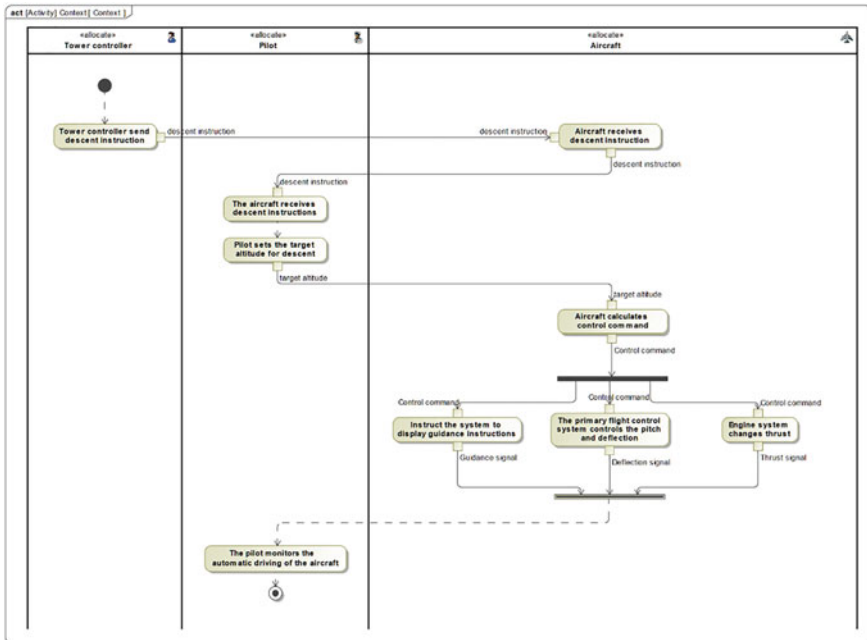


Fig. 3 The activity diagram of aircraft descending scenario

element and the child requirement element to express the result of the requirement decomposition.

3 System Level Functional Modeling

3.1 Structure Modeling

Based on the activity diagram model described in Sect. 2.2, the aircraft structure involved in the activity diagram can be clarified. According to the constituent relationships of each system, the system level structure model can be established by BDD and IBD.

BDD can represent the decomposition relationships between the various levels of the system. For example, there is a hierarchical relationship between the PFCS and the aileron control system in the physical architecture, which can be represented by the Directed Composition. An example of BDD is given below taking the PFCS as an example, as shown in Fig. 4.

In BDD, only the definition of each block and its decomposition relationships can be understood. Only through the IBD can system engineers see the attributes, interfaces, operations of each block and how it is connected to external entities or internal blocks. The IBD of aircraft systems is given below, as shown in Fig. 5.

In Fig. 5, the PFCS has 8 interfaces in total, of which p_hdy is connected to the hydraulic system, receiving hydraulic energy flow; p1, p3, p4, and p5 are associated with the avionics system and transmit signals such as flight status and autotrim. The p2 interface is connected to the power system for receiving electric energy; po1 and po2 are responsible for transmitting the surface position signal measured by PFCS to the indicating/recording system.

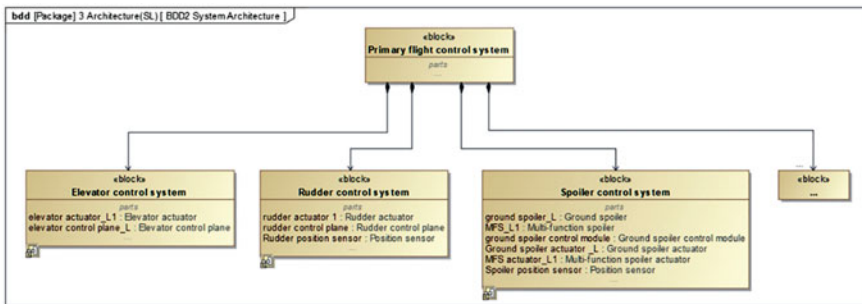


Fig. 4 The BDD of primary flight control system

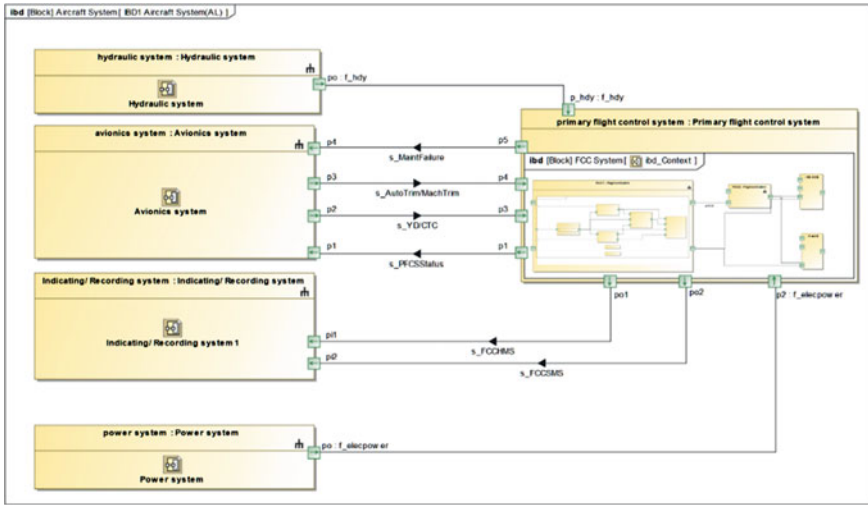


Fig. 5 The IBD of aircraft systems

3.2 Behavior Modeling

Gero et al. [16] believe that behavior describes how a structure fulfills its function. However, Umeda et al. [17] argue that not all functions can be described in terms of input and output of material, energy, and information. They believe that a function cannot be independent of behavior, so they define the function as sequential state transitions over time where a state consists of three elements; entities, attributes of entities, and relations between entities.

Similarly, in SysML, the behavior model is typically represented by two diagrams: activity diagrams and state machine diagrams. The activity diagram has been mentioned in Sect. 2.2. The difference between the state machine diagram and the activity diagram is that the state machine diagram focuses on how the structure in the system changes state according to events that occur over time. The state machine diagram can clearly indicate the triggering conditions of the system when the state changes. Figure 6 shows the state changes experienced by the aircraft during the cruise phase and a series of actions performed in each state.

3.3 Parameter Modeling

When defining a block in BDD, the value attribute of the block has been established. When the system performs activities or changes states, its parameters are usually changed and transferred. Therefore, it is necessary to establish a standardized parameter model (Fig. 7).

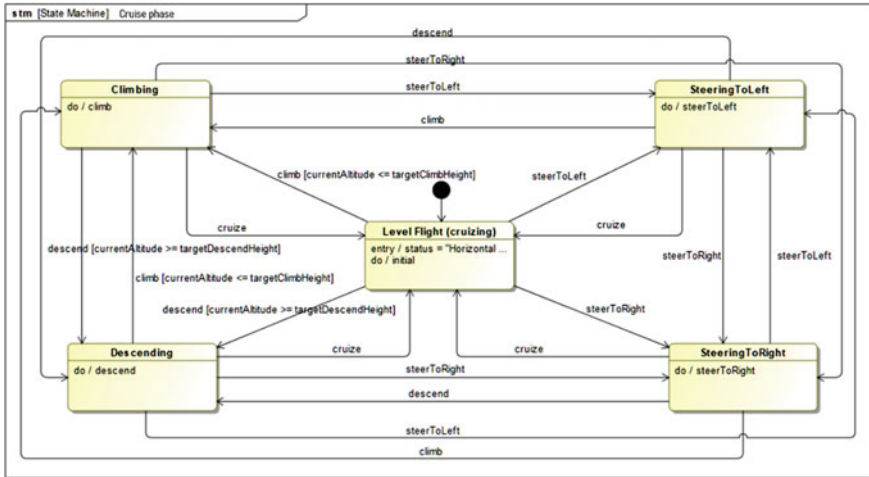


Fig. 6 The state machine diagram of aircraft in the cruise phase

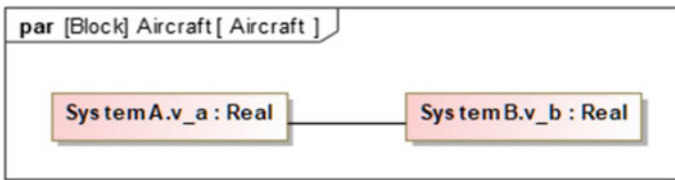


Fig. 7 The parameter diagram

In SysML, transfer parameters and parameter diagrams are used to represent the passing of parameters. The parameter diagram is a specific IBD that shows the internal structure of the module, but it focuses on the binding relationship between the value attribute and the constraint parameter. An example of the parameter diagram is shown in Fig. 10. In the figure, v_a and v_b are a parameter of system A and system B respectively, and the type of the two parameters is real. The two parameters are connected via a Binding Connector relationship. Mathematically, it means that the two parameters are equal. In the functional model, it means that when the value of one parameter changes, the changed parameter value can be transmitted to another system.

4 Case Study

Based on the proposed scenario-based functional modeling approach, a complete functional model of the primary flight control system controlling the spoiler

extending and retracting in the aircraft deceleration on the ground scenario is established, and the simulation and analysis of the model are carried out.

4.1 Aircraft-Level Functional Modeling

Scenario definition. In this scenario, the main part of the system is the aircraft system, the actor is the pilot, the goal is to slow down the aircraft to stop, and the location is the airport runway. The precondition of the scenario is that the aircraft has landed, and the postcondition is the aircraft stop at the parking area. Thus, a set of contextual elements of the scenario can be established, as shown in Fig. 8.

Scenario modeling. First, create a “context” Block, which is the operating environment of the aircraft. Then create an “aircraft” object and establish all stakeholders—pilot. Finally, associate the aircraft with the pilot in the IBD. The pilot controls the aircraft to decelerate on the ground through the `s_groundDecelerationCommand` signal. The aircraft sends the flight status signal `s_flightStatus` to the pilot. The external environment of the aircraft in the ground deceleration scenario is clearly defined, as shown in Fig. 9.

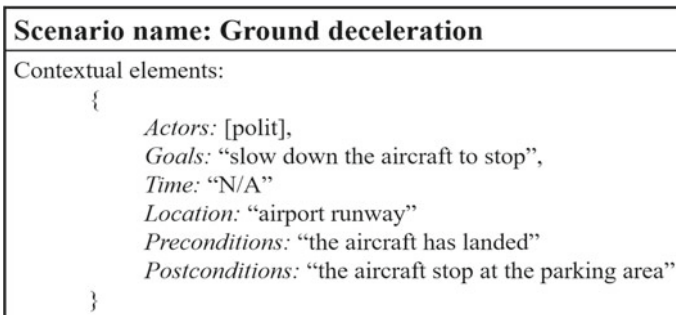


Fig. 8 A set of contextual elements for the deceleration on the ground scenario

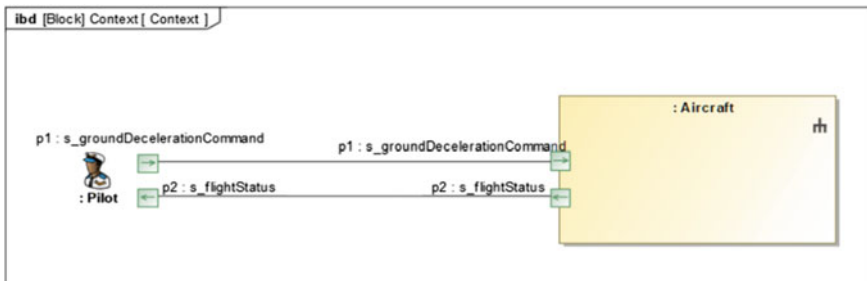


Fig. 9 Aircraft operating environment in the deceleration on the ground scenario

Based on the general division of aircraft, the systems involved in this scenario can be defined as primary flight control system, electrical power system, hydraulic system, landing system, and indication/recording system. In order to achieve the goal, slow down the aircraft to stop, the aircraft needs to perform the following activities. First, pilot send ground deceleration command. After the aircraft receives the instruction, the PFCS requests WOW and WS signals from the landing gear system, and then PFCS detect whether the aircraft is on the ground. If it is No, continue to monitor the WOW signal; if it is Yes, then Landing system send WS signal and PFCS detect whether the wheel speed is above 45 knots. If it is No, continue to monitor the WS signal; if it is Yes, the power system and hydraulic system provide electrical and hydraulic energy respectively. After receiving the energy flow, PFCS controls the spoilers to extend, and at the same time continues to detect whether the wheel speed is less than 45 knots. When the wheel speed is less than 45 knots, PFCS controls the spoilers to retract, and then ends the entire activity.

In the process of PFCS controlling the spoiler movement, it sends the signal of spoiler position to the indicating/recording system. The indicator/recording system displays the flight status, which is received by the pilot. Figure 10 shows the details of the activities.

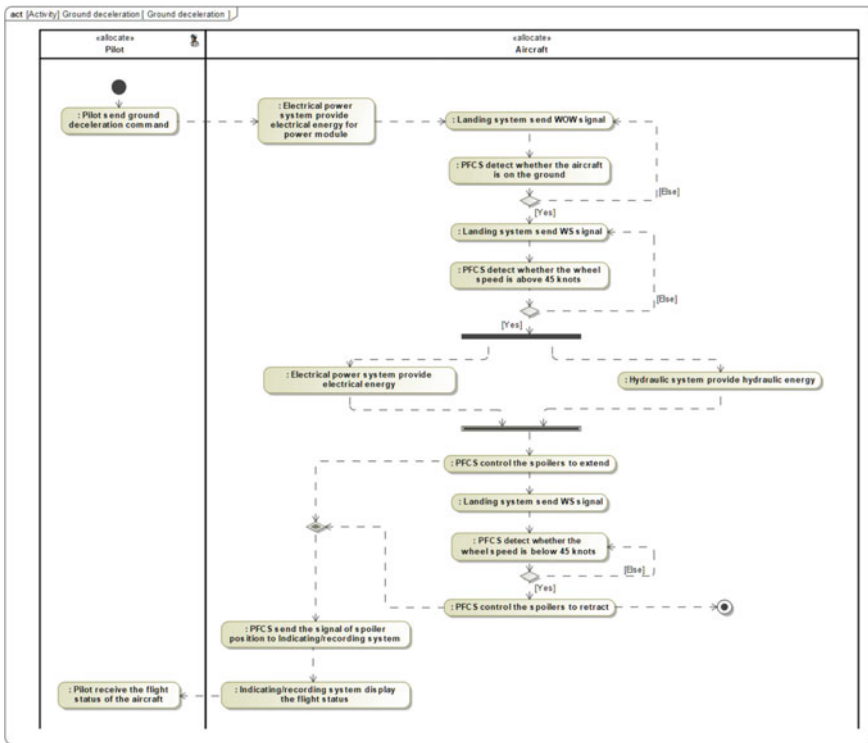


Fig. 10 The activity diagram of the deceleration on the ground scenario

Requirement modeling. According to the activities performed by the aircraft, the user requirements in the scenario can be defined. First, the aircraft-level user requirement is “the aircraft can slow down on the ground.” In response to this requirement, a parent requirement element of controlling ground deceleration is established.

This requirement can be decomposed to five system-level requirements: Control the main flight control system, control landing system, and other three requirements related to the power system, hydraulic system, and indicating/recording system. For PFCS, subsystem-level requirement decomposition is continued. The details are shown in Fig. 11.

4.2 System-Level Functional Modeling

Structure modeling. Based on the Flight Crew Operation Manual (FCOM) and ATA100, a deeper structural decomposition of PFCS is carried out at the system level, which mainly includes the following subsystems: flight control computer, spoiler control system, elevator control system, rudder control system, aileron control system, and horizontal stabilizer trim system. Among them, the flight control computer and spoiler control system are mainly used in deceleration on the ground scenario. The flight control computer can be decomposed into two components: power module and computer module. The spoiler control system mainly includes: ground spoiler, ground spoiler actuator, ground spoiler control module, and spoiler position sensor. The system-level structural model BDD is shown in Fig. 12.

Once the module elements are defined, IBD can be used to establish the ports and connections of each module. First, establish the IBD of the aircraft, as shown in Fig. 13. The aircraft itself has two ports, the p1 port’s direction is in, through this port, the aircraft can receive the s_groundDecelerationCommand signal from the

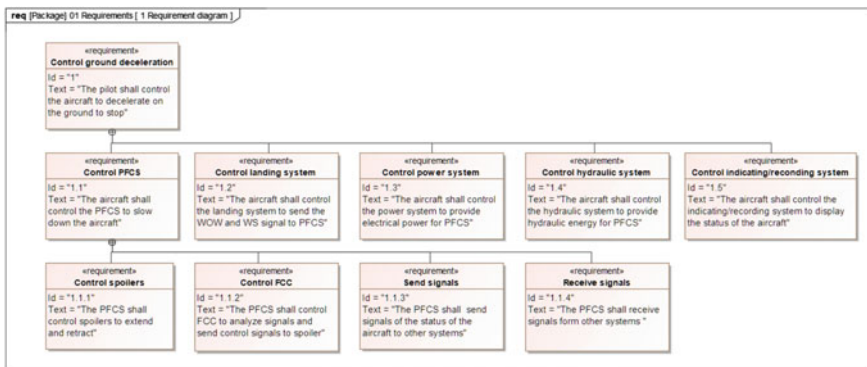


Fig. 11 The requirement diagram of ground deceleration scenario

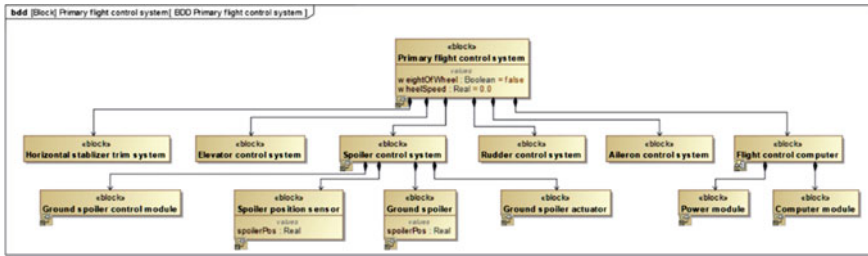


Fig. 12 The BDD of PFCS structure

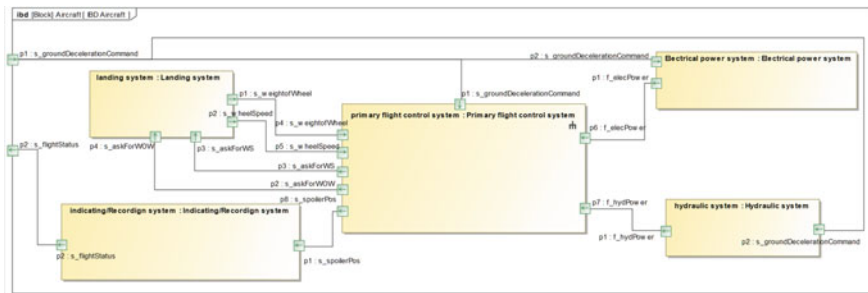


Fig. 13 The IBD of flight control system

pilot; the p2 port direction is out, the aircraft sends s_flightStatus to the pilot through this port.

PFCS module has eight ports. Port p1 receives command signal; p2–p5 are where the PFCS interacts with the landing system; p6 and p7 are used to receive electric energy and hydraulic energy from the power system and the hydraulic system; spoiler position signals are sent by p8 to the indication/recording system. Other systems also have ports for interacting with the PFCS.

Similarly, IBD is used to represent the internal structural attributes of PFCS and the relationship between internal blocks, as shown in Fig. 14. There are a total of 7 ports outside the flight control computer subsystem and 4 ports for the spoiler control subsystem. Inside the subsystem, the ports for the interaction of each module are also defined.

Behavior modeling. In IBD, the connections of the internal blocks and the transmission path of materials, energy, and information are represented. Then, the state machine diagrams are built to represent their state changes in this scenario, as well as the actions performed in different states. Due to the numerous systems and components, the state machine diagrams of the PFCS, spoiler control system, and ground spoiler are selected as the typical examples here, as shown in Fig. 15.

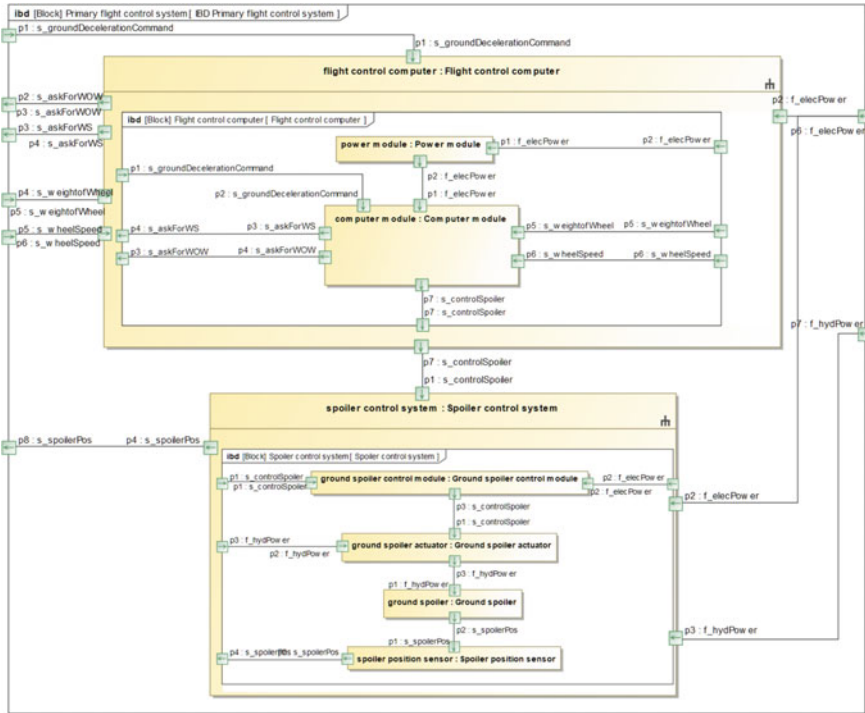


Fig. 14 The IBD of PFCS

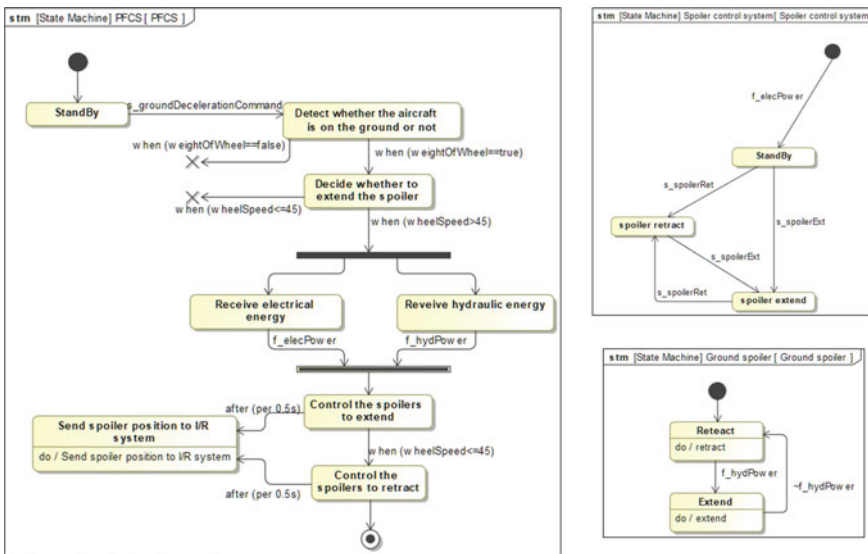


Fig. 15 The state machine diagrams of PFCS, spoiler control system, and spoiler

On the left is the state machine diagram of PFCS. First, the PFCS enters the StandBy state. After receiving the `s_groundDecelerationCommand` signal, the PFCS enters the Detect whether the aircraft is on the ground or not state. When `weightOfWheel == false`, exit the current state machine. If `weightOfWheel == true`, continue to determine whether the aircraft wheel speed is greater than 45 knots. If it is greater, control the spoiler to extend after receiving electrical energy from the power supply system and hydraulic energy from the hydraulic system. After the wheel speed is less than 45 knots, control the spoiler to retract and end the state machine. In the process of extending and retracting the spoiler, PFCS needs to send the spoiler position signal to the indicator/recording system every 0.5 s.

The upper right is the state machine diagram of the spoiler control system. First, the spoiler control system enters the StandBy state after receiving electrical power, and then enter spoiler extend and spoiler retract states after receiving the corresponding control commands `s_spoilerExt` and `s_spoilerRet`. At the same time, the spoiler control system can switch between these two states through the `s_spoilerExt` and `s_spoilerRet` instructions.

The bottom right is the state machine diagram of the spoiler. Because the spoiler only has two states, extend and retract, it is only necessary to switch between these two states. It is worth mentioning that the trigger conditions for the state switching of the spoiler are the two hydraulic energy `f_hydPower` and `~ f_hydPower`, where `~` represents the opposite direction.

Parameter modeling. In scenario modeling, two parameters in this model—weight of wheel and wheel speed are mentioned. The weight of wheel is used to judge whether the aircraft touches the ground, and the wheel speed is used to judge whether the aircraft needs to slow down by extending the spoiler. As shown in Fig. 16, the parameter type of WOW is Boolean, and its default initial value is false, which means that the aircraft is not grounded. The parameter type of WS is real, and the default initial value is 0. When the aircraft touches the ground, the WOW will change from false to true, and will be sent from the landing gear system to PFCS through port p1. Similarly, the landing system will measure the wheel speed and send it to PFCS through port p2.

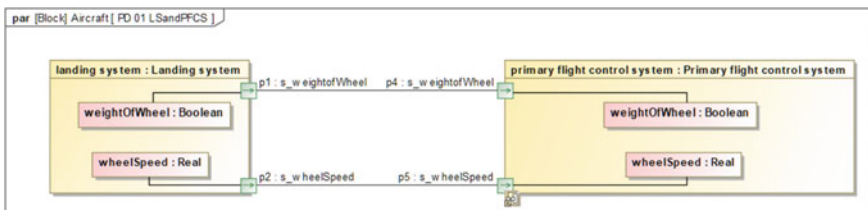


Fig. 16 The parameter diagram of WOW and WS

4.3 Functional Simulation of PFCS

This section will simulate the functional model established in the previous section to verify the interactions among the system, the user, and the operating environment as well as the internal interactions among systems.

As shown in Figs. 17 and 18, the simulation results of interactions between the pilot and the aircraft as well as among various systems inside the aircraft are given. First, the pilot sends the `s_groundDecelerationCommand` to the aircraft, which is sent to the PFCS, power system, and hydraulic system respectively. Subsequently, the power system and hydraulic system provide electrical energy and hydraulic energy to the PFCS. After receiving the command, the PFCS requests the WOW and WS signals from the landing system, and returns the WOW parameter to true and the WS parameter to 60.0, as shown in Fig. 19. Then PFCS controls the extending of

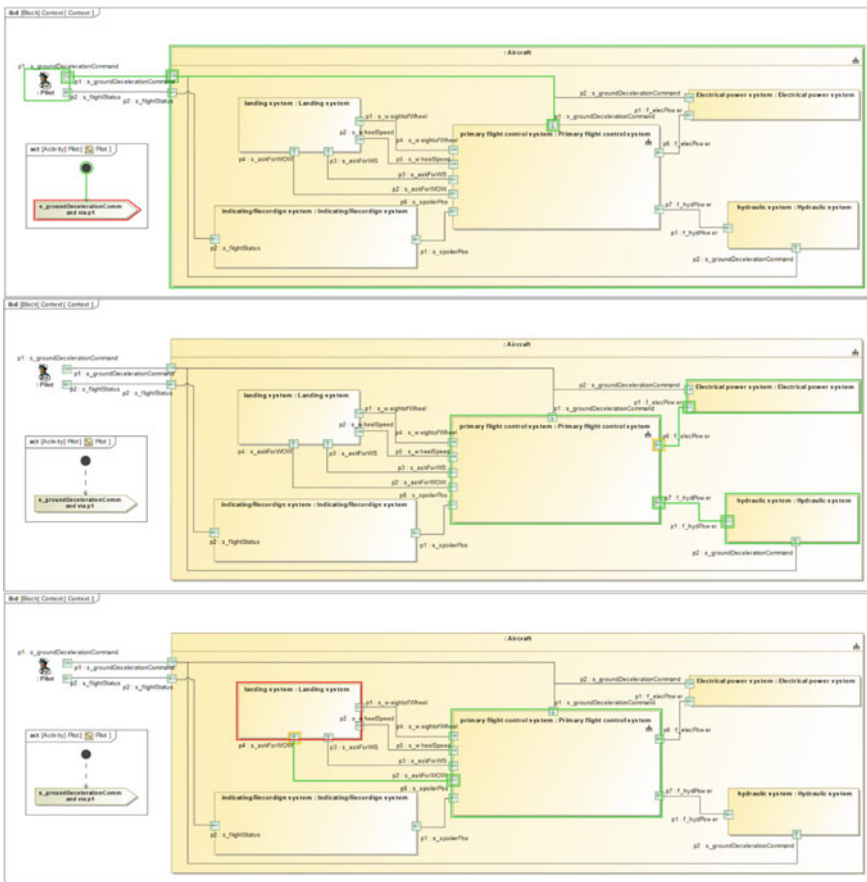


Fig. 17 The simulation process of the functional model (1)

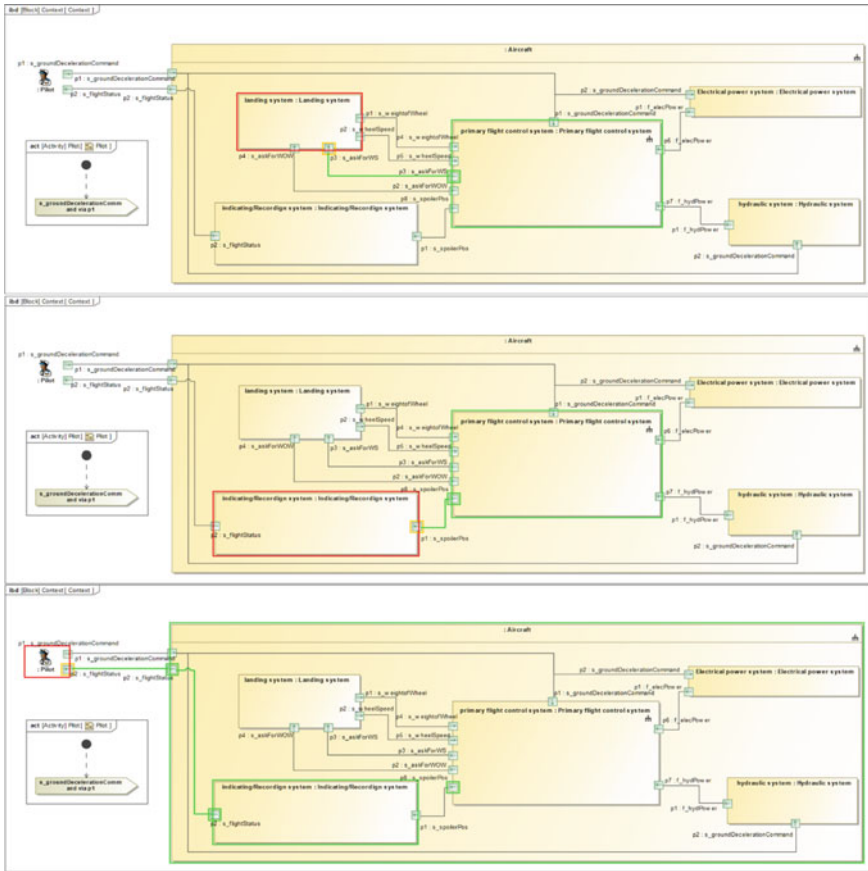


Fig. 18 The simulation process of the functional model (2)

the spoiler through the spoiler control system and retracts the spoiler after the wheel speed drops below 45 knots. During the process of controlling the spoiler, the PFCS will send the spoiler position to indicating/recording system every 0.5 s, and the I/R system will send the flight status to the pilot by displaying the s_flightStatus signal.

The simulation process and state change of spoiler control system and spoiler is shown in Figs. 20 and 21.

First, under the effect of electric energy, the spoiler control system enters the StandBy state; then, after receiving the s_spSpoilerExt command from the flight control computer, the spoiler control system enters the spoiler extend state, and the spoiler

Name	Value
Context	Context@159e4a92
Pilot	Pilot@1821b2a7
Aircraft	Aircraft@664bf4b7
Electrical power system : Electrical power system [Se...	Electrical power system@4115f226
hydraulic system : Hydraulic system [Send hydraulic e...	Hydraulic system@31eaac1e
indicating/Recordign system : Indicating/Recordign sy...	Indicating/Recordign system@289d2810
landing system : Landing system [StandBy]	Landing system@70d02534
weightOfWheel : Boolean	<input type="checkbox"/> false
wheelSpeed : Real	0.0000
primary flight control system : Primary flight contro...	Primary flight control system@73afa047
weightOfWheel : Boolean	<input type="checkbox"/> false
wheelSpeed : Real	0.0000
flight control computer : Flight control computer	Flight control computer@6420db1f
spoiler control system : Spoiler control system	Spoiler control system@3602a4c

Name	Value
Context	Context@22421be0
Pilot	Pilot@28ba7090
Aircraft	Aircraft@3c5e2cd1
Electrical power system : Electrical power system [Se...	Electrical power system@1298363b
hydraulic system : Hydraulic system [Send hydraulic e...	Hydraulic system@652f2665
indicating/Recordign system : Indicating/Recordign sy...	Indicating/Recordign system@63c6222a
landing system : Landing system [Send WS signal]	Landing system@344b4c2f
weightOfWheel : Boolean	<input checked="" type="checkbox"/> true
wheelSpeed : Real	60.0000
primary flight control system : Primary flight contro...	Primary flight control system@7346efb8
weightOfWheel : Boolean	<input checked="" type="checkbox"/> true
wheelSpeed : Real	60.0000
flight control computer : Flight control computer	Flight control computer@6d3a2128
spoiler control system : Spoiler control system	Spoiler control system@309d1ff

Fig. 19 The parameter value change of WOW and WS

is released at this time. After the speed is reduced, the spoiler control system receives the s_spoilerRet command, enters the spoiler retract state, and retracts the spoiler. It is particularly worth mentioning that if repeated retracting and extending occurs in the deceleration process, or the position of spoiler is adjusted, the spoiler control system can still switch the state between spoiler extend and spoiler retract through instructions.

The state of the spoiler is retract and extend. After startup, spoiler enters in retract state by default. When the spoiler control system starts to control the extending of the spoiler to slow down the aircraft, the spoiler changes to the extend state through the hydraulic energy, and can be changed back to the retract state under the effect of the reverse hydraulic energy.

5 Conclusion

This study establishes a scenario-based functional modeling approach for complex civil aircraft systems, which effectively represent functional logic, especially involved in complex interactions among the system, the user, and the operation environment as well as among various systems. The case study of the primary flight

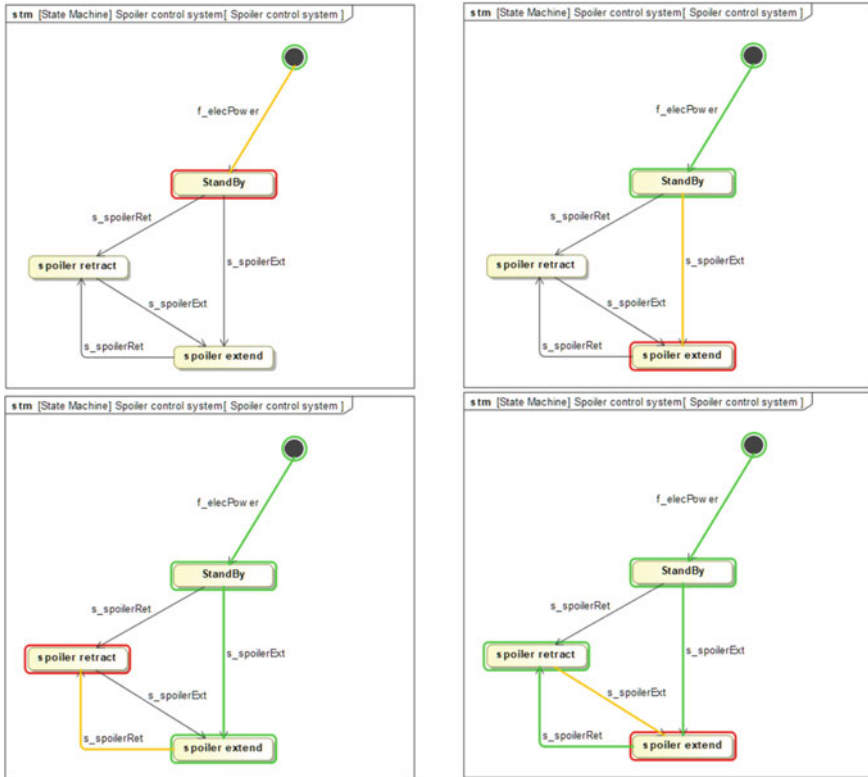


Fig. 20 Spoiler control system simulation

control system under the aircraft deceleration on the ground scenario proves that the proposed functional modeling approach can help engineers formalize the generated functional architecture solutions and establish the complete and traceable functional model of requirements, structure, behavior, and parameter by using diagram models of SysML.

Based on the functional modeling approach in this paper, the future work is to develop an interface integrated with computing software, and use the computing software to establish a functional model with high fidelity, so as to support the method more effectively.

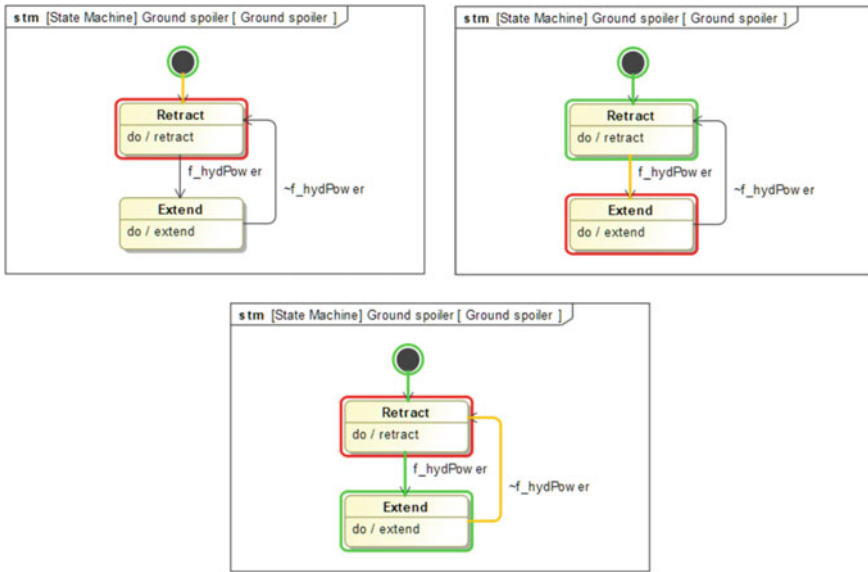


Fig. 21 Spoiler state machine simulation

Acknowledgements This paper is sponsored by National Natural Science Foundation of China (51875346), and the SJTU-COMAC Joint Foundation for Systems Engineering of Commercial Aircraft.

References

1. Gao J, Feng H (2018) Civil aircraft flight control system, 1st edn. Beijing University of Aeronautics and Astronautics Press, Beijing
2. Zhao L, Ye J, Guo W, Zhao Y (2021) Simulation of civil aircraft take-off scene based on MBSE. *J Syst Simul.* <https://doi.org/10.16182/j.issn1004731x.joss.20-0484>. Accessed 24 April 2021
3. Zheng D, Zhang Z, Liu J (2016) DMU technology of aircraft design. *Aeronaut Manuf Technol* 05:83–86
4. Erden M, Komoto H, Beek TJ, D’Amelio V, Echavarria E, Tomiyama T (2008) A review of function modeling: approaches and applications. *Artif Intell Eng Des Anal Manuf* 22(2):147–169
5. Eisenbart B (2014) Supporting interdisciplinary system development through integrated function modelling. PhD dissertation. University of Luxembourg
6. Srinivasan V, Chakrabarti A, Lindemann U (2012) A framework for describing functions in design. In: 12th international design conference, Dubrovnik, 21–24 May 2012. Faculty of Mechanical Engineering and Naval Architecture, Croatia, pp 1111–1121
7. Carroll J (2000) Five reasons for scenario-based design. *Interact Comput* 13:43–60
8. Campbell MI, Cagan J, Kotovsky K (2003) The A-design approach to managing automated design synthesis. *Res Eng Design* 14:12–24
9. Pahl G, Beitz W (2007) *Engineering design: a systematic approach*, 3rd edn. Springer, London

10. Xue F, Wang L, Miao W, Liu W (2019) Design of airborne flight management software based on MBSE. *Aeronaut Comput Tech* 49(05):111–116
11. Gui F, Chen Y (2021) A scenario-integrated approach for functional design of smart systems. *Artif Intell Eng Design Anal Manuf*, 1–15. <https://doi.org/10.1017/S0890060420000487>
12. Kaindl H (2000) A design process based on a model combining scenarios with goals and functions. *IEEE Trans Syst Man Cybern Part A: Syst Humans* 30(5):537–551
13. Alexander IF, Stevens R (2003) *Writing better requirements*. Pearson Education Inc., London
14. Pohl K (2010) *Requirements engineering: fundamentals, principles, and techniques*. Springer Publishing Company Inc., New York
15. Delligatti L (2014) *SysML distilled: a brief guide to the systems modeling language*, 1st edn. Pearson Education Inc., London
16. Gero JS (1990) Design prototypes: a knowledge representation schema for design. *AI Mag* 11(4):26–36
17. Umeda Y, Ishii M, Yoshioka M, Shimomura Y, Tomiyama T (1996) Supporting conceptual design based on the function-behaviour-state modeller. *AI EDAM* 10(4):275–288

Interfacial Properties of Stitched Three-Dimensional Woven Composite/Titanium Alloy Hybrid Board



Chongjing Li

Abstract The effects of stitching types (trajectory of stitching), stitch fiber materials, and the twist of stitches on interfacial shear, short-beam strength, and interlaminar fracture toughness of three-dimensional (3D) woven composite/titanium alloy hybrid board were investigated experimentally. The results revealed that when considering interlaminar shear properties: stitching types have little effect on interlaminar shear properties of hybrid laminates; the difference of ultimate load and strength is great when different stitch fiber materials are used, and aramid fiber are the most; the ultimate load and strength can also be greatly increased by twisting the stitches, and the maximum load and ultimate strength of the stitches with twist of 30m^{-1} are the highest, but excessive twisting will lead to the decrease of the ultimate load and strength of the structure. When considering the strength performance of the short beam: the maximum load and the strength of the short beam do not change significantly with the change of stitching types, stitch fiber materials, and the twist of stitches. When the interlaminar fracture toughness is considered: the interlaminar fracture toughness is increased by stitching, and the delamination resistance of the sample strengthened by carbon fiber stitch is stronger; over-twisting of stitches results in a decrease in the delamination resistance. The results revealed that the failure mode of the interlaminar shear test specimens is all shear failure of stitches. The failure mode of short-beam strength specimens is the interlaminar shear failure of 3D braided laminates. And there are three failure modes in the interlaminar fracture toughness test: the three-dimensional braided plate laminated fracture at the precrack tip; part of the stitches are tensile fracture, and the three-dimensional braided plate was layered fracture; all the stitches were tensile fracture, and the 3D braided laminates were peeled off from the titanium alloy plates. The formation of the three modes was mainly related to the stitch fiber materials and the degree of twist.

C. Li (✉)

Shanghai Jiao Tong University, Shanghai, China
e-mail: 1696650294@sjtu.edu.cn

Keywords Three-dimensional woven composite/Ti alloy hybrid · Failure mechanism · Interface properties

1 Introduction

Stitched composites are one of the most promising textile composites. The stitched composite material strengthens the mechanical properties in the thickness direction by using stitches in the thickness direction and overcomes the weak impact resistance and low damage tolerance in the thickness direction of ordinary laminates. With the rapid development of composite materials in the aerospace field, stitched composite materials have good application prospects in the field of composite materials.

However, although stitching enhances the mechanical properties in the thickness direction, during the stitching process, the stitching will cause bending deformation and damage to some of the fibers in the plane, which affects the in-plane mechanical properties [1].

For the main parameters affecting the properties of stitched composites, Weimer and Mitschan [2] made a detailed summary. According to this, Tianjun [3] divides the factors about stitching into three major parts: machinery, materials, and stitching technology.

- Mechanical factors: the arrangement mode of the sewing machine needle, the number of needles, the feeding mode, and the way the machine presses the fabric.
- Material factors: material, line density, structure, and number of strands of the stitch.
- Sewing process factors: bottom thread tension, upper thread tension, stitching trajectory, stitching pitch, stitching spacing, stitching direction, stitching speed, and stitching angle.

Different parameters together affect the final properties of the stitched composite. At present, some related studies at home and abroad focus on individual or multiple important parameters and have achieved relatively obvious results.

For the study of stitch fiber materials, Tan et al. [4, 5] investigate and evaluate the interlaminar fracture toughness of laminated composites reinforced by through-the-thickness stitching using different stitch fiber materials—Carbon, Kevlar, and Vectran, using the DCB test. And they came up with a four-step stitch fracture process: interfacial debonding, slack absorption, fiber breakage, and pull-out friction. They came to the conclusion that the relationship between GIC and stitch density follows a linear law. Ravandi et al. [6] studied the effect of through-the-thickness stitching using natural fibers on the interlaminar fracture toughness of flax fiber/epoxy composite laminates by DCB experiment. The results revealed that cotton thread stitch does not necessarily improve the interlaminar fracture toughness of the composite, but it can be improved by stitching with flax yarn. It can be seen that the influence of stitch fiber materials on the interlaminar properties of composites by through-the-thickness

stitching is significant; however, there are a few studies on the influence of stitch fiber materials on other properties of stitched composites.

At present, there are many researches on the effect of stitch density and stitch thread thickness on the properties of stitched composites. Tan et al. [7] used ultrasonic C-scan to study the damage progression and failure characteristics of stitched composites under out-of-plane loading. The results show that damage initiation occurs at a lower load due to the presence of resin-rich regions. During damage propagation, the rate of delamination growth is inversely related to stitch density. The final failure mechanism in the unstitched and moderately stitched composite is mainly delamination failure; while densely stitched composite failed by indenter penetration comprising of in-plane fiber fracture and matrix crushing. In addition, they also studied the influence of stitch density and stitch thread thickness on the impact resistance of laminated composites reinforced by through-the-thickness stitching [8]. Herwan et al. [9] investigated the influence of stitch density and stitch thread thickness on the Mode II delamination properties of Vectran stitched composites. The results show that, in densely stitched laminates (high stitch density) with thicker stitch thread, G_{IIC} values were improved significantly. Joshi et al. [10] studied the influence of stitch densities on the behavior of through-the-thickness-reinforced stitched laminates under in-plane tensile loading and found that the increase of stitch density improves the strength and stiffness suppressing crack propagation under tensile loading. Riccio et al. [11] carried out three-point bending tests on a skin-stringer configuration by considering stitching technique, the pitch, and the yarn diameter. The numerical results have confirmed that stitching can delay the crack initiation and propagation, increase the stiffness of the structure, and reduce the delamination area.

As for the study of stitch pattern, Yanan et al. [12] mentioned that stitch pattern is not the key point, but it should be stitched close to the free edge of the fabric. This view can be verified by the study of Karahan et al. [13], who simultaneously studied the influence of stitch density and pattern on the tensile strength of composite samples, and observed that higher tensile strength occurs with low stitch densities, and there is no significant effect of stitching direction or pattern on tensile strength and modulus of stitched samples. Joshi et al. [14] conducted tensile tests with different stitching directions (longitudinal and transverse) around the notch and found that the damage was all initiated by matrix cracks in the perpendicular direction of the loading axis on the notch. Longitudinally stitched laminates have higher strength than transversely stitched laminates.

At present, domestic research on the twist of stitches is mainly at the level of experiments. The effects of different twists of stitches on the in-plane tensile properties, bending properties, and interlaminar shear properties of composite materials are mainly studied through experiments.

Among them, Longying [15] also took Kevlar stitches as research objects and experimentally studied the permeability and breaking strength of Kevlar stitches with different twists. Jiping [16] used scanning electron microscopy to observe the combination of Kevlar stitch and resin interface with different twists. In addition, they pointed out that the effect of stitching on in-plane performance depends on the

stitch method, stitch twist, and stitch density. Just as the results of Yang Longying and Chen Jiping’s experiments, common stitches are not simply using one or two strands. Twisting more than two strands together can strengthen the stitch, but when the twist of the stitch is different, it will affect the permeability of the resin, and the strength of the stitch will also be different. Therefore, the effect of preventing the delamination is different when the laminate is delaminated.

It can be seen that there are many studies on the influence of stitch density, stitch direction, and stitch thread thickness on the properties of stitched composites. There are a few studies on the effects of different stitching types, stitch fiber materials, and twists. In this paper, the influence of the three kinds of stitching parameters on the interface properties of 3D woven composite/titanium alloy hybrid plate is mainly studied.

2 Materials and Methods Used in the Experiment

2.1 Three Stitch Parameters

2.1.1 Stitching Types

There are three types: ordinary stitching, improved lock stitching, and chain stitching. The trajectory stitching is shown in Fig. 1.

2.1.2 Stitch Fiber Materials

Three kinds of stitch fiber materials were used in this study: carbon fiber, polyimide fiber (PI fiber), and aramid fiber. Carbon fiber is widely used in the aerospace field because of its high tensile strength and high modulus. PI fiber is characterized by high

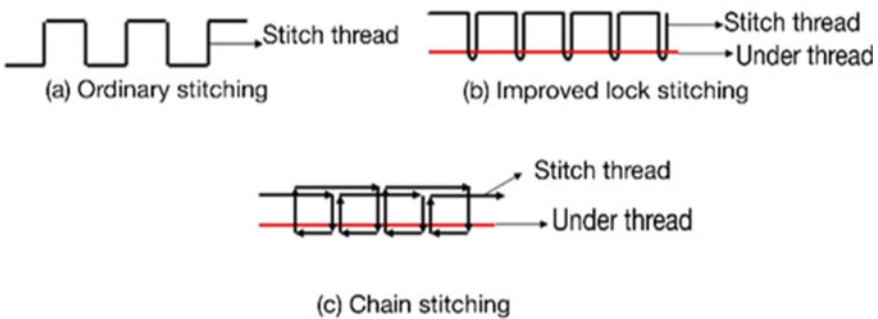


Fig. 1 The stitching trajectory of different stitching types

thermal stability and low temperature resistance. Aramid fiber has the characteristics of high toughness, easy weaving, and good impact resistance, and because its price is relatively cheap, it is widely used in the field of composite materials.

2.1.3 Twist of Stitches

The twist T is the number of twists per unit length (m^{-1}). Pitch h refers to the distance between two adjacent threads of the yarn. The relation between twist and pitch is $T = 1/h$.

It is found from the literature that there is less research on the effect of twist of stitch on the properties of stitched composites. In fact, the twist of the stitch will affect the degree of bonding between the stitch and the resin, and the mechanical properties of the stitch itself. The effect on the performance of stitched composites cannot be ignored.

2.2 The Material and Configuration of the Test Piece

The experimental component materials used in this study are consistent with those used in reference [17]. In the hybrid area, the 3DWC plates and the Ti plates were connected by stitches only.

The test is divided into three parts: interlaminar shear strength test, short-beam strength test, and Mode I fracture toughness test. The effects of stitching types, stitch fiber materials, and twist on the interface properties of the hybrid broad were investigated.

2.2.1 Sample Configuration of Interlaminar Shear Strength Test

The schematic diagram of the experimental pieces is as shown in Fig. 2. From top to bottom, there are a single 3DWC laminate I, two identical Ti plates I and II, and 3DWC laminate II. The central two Ti plates are prefabricated with holes of the same form for the stitches to pass through.

2.2.2 Sample Configuration of Short-Beam Strength Test

The schematic diagram of the experimental pieces is as shown in Fig. 3. From top to bottom, there are a single 3DWC laminate, Ti plates, and 3DWC laminate. The central Ti plates are prefabricated with holes of the same form for the stitches to pass through.

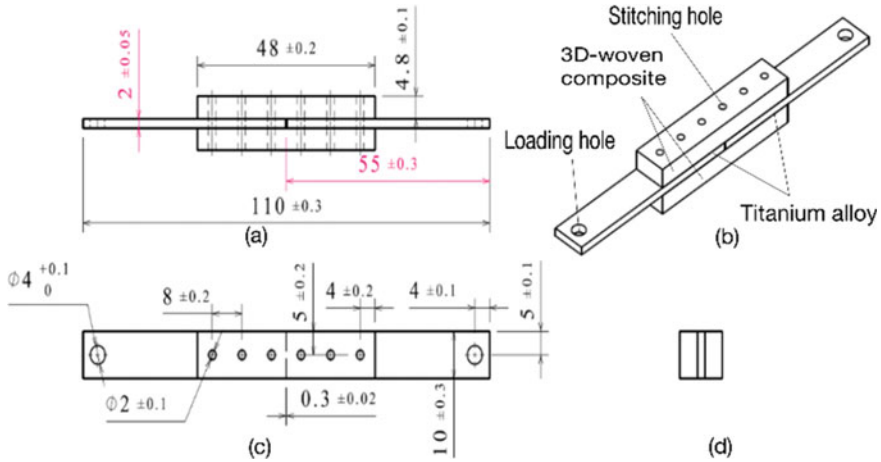


Fig. 2 Experimental piece of interlaminar shear strength test a front view, b equiaxial test view, c top view, and d side view

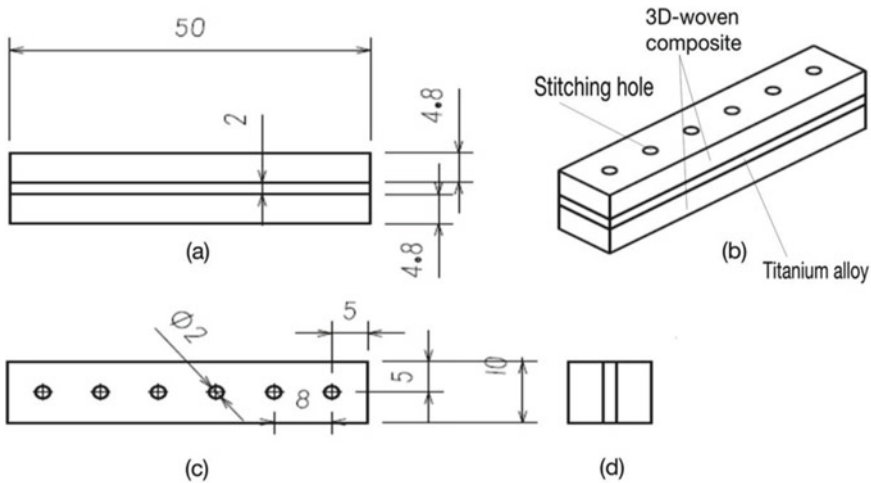


Fig. 3 Experimental piece of short-beam strength test a front view, b equiaxial test view, c top view, and d side view

2.2.3 Sample Configuration of Mode I Fracture Toughness Test

The schematic diagram of the experimental pieces is as shown in Fig. 4. From top to bottom, there are a single 3DWC laminate (with loading block), Ti plates, and 3DWC laminate (with loading block). The central Ti plates are prefabricated with holes of the same form for the stitches to pass through.

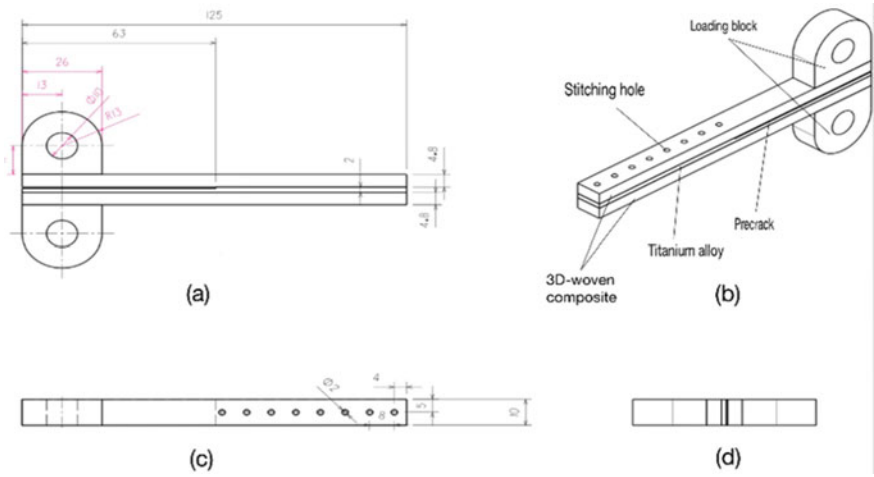
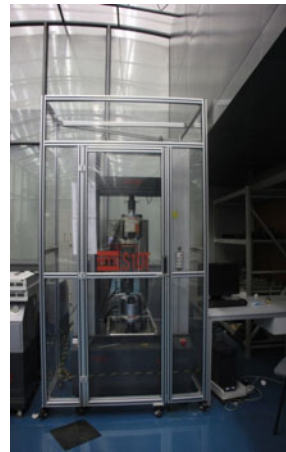


Fig. 4 Experimental piece of Mode I fracture toughness test **a** front view, **b** equiaxial test view, **c** top view, and **d** side view

Fig. 5 UTM5105X microcomputer controlled electronic universal mechanical testing machine



2.3 The Experimental Method

In this study, a UTM5105X microcomputer controlled electronic universal mechanical testing machine is used, as shown in Fig. 5. The testing machine is composed of a host machine, an overall operating platform, and testing software and has a variety of testing functions. The experimental load and displacement of the upper beam are recorded in real time by the testing machine. The main technical parameters of the testing machine are as follows: the maximum load is 100 kN; load accuracy is within 1% set value; the relative error of the test force is within $\pm 0.5\%$; the relative error of the deformation value is within $\pm 0.5\%$.

Fig. 6 Loading process of interlaminar shear strength test

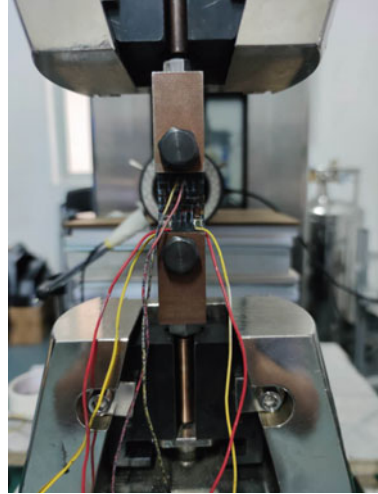
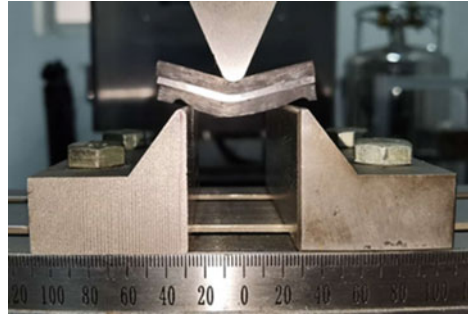


Fig. 7 Loading process of short-beam strength test



2.3.1 Interlaminar Shear Strength Test

The test was conducted according to ASTM standard: D3528/D3528-96 Standard Test Method for Strength Properties of Double Lap Shear Adhesive Joints by Tension Loading.

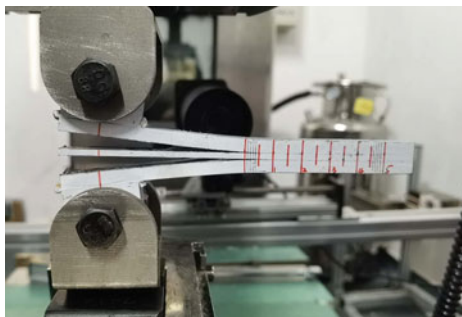
The experimental device is shown in Fig. 6. The loading is controlled by displacement and the loading rate is set at 2 mm/min.

2.3.2 Short-Beam Strength Test

The test was conducted according to ASTM standard: D2344/D 2344M-00(06) Standard Test Method for Short-Beam Strength of Polymer Matrix Composite Materials and Their Laminates.

The experimental device is shown in Fig. 7. The loading is controlled by displacement and the loading rate is set at 1 mm/min.

Fig. 8 Loading process of Mode I fracture toughness test



2.3.3 Mode I Fracture Toughness Test

The test was conducted according to ASTM standard: D5528-13 Standard Test Method for Mode I Interlaminar Fracture Toughness of Unidirectional Fiber-Reinforced Polymer Matrix Composites.

Water-based correction solution is applied to both sides of the sample to allow for observation of delamination initiation. An optical microscope is placed on one side of the specimen to observe the layered frontiers that extend along one side during the test. The loading was controlled by displacement and the loading rate was set at 2 mm/min. The experimental device is shown in Fig. 8.

3 Results and Discussion

The mechanical parameters of the 3DWC composite material plate used in this study were obtained by the static test in advance, as shown in Table 1. Poisson's ratio of the material is 0.038.

The results revealed the following for 3D woven composite/titanium alloy hybrid samples:

- (1) Interface shear: compared with ordinary stitching, the maximum load and ultimate strength of improved lock stitching and chain stitching are slightly increased. Compared with PI fiber, the maximum load and ultimate strength of carbon fiber and aramid fiber increased obviously, the maximum load and ultimate strength of aramid fiber increased by 135.6 and 136.8%, respectively. Compared with the untwisted stitches, the ultimate load and strength of the test piece are increased by twisting. The maximum load and ultimate strength of the twist of 30 m^{-1} are increased by 211.2% and 213.1%, respectively.
- (2) Short-beam strength: the maximum load and the strength of the short beam do not change significantly with the change of stitching types, stitch fiber materials, and the twist of stitches.

Table 1 3DWC composite material parameters

Performance	Properties	Value (MPa)
Warp tensile	Tensile strength	1086.4
	Tensile modulus	84400
Weft tensile	Tensile strength	567
	Tensile modulus	60100
Warp compression	Compressive strength	459
	Compression modulus	71163.8
Weft Compression	Compressive strength	398.3
	Compression modulus	52487.7
Shear	Shear strength	98.26
	Shear modulus	5091850
Bending	Flexural strength	397.23
	Flexural modulus	41.22

**Fig. 9** Interlaminar shear specimen failure

- (3) Interlaminar fracture toughness: the existence of stitches makes crack propagation difficult, and stitching greatly strengthens the delamination resistance of the sample. The specimen reinforced with carbon fiber stitches has better delamination resistance. Over-twisting of the stitches damages the tensile properties of the stitches and leads to the decrease of the delamination resistance of the samples.

3.1 Influence of Stitching Parameters on Interlaminar Shear Properties

The failure mode of this series of test samples is stitch shear fracture, as shown in Fig. 9. Take out the damaged sample for enlarged observation, as shown in Fig. 10. The stitch was not pulled out. Due to the low strength of the epoxy resin in the stitch hole, it was crushed in the loading process, and the stitch hole could not support the stitches. In this case, the shear stress on the stitches was applied by 3DWC, the fracture point of the stitch was not located on the surface of 3DWC, but was offset along the axial direction of the stitch, and there were different lengths of threads at the fracture point.

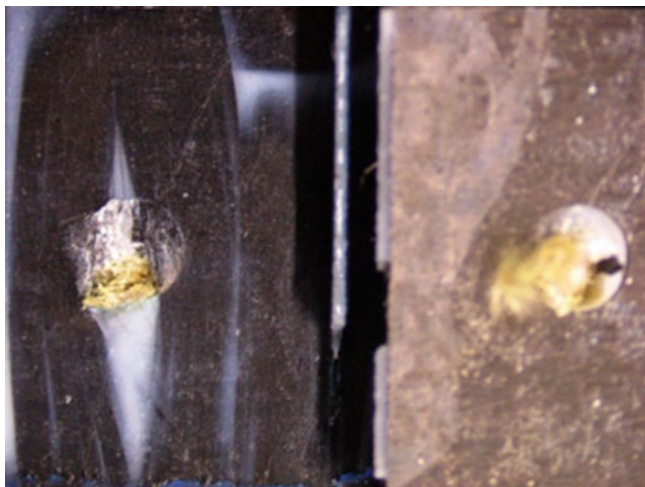


Fig. 10 Enlarged view of interlaminar shear specimen failure

3.1.1 Stitching Types

Because of the three stitching types, the test was divided into three groups, each group containing six samples. All three groups used carbon fiber stitches with twist of 30 m^{-1} . The maximum load and interlaminar shear strength are shown in Table 2. It can be seen that both improved lock stitching, and chain stitching can improve the ultimate load and strength of the test piece. Compared with ordinary stitching, the maximum load of chain stitching was increased by 7.8%, and the maximum load of improved lock stitching was increased by 8.5%. Compared with ordinary stitching, the strength of chain stitching was increased by 7.7%, and the strength of improved lock stitching was increased by 8.7%. The load-displacement curves of the samples are shown in Figs. 11, 12, and 13.

3.1.2 Stitch Fiber Materials

The experiment was divided into three groups, each containing four samples. The improved lock stitching was used in all three groups with twist of 30 m^{-1} . The maximum load and interlaminar shear strength are shown in Table 3. It can be seen that both carbon fiber and aramid fiber increase the ultimate load and strength of the test pieces. Compared with PI fiber, the maximum load of carbon fiber is increased by 39.9% and that of aramid fiber is increased by 135.6%. Compared with PI fiber, the strength of carbon fiber is increased by 40.6%, and the strength of aramid fiber is increased by 136.8%. The load-displacement curves of the samples are shown in Figs. 14, 15, and 16.

Fig. 11 Load-displacement curve of ordinary stitching

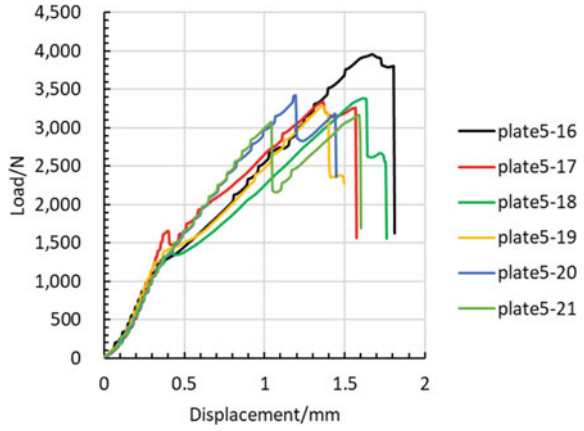


Fig. 12 Load-displacement curve of chain stitching

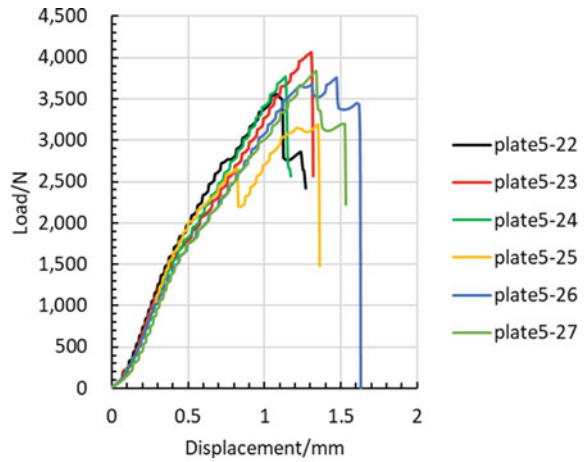


Fig. 13 Load-displacement curve of improved lock stitching

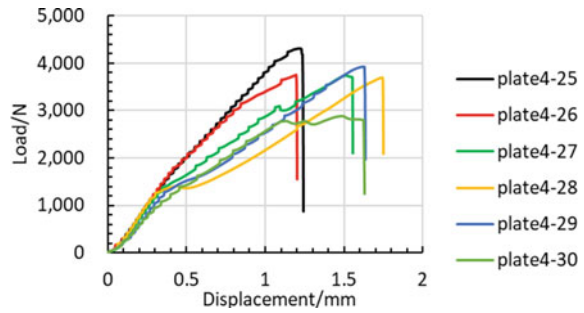


Fig. 14 Load-displacement curve of carbon fiber

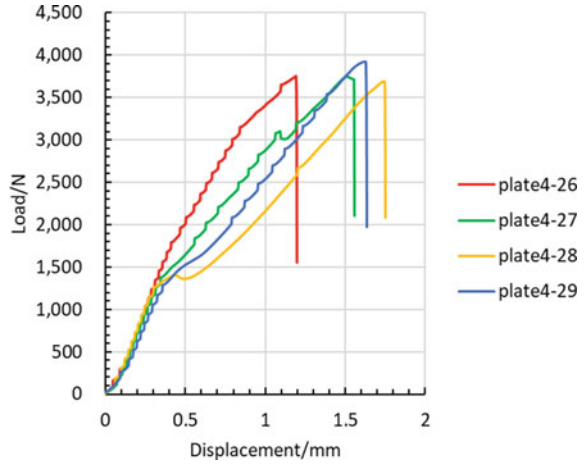


Fig. 15 Load-displacement curve of PI fiber

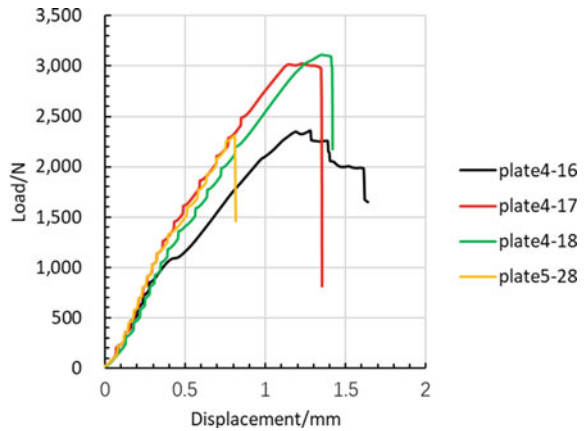


Fig. 16 Load-displacement curve of aramid fiber

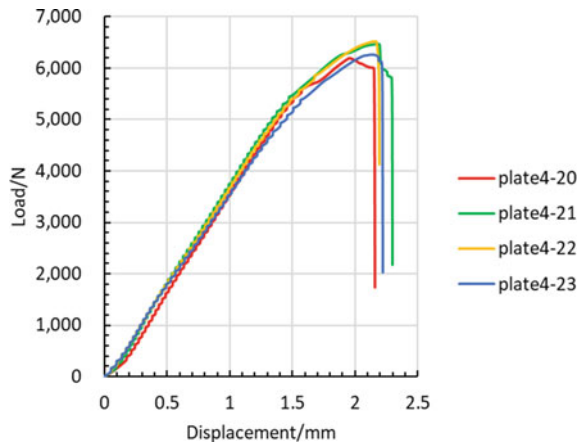


Table 2 Interlaminar shear performance of different stitching types

Stitching types	Specimen number	Ultimate load/N	Ultimate strength/MPa
Ordinary stitching	Plate 5–16	3963.1	8.25
	Plate 5–17	3338.3	6.98
	Plate 5–18	3384.3	7.09
	Plate 5–19	3287.2	6.84
	Plate 5–20	3424.7	7.17
	Plate 5–21	3173.3	6.63
	Mean value	3428.5	7.2
	Standard deviation	276.0	0.6
	Coefficient of dispersion/%	8.1	7.9
Chain stitching	Plate 5–22	3558.7	7.43
	Plate 5–23	4061.9	8.48
	Plate 5–24	3771.7	7.86
	Plate 5–25	3188.7	6.64
	Plate 5–26	3757.2	7.84
	Plate 5–27	3836.8	8.02
	Mean value	3695.8	7.71
	Standard deviation	296.4	0.63
	Coefficient of dispersion/%	8.0	8.1
Improved lock stitching	Plate 4–25	4313.98	9
	Plate 4–26	3754.52	7.86
	Plate 4–27	3746.38	7.85
	Plate 4–28	3692.04	7.76
	Plate 4–29	3926.78	8.17
	Plate 4–30	2889.26	6.04
	Mean value	3720.5	7.78
	Standard deviation	466.6	0.97
	Coefficient of dispersion/%	12.5	12.43

3.1.3 Twist of Stitches

Three levels of twist were used in the test: no twist, 30 m^{-1} , and 60 m^{-1} . The experiment was divided into three groups, each containing four samples. All three groups used improved lock stitching with aramid fiber as stitch material. The maximum load and interlaminar shear strength are shown in Table 4. It can be seen that the twisting of stitches increases the ultimate load and strength of test pieces. Compared with no twist, the maximum load of twist of 60 m^{-1} and 30 m^{-1} twist are increased by 12.2%

Table 3 Interlaminar shear performance of different stitch fiber materials

Stitch fiber materials	Specimen number	Ultimate load/N	Ultimate strength/MPa
Carbon fiber	Plate 4–26	3754.52	7.86
	Plate 4–27	3746.38	7.85
	Plate 4–28	3692.04	7.76
	Plate 4–29	3926.78	8.17
	Mean value	3779.9	7.9
	Standard deviation	101.8	0.2
	Coefficient of dispersion/%	2.7	2.3
PI fiber	Plate 5–28	2306.48	4.81
	Plate 4–16	2363.68	4.9
	Plate 4–17	3029.18	6.28
	Plate 4–18	3109.92	6.51
	Mean value	2702.3	5.6
	Standard deviation	426.0	0.9
	Coefficient of dispersion/%	15.8	15.9
Aramid fiber	Plate 4–20	6196.96	12.91
	Plate 4–21	6472.62	13.61
	Plate 4–22	6525.86	13.63
	Plate 4–23	6270.66	13.12
	Mean value	6366.5	13.3
	Standard deviation	157.7	0.4
	Coefficient of dispersion/%	2.5	2.7

and 211.2% respectively. Compared with no twist, the strength of twist of 60 m^{-1} and 30 m^{-1} are increased by 11.9% and 213.1% respectively. The load-displacement curves of the samples are shown in Figs. 17, 18, and 19.

3.2 Influence of Stitching Parameters on Short-Beam Shear Strength

All the samples in this group are interlaminar shear failure. The typical failure photos of the test part are shown in Fig. 20. It can be seen that the failure forms of the samples are interlaminar shear failure at the interface between braided materials and titanium alloy plates. Some samples have stitches pulled out, and slight compression and tensile failure occur on both sides of the loading site.

Table 4 Interlaminar shear performance of different twists of stitches

Twist (m^{-1})	Specimen number	Ultimate load/N	Ultimate strength /MPa
30	Plate 4-21	6472.62	13.61
	Plate 4-22	6525.86	13.63
	Plate 4-23	6270.66	13.12
	Mean value	6423.0	13.5
	Standard deviation	134.6	0.3
	Coefficient of dispersion/%	2.1	2.1
60	Plate 7-16	2168.76	4.51
	Plate 7-17	2147.2	4.46
	Plate 7-19	2633.18	5.46
	Mean value	2316.4	4.8
	Standard deviation	274.6	0.6
	Coefficient of dispersion/%	11.9	11.7
0	Plate 7-24	2170.08	4.52
	Plate 7-26	2151.38	4.49
	Plate 7-27	1869.56	3.88
	Mean value	2063.7	4.3
	Standard deviation	168.4	0.4
	Coefficient of dispersion/%	8.2	8.4

Fig. 17 Load-displacement curve of twist of $0 m^{-1}$

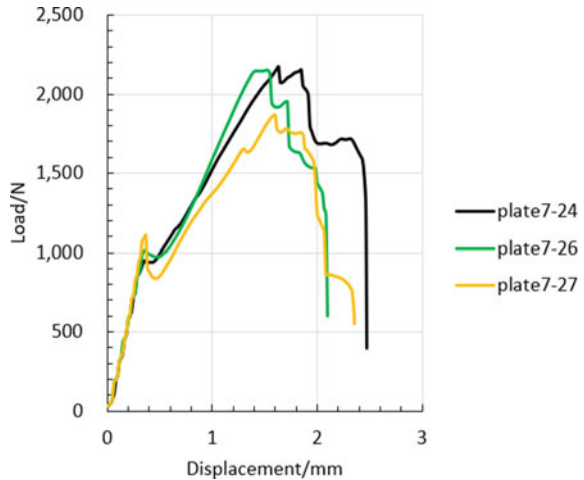


Fig. 18 Load-displacement curve of twist of 30 m^{-1}

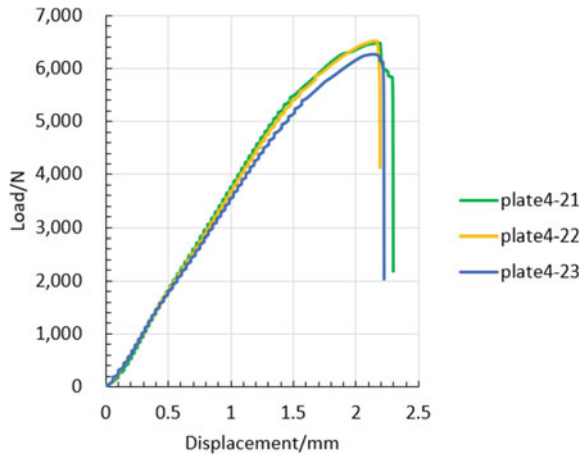
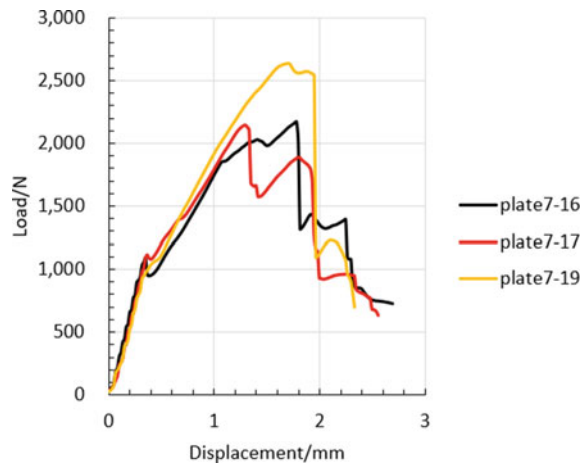


Fig. 19 Load-displacement curve of twist of 60 m^{-1}



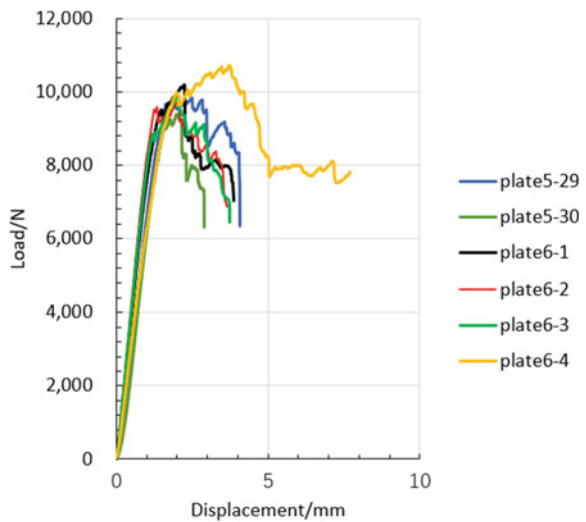
3.2.1 Stitching Types

Because of the three stitching types, the test was divided into three groups, each group containing six samples. All three groups used carbon fiber stitches with twist of 30 m^{-1} . The maximum load and short-beam strength are shown in Table 5. It can be seen that both improved lock stitching, and chain stitching can improve the ultimate load and short-beam strength of the test pieces. Compared with ordinary stitching, the maximum load of chain stitching is increased by 10.8%, and the maximum load of improved lock stitching is increased by 3.0%. Compared with ordinary stitching, the strength of short beam with chain stitching was increased by 11.5% and that with improved lock stitching was increased by 2.9%. The load-displacement curves of the samples are shown in Figs. 21, 22, and 23.



Fig. 20 Failure of short-beam shear specimen

Fig. 21 Load-displacement curve of ordinary stitching



3.2.2 Stitch Fiber Materials

The experiment was divided into three groups, each containing four samples. The improved lock stitching was used in all three groups with twist of 30 m^{-1} . The maximum load and interlaminar shear strength are shown in Table 6. It can be seen that both carbon fiber and PI fiber increase the ultimate load and strength of the test pieces. Compared with aramid fiber, the maximum load of carbon fiber is increased by 8.2% and that of PI fiber is increased by 3.4%. Compared with aramid fiber,

Table 5 Short-beam shear strength of different stitching types

Stitching types	Specimen number	Ultimate load/N	Short-beam shear strength/MPa
Ordinary stitching	Plate 5–29	9832.9	63.44
	Plate 5–30	9379.9	60.35
	Plate 6–1	10188.8	64.89
	Plate 6–2	9848.3	63.54
	Plate 6–3	9827.4	63.42
	Plate 6–4	10719.2	68.81
	Mean value	9966.1	64.1
	Standard deviation	449.7	2.8
	Coefficient of dispersion/%	4.5	4.3
Chain stitching	Plate 6–14	10391.4	66.61
	Plate 6–15	10841.6	69.94
	Plate 6–16	10688.4	68.8
	Plate 8–16	11509.7	75.06
	Plate 8–17	11524.4	74.84
	Plate 8–18	11311	73.51
	Mean value	11044.4	71.5
	Standard deviation	471.6	3.5
	Coefficient of dispersion/%	4.3	4.9
Improved lock stitching	Plate 3–1	10164.8	64.34
	Plate 3–2	9331.5	60.48
	Plate 3–3	10182	65.49
	Plate 3–4	10835.4	69.27
	Plate 3–5	10660.3	68.84
	Plate 3–6	10408.2	67.17
	Mean value	10263.7	65.9
	Standard deviation	527.3	3.3
	Coefficient of dispersion/%	5.1	5.0

the strength of carbon fiber is increased by 8.7%, and the strength of the PI fiber is increased by 4.3%. The load-displacement curves of the samples are shown in Figs. 24, 25, and 26.

3.2.3 Twist of Stitches

The experiment was divided into three groups, each containing four samples. All three groups used improved lock stitching with aramid fiber as stitch material. The

Fig. 22 Load-displacement curve of chain stitching

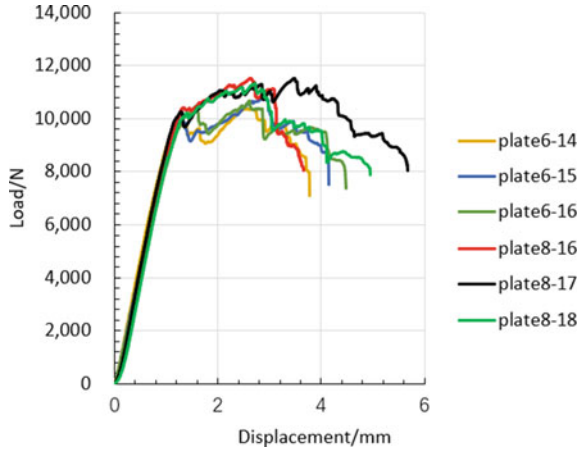


Fig. 23 Load-displacement curve of improved lock stitching

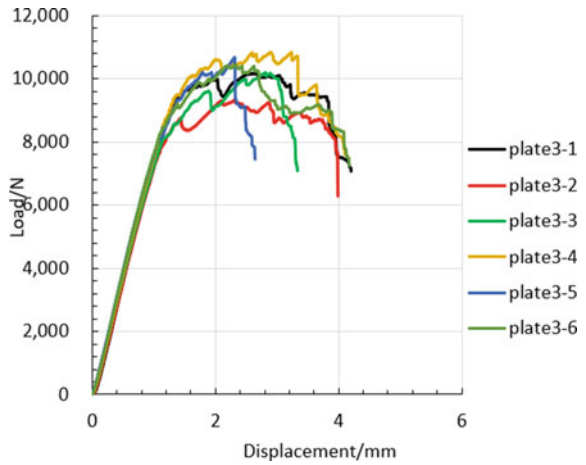


Fig. 24 Load-displacement curve of carbon fiber

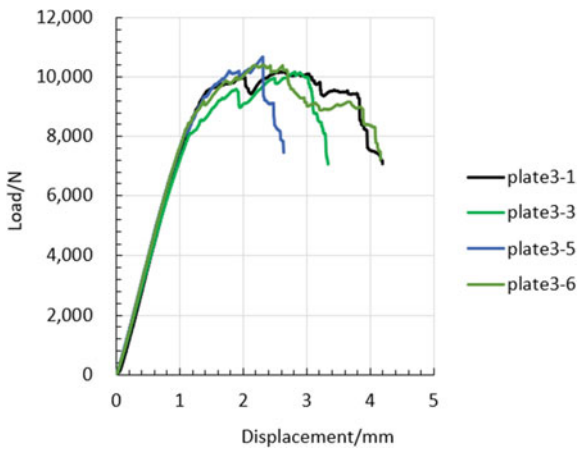


Table 6 Short-beam shear strength of different stitch fiber materials

Stitch fiber materials	Specimen number	Ultimate load/N	Short-beam shear strength/MPa
Carbon fiber	Plate 3-1	10164.8	64.34
	Plate 3-3	10182	65.49
	Plate 3-5	10660.3	68.84
	Plate 3-6	10408.2	67.17
	Mean value	10353.8	66.5
	Standard deviation	232.5	2.0
	Coefficient of dispersion/%	2.2	3.0
PI fiber	Plate 3-13	9909.2	64.01
	Plate 3-14	9568.7	61.85
	Plate 3-15	10049.8	64.12
	Plate 6-5	10057	65.21
	Mean value	9896.2	63.8
	Standard deviation	228.7	1.4
	Coefficient of dispersion/%	2.3	2.2
Aramid fiber	Plate 3-7	9485.5	60.07
	Plate 3-9	9865.5	62.16
	Plate 3-10	9464.4	61.48
	Plate 3-11	9478.3	60.88
	Mean value	9573.4	61.1
	Standard deviation	194.9	0.9
	Coefficient of dispersion/%	2.0	1.5

Fig. 25 Load-displacement curve of PI fiber

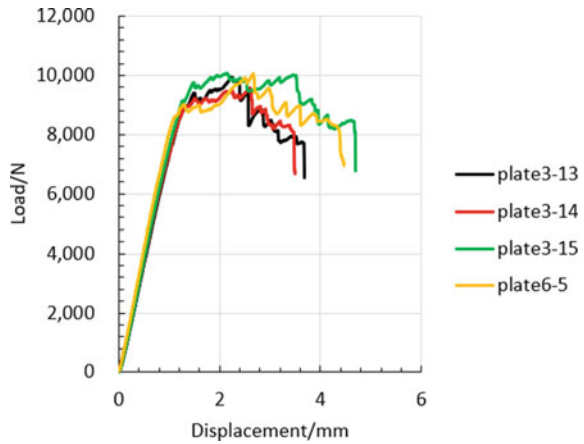


Fig. 26 Load-displacement curve of aramid fiber

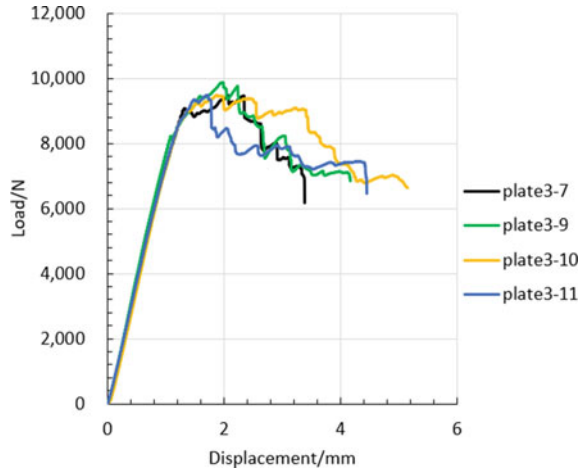
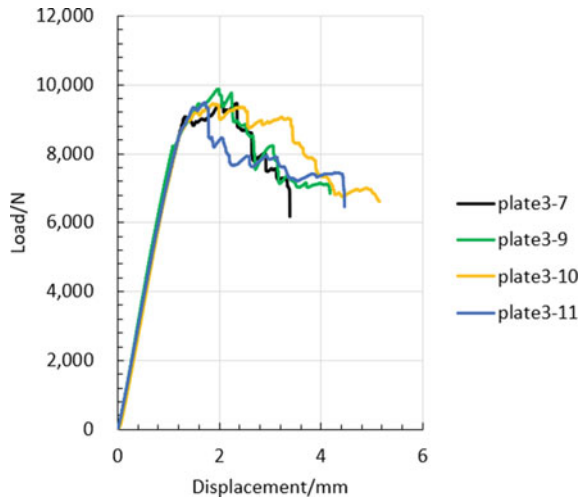


Fig. 27 Load-displacement curve of twist of 30 m^{-1}

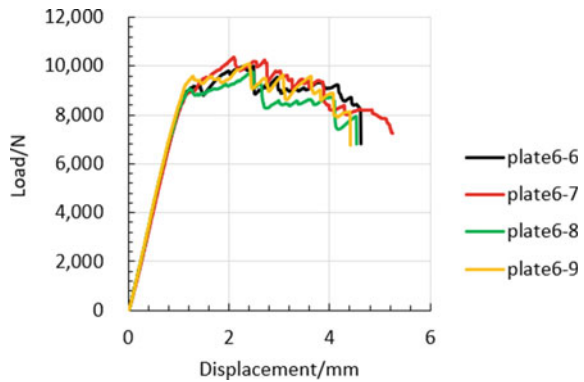


maximum load and short-beam shear strength are shown in Table 7. It can be seen that the twisting of stitches does not improve the ultimate load and strength of the test pieces. Compared with twist of 30 m^{-1} , the maximum load of twist of 60 m^{-1} and no twist are increased by 5.0% and 12.2%, respectively. Compared with twist of 30 m^{-1} , the strength of twist of 60 m^{-1} and no twist are increased by 5.5% and 14.1%, respectively. The load-displacement curves of the samples are shown in Figs. 27, 28, and 29.

Table 7 Short-beam shear strength of different twists of stitches

Twist (m^{-1})	Specimen number	Ultimate load/N	Short-beam shear strength/MPa
30	Plate 3-7	9485.5	60.07
	Plate 3-9	9865.5	62.16
	Plate 3-10	9464.4	61.48
	Plate 3-11	9478.3	60.88
	Mean value	9573.4	61.1
	Standard deviation	194.9	0.9
	Coefficient of dispersion/%	2.0	1.5
60	Plate 6-6	10019	64.39
	Plate 6-7	10352.7	66.19
	Plate 6-8	9759	62.6
	Plate 6-9	10084	64.77
	Mean value	10053.7	64.5
	Standard deviation	243.8	1.5
	Coefficient of dispersion/%	2.4	2.3
0	Plate 9-1	10711.58	69.02
	Plate 8-19	10426	67.81
	Plate 8-20	10814.5	70.43
	Plate 8-21	11012.5	71.86
	Mean value	10741.1	69.8
	Standard deviation	244.4	1.8
	Coefficient of dispersion/%	2.3	2.5

Fig. 28 Load-displacement curve of twist of $60 m^{-1}$



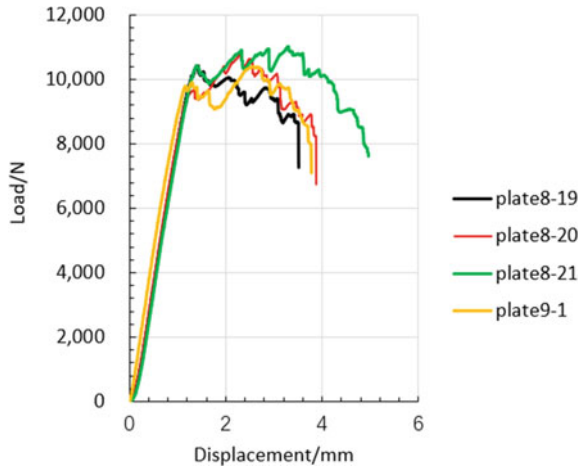


Fig. 29 Load-displacement curve of twist of 0 m^{-1}

3.3 Influence of Stitching Parameters on Mode I Fracture Toughness

Since the specimens are connected by stitches, crack propagation is not a continuous process. The crack grows rapidly before the stitch and very slowly when it meets the stitch. The values of Mode I fracture toughness calculated by the modified beam theory or the beam theory are not relevant. Therefore, the failure modes and the corresponding load-displacement curves of the samples are listed, in which the fracture of the stitches corresponds to the steep drops of the load in the load-displacement curves. There are three main modes of specimen failure in the test:

The three-dimensional braided plate laminated fracture at the precrack tip. As shown in Fig. 30, name this mode A.

Parts of the stitches are tensile fracture, and the three-dimensional braided plate was layered fracture. As shown in Fig. 31, name this mode B.

All the stitches were tensile fracture, and the 3D braided laminates were peeled off from the titanium alloy plates. As shown in Fig. 32, name this mode C.

3.3.1 Stitching Types

The test was divided into three groups, with ten samples in the ordinary stitching group and six samples in each other group. All three groups used carbon fiber stitches with twist of 30 m^{-1} . It can be seen from Table 8 that most failure modes of the hybrid plate are mode A. Even in mode B, the number of fractures in the stitches is less. It can be seen that the existence of stitches makes it difficult to extend the crack,

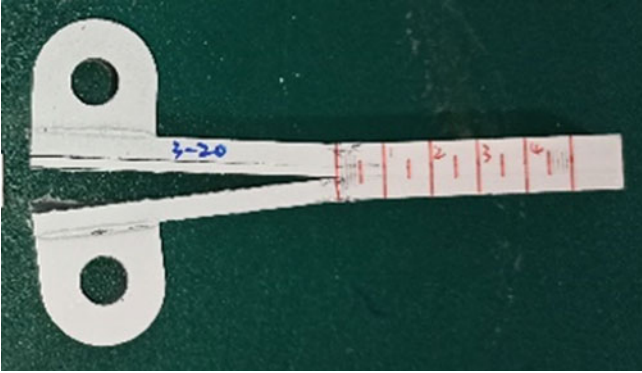


Fig. 30 Interlaminar fracture sample Mode A



Fig. 31 Interlaminar fracture sample Mode B

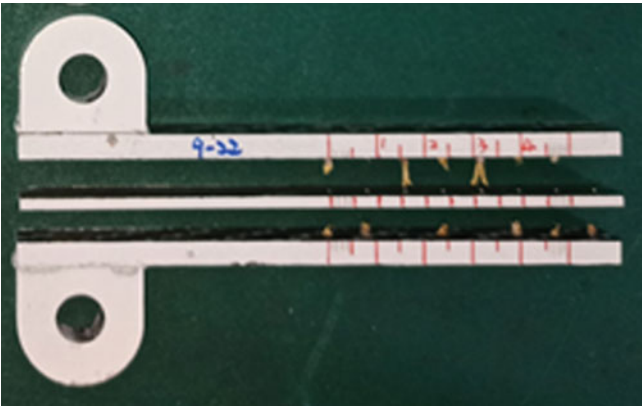


Fig. 32 Interlaminar fracture sample Mode C

Table 8 Failure modes of Mode I fracture toughness test with different stitching types

Stitching types	Specimen number	Failure modes
Ordinary stitching	Plate 3–16	A, the composite material is not delaminated
	Plate 3–17	B
	Plate 3–18	A, the composite material is not delaminated
	Plate 3–19	A
	Plate 3–20	A
	Plate 3–21	A
	Plate 3–22	A
	Plate 3–23	A, the composite material is not delaminated
	Plate 3–24	A
	Plate 3–25	A
Chain stitching	Plate 6–24	A
	Plate 6–25	A
	Plate 6–26	B, 3 stitches were tensile fracture
	Plate 6–27	B, 2 stitches were tensile fracture
	Plate 6–28	Loading block debonded
	Plate 6–29	A
Improved lock stitching	Plate 6–18	A
	Plate 6–19	B
	Plate 6–20	B
	Plate 6–21	A
	Plate 6–22	A
	Plate 6–23	A

and the stitches greatly strengthen the anti-delamination ability of the samples. The load-displacement curves of the samples are shown in Figs. 33, 34, and 35.

3.3.2 Stitch Fiber Materials

The experiment was divided into three groups, the PI fiber group contained four samples and the other groups had six samples. The improved lock stitching was used in all three groups with twist of 30 m^{-1} . It can be seen from Table 9 that the failure mode of the carbon fiber stitch material group is mostly mode A, the PI fiber group is mode C, and the aramid fiber group is mode B. The main reason lies in the tensile property of the stitches, and the carbon fiber is stronger than the aramid fiber and PI fiber. It can be concluded that the specimen reinforced with carbon fiber stitches has

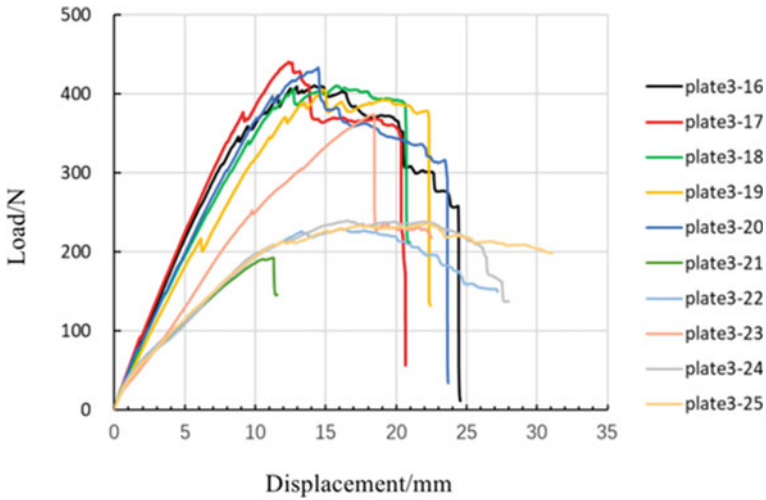
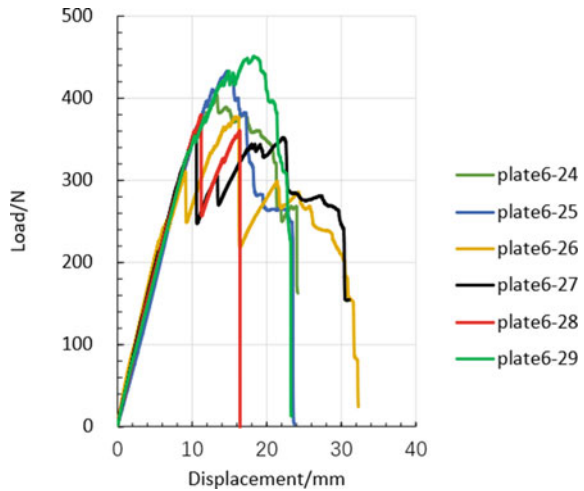


Fig. 33 Load-displacement curve of ordinary stitching

Fig. 34 Load-displacement curve of chain stitching



stronger delamination resistance. The load-displacement curves of the samples are shown in Figs. 36, 37, and 38.

3.3.3 Twist of Stitches

The experiment was divided into three groups. There are six samples in twist of 60 m^{-1} group and four samples in each other group. All three groups used improved lock stitching with aramid fiber as stitch material. As can be seen from Table 10,

Fig. 35 Load-displacement curve of improved lock stitching

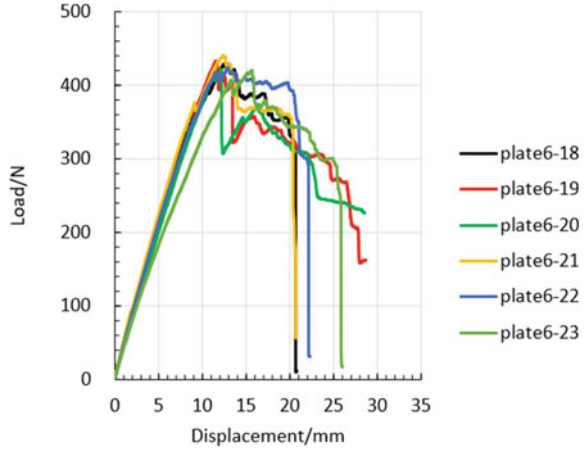


Table 9 Failure modes of Mode I fracture toughness test with different stitch fiber materials

Stitch fiber materials	Specimen number	Failure modes
Carbon fiber	Plate 6–18	A
	Plate 6–19	B
	Plate 6–20	B
	Plate 6–21	A
	Plate 6–22	A
	Plate 6–23	A
PI fiber	Plate 9–20	C
	Plate 9–21	C
	Plate 9–22	C
	Plate 9–23	C
Aramid fiber	Plate 6–30	A
	Plate 6–31	B, 2 stitches were tensile fracture
	Plate 6–32	B, 1 stitch was tensile fracture
	Plate 9–17	B, 3 stitches were tensile fracture
	Plate 9–18	B, 2 stitches were tensile fracture
	Plate 9–19	B, 2 stitches were tensile fracture

Fig. 36 Load-displacement curve of carbon fiber

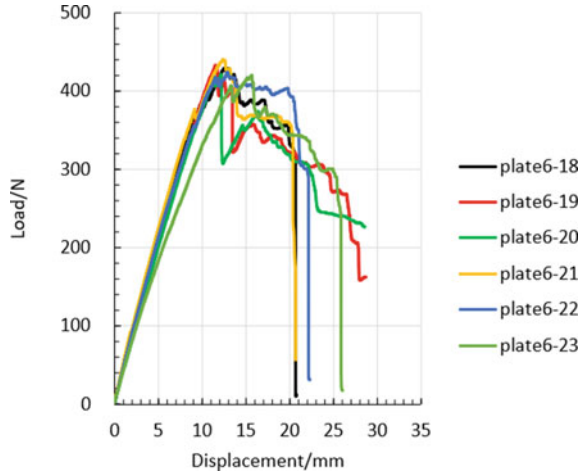
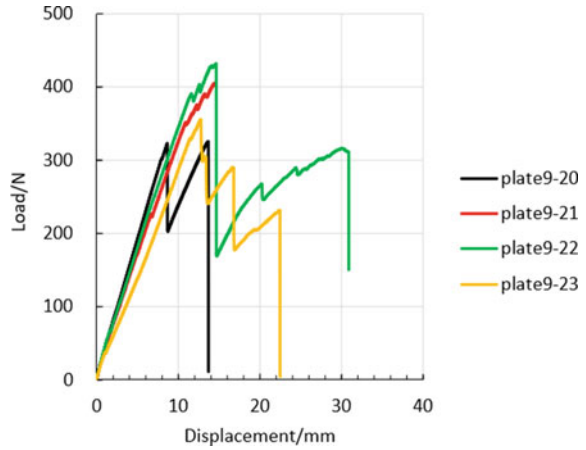


Fig. 37 Load-displacement curve of PI fiber



most of the failure modes of the untwisted and twist of 30 m^{-1} stitches are mode B, while the failure modes of the twist of 60 m^{-1} stitches are mode C. It can be seen that excessive twisting of the stitches damages the tensile properties of the stitch, leading to a decrease in the delamination resistance of the samples. The load-displacement curves of the samples are shown in Figs. 39, 40 and 41.

Fig. 38 Load-displacement curve of aramid fiber

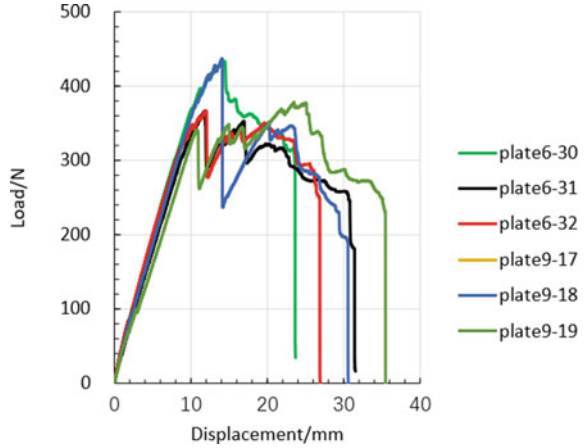


Table 10 Failure modes of Mode I fracture toughness test with different twists of stitches

Twist of stitches (m^{-1})	Specimen number	Failure modes
30	Plate 6–30	A
	Plate 6–31	B, 2 stitches were tensile fracture
	Plate 6–32	B, 1 stitch was tensile fracture
	Plate 9–17	B, 3 stitches were tensile fracture
	Plate 9–18	B, 2 stitches were tensile fracture
	Plate 9–19	B, 2 stitches were tensile fracture
60	Plate 9–24	B, 1 stitch was tensile fracture
	Plate 9–25	C
	Plate 9–26	C
	Plate 9–27	B, 2 stitches were tensile fracture
0	Plate 9–32	A
	Plate 10–17	B, 1 stitch was tensile fracture
	Plate 10–18	B, 5 stitches were tensile fracture
	Plate 10–19	B, 2 stitches were tensile fracture

Fig. 39 Load-displacement curve of twist of 30 m^{-1}

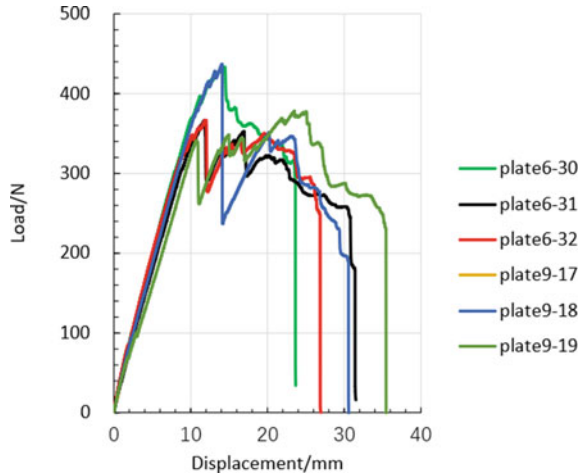
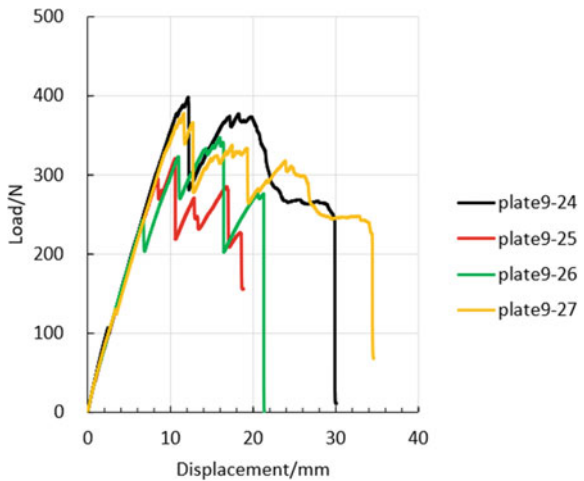


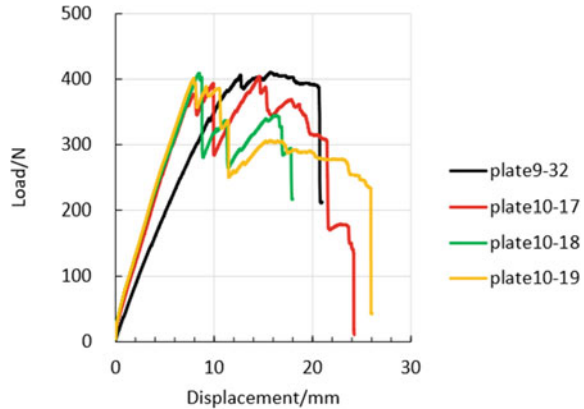
Fig. 40 Load-displacement curve of twist of 60 m^{-1}



4 Conclusion

- (1) When considering interlaminar shear properties: compared with PI fiber, the maximum load and ultimate strength of aramid fiber increased by 135.6% and 136.8%, respectively. Compared with the untwisted stitches, the maximum load and ultimate strength of the twist of 30 m^{-1} are increased by 211.2% and 213.1%, respectively. Excessive twisting of the stitches will lead to a decrease in the ultimate load and strength of the structure, so twist of 30 m^{-1} is the best in this study.
- (2) When considering the strength performance of the short beam: the maximum load and the strength of the short beam do not change significantly with the

Fig. 41 Load-displacement curve of twist of 0 m^{-1}



change of stitching types, stitch fiber materials, and the twist of stitches. In general, chain stitching and untwisted carbon fiber stitches strengthen the short beam with the best strength.

- (3) When the interlaminar fracture toughness is considered: the interlaminar fracture toughness is increased by stitching, and the delamination resistance of the sample strengthened by carbon fiber stitch is stronger; over-twisting of stitches results in a decrease in the delamination resistance. Therefore, the twist of the stitches should be controlled below 60 m^{-1} .
- (4) The results revealed that the failure mode of the interlaminar shear test specimens is all shear failure of stitches. The failure mode of short-beam strength specimens is the interlaminar shear failure of 3D braided laminates. And there are three failure modes in the interlaminar fracture toughness test: the three-dimensional braided plate laminated fracture at the precrack tip; part of the stitches are tensile fracture, and the three-dimensional braided plate was layered fracture; all the stitches were tensile fracture, and the 3D braided laminates were peeled off from the titanium alloy plates. The formation of the three modes was mainly related to the stitch fiber materials and the degree of twist.

References

1. Hongyan G (2014) Study on in-plane stiffness and strength prediction model of stitched composite materials. Nanjing University of Aeronautics and Astronautics
2. Weimer C, Mitschang P (2001) Aspects of the stitch formation process on the quality of sewn multi-textile-preforms. *Compos A Appl Sci Manuf* 32(10):1477–1484
3. Tianjun N (2008) Research on flow infiltration properties and mechanical properties of warp-knitted axial suture composite materials. Donghua University
4. Tan K, Watanabe N, Iwahori Y (2011) Stitch fiber comparison for improvement of interlaminar fracture toughness in stitched composites. *J Reinf Plast Compos* 30(2):99–109

5. Tan K, Watanabe N, Sano M et al (2010) Interlaminar fracture toughness of vectran-stitched composites-experimental and computational analysis. *J Compos Mater* 44(26):3203–3229
6. Ravandi M, Teo WS, Tran LQN et al (2016) The effects of through-the-thickness stitching on the Mode I interlaminar fracture toughness of flax/epoxy composite laminates. *Mater Design* 109:659–669
7. Tan KT et al (2013) Effect of stitch density and stitch thread thickness on damage progression and failure characteristics of stitched composites under out-of-plane loading. *Compos Sci Technol* 74:194–204. <https://doi.org/10.1016/j.compscitech.2012.11.001>
8. Tan KT, Watanabe N, Iwahori Y (2012) Impact damage resistance, response, and mechanisms of laminated composites reinforced by through-thickness stitching. *Int J Damage Mech* 21(1):51–80. <https://doi.org/10.1177/1056789510397070>
9. Herwan J et al (2014) Effects of stitch density and stitch thread thickness on mode II delamination properties of Vectran stitched composites. *Plast, Rubber Compos* 43(9):300–308. <https://doi.org/10.1179/1743289814Y.0000000103>
10. Joshi P, Kondo A, Watanabe N (2017) Progressive failure analysis of carbon-fibre/epoxy composites laminates to study the effect of stitch densities under in-plane tensile loading. *Plast, Rubber Compos* 46(4):147–154. <https://doi.org/10.1080/14658011.2017.1300124>
11. Riccio A et al (2017) On the use of selective stitching in stiffened composite panels to prevent skin-stringer debonding. *Compos: Part B Eng* 124:64–75. <https://doi.org/10.1016/j.compositesb.2017.05.052>
12. Yanan J, Xiaojiu L, Fuyun D (2002) Research on the properties of three-dimensional seam composite materials. *J Textile Sci* 2002(02):96-98 + 3
13. Karahan M et al (2013) Influence of stitching parameters on tensile strength of aramid/vinyl ester composites. *Mater Sci/Medziagotyra* 19(1):67–72. <https://doi.org/10.5755/j01.ms.19.1.3829>
14. Joshi P, Kondo A, Watanabe N (2016) Numerical analysis to study the effect of through thickness reinforcement with different stitch orientations on open-hole laminates. *Plast, Rubber Compos* 45(10):445–454. <https://doi.org/10.1080/14658011.2016.1245011>
15. Longying Y (2017) The influence of Kevlar suture twist on the mechanical properties of stitched composites. In: Chinese aeronautical society. In: Proceedings of the 2017 (3rd) China aerospace science and technology conference (Suppl). Chinese Aeronautical Society: Chinese Aeronautical Society, p 5
16. Chen Jiping S, Jiazhi ZY (2013) Effect of suture twist on the infiltration and mechanical properties of chain-stitched composite materials. *FRP/Compos Mater Z2*:21–26
17. Yirong L, Huayong Z, Xiuhua C, Hai W (2020) Failure mechanism of stitched three dimension woven composite/Ti alloy hybrid boardjoint under shear load. *J Mater Eng* 202,48(11):162–169

Economic Analysis of Continuous Climb Operation



Donglei Xu, Gang Xiao, and Dongjin Ding

Abstract Due to the limitations of ground facilities and ATC technology, the existing departure and arrival procedures usually adopt the procedures of step climbing and descent. The level flight process increases the operational cost for the aircraft, especially during the climbing phase where a maximum thrust is needed. Trajectory-based operation (TBO) provides a solution to improve the efficiency of flight procedures. The addition of four-dimensional trajectory with time dimension improves the predictability of aircraft operation. Before it is widely used, it is of great significance to evaluate economic benefits. In this research, a method of economic evaluation of continuous climb program (CCO) is proposed. The CCO model is built by using aircraft performance data, and then the fuel cost and time cost are calculated and analyzed based on the cost index (CI). Through the simulation analysis of specific paths, the result shows that CCO procedure has a significant improvement in economy compared with the traditional climb, which is helpful for the future implementation of new air traffic control service.

Keywords Flight procedure · Continuous climb operation · Economic analysis · Cost index · Fuel consumption

1 Introduction

Economic characteristics describes the flight procedure in terms of operating cost effectiveness, especially in terms of reducing fuel consumption and shortening flight time and distance. This leads to the two main economic measurement for flight procedure: fuel cost and time cost. Previous research mainly focuses on the calculation and trade-off between fuel–time costs. Fuel consumption is closely related to the thrust

D. Xu · G. Xiao (✉) · D. Ding
Shanghai Jiao Tong University, Shanghai 200240, China
e-mail: xiaogang@sjtu.edu.cn

D. Xu
e-mail: xudonglei@sjtu.edu.cn

provided by the aircraft, as well as flight velocity and height. For the climb stage, the value of thrust affects the climb speed and altitude, and in turn affects the amount of time to enter the optimal cruise level. A coupling relationship exists between the fuel cost and time cost of the climb procedure, therefore, an integration of the two factors is needed while considering the economic characteristics.

This paper uses the BADA model to calculate fuel consumption of the CCO procedure and uses cost index to construct the economic evaluation model. Then a case study using the model is carried out based on the actual flight from Shanghai to Paris. The second section describes previous researches related to CCO and economic evaluation of flight procedure. The third section introduces the model construction methods, consisting of continuous climb model, fuel consumption model, and cost calculation model. In the fourth section, the method is used for designing and evaluation of CCO procedure of MU553 flight. The simulation results show that CCO has huge benefits in saving fuel and time. The fifth section summarizes the research content and points out the shortcomings and future research directions.

2 Related Research

For aircraft operational cost, calculation elements include fuel cost, trip cost, crew cost, aircraft and ATC costs, maintenance cost, and so on. Factors related to these cost elements are flight hours, aircraft weight, and size, as well as systems and components prices. When it comes to evaluation of the economic characteristics of an operational procedure, the fuel and time cost becomes a crucial point.

For airlines, the concept of Cost Index (CI) [1] which is proposed to calculate the time cost versus fuel cost has been adopted as a way to adjust the navigation strategy to save cost by altering the value of CI, and this method has been widely applied to the Flight Management Computer (FMC) [2].

However, from the operation perspective, the optimal climb efficiency cannot be achieved merely by adjusting CI. Due to limitations of airspace conditions and safety requirements from air traffic control, in most cases step climb is still the major way for aircrafts to depart. After reaching the specified altitude and speed, the aircraft needs to execute level flight until receiving instructions from the air traffic controller, which leads to an increase in operational costs. Therefore, as one of the air traffic stakeholders, ATC needs to make innovations in flight procedures to reduce the level flight during departure and design new instrument flight procedures (IFR) to improve climb efficiency, that in turn contributes to economic aircraft operation.

Continuous climb operation (CCO) is a type of operation for departure achieved through proper airspace design, procedure design, and appropriate ATC clearance. During the operation, the departing aircraft uses optimal engine thrust setting without ATC interference until it climbs to the initial cruise altitude [3]. Over the past two decades, empirical data regarding CCO performance has been collected and analyzed in previous researches. In the United States, Melby et al. [4] analyzed the operating radar data of 34 OEP (Operational Evolution Partnership) airports established by FAA

for approximately 45,000 takeoff and landing routes in one day. It is concluded that the implementation of vertical continuous operation in the critical climb and descent phase saves fuel and flight time. For all OEP airports, an annual economic benefit of 380 million U.S. dollars can be estimated. In Europe, the 2018 EUROCONTROL study revealed that fuel saving from CCO/CDO were up to 340,000 tonnes per year for the airliners, or around €150 million fuel costs [5]. For non-CCO profiles below FL100, a typical level flight of 168 s can consume 15 kg more fuel than CCO profiles.

Models and simulations on CCO have also been developed for academic research. Javier et al. [6] proposed six CCO operation concepts, and implemented CCO simulation analysis at Palma Airport for fuel consumption, climb time, and horizontal flight distance analysis. Comparisons were made among different concepts regarding reducing fuel consumption and time [7]. In terms of the calculation method for fuel consumption and time, Runping G. used the original performance data to obtain the calculation formula of climb fuel consumption by a linear regression fitting equation [8], Ramon and Xavier [9], Judith [10] calculated the fuel consumption savings of CCO optimized trajectory through the correlation coefficient from BADA (Base of Aircraft) model. In addition, there are literatures using QAR data to perform aerodynamic and wind corrections on fuel consumption models, which improves the accuracy of the model [11]. In China, the Civil Aviation Administration of China attaches great importance to energy conservation, emission reduction, and efficiency improvement. The implementation of continuous operation procedures in CDO/CCO is in a stage of combining theoretical exploration and experimentation together, and large-scale trial flights have not yet begun [12].

3 Methodology

3.1 CCO Model

Continuous climb operation (Continuous Climb Operations, CCO) refers to obtaining the initial cruise altitude as soon as possible by setting the optimal speed and thrust by means of continuous climbing [3]. The CCO trajectory is defined as the trajectory executed by the aircraft from the takeoff end point to the initial cruise altitude, including horizontal vertical profile. The horizontal profile follows the existing standard instrument procedures for departure, and climbs and turns through waypoint/navigation stations according to the designated runway and departure route. The vertical profile is a continuous and uninterrupted climb, without ATC control constraints. The profile is affected by the performance of the aircraft, as well as intended flight tasks.

The premise of the basic CCO departure procedure design is that all aircraft climb rates are not restricted. This requires a certain amount of vertical airspace to ensure continuous climb without interference, and the design climb gradient is 60–3000 m/nm. ICAO stipulates the maximum climb rate and minimum climb rate

of the standard departure procedures, and has set up routes that match the climb performance of different aircraft [3], so as to shorten the climb time and improve the efficiency of departure. In this research, the designing of airspace will not be further looked into, and it is assumed that the airspace can support the execution of CCO.

3.2 Aircraft Performance Model

In this section, a fuel consumption model for jet aircraft during continuous climb operation is constructed. BADA (Base of Aircraft Data) is a database consisting of performance data for aircraft developed and maintained by EUROCONTROL. It is based on a kinetic approach to aircraft performance modeling, which models aircraft forces, and is intended for trajectory simulation and prediction in Air Traffic Management research [13].

The parameters used in the model are:

Thr	Thrust, N;
D	Drag, N;
V_{TAS}	True airspeed, m/s;
V_{CAS}	Calibrated airspeed, m/s;
m	Mass, kg;
h	Height, m;
\dot{h}	Vertical speed, m/s;
γ	Aircraft path angle, rad;
g	Gravitational acceleration, 9.80665 m/s ² ;
ρ	Air density, kg/m ³ ;
ρ_0	MSL air density, 1.225 kg/m ³ ;
P	Air pressure, Pa;
P_0	MSL air pressure, 101,325 Pa;
T	Air temperature, °C;
T_0	MSL air temperature, 15 °C;
κ	Adiabatic index of air, 1.4;
R	Real gas constant for air, 287.05287 m ² /K s ²
S	Wing area, m ² ;
C_L	Lift coefficient;
C_D	Drag coefficient;
η	Thrust specific fuel consumption, kg/(min × kN);
C_{f1}	1st thrust specific fuel consumption coefficient, kg/(min · kN);
C_{f2}	2nd thrust specific fuel consumption coefficient, knots;

Total energy model

Following the law of conservation of energy, regarding the aircraft as a mass point, the work done by the external force acting on the aircraft is converted into kinetic

energy and potential energy. The energy model of the aircraft during the climb phase is

$$(Thr - D)V_{TAS} = mgh + mV_{TAS}\dot{V}_{TAS} \quad (1)$$

Generally speaking, the fuel consumption of an aircraft equipped with a turbine engine depends on the amount of thrust. The fuel consumption per unit time and unit thrust η [kg/min•kN] during the climb phase is (the unit of V_{TAS} is knots):

$$\eta = C_{f1}\left(1 + \frac{V_{TAS}}{C_{f2}}\right) \quad (2)$$

Combining the thrust of the aircraft in the climb phase in the flight profile, we can get the fuel consumption per minute f_{climb} [kg/min] (the unit of Thr is kN):

$$f_{climb} = \eta Thr = C_{f1}\left(1 + \frac{V_{TAS}}{C_{f2}}\right) Thr \quad (3)$$

Kinematics model

During the climb of an aircraft, the lift, gravity, thrust, and drag acting on the aircraft will affect the speed and climb rate of the aircraft. From the perspective of fuel consumption, full thrust setting can make the aircraft enter the cruise altitude as soon as possible, providing the optimal fuel economy. The maximum climb thrust of the aircraft can be calculated according to the coefficient of the flight stage of the aircraft, which is given based on different type of aircraft in BADA 3:

$$Thr_{max} = C_{Tc,1}\left(1 - \frac{h}{C_{Tc,2}} + C_{Tc,3} \cdot h^2\right) \quad (4)$$

The aircraft lift and drag are calculated using lift and drag coefficients as follows:

$$\begin{cases} L = C_L \rho V_{TAS}^2 S / 2 \\ D = C_D \rho V_{TAS}^2 S / 2 \end{cases} \quad (5)$$

Considering the airplane is in a horizontal position, therefore lift also equals to mg , so from Eq. (5) we can get the lift coefficient as

$$C_L = 2mg / \rho V_{TAS}^2 S \quad (6)$$

The drag coefficient C_D is related to aircraft configuration, including lift-induced drag and zero-lift drag [14]. BADA 3 specifies the clean configuration during the climb stage, and the drag calculation coefficients of different aircraft types are given in the OPF file. In the nominal case, the formula for calculation of the drag coefficient C_D is as follows:

$$C_D = C_{D_0} + C_{D_2} \times C_L^2 \quad (7)$$

For simpler calculation of the trajectory, the vertical speed \dot{h} can be represented as

$$\dot{h} = \left(\frac{Thr - D}{mg} \right) V_{TAS} \cdot ESF \quad (8)$$

Among which ESF is the energy distribution coefficient, which describes the available power allocated to the climb relative to the acceleration during the climb. According to the selected speed profile, ESF is given as

$$ESF = \left(1 + \frac{V_{TAS}}{g} \frac{dV_{TAS}}{dh} \right)^{-1} \quad (9)$$

In order to simplify the calculation, BADA has defined the ESF value for aircraft not climbing according to the constant CAS or constant M number. For example, when $ESF = 0.3$, 70% of the thrust is used for acceleration, and 30% of the thrust is used for climbing. It is necessary to adjust the value of the ESF to achieve a reasonable climb trajectory.

Considering speed changing during climb, a time period $dt = 1s$ is introduced to calculate the trajectory through the differential formula (10) and (11), and the vertical profile and speed profile can be generated:

$$h(t_{i+1}) = h(t_i) + dh \quad (10)$$

$$V_{TAS}(t_{i+1}) = V_{TAS}(t_i) + dV_{TAS} \quad (11)$$

dV_{TAS} can be represented using ESF :

$$dV_{TAS} = \left(\frac{1}{ESF} - 1 \right) \frac{g}{V_{TAS}} \cdot dh \quad (12)$$

Atmospheric model

The atmospheric condition changes as the aircraft climbs to higher altitude. The formula for calculating air pressure, air temperature and air density at the altitude H of the aircraft is

$$\begin{cases} P = P_0(1 - 0.00003387H)^{3.5009} \\ T = T_0 - 0.0065 \times H \\ \rho = 0.0035P/T + 273.15 \end{cases} \quad (13)$$

The takeoff environmental condition varies from airports to airports. BADA provides International Standard Atmosphere (ISA) data and four types of non-ISA data models. Considering the change in pressure caused by the altitude change, the conversion formula between the true airspeed V_{TAS} and the Mach number M is

$$M = V_{TAS} / \sqrt{\kappa \cdot R \cdot T'} \tag{14}$$

T' represents the air temperature T in K.

3.3 Operational Cost Model

The operational cost model considers fuel cost and time cost as inputs. The fuel cost is calculated by the amount of fuel used multiplied by fuel price. The time cost coefficient is however not easy to obtain, so we use Cost Index (CI) to calculate the time cost. CI is the ratio of aircraft operating time cost to fuel cost. The formula for CI is

$$CI = C_t / 100C_f \tag{15}$$

where C_t represents the hourly time cost in \$/h, and C_f represents the fuel cost per pound in cents/lbs. The determination of CI is generally allocated according to the airline’s task requirements. For example, when the fuel price is high, CI is set to 0, it is the most economical situation for this scenario. When CI is set to 999 or MAX (depending on aircraft type), it is the Minimum Time Mode for Maximum Speed. In this research the Operating Cost (OC) is proposed to calculate the combined fuel and time navigation cost.

Operating Cost (OC) is the cost of operation within the limitation of aircraft performance, ATC procedures, and airspace conditions during the operation of an aircraft. In a single climb phase of a single flight, the formula for defining limited operating cost OC_{climb} is

$$OC_{climb} = C_t t_{climb} + C_f W_f = C_f (CI \times t_{climb} + W_f) \tag{16}$$

where t_{climb} [h] is the time of flight to complete the climb, W_f [lbs] is the total fuel consumption, $C_t t$ is the time cost, and $C_f W_f$ is the fuel cost.

The objective function is constructed as follows: take time as the numerical integration unit, f_{climb} is expressed as the function of time $f_{climb}(t)$, then the fuel consumption and the total time cost for the objective function J can be expressed as

$$J = C_f \int_{t_0}^{t_1} (f_{climb}(t) + CI) dt \quad (17)$$

Constraints should be determined according to specific aircraft type and flight conditions. The goal is to obtain the minimum operational cost. Note that the selection of CI depends on fuel price and hourly time cost. Once it's set, the climb-related data such as velocity is determined.

4 Case Study

4.1 Simulation Object

In this section, the route from Shanghai Pudong Airport to Paris Charles de Gaulle Airport (PVG-CDG) is selected as the simulation object. The selected departure route is PIK-81D, and the en route waypoints are PD301-PD302-PD303-SS303-SS304-SS305-EKIMU-POMOK-SS320-PIKAS [15]. The horizontal profile is determined by the SID procedure. The information of each waypoint is shown in Table 1.

4.2 Numerical Modeling

This section the climb phase of Boeing 777-300ER is modeled. The B77W is a dual-engine wide-body passenger aircraft. The climb performance data of B77W is shown in Table 2 [16].

The next step is to set initial values to parameters in the model. Constraints are divided into two categories: initial conditions and performance constraints. The initial condition is when the aircraft completes the takeoff process, reaches the V_2 speed and the safe above-ground height h_{TO} . The end point of the climb procedure is to reach the Top of Climb (ToC) point and goes into initial cruise phase, the altitude of which is h_{TOC} . In terms of performance constraints, the maximum speed during

Table 1 Waypoint information of SID

Way point	Category	Latitude	Longitude
PD301	RNAV way point	N305944	E1215036
PD302	RNAV way point	N305741	E1214309
PD303	RNAV way point	N310024	E1212825
SS303	RNAV way point	N310413	E1210733
SS304	RNAV way point	N310924	E1210716

the climbing phase shall not exceed TAS $V_m = 490\text{kts}$ (CAS 310kts) for h_{TOC} , and the minimum speed shall not be lower than $V_{stall} = 133\text{kts}$. The initial conditions as well as final states are shown in Table 3.

We use various ESF s for each time step to generate different trajectories as a way to simulate real aircraft operation controlled by pilot. The goal is to find the optimal solution for operational cost, which refers to a minimum result of J . Trajectory simulation results are shown below (see Fig. 1), where 200 iterations are generated

Table 2 B77W performance table for climb

Identification		Configuration			Climb		
ICAO	Engine Type	MTOW [t]	Wing span [m]	Aircraft length [m]	Vlow [kts]	Vhigh [kts]	Mach
B77W	JET	351,534	64.80	73.86	310	310	0.84

Table 3 Initial conditions and final states for different parameters

Variables	Initial value	Final state
t, s	1	Not constrained
V_{TAS}, knots	$V_2 = 168\text{knots}$	V_f
h, ft	$h_{TO} = 35ft$	$h_f = h_{TOC}$
m, kg	217,700 kg	Not constrained

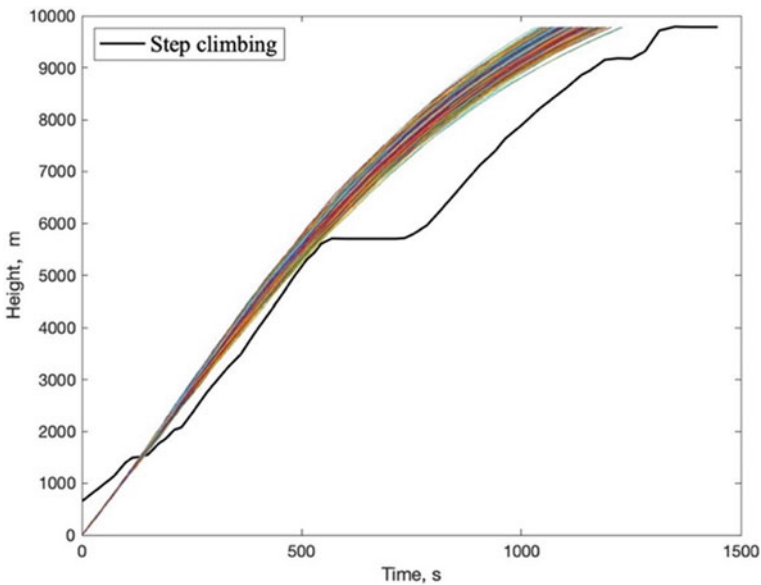


Fig. 1 Tradition step climb and CCO trajectories

with *ESF* ranges from 0.6 to 1.2. The step climbing data is taken from real open-source flight data by ADS-B surveillance. CCO shows improvement in climb time, compared with over 20 min of climb in traditional ways. Without ATC restrictions, such as speed limitation of 250 kts below FL100 and traffic-induced maintaining flight level. However, the separation should be given by ATC previous to takeoff and climb in order to avoid collision between aircrafts, especially those with different climb performance.

The total fuel flow consumption during climb for each iteration is given below (see Fig. 2). The data is sorted out from minimum to maximum. We can see that with shorter climbing time, fewer fuel will be used. This is because using maximum thrust for climb, which is represented as a function of height, and so is the time specific fuel flow.

The fuel flow rate in kg/s for the most time efficient flight trajectory is shown below (see Fig. 3). The result shows that the fuel flow rate decreases as the aircraft climbs up till ToC. This is consistent with the fuel estimation in the flight manual for pilots and calculation tables for FMC. As a result, a level flight in step climb profile of 3 min in Fig. 2 from $t = 500s$ to $t = 680s$ can add up to 42.51 kg more fuel consumed than CCO procedure. The distance traveled at cruise altitude for CCO that covers the level flight range at lower altitude for step climb is proved more fuel efficient, which is a critical economic performance improvement of this operational concept.

After obtaining the total fuel consumption and climb time, the operation cost can be determined. The fuel price is chosen as $\text{€}23.58/\text{lbs}$ [17]. Four different CI

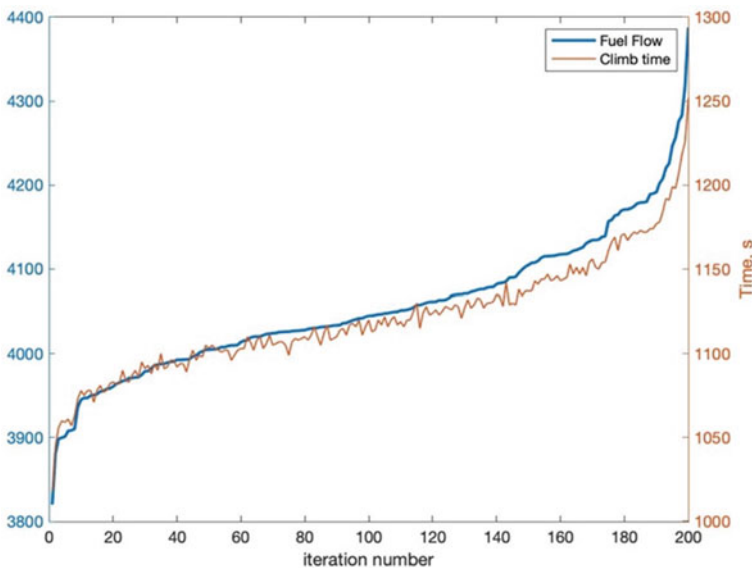


Fig. 2 Total fuel flow of each iteration and corresponding climb time

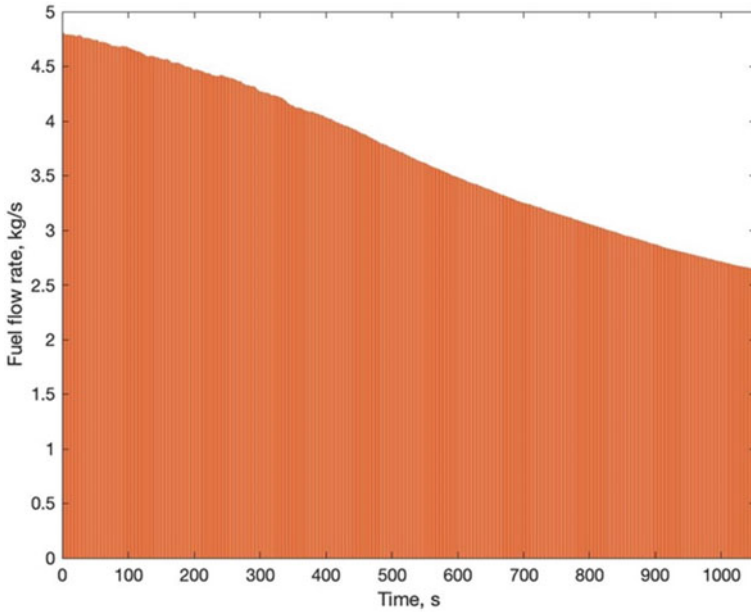


Fig. 3 Fuel flow rate with the change of climbing time

(100, 50, 20, 0) is selected to simulate different navigation strategies for airlines. The economic analysis results are shown in Table 4.

Table 4 CCO economic analysis

Fuel flow [kg]	Time [s]	OC [\$]			
		CI = 100	CI = 50	CI = 20	CI = 0
4109.54	1149	2884.46	2508.16	2282.38	2131.86
4014.56	1105	2806.37	2444.48	2227.35	2082.59
4011.20	1099	2800.69	2440.77	2224.82	2080.85
4136.44	1153	2901.03	2523.43	2296.86	2145.82
3996.19	1093	2788.98	2431.02	2216.25	2073.06
3935.11	1071	2742.88	2392.13	2181.68	2041.38
4111.76	1145	2882.99	2508.00	2283.01	2133.02
4037.16	1112	2822.67	2458.49	2239.99	2094.31
4063.45	1120	2841.56	2474.76	2254.68	2107.96
4064.42	1131	2849.26	2478.86	2256.62	2108.46

5 Conclusion

In this research, a method of economic evaluation of continuous climb operation is constructed, focusing mainly on fuel cost and time cost. BADA 3 is adopted to construct the CCO trajectory as well as fuel consumption model, and is used to calculate total operational cost. The results show that with the maximum thrust setting for climb, the aircraft can reach the initial cruise altitude in shorter time and save a good amount of fuel compared with step climb. For airlines to use in real operation scheduling, this method can be used to implement economic analysis of climb trajectory, in order to reach an optimal cost efficiency.

For different airspace design and operational goals, the CCO procedure can be executed in various manners. In future research, the different operational concepts will be studied, along with multiple aircrafts for CCO integration. In this case, airspace demand and capacity will also be considered in economic analysis of CCO.

Acknowledgements This paper are Sponsored by National Program on Key Basic Research Project (2014CB744903), National Natural Science Foundation of China (61673270), Natural Science Foundation of Shanghai (20ZR1427800), New Young Teachers Launch Program of Shanghai Jiao-tong University (20X100040036), Shanghai Pujiang Program (16PJD028), Shanghai Industrial Strengthening Project (GYQJ-2017-5-08), Shanghai Science and Technology Committee Research Project (17DZ1204304), and Shanghai Engineering Research Center of Civil Aircraft Flight Testing.


References

1. Geoff B, Christine AB, Trevor WT, Jone MCK, John F (2001) Real-time cost management of aircraft operations. *Manag Account Res* 12(3):281–298. <https://doi.org/10.1006/mare.2001.0162>
2. Bill R (2007) Fuel conservation strategies: cost index explained. *AERO, QTR* 2.07, 26–28
3. ICAO (2013) Continuous Climb Operations (CCO) Manual. Doc 9993, AN/495. <https://store.icao.int/en/continuous-climb-operations-cco-manual-doc-9993>
4. Paul M, Ralf HM (2007) Benefit potential of continuous climb and descent operations. AIAA aviation technology, integration and operations conference
5. EUROCONTROL (2020) European CCO/CDO Action Plan. <https://www.eurocontrol.int/publication/european-cco-cdo-action-plan>
6. Javier PC, Rosa V, Victor GC, Sergio M (2015) Continuous climb operations: the following step
7. Javier PC, Victor GC, Rosa V (2016) How do continuous climb operations affect the capacity of a terminal Manoeuvre Area?
8. Runping G, Zhichao L (2015) Research on models for calculating climb and descent performance of aircraft. *J Civil Aviat Flight Univ China* 04:39–43
9. Ramon D, Xavier P (2015) Fuel and time savings by flying continuous cruise climbs. *Transp Res Part D: Transp Enviro*, 35. <https://doi.org/10.1016/j.trd.2014.11.019>
10. Judith R, Stanley F, Hartmut F (2016) Continuous climb operations with minimum fuel burn
11. Qianwen H, Ming Z, Sihan L (2019) Aircraft departure fuel consumption improvement model based on flight data. *IOP conference series: materials science and engineering* 688, 022031. <https://doi.org/10.1088/1757-899X/688/2/022031>
12. Yao X (2019) The application of CCO/CDO procedure in China. *J Civil Aviat* (4), 20–23

13. Angela N, Damir P, Vincent M (2010) BADA: An advanced aircraft performance model for present and future ATM systems. *Int J Adapt Control Signal Process* 24:850–866. <https://doi.org/10.1002/acs.1176>
14. Mohammad S (2017). Drag force and drag coefficient. <https://doi.org/10.1201/9781315366913-3>
15. AIP (2021) Standard Departure chart-instrument/standard instrument departure chart ZSPD-7F: SID RWY34L/34R/35L/35R (ODULO, PIKAS)
16. EUROCONTROL (2021) Aircraft performance database. <https://contentzone.eurocontrol.int/aircraftperformance/details.aspx?ICAO=B77W&NameFilter=boeing>. Accessed 3 May 2021
17. IATA (2021) Jet Fuel Price Monitor. <https://www.iata.org/en/publications/economics/fuel-monitor/>. Accessed 3 May 2021

Formation of Aircraft Control Based on a Combination of the Direct Method and the Inverse Problems Method of Dynamics



O. N. Korsun , A. V. Stulovsky, V. P. Kharkov, S. V. Nikolaev, and Mounq Htang Om

Abstract In this paper, the method for forming optimal program control based on combining dynamics inverse problems method and optimal control direct method is considered. The results of its application are given using the example of the problem of aircraft climb in the minimum time.

Keywords Optimal program control · Direct methods · Population algorithm of numerical optimization · Dynamics inverse problems method

1 Introduction

To date, many different approaches to solving the problem of optimal control are known [1]. So, it seems reasonable that the invention of methods that combine different approaches to control problems would allow us to achieve new results.

The possibility of such an effective combination is considered in this paper, based on the previously proposed version of the direct method [2, 3] and the inverse problems method of dynamics, formulated by Krut'ko [4] and developed later by his followers [5].

Since this work is devoted to the practical implementation, it is performed on the example of a particular problem of optimizing the climb of an aircraft.

O. N. Korsun (✉) · A. V. Stulovsky
State Research Institute of Aviation Systems, Victorenko, 7, 125319 Moscow, Russia

O. N. Korsun · S. V. Nikolaev · M. H. Om
Moscow Aviation Institute, Volokolamskoe shosse, 4, 125993 Moscow, Russia

V. P. Kharkov
Experimental Workshop NaukaSoft, Godovikova, 9, 129085 Moscow, Russia

2 Problem Statement

This problem can be represented as a Lagrange problem with a free end [1]. In general, it is written as follows. The object model is set,

$$\dot{x} = f(x, u, t)$$

where x —the state vector, u —the vector of control, t —time.

At the initial time $t = t_0$, the position of the system in phase space is assumed to be known $x(t_0) = x_0$. The starting time t_0 and ending time T of the motion are fixed.

It is necessary to find a control u that provides the minimum value for the specified functional

$$J(x, \tilde{x}, u) = \int_{t_0}^T F(x, \tilde{x}, u, t) dt$$

where \tilde{x} —the desired values of the state vector.

The considered spatial motion of the aircraft under assumption $\beta = 0$ can be described quite fully by the following 4 differential equations [2, 3]

$$\begin{aligned} \dot{\alpha} &= \omega_z - \frac{qS}{mV} c_{ye}(\alpha) - \frac{P_x}{mV} \sin\alpha + \frac{g}{V} (\sin\alpha \sin\vartheta + \cos\alpha \cos\vartheta \cos\gamma) \\ \dot{V} &= -\frac{qS}{m} c_{xe}(\alpha) + \frac{P_x}{m} \cos\alpha + g(-\cos\alpha \sin\vartheta + \sin\alpha \cos\vartheta \cos\gamma) \end{aligned} \quad (1)$$

$$\dot{H} = V(\cos\alpha \sin\vartheta - \sin\alpha \cos\vartheta \cos\gamma)$$

$$\dot{\psi} = -\frac{1}{\cos\vartheta} \omega_z \sin\gamma$$

where α, β —angles of attack and sideslip, rad;

ω_z —angular velocity with respect to the axis Oz ,

or pitch angular velocity, rad/s;

ϑ, γ, ψ —angles of pitch, roll and yaw, rad;

V —airspeed, m/s;

H —flight altitude, m;

$c_{xe}(\alpha)$ —drag coefficient;

$c_{ye}(\alpha)$ —lift coefficient;

m —aircraft mass, kg;

S —wing surface area, m²;

P_x —projection of thrust force on axis Ox of body-fixed coordinate system, N;

g —gravity acceleration, m/s^2 ;

q —dynamic air pressure, Pa.

The system of differential Eq. (1) is also supplemented by an algebraic equation for the angular velocity in pitch ω_z .

$$\omega_z = \dot{\vartheta} \cos \gamma - \dot{\psi} \cos \vartheta \sin \gamma,$$

where $\tilde{\psi}$ —the desired values of the yaw angle.

In the case of purely longitudinal motion, the yaw angle is set to zero.

For the selected system, the role of control signals is performed by the pitch angle and the projection of the thrust force on the longitudinal axis of the aircraft. The smoothness of these parameters, together with the duration of the considered flight sections in time, allows us to apply spline approximation methods to them, for which are used cubic Hermitian splines [3]. Angle of roll in (1) may be used as an input signal for lateral movement [2, 3]. In the case of pitch movement only it is set to zero.

3 Technique of Program Control Forming

The problem was solved in two different ways in order to compare the obtained results. In the first case, only the direct method was used. The desired control signals—the pitch angle and the projection of the thrust vector were represented over the time interval in the form of cubic Hermitian splines determined by the parameter set on a uniform grid. Fixing the parameter values made it possible to integrate the system (1) and determine the output signals of the system. Based on these output signals, the value of the functional was calculated, which is the sum of the squares of the mismatch of the system's output signals and their desired values.

$$J(V, \tilde{V}, H, \tilde{H}) = \int_{t_0}^T \left((V - \tilde{V})^2 + (H - \tilde{H})^2 \right) dt \quad (2)$$

The search for parameter values that would provide the minimum value for the functional (2) was performed using the particle swarm optimization method [6].

In the second case, the values of the pitch angle were still found using the direct method, while the other component of the control vector—the projection of the thrust vector on the longitudinal axis—was found by the inverse problems method of dynamics. To apply this method, it is necessary to formulate requirements for the transition process of the system from the initial position to the desired trajectory [4]. We require that the discrepancy between the system speed and the desired speed is written off using the formula of the aperiodic link

$$\dot{\Delta} = -\frac{1}{\tau}\Delta, \tag{3}$$

where $\Delta = V - \tilde{V}$ and τ is the transition parameter that gives it the desired dynamic properties.

By expanding in the expression (3) Δ and taking into account the requirement $\tilde{V} = const$, the following equation can be written

$$\dot{V} = \frac{1}{\tau}\tilde{V} - \frac{1}{\tau}V$$

Let's substitute the formula for the velocity derivative [7] into this expression and express the projection of the thrust force from it.

$$P_x = \frac{m}{\cos \alpha \cos \beta} \left[-\frac{qS}{m} c_{xe}(\alpha) + \frac{1}{\tau}(\tilde{V} - V) + g(\cos \alpha \cos \beta \sin \vartheta - \sin \alpha \cos \beta \cos \vartheta \cos \gamma - \sin \beta \cos \vartheta \sin \gamma) \right]$$

This expression determines the value of the thrust projection at each step of system integration (1). At the same time, the minimized functional (2) remains unchanged.

4 Results Description

In this paper, we considered the practical problem of climb with the best operating speed. In the first case, both control signals were determined by the direct method, and the resulting altitude and speed values are shown in Fig. 1.

Analysis of Fig. 1 shows that the direct method finds a solution to the problem of rapid climb, although the speed restores the original value only at the end of section.

In the second case, the required thrust value was found by solving the inverse problem dynamics. The resulting values of the output signals are shown in Fig. 2.

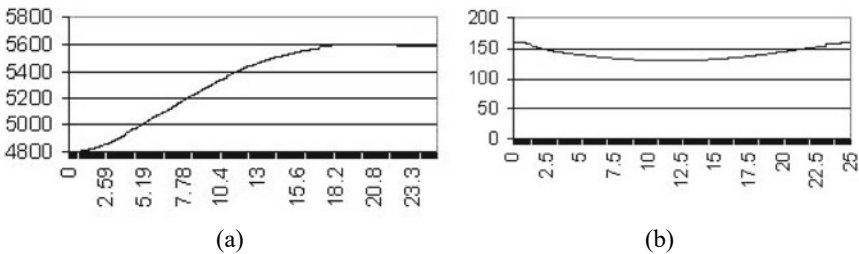


Fig. 1 Output signals of the system (1) as a function of time when generating control signals using the direct method **a** altitude, **b** speed

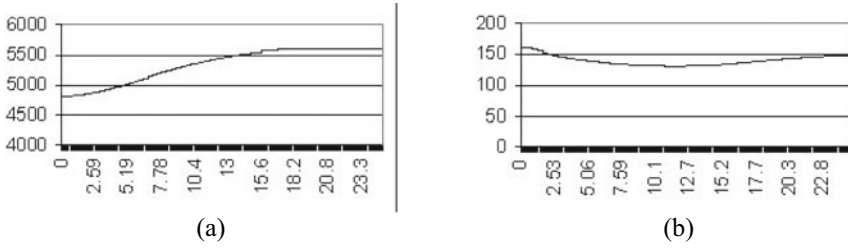


Fig. 2 Output signals of the system (1) as a function of time when forming pitch control by the direct method, and thrust control by the method of inverse dynamics problems **a** altitude, **b** speed

The result corresponds to the first case, but at the end of the section there is a shortage of speed (about 10 m/s). In this case, it must be remembered that the nature of the speed output to the set value is determined by the transition process coefficient.

Therefore, it seems natural to suggest selecting this coefficient, for example, by the same method of swarming particles for the reasons of the minimum value of the functional. The results obtained are shown in Fig. 3.

It is obvious, that when finding the optimal value of the time constant, it was possible to restore the speed by the end of the section (similar to Fig. 1b). A comparison of Figs. 1 and 3 shows that when using the direct method, approximately the same results are obtained as when using the direct method and the inverse problems method of dynamics with time constant optimization together. However, the computational complexity of the second option is significantly lower, since the required thrust in the optimization process is calculated using a simple formula obtained from the inverse problems method of dynamics.

Thus, the paper presents a method for formation of program control of an aircraft for solving the problem of climb using a combination of the direct method and the inverse problems method of dynamics. It is shown that the combined use of both methods may significantly reduce the computational complexity of the direct method without losing the quality of control.

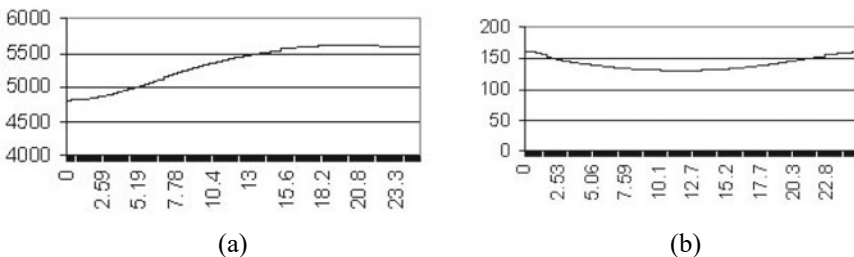


Fig. 3 Output signals of the system (1) as a function of time when forming pitch control by the direct method, and thrust control by the inverse problems method of dynamics, but the coefficient of Eq. (3) is also selected by a swarm of particles **a** altitude, **b** speed

It should be noted that in both cases, the choice of functional significantly affects the search for a solution, so knowledge of the features of the problem to be solved is necessary for the effective operation of the method.

Acknowledgements This work was supported by the Russian Foundation for Basic Research (RFBR), project 20-08-00449.

References

1. Pupkov KA, Egupov ND (2004) Methods of classical and modern theory of automatic control. MGTU im. Baumana, Moscow
2. Korsun ON (2020) Comparative study of pontryagin maximum principle and direct method in aircraft optimal control design. In: IOP conference series: materials science and engineering, vol. 714, p 012011
3. Korsun ON, Stulovskii AV (2019) Direct method for forming the optimal open loop control of aerial vehicles. *J Comp Syst Sci Int* 58(2):229–243
4. Krut'ko PD (2004) Inverse problems of the systems dynamics control. Mashinostrojenie, Moscow
5. Petrov MY (2019) Low-altitude aircraft routing. *J Comp Syst Sci Int* 58(3): 467–473
6. Olsson AE (2011) Particle swarm optimization: theory, techniques and applications. Nova Science Publishers, Hauppauge, USA
7. Bjushgens GS (1998) Aerodynamics, stability and controllability of supersonic aircraft. Nauka, Moscow

Identification of the Engine Thrust Force Using Flight Test Data



O. N. Korsun , B. K. Poplavsky, and Mung Htang Om

Abstract In this article, an algorithm for identifying the thrust force and the coefficients of the aerodynamic drag of the aircraft according to the data of the flight experiment is proposed. In order to ensure identifiability, a special flight maneuver is considered. To reduce the impact of measurement noise, the maximum likelihood estimation is used. The results of the study of the algorithm characteristics based on the flight simulation data are presented.

Keywords Propulsion · Engine thrust · Identification · Flight tests · Flight dynamics · Aerodynamic drag

1 Introduction

The value of the engine thrust is the most important characteristic of an aircraft. However, the existing methods for determining thrust in ground and flight tests have significant limitations.

For example, the errors in the calculation methods based on gas-dynamic models are due to the fact that when setting up these models, data from ground tests are used as a source of a priori information, which do not allow us to fully reproduce the flight conditions [1–3].

To improve the gas-dynamic models and calculate the thrust, flight test data can be used, but this requires an abnormal modification of the engines to install the necessary set of additional sensors [1]. This method is rarely used in practice in recent years due to the high cost and labor intensity.

O. N. Korsun (✉)

State Research Institute of Aviation Systems, Moscow, Russia

O. N. Korsun · M. H. Om

Moscow Aviation Institute, Moscow, Russia

B. K. Poplavsky

Flight Research Institute Named After M.M. Gromov, Zhukovsky, Russia

To overcome these problems, it is proposed to use an approach based on the joint identification of the effective thrust force and the aerodynamic coefficients [4] using an algorithm for obtaining separate estimates of the effective thrust forces based on the methods of flight dynamics and the theory of system identification [5, 6].

2 Algorithm for Obtaining a Separate Estimate of the Effective Thrust Force

To apply the maximum likelihood estimation [6], the parametric identification problem should be formulated as follows:

$$y'(t) = f(y(t), a, u(t)) \quad (1)$$

$$z(t_i) = h(y(t_i), a, u(t_i)) + \xi(t_i) \quad (2)$$

where $y(t)$, $u(t)$ —vectors of output and input signals of dimension n and m , respectively,

$z(t_i)$ —vector of observations of dimension r ,

$\xi(t_i)$ —observation noise, which is a vector normal random sequence of the white noise type with zero mathematical expectation and a known variance matrix $R(t_i)$,

a —vector of unknown parameters to be identified.

The initial conditions $y(t_0)$ are assumed to be known, or are included in the vector of the estimated parameters. It is also assumed that $u(t)$ is a known function of time.

As estimates of the vector of unknown parameters, the values that provide the minimum to the quadratic functional with the matrix of weight coefficients $R(t_i)^{-1}$ are selected:

$$J(a) = \sum_{i=1}^N ((z(t_i) - h(\hat{y}(t_i), a, u(t_i)))^T R^{-1}(t_i) ((z(t_i) - h(\hat{y}(t_i), a, u(t_i)))) \quad (3)$$

The problem of minimizing the functional in the space of identifiable parameters is solved numerically, for example, by the modified Newton method [6].

To solve the problem of obtaining a separate estimate of the thrust force, it is necessary to determine the vectors of input and output signals, as well as the vector of observations.

From the general model of spatial motion [7], we distinguish the equations for flight speed, angle of attack, and pitch angle.

$$\frac{dV(t)}{dt} = a_x(t) \cos \alpha(t) \cos \beta(t) - a_y(t) \sin \alpha(t) \cos \beta(t) + a_z(t) \sin \beta(t);$$

$$\begin{aligned} \frac{d\alpha(t)}{dt} &= \omega_z(t) + (\omega_y(t) \sin \alpha(t) - \omega_x(t) \cos \alpha(t)) \tan \beta(t) - \\ &\quad - \frac{1}{V(t) \cos \beta(t)} (a_x(t) \sin \alpha(t) + a_y(t) \cos \alpha(t)); \\ \dot{\vartheta}(t) &= \omega_y(t) \sin \gamma(t) + \omega_z(t) \cos \gamma(t). \end{aligned} \quad (4)$$

In Eq. (4) $a_x(t)$, $a_y(t)$, $a_z(t)$, there are projections of accelerations on the axis of the associated coordinate system, calculated through the overload projections using the formulas:

$$\begin{aligned} a_x(t) &= g(n_x(t) - \sin \vartheta(t)); \\ a_y(t) &= g(n_y(t) - \cos \vartheta(t) \cos \gamma(t)); \\ a_z(t) &= g(n_z(t) + \cos \vartheta(t) \sin \gamma(t)). \end{aligned} \quad (5)$$

In this considered problem, the maneuver is performed in the longitudinal channel, so the parameters of lateral motion have very small values.

However, equating them to zero, in accordance with the generally accepted approach of flight dynamics, is impractical, because this will lead to additional errors that can be excluded. Therefore, during the numerical solution of the problem, we take them into account, substituting in (4) and (5) the values of these parameters measured in flight. Let's combine the functions obtained from the measurement results into the vector $u(t)$.

$$u(t) = [n_z(t)\omega_x(t)\omega_y(t)\omega_z(t)\gamma(t)\beta(t)]. \quad (6)$$

It should be noted that in the vector $u(t)$, along with the signals of lateral motion, the angular pitch velocity $\omega_z(t)$ is also included, which is necessary for solving the system of Eq. (4).

To calculate the overload projections $n_x(t)$ and $n_y(t)$ on the axis of the associated coordinate system, the following expressions are used.

$$\begin{aligned} n_x(t) &= -\frac{1}{mg} q(t) S \cos \alpha(t) (c_{x0} + c_x^\alpha \alpha(t) + c_x^{\alpha^2} \alpha^2(t)) - \frac{P_{in}}{mg} \cos \alpha(t) + \frac{P_{out}}{mg} \cos \phi_{\delta\theta} + \\ &\quad + \frac{1}{mg} q(t) S \sin \alpha(t) (c_{y0} + c_y^\alpha \alpha(t) + c_y^{\delta_B} \delta_B(t)); \\ n_y(t) &= -\frac{1}{mg} q(t) S \sin \alpha(t) (c_{x0} + c_x^\alpha \alpha(t) + c_x^{\alpha^2} \alpha^2(t)) + \frac{P_{in}}{mg} \sin \alpha(t) + \frac{P_{out}}{mg} \sin \phi_{\delta\theta} + \\ &\quad + \frac{1}{mg} q(t) S \cos \alpha(t) (c_{y0} + c_y^\alpha \alpha(t) + c_y^{\delta_B} \delta_B(t)), \end{aligned} \quad (7)$$

where P_{in} , P_{out} —input and output thrust pulses; $\Phi_{\delta\theta}$ —engine mounting angle;

$c_{x0}, c_x^\alpha, c_x^{\alpha^2}$ —parameters of the parabolic approximation of the drag force coefficient;

$c_{y0}, c_y^\alpha, c_y^{\delta_B}$ —parameters of the linear approximation of the lift force coefficient.

At small angles of attack, the values of the $\cos \alpha(t)$ function are close to 1 and, therefore, it is impossible to estimate the input and output pulses separately.

To ensure the efficiency of the proposed algorithm, the following assumptions are made:

- the value of the input pulse P_{in} is set according to the gas-dynamic model of the engine, so only the output pulse P_{out} is estimated;
- the value of the parameter $c_y^{\delta_B}$ that characterizes the lift force of the elevator, due to its relative smallness, is taken from the bank of aerodynamic characteristics, and is not determined by identification.

Then the vector of parameters to be estimated takes the form:

$$a^T = [c_{x0} \ c_x^\alpha \ c_x^{\alpha^2} \ P_{out} \ c_{y0} \ c_y^\alpha]. \quad (8)$$

Let's consider the equations of observations. Note that the measurements are performed at discrete time. The observation vector will include the pitch angle $\vartheta(t_i)$, the longitudinal overload $n_x(t_i)$, the angle of attack $\alpha(t_i)$, the normal overload $n_y(t_i)$, and the flight speed $V(t_i)$.

Then, the system of equations for the observation model takes the following form

$$\begin{aligned} z_1(t_i) &= \vartheta(t_i) + \xi_\vartheta(t_i); \\ z_2(t_i) &= n_x(t_i) + \xi_{n_x}(t_i); \\ z_3(t_i) &= \alpha(t_i) + \xi_\alpha(t_i); \\ z_4(t_i) &= n_y(t_i) + \xi_{n_y}(t_i); \\ z_5(t_i) &= V(t_i) + \xi_V(t_i). \end{aligned} \quad (9)$$

In the right part of Eq. (9), the notations $\xi_\vartheta(t_i), \xi_{n_x}(t_i), \xi_\alpha(t_i), \xi_{n_y}(t_i), \xi_V(t_i)$ stand for random measurement noises.

In the identification process, the values of $\vartheta(t_i), \alpha(t_i)$, and $V(t_i)$ are obtained by numerical integration of differential Eq. (4), taking into account (5) and (6).

It should be noted that the equations discussed above correspond to a calm atmosphere without wind and turbulence, so the true airspeed and inertial velocity coincide and are equal to $V(t_i)$.

3 Estimation of the Efficiency of the Identification Algorithm Under the Influence of Measurement Noise

The proposed algorithm was tested using flight simulator data. The model was based on the bank of aerodynamic coefficients, the altitude-speed characteristics of the engine, and the algorithms of the integrated flight control system.

The flight test maneuver contained the following steps:

- balance the aircraft in a straight horizontal flight with a constant flight speed;
- transfer of the aircraft into a dive to increase the number of M by 0.02;
- transfer of the aircraft into a climb so that the number of M decreases by 0.04;
- transfer of the aircraft into a dive to increase the flight speed to the initial value of the number of M.

Six test flight maneuvers were performed to test the algorithm. When performing simulation, the time mismatch between the signals did not exceed 1 ms, which was achieved by precise synchronization of the information flows of the flight simulator facilities.

During the calculations, random measurement errors were simulated in the channels of longitudinal and normal overload, angle of attack, and airspeed as normally distributed independent random variables with zero mathematical expectation (mean) and specified standard deviations, which amounted to 0.001 units of overload, 0.06 degrees of angle of attack, and 0.9 km/h of airspeed. Note that when using the data of actual flight experiment, it is recommended to exclude systematic errors of aerometric measurements according to the algorithm [8].

The results of processing according to the proposed algorithm are presented in Table 1. The analysis shows that the identification according to the proposed algorithm provides a good accuracy of identification of the thrust with relative errors less than 1%.

Table 1 Errors in estimating the thrust of the drag coefficients at the noise of the level 1 measurement

Section number	Thrust P, H		C_{x0}		C_x^α		$C_x^{\alpha^2}$	
	Estimate	Relative errors, %	Estimate	Relative errors, %	Estimate	Relative errors, %	Estimate	Relative errors, %
121	6005	0,34	0,02,035	1,75	0,005,952	0,8	0,0,008,066	0,83
122	6000	0,26	0,01,967	1,65	0,005,955	0,75	0,0,008,073	0,91
123	5936	0,81	0,01,944	2,8	0,005,973	0,45	0,0,008,063	0,79
124	5951	0,56	0,01,969	1,55	0,005,959	0,68	0,000,807	0,88
125	5962	0,38	0,01,968	1,6	0,005,995	0,08	0,000,804	0,5
126	5971	0,23	0,01,971	1,45	0,006,022	0,37	0,0,008,012	0,15

4 Conclusion

The processing of the data obtained by flight simulation showed that the proposed algorithm for identifying the thrust force provides an accuracy of identifying the thrust with errors of less than 1%.

One of the reasons for the effectiveness of the maximum likelihood algorithm, which uses numerical integration of the equations of motion, is that the simulation data used for testing are well consistent in time. Based on this, integration does not introduce additional errors, and the algorithm fully shows its positive properties of smoothing the stochastic measurement errors.

Acknowledgements This work is supported by the Russian Foundation for Basic Research (RFBR), project 20-08-00449-a.

References

1. Dobryansky GV, Martyanova TS (1989) Dynamics of aviation gas turbine engines. Ph. Mashinostroenie, Moscow
2. Korsun ON, Leshchenko IA, Eremichev MV (2011) Mathematical modeling of transient processes in an aviation gas turbine engine. *Mechatronics, automation, control*, no 11, p 50–54
3. Kiselev MI, Kamyshin AC, et al (2011) Multivariate mathematical models of the functioning of aircraft gas turbine engines in the phase-chronometric representation. *Metrology*, no 9, p 13–27
4. Korsun ON, Poplavsky BK, Leonov VA (2011) Estimation of the thrust force of aircraft engines according to flight test data on the basis of optimal invariant linear transformations. *Technics of the air fleet*, no 1, p 25–30
5. Jategaonkar RV (2006) Identification of the aircraft system: a time domain methodology. American Institute of Aeronautics and Astronautics, Reston
6. Klein V, Morelli EA (2006) Aircraft system identification: theory and practice. American Institute of Aeronautics and Astronautics, Reston
7. Bjushgens GS (ed) (1998) Aerodynamics, stability and controllability of supersonic aircraft. Nauka, Moscow (In Russian)
8. Korsun ON, Nikolaev SV, Pushkov SG (2016) An algorithm for estimating systematic measurement errors for air velocity, angle of attack, and sliding angle in flight testing. *J Comput Syst Sci Int* 55(3):446–457

Investigation of Plastic Kink-Band in Fiber-Reinforced Composites with Fiber Misalignment Defect



Y. T. Zhang, Y. L. Hu, Y. Yu, Y. Y. Xu, and H. Y. Zhao

Abstract The mechanical behaviors of composites subjected to compressive loads are critical concerns in composite structure designs. Misalignment of fiber orientation is a common manufacturing defect and has significant impact on compressive properties. In this paper, a Representative Volume Element (RVE) with misalignment defect is established with the consideration of Periodic Boundary Conditions (PBCs). A unidirectional lamina with misaligned carbon fibers is investigated based on Finite Element Method (FEM) with consideration of matrix plasticity. Drucker–Prager linear plastic model is utilized to describe elastic-to-plastic behavior of matrix. Parameters of Drucker–Prager model influence the formation and shape of kink-band. The mechanism of kink-band formation and propagation is discussed in this study.

Keywords Misalignment · Plasticity · Drucker–Prager · Kink-band

1 Introduction

Composite materials have high specific strength, high specific stiffness, low density, and low coefficient of expansion. It has been widely used in the primary structure of satellites and aircrafts. However, various defects and damages often occur

Y. T. Zhang · Y. L. Hu · Y. Yu (✉) · Y. Y. Xu · H. Y. Zhao
Aerospace Structure Research Center, School of Aeronautics and Astronautics, Shanghai Jiao
Tong University, Shanghai 200240, China
e-mail: yuyin@sjtu.edu.cn

Y. T. Zhang
e-mail: y.t.zhang0407@sjtu.edu.cn

Y. L. Hu
e-mail: yilehu@sjtu.edu.cn

Y. Y. Xu
e-mail: xyy_654321@sjtu.edu.cn

H. Y. Zhao
e-mail: 1030067zhy@sjtu.edu.cn

during the manufacturing process of composite materials. These defects and damages have significant influence on the reliability of composite materials and restrict their application. There are different types of defects in the composite structures, such as porosity, wrinkle, rich resin, poor resin, and so on.

In this article, the influence of fiber misalignment is discussed and investigated. Micromechanics simulation of composite with misalignment defect is adopted. Under compression, fiber misalignment generates interlaminar shear stresses. With the growth in compressive stress, the fibers can rotate and slide; the matrix undergoes shear deformation [1]. When stress reaches to yielding level, matrix cannot provide sufficient support to fibers. As a result, the system becomes unstable and often presents a drop in load. This shear instability is translated into a localized kink-band with fiber misaligned by an angle [2]. The kink-band will cause compressive stress to decrease, leading to fiber instability. Then the continuous compression after kink-band formation results in fiber breakage, matrix shear failure, or delamination failure [3, 4]. Therefore, compression instability of composite originates from the irregular fiber arrangement during the manufacturing process.

Because of the complexity of manufacturing composite and quality dispersion of different batches, numerical analysis is the most common way to study various mechanical properties of composite [2]. Among the numerical approaches, Finite Element Analysis (FEA) is one of the most commonly used approaches. In this study, FEA method is employed to solve the complex differential equations for investigating compressive behaviors of composites.

Most of the researches focus on 2D model to simulate fiber misalignment model [2, 5, 6], just a few of them use 3D model to predict its mechanical properties [7, 8]. Although it has been proved that important mechanisms such as kink-band, layer delamination, and matrix splitting can be captured by 2D model [6]. Disadvantages of using 2D model are that it can neither capture the complex 3D shear stress state developed between fibers nor the effect of the finite fiber bending rigidity [9]. In this work, a 3D Representative Volume Element (RVE) with fiber misalignment defect is established to simulate the deformation and shear stress distribution.

2 Micro Modeling

2.1 Representative Volume Element

RVE is a common approach used in studying mechanical properties of composites. It was first used by Hill [10]. It is defined as the smallest volume element, which can represent the macroscale constitutive response [11]. Therefore, the RVE shall be able to provide sufficient accuracy of representing the material's macroscale mechanical behavior.

There is an extension in Abaqus called secondary development. It can generate a 3D fiber misalignment model by defining the basic geometry parameters. Model

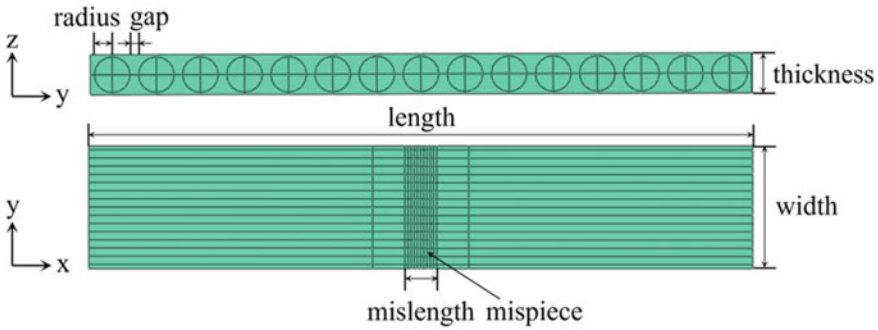


Fig. 1 Geometric parameters of computational model

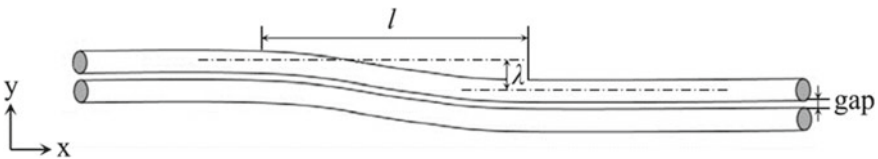


Fig. 2 Local fiber waviness parameters

name and Instance name is needed in model built by Abaqus. Geometric meanings of the relevant parameters are illustrated in Fig. 1.

A RVE is established to represent the mechanical behavior of fiber misalignment. Because prediction of compressive strength with smaller RVE size is found to be misleading [12]. The dimension of this model is $518 \times 96.88 \times 5.87 \mu\text{m}$.

The diameter of fibers is $5.2 \mu\text{m}$ the gap between fibers is $1.2 \mu\text{m}$, and fiber volume is 56%. A half of sinusoidal waviness is considered in the middle of fibers as misalignment defect, as shown in Fig. 2. This fiber misalignment defect is a local waviness that only exist in the middle of fibers, the length l of waviness is $25 \mu\text{m}$. The distance λ from peak to valley of sinusoidal waviness is $0.5 \mu\text{m}$. The ratio λ/l is set to 0.02.

2.2 Materials

Finite element model consists of two types of material, carbon fiber and matrix. Isotropic elastic–plastic material model is applied to matrix, and orthotropic material model is applied to fibers. Moreover, the user-defined subroutine UMAT was adopted to describe the damage of fibers based on the maximum stress criterion. The properties of selected materials are listed in Tables 1 and 2.

Table 1 Elastic properties of fiber

Carbon fiber properties [8]					
E ₁ (GPa)	E ₂ (GPa)	E ₃ (GPa)	ν ₁₂	ν ₁₃	ν ₂₃
276	19	19	0.2	0.2	0.2
G ₁₂ (GPa)	G ₁₃ (GPa)	G ₂₃ (GPa)	X _T (MPa)		
27	7	7	5580		

Table 2 Elastic properties of matrix

Matrix properties	
E (GPa)	ν
4.08	0.38

To consider plasticity in matrix, there are many types of plasticity models available in Abaqus, such as von Mises, Mohr–Coulomb, Drucker–Prager, Gurson–Tvergaard–Needleman (GTN), and Concrete Damaged plasticity model [16].

Besides, for the quasi-brittle material like matrix, soil and concrete, they obtain a pressure-dependent yield surface [8]. Mohr–Coulomb plasticity model is a common one used in engineering application. It has a pressure-dependent yield surface [9]. However, the yield surface of Mohr–Coulomb model on deviatoric principal plane (π -plane) is hexagon, which causes difficulties in numerical implementations due to the sharp corners [13].

The extended Drucker–Prager plasticity model (D-P model) is used to model pressure-dependent yield materials (Under compression, the yield strength is normally higher than the tension yield strength) [6]. Thus, extended D-P model is employed instead, because its yield surface on π -plane is smooth and differentiable.

While, compared to von Mises and GTN model, D-P model can describe a better post-yield behavior of the polymer-matrix under both quasi-static and cyclic loads [6]. Although Concrete Damaged Plasticity model possesses a more detailed explanation on cumulative damage, there is less data about matrix parameters [14]. In conclusion, D-P model will be adopted in this fiber misalignment model.

About D-P model, there are three kinds of shapes of yield surface on the meridional plane. It can be linear, hyperbolic, or general exponent form. When it's going to take epoxy plasticity into consideration, the relation between yield surface and pressure appears to be linear. In this situation, a yield surface with hydrostatic pressure p shows a linear growth. In the linear form, the parameter β represents the slope of the linear yield surface in the $p - t$ stress plane. It is commonly referred to as the friction angle of the material.

Equation of yield surface in meridional plane is described by Eq. (1),

$$F = t - p \tan \beta - C \tag{1}$$

Parameter t is demonstrated by Eq. (2),

$$t = \frac{1}{q} \left[1 + \frac{1}{K} - \left(1 - \frac{1}{K} \right) \left(\frac{r}{q} \right)^3 \right] \tag{2}$$

The D-P model can also simulate non-circular yield surface by changing the parameter K which is the ratio of yield stresses between triaxial tension and compression. Figure 3 shows the influence of K on the shape of the curved surface. In order to ensure that the yield surface maintains a convex shape, $0.778 \leq K \leq 1.0$ is required. In the situation of applying longitudinal compression, there is an approach to match Mohr–Coulomb and Drucker–Prager model parameters, making the two models provide the same failure definition in triaxial compression and tension [13]. The formula of matching θ to β and K is shown in Eqs. (3) and (4). The effect of K on yield surface is shown in Fig. 2.

$$\tan \beta = \frac{6 \sin \theta}{3 - \sin \theta} \tag{3}$$

$$K = \frac{3 - \sin \theta}{3 + \sin \theta} \tag{4}$$

$\tan \theta$ is the slope of Mohr–Coulomb yield surface. The parameter of θ is in the range of $10\text{--}30^\circ$ [15]. For matrix material 977–2, $\theta = 20.77^\circ$ [13].

In Abaqus, the third parameter that D-P model needs to be defined is the dilation angle ψ . The most primitive D-P model requires $\psi = \beta$ and $K = 1$. If $\psi = 0$, inelastic deformation is incompressible. Generally, a real material has to satisfy the restriction that $\tan \psi < 3$, $\psi < 71.5^\circ$. If $\psi = \beta$, this situation is called associated

Fig. 3 Typical yield/flow surfaces of the linear model in the deviatoric plane

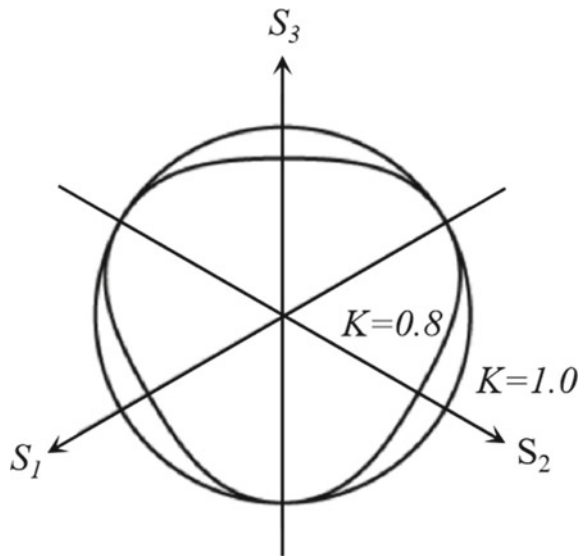
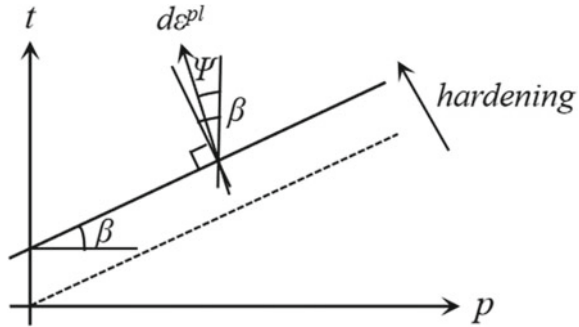


Fig. 4 Linear Drucker–Prager model: yield surface and flow direction in the p – t plane



flow. However, nonassociated flow is usually assumed for polymeric materials, that is, $\psi < \beta$. A geometric interpretation of ψ is shown in the p – t diagram in Fig. 4. $d\epsilon^{pl}$ is the direction of plastic strain.

Parameter G is the flow potential,

$$G = t - p \tan \psi \tag{5}$$

If hardening is defined by the uniaxial compression yield stress σ_c , cohesion of material named d can be expressed as

$$d = \left(1 - \frac{1}{3} \tan \beta \right) \sigma_c \tag{6}$$

And if hardening is defined by the uniaxial tension yield stress σ_t , cohesion of material named d can be expressed as

$$d = \left(\frac{1}{K} + \frac{1}{3} \tan \beta \right) \sigma_t \tag{7}$$

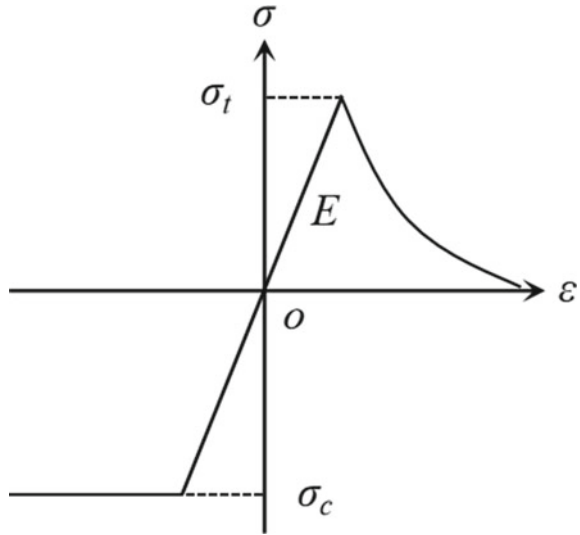
Under a complex stress condition, yield condition of different stress combinations and the plastic constitutive relationship between stress and strain components are the physical relationships on which plastic mechanics problems are analyzed. The constitutive relationship that reflects the plastic stress–strain relationship should generally be given in incremental form. This is because the deformation history needs to be considered in plastic mechanics, and the incremental form can reflect the deformation history and the nature of plastic deformation (Table 3).

For quasi-brittle material like epoxy, the ideal plastic behavior is assumed under compression. The brittle behavior in tension is taken into account by a softening law in Fig. 5 [5].

Table 3 Basic matrix plastic properties [5], [6]

Properties	Plastic properties of matrix
Compression strength (MPa)	100
Ration of triaxial tension to triaxial compression, K	0.7866
Slope of the yield surface, β ($^{\circ}$)	11
dilation angle ψ ($^{\circ}$)	11

Fig. 5 Stress–strain response for matrix



3 Methodology of Micro-mechanical Modeling

3.1 Periodic Boundary Conditions

In order to simulate the deformation of RVE in whole unidirectional laminate, there must have PBCs to be applied on the RVE. PBCs ensure that the deformation in RVE remains periodic under compression.

Once RVE is established, there are nodal coordinates written in Abaqus of all the points on the surface of RVE. Using nodal coordinates as input data to find the maximum and minimum numbers in x, y, and z directions. Sorting nodes to corners, edges, and surfaces by comparing nodes' coordinates to maximum and minimum numbers. There is a detailed picture (Fig. 6) to explain all the names of nodes sets.

In the FE model, there is a half of sinusoidal wave in fibers, leading to the fact that the nodes on front surface and back surface cannot match themselves by coordinates. Therefore, PBCs are applied to four surfaces (left, right, top, and bottom), twelve

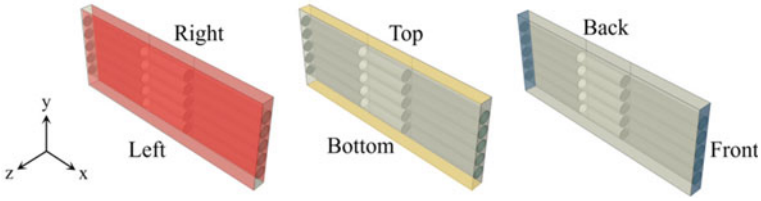


Fig. 6 Set categorization

edges, and eight corners of the RVE. Then the continuity between neighboring RVEs is maintained.

Periodicity requires that opposite faces of RVE deform identically. To achieve this, constraints between the nodes on the opposite surfaces are needed [17]. In Abaqus, equations as shown in Table 4 are employed.

Table 4 PBCs linear constraints equations

Constraint equations: $A \times U_{set1}^{DoF} + B \times U_{set2}^{DoF} = 0$

set1	set2	DoFs	A	B
Left surface	Right surface	1, 2, 3	1	-1
Top surface	Bottom surface	1, 2, 3	1	-1
Front top edge	Back top edge	1, 2, 3	1	-1
Front bottom edge	Back bottom edge	1, 2, 3	1	-1
Front top edge	Front bottom edge	1, 2, 3	1	-1
Top left edge	Bottom left edge	1, 2, 3	1	-1
Top right edge	Bottom right edge	1, 2, 3	1	-1
Top left edge	Top right edge	1, 2, 3	1	-1
Left front edge	Right front edge	1, 2, 3	1	-1
Left back edge	Right back edge	1, 2, 3	1	-1
Left front edge	Left back edge	1, 2, 3	1	-1
Corner 1	Corner 2	1, 2, 3	1	-1
Corner 2	Corner 3	1, 2, 3	1	-1
Corner 3	Corner 4	1, 2, 3	1	-1
Corner 4	Corner 5	1, 2, 3	1	-1
Corner 5	Corner 6	1, 2, 3	1	-1
Corner 6	Corner 7	1, 2, 3	1	-1
Corner 7	Corner 8	1, 2, 3	1	-1

3.2 Periodic Boundary Conditions

Parameter 1 in Table 5 is set as the benchmark mode. To try to compare the effect of different D-P model parameters, different cases in Table 5 are designed to disclose the influence of four parameters on the formation of kink-band. Those cases include the angle of friction β , the ratio of yield stress in triaxial tension to the yield stress in triaxial compression K , the dilation angle ψ , and the final parameter about compression strength of matrix.

After establishing geometric model and applying suitable material model, there is still something that needs to be considered. Some efforts are spent on controlling the mesh quality, a crosshead is swept through fiber direction and divide all the plate equally in z-direction. Furthermore, to improve the calculation efficiency, seeds density is higher on the fiber misalignment and surrounding parts than other positions. The fiber misalignment model after partition is shown in Fig. 7. Elements are discretized using fully integrated brick (C3D8) finite elements to model fibers and matrix.

As a consequence of the large RVE size, the model results in around 8.6 thousand DOFs. The model takes over 2 h to compute. In order to capture the snap-back behavior of kink-band formation, the Riks method is used in the analysis step [5,

Table 5 Different combination of matrix plastic properties

Case	$\beta(^{\circ})$	K	$\psi(^{\circ})$	Compression strength (MPa)
Parameter 1	11	0.7866	11	100
Parameter 2	13	0.7866	11	100
Parameter 3	15	0.7866	11	100
Parameter 4	11	0.91	11	100
Parameter 5	11	0.85	11	100
Parameter 6	11	0.7866	9	100
Parameter 7	11	0.7866	7	100
Parameter 8	11	0.7866	11	130
Parameter 9	11	0.7866	11	70

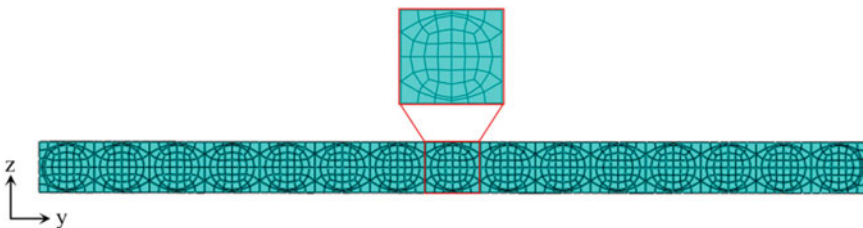


Fig. 7 Misalignment model after partition

8, 12]. This analysis step can effectively analyze the nonlinear buckling process of structure.

Boundary condition for simulating compression behavior is achieved by applying a longitudinal compressive displacement at front surface and fixing displacement of back surface in x -direction. So as to obtain the stress–strain curve of front surface. There is a reference point which exists outside the model, coupling with the front surface and delivering compression force.

4 Computational Results, Validation, and Discussion

4.1 Compressive Failure Mechanism

The analysis of Parameter 1 is conducted to validate the proposed model and reveal kink-band formation mechanism. The typical stress–strain response for misalignment fiber is illustrated in Fig. 8, which reveals four stages of kink-band formation: the initial linear stage I, the peak stress stage II, the snap back stage III, and the plateau stage IV.

After result acquisition, there is an analysis for four stages. In the initial linear stage I, the change in geometry and stress–strain response are controlled by elastic properties, so it shows a straight curve existed in initial stage. When stress among

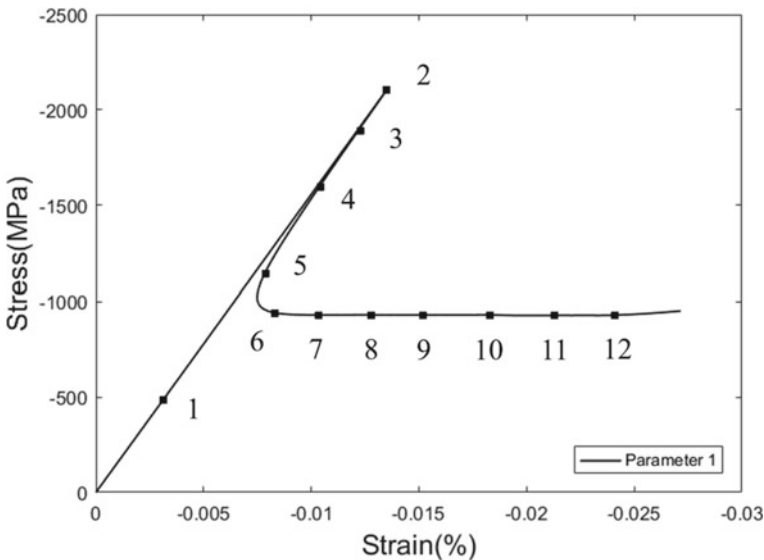


Fig. 8 The stress–strain response of misalignment model corresponding to the number in Fig. 9

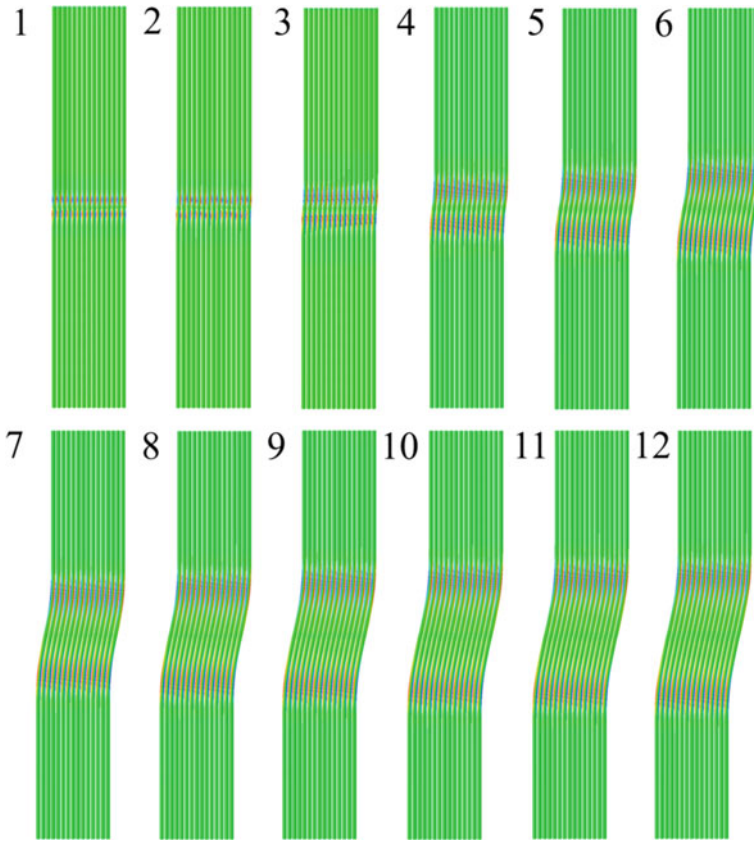
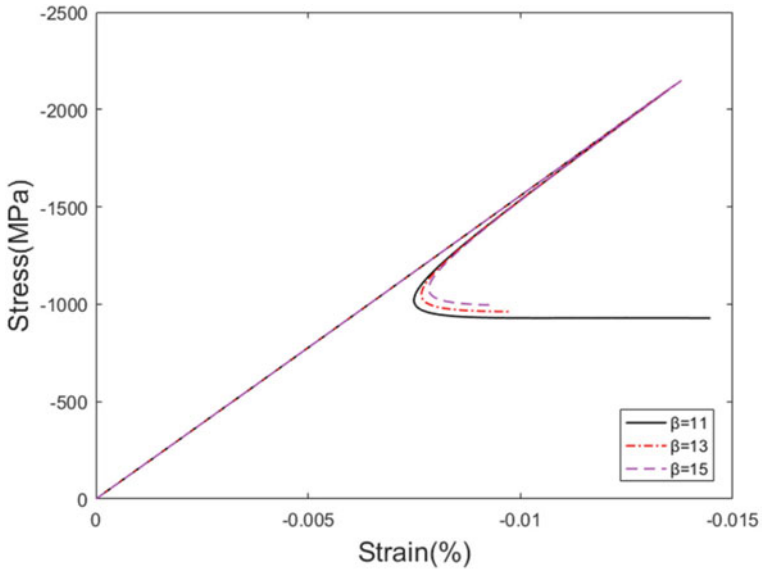


Fig. 9 Development of kink-band formation and S_{xy} in x and y directions

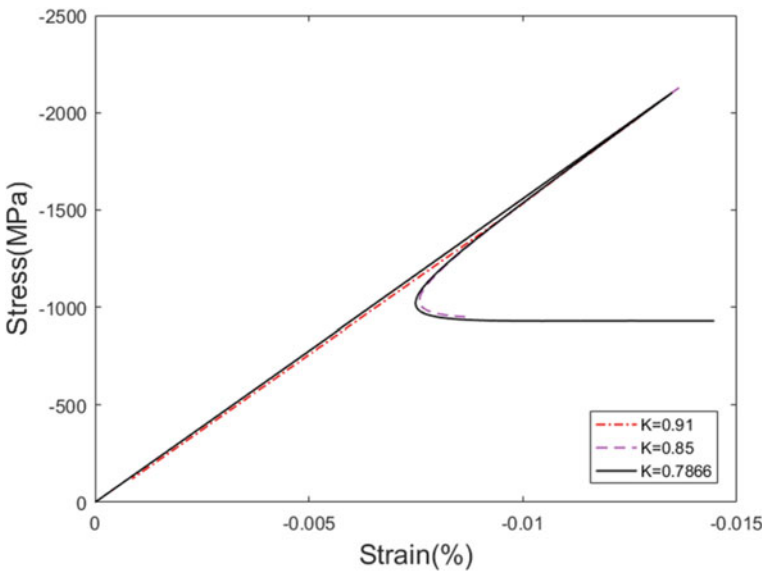
matrix reaches compression strength, matrix gets into the state of ideal plastic deformation. Then the yield band increases up, leading to absence of matrix lateral support, which will cause fiber instability at the same time. The occurrence of fiber instability contributes to a magnificent stress fall, resulting in the generation of snap back stage III. In the last plateau stage IV, the formation of kink-band is observed. With analysis continuing, the dimensions of kink-band are expanding during that stage. In conclusion, the existence of initial fiber misalignment leads to shear stress that further results in matrix damage and the ultimate longitudinal compressive failure.

4.2 Influence of Drucker–Prager Model Parameters

In order to understand the influence of D-P model parameters on the formation of kink-band, finite element analysis is carried out for different parameters in Table 5.

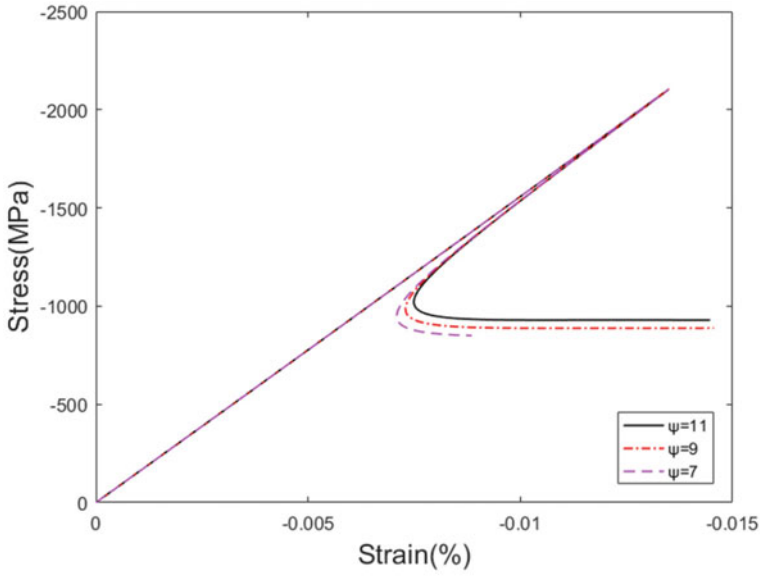


(a)

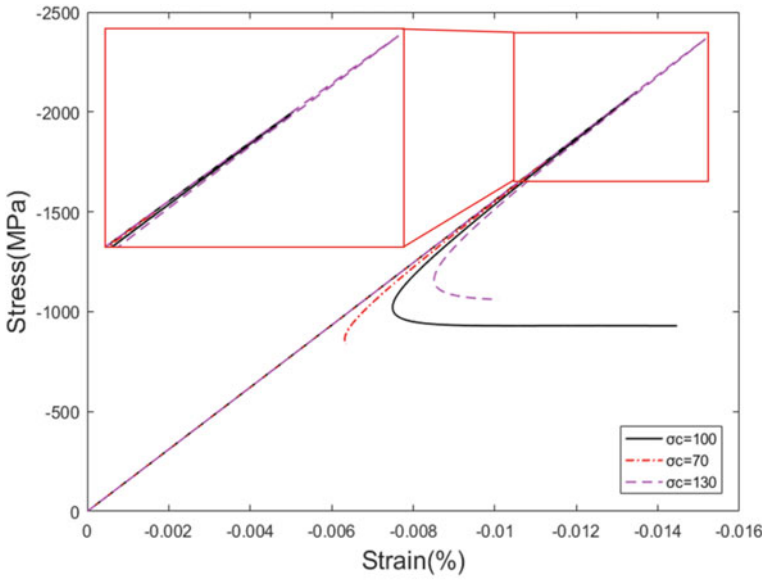


(b)

Fig. 10 The influence of the plastic properties **a** Stress-strain response of different β ; **b** Stress-strain response of different K ; **c** Stress-strain response of different ψ ; **d** Stress-strain response of different compression strength



(c)



(d)

Fig. 10 (continued)

The impact of those parameters on kink-band formation is illustrated in Fig. 10. The slope of the linear yield surface β is the first parameter defined in D-P model. By changing it, the slope of yield surface will be larger. The matrix is easier to yield with a smaller slope. Therefore, the larger initial fiber misalignment results in a lower compressive strength as shown in Fig. 10a.

K is the ratio of yield stress in triaxial tension to the yield stress in triaxial compression, controlling the shape of yield surface. It won't cause some influence on the formation of kink-band. But if its numerical value is beyond some level, matrix will not get into plastic deformation. In another word, there will be no existence of kink-band. As the result in Fig. 10b, when K equals 0.91, there is no kink-band anymore.

The existence of dilation angle ψ controls the direction of hardening. It has some similarity with changing β . Increasing the same order of magnitude causes the stress to increase by the same order of magnitude. The larger ψ it is, the greater stress in plateau stage will be. The maximum stress at peak stage is in management of matrix's compression strength. The reason why there is a drop of stress is that matrix begins to have plastic deformation when stress reaches compression strength. With changing compression strength, the maximum stress in Fig. 10d will be affected. The larger compression strength is, the greater peak stress will be. In the meantime, it can be concluded that compression strength will have some influence on the value of stress when kink-band is formed.

5 Conclusion

In order to explain the formation of kink-band as well as the impact of Drucker-Prager parameters on kink-band, numerical simulation is carried out on commercial software Abaqus. A detailed modeling method is given. The size of kink-band grows in the snap back stage III, until reaching the final dimensions at the plateau stage IV. The various parameters of D-P model have different impacts on the kink-band formation.

Those parameters controlling the formation of yield surface only affect the expansion of kink-band, they do not have impact on the maximum stress that the model could reach. It also can be concluded that the compressive strength of matrix will have impact on peak stress and stress after kink-band formation. In the meantime, computational convergence of model will be influenced, smaller compressive strength leads to slower convergence.

According to the predictions from FEA method, there is some similarity with changing numerical value of β and ψ . Increasing the same order of magnitude causes the stress to increase by the same order of magnitude. It is necessary to do some detailed research on the connection and difference between those two parameters.

Acknowledgements This work is supported by School of Aeronautic and Astronautic, Shanghai Jiao Tong University. Thanks for the detailed instruction from my tutors Dr. Hu and Dr. Yu. Their

insightful suggestions always light me in the lost. The authors also gratefully acknowledge the helpful comments and suggestions of the reviewers, which have improved the presentation.

Funding This work is supported by the National Natural Science Foundation of China under Grant Nos.11902197, and is sponsored by Shanghai Sailing Program under Contract No.19YF1421700.

References

1. Bergana AC, Herráez M (2020) A constitutive model for fiber kinking: formulation, finite element implementation, and verification. *Compos Part A* (129):105682
2. Yanan Y, Yao X, Niu K, Liu B (2019) Compressive failure of fiber reinforced polymer composites by imperfection. *Compos Part A* 106–16
3. Attwood J, Fleck N, Wadley HNG, Deshpande VS (2015) The compressive response of ultra-high molecular weight polyethylene fibers and composites. *Int J Solids Struct* 71:141–155
4. Patel J, Peralta P (2016) Mechanisms for kink band evolution in polymer matrix composites: a digital image correlation and finite element study. In: ASME 2016 international mechanical engineering congress and exposition american society of mechanical engineers
5. Zhou L, Zhao L (2018) A micromechanical model for longitudinal compressive failure in unidirectional fiber reinforced composite. *Results Phys* 10:841–848
6. Paulina D, Venkataraman S (2021) Modeling polymer-matrix composites with fiber waviness defects under cyclic loading. *AIAA SciTech Forum*
7. Naya F, González C (2017) Computational micromechanics of the transverse and shear behavior of unidirectional fiber reinforced polymers including environmental effects. *Compos Part A Appl Sci Manuf* 92:146–157
8. Bishara M, Rolfes R, Allix O (2017) Revealing complex aspects of compressive failure of polymer composites-part I: fiber kinking at microscale. *Compos Struct* 169:105–115
9. Yerramalli C (2004) The effect of fiber diameter on the compressive strength of composites-A 3D finite element based study. *Comput Model Eng Sci* 6:1–16
10. Hill R (1963) Elastic properties of reinforced solids: Some theoretical principles. *J Mech Phys Solids* 11(5):357–372
11. Drugan W, Willis J (1996) A micromechanics-based nonlocal constitutive equation and estimates of representative volume element size for elastic composites. *J Mech Phys Solids* 44(4):497–524
12. Prabhakar P (2013) Interaction between kinking and splitting in the compressive failure of unidirectional fiber reinforced laminated composites. *Compos Struct* 98:85–92
13. Zhang M, Zhang ZD, Wang XD, Du SY (2017) Micro-mechanical analysis about kink band in carbon fiber/epoxy composites under longitudinal compression. *Appl Compos Mater* 24:1011–1028
14. Lee J, Fenves GL (1998) Plastic-damage model for cyclic loading of concrete structures. *J Eng Mech* 124(8):892–900. [https://doi.org/10.1061/\(ASCE\)0733-9399](https://doi.org/10.1061/(ASCE)0733-9399)
15. González C (2007) Llorca, J: Mechanical behavior of unidirectional fiber-reinforced polymers under transverse compression: Microscopic mechanisms and modeling. *Compos Sci Technol* 67(13):2795–2806
16. Lubliner J, Oliver J, Oller S, Ōnate E (1989) A plastic-damage model for concrete. *Int J Solid Struct* 25(3):299–326
17. Sadik O, Peter D (2019) Development of an ABAQUS plugin tool for periodic RVE homogenisation. *Eng Comput* 35:567–577

Methodology for Formation of an Optimized Verification, Validation and Integration Program for an Aircraft Based on Models of Its Architecture



I. A. Konstantinov, V. A. Kaigorodova, and D. S. Shavelkin

Abstract New types of aircrafts embody all the most advanced technical and technological solutions. Architecting commercial aircraft has been always challenging due to the complexity of the product (Li et al. in *Architecting commercial aircraft with a Domain Specific Language extended from SysML*, 2021). The introduction of new technologies is associated with risks in terms of reliability and resiliency. Using traditional design methods in the development of an aircraft, it is impossible to determine all possible scenarios for the aircraft functioning and its systems itself and, as a consequence, to analyze all possible risky states of the aircraft. Each aircraft must meet the requirements that were established to it. This work is devoted to the processes of establishing and verifying these requirements. The principles and methods of integration, verification and validation of technical systems are considered in detail, the importance of these criteria is assessed. This work aims to create prerequisites for the development of an automatic algorithm for verification program and construction of a test certification basis for the aircraft as a whole and its subsystems in particular.

Keywords System engineering · Verification · Validation · System Integration

1 Introduction

The aircraft industry as a whole, as well as each modern aircraft individually, are extremely complex, science-intensive objects. Modern samples of aviation technology embody a huge number of new technologies and achievements of mankind [1]. However, a number of serious requirements are imposed on the aircraft. There are a lot of requirements can be assigned for the aircraft from the different sides, basically these requirements can be grouped into the following components:

- Improvement characteristics for fault tolerance and safety [2];
- Expansion of the aircraft functionality range;

I. A. Konstantinov (✉) · V. A. Kaigorodova · D. S. Shavelkin
Moscow Aviation Institute (National Research University), Moscow, Russia

- Aircraft systems optimization, including reduction of fuel consumption and emissions of harmful emissions into the atmosphere [3].

All of the above requirements are constantly being tightened and refined. Thus, the process of creating new aircraft is impossible without the introduction of new approaches in the aircraft design processes. In order to solve these problems, a separate methodological layer has been created—Systems Engineering.

Systems engineering is an interdisciplinary approach for creating highly complex, knowledge-intensive systems that allows you to combine requirements management models, the creation of life cycle concepts and other important parameters when creating technical systems.

The aircraft being created are extremely different from previous models and generations. Most of these differences lie in the electrification of aircraft, as well as due to the rapid development of computing power, which radically changes the principles of control and operation of all aircraft systems.

The introduction of the above hardware and software solutions has significantly expanded the functionality of the aircraft, which in turn expanded the basis for aircraft testing. One of the problems and prerequisites for this work creation and the development of the methods described in it—is the fact that technical progress develops at a faster rate than the processes and methods for confirming the conformity of the implemented systems.

In the development of new aircraft, it becomes extremely important to use Model—Based Systems Engineering (MBSE) and Model—Based Approach in the development of systems, as well as the creation of architectural models.

One of the key problems is the problem of choosing the optimal testing strategy for the developed technical solutions, as well as their integration, verification and validation (IVV) to higher-level systems.

2 Problem Statement

The program for aircraft testing, as well as separately the systems included in it, is a key stage in the creation of an aircraft. It is these processes that confirm the compliance of the aircraft and its systems with the requirements that were imposed on them. Without a complete test program, which includes confirmation of all possible functional scenarios of the systems' operation, as well as the integrity of the testing methodology, the operation of the aircraft cannot be safe. If, due to some factors, it was possible to test the entire system and cover all the scenarios of the system operations, this verification process will be suboptimal, which will entail significant time and material costs.

One of the significant factors that incline to the need to use a model—oriented systems engineering and a model—oriented approach with the development of model architectures is the fact that in the process of the system's activity, "Emergent" functional states arise. "Emergent" states are a superposition of individual functions

of subsystems and systems from a huge array of all functional states [4]. The number of all possible functional states of systems is extremely large and cannot be analyzed by a person without the help of high-performance computing technology.

Descriptions of the above problems are partially covered in a number of standards, for example, ARP4754A, ARP4761, AS9100, and so on. [5–7]. Many standards, such as ARP4754A, have been specifically designed for the aircraft industry, while some are generic product quality management standards. However, all these standards, although they are applicable to aircraft construction, are nevertheless focused on processes from different angles. Thus, the ARP4754A standard defines methods for ensuring the development of systems from errors in a given system, while the ARP4761 standard conducts security analysis and evaluates security risks. The developed methodology must fully comply with applicable standards and norms.

Many of the principles and methodologies proposed in this study have their origins in software development. It was during the development of software and other information systems that the need arose for the first time to verify and test both the program code in general and its components in particular [4]. An equally acute problem then and now is the integration of program code components into the system. As noted earlier, many of the principles proposed in this work are closely related to software development. A modern aircraft has a fairly serious computing power, which allows it to carry out controlled motion from a multidimensional array of its functional and physical states. Along with the way such processes are implemented in software, such a logic of work can be transferred to physical systems. Indeed, one can see the analogy that the program code, that the aircraft are systems consisting of a large number of subsystems, which must be integrated into the upper-level system. Each of these subsystems and the system as a whole must be verified, and the test set must preserve the integrity of the system configuration and ensure the traceability of requirements for the system and its components.

The implementation of the above algorithm, as well as the analysis of systems and their components with their functional states, is carried out according to the ARCADIA methodology using the Capella tool.

3 Research Method and Expected Results

ARCADIA (ARC—Architecture, A—Analysis, D—Design, I—Integrated, A—Approach) is an engineering method for the design and architectural design of complex and critical systems, including software, electronic, electrical architecture and manufacturing processes. This method facilitates collaboration of all stakeholders at many stages of system development.

It defines a set of practices that guide needs analysis and design in response to operational requirements. At the same time, it can be adapted to the processes and constraints associated with different types of factors.

ARCADIA prioritizes functional analysis as the main way to formalize needs. This includes operational, functional and non-functional requirements, as well as

the final architecture definition based on this functional analysis. ARCADIA is an open source MBSE solution and is also extensible. It can be tailored to specific engineering approaches and integrated with other development tools. It can also be supplemented with ready-to-use add-ons to make it easier to launch new projects, collaborate remote teams, create documents, and more.

The ARCADIA method adopts a structured design approach that establishes a clear separation between needs (operational needs analysis and system needs analysis) and solutions (logical and physical architectures).

ARCADIA recommends three essential, interrelated activities of the same importance:

- Needs analysis and modeling;
- Architectural construction and validation;
- Requirement's design.

Each ARCADIA model can be divided into the several submodel perspectives:

- Operational Analysis (OA);
- System Needs Analysis (SA);
- Logical Architecture (LA);
- Physical Architecture (PA);
- Product Breakdown Structure (PBS).

Each of these submodels is linked to the previous one by traceability/justification links between model elements. The dependencies are always upward: from the SA to the OA, from the LA to the SA, from the PA to the LA, from the PBS to the PA.

In each submodel above, associated with a perspective, the different functional and structural viewpoints are also separated:

- description of the data and interfaces model;
- functional description;
- behavioral structural description;
- structural description of hosting resources.

Each of these descriptions is linked to the previous descriptions of the same submodel by allocation, performance, implementation inks, etc., which will be described next. The dependencies are, there too, always upward: from the functional aspects to the data, from the behavioral to the functional aspects and the data, from the resources to the behavioral aspects (Fig. 1).

Capella workbench is an Eclipse application that implements the ARCADIA method, providing both a domain-based modeling language (DSML) and a dedicated toolbox. It is a systems development toolkit that applies MBSE approaches. This tool helps engineers describe the specification of a system project and present the architecture of this project in a visual form that will be understandable for perception.

One of the key features of Capella is its built-in instructional browser that resembles ARCADIA principles for the user and provides effective instructional guidance.

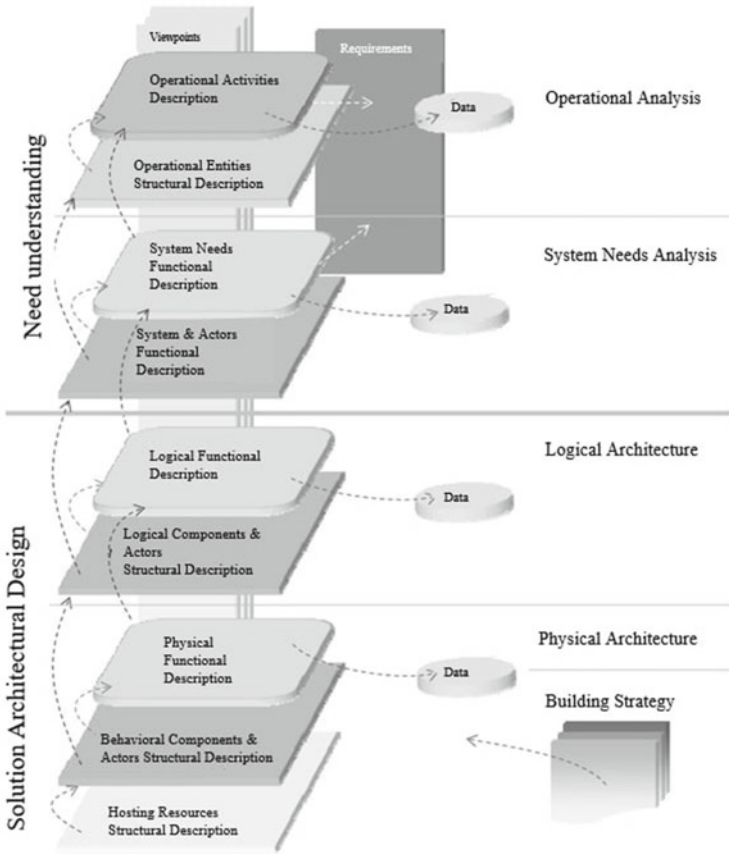


Fig. 1 Suggested logical diagram for ARCADIA methodology

This activity browser provides methodological access to all of Capella’s key activities and thus to the creation of all major diagrams, level by level. This is the main entry point to the model and is intended for both beginners and advanced users.

The purpose of this work is to develop a universal algorithm, the task of which is to form an optimized methodology—a verification program based on models of the system architecture. On the one hand, the task of this algorithm is to analyze the system from the point of view of safety and fault tolerance [8]; on the other hand, the algorithm must automatically write a program for verifying the architecture of the aircraft and its systems. It is required to develop an algorithm for analyzing the architecture of the system in order to obtain an optimal test program and a test program that will guarantee the completeness of coverage of requirements, ensure the completeness of coverage of all possible scenarios of operation and system failures. Besides, in order to specify the subsystem and optimize the IVV (Integration, verification and validation) between the engineering levels, it is necessary to define

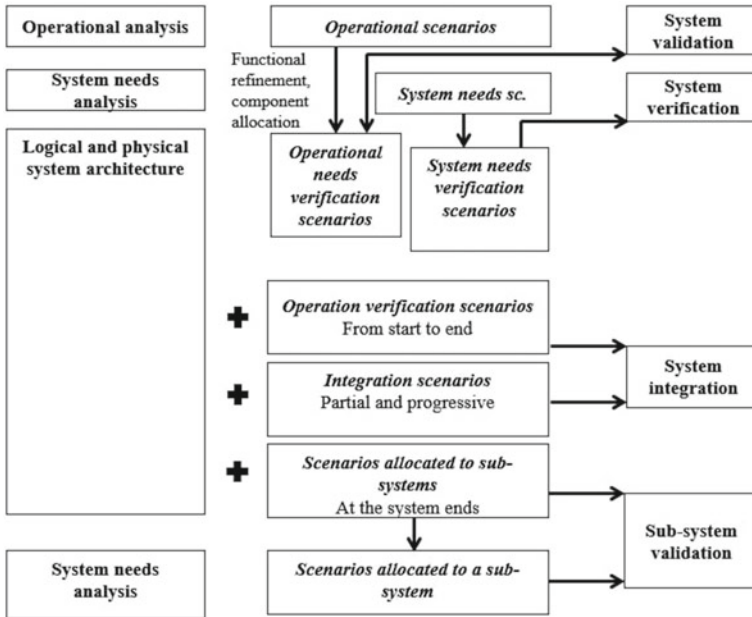


Fig. 2 System development process

scenarios and functional chains focused on each subsystem, which will determine both the behavior expected from the subsystem under operating conditions (as a result of scenarios for calculating parameters determined taking into account the needs), and tests that are delegated by the engineering system to the engineering subsystem as a prerequisite for its integration into the system itself. These scenarios, distributed across subsystems, will be, in particular, a vector for testing each subsystem, as expected by system engineering (Fig. 2).

At the moment, it is quite difficult to clearly and unambiguously formalize the functions of systems and their subsystems; often these understanding ends at the stage of forming a verbal description of these functions, which is unacceptable for creating highly complex systems.

4 Conclusion

The introduction of the above techniques, the development of an algorithm for system verification and the choice of the optimal testing strategy will help to significantly improve the characteristics of reliability and fault tolerance, reduce the time for systems implementation, and reduce the time for testing and testing systems. Since this algorithm is optimized according to various criteria, the introduction of this

procedure in the process of creating new aircraft will significantly reduce the costs of carrying out the above activities.

References

1. Luna S, Lopes A, Yan STH, Zapata F, Pineda R (2013) Integration, verification, validation, test, and evaluation (IVVT&E) framework for system of systems (SoS). <https://doi.org/10.1016/j.procs.2013.09.276>
2. Jean-Luc V (2018) Model-based system and architecture engineering with the arcadia method. UK, London
3. Li H, Zhan C, Wu H, Yu M, Dai J, Zou W (2021) Architecting commercial aircraft with a domain specific language extended from SysML. <https://doi.org/10.1088/1742-6596/1827/1/012100>
4. Basora L, Bry P, Olive X, Freeman F (2021) Aircraft fleet health monitoring with anomaly detection techniques
5. SAE ARP4754 Rev. A, guidelines for development of civil aircraft and systems
6. Guidelines and methods for conducting the safety assessment process on civil airborne systems and equipment ARP4761
7. AS9100—Quality management systems: aviation, space & defense organizations
8. Jimenez JJM, Vingerhoeds R (2019) A system engineering approach to predictive maintenance systems: from needs and desires to logical architecture. <https://doi.org/10.1109/ISSE46696.2019.8984559>

An Investigation on the Flow Mechanism of Complex Fractal Spoiler on Wing



Yanmin Guan and Frank Nicolleau

Abstract As designers aim to increase the aerodynamic efficiency, fractal spoiler may be used on wings for its ability of altering turbulence. The study focuses on analyzing and verifying the feasibility of applying fractal spoilers. The flow mechanism of the flow-through fractal grids is simulated using CFD methods. Both the laminar and turbulent conditions are considered when simulating. The simulation of the wing airfoil provides the velocity distribution to the fractal spoiler. The laminar results help us understand the flow mechanism including wakes, jets, and their interaction behind the grids. In the turbulent results, the importance of the parameter wake interaction length is stated, and compared with former papers. The parameters of the fractal grids are related to a number of flow properties including the turbulence intensity, homogeneity, isotropy, and velocity distribution. These special characteristics suggest that it's feasible to use fractal spoiler on wings as a control method.

Keywords Fractal · Turbulent flow · Spoiler · Wake · Jet

1 Introduction

A fractal is a pattern that continues repeating itself in a smaller scale, and every part of the fractal contains the information of the whole part. Compared to Euclid's simple geometry, objects in the natural world are always irregular and fragmented, such as the leaves, snowflake, and coastline. Complexity is at high level, and the number of distinct scales of length of natural is for all practical purposes infinite [1]. The fractal grids are commonly classified as I-grid, cross-grid, and square grid. Their multi scales and self-similar structure can be considered to mimic the fractal

Y. Guan (✉)

Aerospace Shanghai Jiao Tong University, Shanghai, China
e-mail: mingyueye@sjtu.edu.cn

F. Nicolleau

Aerospace Engineering University of Sheffield, Sheffield, England
e-mail: f.nicolleau@sheffield.ac.uk

in nature's characteristics. Learning from the nature, special engineering design can be gained, which is the idea of "biomimicry".

Flow separation over wings and airfoils has an important impact on aerodynamic efficiency and stall, the control of it is of great importance. Spoilers are upper surface flaps designed to control flow separation to provide aerodynamic braking, and lift dumping at touchdown [2]. They are multifunctional flight control surfaces. And the idea came up with using fractal grids on the spoilers. Instead of altering the whole wing, it would be much easier to alter spoilers so as to control the turbulent flow behind it and improve the aerodynamic efficiency of the wing.

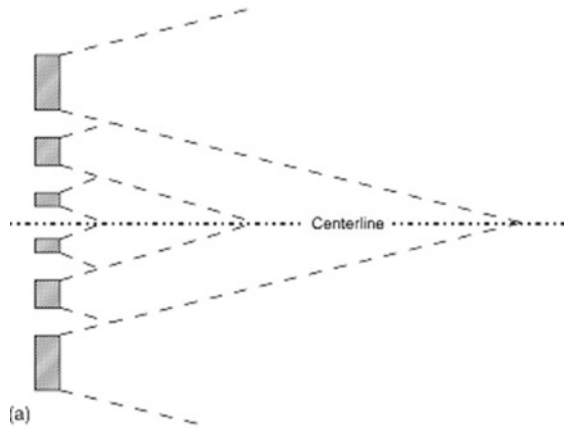
The fractals were studied in engineering first in 1990. The US-based process R&D company Amalgamated Research was the first to use fractals in fluid mixing [3]. Ever since, the fractals were studied more experimentally than theoretically. The fractal square grid was first introduced by Hurst and Vassilicos [4], who were the first to do wind tunnel test about the turbulent flow through the fractal grids. In Imperial College London, they examined the turbulence generated by the fractal grids and found that such grids could to some extent control the transition from laminar to turbulent flow. Besides, several parameters of the fractal grids were related to the turbulence properties downstream such as the turbulence intensity and pressure drop. Among the fractal grids tested, the space-filling fractal (as showed in Fig. 1) generated turbulent flow with the optimum homogeneity. Their theories were later tested and verified by Mazellier and Vassilicos [5], confirming the existence of a typical region where turbulence intensity firstly increased and then decreased. A step further was made by introducing the important wake-interaction length scale. It was shown that the peak of turbulence intensity along the centerline of the two different regions located at about 0.5λ , and the flow profile was inhomogeneous at streamwise distances less than 0.5λ , but became homogenous after 0.5λ . The inhomogeneous region behind the fractal grids originated from the wakes and jets in the flows they generated.

More importantly, they suggested that the turbulence generated from fractal grids had distinct flow mechanism from single-scale fractals. From fractal grids, the smallest wakes are generated by the smallest bars, they then met each near the grids. Larger wakes generated by larger bars mix at distance further. This process repeats itself from the smallest to the largest scales as shown in Fig. 2; this process enhanced the turbulence intensity of fractal-generated flow. Spoilers with different



Fig. 1 Space-filling square grids [6]

Fig. 2 Flow mechanism behind fractal grids [4]



space filling squares were tested in the wind tunnel by Nedic et al. [6], and the parameter of the grids mounted on the spoilers was found to could influence the turbulence they generate, and it is thus possible to use the fractal spoiler as a passive control method.

Introducing multi scales, the fractal-generated turbulence has many different properties from traditional one-scale generated turbulence. The turbulence generated by the fractal square grids was isotropic and homogeneous and decayed exponentially at downstream far enough [7]. The traditional boundary-free turbulent flow obeys the power law. The ratio of the outer to inner length scales of the fractal-generated turbulent was independent of the Reynolds number [8]. However, in traditional Richardson-Kolmogorov cascade picture, the range of scale needed for the turbulence energy to cascade increases with the Reynolds number. In the fractal-generated multiscale turbulent flows, the turbulent flow was found to be independent of the boundary conditions [9].

Although some experimental study has been made, the flow mechanism behind fractals has not been fully understood yet. This article tries to reveal the flow mechanism based on existing theories, and testify the theories of former papers using the CFD method. In view of simplicity and in order to compare our work with former papers, the square grids are chosen as simplified models of the fractal spoilers on the wing.

2 Model Setup

The space-filling fractal with multi scales can be described by five scaling parameters: the grid height H , the number of iterations N , the maximum bar length, the maximum bar thickness, and minimum bar thickness. The fractal dimension here is 2 which proved to generate the most homogeneous turbulence [4]. The scaling parameters

Table 1 Scaling parameters for fractal square grids

N	(mm)	(mm)	(mm)	(mm)	(mm)	(mm)	(mm)	(mm)
1	131.8	65.9			11.7	4.6		
2	131.8	65.9			11.7	4.6		
4	131.8	65.9	33.0	16.5	11.7	4.6	1.8	0.9

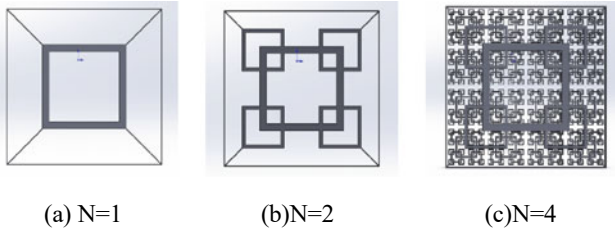


Fig. 3 Fractal Grid Models

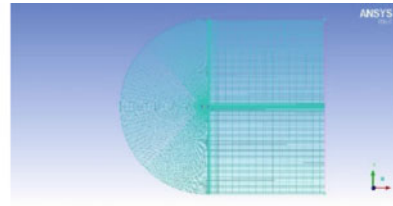
of the fractal grid models in this paper are listed in Table 1. The models are built in SOLIDWORKS as shown in Fig. 3.

Hexahedral meshes are generated manually in the ICFM CFD under two guidelines: (1) Aligning hexahedra elements along each boundary. (2) Improving mesh quality by keeping distortion the smallest. This can be achieved by setting the nodes of all the parallel edges the same, and adjusting the spacing and ratio manually. A former study has shown that the number of five mesh nodes across is enough to simulate the flow around the smallest bars of the fractal grids [10]. Besides, the mesh quality is closely related to the accuracy of the simulation outcome. In ICFM CFD, the mesh quality can be examined by a quality metric ranging from 0 to 1. The quality metric can show where the typical quality of mesh locates so these meshes can be adjusted. The final mesh quality is shown in Fig. 5. We may draw the conclusion that the structured grid is fine enough for simulation. The mesh generation for airfoil and $N = 1, N = 2$ fractal grids are shown in Fig. 4.

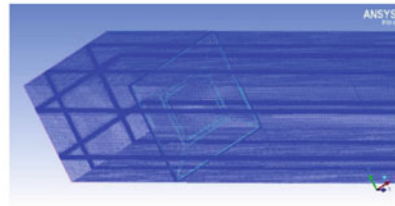
In ANSYS FLUENT, second-order upwind scheme is used, with SST- $\overline{\kappa-\omega}$ turbulence model. The multigrid acceleration method is used, because of its advantage in accelerating the convergence for mesh with large cell numbers and cell aspect ratios.

From the wall $y+$ contour in Fig. 6, in most of the places the wall $y+$ number is lower than 300, which is acceptable. Since SST is the hybrid model and can handle $y+$ from 1 to 300.

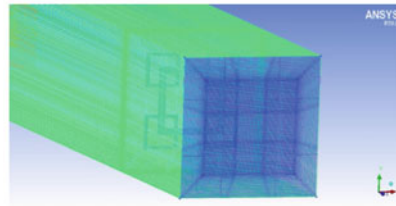
Fig. 4 Mesh Generation



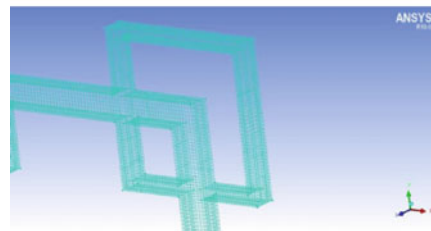
(a) Mesh Generation for Airfoil



(b) Mesh Generation for N=1



(c) Mesh Generation for N=2



(d) Surface Mesh for N=2

3 Results and Discussion

A. *Simulation of the airfoil*

The simulation result of the airfoil is showed in Fig. 7. As showed in Fig. 7(a), the pressure difference of upper and lower surface generate lift, as is explained by Bernoulli's equation. From the vorticity contour of airfoil in Fig. 7(b), the vortex at the wing tail can be observed, the exist of wake enhances the turbulence intensity. What's more, the velocity contour shows that the velocity is around 200 m/s at the

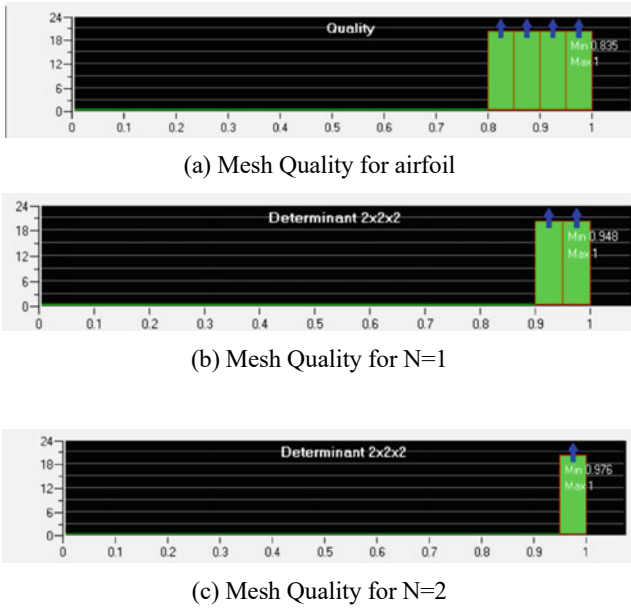
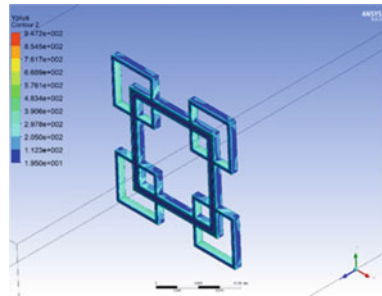


Fig. 5 Mesh Quality

Fig. 6 Wall y + contour



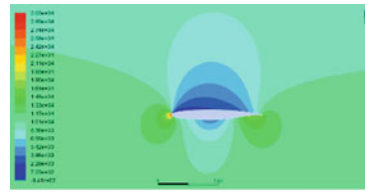
upper surface of the airfoil, where the fractal grids are planned to be mounted on the spoilers.

B. *Laminar results and flow mechanism*

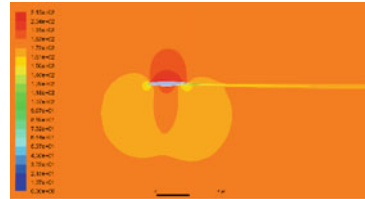
The laminar simulation could help us to understand the fluid mechanism behind the fractal. The red color in the velocity contour in Fig. 8(a) indicates that the velocity is streamwise and the blue color indicates that the velocity is opposite to the streamwise direction. Along with the vorticity contour in Fig. 8(b), we may deduce that there exist wakes at the corner of the model.

The recirculation and wakes phenomena are caused by the flow separation or boundary layer separation. The detachment of the boundary layer of a surface forms

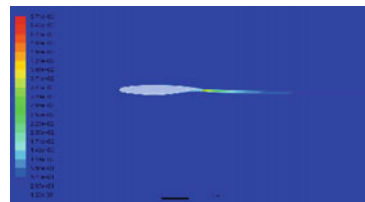
Fig. 7 Simulation results of the airfoil



(a) Static pressure contour

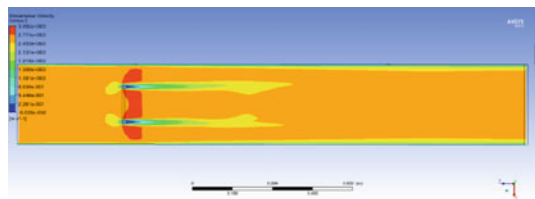


(b) Velocity Contour

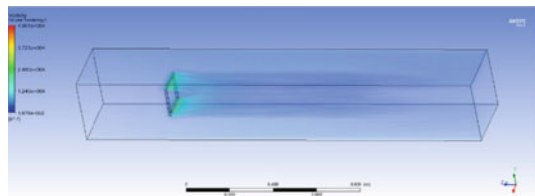


(c) Turbulent kinetic energy contour

Fig. 8 Laminar results for $N = 1$ grid



(a) Streamwise velocity contour of x-z plane at $y=0$



(b) Volume rendering of vorticity

a wake. When flow goes through a sharp corner, the flow separation would always happen because of the sudden expansion and contraction. Wakes always contain large eddy motions which are shed downstream.

As the velocity contour in Fig. 9(a) shows, the flow mechanism behind the $N = 2$ fractal grid is very complicated. Wakes are generated when flow passes the sharp corners of the model. The dark blue color indicates that the local velocity is close to zero, where the recirculation and vortex may exist. The deep red region indicates that when the flow passes through the interval space between the outer grid and inner grid, the jet-like fluid is generated. While the wakes dissipate energy to the surrounding fluids, the jets can travel long distance without dissipating. The vorticity inside the jets are very small and relatively high between the wake and jet. Jet flow also have higher velocity and momentum, and is thus the dominant parts in transferring momentum to downside. In Fig. 9(b), the jets interact and attach toward the wakes. Between the jet and the wake are the shear layers caused by velocity gradient. Besides, the wakes closer to the centerline would meet first while the wakes away from centerline would interact later downside. The jets and wakes influence each other, generating the complicated turbulence with multi scales. (The laminar result for $N = 2$ grids may not be the real case because the jet-like flow usually comes with turbulence.)

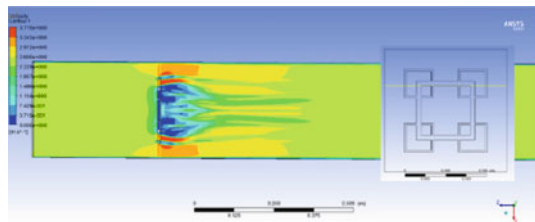
C. *Turbulent results and discussion*

- Flow mechanism

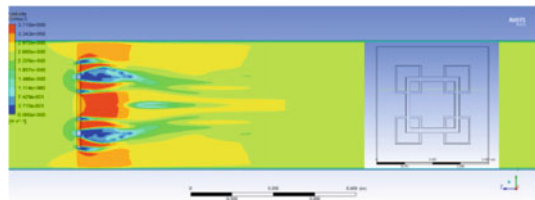
For the turbulent through the $N = 2$ fractal grids, more intense momentum transition can be observed. While the small jets are influenced and attached to the wakes, the two wakes beside the jets are also twisted, as in velocity contour Fig. 10.

The $N = 2$ fractal grids generate turbulent flow with much higher turbulence intensity compared to the $N = 1$ case, as shown in Fig. 11. The velocity along the

Fig. 9 Laminar results for $N = 2$ grid



(a) Velocity contour of x-z plane at $y=0.06$



(b) Velocity Contour of x-z plane at $y=0.04m$

Fig. 10 Velocity contour of $x-z$ plane at $y = 0.04$ m

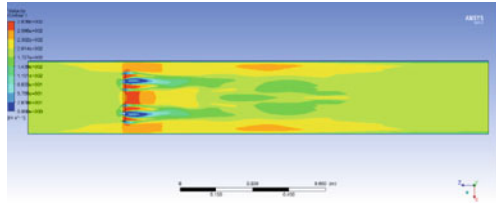
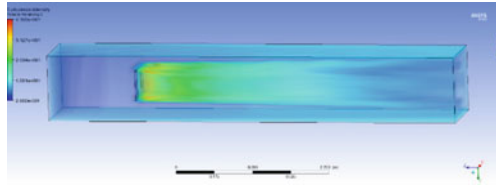
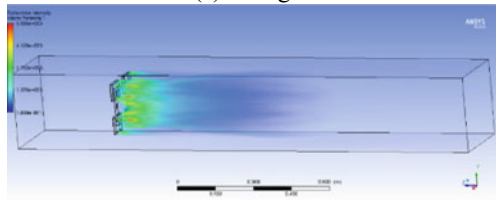


Fig. 11 Turbulence intensity



(a) N=1 grid



(b) N=2 grid

centerline in Fig. 12 shows that the fluid first accelerates due to the influence of jet-like flow, and then decelerates as the jet-like flow diminishes, and accelerates again at around $z = -0.5$ m influenced by the wakes. After the wakes diminish the flow decelerates after about $z = -1.1$ m and finally remains unchanged.

- Isotropy and wake interaction length

Turbulence is characterized by random, disorder, irreversibility, and intermittency. The “similarity hypothesis” [11] has a close relationship with fractal. In the fractal

Fig. 12 Velocity along the centreline

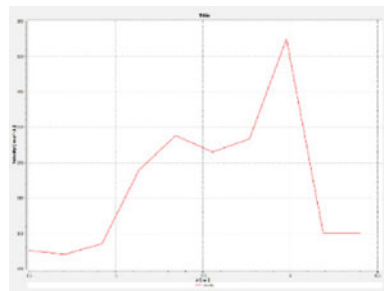
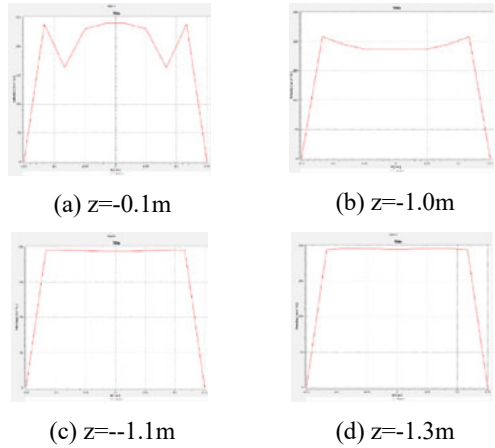


Fig. 13 Longitudinal Velocity change at $y = 0.04$ m



grid, every smaller scale part is similar to the whole grid. In turbulent flow at sufficiently high Reynold number, the statistics of the small-scale universal form of motion that is determined uniquely. The large-scale vortices are anisotropic. The small-scale vortices carry with all structure information about how they were created. When fully developed, they become homogeneous and isotropic.

The presence of velocity gradient causes turbulent flow. By constantly changing the value of z downstream, the lateral velocity gradient always exists, as the longitudinal velocity showed in Fig. 13(a). However, when the value of z is close to -1.1 m, as in Fig. 13(c), the velocity profile acts as almost a line along the longitudinal direction and the velocity gradient disappears.

Combined with Fig. 12, it's natural to assume that after $z = -1.1$ m downstream, the turbulence is isotropic, while before $z = -1.1$ m the turbulence is anisotropic. The important scaling parameter wake interaction length was introduced and determined as in [10]. It indicates the boundary of two distinct flow regions, one is the near-grid region with high anisotropic turbulence, the other is the far-field isotropic turbulence region. Using this parameter, the peak of turbulence intensity along the centerline can be predicted, which is 0.15 m, and that coincide with the numerical simulation results.

- Homogeneity and Prantl mixing length model

On the other hand, the homogeneous flow is defined where the turbulent level at any given location are the same along all directions. From turbulent kinetic energy contour of x - y plane at different z locations in Fig. 14, one can observe that the turbulence is highly inhomogeneous close to the fractal grid, and becomes homogeneous at about $z = -0.6$ m. The inhomogeneous behind the fractal grids is caused by the interaction of the jets and wakes, while the ideal turbulent flow is thought to be both isotropic and homogeneous, and dissipates exponentially. Fully developed, the turbulence generated by fractal grids shows accordance with the Kolmogorov similarity hypothesis.

Fig. 14 Turbulent Kinetic Energy of x–y plane for different location at z

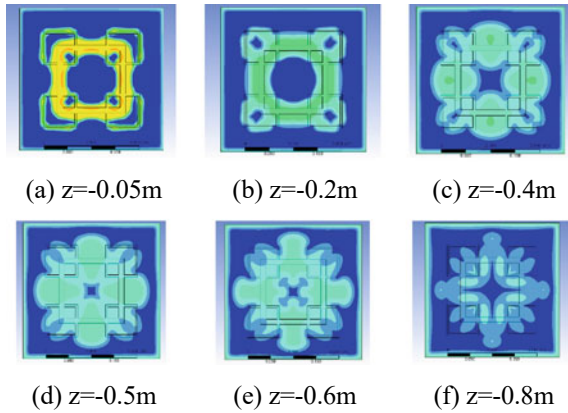
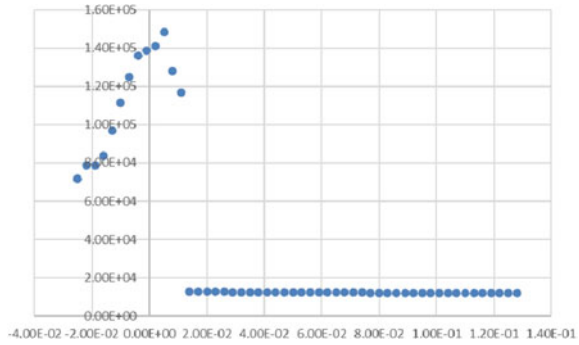


Fig. 15 Streamwise evolution of the maximum absolute vorticity value. The maximum is over the y–z plane at a given z location



The decay of turbulence is visible by plotting the maximum vorticity over the x–y plane as a function of the streamwise coordinate z. Fig. 15 shows that the turbulence generated from fractal have higher vorticity compared to the $N = 1$ case. (From the volume rendering of vorticity in Fig. 16 the max value is 4.95×10^4 for $N = 1$). The maximum plane absolute vorticity value increases rapidly when the flow passes through the fractal grid, and decreases rapidly after about $z = 0.04$ m.

The Prandtl mixing length model developed by Ludwig Prandtl uses the model of mixing length to describe the momentum transfer of the flow in the boundary layer.

Fig. 16 Volume rendering of vorticity

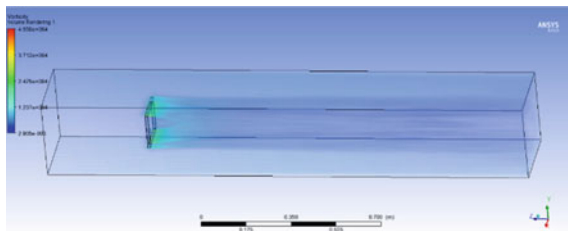
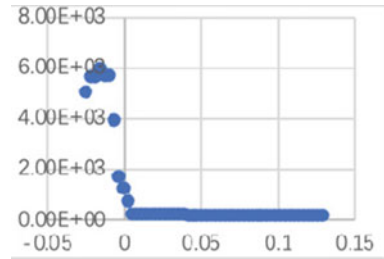


Fig. 17 Streamwise evolution of the maximum of turbulence intensity



The eddy viscosity lays in the boundary layer which is caused by turbulence Reynolds stresses. “The mixing length may be considered as the diameter of the masses of fluid moving as a whole in each individual case; or again, as the distance traversed by a mass of this type before it becomes blended in with neighboring masses [12].”

From the Prandtl mixing length model, the turbulence intensity builds up as a function of the interaction between the wakes shed by the grid bars. In the $N = 1$ case, all the wakes meet at the same streamwise location. On the contrary, in the $N = 2$ fractal case, the wakes generated by the bars are of different sizes and locations and meet at different positions.

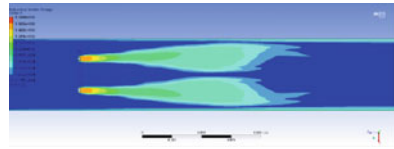
However, if we plot the streamwise evolution of the maximum turbulence intensity as in Fig. 17 it’s hard to find the peak behind the fractal grids as in former paper [8]. The reason behind may be that our iteration number is too low to completely mimic the fractal-generated turbulence. On the other hand, although we are unable to compare several fractal spoilers with different parameters because of the limited condition, we can analyze qualitatively the relationship between the fractal-generated turbulence with the blockage ratio.

- Influence of blockage ratio

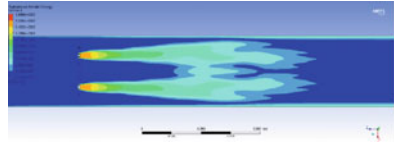
In Fig. 18, the turbulent kinetic energy contour of $x-z$ plane at different y locations are showed. The turbulent downstream is directly influenced by the blockage ratio. It can be observed that where the blockage ratio is low, the jet-like flows become weak, and the turbulence kinetic energy is higher on average. In Fig. 18(d) the main recirculation region actually disappears, an intense region of turbulent mixing is attached to the backside of the spoiler. The interaction of small jet-like flows makes the recirculation regions move downstream and finally disappears.

From the numerical simulation of the fractal-generated turbulence, so many fluid properties are related to the parameter of the fractal grids including the turbulence intensity, homogeneity, isotropy, velocity distribution, etc. The prospect of the fractal grids being used as fractal spoilers is considerable and needs further studies.

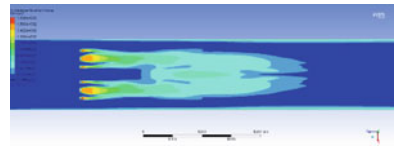
Fig. 18 Turbulent kinetic energy contour of $x-z$ plane at different y



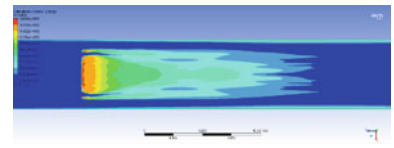
(a) $y=0m$



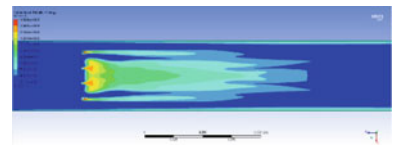
(b) $y=0.02m$



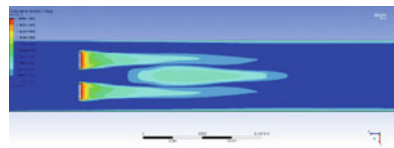
(c) $y=0.04m$



(d) $y=0.06m$



(e) $y=0.08m$



(f) $y=0.1m$

4 Conclusion

After numerical simulation, the outcome of the airfoil, lamina, and turbulent cases are showed and discussed in sequence. The airfoil simulation provides us with the boundary condition to simulate the grids on the fractal spoiler, and helps us to understand the flow mechanism of the wings. The turbulence results introduced the important flow mechanism of wakes and jets and their interaction with us. The important properties of fractal-generated turbulence have been analyzed in this paper include:

- (1) Because of the multiscale nature of the fractal grids, both jets and wakes are generated. The jets are caused by the flow passing through interval space of the fractal grids, while the wakes are generated when the flow goes through sharp corners on the fractal grids. The jets and wakes interact with each other, the smaller wakes meet earlier along the centerline, and the larger wakes meet later. Their interaction together forms the complex and inhomogeneous turbulence behind the fractal grids.
- (2) Downstream the fractal grids, the turbulence change from anisotropic to isotropic at the distance of wake interaction length $[x^* = L_0^2/\epsilon_0]$, and change from inhomogeneous to homogeneous at the distance of about $0.5 [x^*]$.
- (3) The blockage ratio and other parameters of the fractal grids have direct relationship with the turbulence generated by the fractal grids. It's thus possible to use fractal spoilers as control surfaces on the wing to alter the turbulence and the flow properties through the spoilers.

In conclusion, this paper studies the flow mechanism behind the fractal spoiler, tests its unique properties that have been proposed in other papers earlier, and discusses the feasibility of the fractal grids to be fractal wing spoilers. In the future, the author plans to do much more works, including test different kinds of fractal spoilers with different parameters like thickness, iteration, and blockage ratio to find the most suitable fractal grid for the wing spoiler. And if conditions permit the author also intend to do some wind tunnel test to test the feasibility of the fractal spoiler. Moreover, the author is interested in the theory mechanism behind the specialty of the fractal spoiler and intends to analyze it theoretically.

Acknowledgements The authors gratefully acknowledge the helpful comments and suggestions of the reviewers, which have improved the presentation.

References

1. Diab H, Abboud N (1991) The engineering applications of fractals. *SIMULATION* 57(2):89–97
2. Lindsay SD, Walsh P (2019) Experimental investigation of spoiler deployment on wing stall. *Inventi Impact-Autp*

3. Manning R (2008) Fractal breakthrough Ross Manning highlights a potential alternative to current industrial mixers. <https://www.imperial.ac.uk/media/imperial-college/research-centres-and-groups/turbulence-mixing-and-flow-control-group/50853696.PDF>. Last Accessed 23 April 2021
4. Hurst D, Vassilicos JC (2007) Scalings and decay of fractal-generated turbulence. *Phys Fluids* 19(3):035103
5. Mazellier N, Vassilicos JC (2010) Turbulence without Richardson–Kolmogorov cascade. *Phys Fluids* 22(7): 075101
6. Nedic J, Ganapathisubramani B, Vassilicos JC, Borée J, Brizzi LE, Spohn A (2012) Aeroacoustic performance of fractal spoilers. *AIAA J* 50(12):2695–2710
7. George WK, Wang H (2009) The exponential decay of homogeneous turbulence. *Phys Fluids* 21(2): 025108
8. Seoud RE, Vassilicos JC (2007) Dissipation and decay of fractal-generated turbulence. *Phys Fluids* 19(10):105108
9. Weitemeyer S, Reinke N, Peinke J, Hölling M (2013) Multi-scale generation of turbulence with fractal grids and an active grid. *Fluid Dyn Res* 45(6):061407
10. Laizet S, Vassilicos JC (2009) Multiscale generation of turbulence. *J. Multiscale Model* 1:177–196
11. Kolmogorov AN (1962) *J Fluid Mech* 13:82
12. Prandtl L (1926) *Proc Second Int Congr Appl Mech Zur*

Compression Performance of Composite Honeycomb Sandwich Structures with Prefabricated Defects



Zhouyu Zheng, Xiuhua Chen, and Huayong Zheng

Abstract The compression behavior of composite honeycomb sandwich structures with prefabricated defects was investigated via experiments and finite element analysis. An edgewise compression test was carried out on specimens with two types of prefabricated defects: panel layering and panel-core debonding. Maximum load and degree of maximum attenuation were compared. Test results demonstrate that the failure mode is core shear failure, buckling, facesheet compression failure, and end failure. The defect size has little influence on structural mechanical properties, while the type of prefabricated defect does. A 3D finite element model was constructed to investigate the compression behavior of honeycomb sandwich structures with prefabricated defects. Abaqus continuum damage model (ACDM) and cohesive zone model (CZM) methods were compared in panel modeling. This study provides a reliable method for defects repair tolerance assessment of composite honeycomb sandwich panels.

Keywords Composite material · Honeycomb sandwich · Compression performance · Prefabricated defects

Z. Zheng · X. Chen (✉)
Shanghai Jiao Tong University, Shanghai, China
e-mail: chenxiuhua@sjtu.edu.cn

Z. Zheng
e-mail: zzy77jay@sjtu.edu.cn

X. Chen · H. Zheng
Aerospace System Engineering Shanghai, Shanghai, China
e-mail: zhenghrb@126.com

H. Zheng
Shanghai Key Laboratory of Spacecraft Mechanism, Shanghai, China

1 Introduction

1.1 Introduction of Sandwich Structure and Applications in Aerospace

The design of high-load performance components is especially important in the design of high value-added products such as F1 racing cars, airplanes, spacecrafts, and satellites. These structures need strong stiffness, effective stress, and breaking strength while being as light as possible. This kind of performance requires structural effectiveness design. Efficient materials and optimized structural design can maximize structural effectiveness.

The composite material is a multiphase material composed of two or more materials with different properties. Although the constituent materials act as a whole, they can be physically distinguished at the interface [1]. In the conceptual design of all possible composite structures, sandwich structures stand out as a result of the continuous development of numerous artificial sandwich materials. As a special form of panel composite, it consists of several different materials and these materials interconnect to take advantage of the performance of the components to improve overall performance.

The sandwich structural panel is composed of three parts, and the upper and lower surfaces are thin sheets of high strength, and the middle is filled with a thick, light and low strength material. In order to transfer the load in the structural components, the two faces and the core need to be tightly bonded.

Nowadays, the pursuit of high-tech products for lightweight and high performance makes the application of sandwich structures increasingly widespread. In many weight-critical applications, faces often use composite materials. Sometimes, for cost savings, aluminum, iron, and plywood are still in use. Lightweight foam and honeycomb are two popular selections for the core (Figs. 1 and 2).

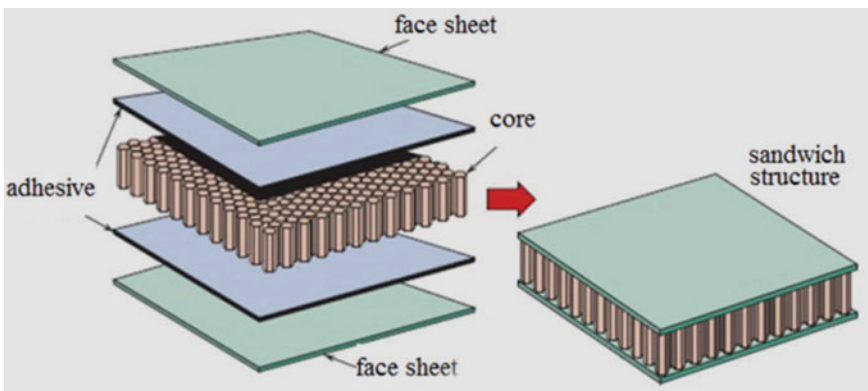


Fig. 1 The geometry for sandwich structure



Fig. 2 Some typical aircrafts using sandwich structure

A large part of high-tech products is concentrated in the aerospace industry. In this area, sandwich structure can be seen in wings, rudder, landing gear, cowling, and so on. From the eye of history and the application fields, sandwich structure has its name in aerospace, and holds a long-term and broader development space. Although it has been used in many aircrafts including the ARJ21 and the C919, it remains its baby step in space engines. However, it has a bright future in the choice of the material for space engines since its high-level performance.

1.2 Failure and Damage of Sandwich Structure

Typically, sandwich constructions in these applications use thin-gage composite laminates which are cocured to honeycomb and foam cores [2]. Due to the nature of these structures, damage tolerance is more complex than conventional laminated structures. Besides typical damage concerns such as through penetration and delamination, additional modes including core crushing and facesheet debonding must also be addressed. This complicates the certification process by introducing undefined Allowable Damage Limits (ADL) and Critical Damage Thresholds (CDT) as related to the ultimate and limit load-carrying capability of the structure. The damage resistance and damage tolerance of sandwich composite structures must be addressed because of the potential threat to structural integrity in both commercial and military applications. This need is further accentuated in view of the increasing use of composite sandwich configurations in general aviation (GA) aircraft where thin skins are typical [3].

For different kinds of loading for sandwich structure, edgewise compression is among the important kinds. This study is mainly based on this kind of loading. Figure 3 shows the damage modes and mechanisms of edgewise compression. The common damage modes and mechanisms are end failure (unacceptable), facesheet buckling failure, facesheet compression failure, facesheet dimpling failure, core compression failure, and core shear failure [4].

Researchers have done lots of work in failure and damage performance of sandwich structure. Fleck and Sridhar [5] performed an edgewise compression on sandwich structures. A number of competing failure modes were observed. The minimum weight design method of sandwich structure was carried out. Mamalis et al. [6]

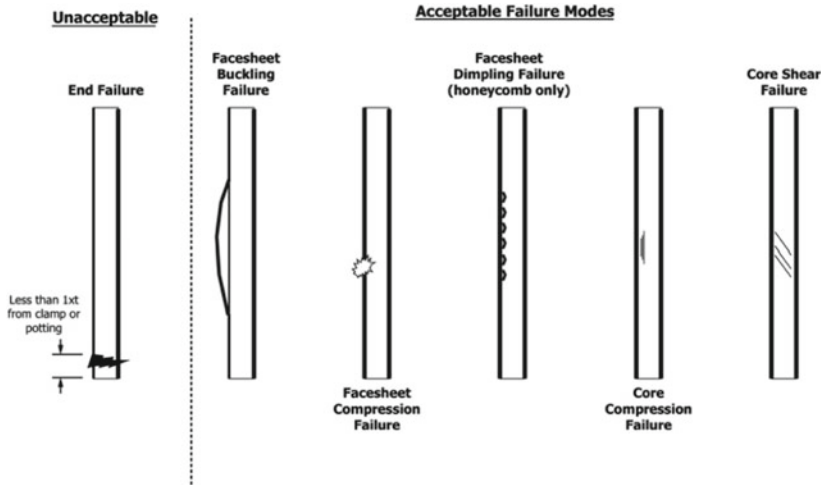


Fig. 3 Failure modes in sandwich columns subjected to edgewise compression [4]

performed edgewise tests on four types of specimens. The results indicated the most efficient failure modes with respect to crash energy absorption is the progressive end-crushing mode. Lei et al. [7] investigated the sandwich

structure through experimental, theoretical and FEA methods. The results showed that, with the increase of slenderness ratio, the critical collapse stress of column is significantly reduced. Mcelroy et al. [8] performed simulations on prediction of delamination-migration. FEA models were designed using: (1) Abaqus continuum damage model (ACDM); (2) Cohesive zone model (CZM); (3) Deformation gradient decomposition model (DGDM). Advantages and disadvantages were compared between these three methods. Guo et al. [9] provided a reliable FEA model for honeycomb sandwich repair. However, sandwich structures with prefabricated defects are not investigated nowadays.

Through edgewise compression test, the failure modes of sandwich structures with prefabricated defects were investigated. 3D FEA model was designed, and different kinds of FEA models are compared to predict the delamination-migration. The size of prefabricated defects changes to predict the damage repair tolerance.

2 Experimentation

2.1 Test Specimen Description

Figure 4 shows the structure of honeycomb sandwich. A 480 mm × 120 mm composite sandwich panel consisting of two ZT7H/5429 laminate facesheets and one Nomex honeycomb core (NRH-2-48) was fabricated. The laminate layup is

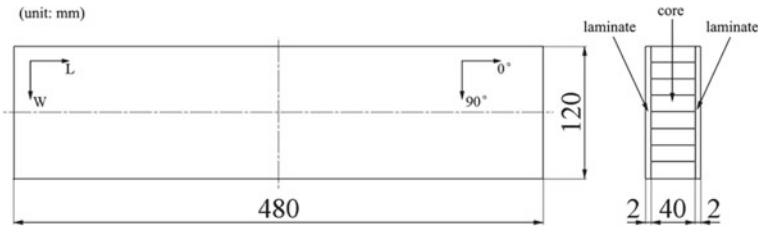


Fig. 4 Diagram of undamaged specimen

given by [45/0/-45/0/45/90/0/-45]s. Ply thickness is 0.125 mm, and each facesheet contains 16 plies. Core thickness is 40 mm. The laminates are co-bonded with the core using J-116A-0.35.

There are two types of defects, including panel layering, panel-core debonding, under investigation. In order to simulate these four types, some prefabricated work has been done as follows:

Figure 5 shows the diagram of the specimen with prefabricated panel layering. Teflon® insert strips, with diameters of 20 mm, 40 mm, 60 mm, were implanted in the laminate at the mid-interface.

Figure 6 shows the diagram of the specimen with prefabricated panel-core debonding. Teflon® insert strips, with diameters of 20, 40, 60 mm, were implanted in the interface of laminate and adhesive layer.

The specimens were separated into 7 groups, each group had 4 specimens. The prefabricated defect type (PDT) and code are listed in Table 1.

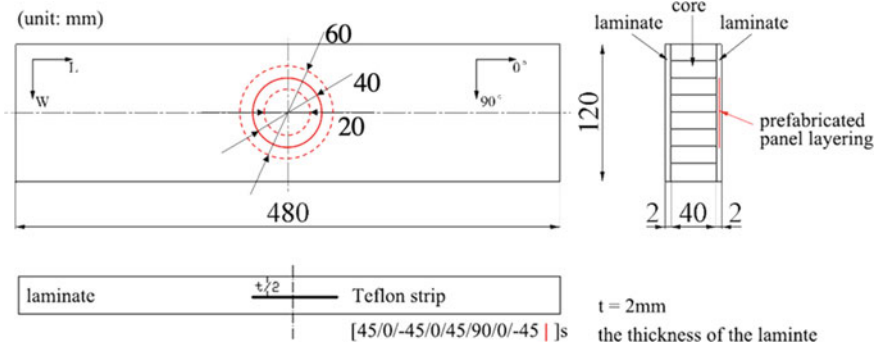


Fig. 5 Diagram of prefabricated panel layering specimen

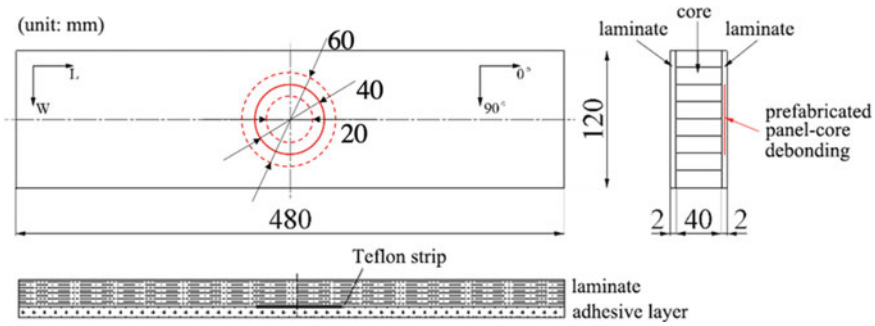


Fig. 6 Diagram of prefabricated panel-core debonding

Table 1 The test group

PDT	Code
No defect	WQ
Prefabricated 20 mm panel layering	WQ-YZMB-20
Prefabricated 40 mm panel layering	WQ-YZMB-40
Prefabricated 60 mm panel layering	WQ-YZMB-60
Prefabricated 20 mm panel-core debonding	WQ-YZBX-20
Prefabricated 40 mm panel-core debonding	WQ-YZBX-40
Prefabricated 60 mm panel-core debonding	WQ-YZBX-60

2.2 Test Procedure

In order to observe the mechanical properties of specimens under edgewise compression, the SUNS® WAW-1000 was used to execute the edgewise compression. The tests followed ASTM C364/C364M-16 [4]. All the tests were executed under RTD condition (Room Temperature Dry: 21 ± 5.5 °C, Moisture absorption is as manufacturing status). Specimens were positioned on flat as shown in Fig. 7. Two steel fixtures were positioned on both ends of the specimens. As is shown in Fig. 8, five points on each facesheet were selected to measure the strain, in order to compare the deformation happening on the facesheets.

2.3 Failure Modes

When the specimen was subjected to edgewise compression, the damage process occurred at the end of laminate, core, and the interface of laminate and core. Table 2 lists the existing failure modes and occurrences. Figure 9 presents the classic picture of each failure mode.



Fig. 7 Edgewise compression test for honeycomb sandwich panel

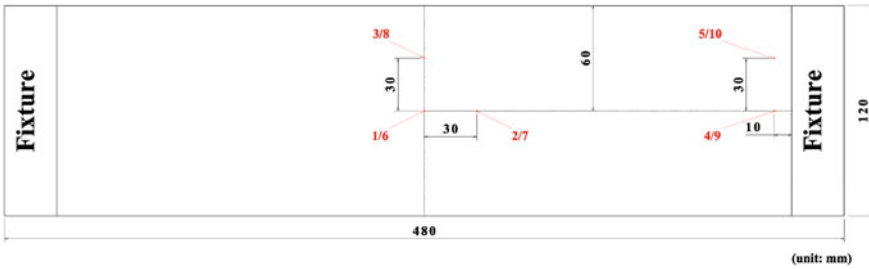


Fig. 8 Positions of strain gauges (channel 1/2/3/4/5 on one side; channel 6/7/8/9/10 on the other side)

Table 2 The existing failure modes and occurrence

Failure mode	Occurrence (no.)
Core shear failure	16
Buckling	10
Facesheet compression failure	7
End failure	7

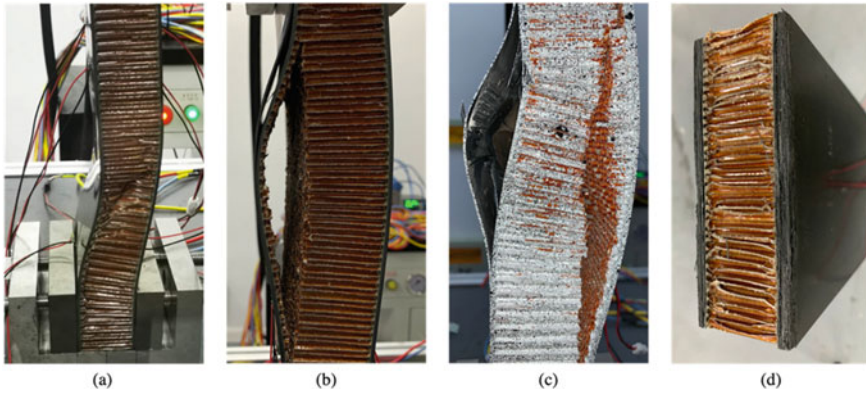


Fig. 9 The classic picture of each failure mode occurred: **a** core shear failure; **b** buckling; **c** facesheet compression failure; **d** end failure

The most common failure mode in the test is core shear failure, buckling is more often in prefabricated panel-core debonding specimens, and facesheet compression is more often in prefabricated panel layering specimen.

2.4 Test Results

The load–displacement curves for seven test groups are shown in Fig. 10. Each group selected one representative specimen.

As is shown in Fig. 11, for prefabricated panel layering group, the ultimate loads are smaller than the no defect group, while in panel-core debonding group, the ultimate loads of 20 mm diameters and 40 mm diameters groups are larger than the no defect group as is shown in Fig. 11. It is an interesting phenomenon, which indicates that defects between the laminate and core may not contribute to ultimate load decreasing to some extent. It will be continued in further study.

Strain-load analysis among the whole specimen was performed. Figure 8 shows 10 strain gauges applied on the surface of the laminate. Channel 1, 2, 3, 4, 6 were selected to analyze the influence of the defect size as is shown in Fig. 12. Overall, the curves are linear. Figure 12b–d is among panel layering group. Non-linear part in curves indicates that initial failure happens in some regions of the specimens, which contribute to strain jitter. Figure 12e–g is among panel-core debonding group. These figures are similar to the no defect group, which also indicates that the panel-core debonding has less influence on structural mechanical properties.

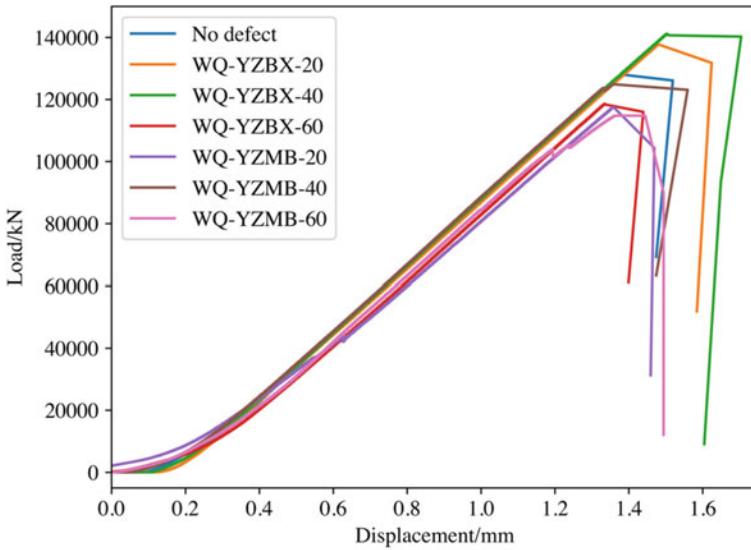


Fig. 10 The load–displacement curves for the test

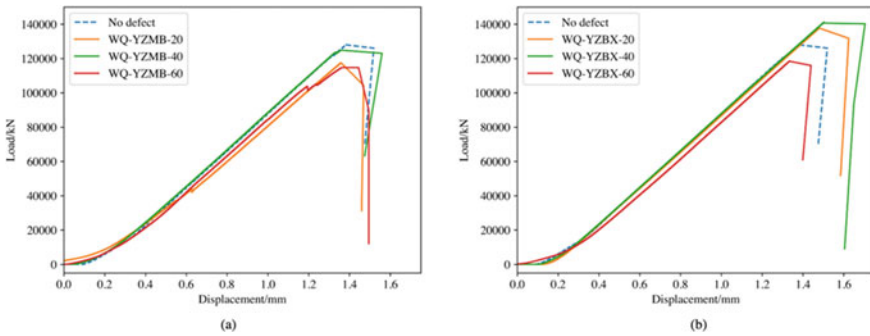


Fig. 11 Comparison of load–displacement curves between different groups. **a** prefabricated panel layering group; **b** panel-core debonding group

3 Finite Element Analyses

The commercial finite element analyses software Abaqus/Explicit® 2019 was used to perform simulations of the edgewise tests. Two kinds of techniques, namely, cohesive zone modeling and the virtual crack closure technique (VCCT) [10–12], were used for numerical delamination simulation. The purpose of these analyses was to compare results from edgewise experiments to finite element models. Abaqus® continuum damage model (ACDM) and Modified cohesive zone model (CZM) were compared in delamination-migration simulation [8]. The prefabricated defect size

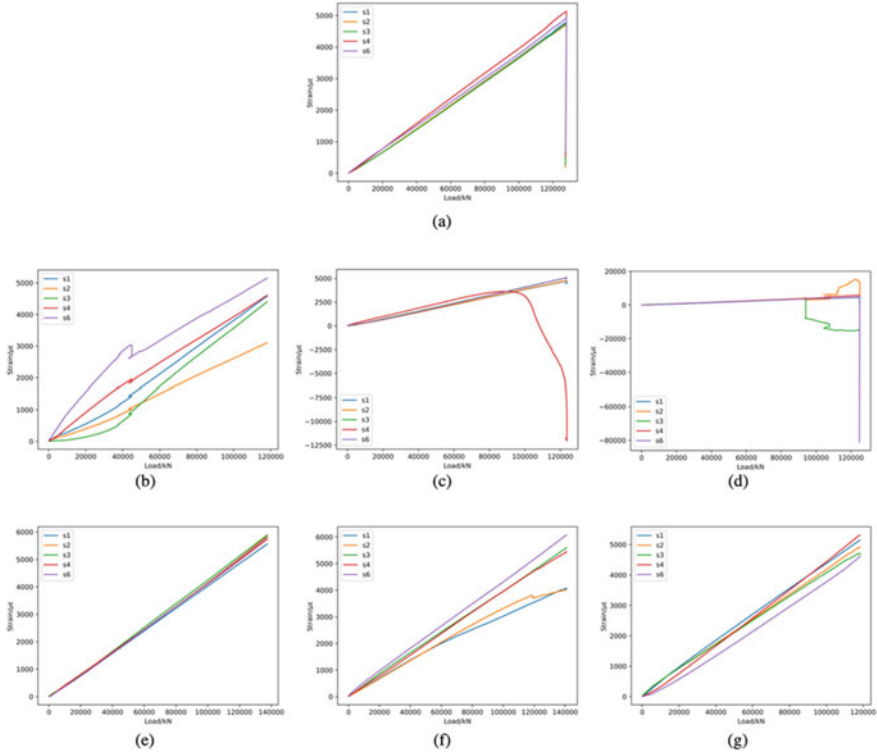


Fig. 12 The curves of strain-load. **a** No defect; **b** Prefabricated 20 mm panel layering; **c** Prefabricated 40 mm panel layering; **d** Prefabricated 60 mm panel layering; **e** Prefabricated 20 mm panel-core debonding; **f** Prefabricated 40 mm panel-core debonding; **g** Prefabricated 60 mm panel-core debonding

varied to investigate the relationship between defect size and ultimate load. Since the study focus was on the laminate, the core and adhesive layering were neglected, the whole model was designed based on laminate.

Continuum shell element was used, and the basic material and strength properties used in analyses are listed in Table 3.

Table 3 Material and strength properties for laminate (ZT7H/5429)

Property	Value	Units	Description
E_{11}	136.00	GPa	Elastic modulus
$E_{22} = E_{33}$	9.12	GPa	
$G_{12} = G_{13}$	5.27	GPa	
G_{23}	3.37	GPa	
ν_{12}	0.31	–	Poisson’s ratio
ρ	1.40	g/cm ³	Density

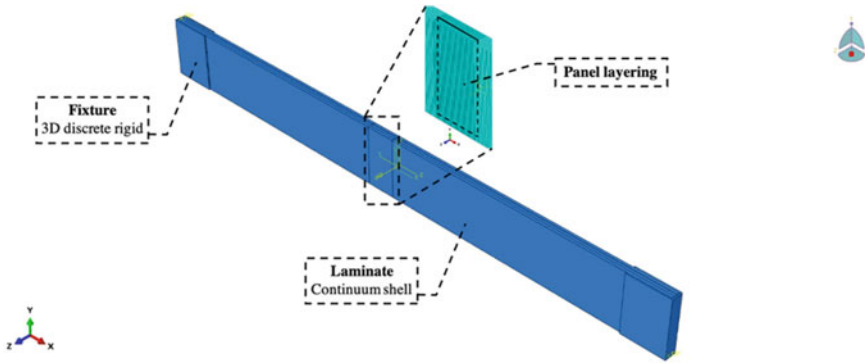


Fig. 13 Finite element model overview (Abaqus screenshot)

As is shown in Fig. 13, a 20 mm × 2 mm × 0.3 mm laminate model was constructed with 3 plies [0/90/0] and rectangular panel layering in the interface of the second and third ply (ply stack direction: +Z). Fixtures were positioned on both ends of the model, using 3D discrete rigid element. The global element size is 0.05 mm. In order to get more accurate result in panel layering part, the part element size is 0.025 mm.

The general interaction of the whole model is no-friction contact, and the general interaction between plies is tie. As is shown in Fig. 14, no-friction contact remains between the interface of the panel layering to simulate the prefabricated defect.

3.1 Comparison of CZM and ACDM

3.1.1 CZM Model

Figure 14a highlights the different but important interaction settings of CZM. A possible damage path was prescribed as highlighted in red line using cohesive zone. As the surfaces start separating from each other, the connectivity stiffness decreases linearly. When the connectivity traction becomes zero, the separation reaches a displacement level, and the surfaces are completely unattached [13]. For damage initiation, a quadratic traction criterion was used to allow for mode mixity and is defined in Eq. (1) [8], where t indicates the normal (n) and in-plane orthogonal shear stress components (s, t).

$$\left\{ \frac{t_n}{Y^T} \right\}^2 + \left\{ \frac{t_s}{S^{12}} \right\}^2 + \left\{ \frac{t_t}{S^{12}} \right\}^2 = 1 \tag{1}$$

The mixed mode critical energy release rate G_c is determined using linear softening in an energy-based Benzeggagh–Kenane (BK) law. Equation (2) shows the basic formulation of BK law:

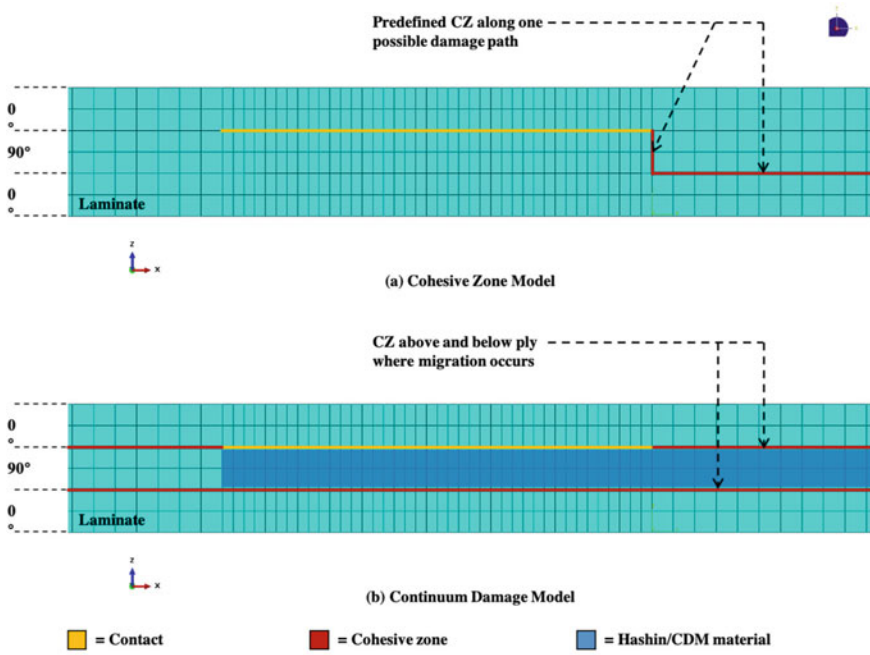


Fig. 14 Laminate damage model detailed besides the panel layering position

$$G_c = G_{IC} + (G_{IIC} - G_{IC}) \left(\frac{G_{II} + G_{III}}{G_I + G_{II} + G_{III}} \right)^\eta \tag{2}$$

where G_I , Mode I energy release rate; G_{II} , Mode II energy release rate; G_{III} , Mode III energy release rate.

Mcelroy et al. [8] simplified Eq. (2), neglecting G_{III} , then the BK law becomes to be

$$G_c = G_{IC} + (G_{IIC} - G_{IC}) \left(\frac{G_{II}}{G_I + G_{II}} \right)^\eta \tag{3}$$

G_I, G_{II} are determined as part of the analysis solution.

The values for these cohesive properties are listed in Table 4.

3.1.2 ACDM Model

Figure 14b highlights the possible damage zone in blue. CDM material stiffness degradation method [14], along with Hashin damage initiation were applied in this zone. The upper and lower boundary of the zone was prescribed as highlighted in red

Table 4 Values for cohesive properties

Property	Value	Units	Description
G_{IC}	0.277	kJ/m ²	Mode I critical energy release rate
G_{IIC}	0.788	kJ/m ²	Mode II critical energy release rate
η	1.634	–	Benzeggagh–Kenane (BK) law exponent
ν	2E-4	–	Viscosity coefficient

Table 5 Values for Hashin damage properties

Property	Value	Units	Description
X^T	2344.00	MPa	Lamina longitudinal tensile strength
X^C	1404.64	MPa	Lamina longitudinal compressive strength
Y^T	76.53	MPa	Lamina transverse tensile strength
Y^C	172.79	MPa	Lamina transverse compressive strength
S^{12}	97.70	MPa	Lamina shear strength

line using cohesive zone (the same as the cohesive property in CZM model). Except this zone, most of the laminates in ACDM used elastic material. The elasticity matrix is shown in Eq. (4) [8]

$$C = \begin{bmatrix} (1 - d_f)E_1 & (1 - d_f)(1 - d_m)v_{12}E_1 & 0 \\ (1 - d_f)v_{12}E_1 & (1 - d_m)E_2 & 0 \\ 0 & 0 & (1 - d_s)GD \end{bmatrix} \quad (4)$$

where $D = 1 - (1 - d_f)(1 - d_m)v_{12}v_{21}$.

The stiffness is reduced by increasing the parameters d_m and d_f . d_m relates to matrix damage and d_f relates to fiber damage. As damage increases, these two parameters increase from zero to 1.0 (maximum value) (Table 5).

0.1 mm displacement load in $-x$ direction was applied to these two models, and the fixed bearing condition was applied on the other end. The displacement cloud figure is shown in Fig. 15.

Under edgewise loading, buckling becomes main failure mode for laminate. In CZM model, the buckling occurred almost in the half of the model which is near the punch, while in ACDM model, the buckling occurred throughout the whole model. In detail, the delamination occurred through the predefined line in CZM model, and relative slip existed among three plies in ACDM model. The x -direction strain of center point of the third ply was selected to investigate the deformation level, along with the load and displacement of loading point, as is shown in Fig. 16.

From Fig. 16a, the ultimate load of ACDM model is greater than CZM. From Fig. 16b, the strain of CZM is greater than ACDM. It can be concluded that the CZM model has a greater influence in structural integrity, and deviation in ultimate load simulation, though CZM provides a more realistic visualization model.

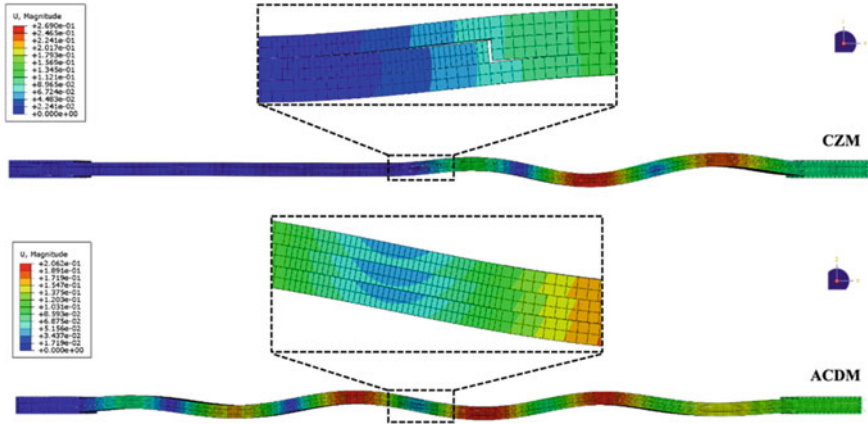


Fig. 15 The cloud figures for the results of ACDM and CZM models in detail

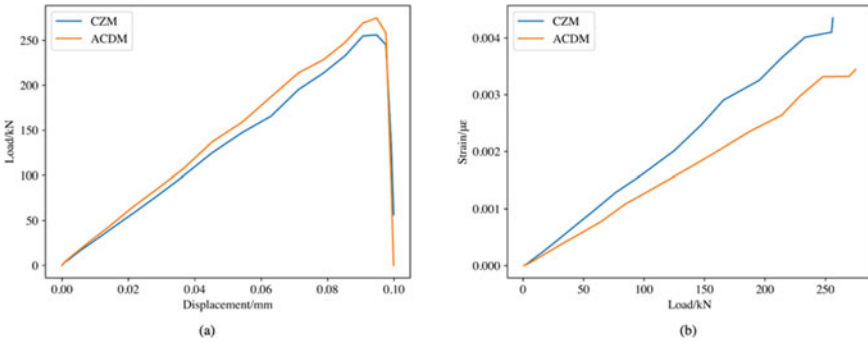


Fig. 16 a The curve of load–displacement; b The curve of strain-load

3.2 The Size of the Prefabricated Defects

Since the whole model to be tested varies in defect size, the relationship between the size of the defect and the delamination, the ultimate load was investigated, which provided a solution for damage tolerance prediction.

In this part, ACDM damage model was used since the CZM model limits the delamination path. Figure 17 shows the position and different sizes of defects.

The load–displacement curves for different defect sizes are shown in Fig. 18. As the size becomes larger, the ultimate load decreases. It indicates that the defect size does influence the structural mechanical properties, especially when the defect is in laminate.

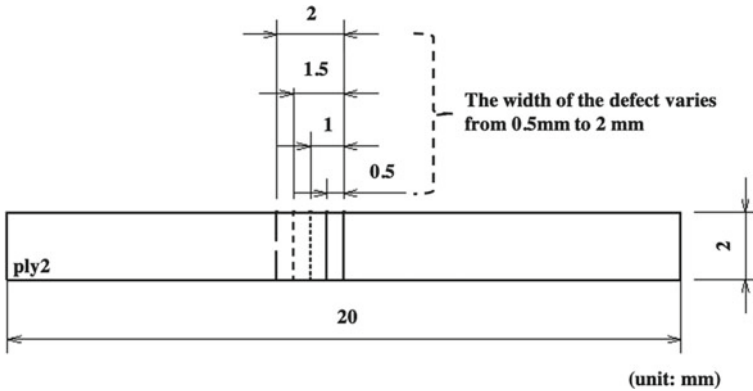


Fig. 17 Diagram for different kinds of prefabricated defects (upper face of ply2)

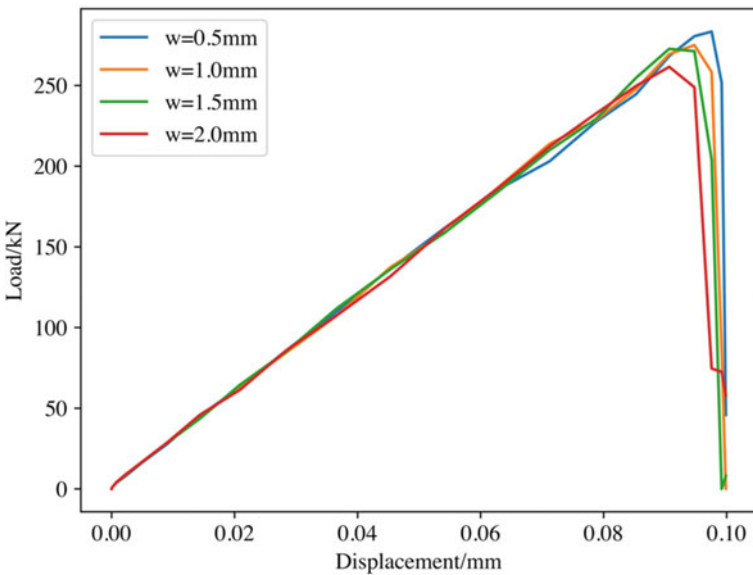


Fig. 18 The load–displacement curves for FEA

4 Conclusion

The whole study was performed using experiment and FEA method. The focus was on the influence of prefabricated defects under edgewise compression applied to honeycomb sandwich structures.

In the experiment section, two types of defects were compared. The results showed that panel layering defect has greater influence on structural mechanical properties than panel-core debonding.

In FEA section, two strength models were introduced and compared. CZM model is more accurate to simulate the delamination when the experiment has been performed. ACDM model has its great performance in delamination–migration prediction. ACDM model was used to study the influence of defect size on structural mechanical properties.

In panel layering group in experiment and varied defect size FEA, load–displacement and strain–stress curves were compared. It can be concluded that, as the size becoming larger, the ultimate load decreases, and the defect size influences the structural mechanical properties, especially when the defect is in laminate.

References

1. Liu XL, Wang BQT (1984) Basics of composite material mechanics. China Construction Industry Press
2. Tomblin JS, Raju KS, Acosta JF (2002) Impact damage characterization and damage tolerance of composite sandwich airframe structures—phase II
3. Administration FA (2004) Bonded repair of aircraft composite sandwich structures
4. ASTM I (2016) ASTM C364/C364M-16, standard test method for edgewise compressive strength of sandwich constructions. West Conshohocken, PA. <http://www.astm.org/cgi-bin/resolver.cgi?C364C364M>
5. Fleck NA, Sridhar I (2002) End compression of sandwich columns. *Compos Part A Appl Sci Manuf*
6. Mamalis AG, Manolacos DE, Ioannidis MB, Papapostolou DP (2005) On the crushing response of composite sandwich panels subjected to edgewise compression: experimental. *Compos Struct* 71(2):246–257
7. Lei H, Yao K, Wen W, Zhou H, Fang D (2016) Experimental and numerical investigation on the crushing behavior of sandwich composite under edgewise compression loading. *Compos Part B* 94(June):34–44
8. Mcelroy M, Leone F, Ratcliffe J, Czabaj M, Yuan FG (2015) Simulation of delamination-migration and core crushing in a CFRP sandwich structure. *Compos A Appl Sci Manuf* 79:192–202
9. Guo X, Guan ZD, Qiu C, Li ZS (2018) Flexural performance of scarf repaired honeycomb sandwich structures. *J Beijing Univ Aeronaut Astronaut* 44(7)
10. Rybicki EF, Kanninen MF (1977) A Finite Element Calculation of Stress Intensity Factors by a Modified Crack Closure Integral. *Eng Fract Mech* 9(4):931–938
11. Rybicki EF, Hernandez TD, Deibler JE, Knight RC, Vinson SS (1987) Mode I and Mixed Mode Energy Release Rate Values for Delamination of Graphite/Epoxy Test Specimens. *J Compos Mater* 21(2):105–123. <https://doi.org/10.1177/002199838702100202>
12. Krueger R (2004) Virtual crack closure technique: history, approach, and applications. *Appl Mech Rev* 57(1)
13. Turon AD, Dávila CG, Camanho PP, Costa J (2007) An engineering solution for mesh size effects in the simulation of delamination using cohesive zone models. *Eng Fract Mech* 74(10):1665–1682
14. Lapczyk I, Hurtado JA (2007) Progressive damage modeling in fiber-reinforced materials. *Compos A Appl Sci Manuf* 38(11):2333–2341

The Assessment of the Prospects of Composite Materials Manufactured by Vacuum Infusion (VaRTM)



A. E. Protsenko, B. B. Safoklov , V. V. Petrov, and O. S. Dolgov

Abstract This paper discusses the data of studies of the strength properties of sandwich panels manufactured by vacuum infusion (VaRTM) and contact molding (CM). In order to assess the prospects of composite products manufactured by vacuum infusion (VaRTM), in comparison with composites obtained by contact molding (CM), in terms of strength and production time, we carried out thermogravimetric studies, studies of the microstructure of the binder on a scanning electron microscope of samples made by the above methods, and study of the VaRTM sample using a high-energy X-ray computational tomograph (VT-600XA).

Keywords PCM · Vacuum infusion · Strength · Electron microscopy · Thermal analysis · X-ray analysis

1 Introduction

In the design of modern aircraft [1] (interior, antenna array fairings, wing fairings, and fuselage), PCM products are widely used, in particular, three-layer honeycomb panels and sandwich panels.

The object of our research is a sandwich panel [2, 3] made of fiberglass corrugated element with shaping trapezoidal PVC foam inserts. Composite material, made of four sheets of fiberglass, was used as the cladding of the structure. In the case of VaRTM [4] sandwich panels, the middle layer and both skins were formed in one process step [5–7]. Using the contact molding method, a middle layer was first produced, onto which the skin was alternately molded.

A. E. Protsenko · V. V. Petrov
Komsomolsk-Na-Amure State University, Komsomolsk-na-Amure, Russia

B. B. Safoklov (✉) · O. S. Dolgov
Moscow Aviation Institute (National Research University), Moscow, Russia
e-mail: safoklovbb@mai.ru

2 Research Materials and Methods

The research was carried out on sandwich panels with a corrugated composite material element and foam shaping inserts in the middle layer (see Fig. 1).

The corrugated element is made of composite material based on glass fabric St-62004, upper and lower cladding of glass fabric T-11, and non-accelerated epoxy vinyl ester binder Dion 9300 FR (Reich Hold).

The middle layer is a three-layer composite material with a zero angle of reinforcement. Skins are made of four layers of fiberglass with reinforcement angles $0/+45/-45/0$. The trapezoidal shaping inserts are made of 40 mm Divinycell H35 PVC foam.

Sandwich panels were manufactured in two ways. Some of the sandwich constructions were made by the non-autoclave method (VaRTM) using a vacuum and infusion unit SVI-20-43 (MSH Techno). Another part of the samples was made by contact molding.

In both cases, reference samples were made for assessing the properties of composite material. Samples were made from twenty layers of glass cloth with a zero angle of reinforcement.

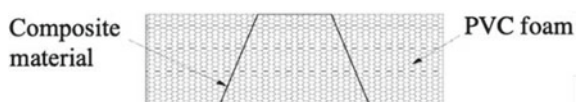
The binder was made from four components according to the following recipe: 100 mass, including Dion 9300 FR, catalyst NORPOL 9802—3 pbw, peroxide NORPOL No. 11—2 pbw, and NORPOL 9854 inhibitor—0.01 pbw. The gelation time during which it is possible under normal conditions to process the mixture is in the range of 120–150 min.

In the case of using VaRTM technology for producing composite materials, curing was carried out in vacuum (0.01 MPa) at room temperature. Holding under vacuum, for additional curing and reducing the likelihood of warpage of the samples, was carried out for 6 h. Holding the product at room temperature in order to achieve complete polymerization of the samples was carried out for ten days. Subsequently, the samples were subjected to heat treatment at 80 °C for 4 h [8].

The obtained samples of sandwich panels were tested for three-point bending in order to determine the ultimate bearing load. Test results were obtained on an Instron 3382 testing machine. The size of the test piece was (410 × 140 × 40) mm. For the tests, supports with a radius of 20 mm were used, installed at a distance of 345 mm from each other. The radius of the knife was also 20 mm. The load was applied to the corrugated composite material elements. The load application rate was 10 mm/min.

The samples were tested for three-point bending in accordance with GOST R 56,810–2015.

Fig. 1 Sample of the middle layer



During determining the hardness, the Brinell method was used. The sample size was $60 \times 60 \times 10$ mm. The test was carried out with a load of 9810 N. The diameter of the loaded steel ball was 10 mm. Tensile strength was determined according to GOST 32,656–2014.

The structure of the sample was studied using a Hitachi S-3400N scanning electron microscope equipped with an electron gun with a tungsten cathode. The measurements were carried out at an accelerating voltage of 3 kV using a secondary electron detector (SE). The study of the structure of the matrix material was carried out at the macro- and meso-levels during delamination of a corrugated composite material element.

The thermogravimetric method was used to establish the matrix-filler ratio in the composite [9]. The samples were analyzed using an STA 409 PC Luxx NETZSCH instrument. The study of the samples was carried out in the air with heating at a rate of $10 \text{ }^\circ\text{C}/\text{min}$ to $600 \text{ }^\circ\text{C}$ in corundum ceramic crucibles.

The VaRTM sample was scanned using a high-energy X-ray computational tomograph (VT-600XA) (cross-sectional relative density characteristics) [10].

3 Results and Discussion

The strength of panels based on sandwich constructions is determined by the strength of all composite materials elements and the quality of the adhesive bonding of foam inserts with composite materials. Table 1 presents the data of strength tests of the witness samples of composite materials.

Composite materials based on Norpol Dion 9300 FR epoxy vinyl ester binder and E-glass linen fabric made by contact molding are significantly inferior in strength characteristics to similar material obtained by the VaRTM method. The static bending tensile strength of VaRTM composite material is 26% higher. In order to identify the reasons for the difference, the samples of materials were examined using the methods of thermal analysis and microscopy.

Thermogravimetric research (see Fig. 2) indicates a significant difference in the matrix/filler ratio in composite materials samples.

When using the VaRTM method, the proportion of the matrix was 28.9%. This is due to the fact that contact molding does not provide sufficient molding pressure, which leads to an increase in the proportion of the binder in the composite material

Table 1 Physical and mechanical properties of PCM

Sample	Hardness (HB)	Bend (σ), MPa	Elongation (σ_p), MPa	Density (ρ) (kg/m ³)
Contact molding method	42	659	635	1613
VaRTM	48	831	829	1934

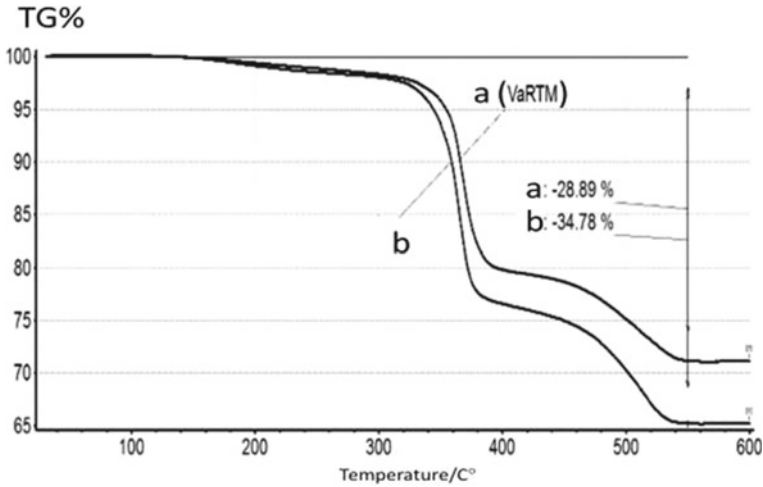
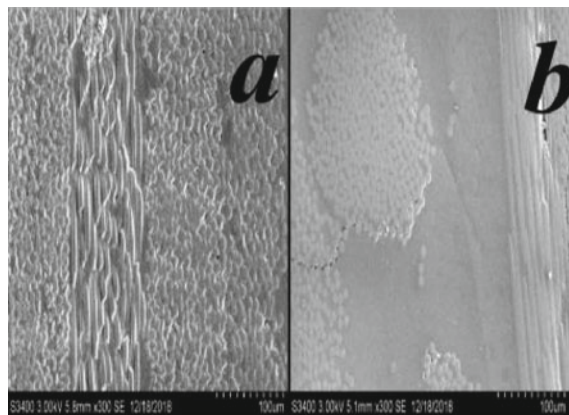


Fig. 2 Thermogravigram of composites obtained by methods **a**-VaRTM and **b**-contact molding

to 34.8%. In turn, this leads to a difference in the density of the obtained samples. Thus, the density of samples obtained by the method of contact molding is 20% less than that of a sample made by the VaRTM method (Table 1).

Investigation of the microstructure of the binder on a scanning electron microscope (see Fig. 3) indicates the presence in the samples obtained by contact molding of a significant number of pores with a diameter of 200–400 μm and reaching 1 mm in length. The packing density of fibers in composite materials differs significantly. In the sample obtained by the VaRTM method, the areas between the fibers, filled with the matrix, are from 10 to 40 μm , while when using the contact molding method, the packing density is much lower and individual fibers can be distinguished in the images. Areas filled with matrix material reach 200 μm .

Fig. 3 Structures of composites obtained by methods: **a**-VaRTM ($\times 300$), **b**-contact molding ($\times 300$)



Tomographic scanning showed that the spread in the values of the relative density (RMS) of the VaRTM sample is 9.1–9.7%. Density characteristics along the sample height are stable. Some leaks are observed, comparable to the thickness of the monolayer (0.01–0.03 mm) (Fig. 4).

In the photographs of Fig. 5, samples made by the contact molding method, an adhesive layer is observed that separates the fiberglass of the corrugated element the skin. On VaRTM samples, the corrugated element and skin form a single monolithic material with a minimum pore content.

The test results of sandwich panels are shown in Table 2.

Figure 6 shows the location of the destruction of the sandwich panels.

Determination of the ultimate bearing load—In both cases, destruction occurs almost at the place of the adhesive joint of foam and composite materials, followed

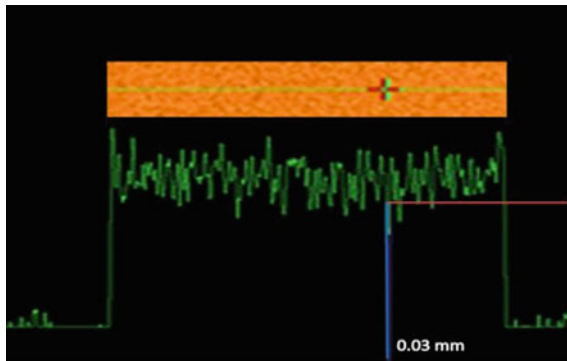


Fig. 4 Histogram of material looseness distribution along the selected section of the composite

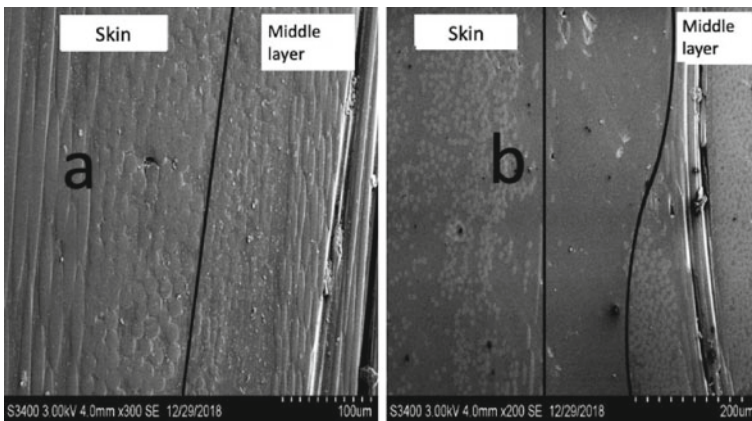
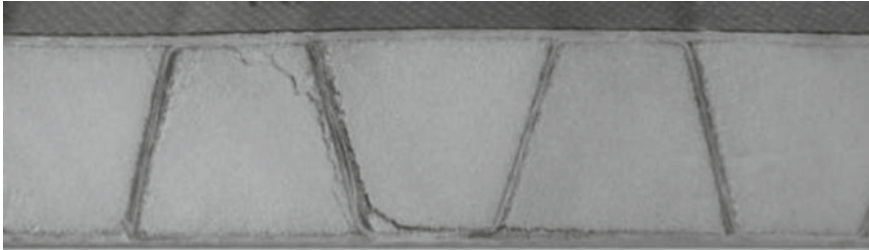


Fig. 5 The contact area of structural elements of the plane integral design obtained by **a**-VaRTM ($\times 300$), **b**-contact molding ($\times 200$)

Table 2 Test results of sandwich panels

Sample	Ultimate strength, MPa	Manufacturing time, h
Contact molding method	4939	20–25
VaRTM	5584	4–6

**Fig. 6** Sample of a sandwich panel after a three-point bending test

by the separation of the foam insert from the laminate. A denser packing of the reinforcing material in composite material obtained by the VaRTM method contributes to an increase in its strength and a more uniform distribution of the load on the brittle polymer matrix, which is also confirmed by the results in [11]. In this case, large unreinforced areas of the matrix between the threads and the layers of glass fabric in the material obtained by contact molding are more prone to destruction areas.

In the process of research, the work time spent on the manufacture of a sample of the sandwich panel 2 m long and 1 m wide was recorded. When using VaRTM, the preparatory operations are carried out once, and despite the fact that in this case the most labor-intensive operation is laying out and sealing the vacuum bag, this method is five times more effective. Also, the undoubted advantage of the vacuum infusion method is that the working personnel does not come into contact with the binder in the process of making the composite, but only at the moment of its mixing.

4 Conclusions

Thus, the results obtained indicate the prospects for the manufacture of sandwich panels in one technological step using the VaRTM method. This technique is especially effective for large-sized products due to the duration of the manufacture of such structures.

In the manufacture of complex structures from polymer composite materials, gluing with additional overlapping bearing layers and fastening with metal plates with bolted joints are often used to connect individual parts. Moreover, these operations lead to an increase in weight and a decrease in radio transparency and the strength of the structure as a whole.

The use of the VaRTM method makes it possible to manufacture large-sized structures in one technological transition directly to size. At the same time, the integrity and solidity of all structural elements are ensured with a simultaneous significant increase in their physical and mechanical characteristics.

References

1. Dolgov OS, Safoklov BB, Aruvelli S (2021) Airdrop of discharged batteries using an unmanned aerial vehicle as a method of increasing the range of an electric aircraft by reducing the mass in flight. *J Aeronaut, Astronaut Aviat* 53(2):235–239
2. Birman V, Kardomateas GA (2018) Review of current trends in research and applications of sandwich structures. *Compos Part B* 142:221–240
3. Zhang F, Liu W, Zhang F (2018) Experimental study on composite sandwich beams with longitudinal GFRP webs. *IOP Conf Ser Mater Sci Eng* T.394(3):032104.6
4. Ding A, Wang J, Ni A, Li S (2018) Compos ageing of sandwich composites with E-glass fibre/vinylester skins and PVC foam core in synergistic environmental agents. *Structure* 202:253–260
5. Taghizadeh SA, Farrokhbadi A, Liaghat GH, et al (2019) Characterization of compressive behavior of PVC foam infilled composite sandwich panels with different corrugated core shapes. *Thin-Walled Struct* 135:160–172
6. Strelets DY, Serebryansky SA, Shkurin M (2019) VA digital approach to aircraft product lifecycle management. In: Twelfth international conference management of large-scale system development (MLSD), pp 1–5
7. Strelets DY, Serebryansky SA, Shkurin MV (2020) Concept of creation of a digital twin in the uniform information environment of product life cycle. In: 2020 13th international conference management of large-scale system development (MLSD), pp 1–4. <https://doi.org/10.1109/MLSD49919.2020.9247749>
8. Protsenko AE, Malysheva DP, Petrov VV (2018) Investigation of the influence of heat treatment on the strength of FGRP used in sandwich constructions. *Key Eng Mater* 773:72–76
9. Friedman HL (1964) Kinetics of thermal degradation of char-forming plastics from thermogravimetry. Application to a phenolic plastic. *J Polym Sci Part C Polym Symp* T.6(1):183–195
10. Safoklov BB., Dolgov OS (2021) Anti/de-icing fluid quality management as an ob-ject to provide safe aircraft takeoff. *J Aeronaut, Astronaut Aviat* 53(2):227–234
11. Protsenko AE, Malysheva DP, Petrov VV (2018) Investigation of the influence of heat treatment on the strength of sandwich structures. *Mater Sci Forum* 926:51–56

Routing Optimization Study for LEO Satellite Networks Using the Hybrid GA-SA Algorithm



Yuxiao Duan, Shufan Wu, Yixin Huang, and Zhongcheng Mu

Abstract With the rapid development of the mega-constellation networks based on the low earth orbit satellites, the shortest path issues in complex networks have gained more and more attention. In this paper, a shortest route solving algorithm based on the hybrid genetic algorithm-simulated annealing algorithm (GA-SA) is proposed. Experimental results show that the proposed hybrid GA-SA method is superior to the single traditional genetic algorithm or simulated annealing algorithm in the computation accuracy while discovering the shortest path between any satellite nodes of different types of topological networks. The new algorithm presents a faster convergence rate and higher accuracy in the simulation of large LEO satellite networks. The proposed algorithm has an advanced global search capability and universal applicability in mega LEO satellite networks.

Keywords Shortest path · Satellite network · GA-SA · Routing algorithm

1 Introduction

Compared with other communication methods, satellite formation communication mainly has the following advantages: (1) enormous communication capacity and long communication distance, (2) all-weather and all-day global coverage, not subject to any complex geographical conditions between the two points of communication, (3)

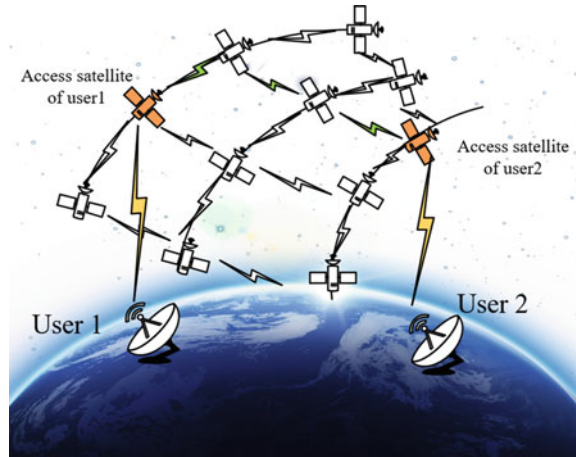
Y. Duan · S. Wu · Y. Huang · Z. Mu (✉)
Shanghai Jiao Tong University, Shanghai, China
e-mail: muzhongcheng@sjtu.edu.cn

Y. Duan
e-mail: duanyx@sjtu.edu.cn

S. Wu
e-mail: shufan.wu@sjtu.edu.cn

Y. Huang
e-mail: huangyxethan@sjtu.edu.cn

Fig. 1 A path connecting two ground users in LEO satellite constellation



unaffected by natural disasters, and (4) high quality and reliability of communication. Therefore, satellite formation networks have a wide range of application prospects.

As illustrated in Fig. 1, we consider the connection between ground users through a LEO satellite constellation. There exist numerous potential routing schemes to deliver data between users through inter-satellite links. Routing schemes with shorter transmission paths can reduce the end-to-end delay and obtain a better quality of service (QoS). Therefore, optimizing the routing choice strategy between a given two nodes in the network plays an important role in addressing the issue of satellite formation communication. Finding inter-satellite links with the shortest communication time can be modeled as a Shortest Path Problem (SPR).

Among the algorithms for solving the SPR problem in satellite communication routing, the classical Dijkstra algorithm [1] and Floyd algorithm [2] are generally accepted at present. However, due to the limitation of time complexity, the search efficiency in solving the SPR problem of large-scale networks is poor. With the deepening of intelligent algorithm research in recent years, some intelligent optimization algorithms have been adopted in satellite communication, such as genetic algorithm [3], ant colony algorithm [4, 5], particle swarm optimization algorithm [6], artificial neural network algorithm [7, 8], and so on.

In 2002, Ahn et al. present the GA approach to solve the SPR problem [3]. In encoding the problem, variable-length chromosomes are used to represent strings and genes to represent parameters. Liu et al. [9] proposed an improved self-adaptive genetic algorithm called DRSP-GA by adjusting the encoding parameters to solve the dynamic stochastic shortest path problem. The final experiment proves that the efficiency of this algorithm is better than the traditional Dijkstra algorithm and A* algorithm in finding the optimal solution when the network changes dynamically. In some application scenarios, it is difficult to determine the weight value in the network path, so Syarif et al. proposed an application of a genetic algorithm in a fuzzy network [10].

A GA-SA hybrid routing algorithm for satellite formation communication is proposed in this paper. The rest of this paper is organized as follows: Sect. 2 models the SPR problem in satellite communication. Section 3 gives a detailed description of the GA algorithm, the SA algorithm, and the hybrid GA-SA algorithm, giving a chromosomal representation of the shortest path problem. Section 4 conducts simulation experiments for satellite formation routing, and the results show that the convergence speed, computational accuracy and precision, and length of routes of GA-SA are better than those of GA algorithm and SA algorithm.

2 Model Description

The satellite formation communication SPR is an NP-hard combinatorial optimization problem. It means that the optimal routing cannot be solved in polynomial time [11]. In this paper, we focus on the case of the undirected graphs model which is commonly adopted in satellite formation.

Generally, the satellite network can be described as $G = (V, E, W_E)$, which is an abstract mathematical object with a set V of n vertices (nodes) and a set E of m edges $\langle i, j \rangle$ (links or arcs). W_E denotes the weight set of the edges. In the SPR problem, the weight set is defined as the inter-sat distance, so solving for the shortest path means finding the one with the minimum sum of weights from the source node to the destination node. Particularly, the source and destination nodes are denoted by S and D , respectively. The connection status between nodes i and j can be represented by a Boolean value x_{ij} , which is 1 when there is a path between the nodes and 0 vice versa. Each edge $\langle i, j \rangle$ has a weight w_{ij} , which is specified by the matrix $W_E = [w_{ij}]$.

The SPR problem can be mathematically represented as the following optimization problem:

$$\begin{aligned}
 \min \quad & \sum_{i=1}^n \sum_{j=1}^n w_{ij} x_{ij} \\
 \text{s.t.} \quad & \sum_{j=1}^n x_{ij} - \sum_{k=1}^n x_{ki} = \begin{cases} 1, & (i = S) \\ 0, & (i = \text{otherwise}) \\ -1, & (i = D) \end{cases} \\
 & x_{ij} = 0 \text{ or } 1 (i, j = 1, 2, \dots, n)
 \end{aligned} \tag{1}$$

In this case, the constraint ensures that the paths satisfying the condition do not pass through the same node between the starting node and the destination node, i.e., there are no loops in the path [3].

3 The Proposed GA-SA Algorithm

As mentioned above, SPR problems are NP-hard, even in the case of only one source node. Hence, a lot of researches have focused on designing efficient heuristic algorithms [12–14]. Among the algorithms to solve the shortest path problem, the genetic algorithm (GA) has been widely studied. GA is proved to be effective for optimal combination and search problems, which can generate abounding feasible solutions by simulating selection, crossover, mutation, inheritance, and other behaviors in nature.

3.1 The Genetic Algorithm

Genetic algorithms (GA) is firstly proposed by Holland [15] in the 1970s. Simple genetic algorithms consist of three basic modules: encoding and decoding, individual fitness assessment, and genetic manipulation, where genetic manipulation includes chromosome duplication, crossover variation, and inversion.

The chromosome is encoded with a positive integer sequence and the obtained original chromosome is an individual in the genetic algorithm. It can be considered as a possible path after decoding. Each locus on the chromosome represents a node in the route graph. Figures 2 and 3 illustrate the encoding and decoding process, where node 1 represents the starting node and node 8 means the destination node. The numbers on the paths indicate the weights, which can also be considered as the length of the paths.

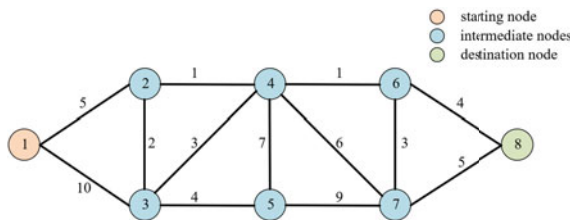


Fig. 2 Example of network topology

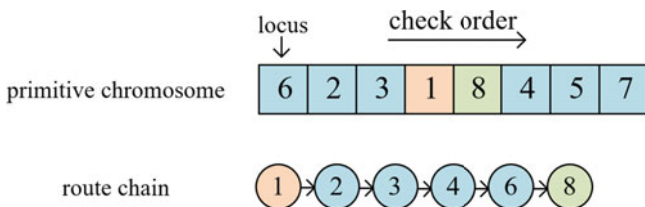


Fig. 3 Decoding of primitive chromosomes

Variable-length chromosomes were used to encode the SPR, which implies that the number of nodes from the start to the end of the different chromosomes is not a constant value. However, the value does not exceed the number of nodes N in the graph. An example of decoding from a topological map using chromosomes is illustrated in Fig. 3. The primitive chromosomes are computer-generated random sequences of integers with non-repetitive loci. The original sequence cannot directly represent a route from the starting node to the destination node and needs to be decoded. The decoding process is as follows: firstly, the starting node needs to be found in the primitive chromosome and used as the starting point in the route chain. Each locus is then checked from left to right to see if there is a pathway to the last node in the route chain, if so, the node is moved to the last point of the path chain, if not, the next locus is checked to see if it can be connected to the route chain. Repeat the above operation until the destination node is connected to the route chain.

Once the route chain is obtained, the value of the fitness function corresponding to that primitive chromosomes can be calculated to evaluate the performance and quality of them. In the SPR problem, the overall weights of the route chain can be used as the fitness function value. Therefore, the fitness function is defined as follows:

$$F_i = \sum_{j=1}^{l_i-1} w_{c_i(j),c_i(j+1)} \tag{2}$$

where F_i represents the fitness value of i -th individual, l_i indicates the length of i -th chromosome, and $w_{c_i(j),c_i(j+1)}$ illustrates the cost between node $c_i(j)$ and $c_i(j + 1)$. The larger the function value is, the longer the length of the route is. The fitness function quantifies the criteria for chromosome performance; the worse a chromosome performs, the lower the probability that its gene will be passed on.

(a) Crossover

In biology, the crossover of homologous chromosomes in individuals is very common. Chromosomes can generate new recombinant chromosomes, which can increase the diversity of the genetic composition of chromosomes and facilitate the selection of offspring that are more adaptable to the environment. Similarly, in GA, the crossover of chromosomes can be used to expand the search range of optimal solutions and thus improve the computational efficiency and accuracy of the algorithm. Figure 4 shows a schematic diagram of the chromosome crossover operation.

Crossover involves the participation of at least two chromosomes. To ensure the invariance of the starting and ending nodes after crossover, these two nodes need to be pruned off first. Then after the crossover is accomplished, the two nodes are inserted at the original position.

As illustrated in Fig. 4, the two chromosomes exchange the genes after the crossover locus. It is possible that duplicate genes appear during the crossover. A simple countermeasure must be taken in this regard: delete the same genes and add the missing nodes. Eventually, recombination is undergone: the start and end nodes are inserted into the original locus to obtain new crossover chromosomes.

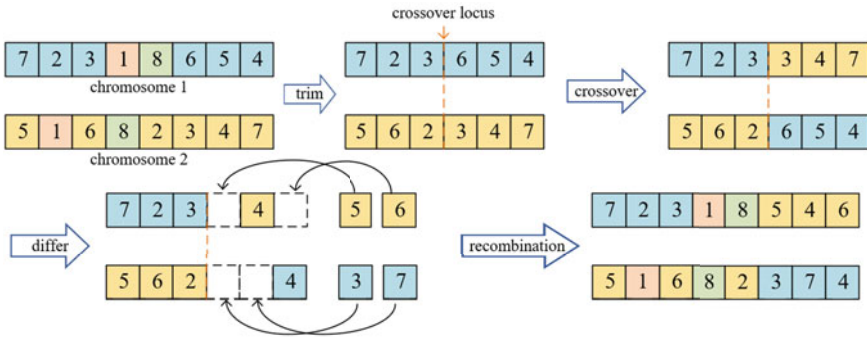


Fig. 4 Schematic diagram of chromosome crossover



Fig. 5 Schematic diagram of chromosome mutation



Fig. 6 Schematic diagram of chromosome inversion

(b) Mutation

Mutations are genetic changes, or flips, that occur on a candidate chromosomes, thereby avoiding the situation of local optima in the process of iteration; Fig. 5 shows the exhaustive process. The number of genes permutation is related to the length of the chromosome, and the mutated chromosome can be considered as a descendant of the original chromosome. First, the mutated locus is randomly selected, and the node corresponding to the locus should not be the starting node and the destination node. Then, the new gene to be mutated is identified. Similar to the crossover operation, node distinction and recombination operation need to be done after the mutation.

(c) Inversion

In addition to crossover and mutation, inversion operation is used for complex problems such as SPR. Inversion is a 180° reversal of the normal order of a region of a chromosome, resulting in a rearrangement of the gene sequence within the chromosome. For shorter chromosomes, the whole chromosome is inverted for simplicity. The inversion operation modifies the decoded route chain of the chromosome, which helps to jump out of the local optimal region and expand the search range. The specific inversion operation is shown in Fig. 6.

3.2 The Simulated Annealing Algorithm

The starting point of the Simulated Annealing (SA) algorithm is based on the similarity of the solid annealing process in physics to the general combinatorial optimization problem. The simulated annealing algorithm starts from a certain high initial temperature, decreases with the temperature, and, in combination with the probabilistic jump property, finds the global optimum of the objective function randomly in the solution space, i.e., the local optimum solution can probabilistically jump out and eventually converge to the global optimum.

The most central part of the simulated annealing algorithm lies in the probabilistic reception of states, which is called the Metropolis-Hastings acceptance criterion:

$$p(\Delta E_i, T_i) = \begin{cases} e^{-\Delta E_i/T_i}, & \Delta E_i > 0 \\ 1, & \Delta E_i < 0 \end{cases} \tag{3}$$

where ΔE_i denotes the difference in internal energy of the state between two temperatures. When the difference is less than 0, it means that the system tends to the equilibrium state and the state is accepted 100%, and when the difference is greater than 0, the state is accepted in a certain state. Algorithm 1 describes a more detailed SA algorithm.

Algorithm 1 Pseudocode for simulated annealing.

Input: initial temperature T_0 , termination temperature: T_f , cooling rate a , maximum iteration i_m

Output: the shortest route and the length

- 1: Generate n random route X_i , initialize temperature T_0 and cooling rate a ;
 - 2:
 - 3: **for** $i=1$ to i_m **do**
 - 4: Create a new solution X'_i , calculate the length of the new route $f(X'_i)$;
 - 5: Compute $\Delta f = \frac{f(X'_i)-f(X_i)}{f(X_i)}$, and decides whether to accept the new route solution based on Metropolis rule:
 - 6: **if** $\Delta f \leq 0$ **then** accept the new route X'_i
 - 7: **end if**
 - 8: **if** $\Delta f > 0$ **then** accept the new route X'_i depending on the acceptance probability function
 - 9: **end if**
 - 10: Update the temperature $T_{i+1} \leftarrow \alpha T_i$ and iteration $i \leftarrow i+1$
 - 11: Sort the paths, the best of which is X_{best}
 - 12: **end for**
 - return** X_{best} ;
-

3.3 The GA-SA Algorithm

However, the simple genetic algorithm has some disadvantages in the process of application, such as (1) the genetic factors (crossover and mutation factors) cannot be changed adaptively with the environment; (2) the results may be affected by the

randomness of the initial population, and if the initial population conditions are poor, it may lead to infeasible solutions such as loops in the path solution [9]; (3) poor convergence of the genetic algorithm in approaching the optimal solution and the premature problem in the suboptimal solution [16]. The SA algorithm, on the other hand, has the features of jumping out of the local optimal region and no strong dependence on the random initial population, which is well suited to make up for the shortcomings of the GA algorithm. Nonetheless, the SA algorithm requires a high initial temperature and a low terminal temperature. It is also very sensitive to the cooling rate. When the cooling rate of the temperature is too fast, it is difficult to acquire a globally optimal solution [17].

In the literature [18], an improved genetic algorithm is adopted in solving the SPR problem by integrating the traditional genetic algorithm with the Dijkstra algorithm and obtains superior solution effects. In this paper, we construct a hybrid algorithm of GA and SA to improve the optimization performance of the algorithm and take advantage of the advantages of each algorithm.

The global search capability of the hybrid algorithm composed of GA algorithm and SA algorithm can be enhanced, so the requirements for the selection of individual parameters in the algorithm are reduced accordingly. When the parameters of the hybrid algorithm are the same as those of the single algorithm, the optimization performance and robustness of the algorithm are greatly improved, and the effect is more significant when the problem size is larger and more complex [17].

The crossover process in the GA algorithm achieves combinatorial optimization and the mutation operation implements random search, while the SA algorithm has a certain probability of jumping out of the local optimal solution and eventually converging to the global optimal. Therefore, theoretically, the GA-SA algorithm can seek the global optimal solution. Algorithm 2 describes a more detailed GA-SA algorithm.

4 Experiments and Discussion

4.1 Experiment Environments Configuration

The topology of satellite communication networks has three main models. Depending on the distance of satellites from the Earth's surface, they are divided into Low Earth Orbit (LEO, 500–2000) satellites, Medium Earth Orbit (MEO, 2000–20000) satellites, and Geostationary Earth Orbit(35768 km) satellites [19]. Among them, LEO satellites, with their relatively low delays, path loss, production, and launch costs, have gradually become a hotspot for research in the fields of satellite broadband Internet and Internet of Things [20, 21].

In this experiment, to validate the effectiveness of the proposed GA-SA algorithm in satellite formation communication, three different numbers of LEO constellations are selected to verify the effectiveness of the algorithm. The specific parameters

Algorithm 2 Pseudocode for GA-SA.

Input: initial temperature T_0 , termination temperature: T_f , cooling rate a , maximum iteration i_m , initial population number: N_{pop} , crossover probability: p_c , mutation probability: p_m , inversion probability: p_i , the length of the Markov chain: L_k

Output: the shortest route and the length

- 1: Generate n random route X_i , initialize temperature T_0 , cooling rate a , and the probability of crossover p_c , mutation p_m and inversion p_f .
- 2: **for** $i = 1$ to i_m **do**
- 3: **for** $l = 1$ to L_k **do**
- 4: **(Crossover)** Randomly select chromosomes for crossover by probability p_c ;
- 5: Compute $\Delta f = \frac{f(X_{i,c}) - f(X_i)}{f(X_i)}$, and decides whether to accept the new route solution based on Metropolis rule;
- 6: **(Mutation)** Randomly select chromosomes for mutation by probability p_m . Create new individual $X_{i,m}$;
- 7: **(Inversion)** Randomly select chromosomes for inverse by probability p_f . Create new individual $X_{i,f}$;
- 8: **if** new individual $X_{i,c}, X_{i,m}, X_{i,f}$ are created **then** go to 10;
- 9: **end if**
- 10: Calculate the difference of fitness function Δf . And decide whether to keep the new individuals according to the Metropolis law;
- 11: Update the temperature $T_{i+1} \leftarrow \alpha T_i$ and iteration $l \leftarrow l + 1$
- 12: Sort the routes, the best of which is X_{best}
- 13: **end for**
- 14: $i \leftarrow i + 1$
- 15: **end for**

return X_{best} ;

Table 1 Parameters of satellites constellation

Number of satellites	Number of orbit planes	Satellites per orbit	Orbit altitude (km)
120	15	8	1100
288	24	12	550
512	32	16	550

of the experimental constellation are shown in Table 1. Figure 7 shows a schematic diagram and the topology of the LEO constellation used for the experiment. Each of these nodes represents a satellite, while the lines between the nodes indicate the inter-satellite links (ISLs).

In the simulation of 512 satellites, the main parameters of the algorithm used are shown in Table 2.

4.2 Results and Discussion

To evaluate the performance of the proposed algorithm, three constellations of different sizes were tested separately. Select node 1 as the starting node. It is important

Fig. 7 Schematic diagram of LEO satellites constellation

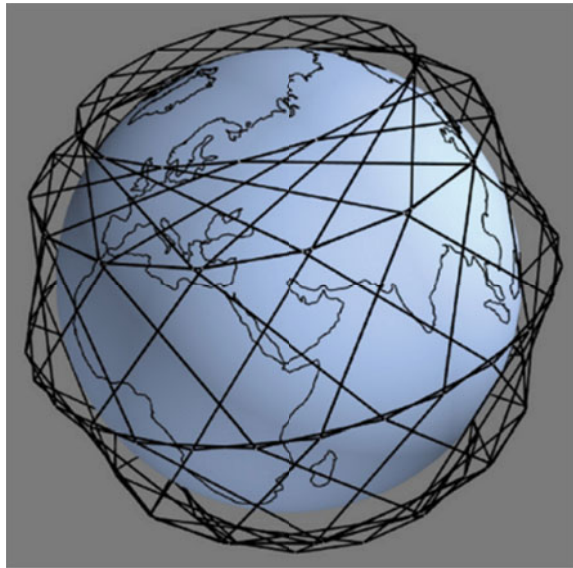


Table 2 Parameters used in the simulation

Parameters	Algorithm		
	GA	SA	GA-SA
Population	300	–	300
Crossover probability	0.85	–	0.85
Mutation probability	0.4	–	0.4
Inverse probability	0.5	–	0.5
Number of iterations	360	–	–
Initial temperature	–	10000	10000
Cooling rate	–	0.95	0.95
Terminal temperature	–	10^{-4}	10^{-4}
Markov chain length	–	20	20

to note that the test path is the longest ‘theoretical shortest path’ in the topology starting from node 1 (i.e., the toughest case starting from node 1). If the algorithm performs well for the toughest case of the constellation, it should also do well in solving the shortest paths between other nodes in this topology. The following table shows the results of running the GA, SA, and GA-SA algorithms in three constellations of different sizes. In Table 3, the optimal path length and the average path length are obtained separately for each constellation using different algorithms. The average path length is the mean of the path lengths obtained after the algorithm is

Table 3 The comparative results of three constellations

Constellation size	Testing size	Algorithm	Optimal route length	Average route length	Theoretically optimal route length
120	1->69	GA	35959.48	35959.48	35959.48
		SA	35859.48	35959.48	
		GA-SA	35959.48	35959.48	
288	1->151	GA	35330.05	36039.20	34543.34
		SA	34543.34	34760.92	
		GA-SA	34543.34	34543.34	
512	1->265	GA	35406.51	39789.52	34667.75
		SA	34767.01	36124.80	
		GA-SA	34667.75	34667.75	

run ten times with random initial values, and this index reflects the probability of the algorithm finding the optimal solution each time. The theoretical optimal path is obtained by the traditional Dijkstra algorithm and is used to compare the accuracy of the results obtained by intelligent algorithms.

As can be seen from Table 3, all three algorithms are successful in finding the global shortest path between two points on a relatively small constellation (120 satellites). When the constellation size becomes larger, with 288 satellites, it is already difficult for the GA algorithm to reach the theoretically optimal solution. The best results in ten simulations are also slightly larger than the global optimal solution. The SA algorithm, meanwhile, can still reach the optimal solution at that constellation, but it does not find the global optimum in every run, and occasionally falls into a local optimum that cannot be jumped out. Further, from the simulation results of the constellation of 512 satellites, only the GA-SA algorithm can obtain the theoretical optimal solution, while neither the GA algorithm nor the SA algorithm can search for the global optimal solution.

Figure 8 shows the shortest paths obtained by the three algorithms for the constellation of 512 satellites with the increasing number of iterations.

It can be seen from Fig. 8 that the GA algorithm has a faster converge rate. However, its convergence value is a local optimal solution, and it eventually fails to reach the globally optimal solution. This reflects the characteristic that the GA algorithm searches fast but tends to converge prematurely. The SA algorithm has a strong search capability and can effectively jump out of the current local optimal solution. Therefore, the search curve of the SA algorithm in the figure is updated frequently and the final convergence value is better than that of the GA algorithm. The proposed GA-SA algorithm, on the other hand, combines the advantages of the above two algorithms, with a wide search range, fast convergence, and jumping out of the local optimal solution. Therefore, the GA-SA algorithm can reach the global optimal solution within a given number of iterations. And it can be seen in Table 3 that the average optimal path length in the simulation of 512 satellite constellations is the same as

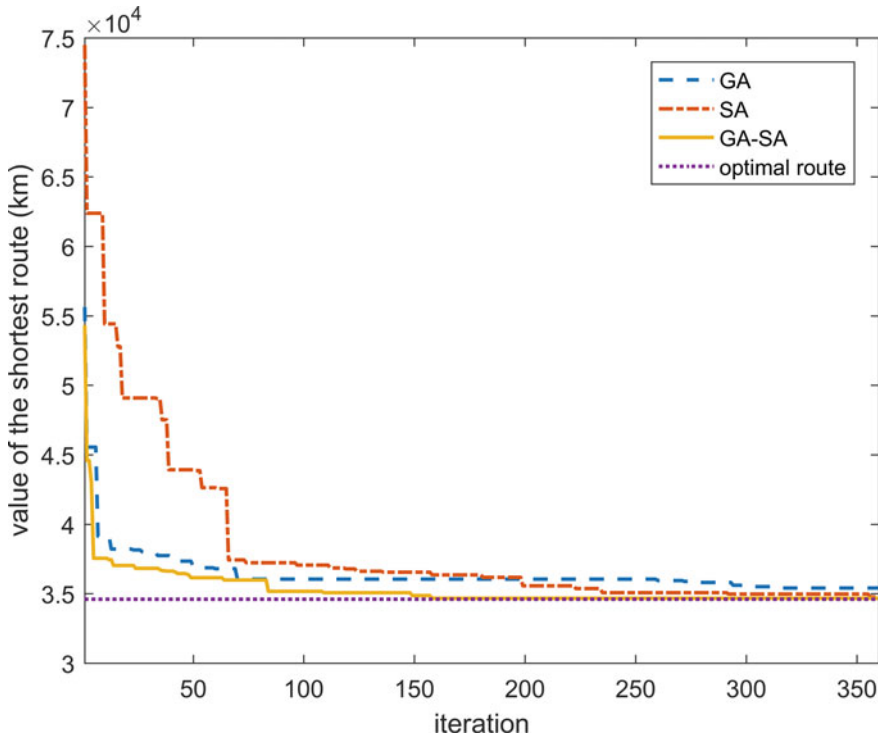


Fig. 8 Comparison of three different algorithms

Table 4 Optimal routes under GA, SA, and GA-SA

Algorithm	Optimal route
GA	1->497->512->511->510->509->493->477->461->445->429->413->397->381->365->349->333->317->301->300->284->268->267->266->265
SA	1->16->15->14->510->509->493->477->461->445->429->413->397->381->365->349->333->317->301->285->269->268->267->266->265
GA-SA	1->2->3->4->5->21->37->53->69->85->101->117->133->149->165->181->197->213->229->245->261->262->263->264->265
Dijkstra	1->2->3->4->5->21->37->53->69->85->101->117->133->149->165->181->197->213->229->245->261->262->263->264->265

the theoretical optimal path length, which means that the accuracy and reliability of the GA-SA algorithm for the shortest path search are also the highest. Table 4 shows the detailed path of the optimal solution under different algorithms.

5 Conclusion

As a typical application domain, the optimal routing discovery algorithm is essential for LEO satellite communication networks. The main contribution of this paper is proposing a hybrid GA-SA algorithm to the satellite routing discovery problem. The objective of this paper is to optimize the routing of the satellite communication network to search for the shortest path between two user access satellites. Since the traditional genetic algorithm is prone to premature, and the simulated annealing algorithm has stronger search capability characteristics, the GA-SA algorithm is proposed in this paper to solve the SPR and optimize the route scheme. Experimental results show that the convergence speed, computational accuracy and precision, and length of routes of GA-SA are better than those of the GA algorithm and SA algorithm. In addition, as the complexity and number of nodes of the network increase, the advantage of the proposed GA-SA becomes more apparent.

References

1. Li X, Li G, Zhang S (2010) Routing space internet based on Dijkstra's Algorithm. In: 2010 second international conference on networks security, wireless communications and trusted computing, vol 2, pp 118–121
2. Wei D (2010) An optimized floyd algorithm for the shortest path problem. *J Netw* 5(12):1496
3. Ahn CW, Ramakrishna RS (2002) A genetic algorithm for shortest path routing problem and the sizing of populations. *IEEE Trans Evol Comput* 6(6):566–579 (2002). <https://doi.org/10.1109/TEVC.2002.804323>. (Conference Name: IEEE Transactions on Evolutionary Computation)
4. Long F, Sun F (2006) An improved ant colony algorithm and its application in routing computation of satellite networks. In: The proceedings of the multiconference on "Computational Engineering in Systems Applications", vol 2, pp 1567–1573. <https://doi.org/10.1109/CESA.2006.4281885>
5. Yang WC, Yao S (2021) A multi-path routing algorithm based on ant colony optimization in satellite network. In: 2021 IEEE 2nd international conference on big data, artificial intelligence and internet of things engineering (ICBAIE), pp 139–144. <https://doi.org/10.1109/ICBAIE52039.2021.9389995>
6. Mohemmed AW, Sahoo NC, Geok TK (2008) Solving shortest path problem using particle swarm optimization. *Appl Soft Comput* 8(4):1643–1653
7. Ali MKM, Kamoun F (1993) Neural networks for shortest path computation and routing in computer networks. *IEEE Trans Neural Netw* 4(6):941–954. <https://doi.org/10.1109/72.286889>. (Conference Name: IEEE Transactions on Neural Networks)
8. Sun W, Liang J, Xiao N, Ding R, Zhang Z (2019) Intelligent routing scheme for SDN satellite network based on neural network 563, 052,087. <https://doi.org/10.1088/1757-899X/563/5/052087>. <http://adsabs.harvard.edu/abs/2019MS%26E..563e2087S>. (Conference Name: Materials Science and Engineering Conference Series)
9. Liu Z, Kong Y, Su B (2016) An improved genetic algorithm based on the shortest path problem. In: 2016 IEEE international conference on information and automation (ICIA), pp 328–332 (2016). <https://doi.org/10.1109/ICInfA.2016.7831845>
10. Hassanzadeh R, Mahdavi I, Mahdavi-Amiri N, Tajdin A (2013) A genetic algorithm for solving fuzzy shortest path problems with mixed fuzzy arc lengths. *Math Comput Model* 57(1–2):84–99
11. Madkour A, Aref WG, Rehman FU, Rahman MA, Basalamah S (2017) A survey of shortest-path algorithms. [arXiv:1705.02044](https://arxiv.org/abs/1705.02044) [cs]

12. Fu L, Sun D, Rilett LR (2006) Heuristic shortest path algorithms for transportation applications: state of the art. *Comput Oper Res* 33(11):3324–3343
13. Polychronopoulos GH, Tsitsiklis JN (1996) Stochastic shortest path problems with recourse. *Networks* 27(2):133–143
14. Chen Xi, Fei Qi, Li Wei: A new shortest path algorithm based on heuristic strategy. In: 2006 6th world congress on intelligent control and automation, vol 1, pp 2531–2536. <https://doi.org/10.1109/WCICA.2006.1712818>
15. Holland JH et al. (1992) *Adaptation in natural and artificial systems: an introductory analysis with applications to biology, control, and artificial intelligence*. MIT Press
16. Application of GA/GA-SA based fuzzy automatic generation control of a multi-area thermal generating system. *Electric Power Syst Res* 70(2):115–127. <https://doi.org/10.1016/j.epsr.2003.11.013>. <https://www.sciencedirect.com/science/article/abs/pii/S0378779603002980>. (Publisher: Elsevier)
17. Yang Z, Xia H, Su F, Zhao J, Feng F (2020) Application of genetic algorithm in modeling of shortest path problem. In: 2020 Chinese automation congress (CAC), pp 3447–3450. <https://doi.org/10.1109/CAC51589.2020.9327269>. ISSN:2688-0938
18. Zhu X, Luo W, Zhu T (2014) An improved genetic algorithm for dynamic shortest path problems. In: 2014 IEEE congress on evolutionary computation (CEC), pp 2093–2100. <https://doi.org/10.1109/CEC.2014.6900496>. ISSN:1941-0026
19. Dong X, Shi H (2008) A shortest path algorithm based on mobile agent in LEO satellite network. In: 2008 4th international conference on wireless communications, networking and mobile computing, pp 1–5. <https://doi.org/10.1109/WiCom.2008.1017>. ISSN:2161-9654
20. Qu Z, Zhang G, Cao H, Xie J (2017) LEO satellite constellation for internet of things. *IEEE Access* 5:18391–18401. <https://doi.org/10.1109/ACCESS.2017.2735988>. (Conference Name: IEEE Access)
21. Su Y, Liu Y, Zhou Y, Yuan J, Cao H, Shi J (2019) Broadband LEO satellite communications: architectures and key technologies. *IEEE Wirel Commun* 26(2):55–61. <https://doi.org/10.1109/MWC.2019.1800299>. (Conference Name: IEEE Wireless Communications)

Siamese U-net with Attention Mechanism for Building Change Detection in High-Resolution Remote Sensing Images



Yiren Song, Zhongliang Jing, and Minzhe Li

Abstract Building change detection in high-resolution remote sensing images is very important for illegal building management and urban supervision. Recently, with the development of neural network and the increase of RS data, there are more and more change detection methods based on deep learning. Most of the existing change detection algorithms based on deep differential feature analysis which detect all semantic changes in two-temporal images, not specifically designed for building change detection and unable to give an accurate mask for building changes area. In this paper, we propose a Siamese U-net with attention mechanism for building change detection in high-resolution bi-temporal remote sensing images. By introducing scene-level building segmentation, we improve the boundary integrity and internal compactness of the final changed building. Our method was applied to WHU dataset and have outstanding building change detection results.

Keywords Change detection · Deep learning · Fully convolutional Siamese network · Remote sensing image processing

1 Introduction

Change detection task is to detect pixels with “semantic change” between two images, which are acquired at different times in the same area. Many factors may cause pixel change, such as the color change of the object, the relative motion of the object [1]. Change detection results should not contain non-semantic changes which we don’t need to pay attention to, such as changes caused by camera moves, sensor noise,

Y. Song · Z. Jing (✉) · M. Li
School of Aeronautic and Aerospace, Shanghai Jiao Tong University, Shanghai, China
e-mail: zljing@sjtu.edu.cn

Y. Song
e-mail: songyiren@sjtu.edu.cn

M. Li
e-mail: liminzhe@sjtu.edu.cn

or light change. Building change detection task is detecting the part of the building change from the two-phase image, not only to judge change or not pixel by pixel, but also give an accurate mask for the changing area.

Previous scholars use the post-category comparison method, they subtract the building segmentation results of the two-phase image directly, limited by the accuracy of building segmentation, change detection accuracy rate will be low and there are lots of messy shapes in change detection result which can't be removed in post-processing stage [2]. Some scholars consider building change detection and building segmentation to be quite different tasks, they abandoned the building extraction process and solved building change detection problems in end-to-end methods based on deep learning, such as U-net [3] and FCN [4]. U-net structures have been frequently used in image-based change detection methods and achieve very representative performance. U-net++ [5] network integrates different sizes of U-net structure into one network, which improves the performance of the network. Fully convolutional neural networks are also widely used in semantic segmentation tasks. It uses convolutional layers to replace all fully connected layers in convolutional neural networks. Their output is spatial maps rather than classification scores.

Change detection and semantic segmentation are very similar which are both pixel-to-pixel prediction tasks and get a category map in the end. But it is not reasonable to concatenate the bi-temporal images and then input them directly into FCNs to get the change area. Some scholars use the Siamese network [6, 7] which has better interpretability to solve the problem. Some scholars have applied the attention mechanism to computer vision tasks and have achieved good results [8]. Zhang proposed a deeply-supervised image fusion network [9] for change detection in high-resolution bi-temporal remote sensing images. To improve boundary completeness and internal compactness of objects in the output change maps, multi-level deep features of raw images are fused with image difference features by means of attention modules for change map reconstruction.

In existing change detection datasets like WHU [10] and CDD [11], compared with the number of unchanged pixels and buildings, changed pixels and buildings are quite small, which will cause sample imbalance problems. What's more, network don't have enough changed buildings with label to train, so It's hard to learn how to give an accurate mask for the changed area. Considering building change detection task and building segmentation task have a lot in common, both of them need to extract the features of the buildings in the image and give segmentation results [12, 13]. Previous scholars have achieved good results on the building segmentation dataset such as Inrial [14] and WHU dataset. In this paper, we use a pretrained building segmentation module to improve the result of change detection result. We propose a Siamese U-net with attention mechanism for change detection in high-resolution bi-temporal remote sensing images. Firstly, the two-temporal images are extracted through the building segmentation module. Then, segmentation results and bi-temporal images are sent to the siamese feature extraction module. Finally, the building change detection result is generated in a differential discrimination network.

The contributions of this paper are:

1. We propose a Siamese U-net with attention mechanism for building change detection task. Introducing scene-level building segmentation improves the accuracy of building change detection.
2. We improve the differential discrimination network with attention mechanism, increase the network's attention to building changes areas, and ignore non-building change areas. The outline of the building edge is clearer, the interior compactness is better, and there are fewer false detections of non-building change areas.
3. We use dilation prediction with parameters to balance the change detection speed and accuracy, improve the model's performance at the edge of the input image.

The remainder of this article is organized as follows. Section 2 illustrates the proposed method, including network architecture and implementation details. Section 3 illustrates the experiment and compares building change detection result with the benchmark methods. Finally, Sect. 4 draws the concluding remarks.

2 Methodology

The proposed network architecture is presented in Sect. 2.1. In Sects. 2.2, 2.3, and 2.4, we present the key network components, building segmentation module, siamese feature extraction module, differential discrimination network with attention mechanism, respectively.

2.1 *The Proposed Siamese U-net with Attention mechanism's Architecture*

The network we proposed has three parts, building segmentation module, siamese feature extraction module, differential discrimination network (DDN) with attention mechanism. Firstly, the two-temporal images are sent to the building segmentation module to get the segmentation result. Then, building segmentation results and bi-temporal images are sent to the Siamese feature extraction module to get different levels of depth features. Finally, DDN will give building change detection results pixel by pixel.

2.2 Building Segmentation Module

This paper focuses on building change detection so that in the building segmentation stage, we use a mature solution, U-net++ to get the result. U-net network is a classic segmentation model and U-net++ improved its performance. U-net++ is a deeply-supervised encoder–decoder network where the encoder and decoder sub-networks are connected through a series of nested, dense skip pathways. U-net++ architecture is shown in Fig. 2, the re-designed skip pathways aim at reducing the semantic gap between the feature maps of the encoder and decoder sub-networks, enabling the shallow features with high fineness to be directly input to the deep layer of the network, which improves the accuracy of the segmentation results.

2.3 Siamese Feature Extraction Module

After the building segmentation stage, we have four images, bi-temporal images and their building segmentation result. How to fuse their information to get building change detection is a problem. We tested a variety of network architecture and fusion methods to find a satisfied solution. Finally, we use U-Net with siamese encoder branch as the backbone network. It's not the first time that U-Net is used as a backbone network in the change detection task. In [15], RS images are input into U-Net through an early-fusion strategy. Benefiting from the excellent performance of U-Net in feature extraction and feature fusion, it achieves good results. U-net can be divided into two parts, downsampling and upsampling. Downsampling can increase the robustness to some small disturbances of the input image such as image translation, rotation, reduce the risk of overfitting, reduce the amount of calculation, and increase the size of the receptive field. The effect of upsampling is to restore and decode the abstract features to the size of the original image, and finally get the segmentation result [16].

In this paper, we add a siamese branch to the U-net's encoder. As shown in Fig. 1, we use early-fusion strategy to fuse each temporal image and its building segmentation result. Specifically, overlay the three-channel remote sensing image and the single-channel building detection results along the channel dimension. After that, the siamese feature extraction module will extract the features of these two four-channel images through four downsamplings. Finally, feature T_{1-4} and feature T_{2-4} are stacked to feature D_0 as the input of differential discrimination network (Fig. 2).

In this section, we use early-fusion strategy to fuse each temporal image's feature and building segmentation result, and use late-fusion strategy to fuse the feature we get after the siamese feature extraction module. Due to the high correlation between remote sensing image and building extraction result, we use early-fusion strategy to keep this correlation from being destroyed. However, early-fusion cause features belonging to different images are mixed together prematurely and difficult to recover,

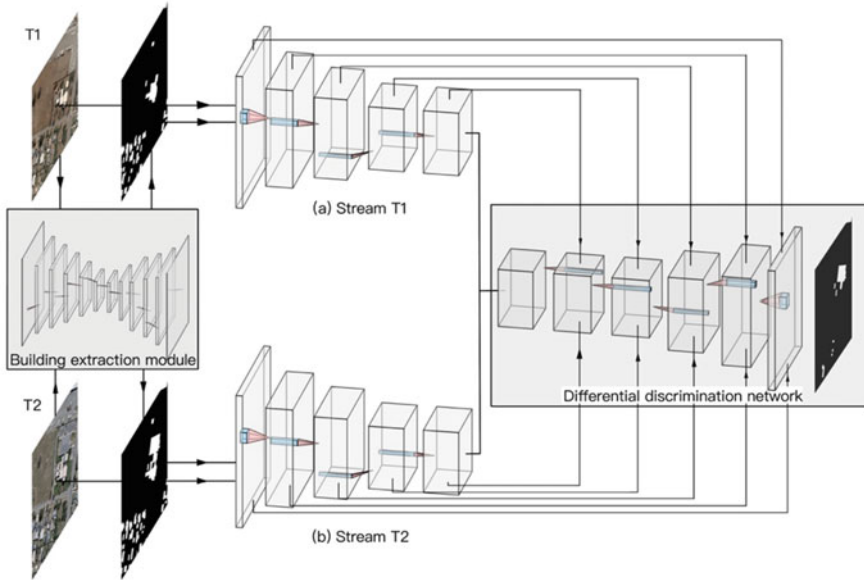


Fig. 1 Network architecture

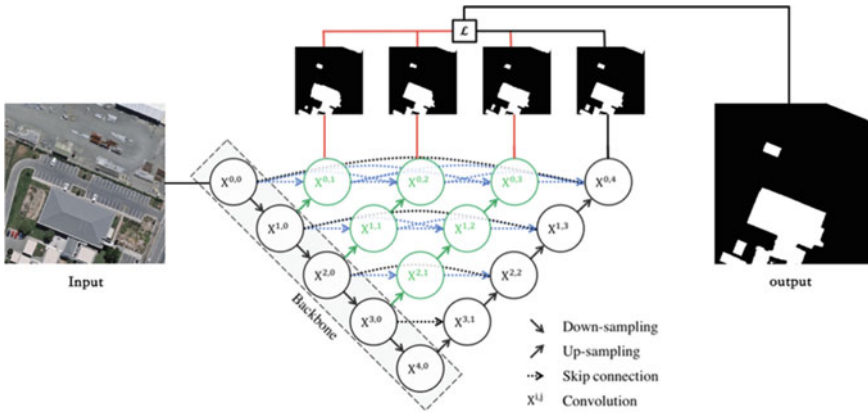


Fig. 2 Building segmentation module architecture

which will cause problem if used for fusing bi-temporal images. Siamese network has better interpretability to solve the problem because, in Siamese network, two branches share the same weights, which means that the methods extracting features of two images are totally the same. The bi-temporal image pairs are generally obtained with the same device and in the same area, which means they have a lot of similarities in feature distribution [17]. So it is reasonable to extract features using the same method.

What's more, parameter sharing reduces the parameters of the feature extraction network by half.

Between siamese feature extraction module and DNN, we use skip connection to pass features to the deep layers of DDN. Shallow features are essential for restoring building outlines and deep features contain more semantic information, which helps DNN to determine whether the building has changed.

2.4 Differential Discrimination Network with Attention Module

In differential discrimination network, we use Siamese feature extraction module's output to judge change or not pixel by pixel and give an accurate mask for the changing area. We used five fully connected layers in differential discrimination network, which is actually very similar to the decoder part of U-net. After multiple downsampling, the high-dimensional features extracted by the Siamese network provide more semantic information which is important to building change detection. However, low-dimensional features passed through the skip connection are critical to maintain the accuracy of the building outline. Actually, If we join the post-processing module to remove isolated changed pixels, the accuracy and F1 score will improve a little. But in order to compare the original performance of the network we proposed, we didn't do this.

CNN is good at extracting features from images, but not all features are useful for building change detection tasks. In building change detection tasks, we hope the neural network will focus on the building area and carefully judge whether the two-phase building part has changed, at the same time ignoring the semantic changes of non-building areas [18]. Therefore, this article uses the attention module to solve this problem. In this paper, we use both position attention module and channel attention module in each fully connected layer of DDN. The position attention module and channel attention module's structure are shown in Fig. 3. In every block of the different discrimination network, giving a feature $A \in R^{C \times H \times W}$, we feed feature A into a convolutional layers to get two new feature maps B and C. Then B and C are reshaped to $R^{C \times H}$. After that we perform a matrix multiplication between the transpose of C and B and then apply a softmax layer to get the spatial attention map $S \in R^{H \times H}$

$$s_{ji} = \frac{\exp(B_i \cdot C_j)}{\sum_{i=1}^N \exp(B_i \cdot C_j)} \quad (1)$$

where i_{ji} measures the i th position's impact on j th position. The more similar the feature representations of the two locations are, the higher the correlation between them. At the same time, we put feature A into the convolutional layer to generate a new feature map $D \in R^{C \times H \times W}$ and reshape it into $R^{C \times H}$. Then we perform a matrix

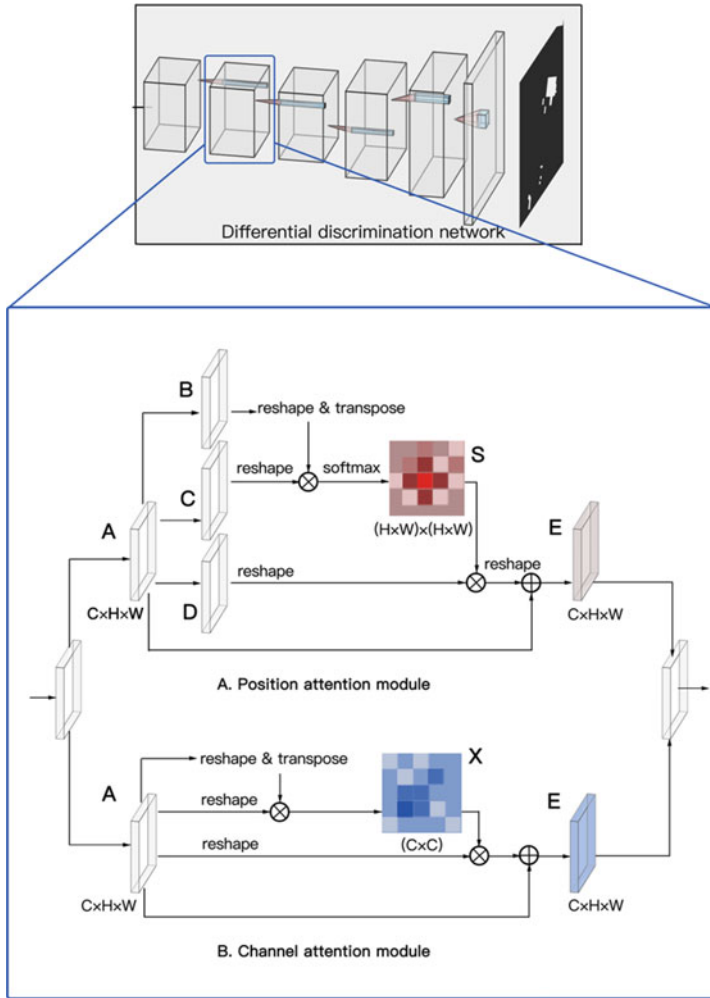


Fig. 3 The details of Position Attention Module and Channel Attention Module

multiplication between D and the transpose of S and reshape the result to $R^{C \times H \times W}$ as follows:

$$E_j = \alpha \sum_{i=1}^N (s_{ji} D_i) + A_j \tag{2}$$

where parameter α is initialized as 0 and gradually learns to gain more weight. It can be concluded from Eq. 2 that the resulting feature E at each location is the weighted sum of the features at all locations and the original feature. Therefore, it

has a global context view and selectively aggregates context based on the spatial attention map. The similar semantic features achieve mutual gains, thus improving intra-class compact and semantic consistency.

The position attention module teaches the network “where to see”, and in the channel attention module, the network will learn “which to see” [19]. Figure 3 illustrates the structure of the channel attention module. Different from the position attention module, channel attention map $X \in R^{C \times C}$ is calculated directly from the original features $A \in R^{C \times H \times W}$. Specifically, we reshape A to $R^{C \times N}$ and then perform a matrix multiplication between the transpose of A and A . Finally, a softmax layer is applied to get the channel attention map $X \in R^{C \times C}$.

$$x_{ji} = \frac{\exp(A_i \cdot A_j)}{\sum_{i=1}^C \exp(A_i \cdot A_j)} \quad (3)$$

where X^{ij} measures the i th channel’s impact on the j th channel. In addition, we perform a matrix multiplication between A and the transpose of X , then reshape their result to $R^{C \times H \times W}$. After that, we multiply the result by a scale parameter β as follows:

$$E_j = \beta \sum_{i=1}^C (x_{ji} A_i) + A_j \quad (4)$$

Similar to parameter α , parameter β gradually learns a weight from 0. Equation 4 illustrates that the final feature of each channel is a weighted sum of the features of all channels and original features, which models the long-range semantic dependencies between feature maps. Experimental results in Sect. 3 will show that our attention module can well alleviate the misdetection problem caused by dual-temporal image registration, and is robust to changes in color and scale.

3 Experiments

3.1 Dataset and Evaluation Metrics

WHU is a special dataset for us, which contains the bi-temporal building extraction Label and change label we need. The dataset contains two aerial images (0.2 m/pixel, $15,354 \times 32,507$) and provides a change vector, a change raster map, and two corresponding building vectors of these two aerial images. So it was widely used in building extraction task. The second important application of the WHU dataset is building change detection. We divide the original image into several 512×512 pixel image pairs for training. We use four indicators to evaluate our model’s performance, they are: Precision (P), Recall (R), F1-Score (F1), and Overall Accuracy (OA). They

are defined as follows: (where TP, TN, FP, and FN, respectively, indicate the number of true positives, true negatives, false positives, and false negatives.) Building change area pixels are positive, while others are negative.

$$P = \frac{TP}{TP + FP} \quad (5)$$

$$R = \frac{TP}{TP + FN} \quad (6)$$

$$F1 = \frac{2PR}{P + R} \quad (7)$$

$$OA = \frac{TP + TN}{TP + TN + FP + FN} \quad (8)$$

3.2 Building Segmentation Module Training

In the process of training the building segmentation module, we applied a transfer learning strategy with fine-tuning the WHU dataset. We use 75% of the images for model fine-tuning and the rest for prediction. The network parameters are initialized by the pretrained U-net++ on the Inrial dataset. Compared with training with random initial weights on WHU dataset directly, the transfer learning strategy's convergence is better, which saves more calculation time and obtains a higher accuracy and F1 score (Table 1).

From Fig. 4 and Table 2, we can find that even if our building segmentation module's performance is satisfied, both overall accuracy and F1 score are over 90%, but we can't subtract the T1 and T2 building segmentation result directly to get change detection result. Change detection results' accuracy is determined by the accuracy of building segmentation. Only if the building segmentation module gives us the perfect building mask, registration errors can be eliminated totally, and we can get good change detection result. Unfortunately, it's impossible. But it doesn't mean that building segmentation result is useless in building change detection task. Actually, we need to find out how to use an inaccurate mask to improve change detection's performance. In addition, our method should be robust enough even if the building segmentation result is bad such as the fourth row in Fig. 2.

Table 1 Building segmentation module's performance on different dataset

Dataset	OA	Precision	Recall	F1 score
Inrial	0.975	0.884	0.876	0.881
WHU	0.982	0.905	0.912	0.907

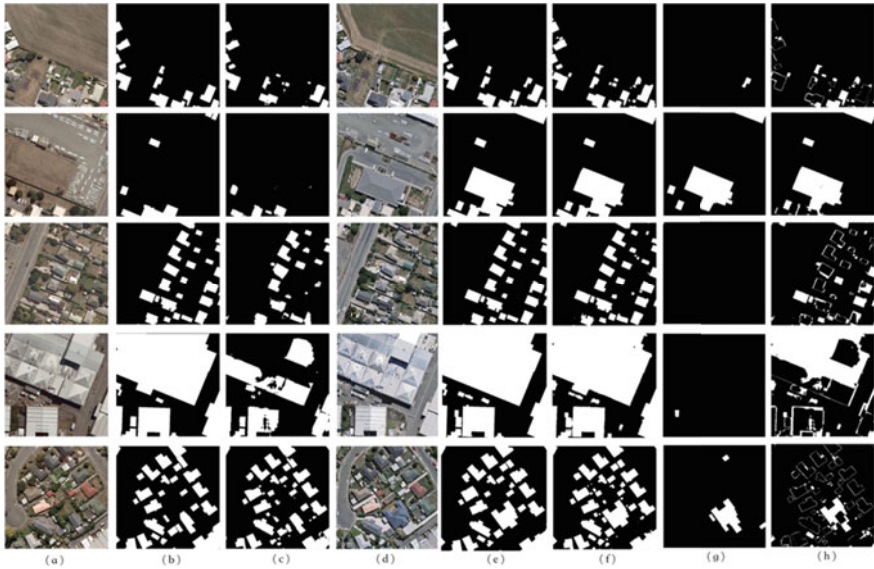


Fig. 4 a T1 image b T1 building segmentation ground truth c T1 building segmentation result d T2 image e T2 building segmentation ground truth f T2 building segmentation result g change area ground truth h The result of sub

Table 2 The relationship between the input images' size and the F1 score

Input images' size	128*128	256*256	512*512	1024*1024
Accuracy	0.796	0.836	0.841	0.820

3.3 Building Change Detection Training

3.3.1 Data Augmentation

We use a set of image preprocesses for data augmentation: (1) image rotation: bi-temporal image pairs are rotated 90°, 180°, and 270°; (2) image flipping: bi-temporal image pairs are horizontally flipped, (3) image blurring: a Gaussian blur filter is applied to T1 images to produce blurred T1 images; (4) image noise adding: we randomly add 400 salt and pepper noises to T1 and T2 images.

3.3.2 Find Appropriate Input Image Size

The size of buildings in remote sensing images is different, many large buildings will be split by sliding windows. These small pictures may only include the roof, glass, and asphalt waterproof layer of the building, but there is a lack of background

information, which is helpful for the network to identify whether it's a part of the building or not. These images will affect the accuracy of building extraction. If we choose a bigger sliding window to cut the original remote sensing image, the video ram will not be enough. If we downsample large-size image input to 512*512 pixels simply, although we get more background information around buildings, we will lose lots of detail which is useful. So, we should choose appropriate input image size to keep a balance between background information and detail texture. So we design experiments to explore the relationship between the input images' size and the accuracy of change detection. From Table 2, we can find that for our proposed model and WHU dataset, 512*512 pixels are a suitable input size.

3.3.3 Parameter Setting

Due to the memory limitation, remote sensing images needed to be cropped into tiles and then input into the network for training. We used a sliding window with a size of 512*512 pixels. The batch size was set to 3. We initialize the learning rate to 0.001 and used Adam as the optimizer. After each epoch finished, we calculated the loss of validation set. After three epochs, if the loss of validation set did not decrease, the previous learning rate was multiplied by the attenuation coefficient of 0.5. We used a Nvidia GPU 1080Ti to train our model and the entire training process took about 18 h.

3.3.4 Building Extraction module's Influence

Our model training process is divided into two stage. The first stage is training the U-net++ segmentation network as a building segmentation module. Secondly, using the segmentation result and two-temporal remote sensing images to train the change detection model together. In order to explore the influence of the building extraction module's performance on the change detection accuracy, we conducted the following experiments. We get building extraction results with an F1 score of approximately 0.6, 0.7, 0.8, 0.9, 1.0 (building segmentation ground truth) from the same building extraction model with different training epochs. The experiment results as Table 3, the change detection accuracy is greatly affected by the building extraction accuracy. The higher the building extraction accuracy, the higher the change detection accuracy.

Table 3 The influence of the building extraction module's performance on the change detection accuracy

building segmentation network training epoch	18	29	61	104	–
building segmentation F1 score	0.591	0.704	0.810	0.907	1.0
Change detection F1 score	0.743	0.771	0.804	0.841	0.924

3.3.5 Dilation Predict

The above experiments have shown that the background information in remote sense images is important for building change detection. However, buildings at the edge of each input picture are cut into small pieces when the data set is divided, making the neural network unable to obtain sufficient background information. For a small regular shape on the edge of the picture, it is difficult for the model to judge whether it is part of the building, which is also a challenge for humans. In addition, for a large-size remote sensing image, whether in building extraction or change detection task, due to memory limitations, we need to use a sliding window method to divide the original image into several 512*512 pixels size small images as input. This operation will cause many buildings to be cut apart and detected in two or more sliding windows. Since the model's performance at the edge of the sliding window is not as good as the central area, this will affect the result of large-size remote sensing images.

We use dilation prediction to solve the problem. Only the center area of the sliding window will be saved as the final change detection result. We set the parameter α to balance the speed and accuracy, when α is set to 0.5, only a square area with $0.5*512 = 256$ pixels side length will be saved, which is 1/4 area of the input image. The accuracy will be higher, but at the same time, it will cost 4 times the time. When α is set to 1, dilation predicts will be banned. Through experiments, we found that α smaller than 0.5 does not significantly improve the detection result, but the time cost will increase greatly (Fig. 5).

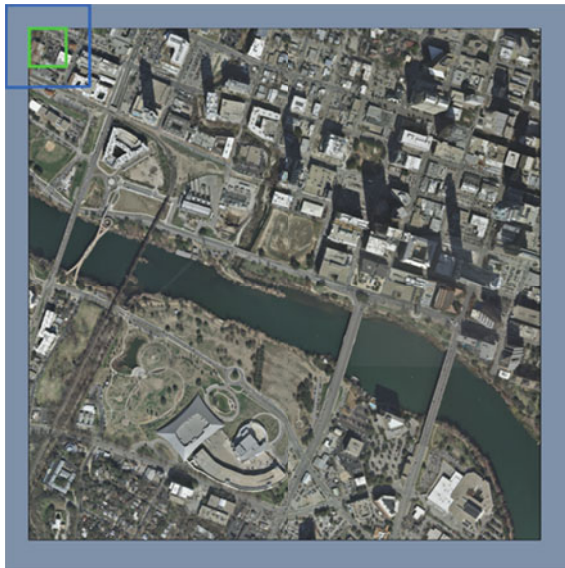


Fig. 5 A example of dilation predict

3.4 Benchmark Methods

To evaluate the method we proposed in this paper, we perform change detection using the following three benchmark methods and compare their performances on the WHU dataset:

- (1) U-net++_MSOF
U-net++_MSOF [15] is proposed based on the architecture of U-net++ . U-net++_MSOF is an early-fusion model which concatenates bi-temporal images directly as input. By fusing the output results of multiple levels of U-net++, this method is superior to all other latest change detection methods on the WHU dataset.
- (2) FC-Sima-conc
Fully convolutional Siamese-Concatenation (FC-Siam-conc) [20] is proposed by Caye Daudt et al. for remote sensing change detection. This method applies a Siamese encoding stream to extract deep features from bi-temporal images, and then concatenate the extracted deep features, finally, DDN will give the CD result using concatenated deep features.
- (3) Fully convolutional Siamese-Difference (FC-Siam-diff) [20] has a similar network architecture with FC-Siam-conc. The difference lies in that FC-Siam-diff concatenates the absolute value of deep feature differences in the decoding stream, Instead of concatenating both deep features from the encoding stream, what FC-Siam-diff extracted is the difference feature in bi-temporal images.

As shown in Figs. 6 and 7, the method proposed in this paper can detect the building change area very well both on large and small area change detection task. When detecting large area change, our method successfully returns the changed areas with complete boundaries and high internal compactness. In the case of small area changes in Fig. 7, almost all the small changed buildings are distinguished in the change maps. From Fig. 8 and Table 4, we can find that our method achieves the best performance with the highest OA (0.984), P (0.850), and F1 (0.841) on the WHU dataset compared with three benchmark methods.

4 Conclusions

In this paper, we propose a Siamese U-net with an attention mechanism for building change detection in high-resolution bi-temporal remote sensing images. We improve the boundary integrity and internal compactness of the final changed building by introducing scene-level building segmentation. In experiments, our method gets better performance in the WHU dataset compared with other benchmark methods. In addition, we use a variety of methods to improve the performance of the proposed

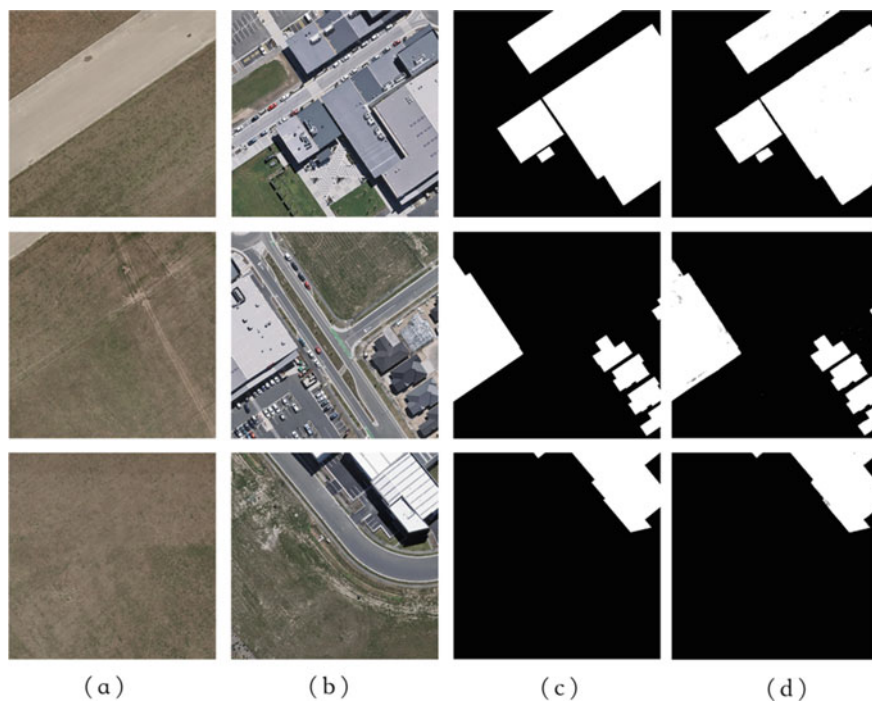


Fig. 6 Examples of large area change detection task. **a** T1 image **b** T2 image **c** ground truth **d** change detection result

method including the position attention module and channel attention module, dilation predict. In the future, we will try to use a transfer learning strategy to solve the problem of change detection and improve the generalization performance of our method.

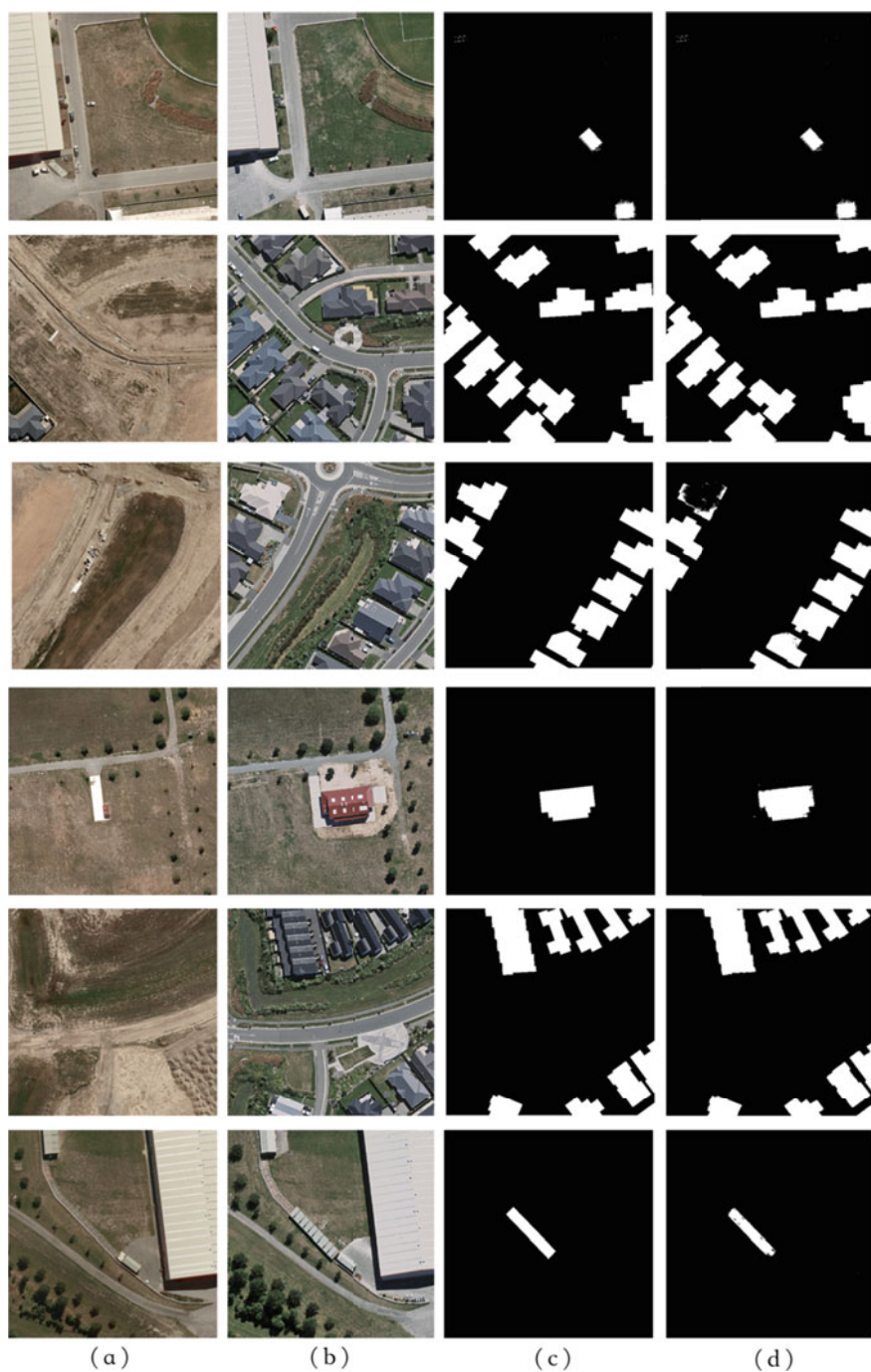


Fig. 7 Examples of small area change detection task. **a** T1 image **b** T2 image **c** ground truth **d** change detection result

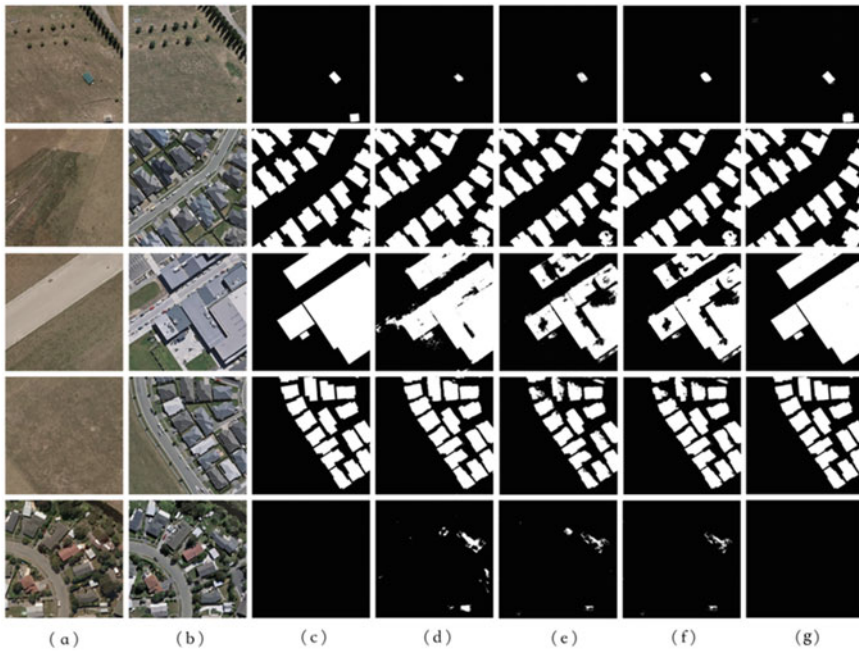


Fig. 8 Change detection result of our method and three benchmark methods. **a** T1 image **b** T2 image **c** ground truth **d** U-net++_MSOF **e** FC-Sima-diff **f** FC-Sima-conc **g** Our method

Table 4 Quantitative evaluation results of different approaches

Methods	OA	Precision	Recall	F1 score
U-net++_MSOF	0.976	0.832	0.849	0.832
FC-Sima-diff	0.973	0.804	0.822	0.800
FC-Sima-conc	0.978	0.822	0.842	0.823
Our Method	0.984	0.850	0.848	0.841

References

1. Chen H, Wu C, Du B et al (2019) Change detection in multisource VHR images via deep siamese convolutional multiple-layers recurrent neural network. *IEEE Trans Geosci Remote Sens* (99):1–17
2. Tewkesbury AP, Comber AJ, Tate NJ et al (2015) A critical synthesis of remotely sensed optical image change detection techniques. *Remote Sens Environ* 160:1–14
3. Ronneberger O, Fischer P, Brox T (2015) U-net: convolutional networks for biomedical image segmentation. Springer, Cham
4. Long J, Shelhamer E, Darrell T (2015) Fully convolutional networks for semantic segmentation. *IEEE Trans Pattern Anal Mach Intell* 39(4):640–651
5. Zhou Z, Siddiquee M, Tajbakhsh N et al (2018) UNet++: a nested U-net architecture for medical image segmentation. In: 4th deep learning in medical image analysis (DLMIA) Workshop

6. Jia L, Gong M, Kai Q et al (2016) A deep convolutional coupling network for change detection based on heterogeneous optical and radar images. *IEEE Trans Neural Netw Learn Syst* (99):1–15
7. Zhan Y, Fu K, Yan M et al (2017) Change detection based on deep siamese convolutional network for optical aerial images. *IEEE Geosci Remote Sens Lett* 14(10):1845–1849
8. Lee H, Lee KS, Kim J et al (2021) Local similarity Siamese network for urban land change detection on remote sensing images. *IEEE J Select Top Appl Earth Obs Remote Sens* (99):1–1
9. Cz A, Peng Y, Dt E et al (2020) A deeply supervised image fusion network for change detection in high resolution bi-temporal remote sensing images. *ISPRS J Photogramm Remote Sens* 166:183–200
10. Ji S, Wei S et al (2019) Fully convolutional networks for multisource building extraction from an open aerial and satellite imagery data set. *IEEE Trans Geosci Remote Sens* 57(1):574–586
11. Daudt RC, Saux BL, Boulch A et al (2018) Urban change detection for multispectral earth observation using convolutional neural networks. *IGARSS 2018-2018 IEEE international geoscience and remote sensing symposium*
12. Wu G, Shao X, Guo Z et al (2018) Automatic building segmentation of aerial imagery using multi-constraint fully convolutional networks. *Remote Sens* 10(3):407
13. Guo E, Fu X, Zhu J et al (2018) Learning to measure change: fully convolutional siamese metric networks for scene change detection
14. Maggiori E, Tarabalka Y, Charpiat G et al (2017) Can semantic labeling methods generalize to any city? The Inria Aerial image labeling benchmark. *Igarss IEEE international geoscience & remote sensing symposium*. IEEE
15. Peng D, Zhang Y, Guan H (2019) End-to-end change detection for high resolution satellite images using improved UNet++. *Remote Sens* 11(11):1382
16. Rahman F, Vasu B, Cor JV et al (2018) Siamese network with multi-level features for patch-based change detection in satellite imagery. *IEEE GlobalSIP 2018*. IEEE
17. Zhang M, Shi W (2020) A feature difference convolutional neural network-based change detection method. *IEEE Trans Geosci Remote Sens* (99):1–15
18. Fu J, Liu J, Tian H et al (2020) Dual attention network for scene segmentation. In: 2019 *IEEE/CVF conference on computer vision and pattern recognition (CVPR)*. IEEE
19. Long C, Zhang H, Xiao J et al (2016) SCA-CNN: spatial and channel-wise attention in convolutional networks for image captioning. In: 2017 *IEEE conference on computer vision and pattern recognition (CVPR)*. IEEE
20. Daudt RC, Saux BL, Boulch A (2018) Fully convolutional Siamese networks for change detection. IEEE

Analysis of Influencing Factors in Finite Element Simulation of High-Speed Impact of Micro-particles in Space Protection



Wei Wang , Shufan Wu , Zhongcheng Mu , and Jiyuan Yi 

Abstract The research on high-speed impact of microparticles has always been a hot topic in the fields of space protection, additive manufacturing, and medicine. It is the premise of the research to make clear the reliable analysis method of microparticle impact process and get the accurate results of interface response. In this paper, the finite element simulation model is established for the high-speed impact of copper particles on copper substrate, and the accuracy of the finite element model is verified by comparing the analysis results with the results in the literature. Furthermore, the time evolution curve of the response results influenced by factors such as meshing density, initial temperature setting, and particle size are studied under the condition of two-dimensional simulation. Based on this, the influence trend of the process of microparticles impacting the substrate is summarized. This study has a very important reference significance for the research and application of space protection, cold spraying additive manufacturing, medical percutaneous drug delivery, and other fields.

Keywords Microparticle impact · Space protection · Finite element analysis · Influencing factor analysis · Response results

W. Wang · S. Wu (✉) · Z. Mu · J. Yi

School of Aeronautics and Astronautics, Shanghai Jiao Tong University, Shanghai, People's Republic of China

e-mail: shufan.wu@sjtu.edu.cn

W. Wang

e-mail: wangwei_up@sjtu.edu.cn

Z. Mu

e-mail: muzhongcheng@sjtu.edu.cn

J. Yi

e-mail: sjtuyjy@sjtu.edu.cn

1 Introduction

Understanding the behavior of matter in high-speed impacts is key to solving fundamental problems ranging from space debris protection, ballistic penetration, and 3D printing to biomedical percutaneous drug delivery [1–4]. With the rise of new fields such as space protection and 3D printing, more and more attention has been paid to the study of the high-speed impact process of microparticles. It is very important for the application of this technology to study the motion change, energy distribution, bonding, and mechanism of the microparticles impacting the substrate at high speed [5].

Microparticle collisions can produce a variety of phenomena that are influenced by factors such as the velocity and angle of impact, the size and shape of the particles, and the types of materials involved. Phenomena resulting from impact include permanent indentation, substrate surface erosion, wear, particle adhesion on the substrate surface, and material erosion due to damage. Depending on the type of process and expectations of the outcome, these effects can be either harmful (breaking the surface) or beneficial (strengthening the surface) [5, 6].

At the same time, it is found that when the particle velocity is higher than a certain critical value, the particles can be deposited into the substrate. When the velocity is lower than this critical value, the particles rebound on the substrate and cannot be deposited. The critical velocity required for particle deposition is not only related to the chemical composition and mechanical properties (hardness, yield strength, strain hardening index, etc.) of the material, but also related to the temperature of the particle and the substrate [7, 8].

Assadi et al. [9] combined the experimental results of the existence of critical velocity in the cold spraying particle deposition process with the numerical results of the high-speed particle collision process and found that when the particle velocity is greater than the critical velocity, the adiabatic shear flow will be unstable [10]. Therefore, they took this velocity as the actual critical velocity of particle deposition in cold spraying. The famous theory of interfacial adiabatic shear instability leading to particle bonding is proposed. The theory is the most widely influential on the particle bonding formation principle of cold spraying. At the same time, SCHMIDT et al. [11], based on this theory, predicted the critical velocity required for deposition of different materials and further developed an empirical formula relating the critical velocity to material properties and temperature.

Because the impact duration of a single particle is very short and cannot be verified by experiments, numerical simulation is needed to study the impact process. However, finite element simulations often fail to provide reliable results, especially when the process involves high strain rates, large deformation, and severe deformation of the finite element mesh. The simulation results depend on the finite element mesh size and orientation and other model parameters. It is necessary to evaluate the reliability of available finite element modeling methods.

In this paper, the Lagrange finite element simulation model is established in ABAQUS to simulate the whole impact process, and the established two-dimensional

simulation model is compared with the literature results [12], and the reliable results are verified. Then, the influence of mesh size, initial temperature setting, and particle size on the response results under the two-dimensional simulation condition is studied. Based on this, some suggestions on the impact process of microparticles are given. The work in this paper provides a good reference for the design method of the additive manufacturing process and has a strong reference significance for the research of space protection and biomedicine-related fields.

2 Finite Element Modeling

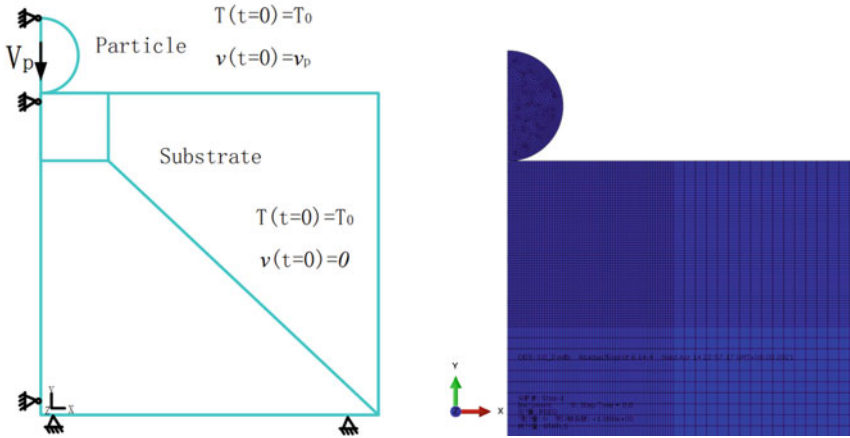
2.1 Simulation Settings

The deformation characteristics of single-particle collisions are studied by using commercial finite element software ABAQUS/Explicit. A two-dimensional axisymmetric Lagrange model is used to simulate the dynamic impact process. Both particles and substrates are assumed to be at room temperature (298.15 K) before the collision. The current particle mesh size is set to 50 elements in the diameter direction, $d_p/50$. The size of the elements within the particle and near the impact zone of the substrate remains uniform. In order to improve the calculation efficiency, the size of the element in the substrate is consistent with the size of the particle element in the impact zone to facilitate the convergence of the analysis results. The mesh size is increased when it is far away from the impact area to reduce the computation (Table 1).

In the first part of the study, the particle diameter is 50um in all the simulations. The substrate is modeled as a cylinder with a radius and height 25 times the particle radius so that waves reflected from the substrate and the far edge could only reach the impact zone after the particle bounced. The underside of the substrate is fixed in all degrees of freedom, while the sides are free. The velocity and displacement of the particles are only in the vertical direction, and the other directions are constrained.

Table 1 Default Settings in finite element simulation

Factor	Setting
Solution procedure	Dynamic-Temp-Disp-Explicit
Hourglass control	Stiffness
Element distortion Control	Length ratio: 0.1
ALE adaptive meshing	NO (exclusively without distortion control)
Interface friction	Coefficient of friction (COF): 0.2
Material damage	YES
Meshing size	1/50d _p



(a) Boundary conditions of the model.

(b) The state of the finite element model.

Fig. 1 Boundary conditions and finite element models

In a two-dimensional axisymmetric simulation with displacement and temperature coupling considered, the four-node reduced integral element (CAX4RT) is used to perform the fully coupled thermal stress analysis. The effect of particle gravity in the process is ignored. The friction coefficient between particles and matrix is 0.2. The surface–surface contact algorithm is used in the two-dimensional axisymmetric simulation (Fig. 1).

2.2 Model and Parameters

Plasticity model. The J-C plastic model is adopted for the flow stress of the material. The dynamic yield criterion includes strain, strain rate hardening, and temperature softening effect. The model expression is as follows [13]:

$$\sigma = (A + B\varepsilon_p^n)(1 + C\ln(\dot{\varepsilon}^*)) (1 - (T^*)^m) \tag{1}$$

Among them, σ is the flow stress, ε_p is the equivalent plastic strain, $\dot{\varepsilon}^* = \dot{\varepsilon} / \dot{\varepsilon}_0$ is the dimensionless strain rate, $\dot{\varepsilon}_0$ is the reference strain rate, which is generally 1, and T^* is the homologous temperature in general and is defined as [13]

$$T^* = \begin{cases} 0 & \text{for } T < T_r \\ (T - T_r) / (T_m - T_r) & \text{for } T_r < T < T_m \\ 1 & \text{for } T > T_m \end{cases} \tag{2}$$

Among them, T_R is the reference temperature, and T_m is the melting temperature of the material. Take the lowest temperature concerned in the test, A, B, n, C, and m are material constants, and $\dot{\epsilon}_0$ and T_R are calibration parameters.

In materials, plastic deformation causes a temperature rise because most of the energy in the plastic deformation is lost as heat. For most metals, experiments show that the ratio of plastic deformation to heat (inelastic heat fraction) is about 0.9. This means that 10% of the total work of deformation enters the material as defects. Therefore, 90% of plastic strain energy is assumed as heat dissipation in this study.

Failure model. Ductile damage and shear damage can be used in the failure model to withstand strain rate deformation. Ductile damage is caused by the nucleation, growth, and coalescence of cavities, while shear damage is based on the locality of shear bands, and the equivalent plastic strain is used as the control parameter of failure for both. The equivalent plastic strain is expressed by the plastic strain rate as follows:

$$\epsilon_p = \epsilon_{p0} + \left(\frac{2}{3}\right)^{1/2} \int_0^t \left(\dot{\epsilon}_{ij}^p \dot{\epsilon}_{ij}^p\right)^{1/2} dt \tag{3}$$

Among them, ϵ_{p0} is the initial equivalent plastic strain, t is the time, and $\dot{\epsilon}_{ij}^p$ is the plastic strain rate component. The equivalent plastic strain is calculated from the strain rate component and is a monotonically increasing value. When the value of the state parameter w_D is 1, the failure is considered to have occurred. The state parameter w_D is defined as follows:

$$w_D = \sum \frac{\Delta \epsilon_p}{\epsilon_D^p} \tag{4}$$

wherein $\Delta \epsilon_p$ is the increase of the equivalent plastic strain increment, ϵ_D^p is the increment corresponding to the failure strain, and then all the increments are accumulated.

The Johnson–Cook damage model is adopted as the ductile damage criterion, in which the failure strain is taken as the function of stress triaxiality (p/q), strain rate, and temperature. Therefore, the failure strain has the following form:

$$\bar{\epsilon}_D^{pl} = \left[d_1 + d_2 \exp(-d_3 \frac{p}{q}) \right] (1 + d_4 \ln \dot{\epsilon}^*) (1 + d_5 T^*) \tag{5}$$

wherein p is compressive stress (with positive tension), q is VonMises stress, $\dot{\epsilon}^*$ is dimensionless strain rate, T^* is homologous temperature, and $d_1 - d_5$ is the material parameter.

The combined effect of hardening and softening of shear damage can be quantitatively expressed by the J-C plasticity model, combined with the following formula to calculate the heat conversion of plastic work:

$$\int_{T_0}^T \rho C_p dT = \beta \int_{\epsilon_{p0}}^{\epsilon_p} \sigma d\epsilon \tag{6}$$

wherein T is the temperature, ρ is the density, C_p is the specific heat capacity, β is the inelastic heat share, and the subscript “0” represents the initial value.

The property parameter. Oxygen-free high conductivity (OFHC) copper is used as both particle and substrate material in all simulations because of the availability of material properties, especially for high strain rate regimes. The J-C model parameters for OFHC copper are taken from Ref. [11] (Table 2).

Table 2 The material properties

Material properties	Copper	Unit
Density	8960	Kg/m ₃
Elastic Modulus	126	GPa
Poisson’s Ratio	0.335	
A	90	MPa
B	292	MPa
n	0.31	
C	0.025	
m	1.09	
Melting Temp	1356	k
Reference Temp	298	k
d1	0.54	
d2	4.89	
d3	3.03	
d4	0.014	
d5	1.12	
Specific Heat	383	J/kgK
Thermal Conductivity	401	W/mk
Inelastic Heat Fraction	0.9	

2.3 Model Simulation Analysis and Verification

As shown in the boundary condition diagram above, axisymmetric boundary conditions are set for the two-dimensional model, the velocity of the particles is 500 m/s, and the horizontal displacement is limited. The substrate surface adopts fixed constraints, symmetrical boundary constraints, horizontal movement, and displacement. The temperature of the particles and substrate was set at room temperature of 298.15 K. Finally, the equivalent plastic strain (PEEQ) and temperature distribution cloud diagram at the end of particle impact are obtained as follows (Figs. 2 and 3).

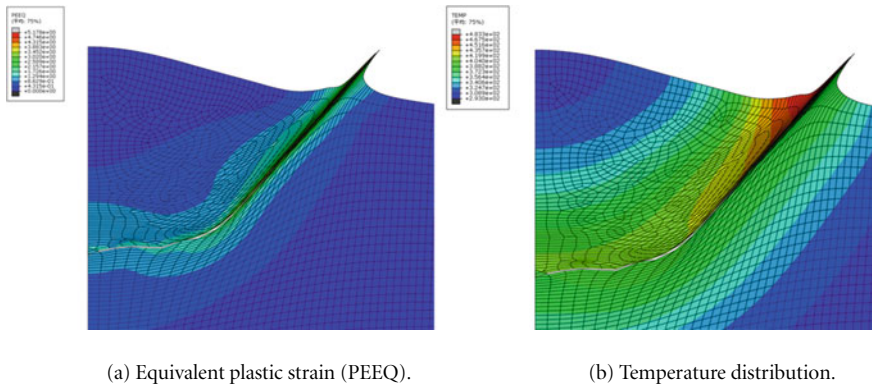


Fig. 2 Equivalent plastic strain (PEEQ) and temperature distribution nephogram

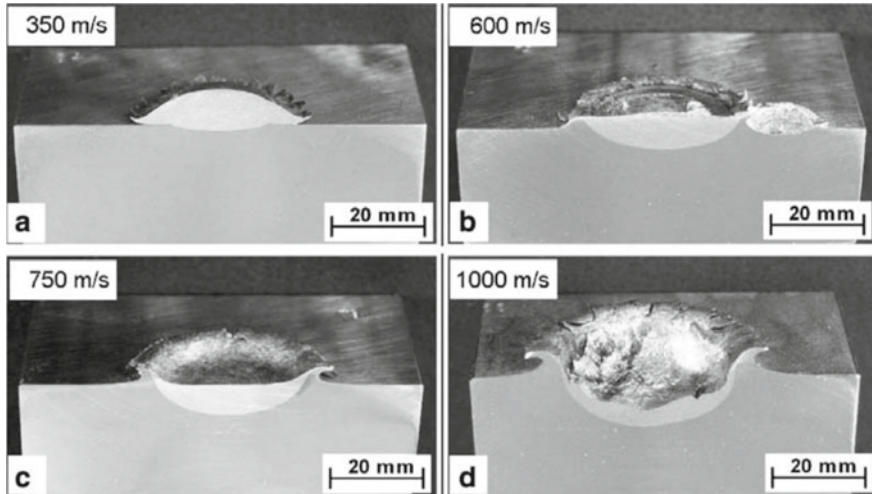


Fig. 3 Macropictures of cross-sections of copper ball impacts to low carbon steel plates with different velocities by Schmidt et al.

Comparing the simulation results with the impact cross-section morphology obtained by Schmidt et al. [11], it can be seen that the interface shape and damage situation in the two results are generally consistent. Through observation, we can know that the impact interface is compact in the middle area of the particle and matrix interface, and there is material overflow near the edge. By comparing the simulation results with the analysis results in Ref. [12], it is found that the response value and response distribution of the impact interface are almost the same, which proves the reliability of the model.

3 Analysis of Influencing Factors

3.1 Effect of Meshing Density

It is found that the mesh size of the impact interface in the two-dimensional finite element model has a certain influence on the simulation results, which will affect our judgment of the critical velocity and response. Based on this, the influence of meshing size on simulation results will be studied. In the analysis, the mesh size of the contact interface between particles and substrate will be kept the same, the interface temperature is set as room temperature, the impact velocity is 500 m/s, and the particle diameter is 50 microns, which will remain unchanged in the analysis. The mesh number of the particle along the diameter direction is set as 25/d, 40/d, 50/d, 60/d, and 80/d, and the mesh size of the contact area of the substrate is consistent with the particle meshing size. The maximum equivalent plastic strain and temperature of the reference point at each meshing density were obtained, as shown in the Table 3.

The evolution curves of the response values of the reference points under different meshing densities are drawn in the same figure. The left vertical axis represents the temperature value (K), and the right vertical axis represents the equivalent plastic strain value (PEEQ). The results are shown in the Fig. 4.

As can be seen from the Fig. 4, the maximum temperature at the interface where particles impact the substrate increases with the increase of meshing density and eventually tends to a uniform and stable value (about 450 K) within the 200 ns impact time. Therefore, it can be inferred that the meshing density has a certain influence on the accurate judgment of the critical velocity, which needs to be taken

Table 3 The response results of each meshing density

Meshing density	Max TEMP(K)	Max PEEQ
25/d	495.729	3.06142
40/d	518.601	4.11615
50/d	534.254	4.35581
60/d	579.368	4.42574
80/d	596.524	4.80575

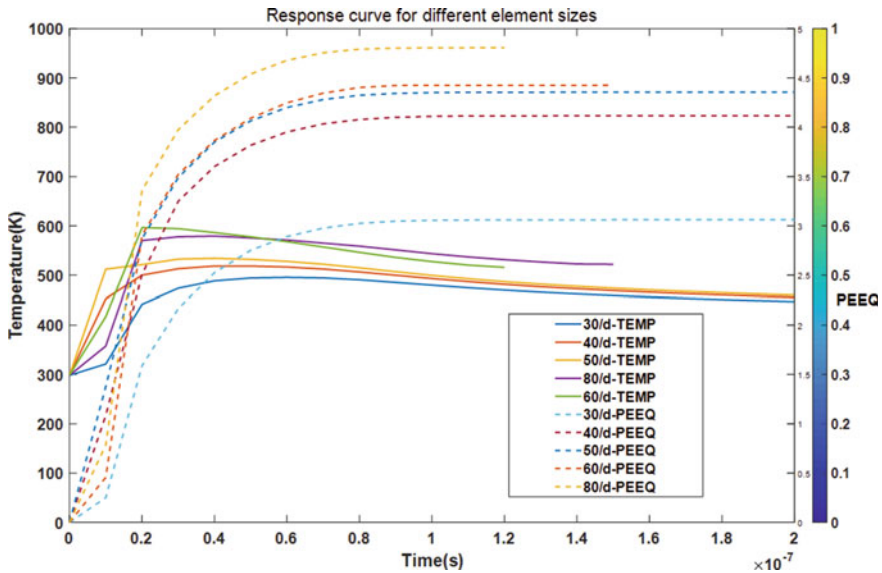


Fig. 4 The evolution curves of the response values of the reference points under different meshing densities

into account in the analysis. It is worth noting that the calculation of 80/d and 60/d meshing density conditions is terminated due to large deformation caused by excessive meshing density. However, as can be seen from the evolution curve, the final values of the curves will also tend to a stable value.

At the same time, the equivalent plastic strain at the reference point gradually increases with time and eventually approaches a stable value, respectively. Moreover, with the increase of meshing density, the maximum plastic strain increases from about 3.1 to 4.8. In addition, when the meshing size is large, the equivalent plastic strain increases greatly with the increase of meshing density. When the meshing size is gradually refined, the equivalent plastic strain increase becomes slow.

3.2 Effect of the Initial Temperature Setting

The experimental results show that the powder deposition efficiency can be improved by strengthening preheating spraying powder. Based on the adiabatic shear critical velocity formula, the critical velocity required for particle deposition can be significantly reduced by appropriately increasing the particle temperature, which is consistent with the two conclusions. Therefore, at different ambient temperatures, the critical velocities of the particles impacting on the substrate are different, which will inevitably lead to changes in the response results. Therefore, it is of great significance to clarify the influence mechanism of temperature change on response results.

Next, speeds of 400, 500, and 600 m/s are set at four temperature conditions of 298.15 K (room temperature), 400, 500, and 600 K for analysis. The results of maximum interface temperature and maximum equivalent plastic strain are shown in the Table 4.

The evolution curves of the response values of the reference points under different initial temperature settings are drawn in the same figure. The left vertical axis represents the temperature value (K), and the right vertical axis represents the equivalent plastic strain value (PEEQ). The results are shown in the Fig. 5.

Figure 5a shows that under the condition of 400 m/s, with the increase of particle–substrate temperature, the temperature evolution value at the reference point increases, and the equivalent plastic strain value also increases. It can be seen from the figure that there is an approximately linear relationship between the increase of ambient temperature and the increase of the final response temperature. Figure 5b shows that under the condition of 500 m/s, as the particle–substrate temperature increases, the temperature evolution value at the reference point increases, and the equivalent plastic strain value also increases. It can be seen from the figure that there is an approximately linear relationship between the increase of ambient temperature and the increase of the final response temperature. Figure 5c shows that at 600 m/s, with the increase of particle–substrate temperature, the temperature evolution value at the reference point increases, and the equivalent plastic strain value also almost increases. Unreasonable results were obtained at room temperature and 400 K, which should be attributed to the change of interface response region caused by different temperature conditions.

By comprehensive comparison of the above three figures, it is found that with the increase of impact velocity, the temperature response value and the equivalent plastic strain value at the reference point also increase. At the same time, the temperature response value and equivalent plastic strain of each response curve eventually tend to a stable value, respectively. It is of great significance to the research of aircraft protection and cold spraying additive manufacturing.

3.3 Effect of Particle Size

Next, five particle sizes of 30, 40, 50, 70, and 80 μm are set at room temperature for analysis. The velocity of the particles is 400 m/s, 500 m/s, and 600 m/s, respectively.

Table 4 The results of maximum interface temperature and maximum equivalent plastic strain

Velocity (m/s)	Temperature (K)			
	298.15	400	500	600
400	509.916/3.559	597.265/3.9513	679.737/4.1111	742.976/4.8904
500	534.254/4.3558	658.701/4.9028	759.532/5.5879	850.990/6.6113
600	725.203/5.5369	841.545/6.3050	650.958/6.2000	1011.93/6.4316

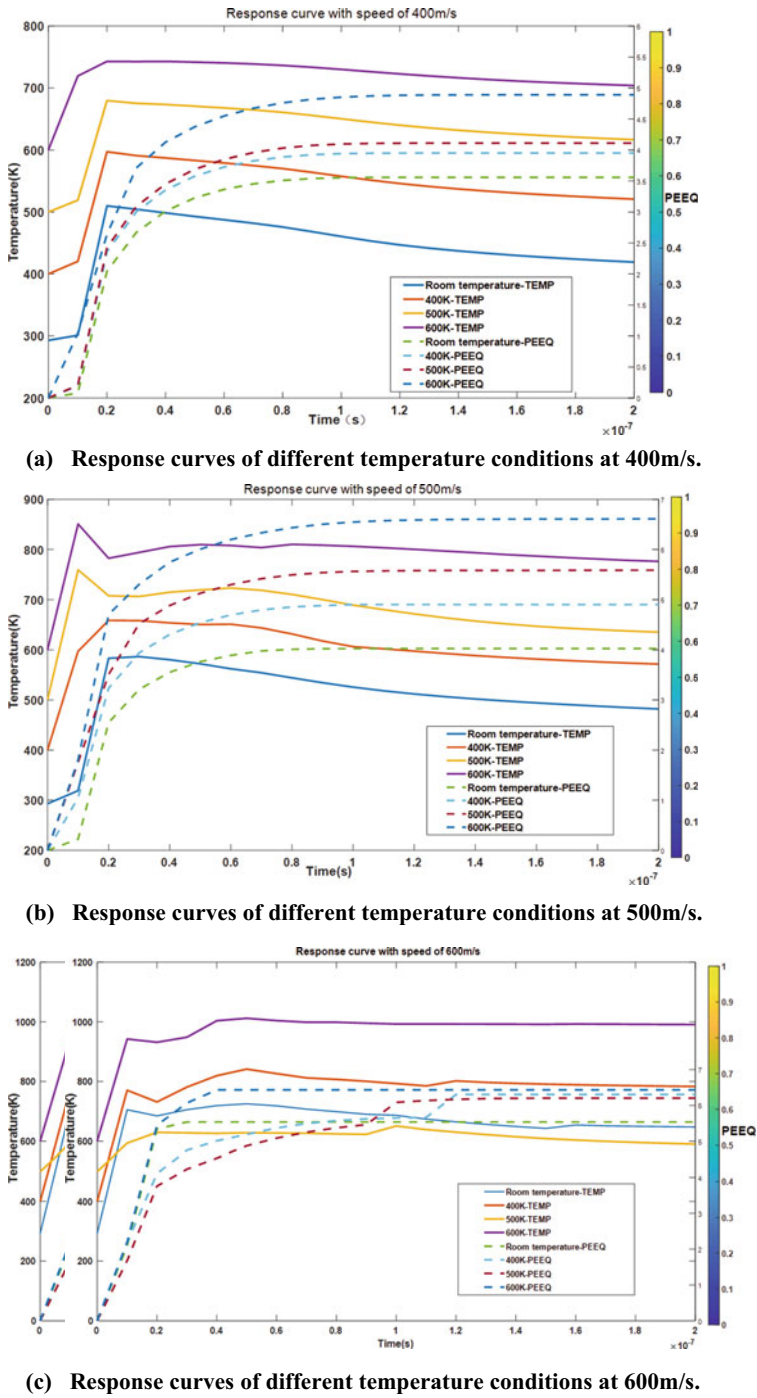


Fig. 5 Response curves of different temperature conditions

The maximum temperature and maximum equivalent plastic strain at the interface are shown in the Table 5.

The temperature and equivalent plastic strain evolution curves of different particle sizes at three speeds are shown in the same figure, and the results are as follows:

Figure 6a shows that under the condition of 400 m/s, with the increase of particle size, the temperature evolution value at the reference point increases, and the equivalent plastic strain value also increases. Figure 6b shows that under the condition of 500 m/s, the temperature evolution value at the reference point increases approximately along with the increase of particle size, and the equivalent plastic strain value also increases. Figure 6c shows that at 600 m/s, with the increase of particle–substrate temperature, the temperature evolution value at the reference point increases, and the equivalent plastic strain value also almost increases. The unreasonable equivalent plastic strain occurs under the particle size of 70 μm and 50 μm , which should be attributed to the change of the interface response region caused by different particle size conditions, thus affecting the corresponding position of the reference point.

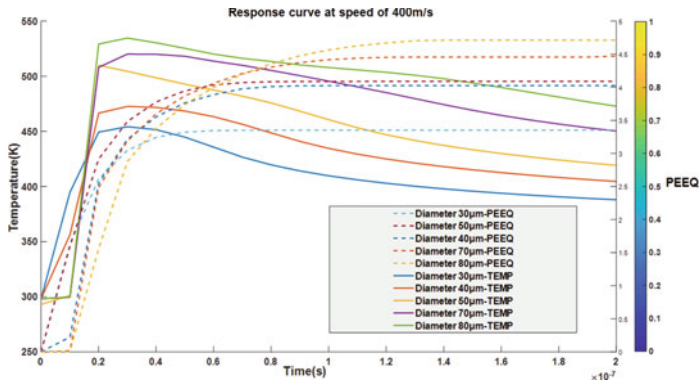
By comprehensive comparison of the above three figures, it is found that with the increase of impact velocity, the temperature response value and the equivalent plastic strain value at the reference point also increase. With the increase of velocity, the particle size has little effect on the response temperature and equivalent plastic strain, and the result has no obvious change. At the same time, the temperature response value and equivalent plastic strain of each response curve eventually tend to a stable value, respectively.

4 Conclusion

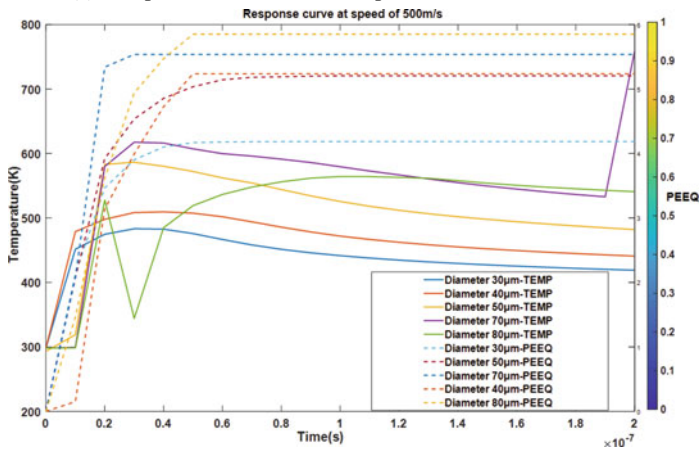
In this paper, a two-dimensional finite element model of impact dynamics is established for the particle impact substrate. J-C plasticity model and failure model were adopted to obtain a two-dimensional finite element model with reliable calculation results. Based on the two-dimensional finite element model, the evolution curve of the influence of meshing density, interface ambient temperature, and particle size on the analysis results is studied. The research results focused on the temperature and equivalent plastic strain values at the reference point of the impact interface, and the following conclusions are drawn:

Table 5 The maximum temperature and maximum equivalent plastic strain at the interface

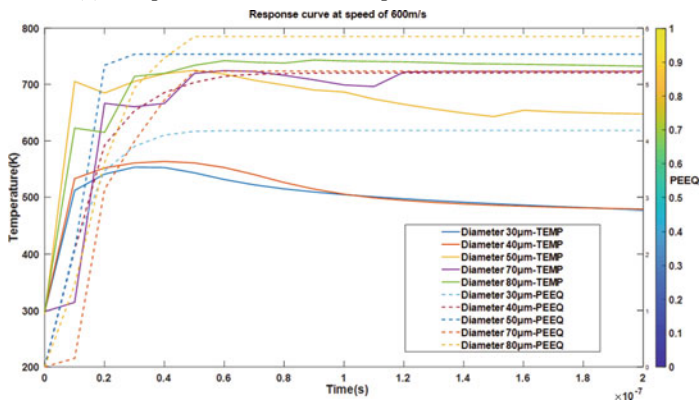
Velocity (m/s)	Particle size (μm)				
	30	40	50	70	80
400	454.2/2.918	472.6/3.385	509.9/3.559	520.1/4.149	534.6/4.658
500	483.3/3.351	509.5/4.088	534.2/4.3558	758.7/4.471	564.3/4.711
600	553.1/4.184	563.3/5.205	725.2/5.5369	724.5/5.237	743.4/5.850



(a) Response curves of different particle size at 400m/s.



(b) Response curves of different particle size at 500m/s.



(c) Response curves of different particle size at 600m/s.

Fig. 6 Response curves of different particle sizes

- (1) The maximum temperature at the interface where particles impact the substrate increases with the increase of meshing density and eventually tends to a uniform and stable value (about 450 K) within the 200 ns impact time. Therefore, it can be inferred that the meshing density has a certain influence on the accurate judgment of the critical velocity, which needs to be taken into account in the analysis;
- (2) With the increase of particle–substrate temperature, the temperature evolution value at the reference point increases, and the equivalent plastic strain value also increases.
- (3) With the increase of particle size, the temperature evolution value at the reference point increases, and the equivalent plastic strain value also increases.

From the above conclusions, it can be seen that the meshing density will affect the accuracy of the analysis results to some extent when the two-dimensional finite element is used to analyze the impact response results. At the same time, the temperature and the maximum plastic strain response of the interface change regularly under the conditions of different temperatures and different particle sizes when the particles impact the substrate. The above work provides a certain reference for the research and application of space protection, additive manufacturing, and biological transdermal drug delivery.

Acknowledgements The authors gratefully appreciate the financial support from the National Natural Science Foundation of China (No.11972234).

References

1. Mostafa HG, David V, Nelson KA et al (2018) In-situ observations of single micro-particle impact bonding. *Scripta Mater* 145:9–13
2. Li WY, Cao CC, Wang GQ et al (2019) ‘Cold spray +’ as a new hybrid additive manufacturing technology: a literature review. *Sci Technol Weld Join* 1–26
3. Mostafa HG, David V, Champagne VK et al (2018) Response to comment on “Adiabatic shear instability is not necessary for adhesion in cold spray.” *Scripta Mater* 162(15):515–519
4. McDonnell JAM (1999) HVI phenomena: applications to space missions. *Int J Impact Eng* 23(1-part-P2):597–619
5. Assadi* H, Kreye H, Gärtner F et al (2016) Cold spraying—a materials perspective. *Acta Mater* 116:382–407
6. Li WY, Liao HL, Li CJ et al (2006) On high velocity impact of micro-sized metallic particles in cold spraying. *Appl Surf Sci* 253(5):2852–2862
7. Dewar MP, McDonald AG, Gerlich AP (2012) Interfacial heating during low-pressure cold-gas dynamic spraying of aluminum coatings. *J Mater Sci* 47(1):184–198
8. Kim KH, Watanabe M, Kuroda S (2010) Bonding mechanisms of thermally softened metallic powder particles and substrates impacted at high velocity. *Surf Coat Technol* 204(14):2175–2180
9. Assadi H, Gärtner F, Stoltenhoff T et al (2003) Bonding mechanism in cold spraying. *Acta Mater* 51:4379–4394
10. Grujicic M, Zhao CL, Derosset WS et al (2004) Adiabatic shear instability based mechanism for particles/substrate bonding in the cold—gas dynamic spray process. *Mater Des* 25(8):681–688

11. Schmidt T, Gartner E, Assadi H et al (2006) Development of a generalized parameter window for cold spray deposition. *Acta Mater* 54(3):729–742
12. Li WY, Chao Z, Li CJ et al (2009) Modeling aspects of high velocity impact of particles in cold spraying by explicit finite element analysis. *J Therm Spray Technol* 18(5–6):921
13. Johnson GR, Cook WH (1985) Fracture characteristics of three metals subjected to various strains, strain rates, temperatures and pressures. *Eng Fract Mech* 21(1):31–48

SatMVS: A Novel 3D Reconstruction Pipeline for Remote Sensing Satellite Imagery



Jiacheng Lu, Yuanxiang Li, and Zongcheng Zuo

Abstract Recently, 3D reconstruction based on satellite imagery has been a hot topic in the remote sensing community. Its output called the digital surface model (DSM) can be widely used in urban planning, military navigation, and so on. Nowadays, almost all satellite image 3D reconstruction pipelines are based on traditional stereo matching algorithms which have low accuracy and long runtime. In contrast, the neural networks based on multi-view stereo (MVS) have shown great reconstruction performance in the computer vision community. To transfer the advanced MVS neural networks to the remote sensing community, we propose a novel 3D reconstruction pipeline called SatMVS. First, the input satellite images and their rational polynomial camera parameters (RPC) are cropped into small tiles according to the designated output DSM region. Second, the RPC parameters are converted to the projection matrix for the homography transform which is the core step in MVS neural networks. Third, the advanced MVS neural network is applied to estimate height maps from satellite images. At last, all inferred height maps from small tiles are converted to 3D points in Universal Transverse Mercator (UTM) coordinate system and fused to get the final complete DSM. In order to train and test SatMVS, we build a novel satellite imagery 3D reconstruction dataset called SatMVS3D dataset, which contains satellite images, RPC parameters, and height map ground truth that covers about 3km². The experimental results on the SatMVS3D dataset demonstrate that our proposed pipeline can provide robust reconstruction performance.

Keywords 3D reconstruction · Digital surface model · Remote sensing · Multi-view stereo neural networks · SatMVS · SatMVS3D dataset

J. Lu · Y. Li (✉) · Z. Zuo
Shanghai Jiao Tong University, Shanghai, China
e-mail: yuanxli@sjtu.edu.cn

J. Lu
e-mail: LUJIACHENG@sjtu.edu.cn

Z. Zuo
e-mail: jason.zuo@sjtu.edu.cn

1 Introduction

In recent years, more and more remote sensing satellites such as Pléiades, WorldView, and QuickBird have been launched to space. These satellites continuously provide researchers high-resolution optical images, which can be used in earth surface 3D reconstruction tasks. Inputs of satellite image 3D reconstruction are several (usually two) optical images and their camera parameters, and the output is DSM of the imaged area.

Satellite stereo pipeline (S2P) [3] is the state-of-the-art satellite image 3D reconstruction pipeline. It includes five steps, image cropping, local point refinement, stereo rectifying, stereo matching, and triangulation. The stereo matching algorithm is the most important step of the whole pipeline. Traditional stereo matching algorithms are divided into three types according to the different matching cost aggregation methods: local method, global method, and semi-global method. Local methods aggregate matching costs by using adjacent pixels [14, 20]. Global methods [10, 11] construct an energy function and try to minimize it to find the best disparity. The semi-global method [5] uses scan line optimization technology to do dynamical planning along 16 directions and seeks the minimum value of semi-global energy. However, all the above traditional stereo matching algorithms are not accurate enough, especially when there exist occlusion and weak texture areas (like lakes and plains) in the image. What's more, these stereo matching algorithms can only deal with two images one time. More than three images have to be divided into multiple input image pairs and the output DSMs are then fused to generate the final DSM, which reduces the pipeline's efficiency.

In the past few years, due to the strong feature learning and regression ability of deep neural networks, more and more researchers in the computer vision community try to apply the convolutional neural networks (CNN) into the 3D reconstruction task. SurfaceNet [9] is the first end-to-end training MVS network. It uses perspective projection to convert the image into a 3D colored voxel cube and then uses convolution and up-convolution operation to indicate if a voxel is on the surface. DeeMVS [7] takes an arbitrary number of posed images as input, then it aggregates the cost using encode-decode structure with skip connection, and finally, full connection conditional random field is applied to estimate the depth. Most recently, the MVS neural networks based on 3D cost volumes are more and more popular with high reconstruction accuracy [4, 16, 17]. These networks use homography transform and variance cost metric to build 3D cost volume from the image features and then use 3D CNN to regress and predict the depth map.

With more input information (no less than three images of the same area) and the strong feature learning ability, MVS neural networks tend to have high reconstruction accuracy in the indoor scene dataset. However, multiple problems exist when we try to directly apply them to the satellite images 3D construction task.

- Image size: satellite images tend to have a much larger size than common indoor scene images.

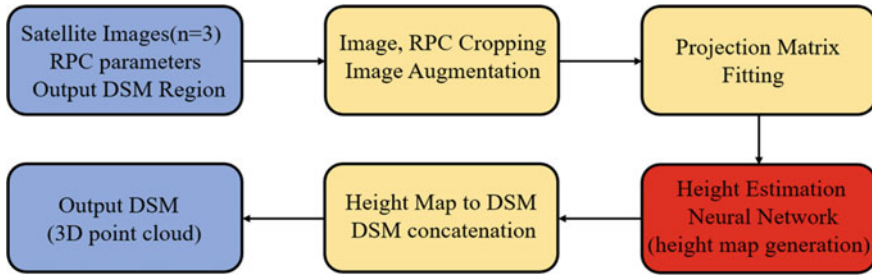


Fig. 1 SatMVS pipeline overview (blue parts are the pipeline’s input and output, orange parts are the preprocessing and postprocessing steps, and the red part is the core step of the whole pipeline)

- Camera parameters: in order to hide satellite camera intrinsic parameters and orbit information, satellite image providers tend to provide RPC parameters instead of a strict image geometry model.
- Depth range: the depth of an indoor scene tends to vary from several meters to tens of meters, while the distance between satellite camera and earth is hundreds of miles.
- Public datasets: none public satellite MVS dataset has been published so far, which makes it difficult to train and test MVS neural networks using the satellite images.

In order to solve the above problems, we proposed a novel pipeline (see Fig. 1). First, we crop the large satellite image into small tiles with size 384×480 according to projection coordinates of the spatial virtual grid on the image plane. Second, we fit the projection matrix under UTM coordinate to replace the original RPC parameters. Third, we design the height estimation model to predict the height map of the input image tile. Finally, we reproject the height map to the initial DSM (in UTM coordinate system) and concatenate all small DSM tiles into the final complete DSM.

The main contributions of this paper are as follows:

- SatMVS: a novel 3D reconstruction pipeline for remote sensing satellite imagery that transfers the advanced MVS neural network to the satellite image 3D reconstruction task.
- SatMVS3D: a novel satellite image MVS dataset is built for training and testing the SatMVS pipeline.

The rest of the paper is organized as follows. Section 2 introduces the related work. Section 3 describes our proposed pipeline SatMVS in detail. Section 4 introduces the first trainable satellite image MVS dataset-SatMVS3D. Section 5 shows some experimental results of the SatMVS pipeline on the SatMVS3D dataset. The last section summarizes our work and describes the prospects of future work.

2 Related Works

2.1 Cost Volume-Based MVS Neural Networks

MVSNet [16] presents the first cost volume-based architecture for depth map inference from multi-view images. In this network, image features are first extracted using eight 2D convolution layers, then multi-feature volumes are constructed based on the plane sweep algorithm[2]. Then multiple feature volumes are aggregated into one cost volume using variance cost metric, and 3D convolution is applied to regularize and regress the final depth map.

The feature volume and cost volume mentioned above are constructed through three steps. First, the reference image’s features are copied N times along the principal axis of the reference camera to generate the N hypothesis plane with a designated depth interval. Then source images’ features are pixel-by-pixel wrapped to these hypothesis planes through a 3×3 homography matrix $H_i(d)$ (see Eq. 1), in order to align with the reference image’s feature. Third, multiple feature volumes are merged into one single cost volume (cost represents the difference of reference and source images’ features at a certain depth).

$$H_i(d) = k_i R_i \left(I - \frac{(t_1 - t_i) n_1^T}{d} \right) R_1^T K_1^{-1} \quad (1)$$

k_i , R_i , and t_i refer to the camera intrinsic, rotation, and translation matrix of the source image, respectively. n_1 denotes the principal axis of the reference camera and d denotes the hypothesis depth.

The cost volume-based MVS networks have high computation complexity due to cost volume’s large size and 3D convolution’s high computation cost. In RMVSNet [17], the 3D convolution is replaced by the 2D GRU time-series module to reduce model complexity. Fast-MVSNet [19] uses sparse cost volume to predict sparse depth map (1/8 of original image size) and then densifies it using propagation module. These approaches show great performance in indoor datasets like DTU [8], Tank, and Templates [12].

Recently, some researchers have tried to apply MVS neural networks into DSM generation. Liu and Ji [13] build WHU aerial dataset and design the REDNet with a recursive encoder-decoder structure. The experiments on the WHU dataset show that REDNet has high-precision 3D earth surface reconstruction result. MS-REDNet [18] designs three-stage depth estimation architecture on the basis of REDNet to reconstruct the 3D building model from aerial images. But this DSM generation only works on aerial images instead of satellite images. Some unique differences in the satellite image 3D reconstruction task are not solved. In contrast, we address these differences in our proposed pipeline.

2.2 RPC Parameters

The strict camera geometry model is also known as the pinhole camera model in the computer vision community, which takes the following form:

$$Z \begin{bmatrix} u \\ v \\ 1 \end{bmatrix} = K \begin{bmatrix} R & t \\ 0^T & 1 \end{bmatrix} \begin{bmatrix} X_c \\ Y_c \\ Z_c \\ 1 \end{bmatrix} \quad (2)$$

where $[X_c, Y_c, Z_c]$ is the 3D point's world coordinate, $[u, v]$ is the corresponding output image pixel coordinate, Z is the depth of the 3D point from the world coordinate system to the camera plane. K includes the focal length and optical center position, (R, t) includes the rotation and translation from world coordinate system to camera coordinate system.

However, when it comes to remote sensing satellite images, the pinhole camera model isn't applicable because the core parameters and orbit parameters of some satellite sensors belong to confidential information. RPC parameter model [6] is the most widely used to replace the pinhole camera model. In RPC, the geodetic coordinates of the ground point and its corresponding image point coordinates are associated with four ratio polynomials (see Eq. 3) which include 80 coefficients and 10 normalized parameters.

$$X = \frac{num_u(P, L, H)}{den_u(p, L, M)} Y = \frac{num_v(P, L, H)}{den_v(p, L, M)} \quad (3)$$

3 SatMVS Pipeline

This section aims at describing each step of our proposed SatMVS pipeline in detail, which includes four steps: image cropping, projection matrix fitting, height estimation network, and height map to DSM.

3.1 Image Cropping

The original size of satellite images tends to be large and vary with the satellite image providers, but the MVS neural network only accepts fixed small size as input. Hence, we must crop the original image into small tiles. Satellite images' large size and different shooting posture of satellite camera can lead to dozens to hundreds of coordinate offsets of corresponding points in different images (as shown in Fig. 2).

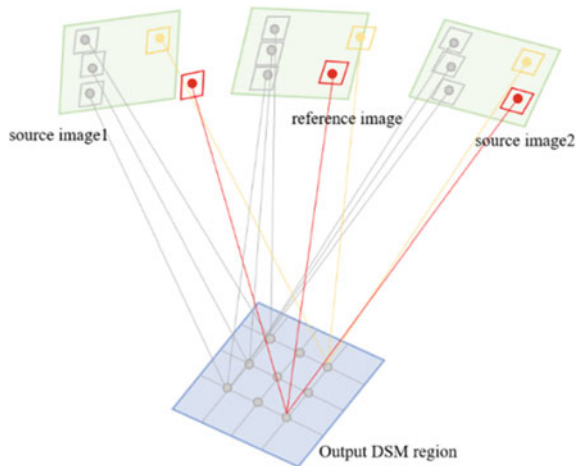


Fig. 2 Coordinate offset of corresponding points in different images (image size 3001×3001)

The offset means we can't simply crop the images according to the certain interval in the image plane because the input images of MVS neural networks should cover the same area in the scene.

Instead, we build 2D virtual grid (2D plane point (east and north) in UTM coordinate system) with the certain interval in the designated output DSM region. Then combining the average height in RPC parameters, we get 2D virtual grid of 3D points (east, north, and height). Then these points are converted to the geodetic coordinate system (latitude, longitude, and height). Then, we project these points to the three input image planes (see Fig. 3) and crop tiles centered on these projection points with standard size 384×480 . Finally, we abandon the group of tiles in the following two cases: (1) once part of one tile is out of the image boundary (see the yellow part in Fig. 3); (2) the projection point is totally out of the image boundary (see the red part in Fig. 3).

Fig. 3 Image cropping based on virtual grid projection from object space



3.2 Projection Matrix Fitting

The plane sweep module is the core step of the cost volume-based MVS neural networks. It mainly relies on the homography matrix (see Eq. 1) to warp the source images' features and align them with the reference image's features. However, we can't directly get the homography matrix from RPC parameters due to the missing of camera internal and external parameter matrix. What's more, the large average value (hundreds of kilometers) and small variance (hundreds of meters) of depth d in Eq. 1 make the homography transform with different depth d doesn't work.

$$Z \begin{bmatrix} x \\ y \\ 1 \end{bmatrix} = \begin{bmatrix} P1 & P2 & P3 & P4 \\ P5 & P6 & P7 & P8 \\ P9 & P10 & P11 & P12 \end{bmatrix} \begin{bmatrix} X_w \\ Y_w \\ Z_w \\ 1 \end{bmatrix} \quad (4)$$

When a large satellite image is cropped into the small tiles, the area imaged by the small tile tends to be less than 1km^2 . It is feasible to fit RPC parameters in one Cartesian coordinate system. UTM is a kind of Cartesian coordinate system, which has been widely used in topographic maps. Thus, we try to convert the RPC parameters into a projection matrix (see Eq. 4) in the UTM coordinate system.

With the scale and offset information of height, latitude, and longitude included in the RPC parameters,

we first get the 3D boundary of height, latitude, and longitude and construct 3D virtual grid within the boundary with designated interval. Then we get the corresponding image coordinate of each 3D point in the virtual grid. Then we convert the 3D virtual grid from a geodetic coordinate system to UTM coordinate system. Finally, the least square method SVD is applied to solve this matrix. What's more, the Z value (the distance between the camera plane and earth surface, see Eq. 5) in the equation can be treated as constant due to its large average value (hundreds of kilometers) and small variance (hundreds of meters); hence, we compute the average Z value after getting the projection and store it as constant together with the projection matrix.

$$z = p_9 * X_w + p_{10} * Y_w + p_{11} * Z_w + p_{12} * 1 \approx constant \quad (5)$$

3.3 Height Estimation Model

The original MVS neural networks are used to predict depth map (each pixel's depth from the camera plane) from the input images. Here, in our model, we directly predict the height map (each pixel's height from the earth's surface). The detailed structure of our height estimation model is shown in Fig. 4.

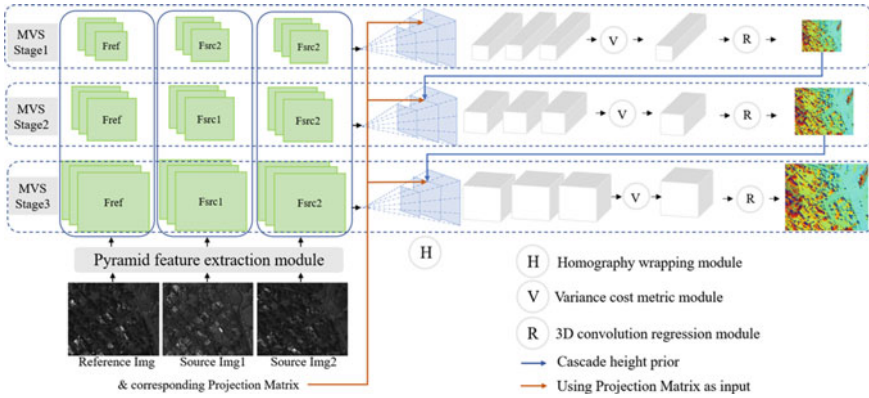
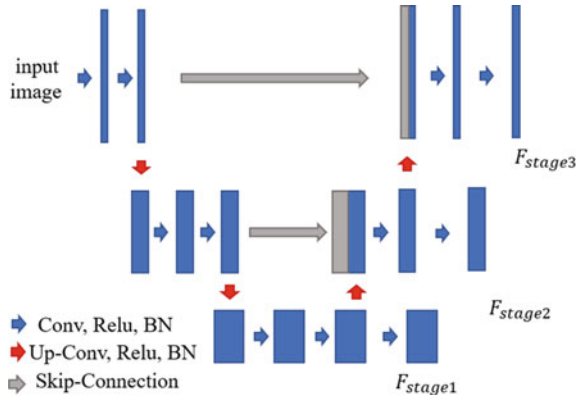


Fig.4 The detailed structure of the height estimation model

3.3.1 Pyramid Feature Extraction Module

Three input images share the same feature extraction convolutional layers weight. We refer to the classic U-Net structure [15] to extract pyramid features (see Fig. 5). Nine 2D convolutional layers are first used to extract features of stage1. The output feature channel of each layer is {8,8,16,16,16,32,32,32,32}. The stride of the third and sixth layers is set as 2 in order to down-sample the feature map. Then the eighth layer is up-sampled through the up-convolution layer with stride 2 and then concatenates with the fifth layer in order to get the feature of stage2. The feature of stage3 is extracted in the same way. The sizes of the output feature map are 1/4, 1/2, and 1 of the original image size, and the feature channels are 32, 16, and 8, respectively.

Fig.5 Pyramid feature extraction module



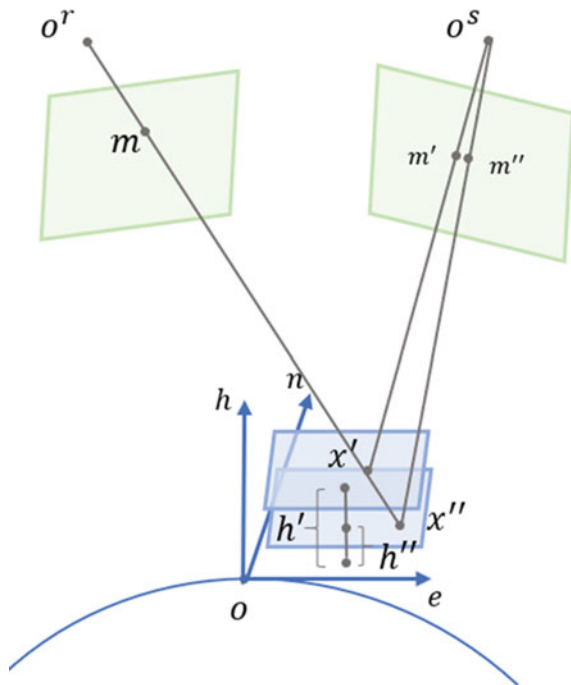
3.3.2 Height Estimation Module

As introduced in Sect. 3.2, we convert the RPC parameters into a projection matrix in the UTM coordinate system. Instead of aligning features along the depth direction, we align features along the height direction of the UTM coordinate system (see Fig. 6). The rationality of this way lies in the fact that the depth value of the projection matrix is almost constant due to the extremely large depth distance of the satellite image (see Eq. 4).

With certain image coordinate (x, y) in reference image and height Z_w , and reference image's projection matrix, we can get X_w, Y_w with Eq. 6 (constant z is an average value of z when fitting the projection matrix). Then we use (X_w, Y_w, Z_w) and projection matrix of the source image as input to get the image pixel coordinate of the source image. Through this way, we can apply homography transform between reference and source images.

$$\begin{bmatrix} X_w \\ Y_w \end{bmatrix} = \begin{bmatrix} p_1 & p_2 \\ p_5 & p_6 \end{bmatrix}^{-1} \begin{bmatrix} x * constant\ z - p_4 - p_3 * Z_w \\ y * constant\ z - p_8 - p_7 * Z_w \end{bmatrix} \quad (6)$$

Fig.6 Homography transform using the projection matrix



3.3.3 Variance Cost Metric

The values of the same position in three feature volumes are the features of each image at a certain height. The similarity of features in the same position represents the probability of the real height of the image pixel. To quantitatively describe this similarity, we aggregate the three feature volumes into one cost volume with the following equation. The smaller the cost value is, the more similar the features are.

$$c_i = \frac{\sum_{i=1}^N (V_i - \bar{V}_i)^2}{N} \quad (7)$$

where c_i is cost value of each position, V_i is feature value of feature volume, and \bar{V}_i is average feature value.

3.3.4 3D Convolution Regression

Each value in cost volume represents the similarity of features between reference images and source images. We follow the regression method in [16]. The multi-scale 3D CNN is applied to regularize the cost volume. The output volume has one single channel, and then the softmax operation is applied along the height direction to calculate the probability at each hypothesis height of the image pixels. Finally, the height map is calculated with the following equation.

$$H = \sum_{i=1}^n h_i * p_i \quad (8)$$

3.3.5 Cascade Module

Our model consists of three stages. Each stage has an estimated height map (1/4, 1/2, and 1 of input image size). In the first stage, the hypothesis height range of plane sweep is preset. In the second stage and the third stage, the depth of each pixel in plane sweep totally depends on the height prediction value of the previous stage. In addition, the number of assumed depth planes in the three stages is 48, 16, and 8, respectively. Thus, we can get the height map from coarse to fine and finally reduce the computational complexity of the model.

3.3.6 Loss Function

The loss of each stage is in Eq. 9. p_{valid} represents the image pixels that contain height ground truth. h_{gt} is pixel's height ground truth. h_{est} is pixel's estimated height. The $Loss_i$ is defined as L1 distance between h_{est} and h_{gt} .

$$Loss_i = \sum_{p_{valid}} |h_{est} - h_{gt}| \quad (9)$$

The total loss is the weighted sum of three stages. The weight λ_i is 0.5, 1, and 2, respectively.

$$Loss = \sum_{i=1}^3 \lambda_i Loss_i \quad (10)$$

3.4 Height Map to DSM

After getting the height map, with image pixel coordinate (u, v) and estimated height h in the height map, we can directly get the 3D point's coordinate (X_w, Y_w, Z_w) using Eq. 6.

Finally, we put all small DSMs generated by small pictures together to make the whole DSM in the designated region.

4 SatMVS3D Dataset

4.1 IAPRA MVS3DM Dataset

The IAPRA MVS3DM dataset [1] is the benchmark dataset that supported the 2016 IAPRA Multi-view Stereo 3D Mapping Challenge. It includes 47 optical images of worldview-3 satellite. These images cover about 100 km² with 0.3 m pixel resolution. The area imaged is near San Fernando, Argentina. It also includes airborne lidar ground truth with 0.2 m resolution, and this airborne lidar covers about 20 km².

4.2 Novel SatMVS3D Dataset

The original IAPRA MVS3DM dataset can't be directly used to train the pipeline's height estimation model, because the optical satellite images lack corresponding height map ground truth that used to be the label value during training. Hence, we created the trainable SatMVS3D dataset on the basis of the IAPRA MVS3DM dataset, including four main steps.

First, eight sites from the large lidar ground truth area are chosen. These eight sites totally cover about 3 km². Each site has more than 40 optical images. The distribution of these sites is shown in Fig. 7 and the detailed information of each site is shown in Table 1.

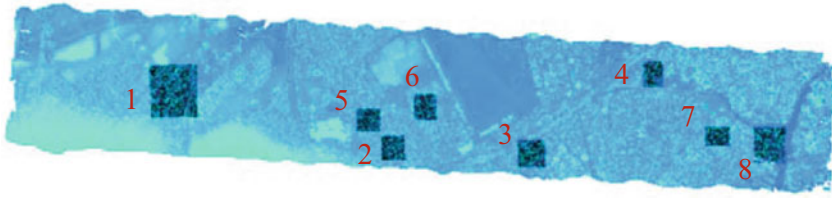


Fig. 7 Distribution of eight sites of SatMVS3D dataset (background is the airborne lidar ground truth covering area)

Table 1 Overview of the SatMVS3D dataset

	Views	Image size	Cover area (km ²)	Cropped subsites
Site1	50	3001 × 3001	0.84	132
Site2	50	2001 × 2001	0.31	44
Site3	43	2001 × 2001	0.29	42
Site4	42	2001 × 2001	0.32	47
Site5	50	2001 × 2001	0.32	48
Site6	50	2001 × 2001	0.34	50
Site7	42	2001 × 2001	0.27	43
Site8	40	2001 × 2001	0.24	33

Second, we convert the point cloud ground truth from UTM coordinate to the geodetic coordinate, and then we convert the point coordinates through the RPC parameters of satellite images to the image coordinate (u, v), to generate the height map ground truth for each site.

Third, the large satellite images with their height maps are cropped to standard small tiles following the way in Sect. 3.1 with size 380 × 484.

Fourth, we generate the projection matrix for each image tile following the way in Sect. 3.2.

Finally, sites 2, 4, 5, 6, 7, and 8 are allocated as the training set, which consists of 265 cropped subsites, and sites1 and 3 are allocated as test set, which contains 174 cropped subsites.

5 Experimental Results

In this section, we train and test our proposed pipeline SatMVS on the SatMVS3D dataset. We first test the accuracy of the fitted projection matrix, then we test our height estimation model in the test sites of the SatMVS3D dataset. Finally, we generate the complete DSM through the whole pipeline.

Table 2 Reprojection error of fitted projection matrix

	Minimum value	Maximum value	Average value
Site1-2	8.81*10e-8	0.062	0.013
Site1-3	4.64*10e-7	0.069	0.015
Site1-21	1.02*10e-6	0.080	0.016
Site1-74	1.74*10e-7	0.105	0.024
Site1-119	1.22*10e-6	0.063	0.015

5.1 Projection Matrix Fitting Accuracy

5.1.1 Reprojection Error

Five sub-sites of site1 are used to check the accuracy of the projection matrix. Following procedures in Sect. 3.3.2, we first fit the projection matrix from 3D virtual grid point and corresponding image pixel coordinate (u, v) (project through RPC parameters). Then, then the image pixel coordinate and height value Z_w in 3D virtual grid are used to get the other two dimension's coordinates X_w, Y_w through Eq. 6. Finally, the new image pixel coordinate (u', v') are calculated through Eq. 4. We calculate the reprojection error using the following form.

$$Err = \sqrt{(u' - u)^2 + (v' - v)^2} \quad (11)$$

As shown in Table 2, the reprojection error is less than one-tenth pixels.

5.1.2 Homography Transform via Projection Matrix

Besides the reprojection error, the homography transform based on the projection matrix of the reference image and source image has great significant importance to height estimation. Figure 8 shows the transform from the source image to the reference image (here we transform the original image instead of extracted feature). The third to fifth pictures represent transform with designated height, while the last picture represents transform with height ground truth of each pixel. The last picture demonstrates the accuracy of reprojection based on projection matrix; what's more, it also demonstrates that feature difference is smallest only when features of the source image are transformed with an accurate height of each pixel in the reference image.

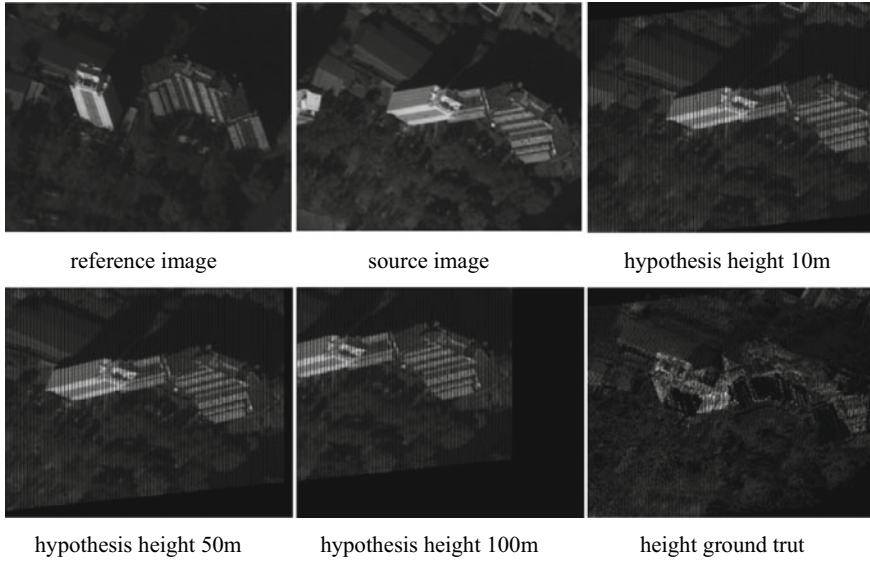


Fig. 8 Visualization of homography transform

5.2 Height Estimation Model Performance

5.2.1 Implemental Details

The height estimation model is the core of the whole pipeline. We evaluate our model on the SatMVS3D dataset. Six sites of the SatMVS3D dataset are used to train the networks, and the other two sites are used to test. During training, the inputs are three satellite images with size 384×480 , the corresponding height map, and the fitted projection matrix. The final output is the estimated height map with the same size as input images. According to the height ground truth, we set the first stage's height range at $[10, 70]$ meters. During three iteration stages, the number of height hypotheses is 48, 32, and 8, and the depth intervals are 1.25 m, 0.625 m, and 0.3125 m, respectively (the depth interval of the first stage is calculated as $(70-10)/48$). In the training stage, the batch size was set as 2. RMSProp was chosen as the optimizer, and the learning rate was set at 0.001. All the experiments were conducted on one single Geforce 1080Ti platform.

5.2.2 Metrics

Accuracy and completeness are the main evaluation metrics in the 3D reconstruction task. Accuracy is the median value of the L1 distance between the predicted height and the ground truth height, and the pixels with none value are ignored. Completeness

Table 3 Quantitative reconstruction results of height estimation models

	Acc (m)	Com (<1 m) (%)	Com (<3 m) (%)
MVSNet	1.02	48.6	76.7
RMVSNet	0.89	51.7	80.2
Ours	0.82	54.3	85.5

is defined as the percentage of lidar points whose error is less than a certain threshold. Here, we choose the 1 and 3 m as two thresholds.

5.2.3 Result on SatMVS3D Dataset

MVSNet [16] and RMVSNet [17] are used to compare with our height estimation model. They are trained and tested on the same platform and have the same input (three input images and fitted projection matrix). Quantitative results are shown in Table 3. The results show that our height estimation model has better accuracy and completeness than MVSNet and RMVSNet. That's because the multi-stage architecture ensures that the height map is estimated in a coarse-to-fine way. As shown in Fig. 9, the reconstruction result of our height estimation model includes more details and more complete earth surface information.

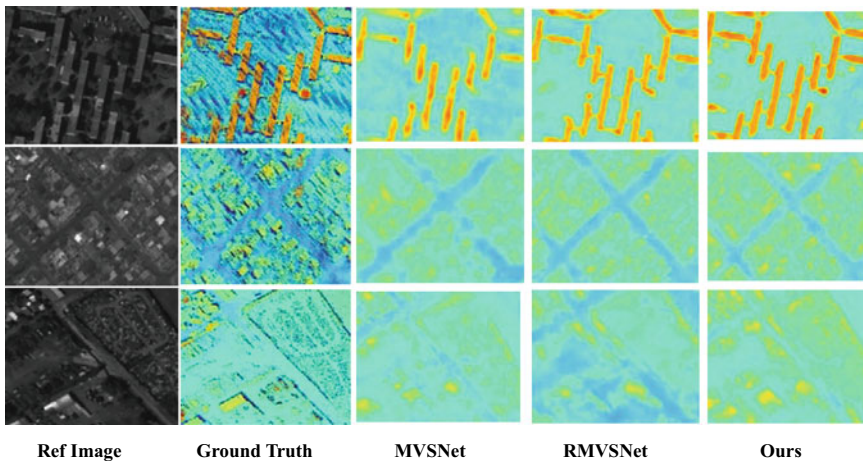


Fig. 9 The inferred height map of height estimation networks

5.3 Whole Pipeline Performance

Finally, we test our whole pipeline comparing with S2P in the site 3 of SatMVS3D dataset. Both S2P and our pipeline take the uncropped large image as input. The input image number of S2P is set as 2 and 3. For three input images, S2P treats them as two image pairs and generates two DSM and finally combines them using median filtering. While our pipeline just takes three images as input. Besides accuracy and completeness, the runtime of the S2P and our pipeline is also compared in this section. It is noteworthy that runtime is compared using the processing time in the whole input image, while the accuracy and completeness are compared on the certain region of the input image (see Fig. 10, red box region).

Quantitative results are shown in Table 4. The accuracy and completeness of S2P remarkably increase with the input image number. While the runtime multiply increases. Compared with S2P, our pipeline SatMVS has higher accuracy when the input image number of S2P is 2 and slightly less accuracy when the input image number is 3. What's more, the completeness with 1 and 3 m threshold of SatMVS is higher than S2P. The reason for this result is that S2P's output DSM contains much invalid regions with none value. These regions are not involved in the calculation of

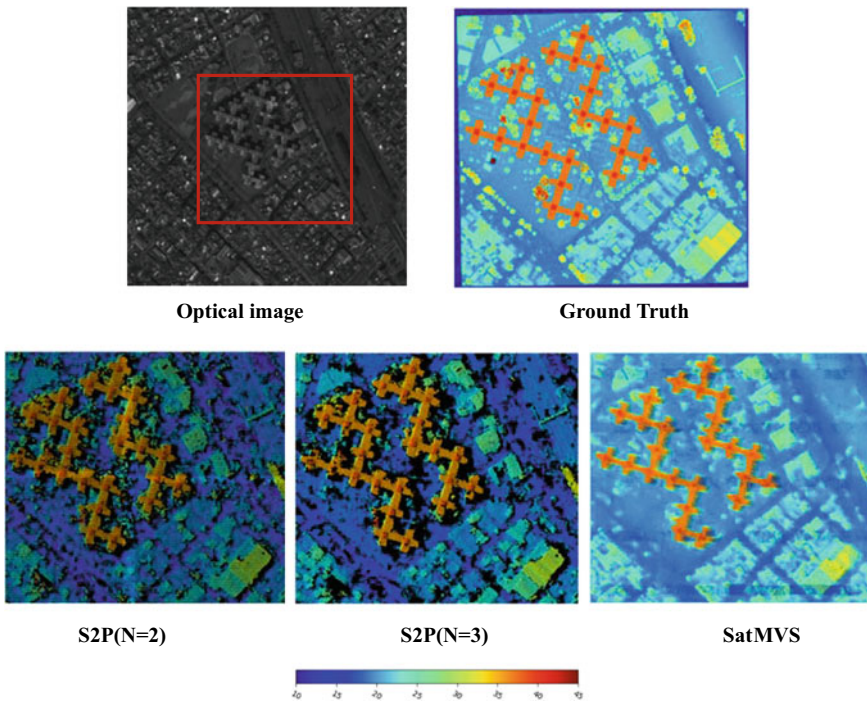


Fig. 10 DSM generated by the whole pipeline (red box region in reference images is used to calculate the accuracy and completeness of output DSM)

Table 4 Quantitative DSM performance of whole pipelines

Method	Accuracy(m)	Com (<1 m) (%)	Com (<3 m) (%)	Runtime(min)
S2P (N = 2)	2.29	5.83	22.59	0.76
S2P (N = 3)	0.85	27.24	43.39	1.93
SatMVS (Ours)	1.03	42.3	81.1	0.52

accuracy. In contrast, our pipeline SatMVS infers height for each pixel of the image with almost none void region, which boosts the completeness of output DSM. What's more, the runtime of SatMVS is always less than S2P which means higher efficiency of our pipeline. Finally, from the visualization of output DSM shown in Fig. 10, it's clear that DSM generated by SatMVS has much less invalid region than S2P.

6 Conclusion

The main purpose of the paper is to transfer advanced multi-view stereo neural networks from the computer visions community to the remote sensing community to elevate the accuracy of the digital surface model. To achieve this goal, we propose a novel pipeline SatMVS which includes image cropping, projection matrix fitting, height estimation neural network, and height Map to DSM steps. What's more, we build the world's first trainable satellite image MVS dataset called SatMVS3D. The experiments of SatMVS on SatMVS3D dataset show that although with slightly less accuracy, the novel pipeline has better completeness and efficiency than the traditional stereo-matching-algorithm-based pipeline.

References

1. Bosch M, Kurtz Z, Hagstrom S, Brown M (2016) A multiple view stereo benchmark for satellite imagery. In 2016 IEEE applied imagery pattern recognition workshop (AIPR), 1–9. <https://doi.org/10.1109/AIPR.2016.8010543>
2. Collins RT (1996) A space-sweep approach to true multi-image matching. In: Proceedings CVPR IEEE computer society conference on computer vision and pattern recognition, pp 358–363. <https://doi.org/10.1109/CVPR.1996.517097>
3. de Franchis C, Meinhardt-Llopis E, Michel J, Morel J-M, Facciolo G (2014) An automatic and modular stereo pipeline for pushbroom images. In: ISPRS annals of the photogrammetry, remote sensing and spatial information sciences. Zürich, Switzerland
4. Gu X, Fan Z, Zhu S, Dai Z, Tan F, Tan P (2020) Cascade cost volume for high-resolution multi-view stereo and stereo matching. In: Proceedings of the IEEE conference on computer vision and pattern recognition, pp 2495–2504
5. Hirschmuller H (2005) Accurate and efficient stereo processing by semi-global matching and mutual information. In: 2005 IEEE computer society conference on computer vision and pattern recognition (CVPR'05), 2:807–814. <https://doi.org/10.1109/CVPR.2005.56>

6. Hu Y, Tao V, Croitoru A and (2004) Understanding the rational functional model: methods and application. *Int Arch Photogramm Remote Sens* 20(6):119–124
7. Huang P, Matzen K, Kopf J, Ahuja N, Huang J (2018) DeepMVS: learning multi-view stereopsis. In: 2018 IEEE/CVF conference on computer vision and pattern recognition, pp 2821–30. <https://doi.org/10.1109/CVPR.2018.00298>
8. Jensen R, Dahl A, Vogiatzis G, Tola E, Aanæs H (2014) Large scale multi-view stereopsis evaluation. In: 2014 IEEE conference on computer vision and pattern recognition, pp 406–413. <https://doi.org/10.1109/CVPR.2014.59>
9. Ji M, Gall J, Zheng H, Liu Y, Fang L (2017) SurfaceNet: an end-to-end 3D neural network for multiview stereopsis. In IEEE international conference on computer vision (ICCV), pp 2326–2334
10. Sun J, Zheng N-N, Shum H-Y (2003) Stereo matching using belief propagation. *IEEE Trans Pattern Anal Mach Intell* 25(7):787–800. <https://doi.org/10.1109/TPAMI.2003.1206509>
11. Klaus A, Sormann M, Karner K (2006) Segment-based stereo matching using belief propagation and a self-adapting dissimilarity measure. In: 18th international conference on pattern recognition (ICPR'06), vol 3, pp 15–18. <https://doi.org/10.1109/ICPR.2006.1033>
12. Knapitsch A, Park J, Zhou Q-Y, Koltun V (2017) Tanks and temples: benchmarking large-scale scene reconstruction. *ACM Trans Graph* 36(4):78:1–78:13. <https://doi.org/10.1145/3072959.3073599>
13. Liu J, Ji S (2020) A novel recurrent encoder-decoder structure for large-scale multi-view stereo reconstruction from an open aerial dataset. In: Proceedings of the IEEE/CVF conference on computer vision and pattern recognition, pp 6050–6059
14. Mei X, Sun X, Dong W, Wang H, Zhang X (2013) Segment-tree based cost aggregation for stereo matching. In: 2013 IEEE conference on computer vision and pattern recognition, pp 313–20. <https://doi.org/10.1109/CVPR.2013.47>
15. Ronneberger O, Fischer P, Brox T (2015) U-net: convolutional networks for biomedical image segmentation. In: Medical image computing and computer-assisted intervention–MICCAI 2015, pp 234–241. https://doi.org/10.1007/978-3-319-24574-4_28
16. Yao Y, Luo Z, Li S, Fang T, Quan L (2018) MVSNet: depth inference for unstructured multi-view stereo. In: Proceedings of the European conference on computer vision (ECCV), pp 767–783
17. Yao Y, Luo Z, Li S, Shen T, Fang T, Quan L (2019) Recurrent MVSNet for high-resolution multi-view stereo depth inference. In: Proceedings of the IEEE conference on computer vision and pattern recognition, pp 5525–5534
18. Yu D, Ji S, Liu J, Wei S (2021) Automatic 3D building reconstruction from multi-view aerial images with deep learning. In *ISPRS J Photogramm Remote Sens* 171(January):155–170. <https://doi.org/10.1016/j.isprsjprs.2020.11.011>
19. Yu Z, Gao S (2020) Fast-MVSNet: sparse-to-dense multi-view stereo with learned propagation and gauss newton refinement. In: 2020 IEEE/CVF conference on computer vision and pattern recognition (CVPR), pp. 1946–1955. <https://doi.org/10.1109/CVPR42600.2020.00202>
20. Zhang K, Lu J, Lafruit G (2009) Cross-based local stereo matching using orthogonal integral images. *IEEE Trans Circuits Syst Video Techno* 19(7):1073–1079. <https://doi.org/10.1109/TCSVT.2009.2020478>

A Kinematics Analysis of Actuation System Based on DCM Method



Yige Liu and Xiaohua Liu

Abstract The actuator system of gas turbine compressor is composed of several spatial linkages. This study aims to investigate the relationship between the deflection angle of Variable Stator Vane (VSV) and the stroke of hydraulic system using the Direction Cosine Matrix (DCM) method. The actuator system is divided into two parts, and the kinematic models are established respectively. In this work, a motion simulation is carried out to verify the theoretical model. The results show that the theoretical calculation results are completely consistent with the simulation results. This kinematic model can be applied to further optimization of actuation characteristics.

Keywords Gas turbine compressor · Actuator system · Kinematic analysis

1 Introduction

In order to avoid surging and improve stability under variable working conditions, VSVs are commonly used in multistage axial compressor design. The VSVs are driven to rotate by the compressor VSVs' actuator system, deflecting the flow into compressor and adjust the attack angle. If the VSVs' actuator system is not set properly, the blade adjustment angle will deviate greatly from the design point, which will harm the work of gas turbine. Incorrect operation of change setting system of

Y. Liu · X. Liu (✉)
Shanghai Jiao Tong University, Shanghai, China
e-mail: Xiaohua-Liu@sjtu.edu.cn

Y. Liu
e-mail: yige_liu@sjtu.edu.cn

Y. Liu
Shanghai Electric Power Generation Group, Shanghai, China

X. Liu
Key Laboratory (Fluid Machinery and Engineering Research Base) of Sichuan Province, Chengdu, China

variable vanes could make unstable work of compressor and engine. [1] Therefore, it is necessary to optimize the structural parameters of each component in the design stage, to make the stroke of the actuator and the deflection angle of the adjustable stator conform to the law as much as possible. Scholars at home and abroad have done a lot of work in numerical simulation [2–4].

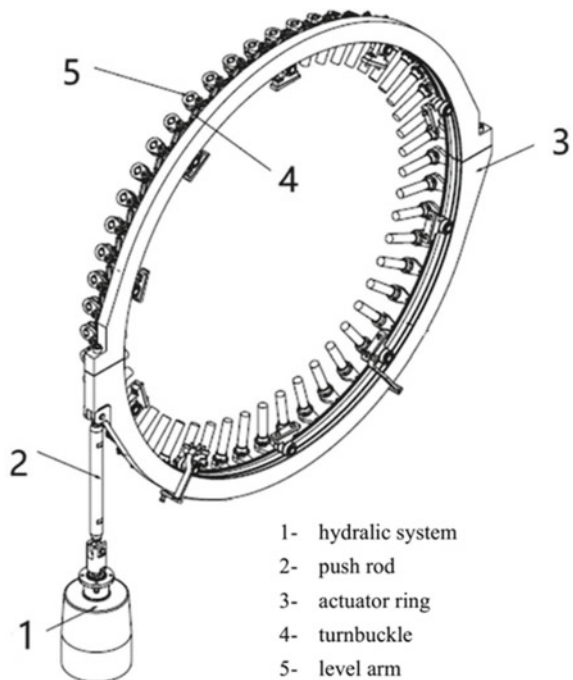
The DCM is formed by the directional cosine between the base vectors of two groups of different orthonormal bases. It is convenient to use DCM in transforming coordinates between the coordinate systems attached to body frame and global frame.

The kinematic model between the deflection angle of the lever arm and the stroke of the hydraulic actuator is established through theoretical derivation using the DCM method in this paper, which provides a theoretical reference for the further optimization design of the actuator system. Motion analysis with Simcenter 3D Motion is applied to prove the validity of the kinematic model.

2 Actuator System and Kinematic Model

The actuator system of a certain type gas turbine is composed of hydraulic system, pushrod, actuator ring, turnbuckle, level arm, and other parts, referring to Fig. 1.

Fig. 1 Structure of actuator system



In the working process of the actuator system, each component has a small deformation; rigid body hypothesis is suitable for the analysis.

In order to analyze the motion law of the multi-body system, it can be decomposed into two closed-loop systems, namely, the VSV-Lever-turnbuckle-Actuator Ring and Actuator Ring-Pushrod-Hydraulic System.

2.1 VSV-Lever-Turnbuckle-Actuator Ring and Kinematic Model

The VSV-Lever-Turnbuckle-Actuator Ring part can be regarded as a closed-loop spatial linkage mechanism, including 2 revolute joints on the VSV and Actuator Ring and 2 spherical joints on the both ends of the turnbuckle. So, it is a RSSR mechanism, as shown in Fig. 2.

The dimensions of the VSV-Lever-turnbuckle-Actuator Ring part and the parameters of the RSSR mechanism are listed in Table 1. *Initial position* means the lever is parallel to the compressor axis.

Fig. 2 Kinematic Model of VSV-Lever-Turnbuckle-Actuator Ring

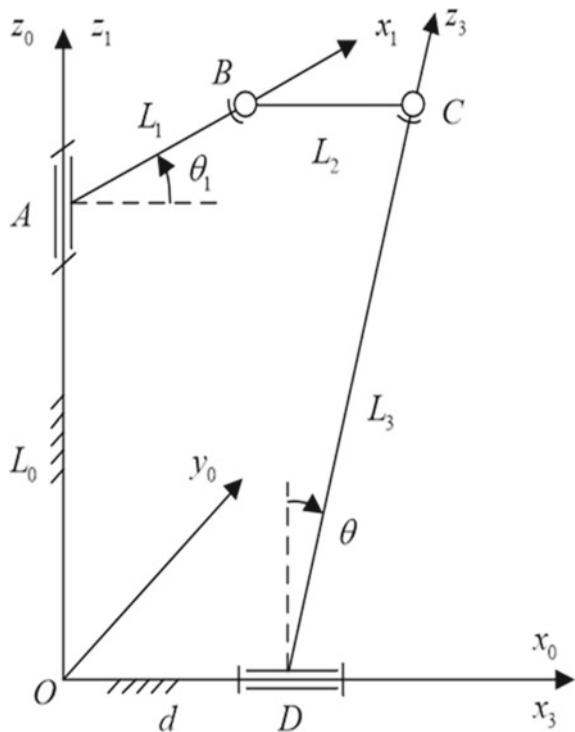


Table 1 Summary of parameters of RSSR mechanism and actual dimensions

Parameters	Name	Unit
L_0	Distance between lever ball head center and GT axis in initial position	mm
L_1	Lever length	mm
L_2	Turnbuckle length	mm
L_3	Distance of ring ball head center to ring centerline	mm
d	Axial distance between vane shaft axis and ring ball center	mm
θ	Vane's deflection angle	°
θ_1	Actuator ring's deflection angle	°

The functional relationship between input angle θ_1 and output angle θ is established by the third-order DCM. For convenience, the sign of input and output angle is determined by the right-hand rule.

For the global coordinate system $Ox_0y_0z_0$, $Ax_1y_1z_1$ can be regarded as the rotation angle θ_1 around the axis Z. Therefore, the DCM for coordinate transformation from coordinate system 1 to 0 is

$$\begin{bmatrix} C_{01}^{\theta_1} \end{bmatrix} = \begin{bmatrix} \cos \theta_1 & -\sin \theta_1 & 0 \\ \sin \theta_1 & \cos \theta_1 & 0 \\ 0 & 0 & 1 \end{bmatrix} \quad (1)$$

Similarly,

$$\begin{bmatrix} C_{03}^{\theta} \end{bmatrix} = \begin{bmatrix} 1 & 0 & 0 \\ 0 & \cos \theta & -\sin \theta \\ 0 & \sin \theta & \cos \theta \end{bmatrix} \quad (2)$$

Since the coordinates of B and C are constrained by the fixed length L_2 of the turnbuckle in the actual motion of the mechanism, the coordinates of B and C need to meet the following equation:

$$|BC| = (x_B - x_C)^2 + (y_B - y_C)^2 + (z_B - z_C)^2 = L_2^2 \quad (3)$$

The coordinates of point B and C can be expressed by input angle θ_1 and output angle θ ,

$$\begin{bmatrix} x_B \\ y_B \\ z_B \end{bmatrix} = \begin{bmatrix} 0 \\ 0 \\ L_0 \end{bmatrix} + \begin{bmatrix} C_{01}^{\theta_1} \end{bmatrix} \begin{bmatrix} L_1 \\ 0 \\ 0 \end{bmatrix} = \begin{bmatrix} L_1 \cos \theta_1 \\ L_1 \sin \theta_1 \\ L_0 \end{bmatrix} \quad (4)$$

$$\begin{bmatrix} x_C \\ y_C \\ z_C \end{bmatrix} = \begin{bmatrix} d \\ 0 \\ 0 \end{bmatrix} + [C_{03}^{-\theta}] \begin{bmatrix} 0 \\ 0 \\ L_3 \end{bmatrix} = \begin{bmatrix} d \\ L_3 \sin \theta \\ L_3 \cos \theta \end{bmatrix} \tag{5}$$

From Eqs. (3)-(5) and rearranging, we have

$$A \sin \theta + B \cos \theta + C = 0 \tag{6}$$

where

$$A = -\sin \theta_1$$

$$B = -\frac{L_0}{L_1}$$

$$C = \frac{L_0^2 + L_1^2 - L_2^2 + L_3^2 + d^2}{2L_1L_3} - \frac{d \cos \theta_1}{L_3}$$

Therefore,

$$\theta = 2 \arctan \frac{A \pm \sqrt{A^2 + B^2 - C^2}}{B - C} \tag{7}$$

The sign \pm in Eq. (7) should be determined according to actual mechanism. In this case, a minus sign is applied in Eq. (7).

2.2 Actuator Ring-Pushrod-Hydraulic System and Kinematic Model

The actuator ring connects the hydraulic system through the pushrod 5 with two revolute joints. Because the hydraulic system moving in a straight line, and the motion planes of several components are parallel to each other, the Actuator Ring-Pushrod-Hydraulic System part can be simplified as a closed-loop planar slider mechanism, as shown in Fig. 3.

The dimensions of the VSV-Lever-Turnbuckle-Actuator Ring part and the parameters of the Planar slider mechanism are listed in Table 2.

For the global coordinate system Dxy , $Dx'y'$ can be regarded as the rotation angle γ around the axis Z . Therefore, the coordinates of point E and F can be expressed by γ

$$\begin{bmatrix} x_{E'} \\ y_{E'} \end{bmatrix} = \begin{bmatrix} \cos \gamma & -\sin \gamma \\ \sin \gamma & \cos \gamma \end{bmatrix} \begin{bmatrix} L_4 \\ 0 \end{bmatrix} = \begin{bmatrix} L_4 \cos \gamma \\ L_4 \sin \gamma \end{bmatrix} \tag{8}$$

Fig. 3 Kinematic Model of Actuator Ring-Pushrod-Hydraulic System

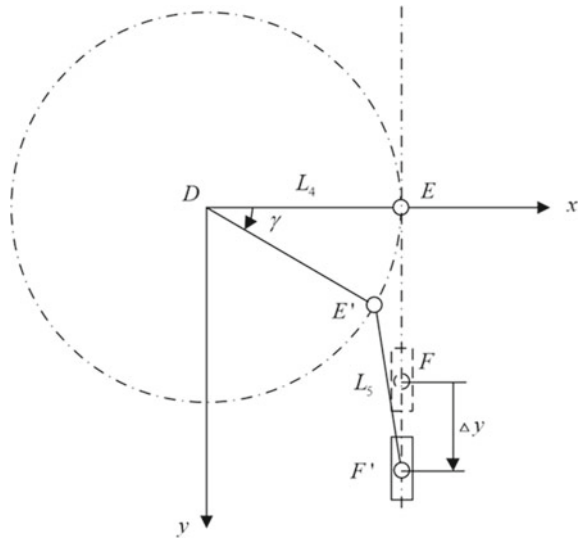


Table 2 Summary of parameters of Planar slider mechanism and actual dimensions

Parameters	Name	Unit
L_4	Distance between Pushrod application point and GT axis	mm
L_5	Pushrod length	mm

$$\begin{bmatrix} x_{F'} \\ y_{F'} \end{bmatrix} = \begin{bmatrix} L_4 \\ L_5 \end{bmatrix} + \begin{bmatrix} 0 \\ \Delta y \end{bmatrix} = \begin{bmatrix} L_4 \\ L_5 + \Delta y \end{bmatrix} \tag{9}$$

Similarly, the coordinates of E' and F' are constrained by the fixed length L_5 of the connecting rod in the actual motion of the mechanism, the coordinates of E' and F' need to meet the following equation:

$$|E'F'| = (x_{E'} - x_{F'})^2 + (y_{E'} - y_{F'})^2 = L_5^2 \tag{10}$$

From Eqs. (3)-(5) and rearranging, we have

$$\Delta y^2 + D\Delta y + E = 0$$

where

$$D = 2(L_5 - L_4 \sin \gamma)$$

$$E = 2L_4^2(1 - \cos \gamma) - 2L_4L_5 \sin \gamma$$

Table 3 Parameters of a certain actuator system

Parameters	Value	Unit
L_0	600	mm
L_1	80	mm
L_2	35	mm
L_3	600	mm
L_4	685	mm
L_5	400	mm
D	80	mm

Therefore,

$$\Delta y = \frac{-D \pm \sqrt{D^2 - 4E}}{2} \tag{11}$$

The sign \pm in Eq. (10) should be determined according to actual mechanism. In this case, a minus sign is applied in Eq. (10).

In the initial position, where input angle in RSSR mechanism $\theta_1 = 0$. The corresponding output angle is recorded as θ_{ini} . Then the input angle of the second closed-loop system

$$\gamma = \theta - \theta_{ini} \tag{12}$$

From Eqs. (7)–(11) and (12), we have the kinematic model between actuator system stroke and VSVs deflection angle.

3 Motion Analysis with Simcenter 3D Motion

Considering a certain type of gas turbine actuator system. The actuator system’s parameters are listed in Table 3.

The results of *Strokes* in different input angles obtained from the kinematic model and motion simulation are in good agreement, as shown in Fig. 4. Therefore, the theoretical analysis model established in this paper is credible.

4 Conclusion

1. By dividing the adjustable vane actuator into two parts and abstracting it into a connecting rod mechanism and a slider mechanism, the kinematic model of the VGV’s deflection angle and the stroke of the hydraulic system is established by DCM method.

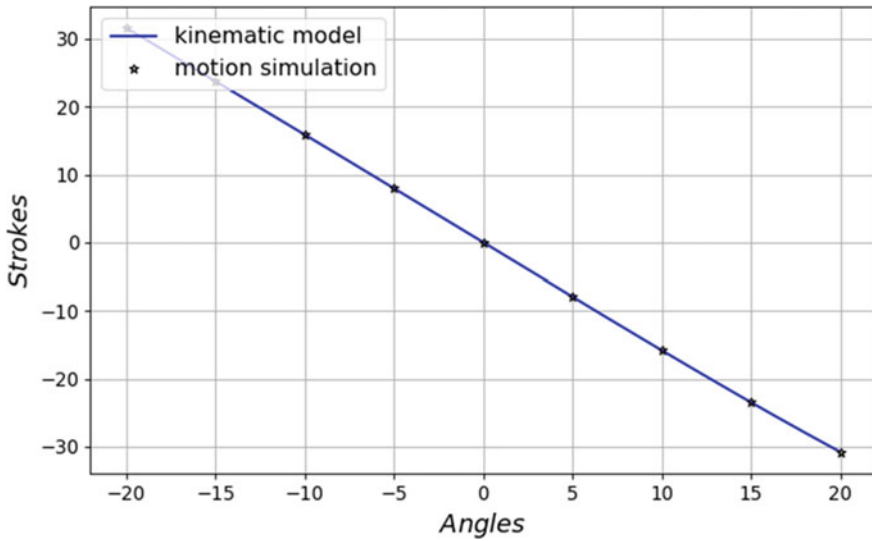


Fig. 4 The results of kinematic model and motion simulation

2. The correctness of the kinematic model is verified by numerical simulation using Simcenter 3D software.
3. This model reveals the role of the structural parameters in the actuation process and provides a theoretical model for further optimizing the characteristics of the actuator.

Acknowledgements This work is partially supported by National Natural Science Foundation of China (No.51976116), Natural Science Fund of Shanghai (No.19ZR1425900), and the Open Research Subject of Key Laboratory (Fluid Machinery and Engineering Research Base) of Sichuan Province (No. rszjj2019022).

References

1. Wirkowski P (2007) Influence of changes of axial compressor variable stator vanes setting on gas turbine engine work. In: V international scientifically-technical conference POLISH CIMAC Explo-Diesel & Gas Turbine'07, vol 2007, pp 511–518
2. Liang S, Yin X, Wang H (2016) Parametric design of stator blade jointly adjusting mechanism based on ADAMS. *Aeroengine* 42(1):65–69. (in Chinese)
3. Yu J, Sun J, Ji F et al (2019) Motion analysis and optimization of jointly adjusting mechanism of aero-engine stator vane. *J Aerosp Power* 34(6):1193–1200
4. Hu M, Zheng L (2014) Simulation analysis of single-stage variable stator vane system based on CATIA and ADAMS. *Aeronauti Manuf Technol* 22(8):98–101. (in Chinese)

Al-Mg-Sc (1570) Alloy Structure Formation Process



V. M. Greshnov, F. F. Safin, R. I. Shaikhutdinov, and I. R. Yanova

Abstract The way of metalworking of one Al-Mg-Sc aluminum alloy is presented. Steps for achieving required structural properties are shown. The results of plastic deformation modeling and microstructure experiments from preproduction stamping are given.

Keywords Metalworking · Strain hardening · Plasticity · Constitutive equations · Aluminum alloys

1 Introduction

In improving aircraft details performance new alloys are constantly being developed. A number of requirements are imposed on aluminum alloys in aircraft structures, such as weldability, corrosion resistance, decent amount of plasticity, metallurgy, and machine-tool manufacturability, and heat resistance. Of course, ready product should have great strength properties. Recently, research and development by specialists from RSC Energia, OJSC VILS, together with Kamensk-Uralsky Metallurgical Plant, and a number of other organizations, have made it possible to develop and introduce into production a new aluminum thermally unhardened corrosion-resistant alloy 1570 of the Al-Mg-Sc system [1, 2].

From alloy 1570, in particular, large-sized, geometrically complex, power stamped-welded structures with a minimum flight weight were made. Also, alloy 1570 in the form of forgings was used in the construction of spacecraft for power parts (beams, brackets) of the instrument compartment. High performance of sheets made of alloy 1570 in large-sized welded tanks was established. Alloys of the Al-Mg-Sc have decent strength characteristics which makes them especially good as a structural material.

V. M. Greshnov · F. F. Safin · R. I. Shaikhutdinov (✉) · I. R. Yanova
Ufa State Aviation Technical University, Ufa, Russia

V. M. Greshnov
e-mail: Greshnov_VM@list.ru

Thus, the urgent task is to search for opportunities for additional technological hardening of the alloy in the manufacture of products from it.

Since the alloy 1570 is not thermally hardened, the only way of hardening is strain hardening thermomechanical treatment using the mechanisms of dislocation and grain boundary hardening. In this regard, it is of interest to obtain a microcrystalline structural state of the alloy (grain size 0.2–5.0 μm) using large and severe deformation, when grain-boundary hardening makes a significant contribution.

To tackle this task, we investigated structural properties of the 1570 alloy imposed by plastic deformation, and suggested steps for achieving required properties. With the usage plastic deformation simulating we have found the rational stamping procedure. After obtaining blanks, we examined its properties, and microstructure as well as for ready part manufactured from that blanks. The paper reports results of the study.

2 Materials and Methods

Initially, the workpieces were hot-pressed 1570 alloy rods with diameters of 30 and 40 mm. The chemical composition of the alloy is given in Table 1.

Mechanical properties were defined on classic tensile, and compression tests under elevated temperatures on Instron 5982. Initial state mechanical properties are collected in Table 2. Temperature monitoring was performed with the usage of the device Center 306. Temperature fluctuations over the furnace volume did not exceed ± 5 °C. The traverse speed was 2 mm/min. The average strain rate was 4.3

Table 1 Chemical composition of 1570 alloy

Al	Base
Ni	0.01–0.05
Be	0.0001–0.005
Mg	5.6–6.3
Sc	0.18–0.3
Zr	0.05–0.12
Cr	0.05
Ti	0.01–0.03
Fe + Si	0.05–0.2
Co	0.01–0.05

Table 2 Mechanical properties of 1570 in initial state

T, °C	Yield stress, MPa	UTS, MPa	Elongation, %	Area contraction, %
20	300	440	20	40

$\times 10^{-3} \text{ s}^{-1}$. These experiments were conducted on the equipment of the collective use center “Nanotech”.

The study of the influence of the modes of thermomechanical processing on the mechanical properties, and structure was carried out using a hydraulic press for isothermal stamping with a nominal force 6.3 kN.

Electron microscopic studies of the fine structure of the samples were carried out using a JEOL JEM-2100 transmission electron microscope in bright, and dark fields at magnifications of $\times 5000$, $\times 8000$, $\times 15,000$. Thin samples (foils) were used for the analysis. In order to obtain foils, plates were cut out on an electroerosive wire-cutting machine with a thickness of 0.3 mm, followed by mechanical thinning to a thickness of 0.15 mm. The surface of the obtained samples was prepared by electropolishing ($T = -25 \dots 30 \text{ }^\circ\text{C}$, $U = 20 \text{ V}$) on a Struers TenuPol-5 installation in a solution of 30% nitric acid with H_2O and 70% methanol (CH_3OH).

Simulating of plastic deformation was conducted on SFTC Deform-3D software where finite element method is implemented for the classical boundary problem of 3D equilibrium equations for plasticity problems.

The theory of irreversible plastic deformation [3, 4] was applied for dislocation density, grain size, and yield stress prediction. For dislocation density, and grain size predictions the following formulae are used, respectively:

$$\rho_S = \beta m G b \left(\frac{(\lambda b)^{-1} (\exp(\varepsilon) + \rho_{s0} + A\varepsilon)}{\exp(\varepsilon)} \right)^{0.5},$$

where ε —deformation intensity; G —shear modulus, ρ_{s0} —initial dislocation density, b —Burger’s vector; β , λ , A —model constants. One needs to look [3, 4] for further details.

$$d = 10/\sqrt{\rho_S}$$

3 Results and Discussion

It is known that the hardening of metal during thermomechanical treatment with the use of high strain rates occurs due to two mechanisms—dislocation hardening, and grain-boundary hardening with the dispersion of structural components, mainly due to significant grain refinement (linear grain size $d = 0.3\text{--}5.0 \text{ }\mu$), and at the same time, an increase in the area of grain and subgrain boundaries. According to the Hall–Petch’s law a decrease in the grain size leads to an increase in the flow stress.

Since the 1570P alloy is not thermally hardened, the only hardening technology is plastic structure formation. Thus, the problem of plastic structure formation of the

alloy is formulated as follows: using the ranges of large and severe plastic deformation, it is necessary to transform the initial inhomogeneous microstructure of the alloy with an average linear grain size of microns into a microcrystalline structure with equiaxed grains with an average linear size of the order of 1.0–1.5 μ .

In this case, the workpieces must be deformed in such a way that, after plastic processing, the shape and dimensions of the workpieces remain the same (before processing). The finer grain should provide improved room temperature toughness characteristics.

Taking into account the conditions of small-scale production and patent research, the following metalworking procedures are proposed, which are illustrated in Fig. 1.

The temperature regime was chosen, dies are designed, and preproduction stamping was performed (Fig. 2).

Deform 3D stamping procedure plastic deformation results are given in Fig. 3. The theoretical grain size and yield stress estimation are obtained (Fig. 4). For calculations the following model constants were used: $\rho_{s0} = 7.5 \cdot 10^{10} \text{ sm}^{-2}$, $\lambda = 1.6 \cdot 10^{-4} \text{ sm}$, $A = 5.1 \cdot 10^{10} \text{ sm}^{-2}$, $\beta = 0.4$, $m = 3.1$, $b = 3 \cdot 10^{-8} \text{ sm}$. Shear modulus for alloy at $T = 20 \text{ }^\circ\text{C}$ was equal to $G = 2700 \text{ MPa}$.

The end result of stamping was used to manufacture a part, and its mechanical properties, grain size, and microstructure were examined. The result of examination is illustrated in Figs. 5 and 6.

4 Conclusion

Analysis of the above results shows that proposed stamping steps of plastic structure formation stably ensures the production of cylindrical billets with diameters of 30 and 40 mm and lengths of 165–190 mm in a microcrystalline structural state (grain size 0.2–0.35 microns) (200–350 nm) with the presence of nanoscale (100 nm) grains and particles. This microcrystalline structure provides an increase in the static strength characteristics at $T = 20 \text{ }^\circ\text{C}$: $\sigma_Y = 370 \dots 540 \text{ MPa}$; $UTS = 557 \text{ MPa}$ with enough characteristics of plasticity for further metal forming manufacturing. In this case, the main mechanisms of hardening are dislocation and grain-boundary ones. The results of this work formed the basis of a patent №201,712,069 in Russia “Method of plastic structure formation of cylindrical dimensional blanks”.

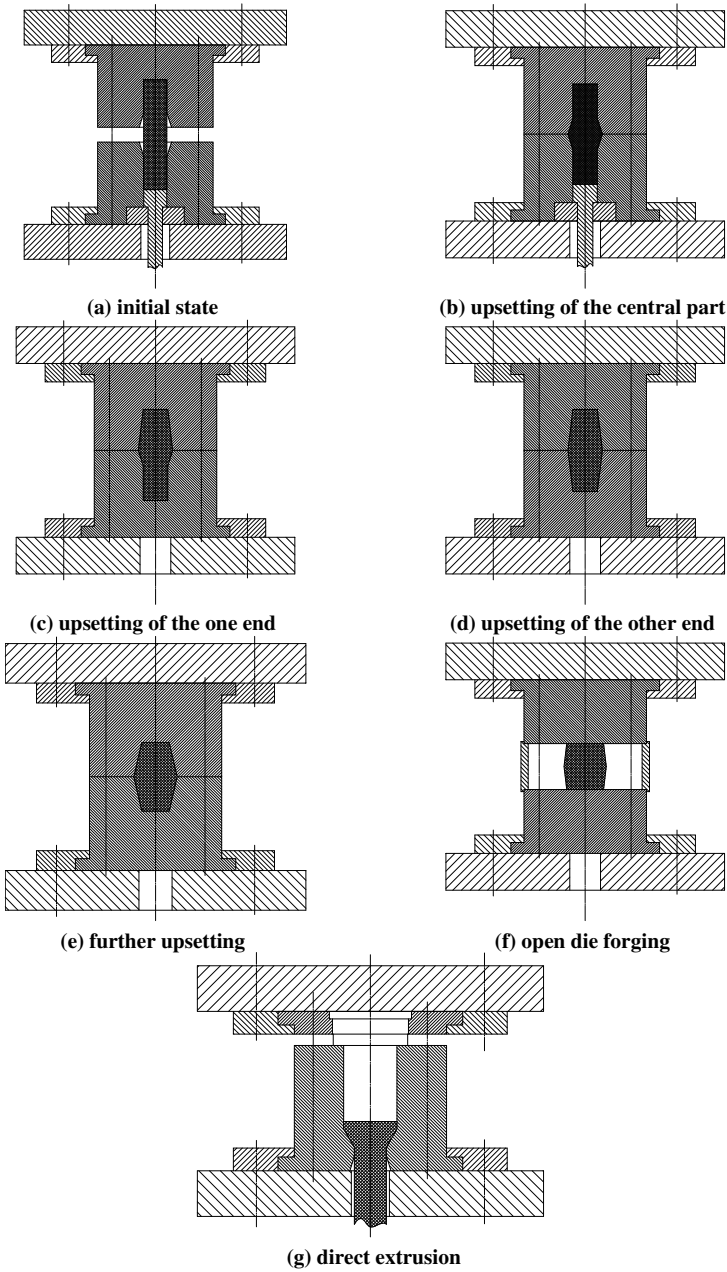
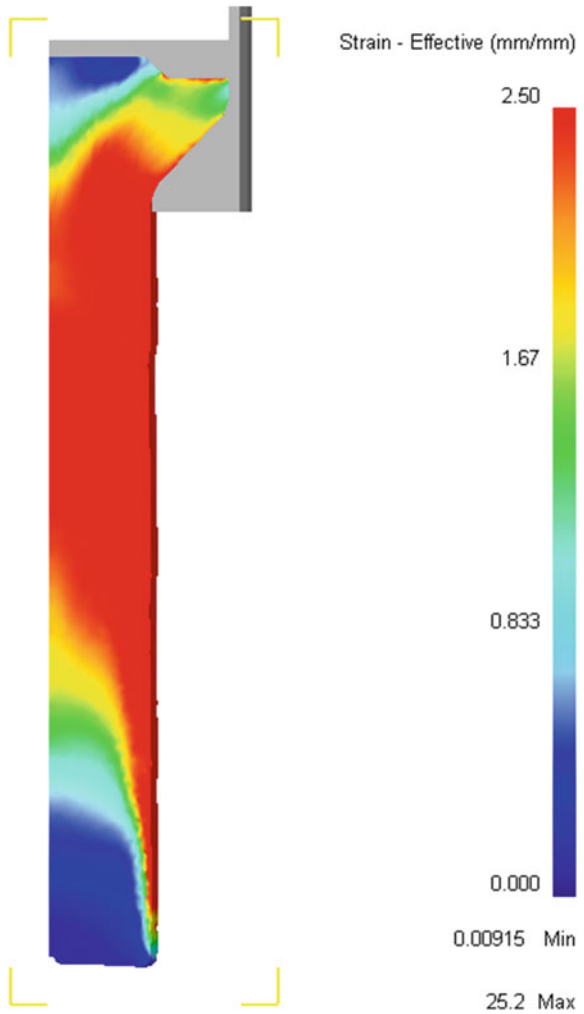


Fig. 1 Stamping steps proposed



Fig. 2 Some stamping steps results

Fig. 3 Deformation intensity after extrusion



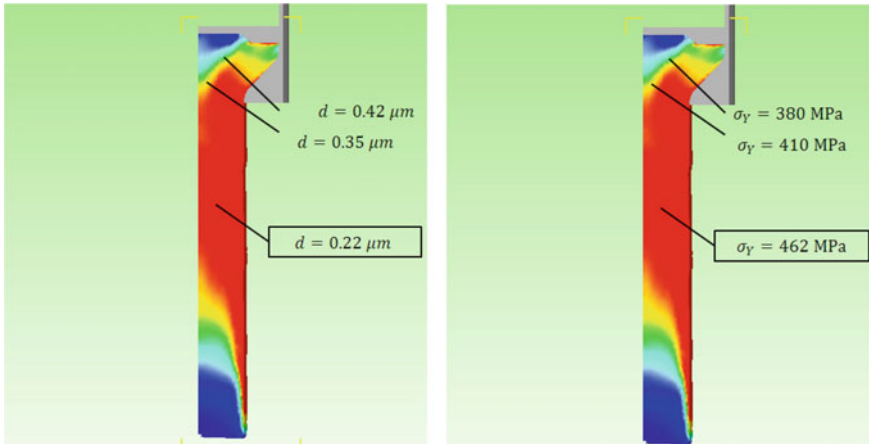


Fig. 4 Theoretical estimation of grain size, and yield stress

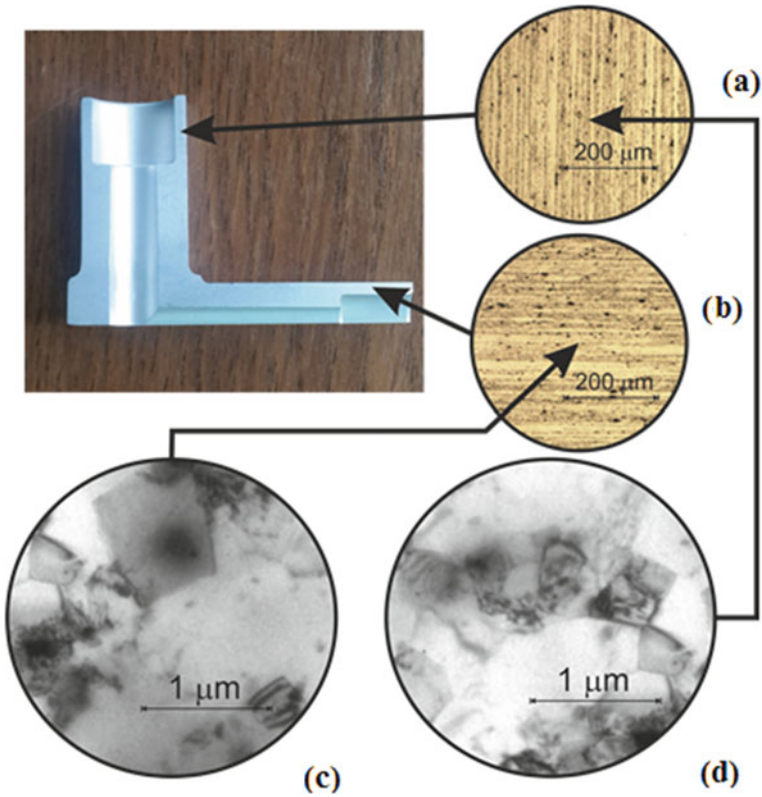


Fig. 5 Macro- and microstructure of a part: magnification in an optical microscope X10 (a, b); magnification in a transmission electron microscope X5000 (c, d)

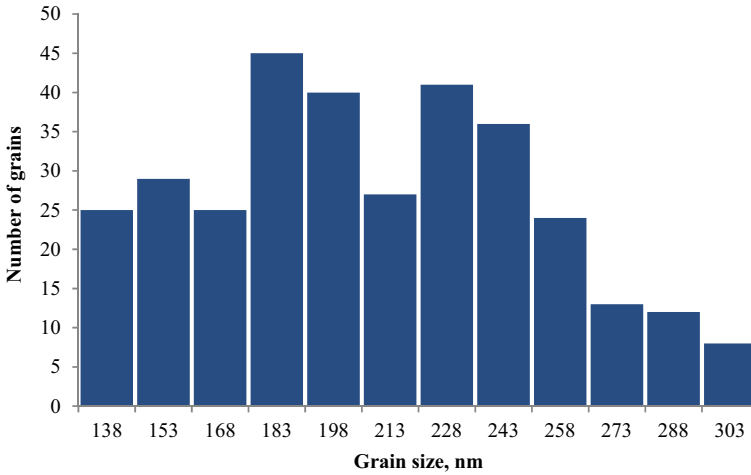


Fig. 6 Grain size distribution on chosen spots of the part

References

1. Bronz AV, Efremov VI, Plotnikov AD, Chernyavskii AG (2014) Alloy 1570C—a material for hermetic constructs of the perspective reusable products of RSC Energia. *Kosm Tekh Tekhnol* 4:62–67
2. Filatov YuA, Plotnikov AD (2011) Structure and properties of deformed semi-finished products from aluminum alloy 01570C of the Al–Mg–Sc system for the RSC Energia product. *Tekhnol Legk Splavov* 2:15–26
3. Greshnov VM (2018) Physical and mathematical theory of large irreversible deformations of metals. Fizmatlit, Moscow
4. Greshnov VM (2013) Foundations of the physical and mathematical theory of irreversible deformations of metals. Structural and phenomenological approach. Palmarium Academic Publishing, Chicinau, Saarbrücken

Verifying Aluminum-Air Fuel Cell for Unmanned Aerial Vehicle During Operation in the Field



Elizaveta S. Ryzhova , Konstantin V. Pushkin, and Ejen Gurev

Abstract This work describes the effects of changes in water based electrolyte composition on the performance of the aluminum-air chemical current source. A study of the operation of a power source was carried out on the basis of various water samples from publicly available sources. The possibility of using a power plant with an aluminum-air chemical current source in the field has been confirmed.

Keywords Aluminum-air · Chemical current source · Fuel cell · Power plant · UAV

1 Introduction

There is a growing trend in the market for services [1] using unmanned aerial vehicles (UAVs). The modern development of aerospace technology requires the creation of new highly efficient, environmentally friendly autonomous energy sources, including for UAVs. At the moment, the problem of creating a UAV without an internal combustion engine, which involves noise, interference, vibration, fire hazard, but with the use of electric motors, remains urgent. The electric motor and its chemical current source are less explosive, practically do not emit thermal radiation, and have a lower mass. Reducing the mass of the UAV is possible with the use of advanced energy sources. Lithium-ion batteries are widely used as energy sources, but fuel cells—primary chemical energy sources—are lighter. Among the fuel cells, air-aluminum fuel cells (AA FC) have high energy characteristics, which are also the safest to use and promising for development and use on UAVs.

E. S. Ryzhova (✉)

Department of Aircraft Design, Shanghai Jiao Tong University, Shanghai, China

e-mail: Lishen-rishowa@sjtu.edu.cn

E. S. Ryzhova · K. V. Pushkin · E. Gurev

Department of Aircraft Engineering, Moscow Aviation Institute, Moscow, Russia

2 Purpose of the Study

The main component of the electrolyte for AA FC is water. Before the start of this study, it was assumed that for the operation of AA FC in a UAV, and it is possible to use water from rivers, melted snow, water pipes, wells, rainwater, etc., thereby reducing the transferred mass of consumable components of AA FC.

The purpose of this work is to test the performance of the AA FC for UAVs when operating on alkaline electrolytes prepared from water available in field conditions.

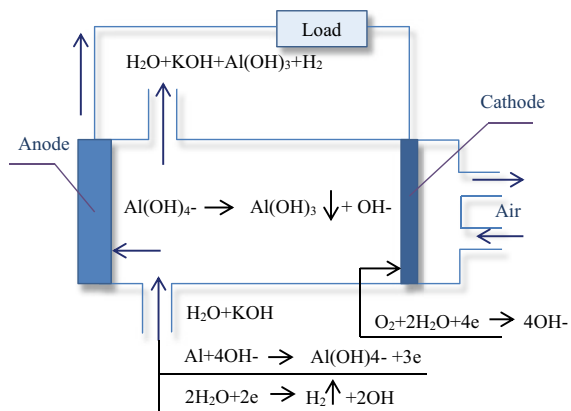
3 How the AA FC Works

The possibility of an electrochemical reaction between aluminum and oxygen with the generation of electricity is provided in an electrochemical cell (Fig. 1), in which aluminum is immersed in an electrolyte and used as an anode, and oxygen is supplied to a special gas diffusion cathode, which capable of passing gaseous oxygen, but impermeable to the electrolyte.

4 Selection of Components for AA FC

The minimum polarization and the most negative value of the anode potential, as well as the minimum corrosion of the anode, are the main criteria in the search for the best anode components. In studies [2] MAI showed that it is promising to use hosted pure aluminum A995 in such an installation. But its corrosion in purely alkaline electrolytes is high, so it must be suppressed by the introduction of inhibitors [4]. After research [3], the following anode-electrolyte combination was identified as the

Fig. 1 Schematic diagram of air-aluminum fuel cell

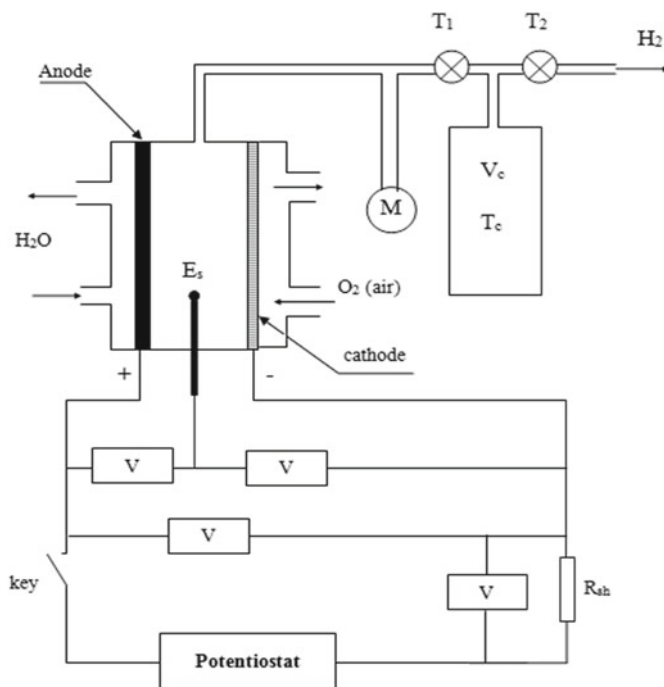


best: A995 + 4M KOH solution + tartrate ion. Electrolytes for the experiments were made on the basis of water samples from different regions of Russia.

5 Methods

Figure 2 shows an experimental setup.

Currently, there are no direct methods for measuring the corrosion rate of the anode. Volumetric and mass methods were used to determine corrosion in this work.



- H_2O – water from the thermostat;
- T_1, T_2 – gas taps;
- M – manometer;
- V_c – calibrated volume;
- T_c – temperature in a calibrated volume;
- E_s – reference electrode;
- R_{sh} – measuring shunt;
- V – voltmeters placed in the circuit.

Fig. 2 Experimental setup

The amount of hydrogen released during the reaction depends on the amount of corroded metal. The corrosion current density is determined by the formula.

Displayed equations are centered and set on a separate line.

$$j_{\text{corr}} = \frac{2 \cdot 9,81 \cdot \Delta P \cdot V_T \cdot F}{R \cdot T_T \cdot S \cdot \Delta \tau} \quad (1)$$

The gravimetric method is used to measure the mass loss of the electrode while in the electrolyte.

Then the average corrosion current density is calculated by the ratio

$$\overline{j_{\text{corr}}} = \frac{3 \cdot F \cdot W_K}{\mu_{Al}} \quad (2)$$

Next, we get indirect values from the measurement results, which are subsequently processed.

The discharge current density is determined by the formula

$$j = \frac{I}{S} \quad (3)$$

The corrosion rate is calculated by the formula

$$W_K = \frac{m_{al}^0 - m_{al}^k - M_{al}^{CF}}{S \cdot \tau} \quad (4)$$

The potentials of the electrodes were converted to a standard hydrogen scale in accordance with equation:

$$\phi_{\text{SHE}} = \phi_{\text{Ag/Cl}} + E \quad (5)$$

In statistical processing, a confidence level of 95% is accepted. The approximating equation was found by the least squares method.

Table 1 shows the numbering of the electrolytes used for experiments based on different water samples.

In the course of the study, the dependences “current (current density) potential” were plotted for samples of anodes and cathodes used in experiments when working with electrolytes based on various water samples. To obtain more accurate results, each experiment was carried out at least three times. Based on the results obtained, graphs of current–voltage characteristics for anodes (Fig. 3) and cathodes were built.

The results were processed by the methods of mathematical statistics, and the confidence intervals were determined. Based on the average values of the anodic and cathodic potentials for each electrolyte, a graph of the dependence of the total voltage across the cell on the current was built (Fig. 4).

Table 1 Water samples

	A. Urban polluted environment	B. Outside the city	C. Sparsely populated and slightly polluted cities	
1. Tap water	1A	1B	1C	–
2. Melted snow	2A	2B	2C	–
3. Water from rivers and lakes	3A	3B	3C	–
4. Distilled water	–	–	–	4

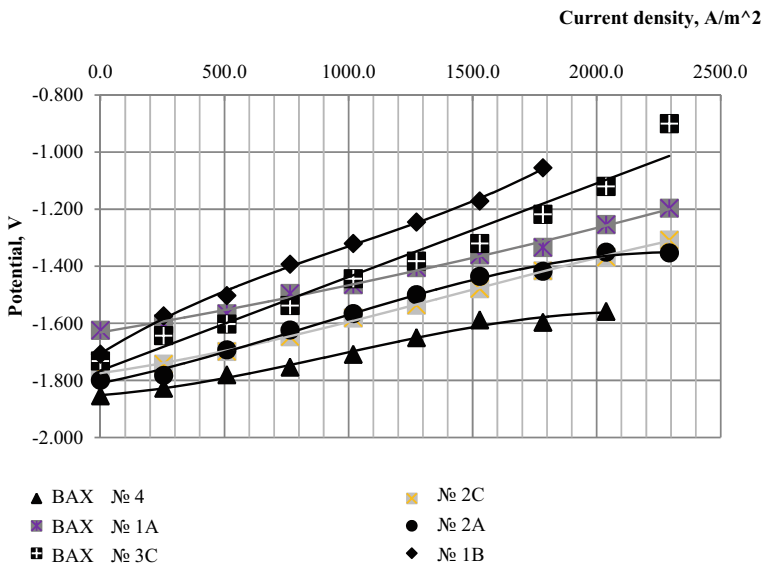


Fig. 3 Volt-ampere characteristics of the anode

Using an emission spectrometer, the composition of water samples was analyzed for the content of metallic elements in order to determine their possible effect on the energy characteristics of AA FC.

Alkalis easily dissolves the protective oxide film on the aluminum surface, and it begins to react with water, as a result of which the metal dissolves with the release of hydrogen (aluminum corrosion with hydrogen depolarization). To increase the usefulness of aluminum, it is necessary to reduce the rate of corrosion. Therefore, in the course of the experiments, the volume of hydrogen evolution was monitored, and the dependences of the corrosion current density on the discharge current density were also plotted (Fig. 5).

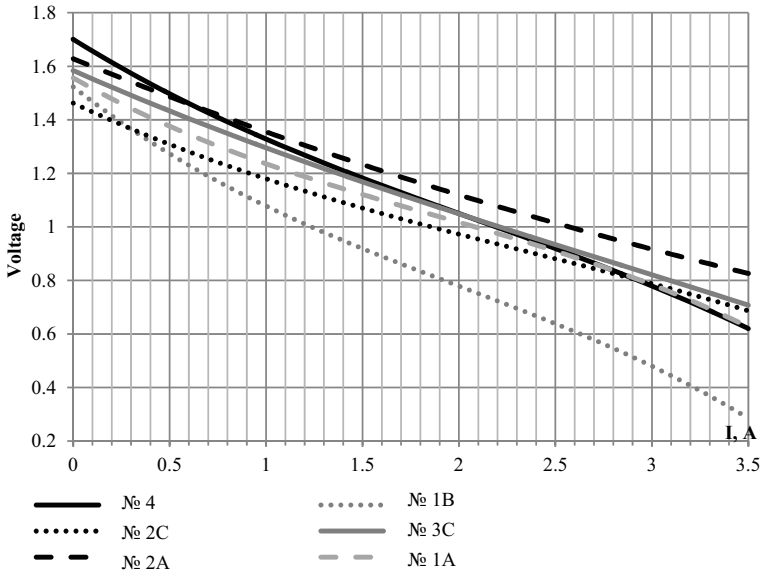


Fig. 4 Total cell voltage

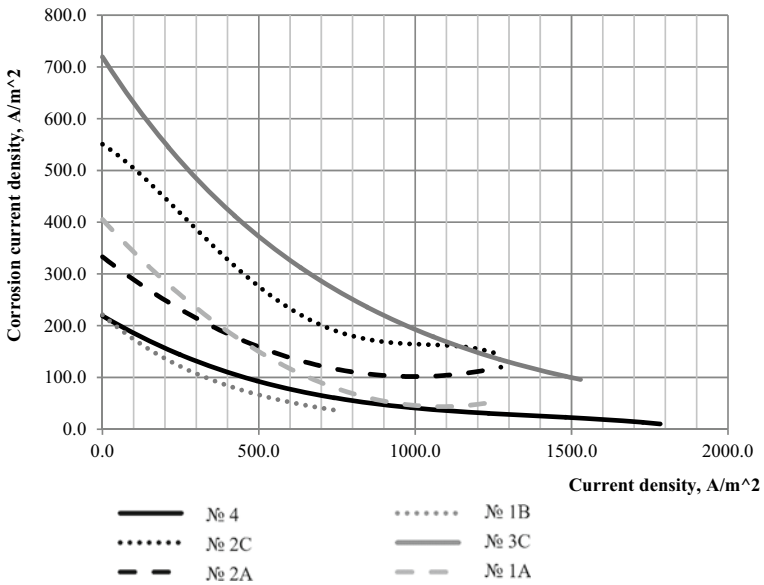


Fig. 5 Corrosion

6 Results

Based on the results of the study, it was concluded that water taken from generally available sources for the preparation of electrolyte in the field affects the energy characteristics of AA FC. The polarization of the anode increases when working in electrolytes prepared on the basis of tap water. These samples show a high content of calcium and sulfur. Water samples taken in a polluted urban environment increase the cathode polarization. Such samples have a high content of rhodium and rubidium. The composition of all electrolyte samples influenced the increase in the corrosion of the anode.

7 Conclusion

For unmanned aerial vehicles, it is possible to prepare electrolytes for AA FC in the field. The use of water from melted snow is optimal since the characteristics of AA FC when operating in electrolytes based on it correspond to the performance characteristics when using pure electrolytes based on distilled water.

Acknowledgements This work was partially supported by Department 908 “Physical Chemistry” and Department 208 “Rocket electric motors, power and energy-physical installations” of the Moscow Aviation Institute. The authors are also grateful to Sevruck SD and Farmakovskaya A.A. for advice, support, and useful recommendations for improving the work.

References

1. MarketsandMarkets Research Private Ltd. (2019) Unmanned Aerial Vehicle (UAV) Market by vertical, class, system, industry (Defense & Security, Agriculture, Construction & Mining, Media & Entertainment), Type, mode of operation, range, point of sale, MTOW and region-global forecast to 2025. <https://www.marketsandmarkets.com/Market-Reports/unmanned-aerial-vehicles-uav-market-662.html>. Accessed 20 April 2020
2. Okorokova NS, Pushkin KV, Sevruck SD, Farmakovskaya AA (2012) The modeling of physical and chemical processes in the current sources with an aluminum anode of the power plants for aerospace systems. *Aerospace MAI J* 5:65–71
3. Pushkin KV, Sevruck SD, Okorokova NS, Farmakovskaya AA (2018) The most efficient corrosion inhibitors for aluminum anode of electrochemical cell used as a controlled hydrogen generator. *Periodico Tche Quimica* 414–425
4. Ryzhova ES (2017) Study of the influence of the prospective organic corrosion inhibitor of the aluminum anode on the characteristics of the hydronic chemical current source. *Gagarin Readings 2017: Abstracts*, Moscow, April 05–19, 2017. Moscow Aviation Institute (National Research University), Moscow, pp 593–594

Design Methodology Based on the RFLA Approach



Ezhen Gurev, Alexander Dolotovskiy, Maria Voitishina, and Dmitry Slezkin

Abstract Throughout the entire existence of avionics, the role of software in aircraft systems was constantly increasing, and the aircraft systems themselves are becoming more and more complex, while the complexity increases not only in the implementation but also in the integration of systems.

This has led to the conclusion that on-board software is to be developed by large teams, and the mutual influence of hardware and software, as well as various subsystems, must be taken into account. Inevitably, the projects began to face the following difficulties:

- Dependence on bench software, simulators, and physical prototypes;
- Communication both within the development team and between teams and businesses;
- Opacity of the relationship between the initial requirements and the result;
- Avalanche-like increase in the complexity of the source code;
- High costs for system verification and validation;
- Problems with the qualification of heterogeneous development tools.

The solution to these difficulties is the use of model-based design, which is a modern approach to the development of large, complex, and highly reliable systems. The essence of the method is the systematic application of models at all stages of the product life cycle, from design to implementation. In the course of development, models of systems and subsystems are created at different levels of the hierarchy,

E. Gurev (✉)

Moscow Aviation Institute (National Research University), Moscow, Russia

e-mail: EE_Gurev@ssj.irkut.com

E. Gurev · A. Dolotovskiy · M. Voitishina · D. Slezkin

Regional Aircraft–Branch of the Irkut Corporation, Moscow, Russia

e-mail: A_Dolotovskiy@ssj.irkut.com

M. Voitishina

e-mail: M_Voytishina@ssj.irkut.com

D. Slezkin

e-mail: D_Slyozkin@ssj.irkut.com

including models of both the physical part and the algorithms themselves. Such models are used to evaluate the interaction of the algorithm, the physical part, and the external environment. This allows to validate and verification algorithms at the early stages of the project without the use of physical prototypes.

With model-oriented design, the following results are achieved:

There is a need to fully convey to the supplier the requirements for the developed aircraft system or component.

Distribution of responsibility between the integrator and the supplier. As a result, the correct certification in accordance with P-4754A [1, 2].

Reduction of labor costs and time for algorithms implementation on the target microprocessor platform, due to automatic program code generation (for example, using MATLAB, Simulink).

Validation of system requirements by creating a system model and performing tests on it.

Debugging and testing algorithms at the system model level, which ensures that most development errors are found at the preliminary design stage, rather than at the product prototype testing stage.

Traceability of requirements, model, program code, and test scenarios, which is one of the conditions for compliance with industry standards for embedded systems development.

Keywords MBSE · Aircraft design · Requirements · Functions · Logic · Architecture · RFLA

1 Introduction

This research paper describes the approach to the development of aircraft and aircraft systems, the definition of requirements, functions, logic, and architecture of aircraft and its systems.

The methodology applies to all departments involved in the development and/or certification/life cycle processes of on-board systems and aircraft systems.

This methodology can be the basis for the development of plans, standards, and techniques in accordance with ARP-4754A, DO-178C, and DO-331, as well as requirements and instructions to suppliers for the development of software for on-board systems and aircraft systems [3, 4].

The term “Architecture” in this article should be understood as design, constructive, or organizational solutions established to achieve the goal, changes in which require the return of the development process to the previous stage of the life cycle.

2 Model-Oriented Design for the Development of Complex Systems in Accordance with DO-178C and DO-331

Model-oriented design is a modern approach to the development of large, complex, and highly reliable systems. The essence of the method is the systematic application of models at all stages of the software life cycle, from design to implementation. In the course of development, in accordance with this approach, models of systems and subsystems are created at different levels of the hierarchy, including models of both the physical part and the algorithms themselves. Such models are used to evaluate the interaction of the algorithm, the physical part, and the external environment. Also, validation and verification of algorithms are carried out at the early stages of the project without the use of physical prototypes [5, 6].

Effects of model-based design [7–10]:

- Reduce labor and algorithm development time
- Reduce labor costs and time for implementing algorithms on the target microprocessor platform, thanks to automatic C-code generation
- Validation of system requirements by creating a system model and performing tests on it
- Debugging and testing algorithms at the system model level, which ensures that most development errors are found at the preliminary design stage, rather than at the prototype device testing stage
- Transparency of the relationship between requirements, model, C-code, and test scenarios, which is one of the conditions for compliance with industry standards for embedded systems development.

3 Design Methodology Based on the RFLA Approach

3.1 The Main Components of the Development Process

The development process can be described using four main components (see Fig. 1):

- R (Requirements)—the process of developing and managing requirements;
- F (Functional)—the process of describing the functional architecture;
- L (Logical)—the process of describing the logical interaction of the functional components of the system

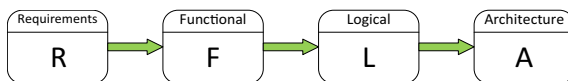


Fig. 1 The main components of the development process

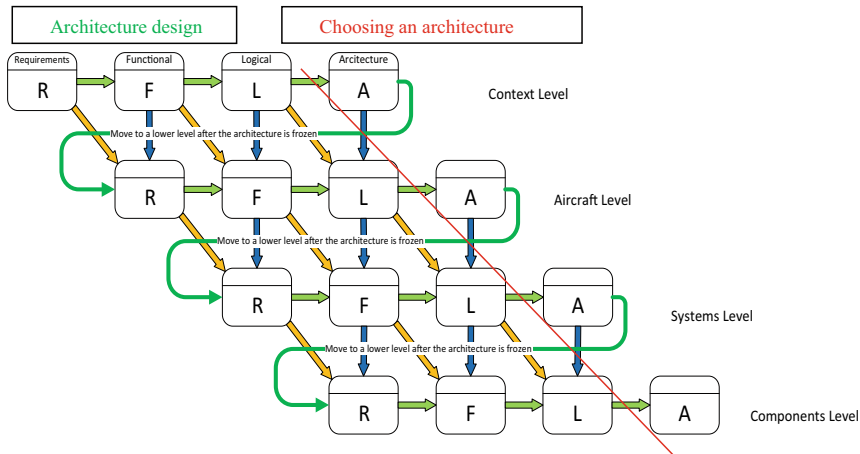


Fig. 2 General process of aircraft and its systems development

- A (Architecture)—the process of describing the physical architecture and implementation of the product;

These components of the product development process are necessary to identify architectural solutions that meet the goals of the aviation program. Within the framework of the RFLA approach, an unambiguous relationship is established between all information objects created during product development (the green arrows in Fig. 1 indicate not only transitions between processes but also links between documents created within the framework of these processes) [2].

RFLA is based on the application of a system approach in design processes, namely, the decomposition of complex systems into abstract levels and hierarchies (system, subsystem, and component).

By using the RFLA approach at all levels of the hierarchy and maintaining the relationships between the created documents in the development process, you can build a common development process for the aircraft and its systems. This process is shown in Fig. 2.

Each component of the process is described by a set of electronic documents such as mathematical models, three-dimensional models, drawings, diagrams, sketches, and project documents.

3.2 General Process of Aircraft and Its Systems Development

Development is performed by sequentially executing a chain of R-F-L-A processes at each level of the system hierarchy. The transition to the level below is carried out only after defining the requirements, functions, logical, and physical description of the architecture at the level of consideration.

Green arrows indicate the progress of the development process.

The yellow arrows indicate the direction of decomposition of requirements, functions, and logic as you move from the top level to the component level.

Blue arrows indicate the effect that the upper levels have on the lower ones. When you move from the top level of consideration to the bottom, you will see derived requirements, functions, and logic.

At the highest level (context level), requirements are defined more abstractly as customer needs, marketing and software requirements, and goals.

Requirements are decomposed into lower levels, such as aircraft level and system level (yellow arrow in Fig. 2).

The functionality is similar path that starts from the top-level functions and continues decomposition of functions in the direction of the functions of the level of system elements (a yellow arrow in Fig. 2).

Logical and physical architecture description is defined at each level, thus to ensure the functionality of the level to attain the goals at this level.

When choosing a logical and physical description of the architecture, it is recommended to use ready-made solutions that have shown effectiveness from the experience of similar developments. In this case, in accordance with the RFLA approach, the function defined at the level above becomes an additional source of derived requirements for development at the level below (the blue arrow in Fig. 2).

The transition to the next level of consideration should be made only after the development of a logical and physical description of the architecture. At the same time, the distribution of requirements and functions between the systems is carried out, in order to consistently determine their architecture.

After the design is completed at the current system level, we freeze the physical architecture (the way requirements, functions, and logic are implemented), which imposes additional requirements that limit the design options at lower levels.

The result of the decomposition is a tree of requirements and a tree of functions of the aircraft and its systems, which are related to each other. This ensures the completeness of the description of the requirements and functionality of the designed product.

The result of the RFLA approach can be

- (R) Documented requirements, models of requirements;
- (F) Documented product functional descriptions, function diagrams;
- (L) Documented descriptions of the logical interaction of functions (functional models, circuit diagrams, specification models, functional programs);
- (A) Descriptions of the physical implementation of the architecture: drawings, 3D models, etc.

4 Examples of Development According to the RFLA-Approach

4.1 Example of Forming a Flow of Requirements, Functions, Logic, and Architecture at the Aircraft Level

Based on the marketing requirements, the R1 requirement and the F1 function of the aircraft level must be developed:

R1 The aircraft must turn 180° on the TBD (To Be Determined) artificial runway wide

F1 (To meet the R1 requirement, it must be provided) Control of the aircraft on the ground

F1. 3 Control of the movement around the center of mass of the aircraft when moving on the ground

F1. 3.1 Control of the movement around the center of mass in the track channel

On the basis of a combination of requirements, functions, and analysis of existing solutions, a logical description of the relationships between the architecture of the proposed product should be prepared:

L1 (To meet the R1 requirement as part of the F1 function), the aircraft movement must be controlled by its systems when moving on the ground

Based on the combination of the requirement, function, logical description, and analysis of existing solutions, a description of the physical representation of the architecture of the intended product should be prepared:

A1 (To meet the R1 requirement as part of the F1 function, taking into account the logical description of L1), the aircraft must be equipped with a landing gear complex with a controlled rotary front support and a wheel brake control system for the use of differential braking

This algorithm is shown in Fig. 3.

4.2 Example of system-level decomposition

Decomposition of requirements and functions based on the selected architecture gives rise to several branches of the requirements and functions of Fig. 4.

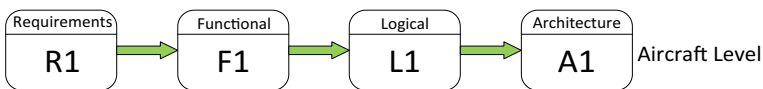


Fig. 3 Example of forming a flow of requirements, functions, logic, and architecture at the aircraft level

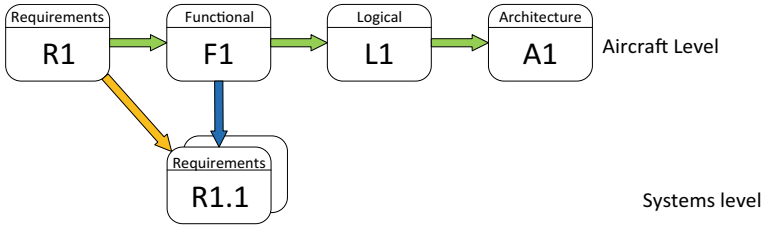


Fig. 4 Example of decomposition of requirements to the system level

The requirement level of the aircraft R1, given functions F1, L1 logic, and architecture A1 needs to define system requirements:

-
- R1.1 control system with brake wheels has to manage the movement of an aircraft on the ground during taxiing and the rotation of the wheels of the front support on TBD angles

 - R1. 2 the brake wheel control system must provide separate control of the brakes of the wheels of the left and right landing gear

 - R1. 3 the integrated control system should provide control of the aircraft on the ground using the rudder

The system-level requirements should define the functions of the systems, taking into account the physical concept of the principles of the flight dynamics of the aircraft, which divides the movement into trajectory and movement around the center of mass (see Fig. 5).

-
- F1. 1 Control of the front landing gear rotation at TBD speeds (to meet the R1.1 requirement)

 - F1.2 Control of the differential braking (to meet the R1. 2 requirement)

 - F1.3 Control of the rudder movement by braking (to meet the R1.3 requirement)

Similar to the aircraft-level consideration, the combination of requirements, functions, and analysis of existing solutions should determine the logical description of the system architecture relationships (see Fig. 6):

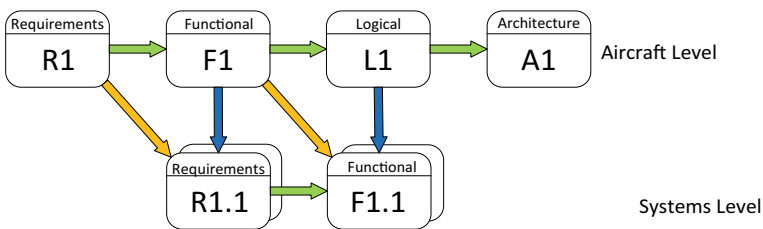


Fig. 5 Example of decomposition of functions at the system level

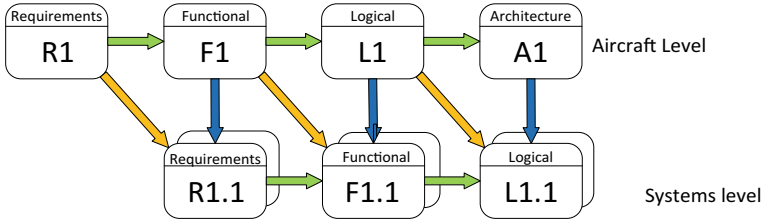


Fig. 6 Example of the process of defining logics at the system level

L1.1 control function F1.1 at large angles is performed when the movement of an aircraft on the ground at a speed of less than TBD

L1.2 control function F1.2 is the movement of an aircraft on the ground at a speed of less than TBD

L1.3 control function F1.3 is performed, the management plane pedals and the automatic control on earth

In the same way, the architecture of the systems that provide control on the ground should be determined:

A1. 1 (To fulfill the requirement R1. 1 in the framework of the function F1. 1, taking into account L1.1) To control the rotation of the wheels of the front chassis support at large angles, wheel control handles are provided that have an interface with the front wheel control system

A1. 2 (To meet the requirement R1. 2 in the framework of the F1.2 function, taking into account L1. 2), the right pedal of the control station with the brake wheel control system is provided for controlling the brakes of the wheels of the right chassis support, and the left pedal of the control station with the brake wheel control system is provided for controlling the brakes of the wheels of the left chassis support

A1. 3 (To meet the requirement R1.3 in the framework of the F1.3 function, taking into account L1.3), the control station pedals with an integrated control system are provided for steering the rudder

The above example is illustrated in Fig. 7.

Further decomposition of requirements and functions into the next levels of consideration should be carried out according to a similar methodology.

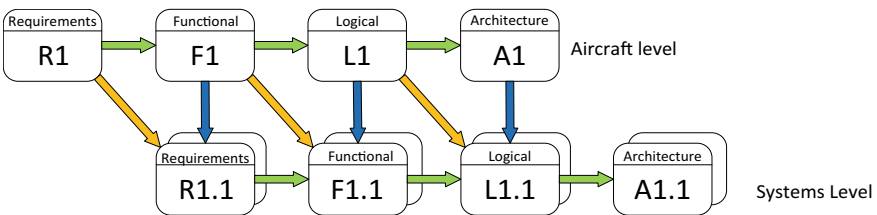


Fig. 7 Example of the system architecture definition process

5 Conclusion

The purpose of this approach is to ensure the level of quality of aircraft development required by the aviation authorities.

To achieve this goal, you need to solve the following tasks:

- Develop requirements for all levels of the system hierarchy;
- Develop functional models for all levels of the system hierarchy;
- Develop models of interaction of functional elements;
- Develop architectural descriptions for all levels of the system hierarchy;
- Ensure traceability of the relationships between the descriptions of all these models, as well as their components, throughout the entire life cycle of the aircraft.

References

1. SAE ARP4754A-Guidelines for Development of Civil Aircraft and Systems, 12/2010
2. Esdras G, Liscouët-Hanke S (May 2015) Development of core functions for aircraft conceptual design: methodology and results. In: Conference: Canadian aeronautics and space institute AERO 2015 conference at: Montreal, Canada
3. Federal Aviation Administration (FAA), Requirements Engineering Management Handbook DOT/FAA/AR-08/32, June 2009
4. SAE ARP4761-Guidelines and Methods for Conducting the Safety Assessment. Process on Civil Airborne Systems and Equipment, 12/1996
5. RTCA DO-178C, Software Considerations in Airborne Systems and Equipment Certification SC-205 5 January 2012
6. RTCA DO-331 Model-Based Development and Verification Supplement to DO-178C and DO-278A, dated December 13, 2011
7. International Council on Systems Engineering (INCOSE), Systems Engineering Handbook, INCOSE-TP-2003-016-02, Version 2a, 1 June 2004
8. Siemens PLM, Systems Engineering und PLM, ISSN 2193-8415
9. IBM Product Lifecycle Management, Collaborative Systems Engineering, PLS03029-USEN-01
10. Thierry Ambroisine, Dassault Systèmes, Mastering increasing product complexity with Collaborative Systems Engineering and PLM, embedded world conference 2013

Research on Technological Potential for Using Aluminum Alloy Wire in Airborne Smart Cables



I. G. Roberov, V. S. Grama, M. A. Kiselev, V. V. Kosyanchuk,
and E. Yu Zybin

Abstract A prerequisite for creating a competitive aircraft is to ensure low operating costs by reducing downtime and rational organization of aircraft maintenance and repair through continuous monitoring, diagnostics, and prediction of the aircraft health. For the monitoring, diagnosing, and predicting purposes of the aircraft health in recent decades, the list of parameters recorded aboard has been continuously expanding. Great prospects in this direction are associated with the creation and implementation of so-called smart materials that can control their health and even actively resist damage. The article presents the results of research aimed at establishing diagnostic features for wire made of aluminum alloy 1417M that can be easily measured during aircraft operation and are uniquely related to its health. This wire is promising for on-board cable network due to its 30% less weight than copper wire. The article investigates the effect of twisting on the mechanical properties characteristics (conventional yield stress, tensile strength, percentage elongation) and the values of the resistivity of the alloy wire 1417M. The dependences of mechanical characteristics and resistivity on the number of twists were obtained. It has been established that the nature of the dependences obtained is influenced by the diameter of the tested wire. Correlation between resistivity and stress-related properties of alloy is established. The obtained regression equation makes it possible to analyze the voltage change patterns as a function of the strain value by changing the value of

I. G. Roberov · M. A. Kiselev (✉) · V. V. Kosyanchuk · E. Y. Zybin
State Research Institute of Aviation Systems, Moscow, Russia
e-mail: m.kiselev@mstuca.aero

E. Y. Zybin
e-mail: eyzybin@2100.gosniias.ru

V. S. Grama
Russian State Technological University, Moscow, Russia
e-mail: grama@mirea.ru

M. A. Kiselev
Moscow State Technical University of Civil Aviation, Moscow, Russia

the resistivity values during loading of the wire from aluminum alloy 1417M. Therefore, it can be the basis for monitoring, diagnostics, and prediction of the aircraft cable network health.

Keywords Health · Monitoring · Diagnostics · Prediction · Smart · Cable · 1417M alloy · Wire · Twisting · Mechanical properties · Resistivity · Correlation dependence · ICASSE

1 Introduction

One of the results of the constantly tightening requirements to reduce harmful emissions and the harmful aircraft effects on the environment is the intensification of both exploratory research and the realization of certain technologies for a more electric aircraft [1, 2]. Studies aimed at improving, increasing the reliability, and reducing the mass of the aircraft power supply system and the on-board cable network (OCN) seem to be relevant [3, 4]. It should be noted that simply improving specific parameters such as cables is no longer considered a sufficient competitive advantage. From the point of view of operational safety and reduction of aircraft downtime, it is extremely important to ensure the possibility of continuous monitoring and prediction of the health of both the OCN in particular and the aircraft as a whole [5].

The mass of OCN of a modern aircraft is 3–4% of its total mass. A decrease in the mass of OCN can be ensured by using aluminum alloys with high mechanical and electrical properties as the main material, instead of copper. The advantages of aluminum and its alloys include its low density and weight of products, relatively high strength characteristics, good thermal and resistivity, processability, and high corrosion resistance. Replacing copper wires with aluminum ones will reduce the weight of the OCN by up to 30%.

However, the properties of the special aluminum alloy billets achieved now do not allow producing a high-quality wire with a diameter of less than 0.5 mm due to the inhomogeneity and coarseness of the resulting billets structure. This limits the use of aluminum wire for reducing the weight of the OCN.

Operating temperature of OCN wires is within the range of 150–450 °C. The operating temperature of wires made of standard aluminum alloys depends on their properties and usually does not exceed 100 °C that also limits their use in aircraft OCN.

Standard technologies for the billets production from aluminum alloys by casting (direct chill mold) do not allow the production of wire with the required properties. In the USSR to solve this problem a technology including the production of granules, their sintering into an ingot, pressing and further processing to wire was used. Due to the low productivity, low yield of suitable products, high cost and the impossibility of manufacturing wire \varnothing 0.10–0.50 mm, the granule technology was not sufficiently widespread in the production of special aluminum alloys.

The technological process of casting a billet in an electromagnetic mold allow to obtain a wire from heat-resistant aluminum alloys which has high quality characteristics. This technology provides significantly higher productivity, low cost, and the ability to obtain wire \varnothing 0.10–0.50 mm. Cerium additives to aluminum alloys neutralize the effect of iron and silicon, increase strength without loss of resistivity and disperse the alloy structure [6]. The operating temperature of wires made of special aluminum alloys with rare earth metals (REM) can reach 350 °C, which expands the prospects for their use in OCN.

Structural analysis, mechanical tests, and resistivity values of the alloy based on the Al-Ce system confirmed the presence of the properties necessary to obtain lightweight and heat-resistant wires [7, 8].

The sequence of technological processes and operations of cable production must ensure the receipt of a cable or wire of a given design, with specified electrical and mechanical properties and guaranteed reliability. One of the main processes of cable production is twisting—the process of combining individual elements (wires, insulated strands) in which each of them is located along a screw line around the central elements, i.e., twisting wires into conductive strands and insulated strands into cable. The twisting of the production elements occurs due to the combined action of two movements—rectilinear (translational) and rotational [9].

During this process the wires are twisted around their own axis that is they undergo torsion deformation which can cause a change in the mechanical properties of the wire.

2 Problem Statement

The purpose of this work was to study the effect of twisting on the mechanical properties and electrical resistivity of a wire made of alloy 1417M (Al-REM) and to establish a correlation between the characteristics of mechanical properties and resistivity to evaluate the functionality and health of the alloy at various stages of deformation using the electropotential method which in subsequently it can be used to control and predict the health of the OCN, i.e., to create a smart cable. The main idea of smart materials is, firstly, informing about their health (about the occurrence of damage, its location and magnitude—these are the so-called passive smart materials) and, secondly, adapting their design to changing conditions. The basic material from which the smart structural elements are made should have adaptive abilities [10–12].

3 Research Methods and Results

Al-REM alloy (aluminum alloy 1417M) with a cerium and lanthanum content of 6% and 3%, respectively were used as the starting material for the study.

Melting of aluminum alloy ingots 1417M was carried out using the technology of continuous casting into an electromagnetic mold, followed by wire drawing to a diameter of 0.5, 1, and 3 mm.

The microstructure of longitudinal sections of wire samples in the initial state and after twisting at an increase of 1000 times was studied using an OLIMPUS GX-51 system metallurgical inverted microscope.

An electropotential meter “ZOND IGT-98” was used for measuring the resistivity from the potential difference arising when passing current through the sample.

The wire was twisted on a KTS-402 twisting machine at a speed of 10 rpm with a tension force proportional to the wire diameter, 20 N, 40 N, and 120 N, respectively.

For tensile tests in accordance with GOST 10,446–80 “Wire Tensile test method” samples from a wire of each diameter were made in the initial state (without twisting) and after 2, 5, and 10 turns of twisting.

Tensile tests of wire with a diameter of 0.5 mm were carried out on an electromechanical universal test bench UTS-110MK-1 with a maximum load of 1000 N, and wires with a diameter of 1 and 3 mm were carried out on an electromechanical universal test bench UTS-101-50 with a maximum load of 50,000 N.

The tensile strain rate was 10 mm/min. The maximum permissible relative error of load measurement is 0.5%. For each combination of factors (A—wire diameter, B—number of twists) 5 samples ($n = 5$) were tested.

Two-factor dispersion analysis was carried out to assess the materiality of the influence of wire diameter (factor A), the number of twists (factor B), and their interaction on the obtained characteristics of mechanical properties (σ_B , $\sigma_{0.2}$, δ) of aluminum alloy wire 1417M.

The results of studying the microstructure of the 1417M aluminum alloy (Fig. 1) show that the structural components of the material are the α -solid solution of cerium and lanthanum in aluminum (light background) and the eutectic (dark background). Nature changes analysis in the microstructure of the wire during twisting makes it possible to note that as a result of twisting, the crystallites rotate clockwise.

The results of the study of the microstructure of aluminum alloy 1417M (Fig. 1) were found that the nature of the dependence of the average values of the tensile strength σ_t on the number of twists at different values of the wire diameter (Fig. 2)

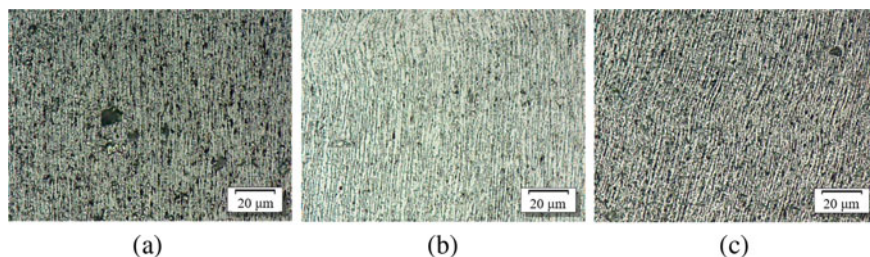


Fig. 1 Microstructure of longitudinal sections of wire samples made of alloy 1417M with a diameter of 3 mm: **a** without twisting; **b** after 5 turns of twisting; **c** after 10 turns of twisting

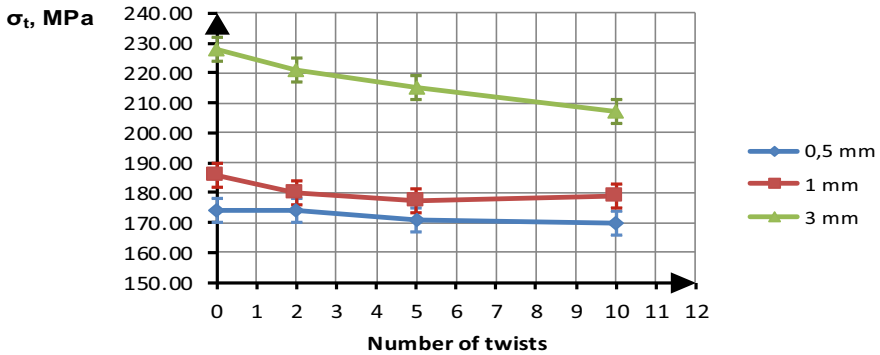


Fig. 2 Dependence of the average values of σ_t on the number of twists for different wire diameters

shows a slight decrease in the strength characteristics with an increase in the number of twists.

The influence of the wire diameter and the number of twisting turns on the tensile strength is significant. The confidence error for the obtained values of the tensile strength σ_t was 6 MPa.

During the experiments, it was found that for all values of the wire diameter, with an increase in the number of twists, the value of the conventional yield stress $\sigma_{0,2}$ has decreasing tendency (Fig. 3).

The influence of the wire diameter and the number of twists on the value of the conventional yield stress are statistically significant.

It was shown that for wire with diameters of 0.5 and 3 mm (with an increase in the number of twists to 10) the percentage elongation changes within the confidence error and for a wire with a diameter of 1 mm it tends to increase (Fig. 4).

As is known, most of the physicochemical properties of metals are functionally related to resistivity which is one of the most important structurally sensitive

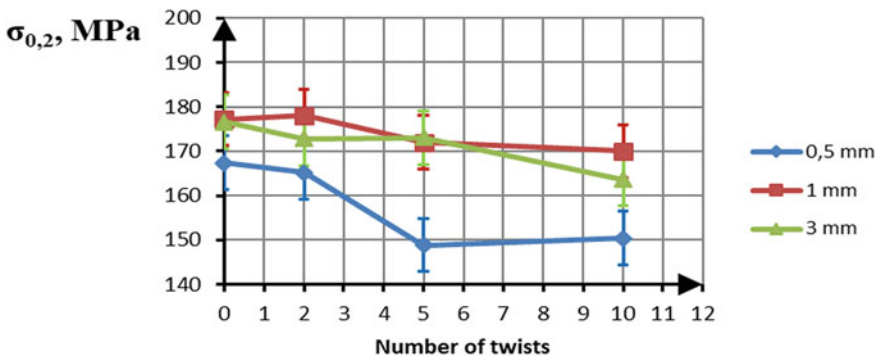


Fig. 3 Dependence of the conventional yield stress $\sigma_{0,2}$ on the wire diameter and the number of twists

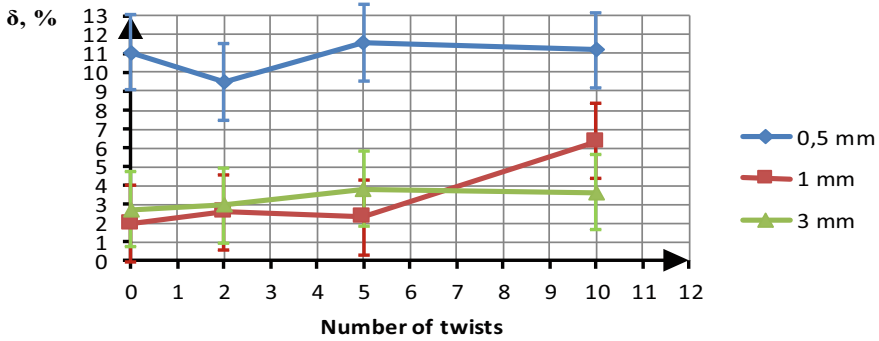


Fig. 4 Dependence of the percentage elongation δ on the wire diameter and the number of twists

characteristics of alloys. This makes it possible, by measuring electrical resistivity, to assess the structural state of the material which corresponds to certain processing modes and, accordingly, to indicators of strength properties.

In the absence of mechanical stresses the metal has the nominal value of the grid period d_0 and corresponding nominal electrical resistivity γ_0 . Under the effect of mechanical stresses change $\Delta\sigma$ there is a change in the period of the metal grid Δd . In the zone of elastic deformations, this change can be considered proportional to the mechanical stress, i.e., changes in resistivity $\Delta\gamma$ also proportional to mechanical stresses $\Delta\sigma$.

At the same time, as the degree of deformation increases, the dislocation density increases, the concentration of point defects and package defects increases which leads to an increase in the resistivity of metal materials associated with electron scattering on crystal grid defects. Thus, by measuring the magnitude of the resistivity in the process of stretching, torsion, compression, etc., it is possible to estimate the structural health of the alloys corresponding to different stages of the deformation process under loading.

To measure the electrical resistance during inflight operation, we can use non-contact methods for measuring quantities functionally related to magnetic or electromagnetic fields caused by the current flowing through the conductor. This allows the implementation of the so-called smart cable braiding for its structural monitoring using on-board wireless sensor networks.

To measure the electrical resistance (conductance) of the wire from the 1417M alloy in our research, an electropotential meter “ZOND IGT-98” was used with an additional mode for periodic measurement of resistivity. In order to record the data obtained during mechanical tests, an appropriate data exchange software was developed, designed to transfer the values of the voltage recorded by the unit in relative units to the personal computer for further processing. To determine the value of resistivity ρ it is necessary to know the ratios $\frac{U}{I}$ and $\frac{S}{l}$, where U —potential difference (V), I —amperage (A), S —cross-sectional area of the sample (m^2), and l —distance between potential electrodes (m).

Then the resistivity ρ is determined by

$$\rho = \frac{U \cdot S}{I \cdot l} \tag{1}$$

However, $\frac{U}{I}$ ratio during measurements is known up to the accuracy of an unknown multiplier k , as U and I are displayed in relative units.

The multiplier k relates the true $\frac{U}{I}$ ratio with displayed $\frac{U_0}{I_0}$ ratio

$$\frac{U}{I} = k \cdot \frac{U_0}{I_0} \tag{2}$$

Then we have the following expression

$$\rho = k \frac{U_0 \cdot S}{I_0 \cdot l} \tag{3}$$

To determine the multiplier k , the resistivity ρ of the wire samples was initially measured in $\mu\Omega$ on the ETS-515 test bench, designed to measure low ohmic resistances and determine the resistivity in accordance with GOST 7229-76. The resistivity in $m\Omega$ measured during the test is reduced to resistivity at 20 °C according to the formula

$$R_{20} = R_{\text{measured}} \cdot K_t = R_{\text{measured}} \cdot \frac{1}{1 + \alpha_R(t_{\text{air}} - 20)}, \tag{4}$$

where K_t —temperature coefficient, α_R —temperature coefficient of resistivity in $^{\circ}C^{-1}$ (for aluminum – 0,00,403), and t_{air} —indoor air temperature in $^{\circ}C$.

Calculation of resistivity in $\mu\Omega$ obtain by the formula:

$$\rho = \frac{R_{20} \cdot S}{l} = \frac{R_{20} \cdot \pi \cdot d^2}{4 \cdot l} = \frac{R_{\text{measured}} \cdot \pi \cdot d^2}{(1 + \alpha_R(t_{\text{air}} - 20))4 \cdot l}, \tag{5}$$

where S —cross-sectional area of the sample in m^2 , l —sample length 1 m, and d —sample diameter in m. According to the passport data, the relative error of resistance measurement is no more than $\pm 0.05\%$.

Then measurements on the same samples were carried out in relative units with the device “ZOND IGT-98”. From the data obtained, the value $k = 4,16 \cdot 10^{-3}$.

Twisting was carried out on a machine for testing materials for twisting KTS 402 which provides twisting to a given number of twists, twisting to failure, twisting followed by untwisting, and twisting to a given degree. Samples for twisting consisted of wires 3 mm in diameter and 300 mm in length in a solid (unannealed) state.

Connection to the sample was carried out using an electropotential converter EPP 20 × 80-SK specially made for this purpose with sliding spring-loaded contacts. The distance between current electrodes is 80 mm and between potential electrodes—20 mm.

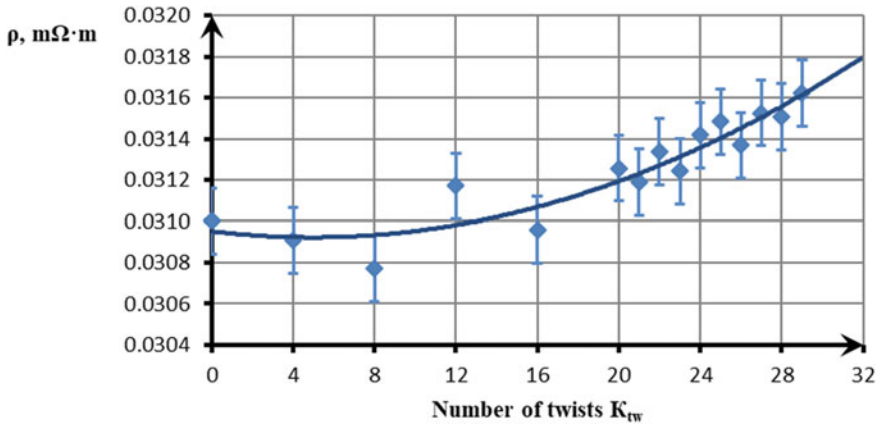


Fig. 5 Dependence of resistivity of aluminum alloy wire 1417M 3 mm diameter on number of twists

Measurements were carried out after twisting wire samples by a certain number of twists ($K_{tw} = 0 \div 29$). Obtained results of single-factor variance analysis with confidence probability $P = 0,95$ indicate that the effect of the number of twists on the value of resistivity is statistically significant, while the total confidence error of the change in resistivity was $1,6 \cdot 10^{-4} m\Omega \cdot m$.

It was found that with an increase in the number of twists, the resistivity tends to increase (Fig. 5). The dependence $\rho = \rho(K_{tw})$ can be represented by a regression equation of the form:

$$\rho = 1 \cdot 10^{-6} \cdot K_{tw}^2 - 1 \cdot 10^{-5} K_{tw} + 0.031 \quad (6)$$

and the coefficient of determination $R^2 = 0,8743$.

After twisting, tensile tests of the samples were carried out and the values of the physical characteristics, parameters of strength, and plasticity properties were determined. The obtained test results indicate that with an increase in the number of twists, the strength properties and plasticity tend to decrease, the nature of the destruction of the samples changes—from ductile to brittle (Fig. 6).

The dependence of the tensile strength on the number of twists $\sigma_t = \sigma_t(K_{tw})$ can be represented by a regression equation of the form:

$$\sigma_t = 0,0002K_{tw}^4 - 0,0176K_{tw}^3 + 0,4481K_{tw}^2 - 4,7342K_{tw} + 224,6 \quad (7)$$

and the coefficient of determination $R^2 = 0,9647$ Fig. 7.

Table 1 shows the results of the correlation analysis of the relationship between the parameters of strength properties and plasticity from resistivity.

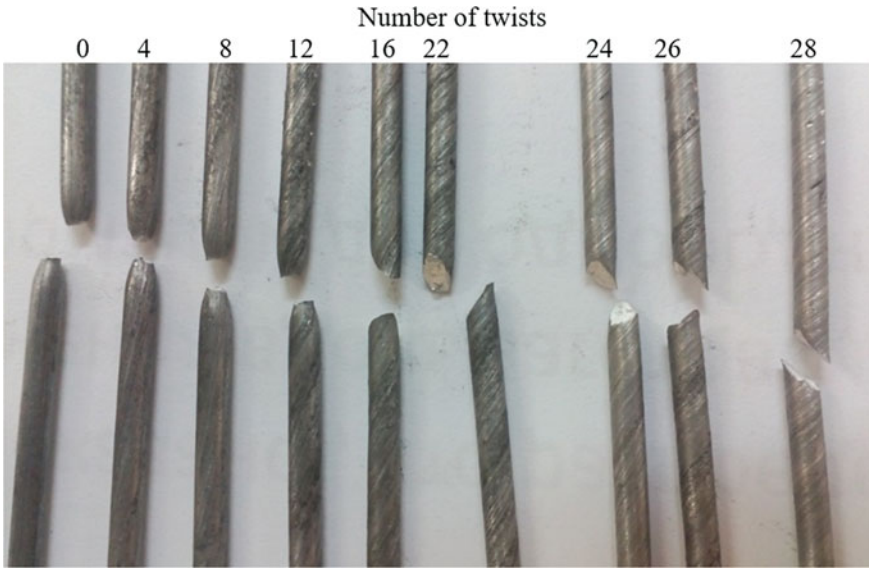


Fig. 6 Change the pattern of samples destruction depending on the number of twists

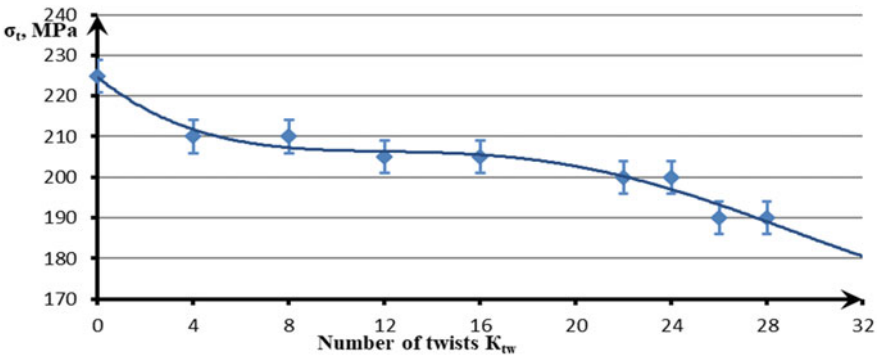


Fig. 7 Dependence of tensile strength σ_t on the number of twists for wire 3 mm in diameter made of alloy 1417M

Table 1 Correlation dependence of strength and plasticity properties from resistivity

	P
σ_t	-0,777
$\sigma_{0,2}$	-0,494
δ	-0,829

Selective coefficient of correlation between resistivity ρ and tensile strength σ_t $r(\rho, \sigma_t) = -0,777$ while for the significance level $\alpha = 0,05$ number of degrees of freedom $f = n - 2 = 7$ critical value of selective correlation coefficient $r_{1-\frac{\alpha}{2}} = 0, 666$. As $|r(\rho, \sigma_t)| > r_{1-\frac{\alpha}{2}}$ then, with a confidence level $P = 0,95$ there is a statistically significant correlation between resistivity ρ and strength σ_t .

As a result of the performed regression analysis, a model of dependence $\sigma_t = \sigma_t(\rho)$ (Fig. 8) was obtained in the form of a sixth-degree polynomial with a coefficient of determination $R^2 = 0, 9978$:

$$\sigma_t = 7 \cdot 10^{20} \rho^6 - 1 \cdot 10^{20} \rho^5 + 1 \cdot 10^{19} \rho^4 - 4 \cdot 10^{17} \rho^3 + 1 \cdot 10^{16} \rho^2 - 1 \cdot 10^{14} \rho + 7 \cdot 10^{11}$$

4 Conclusions

Wire made of alloy 1417M has a combination of the necessary strength and plastic properties for possible use as airborne high-voltage power cables. Based on the studies of samples of wire made of aluminum alloy 1417M, the dependences of torsion on the characteristics of mechanical (conventional yield stress, tensile strength, percentage elongation) and physical (resistivity) properties has been established. It is shown that the nature of the dependences is influenced by the diameter of the wire being tested. For samples of wire from aluminum alloy 1417M diameter 3 mm, correlation between resistivity and strength properties was established. Regression equation is obtained for dependence of tensile strength on electrical resistivity of alloy 1417M. This dependence can be used to estimate the health of OCN

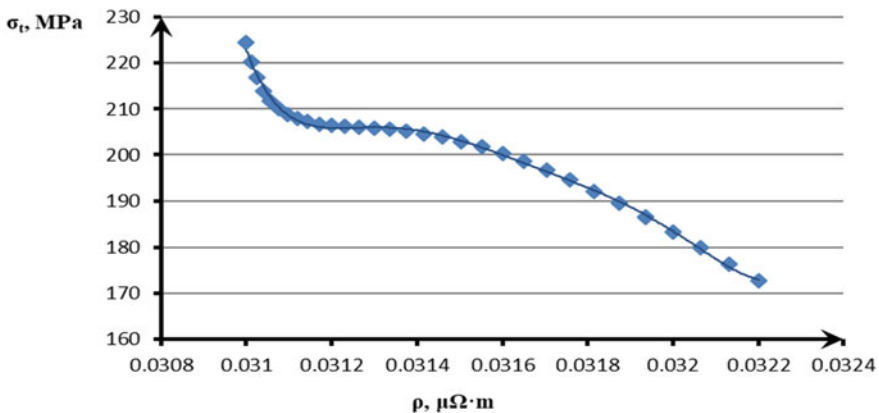


Fig. 8 Dependence of strength of aluminum alloy wire 1417M 3 mm diameter on resistivity

and to predict the residual life of the smart cable from 1417M alloy in the operating conditions of the aircraft.

References

1. Sarlioglu B, Morris CT More electric aircraft: review, challenges, and opportunities for commercial transport aircraft. *IEEE Trans Transp Electr* 1(1):54–64
2. Gubernatorov K, Kiselev M, Moroshkin Y, Chekin A (2020) Architecture of air conditioning system with electric-motor-driven blowers. IN: IOP conference series: materials science and engineering, vol 868(1), p 012023
3. Chekin A, Moroshkin Y, Gubernatorov K, Kiselev M (2019) Impact of reliability of state-of-the-art electrical units on architecture of power supply system of modern aircraft. In: *Proceedings-ICOECS 2019: 2019 international conference on electrotechnical complexes and systems*, p 8949924
4. Ismagilov FR, Vavilov VE, Gusakov DV, Kiselev MA (2018) Design methodology of the aircraft power generation system. In: *Proceedings of the 2nd international conference on electronics, communication and aerospace technology, ICECA 2018*, pp 1923–1928, 8474785
5. Roberov IG, Figurowsky DK, Kiselev MA, Grama VS, Matveev DB, Ivanov VO (2020) Comprehensive diagnostics of the technical condition and assessment of the performance of metallic materials by non-destructive testing methods. *Blank production in mechanical engineering [Kompleksnaya diagnostika tekhnicheskogo sostoyaniya i otsenka rabotosposobnosti metallicheskih materialov metodami nerazrushayushchego kontrolya. Zagotovitel'nyye proizvodstva v mashinostroyenii]*, vol 18, no 4, pp 178–181. (in Russian)
6. Savitsky EM, Terekhova VF (1975) *Metallurgy of rare earth metals*. Mosvka, Science [Metallovedeniye redkozemel'nykh metallov. Mosvka: Nauka], 272 pp. (in Russian)
7. Pervukhin MV (2012) *Electrotechnology and equipment for producing continuously cast ingots in an electromagnetic crystallizer. Theory and practice. [Elektrotekhnologiya i oborudovaniye dlya polucheniya nepreryvnolytkh slitkov v elektromagnitnom kristallizatore. Teoriya i praktika]*, Abstract of the thesis for the degree of Doctor of Technical Sciences, Krasnoyarsk, 36 pp. (in Russian)
8. Figurowsky DK, Pervukhin MV, Romanova EV (2009) The influence of the electromagnetic field in the process of crystallization on the structure of the alloy of the Al-REM system (alloy 1417M) [Vliyaniye vozdeystviya elektromagnitnogo polya v protsesse kristallizatsii na strukturu splava sistemy Al-RZM (splav 1417M)], *Materials of the VII international scientific and technical conference intermatic-2009, Part 2/MIREA*, pp 189–193
9. Leonov VM, Peshkov IB, Ryazanov IB, Kholodny SD (2006) *Fundamentals of cable technology*. Publishing Center “Academy”, Moscow. [Osnovy kabel'noy tekhniki, Moskva: izdatel'skiy tsentr «Akademiya»], 432 pp. (in Russian)
10. Akhras G (2000) Smart materials and smart systems for the future. *Can Mil J* 3:25–32
11. Wadhawan VK (2005) Smart structures and materials. *Resonance* 11:27–41
12. Schulz MJ, Pai PF, Inman DJ (1999) Health monitoring and active control of composite structures using piezoceramic patches. *Composites: Part B*, vol 30, pp 713–725

Study of the Features of the Flight and Technical Characteristics of a Hybrid Airship



S. F. Borodkin, M. A. Kiselev, and M. V. Shkurin

Abstract It is well-known that the forces at work determine the dynamics of aircraft motion. When an airplane is flying, these forces include the total aerodynamic force, the thrust force of the propulsion system, and the force of gravity. Hybrid Airship (HA) differs from an airplane by the presence, in addition to the above, of aerostatic force, the value of which depends, among other things, on the altitude of the HA. The presence of aerostatic force affects the maneuverability of an HA. The proposed article analyzes the changes in the flight and technical characteristics of an HA due to the presence of aerostatic force.

Keywords Flight dynamics · Hybrid airship · Airship · Aero-static force · Turn

1 Introduction

Attempts to create and widely use hybrid airship (HA) made many times in the last century. However, all of them ended without much success. Now we can say that interest in such projects is rebounding [1–6]. The attractiveness of the idea of creating HA lies in the unattainable for aircraft of traditional schemes (planes and helicopters) capabilities of HA in terms of payload capacity, as well as in terms of transportation and unloading to unequipped sites of large-sized cargo (not to be mistaken with the requirements for basing). Achievements to date in terms of construction materials, electric propulsion systems, hydrogen fuel cells, as well as the need to develop the Arctic regions of the Russian Federation (RF), the Northern Sea Route opens new prospects for this type of aircraft. At the same time, a large sailing HA, inertia due to large size and mass requires careful study of issues related to both the actual selection of rational design parameters HA [7, 8] and the calculation of aerodynamic

S. F. Borodkin · M. A. Kiselev
Moscow State Technical University of Civil Aviation, Moscow, Russia

M. V. Shkurin (✉)
Moscow Aviation Institute (National Research University), Moscow, Russia
e-mail: m.shkurin@mai.ru

characteristics HA [9–11]. With the study of the features of the dynamics of flight HA, and, primarily, issues related to the agility HA and the characteristics of its stability and controllability [12, 13].

2 Problem Statement

HA is essentially an aircraft that uses a combination of aerostatic and aerodynamic principles to create lift [14].

The calculation of aerostatic lifting force is based on the laws of Pascal and Archimedes, according to which the expulsive or, as we will call it further, the total aerostatic lifting force is equal to the weight of air displaced by the gas volume W_g

$$Y_{\text{full aship}} = G_a = W_g g \rho_a, \quad (1)$$

where g is the acceleration of gravity and ρ_a is the density of outside air.

The $Y_{\text{full aship}}$ force always directed upwards parallel to the weight of the airship G .

The application point $Y_{\text{full aship}}$ is in the center of the gas volume. The value of $Y_{\text{full aship}}$ does not depend on the type of lift gas used but is determined only by the values of W_g and ρ_a . If the line of action of the aerostatic force does not coincide with the line of action of the airship weight, aerostatic moments occur. Some sources, such as [15], use the concept of aerostatic force, which is the excess of total aerostatic lifting force over the weight of the lifting gas in the volume W_g . Since the weight of the gas, volume is equal to $G_a = W_g g \rho_a$, the value of excess aerostatic lifting force $Y_{\text{ex aship}}$ calculated as follows:

$$Y_{\text{ex aship}} = G_a - G_g = W_g g (\rho_a - \rho_g) = W_g (\gamma_a - \gamma_g) = W_g \gamma_{\text{aship}}, \quad (2)$$

where ρ_g —lifting gas density,

γ_a —specific gravity of outside air,

γ_g —specific gravity of gas,

$\gamma_{\text{aship}} = \gamma_a - \gamma_g$ —specific aerostatic lift force.

The value of $Y_{\text{ex aship}}$ depends on the type of lifting gas and, as follows from (2), in contrast to $Y_{\text{full aship}}$, can be both positive and negative.

As we ascend to altitude, the values of $Y_{\text{full aship}}$ and $Y_{\text{ex aship}}$ decrease in proportion to the decrease of the surrounding HA air density ρ_a . At the flight altitude, where the air density becomes equal to the gas density, the excess aerostatic force becomes zero. For hydrogen, this altitude is about 20 km, for helium it is 15.5 km. At high altitudes, the $Y_{\text{ex aship}} < 0$. This means that the ejection force $Y_{\text{full aship}}$ became less than

the gas weight G_g and flight at these altitudes from the point of view of usefulness of the Y_{exaship} makes no sense.

If helium is used as a lifting gas, then for heights $H \sim 0 \dots 200$ m the value of the specific aerostatic lifting force γ_{aship} can be approximately taken as equal to one. This means that the value of excess aerostatic lifting force Y_{exaship} in [kgf] is numerically equal to the gas volume W_g in [m³], i.e., with $W_g = 10,000$ m³ the value of $Y_{\text{exaship}} = 10,000$ kgf, etc.

Hereinafter, speaking of the aerostatic force, we mean only the total aerostatic lift, i.e., $Y_{\text{aship}} = Y_{\text{full aship}}$. In this case, the weight of the lifting gas G_g will be considered in the value of the total weight HA G . Then the ratio of the aerostatic lift of Y_{aship} to the weight of HA will actually determine the degree of proximity of HA to airship: the closer this ratio is to one the closer HA is to airship and the closer this ratio is to zero the closer HA is to aircraft:

$$K_{\text{aship}} = \frac{Y_{\text{aship}}}{G} = 0 \dots 1$$

Let us estimate the effect of the magnitude of the aerostatic force, as the main distinguishing feature of HA, on:

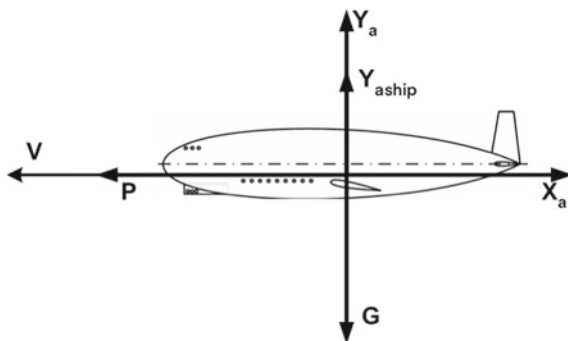
- range of speeds and heights of horizontal straight-line flight;
- takeoff and landing characteristics;
- climb and descent characteristics.

3 Research Methods and Results

Horizontal flight characteristics.

The condition for the constancy of flight altitude HA, written with respect to the required value of aerodynamic lift Y_a , assuming that the angle of attack is small ($\sin \alpha = 0$), according to the force diagram in Fig. 1, is as follows:

Fig. 1 Diagram of forces in horizontal flight



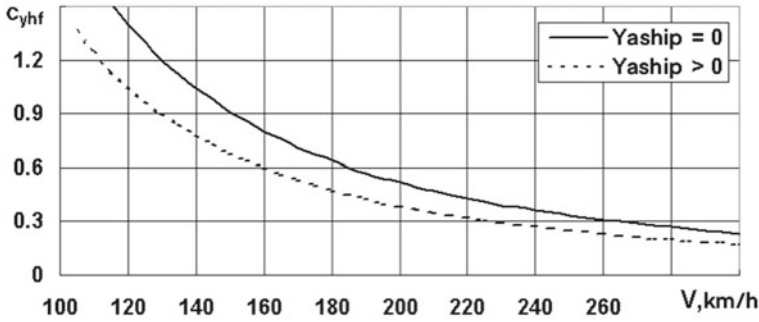


Fig. 2 To the effect of aerostatic force on the required lifting force coefficient in horizontal flight

$$Y_a \approx G - Y_{aship} = G(1 - K_{aship}), \tag{3}$$

From this condition, the values of lift coefficient $c_{y hfHA}$ and velocity V_{hfHA} required for horizontal flight easily found:

$$c_{y hf HA} \approx \frac{2(G - Y_{aship})}{V^2 \rho S} = \frac{2G(1 - K_{aship})}{V^2 \rho S} = c_{y hf aship=0} (1 - K_{aship}), \tag{4}$$

$$V_{hf HA} \approx \sqrt{\frac{2(G - Y_{aship})}{c_y \rho S}} = \sqrt{\frac{2G}{c_y \rho S} (1 - K_{aship})} = V_{hf Y_{aship}=0} \sqrt{1 - K_{aship}}, \tag{5}$$

From (3) to (5) we see that the presence of aerostatic force ($K_{aship} > 0$), other things being equal, reduces the required values of Y_a , which is achieved by reducing either $c_{y hf}$ or V_{hf} by the corresponding number of times. This is illustrated by Fig. 2 with dependence of $c_{y hf}$ on V .

If we take the ratio of aerostatic force Y_{aship} to the weight G equal.

$K_{aship} = 0.25$, then, as follows from condition (3), the required value of lifting force Y_a will decrease by 25% as compared to flight with $K_{aship} = 0$. This is achieved either by a 25% decrease in $c_{y hf}$, or by a 13.4% decrease in V_{hf} : $V_{znHA} = 0.866 V_{hf aship}$, or by a simultaneous change in both $c_{y hf}$ and V_{hf} according to (4) and (5).

When $K_{aship} = 1$, the required value of $Y_a = 0$, and hence $c_{y hf} = 0$ and $V_{hf} = 0$. In this case HA is essentially a dirigible.

If we consider the same horizontal flight speeds, the presence of the aerostatic force, reducing c_{ya} , leads to a decrease in the inductive component of the drag coefficient c_{xi} , and, consequently, to a decrease in the entire drag force X_a (see Fig. 3).

Reducing X_a allows you to realize larger values of tangential overload because

$$n_{xa} = \frac{P - X_a}{G}$$

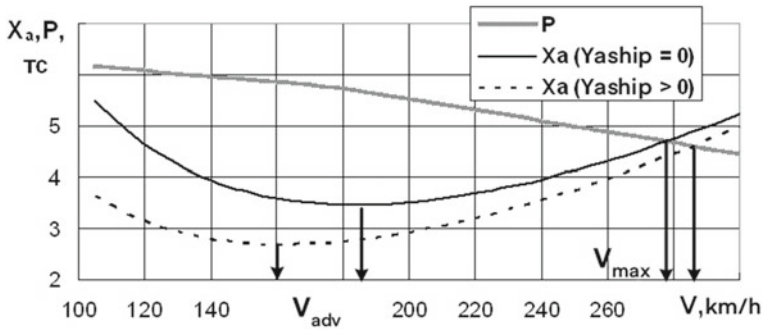


Fig. 3 To the effect of aerostatic force on drag in horizontal flight

The minimum value X_a , corresponding to flight at the most advantageous lift coefficient c_{yadv} , shifted for HA to a lower value of velocity V because

$$V_{adv HA} = V_{adv Y_{aship}=0} \sqrt{1 - K_{aship}}$$

Figure 3 also shows that in the presence of aerostatic force, the maximum flight speed V_{max} increases. As for the minimum allowable, flight speed limit, for HA, as follows from (5), the limit on $V_{min al}$ shifted toward lower values

$$V_{min al HA} = V_{min al Y_{aship}=0} \sqrt{1 - K_{aship}}$$

Thus, the presence of aerostatic force expands the available and operational range of speeds and heights of flight (see Fig. 4).

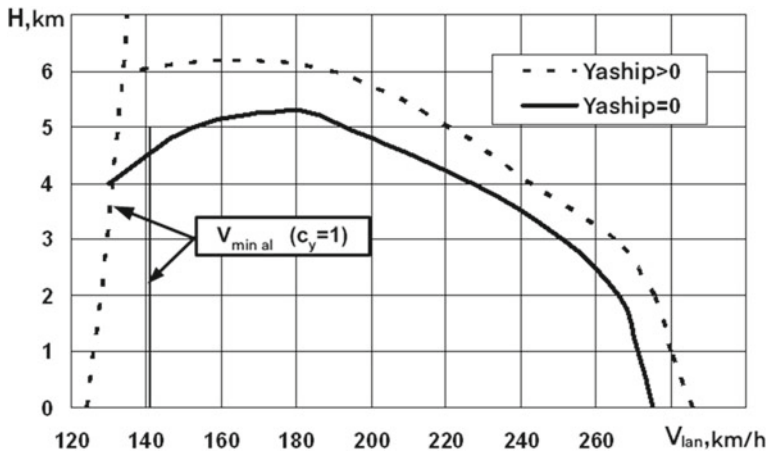


Fig. 4 To the effect of aerostatic force on the operational range of speeds and heights of flight

It should only be remembered that the comparison of HA is made for the same weight and aerodynamic characteristics of the aircraft.

Since, as stated above, with the ascent to altitude aerostatic force decreases, its influence on the horizontal flight characteristics HA.

Takeoff and landing characteristics.

For vertical takeoff of an airplane of vertical takeoff and landing the value of maximum takeoff weight estimated as

$$G_{to} = \frac{\sum P}{1.05 \dots 1.1},$$

whereas for an HA taking off vertically

$$G_{to} = \frac{\sum P}{1.05 \dots 1.1} + Y_{aship},$$

where $\sum P$ is the total vertical thrust of the HA propulsion system.

This means that with the same propulsion thrust of VTOL aircraft and HA, the maximum takeoff weight of HA can be increased by the value Y_{aship} or, with the same takeoff weights, the disposable vertical thrust can be reduced by $(1.05 \dots 1) Y_{aship}$. The same conclusions can draw with respect to the G_{land} weight and thrust of the propulsion system during a vertical landing.

If the HA takes off with a run-up, its breakaway velocity, assuming $\sin \alpha = 0$, is defined as

$$V_{baHA} \approx \sqrt{\frac{2(G_{to} - Y_{aship})}{c_{yba} \rho S}} = \sqrt{\frac{2G_{to}}{c_{yba} \rho S} (1 - K_{aship})} = V_{baY_{aship}=0} \sqrt{1 - K_{aship}}, \tag{6}$$

and takeoff run

$$L_{trHA} \approx \frac{V_{baHA}^2}{2j_{xav}} = L_{trY_{aship}=0} (1 - K_{aship}), \tag{7}$$

where j_{xav} —the value of the average tangential acceleration on takeoff run.

For a landing with a run, we get similar expressions

$$V_{lanHA} \approx \sqrt{\frac{2(G_{lan} - Y_{aship})}{c_{ylan} \rho S}} = \sqrt{\frac{2G_{lan}}{c_{ylan} \rho S} (1 - K_{aship})} = V_{lanY_{aship}=0} \sqrt{1 - K_{aship}}$$

$$L_{run HA} \approx -\frac{V_{lan HA}^2}{2j_{xav}} = L_{run Y_{aship}=0}(1 - K_{aship}),$$

where $j_{xav run}$ —the value of the average tangential acceleration on the run.

It follows from these expressions that if $K_{aship} = Y_{aship}/G = 0.25$, then the above values take on values:

$$\begin{aligned} V_{toHA} &= 0.866V_{toY_{aship}} = 0, & V_{lanHA} &= 0.866V_{lanY_{aship}} = 0 \\ L_{runHA} &= 0.75L_{runY_{aship}} = 0, & L_{lanHA} &= 0.75L_{lanY_{aship}} = 0. \end{aligned}$$

4 Characteristics of Climbing and Descending

The conditions for the constancy of the trajectory angle θ and the flight speed HA in inclined flight, written according to Fig. 5, take the form:

$$Y_a - G \cos \theta + Y_{aship} \cos \theta = 0, \tag{8}$$

$$P - X_a - G \sin \theta + Y_{aship} \sin \theta = 0 \tag{9}$$

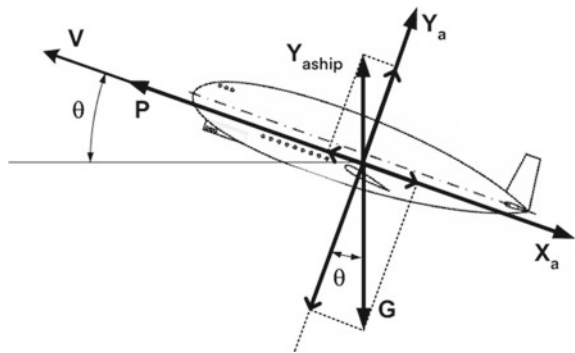
It follows from (8) that in inclined flight HA with some values of θ and V , the values of lifting force Y_a and its coefficients in the presence of aerostatic force, as in horizontal flight, are less than in the absence of it:

$$c_{ytgHA} = \frac{2(G - Y_{aship}) \cos \theta}{V^2 \rho S} = c_{ytgY_{aship}=0}(1 - K_{aship})$$

Smaller values of c_{ytg} correspond to smaller values of c_{xtg} and X_a .

The correlation of forces given in (9) for height gain shown in Fig. 6.

Fig. 5 Scheme of forces in inclined flight



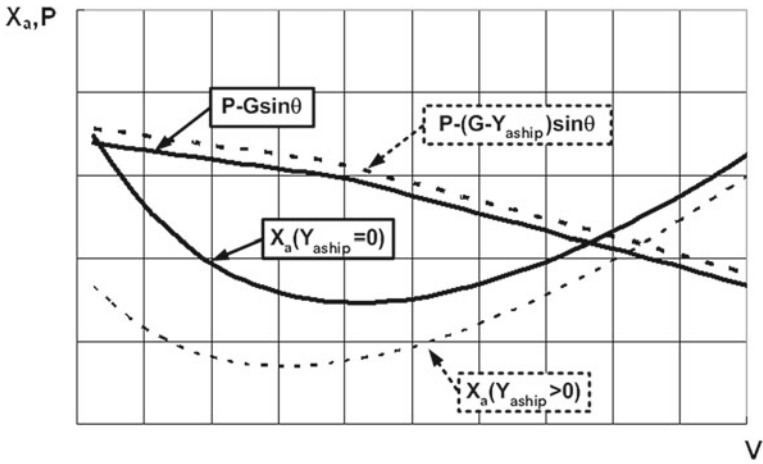


Fig. 6 The effect of aerostatic force on the required and available thrust in inclined flight

From (9) we can obtain an expression for calculating the disposable angle of inclination of the trajectory θ :

$$\sin \theta = \frac{P - X_a}{G(1 - K_{aship})} \tag{10}$$

Figure 7 shows the change in the available angle θ_{av} , and in Fig. 8 the vertical rate of climb $V_y = V \sin \theta_{av}$ from the flight speed during altitude gain.

Thus, when climbing, the presence of aerostatic force at HA increases the disposable angle θ at each flight speed both due to reduction of X_a , and due to $Y_{aship} \sin \theta$, acting in the direction of climbing. Accordingly, the maximum values of both θ_{max} and V_{ymax} increase.

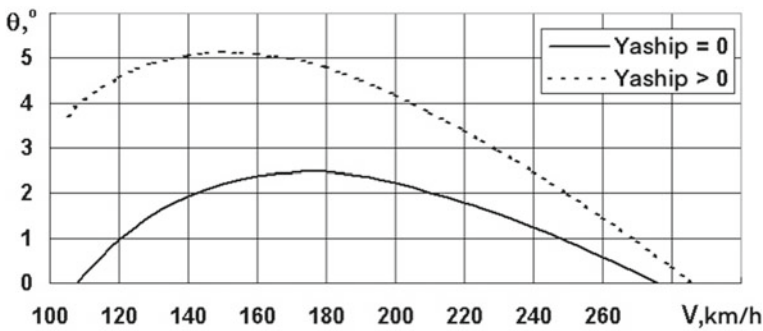


Fig. 7 To the effect of aerostatic force on the value of the available angle of inclination of the trajectory

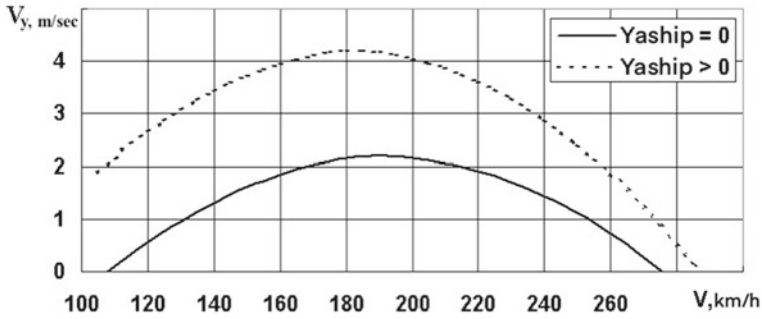


Fig. 8 To the effect of aerostatic force on the rate of lift of the HA

If planning ($P = 0$) is considered, then from (8) and (9) we can find that

$$tg\theta_{pl} = -\frac{X_a}{Y_a} = -\frac{1}{K_{aq}}, \quad tg\theta_{\min pl} = -\frac{X_{adv}}{Y_{adv}} = -\frac{1}{K_{aqmax}}$$

That is, the planning angle at first glance is determent only by the value of the aerodynamic quality of the K_{aq} and does not depend in any way on the aerostatic force. However, the presence of Y_{aship} leads to realization of the same coefficients of lift c_y , as at $Y_{aship} = 0$, but at lower speeds $V_{plHA} = V_{plY_{aship} = 0} \sqrt{1 - K_{aship}}$, i.e., to a shift of dependence $K_{aq}(V)$, and hence dependence $\theta_{pl}(V)$ toward lower values of planning speeds (see Figs. 9 and 10).

Thus, the range of planning angles of HA with aerostatic force has not changed, only the speeds at which they achieved have changed, namely, they have become smaller.

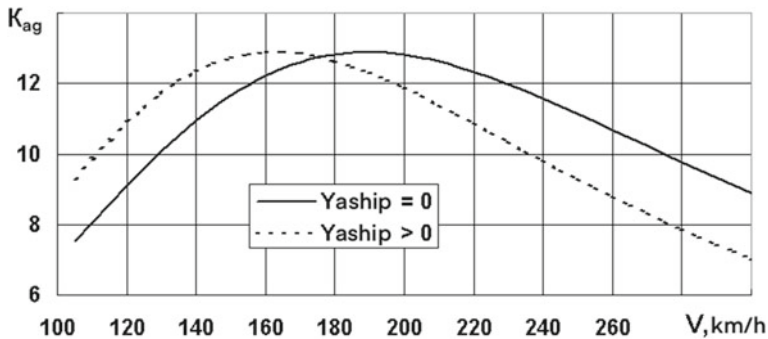


Fig. 9 To the effect of aerostatic force on the aerodynamic quality of the HA

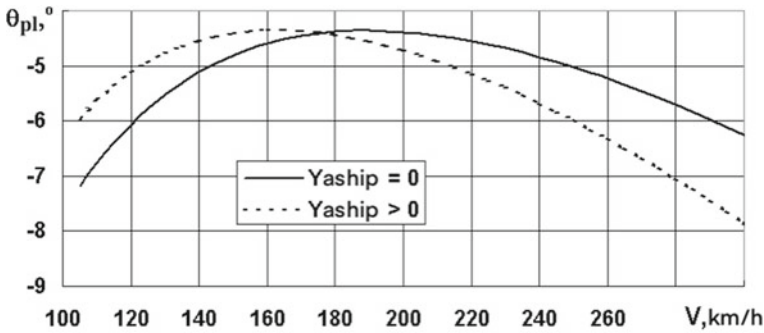


Fig. 10 To the effect of aerostatic force on the planning angles of the HA

5 Conclusions

The presence of aerostatic force in HA leads to a change in the considered APC toward their improvement, namely:

- operational range of altitudes and flight speeds expands;
- field performance improves (V_{land} , L_{land} , V_{loff} , L_{land} decrease);
- climbing characteristics are improved.

The effect of aerostatic force on these APCs is similar to the reduction of HA weight, but without changing its mass.

References

1. Athur D, Newman D, Wheelock J, Hall R (2005) Options for strategic military transportation systems. In: Congressional budget office (US congress), Washington DC
2. Spearman M, Feigh K (1999 June) A hybrid airship concept having twin-hulls and an inboard-wing. In: 13th lighter-than-air systems technology conference, Norfolk, VA, U.S.A
3. Mowforth E (2007) An introduction to the airship. The airship association
4. Liu T, Liou W, Schulte M (2009 March) Aeroship: a hybrid flight platform. *J Aircraft* 46:667–674
5. McElwee W, Miller Jr (1975) The dynairship (structural design criteria and feasibility analysis of an airplane-airship), pp 441–455
6. Dahms J, Bardenhagen A (2017 September) Approach to a synthesis of hybrid unmanned aircraft systems (UAS) in rotastatic configuration. In: 7th EASN international conference on innovation in European aeronautics research, Warsaw, Poland
7. Liu T, Liou WW, Schulte M (2009 March–April) Aeroship: a hybrid flight platform. *J Aircraft* 46(2). <https://doi.org/10.2514/1.39950>
8. Verma AR, Sagar KK, Priyadarshi P (2018 August) Optimum buoyant and aerodynamic lift for a lifting-body hybrid airship. *J Aircraft*. <https://doi.org/10.2514/1.C032038>
9. Andan AD, Asrar W, Omar AA (2012) Aerodynamics of a hybrid airship. AIP conferences proceedings, vol 1440, p 154. <https://doi.org/10.1063/1.4704214>
10. Andan AD, Asrar W, Omar AA (2012 March) Investigation of Aerodynamic Parameters of a Hybrid Airship. *J Aircraft* 49(2):658–662. [https://doi.org/10.2514/1.C031491\(2012\)](https://doi.org/10.2514/1.C031491(2012))

11. Mano S, Premkumar PS, Subhas M, Narashiman L, Pillai SN (2020 November) Aerodynamic characteristics of advanced airship shape—a computational investigation. In: AIP conference proceedings, vol 2270(1), p 040016 <https://doi.org/10.1063/5.0019854>
12. Zhang K, Han Z, Song B (2010 July) Flight performance analysis of hybrid airship: revised analytical formulation. *J Aircraft* 47(4):1318–1330. <https://doi.org/10.2514/1.47294>
13. Wu X (2011) Modelling and control of a buoyancy driven airship. Automatic control engineering. Ecole Centrale de Nantes (ECN); South China University of Technology
14. Svishchev GP (ed) (1994) Aviation: encyclopedia. Big Russian Encyclopedia, Moscow, 736 p
15. Arie MY (1986) Airships. Naukova Dumka, Kiev. No 6

Model-Based Automated Testing Method for Airborne System



Shaofan Zhu, Peipei Xing, and Hao Wang

Abstract This paper is about model-based testing (MBT) method for integration, verification, and validation process of the airborne system. In the context of model-based systems engineering (MBSE), in order to achieve the highly complex virtual integrated testing process, manual test procedure programming is gradually shifting to the MBT method, where test cases are automatically identified, allowing for automated test data analysis and test procedure generation. With a comprehensive exploration and customized development, COMAC has realized the MBT technical process, including modeling rules and requirements formalization, test goal generation methodology, especially implemented the model adapter code development for the communication between the test model and the system under test (SUT), and automated test execution and test result analysis in the two simulation network (RFM2G and high speed Ethernet). Finally, the aircraft ground deceleration scenario is taken as an example to illustrate the whole process, and the outlook on the future work of MBT is given.

Keywords Model-based system engineering · Virtual integrated testing · Model-based testing · Test case · Test procedure · Modeling and simulation · Airborne system

1 Introduction

In the process of virtual integration testing of C919 and CRJ929 aircraft, there is large number of interfaces that need to be configured, stimulated, and tested, the logical architecture between the systems is also extremely complex, which leads to a large amount of labor costs and significantly reduces the reliability of the interaction between human and SUT, such as manual handwriting of test cases, manual configuration, test execution, test coverage analysis, and test report writing. This traditional

S. Zhu · P. Xing (✉) · H. Wang
COMAC Beijing Aircraft Technology Research Institute, Beijing, China
e-mail: xingpeipei@comac.cc

manual writing of test cases and test scripts relies on the level and experience of the test engineer, it is difficult to ensure test adequacy and consistency, and the test efficiency is very low [1].

During recent years, the methodology of MBSE and its supporting tools has been observed by aircraft manufacturers like Airbus, COMAC with growing interest, like the potential of automated generation of target system code, as well as the possible efficiency increase to be gained from MBT, have been investigated. The significance of MBT in the virtual integration test of civil aircraft is huge, such as

- test cases are automatically generated based on the model, which is convenient for test management and maintenance;
- significantly reduce the labor cost required to write, modify test cases, and execute tests;
- realize the traceability of requirements and test verification and assist in obtaining airworthiness certification;
- adaptation flexibility for different existing forms (model/hardware/software) of the system under test.

The MBT paradigm will be adopted more widely in the development and verification processes of avionic systems domain within the next years.

The tool supporting the MBT process is RT-Tester, which supports automated testing of real-time systems. It is a collaboration product between the International Verification System and the University of Bremen's TZI (computing technology), and it has obtained RTCA DO-178B/C certification [2]. Combining the practical engineering experience, COMAC has launched a comprehensive and in-depth technical research and underlying development of MBT, and built several simulation test scenario cases in different simulation environments (such as reflective memory networks (RFM2G), real time simulation databus based on high speed Ethernet).

In Section two of this paper, we shall describe in detail the overall technical architecture and specific implementation process of MBT; a case study derived from aircraft model development process is presented in Section three; and Section four presents the outlook for MBT work and the summary on MBT application issues.

2 Implementation Process for MBT

Model-based testing (MBT) aims to use modeling methods to describe, generate, execute, and analyze results of tests. In the defined test environment, it connects to the actual SUT and executes the test under the guidance of automatically generated test procedures. The final generated result is compared with the expected result in the test procedure to complete the validation of requirements and other related. The overall technical path of MBT is shown in Fig. 1, and each specific process is described in detail below.

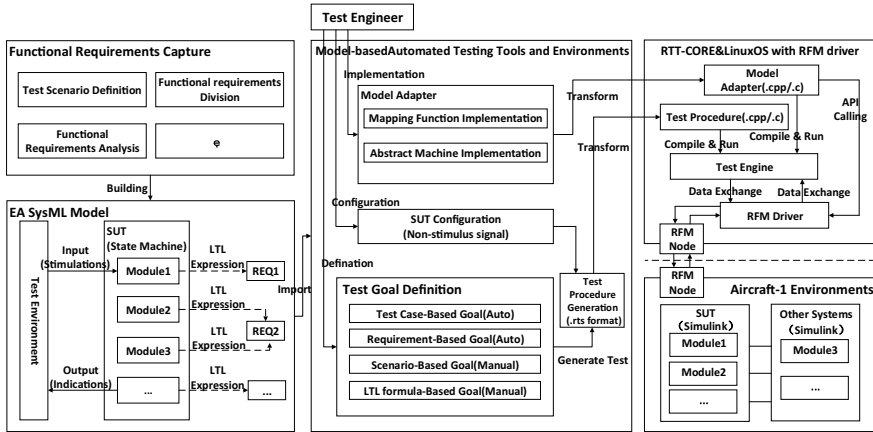


Fig. 1 Overall technical architecture of MBT

2.1 Capture of Functional Requirements

In the functional requirements capture stage, firstly we need to determine the test scenario and extract the corresponding functional requirements in the scenario. The test engineer analyzes these functional requirements and determines the required external environment definition to provide input for the test scenario modeling. These requirements can be imported into the SysML modeling tool, and the test model is developed based on the requirements.

2.2 Building of Test Model

The establishment of test model is the basis of automatic generation of test cases, automatic calculation of test data, and generation of test procedure. Thus, how to ensure the accuracy of modeling and the integrity of requirement expression is the key basis for the effective implementation of MBT.

A test model is used that describes the behavior of the system that should be tested. The SysML language is used to model the SUT and its interactive external environment. The basic elements of building a test model include:

- Class diagram: used to express the various components of the model;
- State machine diagram: used to describe the expected behavior of the SUT;
- Requirements: used to formally express functional requirements that need to be validated;
- Parameters: used to express and transmit the test excitation signal, SUT output signal, and calculation data of the intermediate process.

In order to generate test cases automatically, we need to customize a set of modeling rules to make model elements recognized and imported by MBT tools. A standard modeling strategy is shown in Fig. 2, and the model tree structure is shown in Fig. 3.

2.3 Formalization and Linking of Requirements

Based on the state of the SUT and the description of functional requirements, linear temporal logic (LTL) [3] is used to formalize the requirements. Functional requirements will transform text description into specific logical expression through LTL in the way of state combination, thus resulting in the mapping and traceability from state to requirement.

Fig. 2 A standard modeling strategy

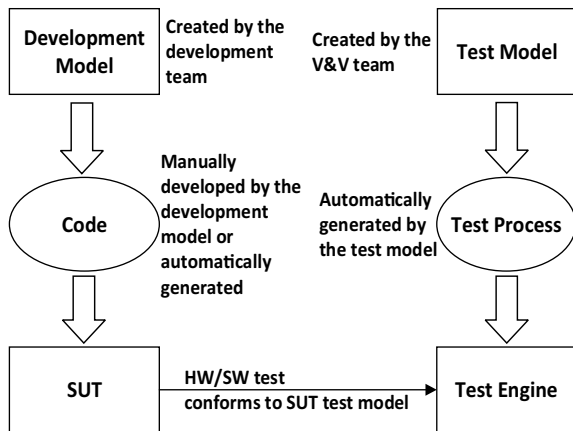
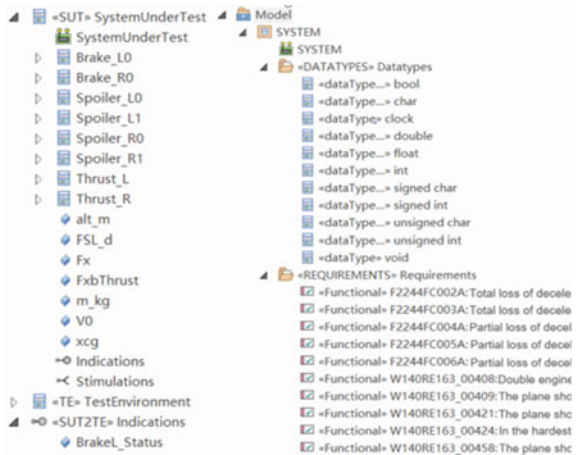


Fig. 3 Model tree structure



The functional requirements are stored in the <<Requirement>> prototype, and each element in the state machine is linked with the requirements, including two types of links [4]:

- Single link: a single state or a single transition is linked to the requirement, which is directly used as the implementation of the formal expression of the requirements;
- Composite link: multi-state, multi-transition, or multi-state-transition are linked to requirements according to certain logical expression. For example, the requirement *After a two-engine shut down, the aircraft should be able to extend at least two pairs of spoilers during landing* is linked to corresponding states through formal expression as follows:

```
<<invariant>>  
{Finally{SpoilerL0_On&&SpoilerL1_On&&SpoilerR2_On}}.
```

2.4 Automated Execution of Tests

2.4.1 Automated Test Case Generation

Test cases can automatically be derived from the test model in form of LTL formulas. MBT tool can import the SysML model and then generate the internal model representation (IMR), which is a special variant of the abstract syntax tree [5]. Transition relation generator traverses the IMR and generates transition relationships and then combines with the test generator to realize automatic generation of test cases based on multiple strategies support or requirements. Different from the traditional test case which describes the whole testing process, the test case generated by MBT defines the precondition and input values, but not the expected outputs, because these are already defined in the model describing the expected behavior of the SUT. The expected outputs are calculated by test oracles that are executed together with a test procedures covering the test cases. According to different forms, test cases can be divided into state, transition, or their combination.

2.4.2 Model Adapter Implementation

The adaptation process of the test is shown in Fig. 4. The abstract interface used in the test model needs to be adapted to the specific software and hardware interfaces. The adapter generator parses all the model interfaces and generates a file with .rts suffix based on the RTTL (RT-Tester Test Language) framework library and then combines with the specific form of SUT, test engineers realize the drive of the test excitation data to SUT and the collection and comparison of the SUT result data by writing the function body. The MBT adapter generator provides an important means to reuse the test models of different SUTs: in many cases, different versions of the

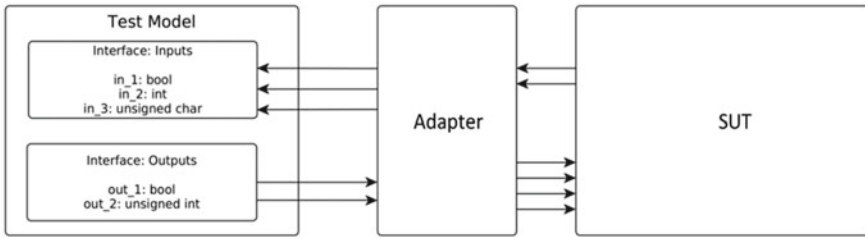


Fig. 4 Test adaptation process

SUT achieve the same function, but the hardware interfaces are different. In this case, you only need to rewrite the adapter function body, and the test model and even the test procedure can be reused directly.

Before generating the test procedure, the basic configuration of the test project is needed, including the selection of code language, the type of API, the operating system, etc., as shown in Fig. 5.

For the SUT or its simulation network, it needs to provide the corresponding API library to realize the model adaptation and interface communication. Figures 6 and 7 show two kinds of simulation network APIs respectively.

- RFM2G: introduce RFM.h2g.h in the test configuration file to read and write the corresponding variables in the RFM2G and develop the corresponding test code to open the board for communication testing;
- Real-time simulation databus: introduce VSAPI.h/VSCAPI.h into the project, set the location of the real-time simulation databus library in the test configuration, and install the required so file on the Linux operating system.

The main framework function code is similar to the Main function, which defines the entire test process, mainly including the command to import the test stimulus

```

37 //
38 // Family and Compiler definitions (if any)
39 //
40 // FAMILY : posix-std | cadu
41 // COMPILER: gcc | g++
42 // LANG : C | C++
43 // ARCHITECTURE: i686 | x86_64
44 //
45 //
46 //
47 // ARCHITECTURE: i686
48 // LANG : c++
49 // COMPILER: g++
50 //
51 // compile flags to be used in all make files for generation
52 // of executable test cases
53 //
54 CFLAGS:
55   -I$(SOFTWAREPATH)
56   -I$(SOFTWAREPATH)/include
57   -I$(RTT_TESTCONTEXT)/inc
58   -I$(find $(RTT_TESTCONTEXT)/inc -type d -not -name CVS -not -name .svn | xargs echo | sed -e 's/| / -I/g'*)
59   -g3 -gdb3
60   -m32
61
62
63 CFLAGS:
64   -Iusr/local/include/boost

```

Annotations in the image:

- Line 47: Operating system selection, choose Linux here
- Line 48: Programming language selection, choose C++ here
- Line 49: ompiler selection, choose C++ compiler here
- Line 60: Define the compiler as 32-bit
- Line 64: The setup tool calls the boost library required for C++ language compilation in the Linux system

Fig. 5 Test configuration

```
1 // This file contains configuration settings to include RFM2G header and library
2
3 // Extend the include path to find the API header files
4 // Note: this is only a sample and must be adjusted.
5 //     more API header files might be needed.
6 // TODO: adjust the following line to point to your installation
7 CFLAGS ; -I$(RTT_TESTCONTEXT)/vs/include
8
9 // Extend the linker path to find the API library
10 // Note: this is only a sample and must be adjusted.
11 // TODO: uncomment and adjust the following line(s)
12 //LDFLAGS ; -L
```

Fig. 6 RFM2G API

```
1 // This file contains configuration settings to include RFM2G header and library
2
3 // Extend the include path to find the API header files
4 // Note: this is only a sample and must be adjusted.
5 //     more API header files might be needed.
6 // TODO: adjust the following line to point to your installation
7 CFLAGS ; -I$(RTT_TESTCONTEXT)/rfm2g-installation/include
8
9 // Extend the linker path to find the API library
10 // Note: this is only a sample and must be adjusted.
11 // TODO: uncomment and adjust the following line(s)
12 //LDFLAGS ; -L<path-to-vrfm2g-v1.30-installation-lib-dir> -l<rfm2g-library-name>
13
14 // The following line must be removed (or commented)
15 // to deactivate the RFM2g driver stubs used for
16 // developing the project.
17 STUBS ; $(RTT_TESTCONTEXT)/RFM2G/stubs
```

Fig. 7 Real-time simulation databus API

data into the SUT model and read the model calculation data and compare it with the test expectations, as shown in Fig. 8.

The interface mapping code realizes the communication mapping between the excitation signal and the SUT and compares the real-time output data. Figure 9 shows the partial codes of data writing and data reading in the real-time simulation databus (left) and RFM2G (right).

```
1 #include "rttInterface.h"
2 #include "MBTAdapterAM.h"
3 #include "MBTAdapterFuncs.h"
4
5 // Model interface
6 extern rttInterface_t *rttIOPost;
7
8 // MBT adapter internal state
9 static rttInterface_t rttIO_MBTAdp_Simulink_Scenario_last = { 0 };
10 static bool_t mbtAdapterEnabled_Simulink_Scenario_last = FALSE;
11 static bool_t triggerFullUpdate_Simulink_Scenario_last = FALSE;
12
13 // Enable MBT adapter AM.
14 @func void enableMBTAdapter_Simulink_Scenario_last() {
15     mbtAdapterEnabled_Simulink_Scenario_last = TRUE;
16     triggerFullUpdate_Simulink_Scenario_last = TRUE;
17     @printf("MBTAdapter(Simulink_Scenario_Last): ENABLE*");
18 }
19
20 // Force complete update of all interface variables.
21 @func void forceUpdate_Simulink_Scenario_last() {
22     triggerFullUpdate_Simulink_Scenario_last = TRUE;
23     @printf("MBTAdapter(Simulink_Scenario_Last): FORCE TE2SUT UPDATE*");
24 }
```

Fig. 8 Main frame code

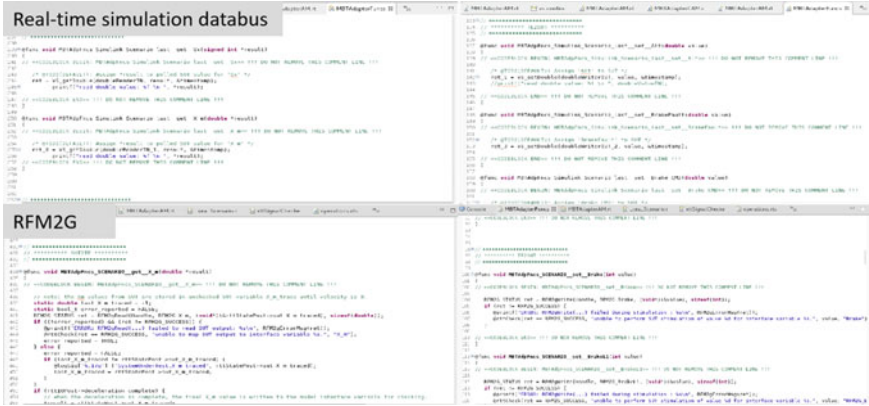


Fig. 9 Interface mapping code development

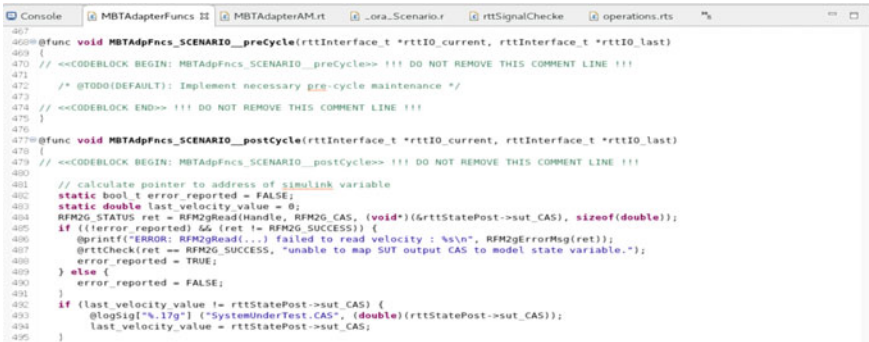


Fig. 10 PostCycle() function code

In addition, functions such as postcycle() and precycle() can be used to implement the real-time feedback mechanisms. As shown in Fig. 10.

2.4.3 Test Goals

After the test engineer imports the target test model into MBT tool, in order to automatically generate the test procedure, the test goals needs to be defined, which can be formulated in the following four ways. The selected coverage goals represent one or more LTL formulas that are used during the test generation to calculate stimulations for the SUT to reach the goal. The number of LTL formulas represented by a goal depend on the type of goal that is defined.

Model-Based Test Goals. Take model elements as test goals, such as components and sub-components of the SUT, states and transitions in the state machine.

Requirements-Based Test Goals. Requirement-based testing is the mainstream means of testing goals definition. It relies on the formal definition of requirements in the model. Taking the requirements as the test goals directly can ensure the traceability of requirement based testing and realize the requirement coverage analysis after testing.

Test Goals Based on Test Scenarios. Describe test scenarios in a textual manner and take it as test goals can solve the problem that scenario models cannot describe dynamic changes well. After the test procedure is generated in this way, model associations will be generated, and test case coverage will also be achieved.

LTL-Based Test Goals. User defined LTL formulas expresses test goals in a similar way to composite links of requirements. It gives engineers more possibilities and flexibility to define test goals. They can use logical symbols to build different model elements to achieve a certain test goal.

Coverage Strategies. Model coverage goals represent a number of test cases and therefore a number of LTL formulas. If a model element coverage goal is selected for a test procedure generation, this model element shall be covered in the specified way by the generated test procedure. How this model element is covered depends on the type of element and on the strategy selected for the goal [6].

- Basic control state coverage (BCS): specify the test goal as the system needs to reach a certain state;
- BCS PAIRS: specify the test goal as the system needs to reach two concurrent states;
- Transition coverage (TR): specify the test goal as the system needs to execute every transition of every state machine;
- High level transition coverage (HLTR): specify the test goal as the system needs to perform the hierarchical transition of each state machine, for transitions from high-level control states, different underlying basic control states can be activated when the transition is triggered;
- Modified condition/Decision coverage (MC/DC): DO-178B/C implements MC/DC coverage test for A-level system.

2.4.4 Automated Generation and Execution of the Test Procedure

Test Procedure Generation. It is necessary to transform the formal verification problem of the test goal into a formula satisfiability problem and make a certain goal formula established through the value calculation of multiple variables, so as to realize the automated calculation of test data and the automated generation of test procedure and report. The test procedure report covers the test goals, the sequence of test stimulus generation, detailed test code, and the expected output results. The

```

1
2
3 @func void stimulator()
4 {
5
6   rttIOPost->Alt = 0.000000;
7   @logSig["%17g"] ("Alt", (double) 0.000000);
8   rttIOPost->BrakeFault = 0.000000;
9   @logSig["%17g"] ("BrakeFault", (double) 0.000000);
10  rttIOPost->Brake_CMD = 0.000000;
11  @logSig["%17g"] ("Brake_CMD", (double) 0.000000);
12  rttIOPost->FSL_L = 0.000000;
13  @logSig["%17g"] ("FSL_L", (double) 0.000000);
14  rttIOPost->FSL_R = 0.000000;
15  @logSig["%17g"] ("FSL_R", (double) 0.000000);
16  rttIOPost->Left_Fault = 0.000000;
17  @logSig["%17g"] ("Left_Fault", (double) 0.000000);
18  rttIOPost->Right_Fault = 0.000000;
19  @logSig["%17g"] ("Right_Fault", (double) 0.000000);
20  rttIOPost->TRL_L = 0.000000;
21  @logSig["%17g"] ("TRL_L", (double) 0.000000);
22  rttIOPost->TRL_R = 0.000000;
23  @logSig["%17g"] ("TRL_R", (double) 0.000000);
24  rttIOPost->X_m_expected = 0.000000;
25  @logSig["%17g"] ("X_m_expected", (double) 0.000000);
26
27  /* End of initial assignments. Add SUT initialization here, i
28
29  rttIOPost->X_m_expected = 270.000000;
30  @logSig["%17g"] ("X_m_expected", (double) 270.000000);

```

Fig. 11 Simulator.rts

```

1
2
3 #include <rtttl.h>
4
5 rttModelVars_t *rttStatePost;
6
7
8 rttInterface_t *rttIOPre;
9 rttInterface_t *rttIOPost;
10
11 void am_timetick_initializeOverwrittenDefaultVariables();
12
13 #ifndef AM_TIMETICK_PREFIX
14 #define AM_TIMETICK_PREFIX am_timetick
15
16 #endif AM_TIMETICK_INIT
17 #func void am_timetick_INIT()
18 {
19   rttIOPre = (rttInterface_t *) calloc(1, sizeof(rttInterface_t));
20   rttIOPost = (rttInterface_t *) calloc(1, sizeof(rttInterface_t));
21   rttStatePre = (rttModelVars_t *) calloc(1, sizeof(rttModelVars_t));
22   rttStatePost = (rttModelVars_t *) calloc(1, sizeof(rttModelVars_t));
23   am_timetick_initializeOverwrittenDefaultVariables();
24   rttStatePost->sut_GAS = 0.0;
25   rttStatePost->sut_Fn = 0;
26   rttStatePost->sut_Fx = 0;
27   rttStatePost->sut_X_m_traced = 0.0;
28   rttIOPost->via = 0;
29   rttIOPost->X_m = 0.0;
30 }
31 #endif
32 #endif AM_TIMETICK_FINAL

```

Fig. 12 Test.rts

generated test code based on RTTL includes several parts, as shown in Figs. 11, 12, and 13.

- Simulator.rts: generate the test stimulus code and the function definition of test sequence according to the defined test goal.
- Test.rts: test timer.
- rttSignalChecker.rts: compare the actual output with the expected value.

Test Compilation and Execution. This process requires the integrated use of two tools, RTT-CORE and RTT-TMS [7]. After generating the test procedure, the generated test code based on RTTL will be converted into C/C++ language code and further compiled into an executable file. Then, run the compiled test code and the SUT model at the same time, load the test stimulus data into the SUT model through the model adapter, execute the test according to the time sequence specified by the generated

```
48 //
49
50 #include "rttExternDecl.h"
51 #include "rttSignalChecker.h"
52
53 #include <math.h>
54
55 #define RTT_MBT_DEBUG
56 #define DBL_MAX 1.79769313486231470e+308
57 #endif
58
59 typedef enum rttmbt_checker_state_t
60 {
61     rttmbt_init_checker = 0,
62     rttmbt_indication_ok = 1,
63     rttmbt_new_expected = 2,
64     rttmbt_new_observed = 3,
65     rttmbt_error_detected = 4
66 } rttmbt_checker_state_t;
67
68 static void rttmbt_assign(void *lhs, void *rhs, rttmbt_signal_types_t
69 rttmbt_equal(void *lhs, void *rhs, rttmbt_signal_types_t
70 rttmbt_valAcceptable(void *observed, void *expected, dt
71 rttmbt_signal_types_t type, double *deviation_ptr);
72 static void logStateChange(const char *signalName, const char *from,
73 void *value, rttmbt_signal_types_t type);
74 static void logNewExpectedValueWarning(const char *signalName, int cu
75 void *expected_val, rttmbt_signal_types_t type);
76 static void logNewObservedValueWarning(const char *signalName, int cu
77 void *observed_val, void *expected_val, double *deviation_ptr);
```

Fig. 13 rttSignalChecker.rts

test procedure, and read out the data of the SUT model for comparison, until the whole test procedure is completed.

The MBT tool runs in Linux environment and needs to rely on a large number of library files. After multiple rounds of debugging, it finally realizes the compilation and running of test code in RFM2G and real-time simulation databus, as shown in Figs. 14 and 15.

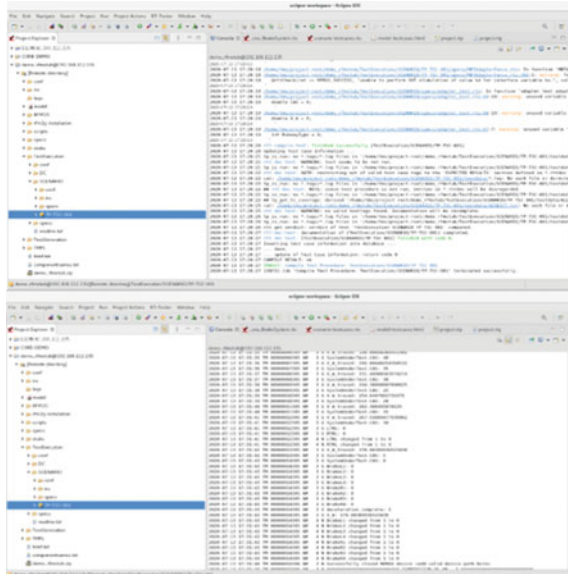


Fig. 14 RFM2G

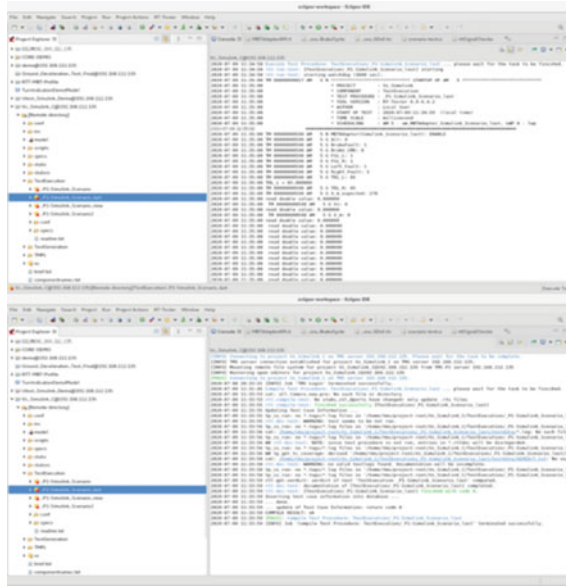


Fig. 15 Real-time simulation databus

2.4.5 Automated Analysis of Test Results and Report Generation

According to the definition of the test procedure, the MBT tool can automatically analyze different types of test coverage: test case coverage and requirement coverage. For requirement-based coverage analysis, the test cases covered by the linked requirements in the test model are all explicit. When all the test cases covered by the requirements are in the pass state after the test code runs, the requirement is in the pass state; otherwise, the requirement is in the fail state [8]. The MBT tool can explicitly show the two-way traceability relationship between requirements and test cases, as well as the traceability relationship between requirements verification results and test case test results. According to the requirement that the test results are not fully covered, we shall further design and adjust the test model and test procedure to achieve complete test coverage for each requirement. Finally, test result reports are generated automatically according to different types of test coverage analysis.

3 Case Study-Aircraft Ground Deceleration Scenario

To illustrate various aspects of MBT for airborne systems, a case study concerning aircraft ground deceleration scenario is presented in this section. The study has been derived from the real ground deceleration control function as used in aircraft, but

Table 1 Functional requirements for ground deceleration

Number	ID	Requirements description
1	W140RE163_001	After a two-engine shut down, the aircraft should be able to extend at least two pairs of spoilers during landing
2	W140RE163_002	The aircraft should be able to deceleration on the ground when the two engines shut down
3	W140RE163_005	The aircraft should provide at least 3 independent methods for ground deceleration control: 1.wheel brake 2.thrust 3.spoiler
4	W140RE163_007	The aircraft should ensure that the thrust is used between 60 knots (TBC) and 160 knots (TBC)

it has been simplified with respect to complexity of the model and retained the characteristics and parameters related to deceleration control function to facilitate the presentation of various MBT features. This process regards the system as a black box, which realizes the validation of functional requirements.

3.1 Requirements Capturing

The four functional requirements in this case come from the items that related to ground deceleration in the aircraft requirements document, as shown in Table 1.

3.2 Test Scenario Modeling

The three most critical systems for realizing the aircraft ground deceleration control function are selected as the SUT: engine, brake, and flight control system (spoiler). Based on the above functional requirements that need to be validated, a test model for the ground deceleration scenario is built. The top-level structure of the model is shown in Fig. 16, the left side represents the interface interaction between the SUT and the test environment, the right side shows the behavior expression of the engine, brake, and flight control system encapsulated in the “Class” module, and the state combination of each system is linked with the functional requirements in the form of a composite link.

The behavior of SUT is presented in the form of a state machine, which expresses the input and output of the current system in this state, as well as the initial and post-conditions to reach this state. As shown in Figs. 17–19.

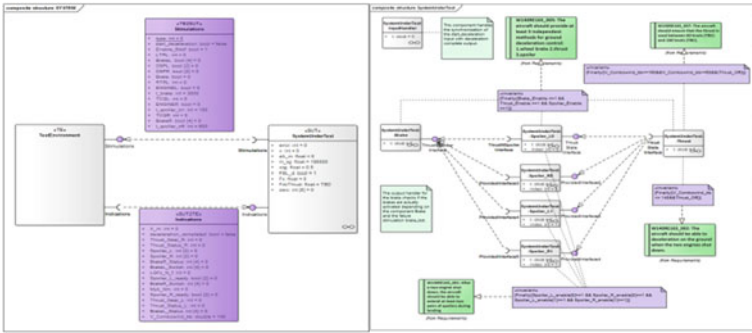


Fig. 16 Top-level structure of ground deceleration scenario model

Fig. 17 Thrust



Fig. 18 Brake

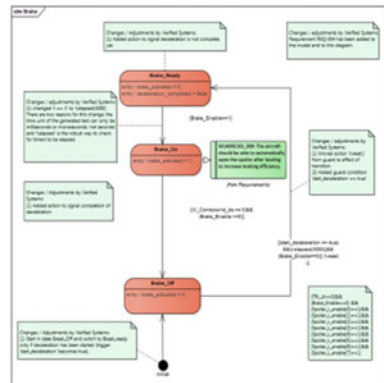
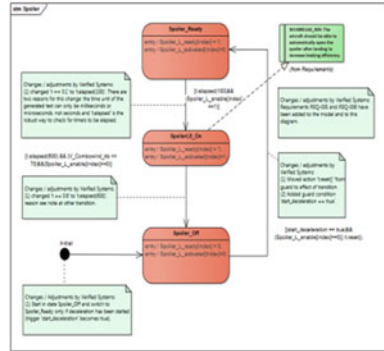


Fig. 19 Spoiler



3.3 Automated Test Generation and Execution

During the ground deceleration test model import, MBT tool automatically identified and generated 154 test cases for the different model coverage strategies (25 BCS, 26 TR, 30 BCS PAIRS, 69 MC/DC, and 4 User-Defined). The test engineer performed basic configuration of the test, called the corresponding API, developed interface mapping code, test code, etc., and then took the requirements formalized by LTL as the test goal, as shown in Fig. 20. The four requirements in the left part of the Goal Editor can be used to add as coverage goals for the test procedure generation. A requirements goal represents the LTL formulas of all test cases that are needed to satisfy the requirement. These are the LTL formulas generated from the model elements that are satisfying the requirement in the test model. These four requirements generated a total of 8 test cases covering the test goals and several test cases that are not explicitly selected as test goals but are implicitly deployed by the generated test procedure.

After a test procedure generation context is configured completely, a test procedure is generated according to this configuration. At the same time, a report is generated that provides information about the test generation results. This report includes the configuration files used for the test generation, how much time was used for the test generation, the expected test execution duration, which of the defined test goals are deployed and which are not, implicitly covered test cases, detailed test code, test procedure stimulations, and expected behavior. Figure 21 shows part of the report. In this study case, we chose to compile the test code in the RFM2G environment,

Console				Goal Editor				RTT-MBT Require				RTT-MBT Test Da				RTT-MBT Test Da				RTT-MBT Require			
Name	Verdict	Headline	Der	Goals	BCS	BCSPAIRS	TR	HITR	MCDC														
1	REQ-001	NOT TESTED		1																			
2	REQ-002	NOT TESTED		2																			
3	REQ-005	NOT TESTED		3																			
4	REQ-007	NOT TESTED		4																			
				5																			
				6																			

Fig. 20 Editing of test goals

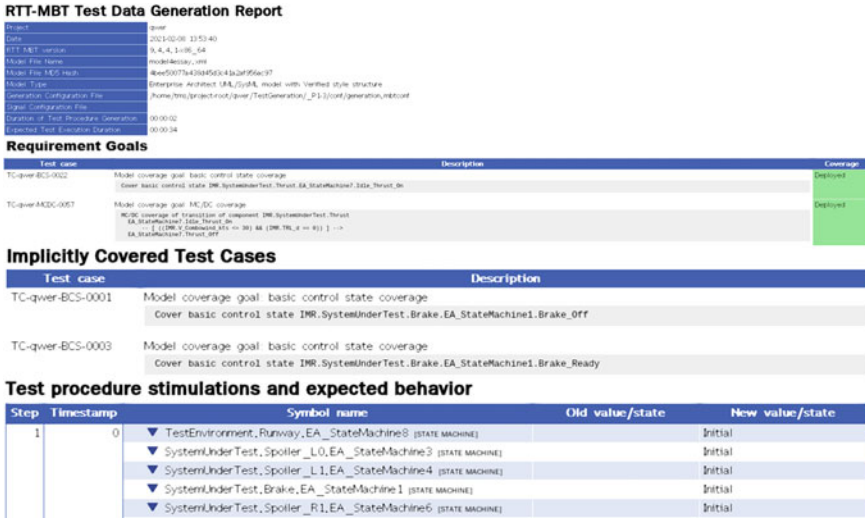


Fig. 21 Automatic generation of test procedures report

execute the entire test according to the generated test procedure, and finally generate a test result report.

3.4 Test Result Coverage Analysis

As shown in Fig. 22, the test case view lists all test cases (8 test cases covered by requirements are intercepted in the figure), their status and their relationships to test procedures. All the test cases are in the pass state, so the test procedure is in the pass state.

The requirement view lists all requirements, their status, and their relationships to test cases. The test cases listed for each requirement have been automatically derived from the model and associated with the respective requirement. As a consequence,

	Name	Verdict	Complexity	Style	Duration	Status
1	./TestExecution/SCENARIO/TP-T...	PASS	MEDIUM	RTL 6.x	3600	COMPLETED
2	TC-RFM2G_Connection-UD-00...	PASS				COMPLETED
3	TC-RFM2G_Connection-UD-00...	PASS				COMPLETED
4	TC-RFM2G_Connection-UD-00...	PASS				COMPLETED
5	TC-RFM2G_Connection-BCS-00...	PASS				COMPLETED
6	TC-RFM2G_Connection-MCDC-0...	PASS				COMPLETED
7	TC-RFM2G_Connection-MCDC-0...	PASS				COMPLETED
8	TC-RFM2G_Connection-MCDC-0...	PASS				COMPLETED
9	TC-RFM2G_Connection-UD-00...	PASS				COMPLETED

Fig. 22 Test case view

1	REQ-001	PASS	COMPLETED
2	TC-RFM2G_Connection-UD-0001	PASS	COMPLETED
3	REQ-002	PASS	COMPLETED
4	TC-RFM2G_Connection-UD-0003	PASS	COMPLETED
5	REQ-005	PASS	COMPLETED
6	TC-RFM2G_Connection-UD-0002	PASS	COMPLETED
7	REQ-007	PASS	COMPLETED
8	TC-RFM2G_Connection-BCS-0022	PASS	COMPLETED
9	TC-RFM2G_Connection-MCDC-0057	PASS	COMPLETED
10	TC-RFM2G_Connection-MCDC-0058	PASS	COMPLETED
11	TC-RFM2G_Connection-MCDC-0059	PASS	COMPLETED
12	TC-RFM2G_Connection-UD-0004	PASS	COMPLETED

Fig. 23 Requirement view

a requirement can be considered as sufficiently covered in many test campaigns, if all test cases listed in the view for the requirement have been exercised in at least one procedure. Test case TC-RFM2G- Connection-UD-0003, for example, is implemented in test procedure Test Execution/SCENARIO/TP-TSC-001, and it contributes to the validation of requirements REQ-002. As shown in Fig. 23, the four functional requirements of ground deceleration that need to be validated in this case have been fully covered.

4 Conclusions

In this paper we have described COMAC’s exploration and practice of MBT technology in the context of virtual integration testing and gave a case to illustrate how MBT can be applied for airborne system. Taking the advantages of MBT tools that have obtained the DO-178B/C tool certification, it can be applied in the desktop simulation integration and testing of the whole aircraft system to realize the automatic generation of life cycle data required for the airworthiness certification process. Finally, the in-depth application of MBT technology in the development of future models will be realized, which can greatly save the manpower cost and improve the test reliability of complex system. It should be noted that the MBT tool cannot achieve combinatorial explosion test configuration and test execution and cannot achieve automatic generation of test oracles and automatic analysis of test result data in black box test verification based on performance requirements.

References

1. Peleska J (2018) Model-based avionic systems testing for the airbus family. In: 2018 IEEE 23rd European test symposium (ETS), pp 1–10. <https://doi.org/10.1109/ETS.2018.8400703>
2. Rasche R, Himmler A, Franke M et al (2018) Interfacing & interchanging-reusing real-time tests for safety-critical systems. In: 2018 AIAA modeling and simulation technologies conference
3. Efkemann C (2014) A framework for model-based testing of integrated modular avionics (PhD thesis), University of Bremen

4. Dahlweid M, Brauer J, Peleska J (2015) Model-based testing: automatic generation of test cases, test data and test procedures from SysML models. SAE technical paper. <https://doi.org/10.4271/2015-01-2553>
5. Peleska J (2013) Industrial-strength model-based testing-state of the art and current challenges. Petrenko A, Schlinglo H (eds) Eighth workshop on model-based testing (MBT 2013), EPTCS, vol 111, pp 3–28
6. Verified Systems International GmbH (2013) RTT-MBT model-based test generator version 9.0-1.0.0-tool qualification report. Technical report verified-INT-007-2013, Verified Systems International GmbH.
7. Peleska J (2013) Industrial-strength model-based testing-state of the art and current challenges. In: Alexander KP, Schlingloff H (eds) Proceedings eighth workshop on model based testing, Rome, Italy, 17th March 2013, vol 111 of electronic proceedings in theoretical computer science, pp 3–28
8. Löding H, Peleska J (2010) Timed moore automata: test data generation and model checking. In: International conference on software testing, verification, and validation, pp 449–458

Design and Modeling of Remotely Piloted Operations (RPO) Mode for Commercial Aircraft



Kelin Zhong, Yong Chen, Yue Luo, and Miao Wang

Abstract The unmanned piloted operations mode is the key development direction of the next generation of commercial aircraft. We propose the remotely piloted operations (RPO) mode of commercial aircraft which combines the autonomous piloting and remotely piloting technology, and describe its organization structure including ground station, airborne intelligent system, and air–ground data link in detail. Then, we take the cruising phase as an example to carry out model-based scenario design and verification. It is found that the RPO mode can basically cover the operations of dual pilots, and autonomous flight in authorized airspace can reduce the workload of the remote pilot and improve airspace utilization and flight safety.

Keywords Remotely piloted operations · Commercial aircraft · Air–ground collaboration · Scenario design

1 Introduction

Since the 1950s, the crew of civil airliners has evolved from a five-person operating mode which consists of captain, first officer, flight engineer, navigator, and radio operator to a dual-pilot operating mode which only contains captain and first officer.

K. Zhong
COMAC Shanghai Aircraft Design and Research Institute, Shanghai, China
e-mail: zhongkelin@comac.cc

Y. Chen · Y. Luo · M. Wang (✉)
Shanghai Jiao Tong University, Shanghai, China
e-mail: miaowang@sjtu.edu.cn

Y. Chen
e-mail: chenyong@comac.cc

Y. Luo
e-mail: luoyue@sjtu.edu.cn

Y. Chen
Commercial Aircraft Corporation of China, Shanghai, China

Nowadays, many experts and scholars at home and abroad have carried out related research on Single-Pilot Operation (SPO) [1]. Further, the unmanned piloted operations mode is the key development direction of the next generation of commercial aircraft [2–4].

Unmanned piloting technology of commercial aircraft are divided into two categories. One is the autonomous piloting technology, also known as Driverless Vehicle, in which the airborne intelligent system autonomously completes the piloting and control of the aircraft. The other is the remotely piloting technology, also known as Unmanned Aerial Vehicle [5]. In this way, the ground operator completes the piloting and control of the aircraft from ground station.

The object of this project is to combine the above two methods. The entire commercial aircraft unmanned pilot uses the airline's remote ground remote pilot control, but in certain specific scenarios and under the authorization of the air traffic control, autonomous flight collaborative decision-making is carried out. The remotely piloted operations mode of commercial aircraft proposed in this paper combines the above two methods. The remote pilot at ground station control the aircraft throughout the flight, but in certain specific scenarios or in the airspace authorized by ATC, autonomous flight and collaborative decision-making is carried out.

2 Organization Structure of Remotely Piloted Operations (RPO) Mode

The flight process organization and management of the commercial remotely piloted aircraft (CRPA) is based on the air–ground collaborative organizing structure of ground station, airborne intelligent system, and air–ground data link. Among them, the ground station is responsible for remote flight mission planning, organization, and management to enhance flight operating and processing capabilities. The airborne intelligent system is responsible for flight environment information collection, flight status organization, and flight operating execution to complete flight information perception, flight status organization, and flight system management [6]. Air–ground data link provides high-speed data transmission, effectively improving air–ground collaborative capabilities, supporting flight environment perception and flight mission decision-making capabilities.

2.1 Ground Station

The ground station provides a means for remote pilot piloting and monitoring CRPA. The remote pilot/ground station and CRPA are connected through command and control link. The flight status information and control commands are transmitted through it.

The ground station consists of a set of equipment for remotely piloting, such as joystick and throttle. In order to reduce the workload of the remote pilot and assist them in better piloting and monitoring, some intelligent equipment is also essential, such as piloting assistance system, human-machine function intelligent distributing system, workload monitoring system, etc.

The remote pilot establishes situational awareness of the flight scene based on the flight data received by the ground station, makes flight decisions, and fulfills the needs of flight missions and goals.

2.2 Airborne Intelligent System

In order to further reduce the workload of remote pilots, CRPA needs to equip more automated equipment to assist remote pilots to ensure flight safety [7]. At the same time, in order to improve airspace utilization and flight safety, CRPA can fly autonomously in traffic areas authorized by air traffic control under the support of airborne intelligent system. If the flight path adjustment caused by weather and other conditions occurring during the period, or the aircraft optimizes the flight path under the current flight environment and status to save fuel, the aircraft can calculate the best flight path by analyzing the status of itself and automatically acquiring the flight intentions of other aircraft in the airspace from ATC and the optimal path will be reported to ATC for the record. Therefore, with the assistance of the airborne intelligent system, the remote pilot in most cases only act as the “remote co-pilot” and monitor the flight of the aircraft.

The airborne intelligent system collects, processes, and organizes the flight environment to construct flight mission status, conditions and results, and downloads the flight environment report, flight status report and system operating report to the ground station for collaborative decision-making.

2.3 Air-Ground Data Link

The air-ground data link provides a communication channel for remote pilots to control CRPA from the ground station. According to the air-ground communication requirements and information types, the air-ground high-speed two-way communication link need to be established to support air-ground mission organization, decision-making, and operating management.

3 Remotely Piloted Operations (RPO) Mode for Commercial Aircraft

Remotely Piloted Operations (RPO) Mode for Commercial Aircraft establishes the cooperative mode of airborne intelligent system, remote pilot, and ATC, aiming at meeting the requirements for flight capability and safety level of dual-pilot mode.

3.1 *Main Operating Ideas of the RPO Mode*

- a. Determine the flight conditions and modes, that means, according to the nominal flight conditions and off-nominal flight conditions, establish the responsibility and flight capability of airborne intelligent system and remote pilot, covering more than 95% of the dual-pilot mode.
- b. Determine the human-machine air-ground collaborative mode, the main purpose of which is to establish the cooperated mode among airborne intelligent system and remote pilot, according to the knowledge and thinking of human (the remote pilot), and the rules and logic of machine (airborne intelligent system), covering test and verification capability of the dual-pilot mode.
- c. Determine the state of single point failure, the main purpose of which is to establish collaborative fault identification among airborne intelligent system and remote pilot, according to the nominal or off-nominal flight of the aircraft and the normal or abnormal capability of the ground remote pilot, covering single point failure handling capability in the dual-pilot driving mode [8].
- d. Determine the cooperation mode with ATC. According to the nominal, off-nominal or autonomous flight of aircraft, establish the cooperation mode among airborne intelligent system, remote pilot, and ATC system to ensure that the existing airspace traffic management mode is not changed.
- e. Determine the capability and status of the ground remote pilot [9], namely, according to the normal or abnormal capability range and behavior of the remote pilot, establish the cooperation mode among airborne intelligent system and remote pilot to realize pilot health and behavior management, covering the dual-pilot driving mode.
- f. Determine the workload of the remote pilot [10]. According to four modes that include nominal flight operation and pilot healthy, off-nominal flight operation and pilot healthy, nominal flight operation and pilot incapacitated, off-nominal flight operation and pilot incapacitated, establish the cooperation mode among airborne intelligent system and remote pilot, to ensure the workload of the remote pilot who instead of the existing dual-pilot is not increased.

3.2 *Air–Ground Collaboration System Architecture*

The biggest difference between RPO mode and the current dual-pilot mode is that there is no pilot and cockpit on board. All flight operations are based on the air–ground collaborative system architecture that relies on the air–ground data link. At this time, the airborne intelligent system is responsible for the collection of flight environment information and the organization of flight status information. The ground station is responsible for flight mission planning and mission operating mode based on the data which passes through the air–ground data link from CRPA to the ground station, thus an information platform is established to complete the integration of environment, tasks and status, and realize the integration and optimization of air–ground mission operations. The air–ground data link provides high-speed data transmission, which can enhance the air–ground coordination capabilities, thereby supporting flight environment perception and flight mission decision-making capabilities.

The ground remote pilot, with the support of the ground station, will realize the following functions [11]:

- (1) Cooperate the ground station mission planning with the airborne information organization. The ground station and the airborne intelligent systems establish a common shared information platform for flight mission organization, operation, and management based on the mission plan to support mission requirements, a common shared information platform for flight environment, conditions, and status based on flight mission composition to support the mission organization, and a common shared information platform for flight management, communication, and surveillance based on the operation of the flight mission to support mission management.
- (2) Integrate the ground station mission operating management and airborne flight status organization. The ground console and the airborne intelligent systems establish a common shared information platform for flight missions, capabilities, and objectives, based on the flight environment condition, to determine mission processing requirements and support mission selection decisions, a common shared information platform for operations, performance, and results of the flight mission based on mission operating status to determine mission operating performance and support mission control decisions and a common shared information platform for flight function types, capabilities, and quality based on the mission processing status to determine functional processing processes and support mission processing decisions.
- (3) Information shared platform and decision-making for flight mission demand. According to the sharing capabilities based on information platform, the ground station and the airborne intelligent systems will establish mission requirement, mission organization, and mission decision-making mode, and determine the adaptability of decisions and flight missions. Based on the coverage capabilities of the information platform, establish mission requirements and mission

organizations and mission decision-making range, and determine the adaptability of decisions and flight environment requirements. Based on the information platform organization capabilities, establish flight mission requirements, mission organization and mission decision-making efficiency, and determine the adaptability of decisions and flight objective requirements.

3.3 *Air–Ground Collaborative Decision-Making Architecture*

According to whether the pilot participates in the flight decision-making, the aircraft flight process is divided into nominal flight process and non-nominal flight process. Among them, the non-nominal flight process requires pilot decision-making, while the nominal flight process does not require pilot decision-making, in which process the flight can be completed using the airborne intelligent system, and the remote pilot just need monitor the flight.

Aiming at the pilot's piloting specification and physical status [12], the RPO mode for commercial aircraft can dynamically adjust the controller of the aircraft to ensure flight safety. It mainly includes the following six situations [13].

- (1) When the remote pilot is in a normal piloting state, who is healthy and operating standardly, and the aircraft is in the nominal flight process, the airborne intelligent system executes control procedures to control the aircraft to complete the flight mission, the remote pilot is responsible for the safety of the aircraft and has complete control of the aircraft. The nominal flight with the assistance of the airborne intelligent system does not require the remote pilot to control the aircraft, and the remote pilot could just monitor the flight with the assistance of the airborne surveillance system. Therefore, airline dispatchers don't need to assist remote pilots in monitoring the aircraft one to one, and can be responsible for the dispatch of multiple aircrafts at the same time, so as to save ground staff costs for airlines.
- (2) When the remote pilot is in a normal driving state, who is healthy and operating standardly, but the aircraft is in the off-nominal flight process in special cases such as flight plan changes, single failure, hydraulic failure, severe weather, etc., the remote pilot must be responsible for the flight safety and take charge of the aircraft, as well as the assistance of the airline dispatcher is needed to complete the safe flight. At this time, the dispatcher must provide one-on-one assistance to the aircraft, and the other aircraft previously assigned by him will be transferred to other dispatchers of the airline. The dispatcher's role at this time is the "remote co-pilot" of the aircraft, and he is responsible for communicating with airlines and air traffic controllers to assist the remote pilot in completing the off-nominal flight processes.
- (3) When the remote pilot is incapacitated such as physical discomfort, non-subjective incorrect operation or leaving the post, and the aircraft is in the nominal flight process, the airborne intelligent system executes control procedures to control the aircraft to complete the flight mission and the backup

remote pilot, take charge of the aircraft, is going to monitor the flight process and be responsible for flight safety. At this point, the backup remote pilot needs to know the basic flight information of the aircraft, so the airline dispatcher must provide one-to-one assistance to the aircraft.

- (4) When the remote pilot is incapacitated and the aircraft is in an off-nominal flight process, the backup remote pilot must take charge of the aircraft, remotely pilot the aircraft and be responsible for flight safety, the airline dispatcher must provide assistance to complete the safe flight. At this time, the dispatcher must provide one-to-one assistance to the aircraft, including communicating with the airline and ATC, and assisting the backup remote pilot to complete the off-nominal flight process.
- (5) When the remote pilot is in an abnormal piloting state (hazardous operating subjectively) and the aircraft is in the nominal flight process, the ground surveillance system should warn the remote pilot that the operation is hazardous, if the malicious operation is continued, the system needs to cut off the control of the current remote pilot and transfer it to the backup remote pilot. At this time, the airborne intelligent system executes the control procedures to control the aircraft, and the backup remote pilot monitors the flight process and is responsible for the aircraft safety. What's more, airline dispatchers provide one-on-one assistance to the aircraft.
- (6) When the remote pilot is in an abnormal piloting state (hazardous operating subjectively) and the aircraft is in an off-nominal flight process, the ground surveillance system should warn the remote pilot that the operation is hazardous, if the malicious operation is continued, the system needs to cut off the control of the remote pilot and transfer it to the backup remote pilot. The backup remote pilot pilots the aircraft and has control of it and is responsible for the safety of the aircraft, but also requires the assistance of the airline dispatcher to complete the safe flight. Dispatchers provide one-on-one assistance to aircraft, including communicating with the airline and ATC, and assisting the backup remote pilot to complete the off-nominal flight process.

4 Air–Ground Collaboration Scenario Design and Verification of CRPA

In this part, we take the cruising phase as an example to carry out model-based scenario design and verification. We perform the air–ground collaborative scenario design of CRPA and verify it through the simulation verification platform. In the airspace authorized by air traffic control, CRPA can conduct route organization autonomously. If there is weather or other conflict during the flight, CRPA will adopt the method of automatic negotiation and decision-making to optimize the trajectory on the premise of obtaining authorization from ATC, while ensuring that it will not conflict with other aircraft, and finally complete the autonomous flight in the authorized airspace. At the same time, the trajectory data generated by the FMS will be

sent to ATC, and ATC sends the data to other aircrafts in the airspace in real time to ensure that other aircrafts will not generate new conflicts in the process of trajectory optimization.

4.1 Simulation Verification Platform

The simulation verification platform includes a system operating model, a flight scene demonstration module, an information synchronization component, and a phase information display module, as shown in Fig. 1. Among them, the system operating model is based on model-driven visual development software, which dynamically simulates the pilot operating layer and system operating layer during the flight through state machine. The flight scene demonstration module is based on a scene simulation modeling software to animate the flight in a vivid way. With the support of the information synchronization component, the flight scene demonstration module transmits flight status information to the system operating model, and the system operating model feedbacks the flight decision result to the flight scene demonstration module, realizing time synchronization and information transmission between models. The phase information display module displays the non-nominal status and processing results during the flight. The co-simulation verification based on model-driven visual development software and scene simulation modeling software has opened up the joint simulation verification of the scene space–time domain, system operating domain, and system logic domain, and improved the rationality and accuracy of the simulation model.

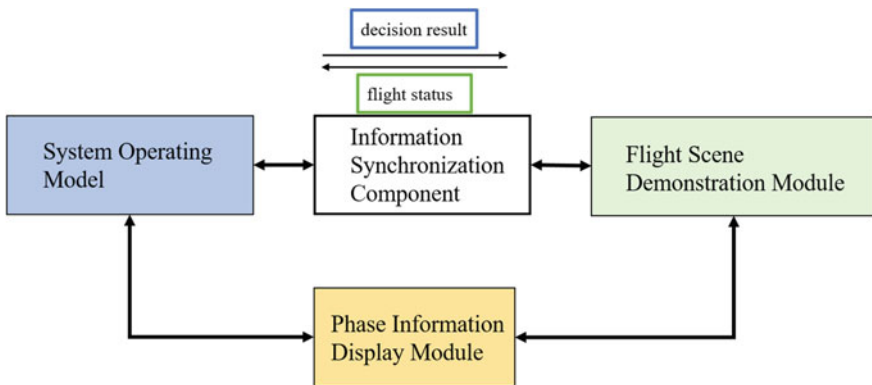


Fig. 1 Structure of the simulation verification platform

4.2 Model Verification and Analysis

Take the flight conflict in the cruising phase as an example, the airborne intelligent system detects the airspace environment and performs conflict calculations. Once the conflict is detected, the remote pilot will be notified immediately, and then asks ATC for help. After receiving the request, ATC assigns the dispatcher for one-to-one assistance. The dispatcher’s role at this time is the “remote co-pilot” of the aircraft, and he is responsible for communicating with airlines and air traffic controllers to assist the remote pilot in completing the off-nominal flight processes. The airborne intelligent system analyzes airspace traffic and provides a variety of conflict resolution for the remote pilot to make decisions. The remote pilot eventually chooses to give way to the conflicting aircraft.

We model the pilot operating layer and system operating layer separately. The pilot operating layer model mainly involves the collaborative interaction among the airborne intelligent system, remote pilots, air traffic control, and airline dispatchers. The system operating layer model mainly involves the cooperative interaction among flight management system, ADS-B, ADS-C, airborne communication system, and ground station decision-making system. The state transition diagram of the airborne communication system is shown in Fig. 2. In addition, the non-nominal conditions that occur during the cruising phase, the selected decision plan and the final processing result are all recorded in the phase information display module, as shown in Fig. 3.

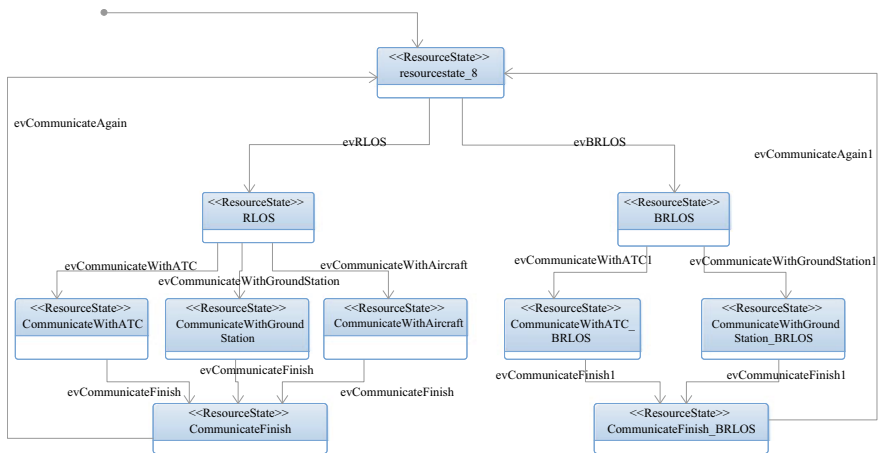


Fig. 2 The state transition diagram of the airborne communication system




	Flight Phase	Non-nominal Condition	Decision Plan	Processing Result
	Cruising Phase	weather conflict	modify the flight path	modify again
	Cruising Phase	SUA	modify the flight path	modify successfully
	Cruising Phase	flight conflict	give way	conflict free

Fig. 3 The phase information display of the cruising phase

5 Conclusion

Co-simulation verification based on model-driven visual development software and scenario simulation modeling software has opened up the space–time domain of the flight scene and the logical domain of the system architecture, completing the synchronization of the time–space state, the synchronization of the action sequence and the dynamic verification. It can be found that the RPO mode can basically cover the operations of dual pilots, and with the support of advanced airborne intelligent systems, 80% of the nominal flight process does not require the remote pilot to pilot, only need to monitor. The data traditionally displayed in the cockpit instrument system has been transmitted through the command and control link to the ground station, which eliminates the need for cockpit configuration and greatly reduces the weight of the aircraft. Autonomous flight in authorized traffic areas can reduce the workload of remote pilot crews and improve airspace utilization and flight safety.

Acknowledgements This work is partially supported by Natural Science Foundation of Shanghai (20ZR1427800), New Young Teachers Launch Program of Shanghai Jiaotong University (20X100040036). The authors also gratefully acknowledge the helpful comments and suggestions of the reviewers, which have improved the presentation.

References

1. Wang M, Xiao G, Wang GQ (2020) Single pilot operation mode technology. *Acta Aeronautica et Astronautica Sinica* 41(4):323541(in Chinese)
2. Lim Y, Bassien Capsa V, Ramasamy S et al (2017) Commercial airline single-pilot operations: System design and pathways to certification. *IEEE Aerosp Electron Syst Mag* 32(7):4–21
3. Malik A, Gollnick V (2016) Impact of reduced crew operations on airlines-operational challenges and cost benefits. The 16th AIAA Aviation Technology Integration and Operations Conference AIAA Aviation (AIAA 2016–3303)

4. Thomas E, Bleeker O (2015) Options for insertion of RPAS into the air traffic system. 2015 IEEE/AIAA 34th Digital Avionics Systems Conference (DASC). Prague, 2015, pp 5B4–1–5B4–14
5. Lachter J, Brandt S, Battiste V, Matessa W, Johnson W (2017) Enhanced ground support: lessons from work on reduced crew operations. *Cognit Technol Work* 07
6. Machuca JP, Miller ME, Colombi JM (2012) A cognitive task analysis-based evaluation of remotely piloted aircraft situation awareness transfer mechanisms. The 2012 IEEE international multi-disciplinary conference on cognitive methods in situation awareness and decision support, New Orleans, LA, 2012, pp 179–182
7. Finke M, Sinapius PB (2016) Application of visual and instrument flight rules to remotely piloted aircraft systems: a conceptual approach. The 2016 IEEE/AIAA 35th digital avionics systems conference (DASC), Sacramento, CA, 2016, pp 1–10
8. Etherington TJ, Kramer LJ, Bailey RE et al (2016) Quantifying pilot contribution to flight safety for normal and non-normal airline operations. The 2016 IEEE/AIAA 35th digital avionics systems conference (DASC), Sacramento, CA, 2016, pp 1–14
9. Evans S, Radcliffe SA (2012) The annual incapacitation rate of commercial pilots. *Aviation Space Environ Med* 83(1):42–49
10. Sprengart SM, Neis SM, Schiefele J (2018) Role of the human operator in future commercial reduced crew operations. //37th Digital avionics systems conference
11. Lim Y, Bassien-Capsa V, Ramasamy S, Liu J, Sabatini R (2017) Commercial airline single-pilot operations: system design and pathways to certification. *IEEE Aerosp Electron Syst Mag* 32(7):4–21
12. Sineglazov VM, Shmelev YN (2013) Qualification level control of remotely piloted aircraft pilots. The 2013 IEEE 2nd international conference actual problems of unmanned air vehicles developments proceedings (APUAVD), Kiev, 2013, pp 134–136
13. Luo Y, Wang M, Xiao G et al Conceptual architecture for remotely piloted operations (RPO) mode in commercial aircraft. *Trans Nanjing Univ Aeronaut Astronaut* 37(02):274–287

The Influence of Wing Deformation on Energy Extraction During Dynamic Soaring



Jiangwei Gao, Weigang An, Fuzhen Shi, Wei Wang, and Jianmin Su

Abstract The wandering albatross's wings have excellent aerodynamic performance, allowing it to travel thousands of miles over the ocean without flapping its wings. In order to explore the correlation between the deformation pattern of the albatross's wings and the energy extraction of dynamic soaring, a single-cycle energy model for dynamic soaring of albatross was established based on the albatross-inspired wing design. After extracting the typical deformation patterns of albatross's wings during dynamic soaring, the energy variation of different patterns in dynamic soaring were calculated based on the single-cycle energy model. Finally, we acquire the optimal wing deformation pattern for different phases of dynamic soaring, which obtains 5% more total energy extraction than the optimal single-cycle fixed deformation pattern. Comparing with the rectangular wing, the total energy extraction increases about 19%. The energy consumption of the low-altitude turn phase was reduced by about 8% compared with the single-cycle fixed deformation pattern and the rectangular wing.

Keywords Albatross · Bionic design · Wing deformation · Energy extraction

1 Introduction

Due to a number of advantages, small unmanned aerial vehicles (UAVs) have gradually become the emphasis of aircraft research in recent years. The bionic research which studies how birds fly by using the wind field in nature as well as applies the research results to improve the flight performance of small unmanned aerial vehicles has gradually become a pop domain.

J. Gao · W. An (✉) · F. Shi · W. Wang
School of Aeronautics, Northwestern Polytechnical University, Xi'an, Shannxi 710072, China
e-mail: gjwxtw@mail.nwpu.edu.cn

J. Su
No. 365 Research Insitute, Northwestern Polytechnical University, Xi'an, Shannxi 710072, China

© The Author(s), under exclusive license to Springer Nature Singapore Pte Ltd. 2023
Z. Jing and D. Strelets (eds.), *Proceedings of the International Conference on Aerospace System Science and Engineering 2021*, Lecture Notes in Electrical Engineering 849,
https://doi.org/10.1007/978-981-16-8154-7_48

627

In nature, albatrosses are able to fly for long periods of time and long distances through dynamic soaring in horizontal gradient wind fields. The explanation of this phenomenon can be summarized into three aspects [1]:

- (1) The albatross's wing shape has excellent aerodynamic performance, which provides excellent lift–drag ratio;
- (2) Albatrosses extract the energy from the wind field on the sea through their unique dynamic soaring trajectories, which helps them to achieve a long-distance flight;
- (3) Albatross can change aerodynamic parameters through wing deformation in dynamic soaring to achieve better flight performance as well as higher energy efficiency.

The albatross's excellent flight performance appeal to a number of researchers. In 2012, Yinfeng Hao from Nanjing University of Aeronautics and Astronautics established a three-dimensional model of a deformed wing by analyzing the wing deformation patterns of albatross in different flight modes, and carried out the aerodynamic analysis of the deformed wing under three mission requirements, respectively [2]. In 2008, Pennycuick analyzed several parameters such as lift–drag ratio and cruise speed of the wandering albatross through the computer simulation [3]. In 2014, Liu Zhaowei et al. from the National University of Defense Technology established a two-dimensional model of albatross wing and discussed the deformation strategy to realize a albatross-inspired wing [4]. In 2018, M. Hassanalian et al. analyzed the aerodynamic characteristics of three albatross wing models with different aspect ratios and wingspans. The selected wing model shows that the increase of aspect ratio results in the increase of lift coefficient and the decrease of drag coefficient [5].

To sum up, the study of the deformation pattern of albatross wings is helpful in exploring the influencing factors of the energy extraction in dynamic soaring, and have great guiding significance for improving the aerodynamic performance and endurance performance of UAV.

This paper is divided into five chapters. In the second chapter, based on the results of the previous work [6], the shape parameter design of the albatross-inspired wing is described. In the third chapter, the horizontal gradient wind field model is selected to establish the single-cycle energy model of dynamic soaring. In Chap. 4, the typical deformation patterns of albatross wings are extracted to calculate the energy variation in four phases of dynamic soaring, respectively, using the single-cycle energy model in Chap. 3, determining the optimal deformation patterns for each phase of dynamic soaring.

2 Albatross-Inspired Wing Design

Refer to the albatross's wings, we established the model of the bionic wing. The content of this chapter is derived from the second chapter of the previous work [6].

First, the GOE-174 airfoil extracted from albatross wings [7] was selected as the airfoil for the bionic wing. The flight Reynolds number was calculated based on the flow environment in which the albatross was flying. The lift-drag ratio of the GOE-174 airfoil was calculated and compared with a series of conventional low-speed airfoils (SD7084, S4083, Clark YM-15, and NACA 2412). The results show that GOE-174 has an excellent lift-drag ratio, make it suitable for bionic airfoil. By decomposing the video of soaring albatross, the shape features of albatross wings were extracted and simplified into three wing segments (Fig. 1).

The ratio parameters of the span length and chord length of each wing segment were obtained from the screenshots, as well as the measured values of the dihedral angle and the sweep angle. Combined with the statistical values of the wing parameters of wandering albatross [8], the values of the span length and chord length of each wing segment were determined. The wing area, average aerodynamic chord length and aspect ratio were calculated to complete the geometrical shape parameterization of albatross wings. The parameterization results are shown in Tables 1 and 2.

According to the selected airfoil and the extracted geometric parameters, a three-dimensional model of the bionic wing is established in CATIA to complete the design of the bionic wing (Fig. 2).

In order to compare the differences in energy extraction results, a rectangular wing model with GOE-174 airfoil as well as same wingspan and aspect ratio is established, shown in Fig. 3.

Fig. 1 Three segments of the albatross’s wing

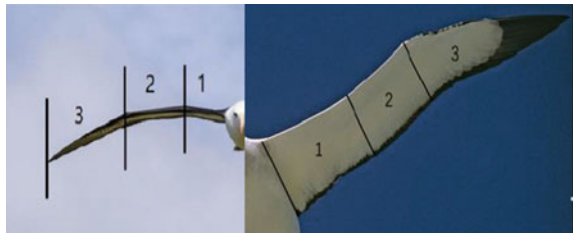


Table 1 The basic parameters of bionic wing

Parameter	Wingspan	Mean aerodynamic chord	Aspect ratio	Wing area
Parameter value	3110 mm	201 mm	15.5	6226 cm ²

Table 2 The 2D parametric model of the bionic wing with 3-m wingspan

Parameter	No.1 segment	No.2 segment	No.3 segment
The span length (mm)	403	317	640
The chord length (mm)	302	241	234
The sweep angle (°)	15	-3.5	23.5

Fig. 2 Bionic wing model

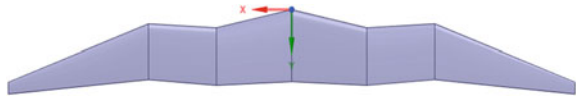
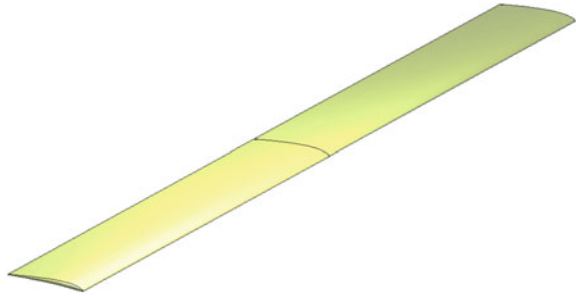


Fig. 3 Rectangular wing model



3 The Single-Circle Energy Model for Dynamic Soaring

3.1 Brief Description of Dynamic Soaring

Due to the existence of gradient wind field over the sea, the typical seabirds, such as albatross and frigate birds, mainly obtain energy from the gradient wind field through dynamic soaring to achieve long-distance flight. The main mode of albatross's dynamic soaring was first proposed by British scientist Lord Rayleigh in 1883 [9]. Lord Rayleigh divided the main mode into four phases: windward climb, high altitude turning, leeward descent, and low-altitude turn. Figure 4 shows a typical Ω -shaped trajectory of dynamic soaring which contains four phases. In order to study

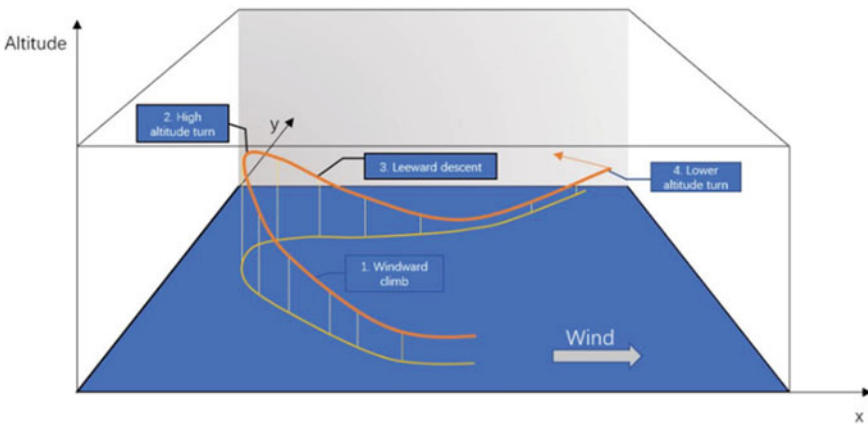


Fig. 4 Typical Ω -shaped trajectory of dynamic soaring

the relationship between wing deformation pattern and dynamic soaring capability, a single period of a typical Ω -shaped trajectory was selected to study the energy extracting performance of bionic wings.

3.2 Wind Field Model Selection

The typical wind field models for horizontal gradient wind contains the following three types: exponential wind field model, logarithmic wind field model, and linear wind field model.

(a) Exponential wind field model

The exponential wind field can be expressed by the exponential function in Eq. (1):

$$V_W(h) = V_R \left(\frac{h}{H_R} \right)^p \quad (1)$$

Equation (2) is used to define the horizontal wind gradient with height changes:

$$\frac{\delta V_W}{\delta h} = p \frac{V_R}{H_R} \left(\frac{h}{H_R} \right)^{p-1} \quad (2)$$

where h is the height, V_W is the horizontal wind speed, H_R is the reference height, V_R is the wind speed at the reference height, and p is the power-law exponent of the exponential function. Reference height and reference wind speed determine the wind speed and wind gradient of the exponential wind field. In researches related to dynamic soaring [10], reference height and reference wind speed are usually taken as 10 m and 10 m/s, respectively. The power-law exponent is used to describe the surface characteristics as well as determines the distribution shape of the wind field model along the height.

(b) Logarithmic wind field model

The logarithmic wind field can be expressed by the logarithmic function in Eq. (3):

$$V_W(h) = V_R \frac{\ln\left(\frac{h}{h_0}\right)}{\ln\left(\frac{H_R}{h_0}\right)} \quad (3)$$

Equation (4) is used to define the horizontal wind gradient with height changes:

$$\frac{\delta V_W}{\delta h} = \frac{V_R}{h \ln\left(\frac{H_R}{h_0}\right)} \quad (4)$$

where h_0 is the roughness factor. Owing to the relationship between logarithm and exponent in mathematics, the logarithmic wind field is similar to the exponential wind field. The reference height and reference wind speed of the logarithmic wind field model are usually taken as 10 m and 10 m/s [11]. The roughness factor, which is similar to p in the exponential wind field model, determines the distribution shape of the wind field model along the height. Generally, the higher the surface roughness is, the higher the h_0 is.

(c) Linear wind field model

The linear wind field can be expressed by the linear function in Eq. (5):

$$V_W(h) = h\beta_w \quad (5)$$

The corresponding horizontal wind gradient is expressed as

$$\frac{\delta V_W}{\delta h} = \beta_w \quad (6)$$

where β_w is a linear gradient as well as the slope of the curve of horizontal wind speed changing with height.

By comprehensive comparison of the three wind field models, the linear model is found imprecise to describe the complex wind field near sea level. The exponential wind field and logarithmic wind field are similar and can be used to approximate the wind field near sea level. For exponential wind field, the wind gradient turn into constant when $p = 1$. Nevertheless, the wind gradient of the logarithmic wind field is always affected by the height, which is closer to the real situation. Moreover, the logarithmic wind field model is also widely used in the simulation research related to dynamic soaring. Therefore, this paper chooses the logarithmic wind field model.

Many researchers used a logarithmic model with h_0 of 0.03, reference height of 10 m and reference wind speed of 10 m/s for dynamic soaring simulation studies [11–13]. Accordingly, the same logarithmic wind field model parameters are selected in this paper.

3.3 The Equations of Motion in the Wind Field

The derivation of motion equation of albatross or unpowered glider in the wind field has been relatively mature. Zhao derived a set of simplified equations of motion with good approximation [14], which has been widely used in dynamic soaring simulation and energy calculation. The EOM is shown in Eqs. (7)–(12).

$$\dot{V}_a = -\frac{D}{m} - g \sin \gamma - \dot{V}_W \cos \gamma \sin \varphi \tag{7}$$

$$\dot{\varphi} = \frac{L \sin \mu}{m V_a \cos \gamma} - \frac{\dot{V}_W \cos \varphi}{V_a \cos \gamma} \tag{8}$$

$$\dot{\gamma} = \frac{L \cos \mu}{m V_a} - \frac{g \cos \gamma}{V_a} + \frac{\dot{V}_W \sin \gamma \sin \varphi}{V_a} \tag{9}$$

$$\dot{x} = V_a \cos \gamma \sin \varphi + V_W \tag{10}$$

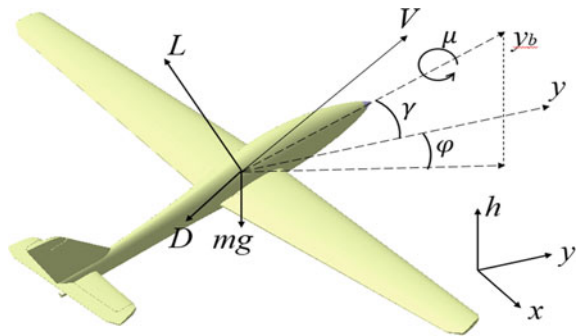
$$\dot{y} = V_a \cos \gamma \cos \varphi \tag{11}$$

$$\dot{h} = V_a \sin \gamma \tag{12}$$

where V_a is airspeed, V_W is wind speed; \dot{V}_a and \dot{V}_W are the derivatives of airspeed and wind speed with respect to time, respectively; m is the weight of the albatross which is taken as 9.44 kg in this paper [8], g is the acceleration of gravity; L and D are the lift and drag, respectively; γ , μ , and φ are the pitch angle, roll angle, and yaw angle of albatross body, respectively; $\dot{\gamma}$ and $\dot{\varphi}$ are the pitch angle rates and yaw angle rates, respectively.

The coordinate system is shown in Fig. 5, where h represents the height. Note that the yaw angle φ is defined as 0 while pointing to the Y-axis forward. For instance, the albatross is in windward climb phase when $\varphi > 0$ as well as in leeward descent phase when $\varphi < 0$.

Fig. 5 The coordinate system of EOM



3.4 The Derivation of Energy Equation in Dynamic Soaring

In this paper, the inertial frame is selected as the reference frame to derive the energy equation of dynamic soaring. In inertial frame, the total energy consists of kinetic energy, and gravitational potential energy, as shown in Eq. (13).

$$E_i = \frac{1}{2}mV_i^2 + mgh = \frac{1}{2}m(\dot{x}^2 + \dot{y}^2 + \dot{h}^2) + mgh \quad (13)$$

where V_i is the inertial velocity. The derivative of Eq. (13) can be expressed as follows:

$$\dot{E}_i = m(\dot{x}\ddot{x} + \dot{y}\ddot{y} + \dot{h}\ddot{h}) + mg\dot{h} \quad (14)$$

After differentiation with respect to time, Eqs. (10)–(12) is substituted into Eqs. (7)–(9):

$$\ddot{x} = -\frac{D}{m}\cos\gamma\sin\psi + \frac{L}{m}(\sin\mu\cos\psi - \cos\mu\sin\gamma\sin\psi) \quad (15)$$

$$\ddot{y} = -\frac{D}{m}\cos\gamma\cos\psi - \frac{L}{m}(\sin\mu\sin\psi + \cos\mu\sin\gamma\cos\psi) \quad (16)$$

$$\ddot{h} = -\frac{D}{m}\sin\gamma + \frac{L}{m}\cos\mu\cos\gamma - g \quad (17)$$

Substituting Eqs. (10)–(12) and (15)–(17) into Eq. (14):

$$\dot{E}_i = -DV_a - D\cos\gamma\sin\psi V_W - L\cos\mu\sin\gamma\sin\psi V_W + L\sin\mu\cos\psi V_W \quad (18)$$

Equation (18) is the energy rate of change in the inertial frame, which is composed of lift, drag, wind speed, airspeed, and attitude angles.

3.5 The Establishment of Single-Circle Energy Model

After ascertaining the wind field model and energy equation, the single-circle energy model of dynamic soaring can be set up. Since the energy equation in dynamic soaring represents the energy rate at each moment, there are two methods to set up the dynamic soaring energy model. The method to obtain energy variation by integrating the energy equation is called the integration method. The result of this method is accurate, though it requires simulation with a given flight trajectory. The large amount of calculation and the lack of parameters for evaluating the energy

extraction make it difficult to simulate the dynamic soaring. Thus, the iterative method can be adopted. According to the energy equation and the time-step advance method, the energy rate of change curve can be drawn. The area under the curve is the energy variation. The energy acquiring performance at different phases can also be evaluated through the variation of the curve.

Researchers often use the typical single-cycle numerical example which is shown in Fig. 6 for the simulation of Ω -shaped dynamic soaring [11–13]. As a complete cycle of 7 s long, this numerical example starts from the second half of the low altitude turn phase as well as ends in the middle of low altitude turn phase.

According to the total time of the numerical example, 0.5 s is taken as a time step length, resulting in 15 data points in total. Each data point corresponds to the corresponding time node in dynamic soaring.

To calculate the energy rate of change in the energy equation, the attitude angle, angle of attack, angle of sideslip, airspeed, height, wind speed, wind gradient, lift, drag, and the mass of the albatross are required at each data points. Referring to the relevant studies of the typical numerical example, the curve of attitude angles, angle of sideslip, airspeed, and height varying with time is shown in Fig. 7. In this paper, 4° is chosen as the angle of attack for calculation since the lift–drag ratio of the bionic wing is the largest when the angle of attack is 4° .

After the change of height is determined, wind speed and wind gradient are calculated by Eqs. (3) and (4), while lift and drag are calculated by Vortex Lattice Method (VLM). In conclusion, the curve of the energy rate and the total energy variation can be obtained from the single-circle energy model.

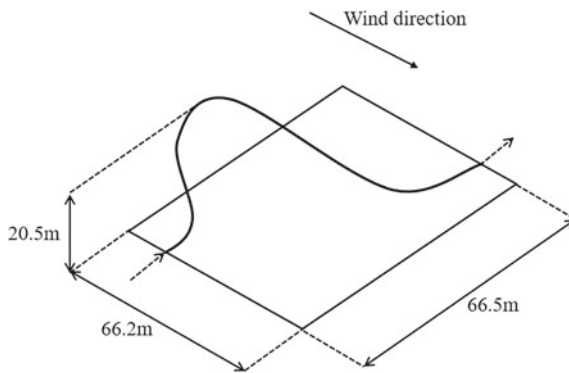


Fig. 6 The typical single-cycle numerical example of Ω -shaped dynamic soaring

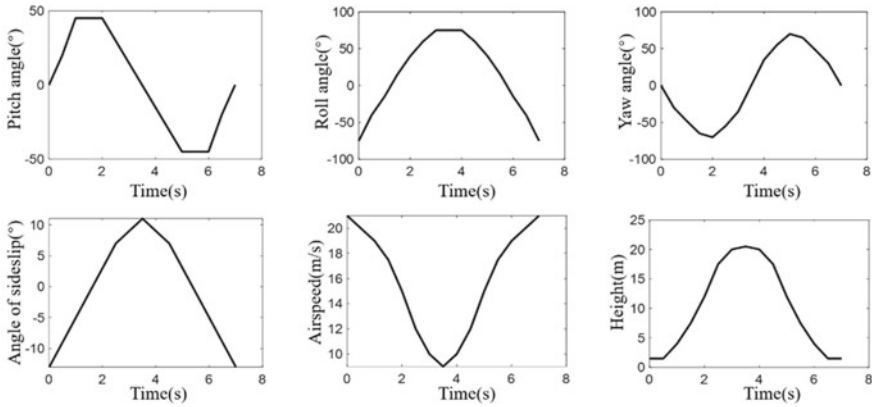


Fig. 7 The curve of attitude angles, angle of sideslip, airspeed, and height in a single cycle of dynamic soaring

4 The Influence of Wing Deformation on Energy Extraction

Refer to the videos, we found that albatrosses often deform their wings by changing the dihedral angle of their wing segment in dynamic soaring. We extracted the dihedral angle of albatross’s wing in dynamic soaring as well as defined the dihedral angle combinations by orthogonal experiment. The energy extraction of disparate dihedral angle combinations is calculated in the four phases of dynamic soaring. The consequence of the bionic wing is compared with the classical rectangular wing. At last, the optimal wing deformation pattern in dynamic soaring is determined.





4.1 The Extraction of Wing Deformation

Based on the bionic wing parameters, ten combinations of the dihedral angle were summarized from a number of albatross dynamic soaring videos. The corresponding bionic prototype are shown in Table 0.3. For instance, 0/-30/-30 demonstrates that the dihedral angles of No.1, No.2, and No.3 wing segments are 0°, -30°, and -30°, respectively (Table 3).

By summarizing the combinations of dihedral angle, the typical values of dihedral angle for each wing segment can be extracted (see Table 4).

In order to explore the influence of different dihedral angle combinations on dynamic soaring performance, $3 \times 6 \times 6 = 108$ combinations need to be analyzed, which is obviously too complicated. The orthogonal experiment method which ensuring the uniformity and representativeness of test samples is adopted to reduce the number of tests. The dihedral angle of three wing segments was selected as the factor as well as the value of the extracted dihedral angles was taken as the level of

Table 3 The dihedral angle combinations and its bionic prototype

The dihedral angle combinations	The bionic prototype	The dihedral angle combinations	The bionic prototype
0/-30/-30		5/-10/5	
5/-30/0		5/-30/-10	

(continued)

Table 3 (continued)





The dihedral angle combinations	The bionic prototype	The dihedral angle combinations	The bionic prototype
5/-5/-5		0/-20/-10	
0/-10/-40		0/-5/-30	

Table 4 The factors and levels of the orthogonal experiment

level	Factor		
	No. 1 dihedral angle(°)	No. 2 dihedral angle(°)	No. 3 dihedral angle(°)
1	0	-5	10
2		-10	0
3	5	-15	-10
4		-20	-20
5	10	-25	-30
6		-30	-40

the corresponding factor. The 18 combinations of dihedral angles (Table 5) obtained from the orthogonal experiment ensure every level of every factor can meet with the levels of other factors once.

4.2 Calculation of Aerodynamic Parameters

Although the computation of CFD software is relatively accurate in the aerodynamic calculation, it spends a great mass of time in meshing. The accuracy of the computation is also affected by parameter setting and meshing. Hassanalian and Melin have verified that the results of VLM are quite accurate for the wing with large sweep angle and dihedral angle by comparing several aerodynamic calculation methods [15, 16]. Considering the relatively low flight speed of the albatross, the VLM is adopted here to calculate the aerodynamic parameters of the wing through the MATLAB program.

VLM is a CFD method which can describe a wing with complex geometry by setting wing parameters. According to the VLM, the wing is modeled as an infinite

Table 5 The design of the orthogonal experiment

Serial number	The dihedral angle combinations	Serial number	The dihedral angle combinations
1	0/-5/-10	10	5/-20/-30
2	0/-10/-40	11	5/-25/-10
3	0/-15/-20	12	5/-30/-40
4	0/-20/10	13	10/-5/-40
5	0/-25/-30	14	10/-10/-10
6	0/-30/0	15	10/-15/10
7	5/-5/-20	16	10/-20/-20
8	5/-10/10	17	10/-25/0
9	5/-15/0	18	10/-30/-30

thin discrete vortex. Each horseshoe vortex starts at infinity behind the wing, moves forward to one of the wing's facets, passes through this facet at the string which establishes the connection between the 1/4 chord length of the wing tip and the 1/4 chord length of the wing root, and then returns to infinity behind the wing. The sweep angle of the wing segment in VLM is defined by the conversion equation in Eq. (19).

$$\beta_i^{\frac{1}{4}} = \arctan\left(\frac{x_i \cdot \tan\beta_i - 1/4(y_i - y_{i+1})}{x_i}\right), i = 1, 2, 3 \quad (19)$$

where x_i , y_i , and β_i are the span length, chord length of wing root, and the sweep angle of corresponding wing segments, respectively. Twelve grid points are set up in the chord direction of the wing and 180 grid points are set up along the span direction of the whole wing. Finally, 2160 grids are set on the bionic wing for calculation.

Through the variation of airspeed and aerodynamic angle given in Chap. 3, the lift coefficient, drag coefficient, lift, and drag of the dihedral angle combinations in four phases can be calculated. For instance, Table 6 shows the lift coefficient, drag coefficient, lift, and drag of the rectangular wing with time.

Table 6 The aerodynamic parameters of the rectangular wing

Time(s)	The lift coefficient	The drag coefficient	Lift(N)	Drag(N)
0	0.7620	0.0291	111.9693	4.2799
0.5	0.7844	0.0294	104.5469	3.9230
1.0	0.7989	0.0297	96.0966	3.5704
1.5	0.8051	0.0298	82.1616	3.0398
2.0	0.8030	0.0298	60.2068	2.2305
2.5	0.7926	0.0296	38.0331	1.4190
3.0	0.7741	0.0293	25.7954	0.9758
3.5	0.7479	0.0289	20.1868	0.7811
4.0	0.7741	0.0292	25.7954	0.9758
4.5	0.7926	0.0296	38.0331	1.4190
5.0	0.8030	0.0298	60.2068	2.2305
5.5	0.8051	0.0298	82.1616	3.0398
6.0	0.7989	0.0297	96.0966	3.5704
6.5	0.7844	0.0294	104.5469	3.9230
7.0	0.7620	0.0291	111.9693	4.2799

4.3 Energy Extraction of Different Deformation Patterns

To analyze the impact of the deformation patterns on energy extraction as well as determine the optimal deformation pattern for bionic wings in dynamic soaring, the energy variation of bionic wings with different deformation are calculated by the single-cycle energy model and aerodynamic parameters given above. With the purpose of facilitating the comparison and analysis, the energy variation in the four phases of dynamic soaring was calculated, respectively. As shown in Table 7, the total energy variation of the bionic wings and the rectangular wing in a single cycle were calculated.

We found 0/-5/-10 having maximum total energy extraction (977.8 J). Sorting the energy variation results from high to low, the dihedral angle combinations with the maximum energy acquisition in each phases is selected and shown in the following:

As shown in Table 8, adopting the maximum energy-harvesting dihedral angles in each stages makes the total energy variation come to 1026.6 J. This result is approximately 5% higher than that of the 0/-5/-10, and approximately 19% higher

Table 7 The energy variation of the different dihedral angles

The dihedral angle combinations	Windward climb (J)	High-altitude turn (J)	Leeward descent (J)	Low-altitude turn (J)	Total energy variation (J)
0/-5/-10	728.8	186.4	659.7	-597.1	977.8
0/-10/-40	669.5	171.2	606.0	-548.5	898.3
0/-15/-20	699.4	178.1	628.7	-588.3	918.0
0/-20/10	708.6	183.1	640.0	-589.6	942.2
0/-25/-30	669.5	171.2	606.0	-548.5	898.3
0/-30/0	691.3	177.7	621.8	-581.7	909.2
5/-5/-20	708.1	180.5	638.1	-589.9	936.8
5/-10/10	721.7	186.6	653.6	-594.3	967.7
5/-15/0	722.3	185.7	653.6	-594.4	967.3
5/-20/-30	660.3	169.0	588.3	-577.2	840.5
5/-25/-10	697.4	178.5	627.4	-585.5	917.9
5/-30/-40	600.1	157.2	526.6	-550.6	733.3
10/-5/-40	635.8	166.3	563.8	-563.4	802.4
10/-10/-10	718.6	184.0	649.4	-592.9	959.1
10/-15/10	711.0	184.0	642.8	-589.6	948.2
10/-20/-20	685.2	174.8	614.5	-581.8	892.7
10/-25/0	699.0	180.0	629.8	-584.2	924.7
10/-30/-30	632.8	162.1	413.1	-618.6	589.5
Rectangular wing	704.4	121.0	634.5	-598.0	861.7

Table 8 The maximum energy variation of the different phases

The part of dynamic soaring	The dihedral angle combinations	Energy variation (J)	Total energy variation(J)
Windward climb	0/-5/-10	728.8	1026.6
High altitude turn	5/-10/10	186.6	
Leeward descent	0/-5/-10	659.7	
Low altitude turn	0/-10/-40	-548.5	

than that of the rectangular wing. Compared with the previous three phases, the 0/-10/-40 in the low-altitude turn phase seems special in deforming extent. Comparing with the 0/-5/-10 and the rectangular wing, the energy consumption of the 0/-10/-40 in the low-altitude turn phase decreases by approximately 8%. To analyze the causes of this phenomenon, the contribution of lift and drag to energy extraction can be obtained from dividing Eq. (18) into Eqs. (20) and (21):

$$\dot{E}_D = -DV_a - D \cos \gamma \sin \psi V_W \tag{20}$$

$$\dot{E}_L = -L \cos \mu \sin \gamma \sin \psi V_W + L \sin \mu \cos \psi V_W \tag{21}$$

Taking the 0/-10/-40 wing as an instance, the energy rate curves contributed by lift and drag is shown as.

As shown in Fig. 8, the lift of inertial frame makes a negative contribution in the low-altitude turn phase (0–0.5 s, 6.5–7 s), which means the increase of lift leads to the increase of energy consumption. However, the drag is always a negative contribution in the inertial frame. In the inertial frame, the numerical comparison of lift contribution and drag contribution shows that the lift of the wing is the main factor affecting

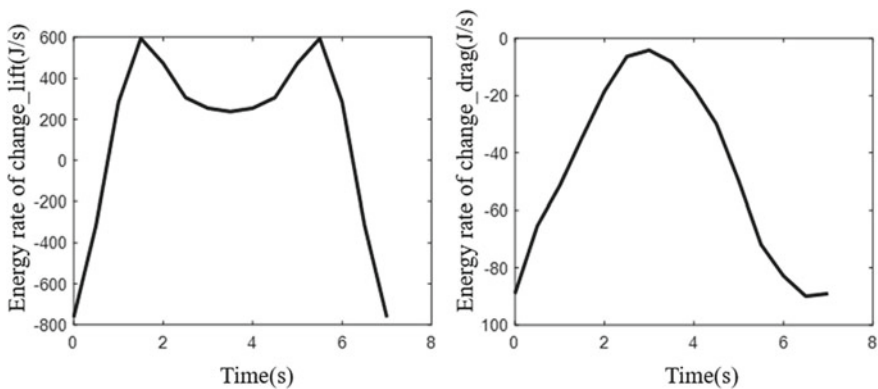


Fig. 8 The energy rate curves contributed by lift and drag

the energy extraction in dynamic soaring. The 0/-10/-40 owns smaller projected area of wing than the previous three phases, reducing lift and energy consumption during low-altitude turn phase.

5 Conclusion

In this paper, after demonstrating the shape parameter design of the albatross-inspired wing based on the results of the previous work [6], the logarithmic horizontal gradient wind field model is selected to establish the single-cycle energy model of albatross in dynamic soaring. The typical deformation patterns of albatross wings were extracted from the video of dynamic soaring as well as simplified by the orthogonal experiment. The 18 kinds of deformation pattern obtained from the orthogonal experiment were used to calculate the aerodynamic parameters by the VLM.

Refer to the established single-circle energy model, the energy variation of the bionic wing and same-sized rectangular wing during the four phases of dynamic soaring were calculated. The 0/-5/-10 deformation pattern has the maximum total energy extraction when the deformation pattern is fixed during the circle. Adopting 0/-5/-10, 5/-10/10, 0/-5/-10, and 0/-10/-40 optimal pattern, respectively, at each phases extract approximately 5% more total energy compared with the 0/-5/-10 fixed as well as approximately 19% more total energy compared with the rectangular wing. Comparing to 0/-5/-10 and the rectangular wing, the energy consumption of the optimal deformation pattern during the low-altitude turn phase is reduced by approximately 8%.

Therefore, based on the bionic wing, adopting different wing deformation patterns in different phases of dynamic soaring can effectively improve the energy extraction in flight and extend the endurance and flight performance of the bionic UAV.

Acknowledgements This work is sponsored by the Foundation of National Key Research and Development Program (2017YFC0822403-4).

References

1. Barnes JP (2004) How flies the albatross—the flight mechanics of dynamic soaring (No. 2004–01–3088). SAE Technical Paper
2. Yinfeng H (2012) Preliminary research on morphing wing based on avian morphology. Dissertation, Nanjing University of Aeronautics and Astronautics
3. Pennycuik CJ (2008) Modelling the flying bird. Elsevier
4. Zhaowei L, Zhongxi H, Juntao Z, Xianzhong G (2014) The very flexible aircrafts and albatross flight. 29th Congress of the International Council of the Aeronautical Sciences
5. Sanchez G, Salazar RD, Hassanalian M, Abdelkefi A (2018) Sizing and performance analysis of albatross-inspired tilt-wing unmanned air vehicle. In: 2018 AIAA/ASCE/AHS/ASC structures, structural dynamics, and materials conference, p 1445

6. Fuzhen S, Weigang A, Wei W, Hang Z, Liu L (2020) Aerodynamic design and optimization of bionic wing based on wandering albatross. In: Proceedings of the international conference on aerospace system science and engineering 2020
7. Qi-hu S, De-ming W, Liang Z (2005) Aerodynamic forces acting on an albatross flying above sea-waves. *Appl Math Mech* 26(9):1222–1229
8. Shaffer SA, Weimerskirch H, Costa DP (2001) Functional significance of sexual dimorphism in wandering albatrosses, *Diomedea exulans*. *Funct Ecol* 15(2):203–210
9. Rayleigh L (1883) The soaring of birds. *Nature* 27(701):534–535
10. Sachs G, Bussotti P (2005) Application of optimal control theory to dynamic soaring of seabirds. In: *Variational analysis and applications*, pp 975–994. Springer, Boston, MA
11. Sachs G (2005) Minimum shear wind strength required for dynamic soaring of albatrosses. *Ibis* 147(1):1–10
12. Bower GC (2011) Boundary layer dynamic soaring for autonomous aircraft: design and validation. Dissertation, Stanford University
13. Duoneng L (2016) Research on mechanism and trajectory optimization for dynamic soaring with fixed-wing unmanned aerial vehicles. Dissertation, National University of Defense Technology
14. Zhao YJ (2004) Optimal patterns of glider dynamic soaring. *Optim Control Appl Methods* 25(2):67–89
15. Stempeck A, Hassanalian M, Abdelkefi A (2018) Aerodynamic performance of albatross-inspired wing shape for marine unmanned air vehicles. In: 2018 Aviation Technology, Integration, and Operations Conference, p 3899
16. Melin T (2000) A vortex lattice MATLAB implementation for linear aerodynamic wing applications. Royal Institute of Technology, Sweden

Acoustics Analysis and Experimental Study on Silencer for Commercial Airplane Air Conditioning System



Xudong Yan, Xuede Sun, and Dawei Wang

Abstract Commercial airplane air conditioning system noise is one of the primary passenger cabin noise sources. Silencers are extensively used to quiet airplane air conditioning system noise. Silencer acoustics performance is influenced by the inner form and acoustic damping materials in silencer. The noise attenuation effect is verified by simulated analysis and laboratory experiment. Acoustics experiment results on airplane show that passenger cabin noise reduces more than 5 dB with silencer.

Keywords Acoustics · Commercial airplane · Air conditioning system · Simulated analysis · Silencer

1 Introduction

Commercial airplane passenger cabin noise influence the passenger hearing comfort and distinct communication. In order to enhance market competitiveness, airplane engineers try every possible way to quiet the passenger cabin noise at the design stage. The primary cabin noise sources of commercial airplane include aeromotor vibration, flight pneumatic noise, and airstream noise from air conditioning system.

Air conditioning system of commercial airplane provides suitable temperature environment for the passengers and flight crew. The airstream in the pipe, rotary part in Ventilating Fan, and Air Cooling Pack can generate much noise. These noises ultimately get into the passenger cabin via air conditioning pipe. Air conditioning system noise is one of the primary passenger cabin noise sources.

Silencers are extensively used to quiet commercial airplane air conditioning noise. Silencers are set at the air conditioning system pipe. The working frequency, noise attenuation effect, and airflow pressure loss are core elements for silencer performance. The silencer property is influenced by the inner form and acoustic damping

X. Yan (✉) · X. Sun · D. Wang
Commercial Aircraft Corporation of China, Ltd. ShangHai Aircraft Design and Research
Institute, Shanghai, China
e-mail: bmw566@qq.com

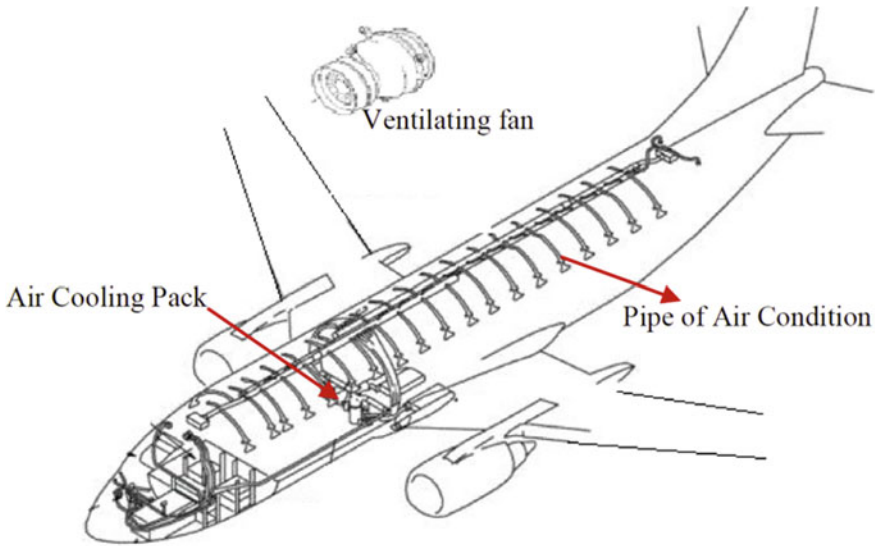


Fig. 1 Airplane air conditioning noise source in passenger cabin

materials in silencer. Silencer inner form and size are optimized to meet the weight and interspaces restrictions requirements.

In this article, silencers with different design parameters are analyzed with finite element tools. Experiments in Laboratory and tests on airplane are also implemented to verify the noise attenuation effect of silencers.

2 Airplane Air Conditioning Noise Source in Passenger Cabin

Airplane air conditioning noise sources in passenger cabin include Air Cooling Pack, Ventilating Fan, and airstream in the Pipe [1]. The frequency of these noises is primarily in the range of 550–8500 Hz. Airplane air conditioning noise source parts are illustrated in Fig. 1. Noise level around ventilating fan is illustrated in Fig. 2.

3 Silencer Acoustics Simulated Analysis

Dissipative silencers are extensively used in commercial airplane. These silencers consist of expansion pipe and acoustic damping materials. The internal form of silencer is illustrated in Fig. 3. Silencer simulated analysis is made by acoustics simulation tool COSOL Multiphysics 5. The simulated model is illustrated in Fig. 4.

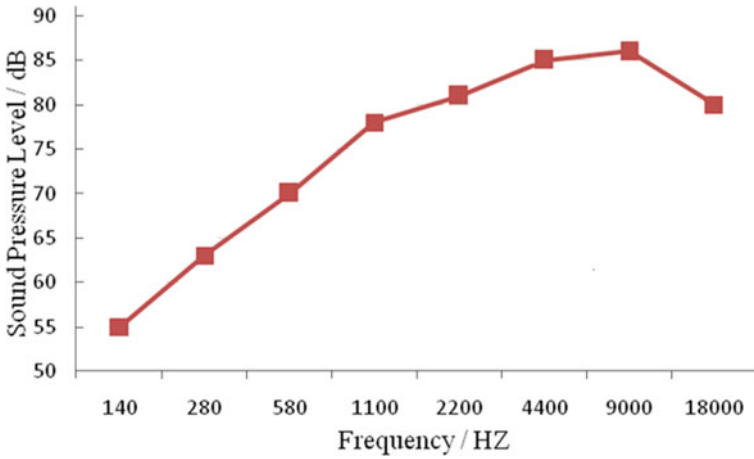


Fig. 2 Noise level around ventilating fan

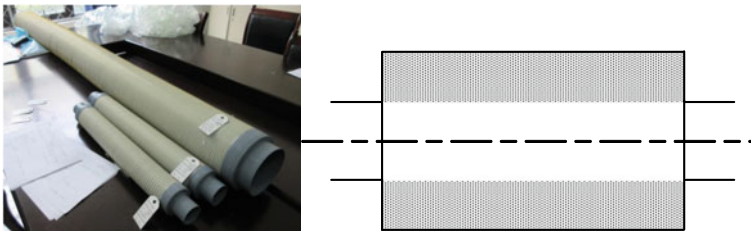
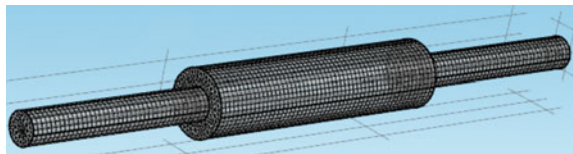


Fig. 3 Airplane silencer internal form

Fig. 4 Simulated model



As illustrated in Figs. 5 and 6, Noise attenuation efficiency of the silencer is influenced by the expansion ratio of pipe and unit weight of acoustic damping materials in silencer. The silencer is via sound transmission path variation and acoustic damping materials to reduce the cabin noise. The larger the expansion ratio of the silencer is, the better the noise attenuation efficiency is. The bigger the unit weight of acoustic damping materials in silencer is, the better the noise attenuation efficiency is. Sound pressure level around frequency 550 Hz of the silencer is illustrated in Fig. 7.

Airflow pressure loss in the pipe is a significant parameter for the air conditioning system. The faster the airflow is, the more noise will get into the passenger cabin. For these reasons, the airstream velocity in airplane air conditioning system pipe is

Fig. 5 Silencer noise attenuation efficiency and expansion ratio N

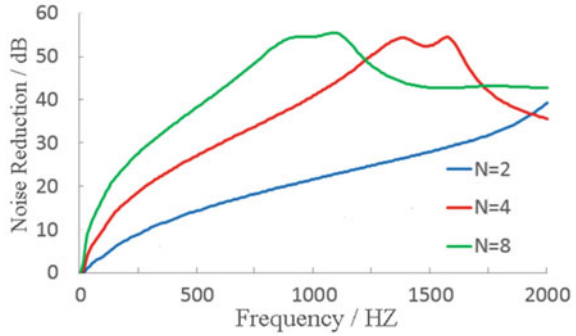


Fig. 6 Silencer noise attenuation efficiency and acoustic damping materials

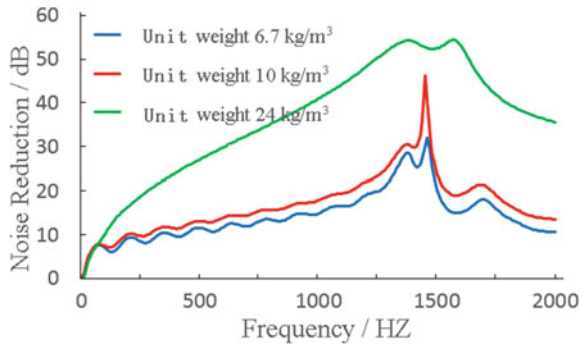
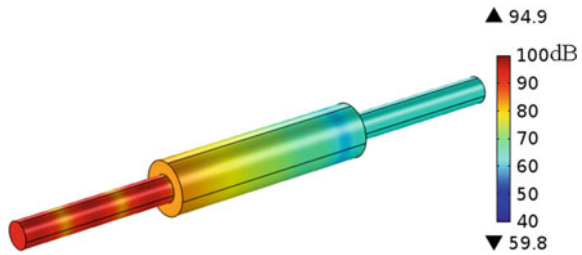


Fig. 7 Sound pressure level around frequency 550 Hz



restricted below 20 m/s. Usually, the airstream velocity in the pipe under cabin floor is around 15 m/s, and the airstream velocity in the pipe above cabin floor is around 10 m/s [2].

In this article, we assume the atmosphere pressure around the silencer is 101 kPa. Airflow gage pressure loss is illustrated in Fig. 8 (velocity at 15 m/s and expansion ratio $N = 2$). As illustrated in Table 1, the faster the airflow is, the more airflow pressure loss will be.

Fig. 8 Air gage pressure (velocity at 15 m/s, expansion ratio $N = 2$)



Table 1 Airflow pressure loss in Silencer (expansion ratio $N = 2$)

Airflow velocity (m/s)	10	15	20
Loss of airflow pressure (Pa)	79.8	176.8	308.9

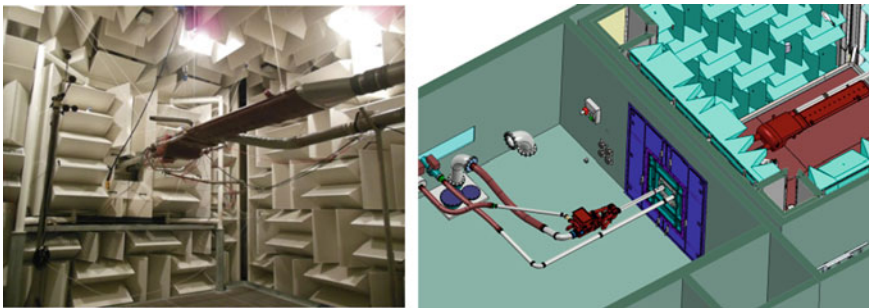


Fig. 9 Acoustics experiment implemented in an anechoic chamber with the airplane air conditioning system part

4 Acoustics Experiment in Laboratory

Acoustics experiment is implemented in an anechoic chamber with airplane air conditioning system part (Air Cooling Pack, Ventilating Fan, and Ventilation Pipe). The laboratory experiment in an anechoic chamber is illustrated in Fig. 9.

The laboratory experiment in an anechoic chamber shows that the primary noise frequency of the air conditioning system is higher than 300 Hz. These noises primarily are from the rotary parts in Ventilating fan and Air Cooling pack. The experiment result at the air outlet of the air conditioning pipe is illustrated in Fig. 10.

5 Acoustics Experiment on Airplane

Acoustics experiment is implemented on airplane with silencer, and experiment result is illustrated in Table 2. The experiment result shows that noise reduction of the silencer is significant, and the cabin noise will reduce more than 5 dB with silencer. The microphone site of acoustics experiment on airplane is illustrated in Fig. 11 [3, 4].

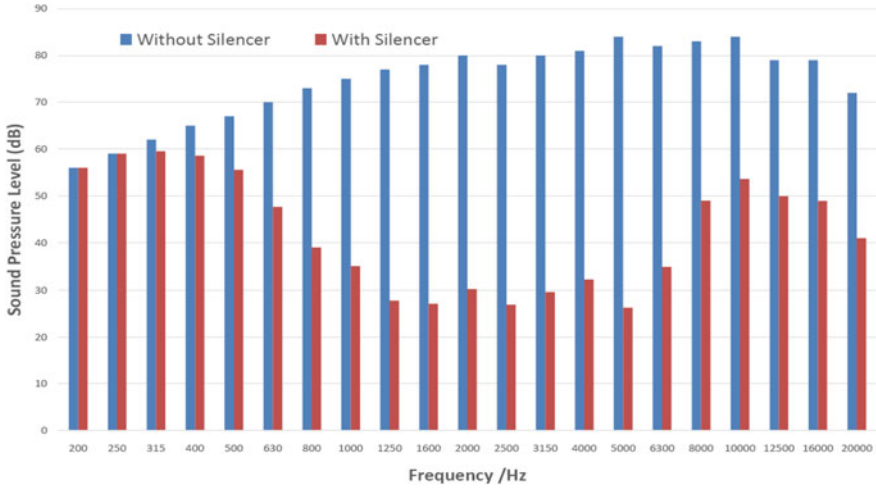


Fig. 10 Laboratory experiment in an anechoic chamber (at air outlet of air conditioning pipe)

Table 2 Acoustics experiment on airplane

	Test position 1	Test position 2	Test position 3	Test position 4	Test position 5
Airplane without silencer / dB	79.72	79.62	80.82	80.31	81.53
Airplane with silencer / dB	71.89	71.13	72.46	72.29	76.16
Noise reduction / dB	7.83	8.49	8.36	8.02	5.37

6 Conclusion and Future Expectations

This article analyzes commercial airplane air conditioning noise sources in passenger cabin and implements silencer acoustics experiment in an anechoic chamber and test on airplane. The conclusion of this article is illustrated below.

- (1) Airplane air conditioning noise in passenger cabin is from rotary part in Air Cooling pack, Ventilating fan, and airstream in Pipe. It is primarily in the frequency range of 550–8500 Hz.
- (2) Noise attenuation efficiency of the silencer is influenced by the expansion ratio of pipe and unit weight of acoustic damping materials in silencer. The larger the expansion ratio of the silencer is, the better the noise attenuation efficiency is. The bigger the unit weight of acoustic damping materials in silencer is, the better the noise attenuation efficiency is.



Fig. 11 Microphone site of acoustics experiment on airplane

- (3) Commercial Airplane passenger cabin noise will reduce more than 5 dB with an air conditioning silencer.

In the future, engineers are trying other measures to quiet the airplane air conditioning noise, including:

- (1) Active noise reduction technology will be used in the noise source part(Ventilating fan, Air Cooling pack, and so on).
- (2) Micropunch form will be designed inside of the noise source part.

References

1. SAE Acoustical Considerations for Airplane Environmental Control System Design (2005) AIR1826, 2005.08
2. SAE Air conditioning Systems For Subsonic Airplanes. ARP85 Revision E (2002) 06
3. Lu K, Zeng X, Yang Y (2013) Acoustics experiment. Machinery industry Press, 06
4. Du G, Zhu Z, Gong X (2011) Acoustics foundation. Nan Jing University Press, 09

Approaches and Numerical Simulation of Cryogenic Environment in Large Space Environment Simulator



Weiwei Shan, Yang Liu, and Ang Li

Abstract The nitrogen system is one of the important systems of space environment simulator. Its function is to provide liquid nitrogen with stable flow and temperature for the shroud during thermal test. To better determine and analyze the design parameters of nitrogen system, software FloMaster was employed to simulate the whole nitrogen system, and the model parameters of single equipment in nitrogen system were studied, so as to determine the key parameters affecting the operation of single-phase closed loop system. Finally, the simulation results were compared with the practical test results.

Keywords Liquid nitrogen · Nitrogen system · Single-phase closed loop · Numerical simulation

1 Introduction

Space environment simulator is the facility where thermal balance tests and thermal vacuum tests are conducted for spacecrafts and assemblies. As one of the most important systems, nitrogen system is designed to supply liquid nitrogen (LN2) for shrouds so that the temperatures of shrouds are always maintained at 100 K during the tests. In general, there are many different kinds of methods to provide LN2 for shrouds according to the temperature demand of shrouds. In the case of shrouds working at 100 K, many researches [1–3] in China believe that open loop working mode can be employed for medium and small size shrouds; as for large size shrouds, closed loop working mode can be employed, by which shrouds can be served enough LN2 circulating flow rate and achieve satisfied temperature uniformity.

On the other hand, the open loop working mode and gravity fluid feeding working mode are mostly chosen for nitrogen system in both small and large space environment simulators [4–12] in some Western countries. These two modes have the advantages of less equipment and less electricity consumption, but liquid nitrogen

W. Shan (✉) · Y. Liu · A. Li
Beijing Institute of Space Environment Engineering, Beijing, China
e-mail: sww_xjtu@163.com

© The Author(s), under exclusive license to Springer Nature Singapore Pte Ltd. 2023
Z. Jing and D. Strelets (eds.), *Proceedings of the International Conference on Aerospace System Science and Engineering 2021*, Lecture Notes in Electrical Engineering 849,
https://doi.org/10.1007/978-981-16-8154-7_50

653

consumption is considerable compared to closed loop working mode. This is because the residual liquid nitrogen is discharged after leaving the shrouds and cannot be recovered any more. Compared with the closed loop, the supplying pressure of open loop is determined by the pressure of the storage tank, the flow rate of liquid nitrogen in shrouds is less than the closed loop, and then temperature uniformity is affected to some extent.

In this paper, the working principle of single-phase closed loop was introduced. With the help of commercial software platform, the single-phase closed loop is numerical simulated, and the critical parameters of the equipment in the system are studied. The numerical study results can be used for the design of nitrogen system of large space environment simulators.

2 System Designing Principles

Under the single-phase closed loop working condition, liquid nitrogen is flowing through the shrouds, and the heat load is taken away by liquid nitrogen at the same time. The whole system can be achieved to simulate the flow and heat transfer process by establishing the mathematical model of each component.

The nitrogen system of the space environment simulator is a set of complicated system including equipment, valves, transducers, and pipelines. Aiming to keep the shrouds at 100 K and provide the stable cold background for the space environment simulator, it is designed to equip liquid nitrogen tanks, liquid nitrogen pumps, valves, the sub-cooler, transducers, safety accessories, and pipelines.

The liquid nitrogen pump is the most power output source of the whole system, which transports the single-phase sub-cooled liquid nitrogen with a certain flow rate and pressure to the shroud. The function of sub-cooler in the whole system is heat exchanger. The atmospheric liquid nitrogen in the inner cooler of sub-cooler is used to cool the high-temperature liquid nitrogen from the shrouds to ensure that the flow in the system is always single-phase liquid nitrogen. The principle of system flow is shown in Fig. 1.

3 System Mathematical Model

In a single-phase closed loop, assuming that single-phase LN2 is incompressible fluid, governing equations are derived as follows.

The mass conservation equation is

$$\frac{\partial}{\partial t} \int_{CV} \rho d\tau + \int_{CS} \rho V \cdot n dS = 0 \quad (1)$$

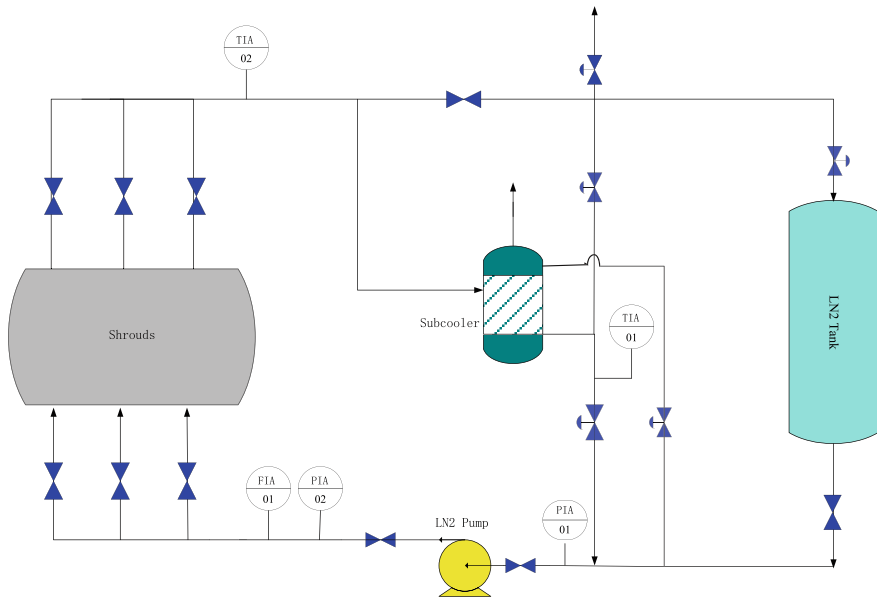


Fig. 1 Schematic of single-phase closed loop system

where assuming that fluid density and velocity at inlet or outlet of pump are homogeneous and velocity direction is perpendicular with outlet surface. Equation (1) can be simplified in Eq. (2) as

$$\dot{m} = \pm |\rho V A| \tag{2}$$

Momentum equation is shown in Eq. (3):

$$F = F_B + F_S = \frac{\partial}{\partial t} \int_{CV} \rho V d\tau + \int_{CS} \rho V V \cdot ndS \tag{3}$$

As for steady flow, it can be simplified as follows:

$$F = \int_{CS} \rho V V \cdot ndS \tag{4}$$

The energy equation is shown in Eq. (5):

$$\frac{dE}{dt} = \dot{Q} + \dot{W} \tag{5}$$

In terms of the flow state of single phase liquid nitrogen in the pipelines, it is considered to be incompressible steady flow. Therefore, Bernoulli equation can be simplified as follows:

$$\frac{\alpha_1 \bar{V}_1^2}{2g} + z_1 + \frac{p_1}{\rho g} = \frac{\alpha_2 \bar{V}_2^2}{2g} + z_2 + \frac{p_2}{\rho g} + h_{LT} \quad (6)$$

where h_{LT} is hydraulic loss, which means the loss of mechanical energy from Sects. 1 and 2.

When the fluid flows through the fluid machinery, such as a pump, because of the input and output of mechanical energy, it is necessary to add a term to consider the influence of shaft work on the total energy head. For the liquid nitrogen closed system, the input shaft work of the liquid nitrogen pump to the fluid is negative.

4 System Equipment

4.1 Liquid Nitrogen Pump

There are various components in FloMaster, which can be selected by users for system simulation. Although it is easy for users to build a model, only by inputting practical and reasonable parameters into the components, can the simulation calculation be accurate and effective. Take liquid nitrogen pump, for example, liquid nitrogen pump is a single-phase high-speed centrifugal pump driven by motor. Based on the flow characteristics of liquid nitrogen pump shown in Fig. 2, users can build a new Suter Curve of LN2 pump by using software FloMaster. Thus, when inputting parameters of LN2 pump, this new performance curve can be chosen and selected (Fig. 3).

4.2 Sub-cooler

Basically, the sub-cooler can be considered to be a heat exchanger, which is composed of a tank and a plate fin heat exchanger. The plate fin heat exchanger is installed inside the tank. The lower temperature LN2 stored in the tank exchanges heat with the higher temperature LN2 returned from the shrouds. Thus, the higher temperature LN2 is cooled down to the required temperature. The heat exchange capacity of the heat exchanger is 50 KW and the flow rate is 24 m³/h.

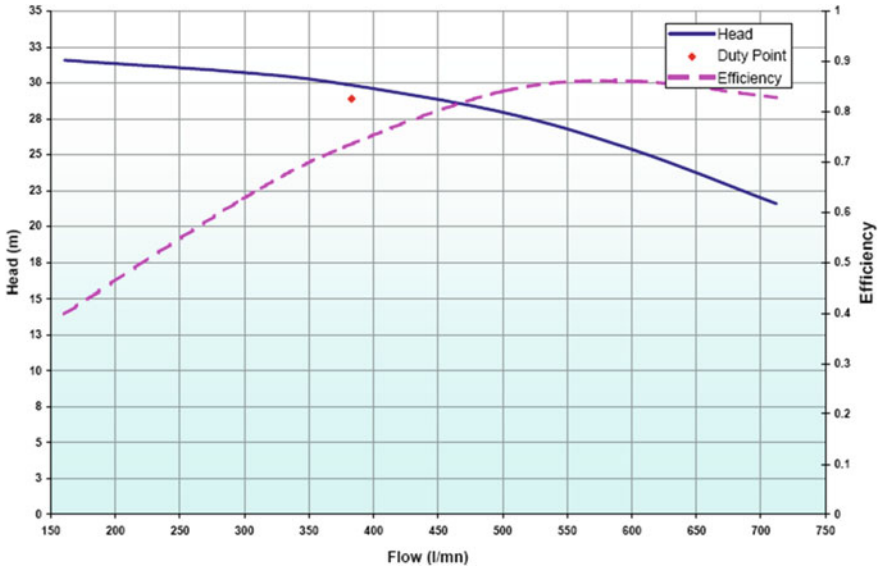


Fig. 2 Characteristic curve of LN2 pump

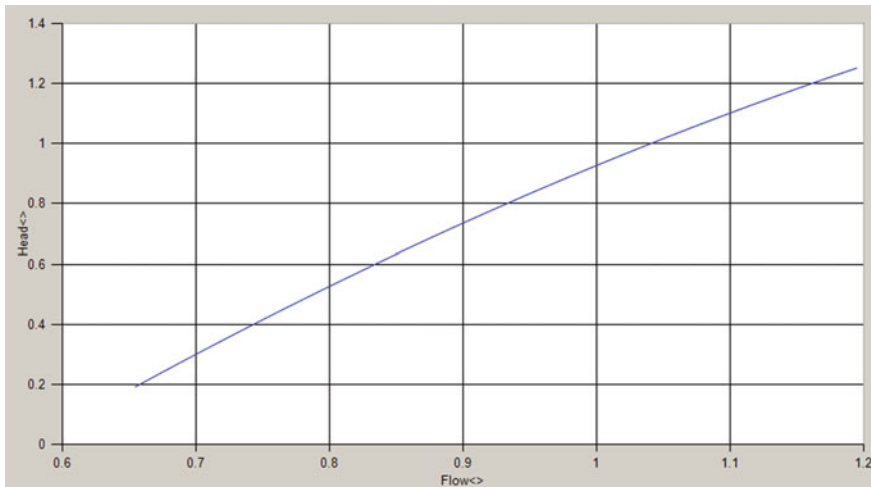


Fig. 3 Suter curve of LN2 pump

4.3 Shrouds

In the numerical simulation, the shroud can be considered as a combination of pressure component and heat exchanger. Its pressure loss is about 0.1 MPa and heat exchange area is 60 m².

4.4 LN2 Tank and Pipelines

LN2 tank offers the stable pressure condition for the closed loop and also liquid nitrogen whenever needed. Pipelines deliver liquid nitrogen or gaseous nitrogen for the shrouds, of which material is SS304 and size is DN50. To diminish the heat radiation between pipelines and the environment, PU heat insulation is the most common way to reduce the heat loss in the range of 5–10 W/m.

5 System Simulations

5.1 Numerical Modeling

Software FloMaster is used to model a medium-sized single-phase closed loop system and simulate the steady state heat transfer of incompressible fluid. The system model is shown in Fig. 4, and the flow and heat transfer results of the whole system are obtained subsequently.

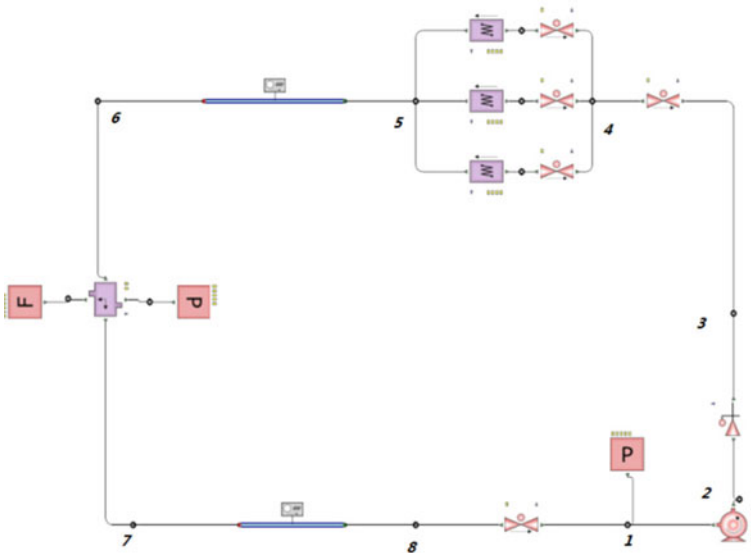


Fig. 4 Numerical model of single-phase loop system

5.2 Simulation Results and Analysis

Under the working condition, the pressure and temperature of each node and the flow rate of the nitrogen system are obtained based on the established simulation model. The pressure list of all nodes is shown in Table 1. It can be seen from the results that the driving power of the whole system comes from the liquid nitrogen pump, and the pressure and flow of its outlet pressure conform to the performance curve of the pump. The temperature list of all nodes is shown in Table 2. As seen in Table 2, the lowest temperature of the whole system appears at the outlet of the sub-cooler; the outlet temperature of the liquid nitrogen of the shroud is higher than the inlet temperature, the reason of which is that the heat load absorbed by the shroud causes the liquid nitrogen temperature to rise. The total flow of the system is 25 m³/h, and the distribution flow in the gate, cylinder, and end shroud is 9.58 m³/h, 6.44 m³/h, and 9.58 m³/h, respectively. The uneven flow distribution in the three parts of the shroud is caused by the difference of pressure loss among the cylinder shroud and the other two shrouds.

Table 1 Pressure list

No	Position of pressure sensor	Pressure value (bar)
1	Inlet pressure of LN2 pump	2.50
2	Outlet pressure of LN2 pump	5.22
3	Pressure after check valve	5.20
4	Inlet pressure of shrouds	5.20
5	Outlet pressure of shrouds	4.79
6	Inlet pressure of sub-cooler	3.84
7	Outlet pressure of sub-cooler	3.51
8	Pressure before inlet valve of LN2 pump	2.51

Table 2 Temperature list

No	Position of temp. sensor	Temperature (°C)
1	Inlet temp. of LN2 pump	-183.135
2	Outlet temp. of LN2 pump	-182.939
3	Temp. after check valve	-182.939
4	Inlet temp. of shrouds	-182.939
5	Outlet temp. of shrouds	-178.75
6	Inlet temp. of sub-cooler	-178.142
7	Outlet temp. of sub-cooler	-183.142
8	Temp. before inlet valve of LN2 pump	-183.135

5.3 Analysis and Comparison with Practical Test Results

In practice, the operating parameters of liquid nitrogen system are shown in the following: liquid nitrogen flow rate of the system is 24.2 m³/h, average temperature of the shroud is lower than—173 °C under no-load condition. Inlet pressure of liquid nitrogen pump: 0.23–0.3 MPa, outlet pressure: 0.47–0.55 MPa. Compared to the simulation results, it is found that the liquid nitrogen flow and system pressure of the whole system are basically consistent, which is in line with the actual operation state. However, in practical operation, the flow between each part of the shroud can be evenly distributed by adjusting the opening of the inlet valve.

6 Conclusions

The working principle of single-phase closed loop system is studied in this paper. One-dimensional numerical simulation of the whole system is carried out by using software FloMaster. The simulation results are in good agreement with the actual operation results, which verify the reliability and practicability of the model. The results show that the flow rate of liquid nitrogen supplied by liquid nitrogen pump can meet the maximum heat load of the shroud in thermal tests, and the temperature of the shroud is lower than 100 K. The research results can provide theoretical guidance for the design and optimization of single-phase closed loop system.

Acknowledgements This work is partially supported by Beijing Institute of Space Environment Engineering. The authors also gratefully acknowledge the helpful comments and suggestions of the reviewers, which have improved the presentation.

References

1. Botao L (2003) Research on LN2 thermal siphon system in large space environment simulator. *Cryog Conf* 2003:123–127
2. Dingzhong Z (2003) Method and application on LN2 thermal siphon system. *Cryog Conf* 2003:183–188
3. Botao L (2002) Nitrogen system design. *China Space Sci Technol* 6(3):61–64
4. Moon GW Shroud system design for a large thermal vacuum chamber. The 49th annual technical meeting and exposition of the institute of environmental science and technology. ESTECH2003
5. Senjiro IIDE (1997) 6M diameter space simulation chamber. In: *Proceedings of the third international symposium on environmental testing for space programmes*, pp 257–262
6. Watson RN (1992) A new thermal vacuum facility at the martin maritta waterton plant. In: *17th Space simulation conference*, pp 165–182
7. LeBlanc P (1992) P. Eng. refurbishment of a large thermal vacuum space simulation chamber. In: *23rd Space simulation conference*, pp 165–182

8. Miyamoto M, Saitoh M Development of a plasma chamber for solar panel testing. In: 24th Space simulation conference
9. Soler Chisabas RS Space thermal and vacuum environment simulation. Space Flight
10. Sathish Kumara S (2018) Thermal vacuum cycling test facility for the qualification of near sun missions solar panels. *Int J Pure Appl Math* 118(16), pp 1291–1308
11. Soler Chisabas RS (2016) Space simulation chambers state-of-the-art. In: 67th International astronomical congress
12. Pollara RA (2014) Improved thermal vacuum chamber temperature performance via gaseous nitrogen thermal conditioning units. In: Proceedings of the 2014 European conference on spacecraft structures, material and environmental testing

Development of Portable Friction Stir Welding Equipment for In-Space Manufacturing



Peng Li , Wei Zhong, Lijie Guo, Jialiang Zhang, Xiaosong Feng, Fei Li, and Weigang Zhao

Abstract Friction stir welding (FSW) technology is a solid-phase joining process with a non-melting pool in the connection area and insensitivity to gravity, so that it is suitable for construction of the structures in space. However, there is still a large gap between the process of FSW in space and on ground. Conventional on-ground FSW process needs large welding forces and power. Besides, the machines are also very bulky. By comparison, the FSW device in space bears the features of light weight, flexibility, portability, and quickly being in-site. To realize the application of space manufacture, the miniaturization and lowering of energy consumption of FSW equipment adapted to space environment are the key issues which need to be solved. Based on the principle of non-tool-tilt friction stir welding (NTFSW), the realization of lightweight FSW equipment has been put forward, and the mechanical mechanism and the structures of portable FSW device have been designed. The key components of the force-amplifying bionic mechanism—the force-amplifying linkage rod (FALR) modeled on masticating jaw bones and the frame modeled on upper jaws or heads—have been designed and optimized with abundant strength and

P. Li (✉)

School of Materials Science and Engineering, Shanghai Jiao Tong University, Shanghai 200240, China

e-mail: lipeng314159@126.com

P. Li · L. Guo · X. Feng · W. Zhao

Shanghai Aerospace Equipment Manufacturer Co Ltd., Shanghai, China

e-mail: guolijie149@163.com

W. Zhong

Aerospace System Engineering Shanghai, Shanghai, China

e-mail: zhongwei6685@163.com

J. Zhang

School of Mechanical Engineering, Donghua University, Shanghai, China

e-mail: zjili@dhu.edu.cn

F. Li

Shanghai Key Laboratory for High Temperature Materials and Precision Forming, Shanghai Jiao Tong University, Shanghai, China

e-mail: lifei74@sjtu.edu.cn

stiffness. The novel FSW device, with mass weight of 41.75 kg and less than 2.7Kw power, is newly patented, which effectively meets the limitations of design goals and ensures the friction stir additive manufacturing system.

Keywords Non-tool-tilt friction stir welding equipment · Biological modeling design · Design · analysis · and evaluation · Portable · Manufacture in space · Repair on-site

1 Introduction

Friction stir welding (**FSW**) technology, originated in the 1990s, from the welding institute **TWI** in Britain, is newly invented by Thomas et al. [1, 2]. As an advanced solid-phase joining technology, it provides a high-performance and high-quality-stability joining method for the processing of materials which are difficult to be welded by melting-phase joining technology. **FSW** has already been able to weld materials, such as aluminum alloys, magnesium alloys, titanium, high-strength steels, and composite materials. It plays an important connecting and assembling role in the manufacture of rockets, airplanes, high-speed trains, and automobiles [3–5]. In particular, in welding aluminum alloy in the field of aerospace, it overcomes the frequent defects existing in traditional material melting welding, such as crack, slag, and porosity, thus making it possible for manufacturing components of rockets and other high-performance aero-products [6–8]. **FSW** will surely be expanded to more product application fields in the future.

FSW was originally implemented by milling machines. Compared with the structure of the gantry machine version and the parallel machine version [9–11], the **FSW** equipment of milling machine version possesses the advantages of simple structures and easy production, so it is still the most popular general structure. Non-tool-tilt friction stir welding (**NTTFSW**) can be implemented directly by milling machines, but the stirring tools of zero-angle may result in substantial defects in welding seams, such as tunnel defects [12]. Therefore, the parameters of the stirring tool of **FSW**, such as the stirring needle thread, the stirring needle angle, and the stirring shoulder, are also needed to be matched with **NTTFSW**.

The conventional **FSW** equipment is often bulky and heavy, which occupies more jigs and fixtures during the welding process. It is difficult to be handheld flexibly and be used to manufacture the components of large-scale products at speed, thus dissatisfying the requirements of mobile scenarios, including the artificial handheld scenarios and the robot handheld ones. In the fields of maintenance and manufacture of large-scale products, it has become a key problem to provide a flexible and portable **FSW** device that can be quickly put into practice of repairing the space station in space [13], manufacturing devices by **FSW** underwater [14] and so on.

Besides in the field of welding, the friction stirring used for manufacturing materials additively, which can be named as the friction stirring additively manufacturing (**FSAM**), is just in its early stage, but it has gained a considerable value of rapidly

manufacturing the large-scale components. The **FSAM**, with the characteristic of solid-state processing, has become an important development direction of the friction stir technology and has tried to be commercialized—for instance, the Meld Manufacturing Corporation uses the patented **MELD** processing to add new materials by FSW to form parts layer by layer [15, 16].

In order to further expand the **FSW** technology to the fields of welding in special environments and to the additive manufacturing processes, more open, light, and modular **FSW** mechanism are needed; therefore, it is necessary to develop a convenient **FSW** device or equipment.

Based on **NTTFSW**, this study develops a Chinese patent [17] of novel portable **FSW** device, whose structure design, analysis, and finite element calculation are shown in this paper, which aims at advancing the research used in field of the manufacturing by **FSW** device in space. The rest of this paper is organized as follows: the basic principles of **FSW** are analyzed based on design points in Sects. 2 and 3, the design results of the novel portable **FSW** equipment are given, including the system design, functional realization, and the detailed capability of the mechanism; in Sect. 4, the key components of the novel portable **FSW** device are analyzed and optimized by finite element analysis method, in order to ensure both strength and stiffness of the axial force amplifier rod and the frame; Sect. 5 is the conclusion of the paper.

2 Basic Physical Processes and Key Points

2.1 Basic Principles of the Processes

The basic principle of **FSW** technology, depicted in Fig. 1, is to use a tool made by the material which is harder than that in the welded workpieces. Set with a stirring shoulder in larger diameter and a stirring needle in smaller diameter, this tool is a multi-diameter shaft, which keeps rotating friction materials to produce mechanical and thermal energy input, and which travels with the stirring tool rotating to form the force and geometry constraint along the surface of workpieces. By adjusting the rotating frequency and travel velocity of the tool, a heating controllable connection can be formed in the workpieces. Furthermore, with the rotating friction between the stirring tool and the workpieces materials, the technology makes a certain temperature distribution in the connection area in the workpieces. The plasticized flow of the materials of the connected workpieces is generated by the travel and relative rotation of the stirring tool. Finally, a solid-phase diffusion and a state of dispersion welding between the materials of the workpieces are generated.

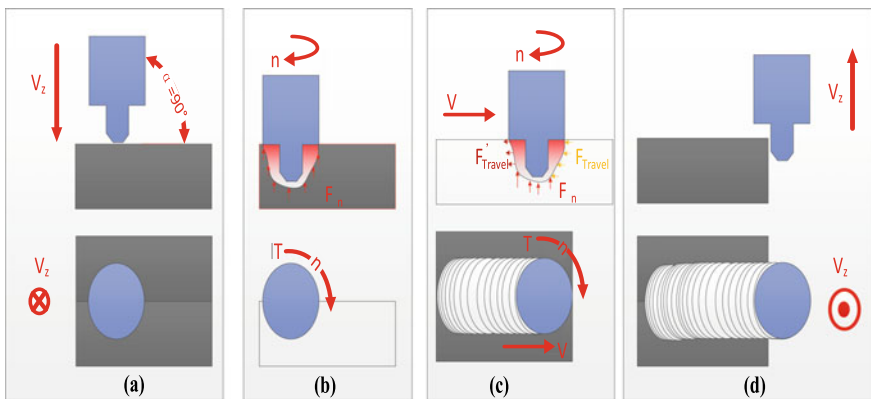
The key to achieving optimum of material microstructure and mechanical performance in the connection area of workpieces depends on the optimal match between the travel velocity V of the stirring tool and the relative rotating speed n of the stirring tool. It is a highly precise and quality-controlled method of solidified connection of

the materials in the workpieces, which is energy-saving, for the controllable temperature gradient generated in the condition of spatiotemporal field of “scanning” the area by the stirring tool. This high degree of precision and easy control of the energy feed are rooted in the energy input by the stirring tool, which has an approximate linear correlation with the welding rotation frequency $f = n/(2\pi)$ and the motion speed V , thus making it easy to grasp the energy feed. Additionally, the joining process involves the superposition of both regular rotational motion and linear motion, by which the motion of the parts’ geometry can also be precisely controlled.

In order to design the FSW equipment, it is a must to carefully analyze the force condition of the stirring tool in each stage of the friction stir process. The FSW process can generally be divided into four stages as depicted in Fig. 1, according to which more details are introduced and analyzed as follows:

(a and b) **From the stirring tool starting to locate the connection track line to the workpieces being touched by the tool, the first stage (a) lasts for an extremely short action time, which belongs to the instantaneous starting stage of the equipment. In the second stage (b), the friction-stirring tool is rotated into the workpieces; meanwhile, the friction begins to generate a thermal field, simultaneously generating the softening and the plasticizing flows of the materials.**

In the first and second stages, the force of the stirring tool depends on the resistance from the workpieces to the stirring tool, which is generated when the stirring tool is rotated and pressed into the workpieces. This resistance Includes: (i) a force of rotating tangential friction, that is, the resistance opposite to the direction of the rotation torque; (ii) an axial force of the stirring tool, that is, the resistance opposite



F_n : The axial force of the stirring tool, that is, the resistance opposite to the downward pressure, et al.; T : Torque of rotating tangential friction; V_z : Velocity close to/remove from the workpiece.; V : Travel velocity; F_{Travel} : Radial force of stirring tool caused by travel; F'_{Travel} : Additional radial force caused by rotation, et al.; $f=n/(2\pi)$; f , the rotating frequency, and n , the rotating speed.; $\theta=(90^\circ-\alpha)$: Angle of the stirring tool-tilt.

Fig. 1 The procedure of Non-tool-tilt friction stir welding

to the downward pressure; (iii) an additional radial force, which is caused by the force of rotor jitter at the moment of starting acceleration, the centrifugal effect of the materials with a certain scale of rotating flow generated by the stirring tool, and other unbalanced states.

- (iii) **In the third stage, the stirring tool continues rotating while scanning the connection track between the pair of workpieces, during which a joint is formed by the progressive contact between the stirring tool in the connection area and the gradual cover of the new solid-phase connection area.**

In the third stage, the force of the stirring tool is subject to the material resistance forces both of the progressive contact of the stirring tool in the area to be connected and of the gradual separation in the new solid-phase connection area. These material resistance forces include: (i) rotating friction torque; (ii) axial force of the stirring tool and (iii) radial force of the stirring tool. At this stage, the force of the stirring tool is generally stable. For example, the source of the force wave is mainly caused by the geometric fluctuations, derived from the structural splicing and trajectory, and the homogeneity of the material microstructure.

- (iv) **In the fourth stage, the joint is completed with the completion of the scanning of the connection track line and the withdrawal of the stirring tool from the workpiece materials.**

In the fourth stage, the withdrawal force of the stirring tool is mainly influenced by the spatial distribution of the materials and the force fluctuations in the local scale area.

2.2 Design Consideration on Practical Application

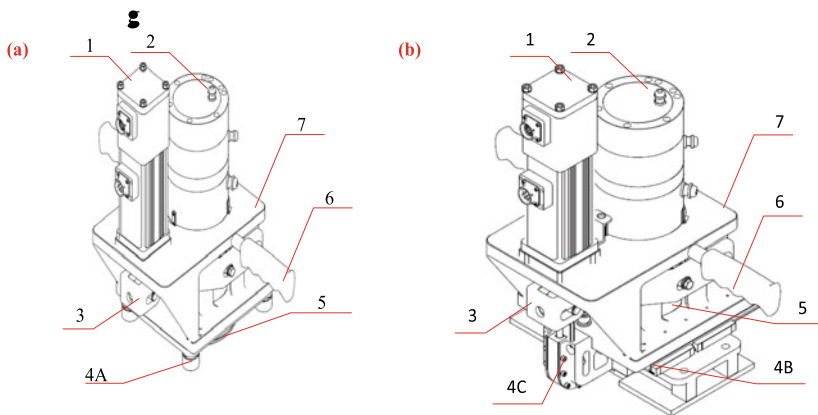
Based on the process analysis of the basic principles above, it is easy to deduce that the axial force, the radial force, and the torque of the stirring tool, fluctuating in a relatively high frequency, present a working condition with the combination of “Pressure-Bend-Twist”. During the FSW process, the task is to achieve a good welding joint mainly through the method of controlling the axial displacement or/and the press force size of the stirring tool. This research is designed based on the hand-held structure, a Chinese patent [17], whose major application scenario is on-site repair. The modular device of this patent can also be embedded to compound with other machine tools. Considering the need for on-site repair, the requirements and difficulties of designing the FSW equipment are listed as follows: (a) the weight of the equipment should be as light as possible, with the mass ≤ 60 kg and the power no higher than 2.7Kw, so that it has the capability to weld the aluminum alloys in the maximum thickness of 6 mm; (b) its configuration should be convenient for hand-holding or hand-guiding by designing a feeding force-amplifying mechanism within the scope of Ergonomics; (c) the forces applied to the reciprocity area of the tool and

the materials should satisfy the process, with a maximum axial force >15000 N and a maximum radial force >5000 N [18]; (d) the stiffness of the structure should be large enough to avoid FSW force fluctuations which will affect the handheld effect, and the strength and the stiffness of the key components should be optimized through analysis and calculation.

3 Results of the Design and Its Development

3.1 General Design of FSW Equipment

The novel FSW equipment, as shown in Fig. 2, is consisted of a traveling system, maintained by a handle, for resisting the radial force, a stirring tool feeding system for axially putting and withdrawing the stirring tool into and from the workpieces, a rotating system with the compact motorized electrical spindle for ensuring the friction thermal of weld under the assistance of the stirring tool, and an axial feeding force-amplifying system (AFFAS), driven by an electrical cylinder, for producing a greater axial force, thus helping implement the axial feeding and the axial driving to the spindle and the stirring tool.



1: Electrical cylinder with roller screws of axial feeding system; 2: Compact motorized electrical spindle of rotating system; 3: Force amplifying linkage rod (*The masticated jaw bone*); 4A: Rolling foot of chassis of travelling driver system; 4B: Rolling guide of chassis of travelling driver system; 4C: Commutator for axial feeding force to travelling force; 5: Mounting end of the stirring tool; 6: handle for manual pushing and pressing; 7: Frame (*The upper jaw and head*).

Fig. 2 Schematic diagram of overall design and walking scheme: **a** Large range of hand push (including manipulator), the left; **b** Small range of machine self-feeding, the right

3.1.1 Traveling Driver System

The traveling system of the novel **FSW** equipment realizes the “scanning” of the welding track of the friction-stirring welding. The equipment is supposed to have two modes—manual pushing and automatic walking [17], and two functions—NTTFSW and friction stir pull/plug welding. As shown in Fig. 2, the differences between the two modes lie in the chassis of the traveling system: Fig. 2a is the type of four rolling feet, while Fig. 2b is the type of two rolling guides. If the welded plate is thin, the offset of the forging force, which is equivalent to the axial force, and the torque can be achieved just by hand pressing. If the welded plate is thick, two rolling guide rails should be laid along the welded parts, and a commutator should be applied to offset the forward resistance, which is the radial force, and the torque.

3.1.2 Axial Feeding System and Driver

According to the principles of the process, an axial feeding system is needed for **FSW** to realize the pressing and withdrawal of the stirring tool. The key components of the **AFFAS** are the force-amplifying linkage rod (**FALR**), an important transmitting and moving part, and the frame, the foundation of fixation and mounting. Considering that the handheld **FSW** equipment in this study has a high structural effectiveness in terms of mechanism function and structure safety, the design is carried out by using the force-amplifying linkage system, which is enlightened by the biological mechanism of animal mouths.

In order to achieve light weight and large application force, an electrical cylinder with roller screws is adopted to drive the linear motion and to make power source of the precise axial feeding system [19]. The servo electric cylinder, **GSX30**, of Lim-Tec Corporation is adopted. It is 4.3 kg in weight, which can output the $F_e = 5620$ N external push/pull force, the $H = 75$ mm motion stroke, and the $V = 127$ mm/s maximum speed. The linear accuracy of **GSX30** is 0.025 mm/300 mm. Considering that the motion stroke of the electric cylinder of this equipment is $H = 75$ mm and the error estimate of the screw bearing in the cylinder is calculated by accumulation, the stiffness of the electric cylinder is 0.00625 mm/75 mm.

3.1.3 Rotational Spindle Driver

A compact motorized electrical spindle [18], adopted in the rotating system, is also specially customized with a rated speed $n = 3500$ rpm, a maximum speed $n_{max} = 8000$ rpm, a maximum axial force $F_n > 15000$ N, and a maximum radial force $F_r > 5000$ N. The requirements of light weight, high speed, high torque, and large load can be achieved through customized design. For example, in order to realize weight reduction, the spindle shell is partially made by aluminum alloy and the core shaft is made of high-strength steel.

3.2 Implement Results of FSW Equipment

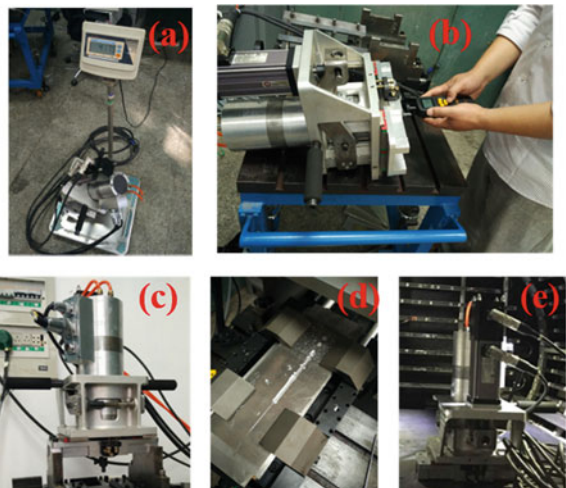
According to the design and the development introduced above, the implement results of the handheld FSW equipment are shown in Fig. 3. As in Fig. 3a, the weight of FSW equipment was reduced from 52 to 41.75 kg, that is, the weight loss rate reaches about 20%. Figure 3b and c demonstrate the routine testing. The conventional test of welding seam is shown in Fig. 3d, which proves that it can weld the Aluminum Alloy 5A06 with the maximum thickness of 6 mm. Figure 3e shows the temperature environmental test which emulates the working condition in space. The results have been verified to be consistent with design objectives; therefore, the equipment is expected to be used in future space manufacturing scenarios, such as the forming, joining, and repairing processes of the in-orbit structure of the space station.

4 Analysis and Evaluation of the Key Designs

4.1 Axial Feeding Force Amplifying Mechanism (AFFAM)

As mentioned before, the key parts of the new portable FSW equipment are the FALR and the frame. In this study, the design of the FALR is ideally similar to the structure of masticated jaw bones, which must maintain a certain strength and stiffness to ensure the precise control of the pressing distance on the stirring shoulder. The frame is similar to the structure of upper jaws and heads, which exerts the reaction forces, bears the large loads, and also holds and provides mounting interfaces and a platform for other parts.

Fig. 3 Verify portable FSW equipment: **a** The test of weight; **b** The test of working rotating speeds; **c** The welding test status on ground; **d** The welding seam; **e** Simulation space state test



In the process of biological evolution, it is significant for heads and jaws to adapt to the environment. In order to provide more evolving space for other organs, strong feeding and chewing system should be developed with light and well-distributed weight. The head and jaw structures of typical creatures are shown in Fig. 4 [20]. The head of *ceratosaurus nasicornis* who is a 6-m sized heavyweight meat-eater of the Jurassic [20] is shown on the left of Fig. 4. Large food intake is presumably achieved by a strong maxillary skull and a mandibular arch and driven by strong lip muscles.

Unlike heavyweight land animals, fish are unable to get enough reaction forces of chewing, tearing, and other activities from grasping the ground, which leads to the evolution of the mechanism with more complicated structures and the weight loss to a larger extent. The typical fish mouth mechanism of haddock *melanogrammus aeglefinus* is shown on the right of Fig. 4 [20]. Fish have evolved a more lightweight mechanism, for the reaction force of water is obviously weaker. In fact, due to the buoyancy effect of fish bladders and other parts, the activities of fish in deep water have similar characteristics of weightlessness, which can be basically equivalent to the mechanical condition of manufacture in space far away from the ground.

The bionically designed **AFFAM** is a hybrid mechanism. As shown in Fig. 5, the serial mechanism of **AFFAM** contains the degree of freedom (**H**) of the electric cylinder movement, and the degree of freedom (**b**) of rs_3 , which is related to the rolling and sliding motion. The parallel mechanism adopts two-stage parallel topology: the first stage consists of a degree of freedom of the rolling and sliding pairs (**rs1**, **rs2**) and a degree of freedom of the rotating pairs (**r1**, **r2**); the second stage is the degree of freedom (**h**) of the moving pairs (**s1**, **s2**, **s3**), which belong to the motorized electrical spindle. The adoption of multistage parallel topology is beneficial to the realization of the stiffness of the overall structure and to the alleviation of the influence of wave dynamics of the welding parts on the handheld effect.

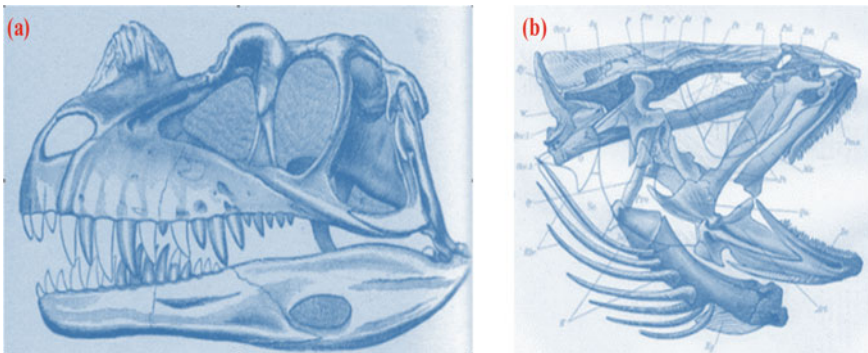


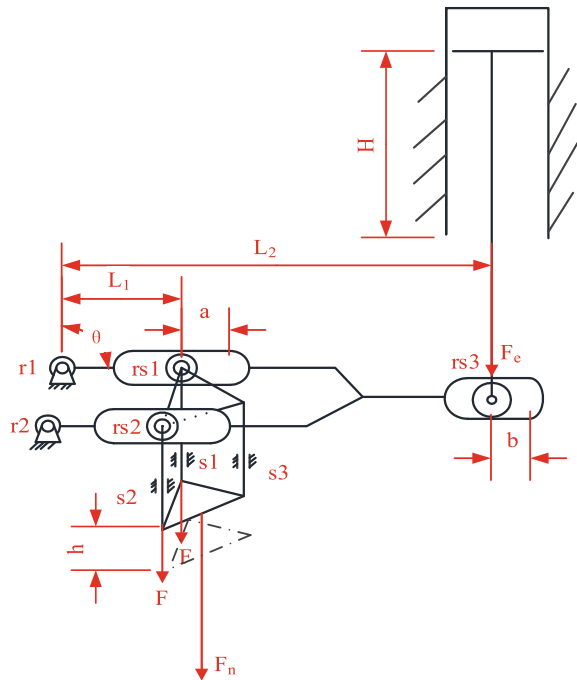
Fig. 4 the head and jaw structure: **a** *ceratosaurus nasicornis* (6-m-sized heavyweight meat-eater of the Jurassic), the left; **b** the haddock *melanogrammus aeglefinus*, the right; reprinted from Ref. [20], copyright 2007, with permission from Springer Science + Business Media, LLC

The output of the electric cylinder is the push/pull force F_e , whose maximum stroke is H . The axial force F_n of the motorized spindle output-end is applied to the stirring tool. The maximum stroke of the up and down movement of the motorized spindle is H . What's more, F is the force on the single ear seat of the motorized spindle, whose maximum linear stroke along the **FALR** is a , while the maximum linear stroke along the **FALR** of the output roller pair of the electric cylinder is b .

Referring to the lever principle, the mechanism above is designed to axially drive the motorized spindle up and down by applying force to the rolling and sliding pairs (**rs1**, **rs2**), which are constituted by the two-ear-blocks of the motorized spindle and the double-forks of the **FALR** modeled on the masticated jaw bones. The double-forks of the **FALR** are connected to the frame modeled after the upper jaw and head through the rotating pairs (**r1**, **r2**). The head and the output shaft of the electric cylinder constitute the rolling and sliding pair **rs3**. The motorized spindle is connected to the frame by three sliding pairs (**s1**, **s2**, **s3**), enabling the motorized spindle to move up and down and to transmit torque to the frame.

By analyzing the schematic diagram of the mechanism in Fig. 5, the transmission ratio of the **AFFAM** is $L2: L1$. Based on the maximum push/pull force $F_e = 5620$ N of the electric cylinder, the **AFFAM** with a transmission ratio of 3 is selected, that is, the ratio of $L2: L1 = 3$, so that the spindle is able to reach up to no less than 15000 N push/pull force, for the push/pull force of the spindle end is 3 times the quantity of that of the electric cylinder. When controlling the **AFFAM**, either the constant-force

Fig. 5 Schematic diagram of the mechanism of the axial feed scheme



mode of the electric cylinder push/pull or the constant-output-speed mode of the electric cylinder push/pull can be adopted. Due to the conservation of instantaneous power of the mechanism, the travel stroke, the speed, and the force of the motorized spindle are proportional to the transmission ratio of the **AFFAM**. After conversion, the force applied to the motorized spindle is proportional to $F_n = 3 * F_e = 16860 \text{ N}$, the motion stroke of the motorized spindle is inversely proportional to $h = H/3 = 25 \text{ mm}$, and the maximum speed of the motorized spindle is inversely proportional to $v = V/3 = 42.3 \text{ mm/s}$.

4.2 Strength and Stiffness Analysis of the **FALR**

4.2.1 Methodology and Design

According to the force analysis of **FSW** at each stage in Sect. 2.1, the **FALR** demonstrates a series of mechanical behaviors, and the axial stiffness of the end of the stirring tool is required to be no more than 0.5 mm/25 mm regarding to the process analysis. Additionally, considering the design that the axial force-amplifying ratio is 3, the axial stiffness of the output shaft of the electric cylinder is required to be less than 1.5 mm/75 mm. Finally, all key components become adequately lightweight and reasonable in structure after optimization.

The software is used in the design to establish a three-dimensional model of the **FALR** which is shown in Fig. 6a. The material used in the **FALR** is **40Cr**, whose mechanical properties are shown in Table 1.

The software **ANSYS 12.0.1** is used for finite element modeling of the **FALR**. In order to improve the optimizing efficiency of the design, tetrahedral mesh is used, in

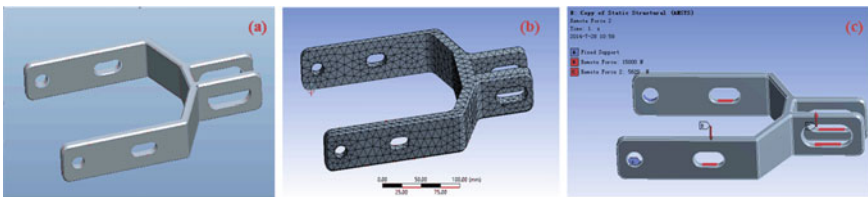


Fig. 6 Design and **FEA** modeling of the force-amplifying linkage rod (The masticated jaw bone): **a** The part model, the left; **b** The meshing, in the center; **c** Constraints and the working force conditions, the right

Table 1 Mechanical properties of alloy steel **40Cr**

Yield strength	Fracture strength	Modulus of elasticity	Poisson's ratio	Micro hardness
790 MPa	984 MPa	210 GPa	0.29	301 HV

which the number of nodes and cells are 7153 and 3730, respectively. The meshing generated by ANSYS is shown in Fig. 6b.

As shown in Fig. 6c, the forces and constraints of the FALR are established according to its process principles in Sect. 2.1, with reference to the force model of the mechanism in Fig. 5 that a fixed constraint is applied to the rotating pairs (r1, r2) on the left of the FALR in order to simplify the stress state. What's more, concentrated forces $F_n = 15000\text{ N}$ and $F_e = 5620\text{ N}$ are applied on the enveloped track planes, which, respectively, contact the pin holes of the two rolling and sliding pairs (rs1, rs2) in the middle of the FALR and the rolling and sliding pair rs3 at the right head of the FALR. Gravity and inertial forces are ignored.

4.2.2 Results and Analysis

On one hand, as shown in Fig. 7a, the cloud map of the stress distribution in the FALR is obtained by FEA solution. The maximum stress, located at the corner of the FALR, is about 255 MPa, which is suitable for use.

On the other hand, regardless of the motorized spindle deformation, the total deformation, 0.964 mm, including the deformation of the FALR, 0.958 mm, and of the motor cylinder itself, 0.006 mm, is converted to the spindle end stiffness of 0.321 mm/25 mm. The cloud map of the deformation distribution of the FALR in Fig. 7b proves that the maximum deformation of FALR, 0.958 mm, lies in the rolling and sliding pair rs3, on which the electric cylinder acts.

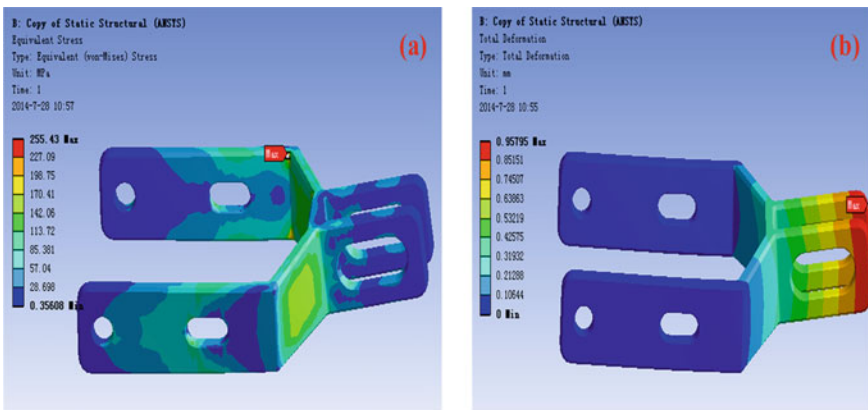


Fig. 7 Preliminary calculation of mechanical behavior of the force-amplifying linkage rod (The masticated jaw bone): a The maximum stress, the left; b The maximum deformation, the right

4.2.3 Effect Evaluation and Suggestions

Based on the statistics above, the maximum stress of the **FALR** is 255 MPa, and the stiffness of the end of the stirring tool is 0.321 mm/25 mm, which does not meet the requirements.

Therefore, in order to enhance the stiffness of the **FALR**, the right head is linked by a block of material; meanwhile, some other geometrical entities are removed appropriately according to the stress distribution to improve the stress path, as shown in Fig. 8a.

The results of the relatively new design of the **FALR** are shown in Fig. 8b and Fig. 8c. The deformation of the new **FALR** at the cashew-nut-shaped pin holes on the right side is less than 0.6 mm, the stiffness of the spindle end is less than 0.2 mm/25 mm, and the new maximum stress is 213 MPa, which are all suitable for use.

4.3 Strength and Stiffness Analysis of the Frame

4.3.1 Methodology and Design

According to the functions of **FSW**, the part model of frame modeled on the upper jaw and head is established, as shown in Fig. 9a. The material of the frame is the forged aluminum **LD10**, which is equal to **AA 2A14**, whose mechanical properties are shown in Table 2.

In order to improve the optimization efficiency, tetrahedral mesh is used in Fig. 9b, with 53,512 nodes and 30,254 cells. Figure 9c shows the load conditions and constraints of the frame. A fixed constraint is applied at the bottom plane, and

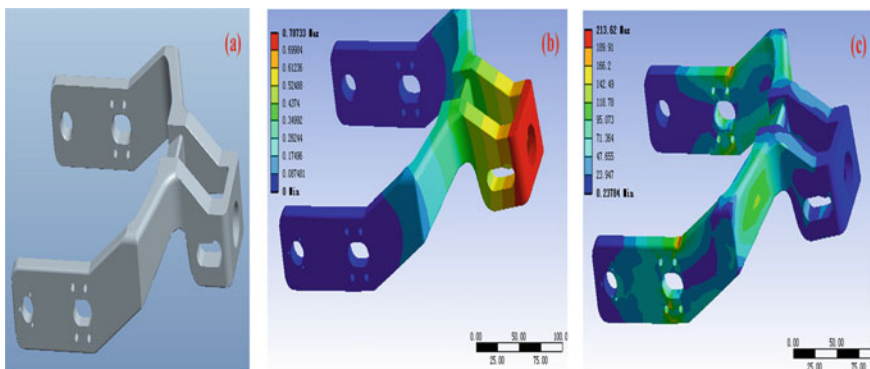


Fig. 8 Optimization and improvement results of the force-amplifying linkage rod (The masticated jaw bone): **a** The improved part model, the right; **b** The ultimate deformation, in the center; **c** Final stress analysis, the right

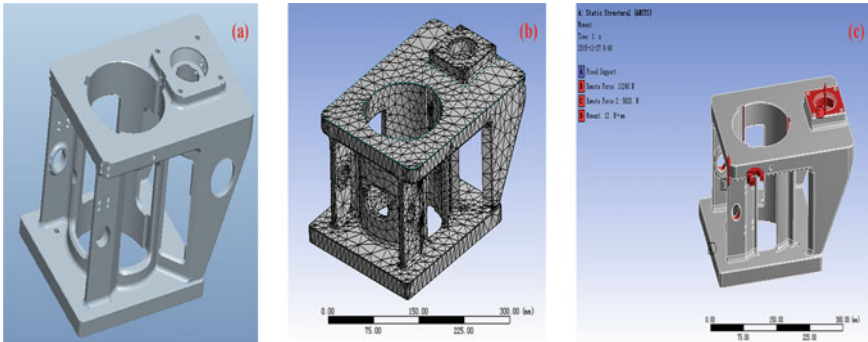


Fig. 9 Design and **FEA** modeling of the Frame (The upper jaw and head): **a** The part model, the left; **b** The meshing, in the center; **c** constraints and force conditions, the right

Table 2 Mechanical properties of forged aluminum **LD10 (2A14)**

Yield strength	Fracture strength	Modulus of elasticity	Poisson’s ratio	Micro hardness
327 MPa	451 MPa	73.1 GPa	0.33	142 HV

a concentrated force of 11240 N is exerted on the mounting hole of the bi-furcation of the **FALR**. A force $F_e = 5620$ N is applied to the mounting hole of the electric cylinder, and a 12Nm torque is applied to the sliding track mounting slot of the spindle. Gravity and inertial forces are ignored.

4.3.2 Results and Analysis

As shown in Fig. 10a, the cloud map of the stress distribution in the frame, with the maximum stress of 48 MPa, is obtained by **FEA** solution. It is shown in the cloud map of the deformation distribution of the frame in Fig. 10b that the maximum deformation, 0.036 mm, is located in the connecting hole of the electric cylinder.

4.3.3 Effect Evaluation and Suggestions

As mentioned above, the maximum strength, 48 MPa, and the maximum deformation, 0.036 mm, are both small enough to meet the demands. The aluminum alloy chosen for the part is adequately lightweight and reasonable in structure, which can be manufactured by five-axis numerical milling machines. Furthermore, the frame can also be designed by topological optimization and be manufactured by additive manufacturing machines, thus achieving a higher degree of lightweight, so that it has the potential to be used in improved versions.

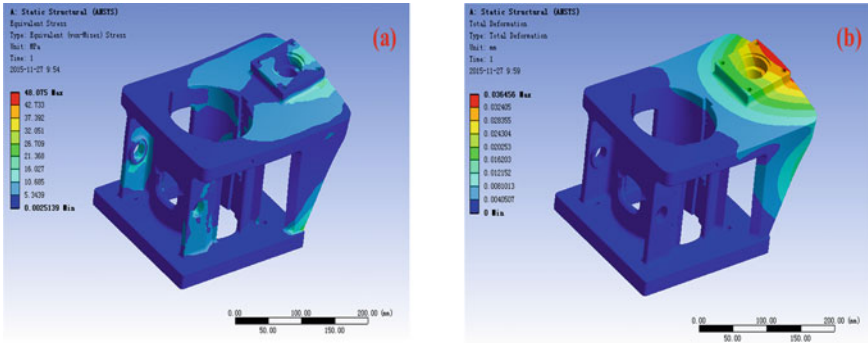


Fig. 10 The computational mechanical behavior of the frame (The upper jaw and head): **a** The maximum stress, the left; **b** The maximum deformation, the right

5 Conclusions

- (1) Based on the analysis of the critical principles of **FSW** and the force-amplifying mechanism inspired by the biological enlightenment of the mechanism of animal mouths, the paper gives a design of a portable **FSW** equipment, which applies the electric cylinder and the motorized spindle, for welding in space in space stations, and analyzes the functional capability of the system and the components in it.
- (2) Through the **FEA** solution, the **FALR** and the frame, modeled, respectively, on the masticated jaw bone and the upper jaw and head, are analyzed and optimized. The improvements are obvious that the weight of the **FSW** equipment is reduced from 52 to 41.75 kg, with the dewatering rate reaching about 20%; besides, it has the capability of welding at most 6-mm-thick aluminum alloys. In line with the research objectives, the **FSW** equipment has been well developed, tested, and validated for operation.
- (3) The **FSW** equipment in this paper provides a very flexible, open, and effective equipment foundation for testing the new technology of **FSW** in space, which can also be suitable for universities and other research facilities to develop freely in new application scenarios, such as in friction stir additive manufacturing, and thus is worth popularization.

Acknowledgements Other efforts about the study described in this paper have also been paid by the following personnel during the years from 2014 to 2015: ZHAO huihui; WEN shanshan; TIAN Hailin; LIU Xinbo; DONG fengbo; WU Rongzong. I would like to extend my heartfelt thanks to them.

This article was written with the help of YAN Xiuyi; ZHANG Jialiang; LI Fei. I would like to extend my heartfelt thanks to them.

The authors also gratefully acknowledge the helpful comments and suggestions of the reviewers, which have improved the presentation.

Contribution of each author **Peng LI:** Methodology, Investigation, Writing—Original draft preparation. **Wei ZHONG:** Validation, Application Background Research. **Lijie GUO:** Funding acquisition, Conceptualization, Supervision Visualization. **Jialiang ZHANG:** Conceptualization, Writing—Reviewing and Editing. **Xiaosong FENG:** Data curation, Resources, Funding acquisition. **Fei LI:** Writing—Reviewing and Editing. **Weigang ZHAO:** Validation and Test.

Term	Definition
Conceptualization	Ideas; formulation or evolution of overarching research goals and aims
Methodology	Development or design of methodology; creation of models
Software	Programming, software development; designing computer programs; implementation of the computer code and supporting algorithms; testing of existing code components
Validation	Verification, whether as a part of the activity or separate, of the overall replication/ reproducibility of results/experiments and other research outputs
Formal analysis	Application of statistical, mathematical, computational, or other formal techniques to analyze or synthesize study data
Investigation	Conducting a research and investigation process, specifically performing the experiments, or data/evidence collection
Resources	Provision of study materials, reagents, materials, patients, laboratory samples, animals, instrumentation, computing resources, or other analysis tools
Data Curation	Management activities to annotate (produce metadata), scrub data and maintain research data (including software code, where it is necessary for interpreting the data itself) for initial use and later reuse
Writing—Original Draft	Preparation, creation and/or presentation of the published work, specifically writing the initial draft (including substantive translation)
Writing—Review and Editing	Preparation, creation and/or presentation of the published work by those from the original research group, specifically critical review, commentary or revision—including pre- or postpublication stages
Visualization	Preparation, creation and/or presentation of the published work, specifically visualization/ data presentation
Supervision	Oversight and leadership responsibility for the research activity planning and execution, including mentorship external to the core team
Project administration	Management and coordination responsibility for the research activity planning and execution
Funding acquisition	Acquisition of the financial support for the project leading to this publication

Data Availability Statements The data that support the findings of this study are available from Shanghai Aerospace Equipment Manufacturer Co., Ltd (SAEM) but restrictions apply to the availability of these data, which were used under license for the current study, and so are not publicly available. Data are however available from the authors upon reasonable request and with permission of SAEM.

References

1. Thomas WM, Nicholas ED (1997) Friction stir welding for the transportation industries. *Mater Design* v18(Nos. 4/6):269–273
2. Thomas WM (1991) Friction stir butt welding. International Patent Application No PCT/GB92 Patent Application, No.9125978.8
3. Gibson BT, Lammlein DH, Prater TJ et al (2014) Friction stir welding: process, automation, and control. *J Manuf Process* v16(1):56–73
4. Mendes N, Neto P, Loureiro A et al (2016) Machines and control systems for friction stir welding: a review. *Mater Design* v90(15):256–265
5. Zeng G, Dong-feng C, Peng W et al (2017) Friction stir welding of packaging container made of SiC_p/Al composites with low volume fraction. *Bulle Chinese Ceramic Soc* v36(05): 1735–1739. <https://doi.org/10.16552/j.cnki.issn1001-1625.2017.05.047>
6. Vairis A, Papazafeiropoulos G, Tsainis A (2016) A comparison between friction stir welding, linear friction welding and rotary friction welding. *Adv Manuf* 4(4):296–304. <https://doi.org/10.1007/s40436-016-0163-4>
7. Boitsov A, Kuritsyn D, Siluyanova M et al (2018) Friction stir welding in the aerospace industry. *Russian Eng Res* v38(12):1029–1033
8. Shtrikman MM, Kornevich AP, Pinskiy AV et al (2018) Friction stir welding of ribbed panels of aircraft airframes. *Weld Int* v32(3):219–222. <https://doi.org/10.1080/09507116.2017.1388048>
9. Teng W, Weizhong G (2019) Modeling and simulation of welding capability for a hybrid friction stir welding equipment. *Mach Design Res* v35(01):175–178
10. Faquan Z, Yongyong L, Ye W et al (2015) Virtual machining function of CNC system for parallel mechanism friction stir welding machine. *Electr Weld Mach* v45(05):6–10
11. Minhong W, Weijia Z, Haitao L et al (2018) Design and motion control of the high precision heavy load friction stir welding robot. *Robot* v40(06):817–824+834. <https://doi.org/10.13973/j.cnki.robot.170560>
12. Ghazanfar B, Awang M, Khan SR et al (2013) Development of a new approach for incorporating tool tilting in friction stir welding. *Adv Mater Res* 701:378–381. <https://doi.org/10.4028/www.scientific.net/amr.701.378>
13. Longhurst WR, Cox CD, Gibson BT et al (2017) Development of friction stir welding technologies for in-space manufacturing. *Int J Adv Manuf Technol* 90:81–91
14. Farzad H, Alireza A, Mohammad A (2017) Effects of processing parameters on microstructure and mechanical behaviors of underwater friction stir welding of Al5083 alloy. *J Manuf Process* v25:77–84. <https://doi.org/10.1016/j.jmapro.2016.11.002>
15. Calvert JB (2015) Microstructure and mechanical properties of WE43 alloy produced via additive friction stir technology. Dissertation, Virginia Polytechnic Institute and State University
16. Hardwick N, Cox C, Schultz JP et al (2018) Meld solid-state joining of different features to cast parts. USA Patent NO.: US20180361501A1
17. Peng L, Chenglin Z, Weigang Z et al (2019) Hand-held du-al-function rotary friction welding device and welding method. Chinese Patent, Patent NO.: ZL201510803669.9
18. Peng L, Chenglin Z, Weigang Z et al (2019) Electric spindle device for rotary friction jointed equipment. Chinese Patent, Patent NO.: ZL201510155438.1
19. Zhang W, Li W, Zheng S et al (2019) Research on Motion Relationships and Transmission Efficiency of Planetary Roller Screw. The Proceedings of the 2018 Asia-Pacific International Symposium on Aero-space Technology (APISAT 2018). pp 2838–2848. https://doi.org/10.1007/978-981-13-3305-7_230
20. Brüßow H (2007) The evolution of eating systems. In: *The quest for food*. Springer, New York, pp 378–393. https://doi.org/10.1007/0-387-45461-6_4